Magnetism: Molecules to Materials III. Edited by J.S. Miller and M. Drillon

ISBNs: 3-527-30302-2 (Hardback); 3-527-60014-0 (Electronic)

Magnetism: Molecules to Materials III

Edited by J. S. Miller and M. Drillon

Magnetism: Molecules to Materials III. Edited by J.S. Miller and M. Drillon

ISBNs: 3-527-30302-2 (Hardback); 3-527-60014-0 (Electronic)

Further Titles of Interest

J. S. Miller and M. Drillon (Eds.)
Magnetism: Molecules to Materials
Models and Experiments
2001. XVI, 437 pages
Hardcover. ISBN: 3-527-29772-3

J. S. Miller and M. Drillon (Eds.)
Magnetism: Molecules to Materials II
Molecule-Based Materials
2001. XIV, 489 pages
Hardcover. ISBN: 3-527-30301-4

J. H. Fendler (Ed.)
Nanoparticles and Nanostructured Films
1998. XX, 468 pages
Hardcover. ISBN: 3-527-29443-0

P. Braunstein, L. A. Oro, and P. R. Raithby (Eds.)
Metal Clusters in Chemistry
1999. XLVIII, 1798 pages
ISBN: 3-527-29549-6

Magnetism: Molecules to Materials III. Edited by J.S. Miller and M. Drillon

ISBNs: 3-527-30302-2 (Hardback); 3-527-60014-0 (Electronic)

Magnetism: Molecules to Materials III

Nanosized Magnetic Materials

Edited by
Joel S. Miller and Marc Drillon

WILEY-VCH

Magnetism: Molecules to Materials III. Edited by J.S. Miller and M. Drillon

ISBNs: 3-527-30302-2 (Hardback); 3-527-60014-0 (Electronic)

Prof. Dr. Joel S. Miller
University of Utah
315 S. 1400 E. RM Dock
Salt Lake City
UT 84112-0850
USA

Prof. Dr. Marc Drillon
CNRS
Inst. de Physique et Chimie
des Matériaux de Strasbourg
23 Rue du Loess
67037 Strasbourg Cedex
France

Library of Congress Card No.: applied for

A catalogue record for this book is available from the British Library.

Die Deutsche Bibliothek - CIP Cataloguing-in-Publication-Data
A catalogue record for this publication is available from Die Deutsche Bibliothek

ISBN 3-527-30302-2

Composition: EDV-Beratung Frank Herweg, Leutershausen. Printing: betz-druck GmbH, Darmstadt. Bookbinding: Wilh. Osswald + Co. KG, Neustadt
Printed in the Federal Republic of Germany.

Magnetism: Molecules to Materials III. Edited by J.S. Miller and M. Drillon

ISBNs: 3-527-30302-2 (Hardback); 3-527-60014-0 (Electronic)

Preface

The development, characterization, and technological exploitation of new materials, particularly as components in 'smart' systems, are key challenges for chemistry and physics in the next millennium. New substances and composites including nanostructured materials are envisioned for innumerable areas including magnets for the communication and information sectors of our economy. Magnets are already an important component of the economy with worldwide sales of approximately $30 billion, twice those of semiconductors. Hence, research groups worldwide are targeting the preparation and study of new magnets especially in combination with other technologically important features, e. g., electrical and optical properties.

In the past few years our understanding of magnetic materials, thought to be mature, has enjoyed a renaissance as it has been expanded by contributions from many diverse areas of science and engineering. These include (*i*) the discovery of bulk ferro- and ferrimagnets based on organic/molecular components with critical temperature exceeding room temperature, (*ii*) the discovery that clusters in high, but not necessarily the highest, spin states because of a large magnetic anisotropy or zero field splitting have a significant relaxation barrier that traps magnetic flux enabling a single molecule/ion (cluster) to act as a magnet at low temperature; (*iii*) the discovery of materials with large negative magnetization; (*iv*) spin-crossover materials with large hysteretic effects above room temperature; (*v*) photomagnetic and (*vi*) electrochemical modulation of the magnetic behavior; (*vii*) the Haldane conjecture and its experimental realization; (*viii*) quantum tunneling of magnetization in high spin organic molecules; (*ix*) giant and colossal magnetoresistance effects observed for 3-D network solids; (*x*) the realization of nanosized materials, such as self-organized metal-based clusters, dots and wires; (*xi*) the development of metallic multilayers and (*xii*) spin electronics for the applications. This important contribution to magnetism and more importantly to science in general will lead us into the next millennium.

Documentation of the status of research, ever since William Gilbert's *de Magnete* in 1600, has provided the foundation for future discoveries to thrive. As one millennium ends and another beckons, the time is appropriate to pool our growing knowledge and assess many aspects of magnetism. This series, entitled *Magnetism: Molecules to Materials*, provides a forum for comprehensive yet critical reviews on many aspects of magnetism which are on the forefront of science today. This third volume reviews the current state of the art in the field of "nanosized materials", including both metallic and organometallic compounds, experimental as well as theoretical points of view.

Joel S. Miller
Salt Lake City, USA

Marc Drillon
Strasbourg, France

Magnetism: Molecules to Materials III. Edited by J.S. Miller and M. Drillon

ISBNs: 3-527-30302-2 (Hardback); 3-527-60014-0 (Electronic)

Contents

Magnetism: Molecules to Materials III. Edited by J.S. Miller and M. Drillon

ISBNs: 3-527-30302-2 (Hardback); 3-527-60014-0 (Electronic)

List of Contributors

Bernard Barbara
Laboratoire de Magnétisme
Louis Néel
CNRS-BP 166
Grenoble 38042
France

Eric Beaurepaire
Institut de Physique et
Chimie des Matériaux
UMR 7504 CNRS-ULP
23 rue du Loess
67037 Strasbourg
France

Jean-Yves Bigot
Institut de Physique et
Chimie des Matériaux
UMR 7504 CNRS-ULP
23 rue du Loess
67037 Strasbourg
France

Patrick Bruno
Max-Planck-Institut für
Mikrostrukturphysik
Weinberg 2
06120 Halle
Germany

Jean-Pierre Bucher
Institut de Physique et de Chimie des
Matériaux de Strasbourg (IPCMS)
UMR 7504 CNRS
Université Louis Pasteur
23 rue du Loess
F-67037 Strasbourg Cedex
France

Dante Gatteschi
Department of Chemistry
University of Florence
Florence
Italy

John Gregg
Clarendon Laboratory
Parks Road
Oxford OX1 3PU
UK

Luca Guidoni
Institut de Physique et
Chimie des Matériaux
UMR 7504 CNRS-ULP
23 rue du Loess
67037 Strasbourg
France

L. Jos de Jongh
Kamerlingh Onnes Laboratory
Leiden University
P. O. Box 9506
2300 RA
Leiden
The Netherlands

Susan M. Kauzlarich
Department of Chemistry
University of California
One Shields Ave
Davis
CA 95616
USA

Fernando Luis
Kamerlingh Onnes Laboratory
Leiden University
P. O. Box 9506
2300 RA
Leiden
The Netherlands
(On leave from the Instituto de Ciencia de Materials de Aragón
CSIC-University of Zaragoza
50009 Zaragoza
Spain)

Fabien L. Mettes
Kamerlingh Onnes Laboratory
Leiden University
P. O. Box 9506
2300 RA
Leiden
The Netherlands

Charles J. O'Connor
Advanced Materials Research Institute
University of New Orleans
New Orleans
LA 70148
USA

Pierre Panissod
Institut de Physique et Chimie des Matériaux de Strasbourg
23 rue du Loess
F-67037 Strasbourg
France

Amy C. Payne
Department of Chemistry
University of California
One Shields Ave
Davis
CA 95616
USA

Ivan Petej
Clarendon Laboratory
Parks Road
Oxford OX1 3PU
UK

Fabrice Scheurer
Institut de Physique et de Chimie des Matériaux de Strasbourg (IPCMS)
UMR 7504 CNRS
Université Louis Pasteur
23 rue du Loess
F-67037 Strasbourg Cedex
France

Roberta Sessoli
Department of Chemistry
University of Florence
Florence
Italy

Jinke Tang
Advanced Materials Research Institute
University of New Orleans
New Orleans
LA 70148
USA

Igor Tupitsyn
Laboratoire de Magnétisme
Louis Néel
CNRS-BP 166
Grenoble 38042
France
(On leave of absence from the Russian Research Center "Kurtchatov Institute"
Moscow 123182
Russia)

David J. Webb
Department of Physics
University of California
One Shields Ave
Davis
CA 95616
USA

Jian H. Zhang
Advanced Materials Research Institute
University of New Orleans
New Orleans
LA 70148
USA

Magnetism: Molecules to Materials III. Edited by J.S. Miller and M. Drillon

ISBNs: 3-527-30302-2 (Hardback); 3-527-60014-0 (Electronic)

1 Nanostructured Magnetic Materials

Charles J. O'Connor, Jinke Tang, and Jian H. Zhang

1.1 Introduction

This survey will critically discuss recent advances in the synthesis, properties and applications of magnetic materials with nanoscale dimensions. Consideration of the different preparative techniques will be followed by a discussion of novel properties and applications likely to fuel research in the coming decades.

1.2 Synthesis

In general, synthetic methods for the fabrication of magnetic materials with nanometer-scale dimensions can be classified into two categories – synthesis from molecular precursors, as with most chemical methods, and synthesis by processing of bulk precursors, for example mechanical attrition. Nanostructured materials can be effectively fabricated by inert gas condensation, pyrolysis, crystallization of amorphous precursors, molecular self-assembly, mechanical alloying, electrolytic plating, plasma deposition, and varieties of solution techniques. Many synthetic techniques developed in the other fields, for example ceramics, electronic materials, catalysts, etc., are applicable to the fabrication of nanostructured magnetic materials. Books are available covering a variety of synthetic techniques [1–5] and numerous review articles on the subject have been published, including one focusing on nanostructured magnetic materials [6]. By use of these techniques many types of nanostructured magnetic materials have been synthesized, including metallic iron, cobalt, nickel, and their alloys, soft and hard ferrites, soft and hard magnets, ferrofluids, and nanocomposites. Because multilayer magnetic materials have been extensively studied in recent years they are not included in this survey, which focuses on synthetic methods for the preparation of nanoparticles and nanocomposites.

Chemical methods, in particular, solution routes, are widely used for the fabrication of nanoparticles and nanocomposites. Some of the most frequently used are precipitation, reduction, pyrolysis, the aerogel–xerogel process, reverse micelle microemulsion, etc. This is partly because of the mild reaction conditions and the less expensive equipment needed. It has been observed that the fabrication technique used has a large influence on the magnetic properties of the nanoparticles obtained, even though they have the same grain size. For example, the reaction temperature

in the fabrication of spinel ferrites affects not only the size and morphology of the particles, but also the relative distribution of magnetic ions on tetrahedral and octahedral sites. As a result the magnetic properties might be significantly altered. Some chemical techniques, for example reverse micelle synthesis, enable substantial control over the size and size distribution of particles. Many old chemical methods have been continuously modified for more effective synthesis. This article surveys recent applications of the synthetic techniques used to prepare nanostructured magnetic materials, with emphasis on solution chemical reactions.

1.2.1 Inert Gas Condensation

One early method for producing nanostructured materials was inert gas condensation from a supersaturated vapor. During inert gas condensation the volatilized monomers are aggregated into clustered by collisions with cold inert gas atoms. This method can be used to prepare nanoparticles of elements, alloys, compounds, and composites. This technique has a few advantages – it can furnish high-purity nanoparticles and it can be used for direct production of films and coatings. Its disadvantage is that it is difficult to produce as large a variety of nanostructured materials as is possible by simpler chemical methods. To produce nanoparticles from the vapor it is necessary to achieve supersaturation. The methods used to produce a supersaturated vapor include thermal evaporation, sputtering, electron beam evaporation, or laser ablation. Some of the most recent synthetic studies using vaporization–condensation processes are introduced here.

Nanoparticles of Fe, Co, and Ni prepared by the inert gas condensation method have different amounts of surface oxidation. Much research has been published on the study of the magnetic interaction between metal core and surface oxide on samples prepared by the inert gas condensation technique [7, 8]. Typically, nanoparticles of iron were prepared by evaporating iron in a tungsten boat at 1500 °C into high purity helium gas at 1 Torr. Upon collision with the inert gas atoms the evaporated atoms lost kinetic energy and condensed as ultrafine powders that accumulated on a cold finger. Passivation was achieved by dosing with oxygen before opening the chamber to air. Detailed low-temperature magnetic study of nanoparticles of iron coated with iron oxide revealed the occurrence of an exchange anisotropy effect between the ferromagnetic core and the iron oxide in the spin-glass state [7]. Normally X-ray diffraction showed the shell oxides of as-synthesized samples to be amorphous. Subsequent annealing at temperatures up to 300 °C resulted in iron oxide thickness of 4–10 nm. Thus the core-shell structure (α-Fe/γ-Fe_2O_3, Fe_3O_4) formed could be used to study magnetic coupling [8].

It is difficult to produce a large quantity of ultrafine particles economically by traditional inert gas condensation techniques. Recently, a modified method called the activated hydrogen plasma–molten metal reaction method has been used for continuous preparation of ultrafine (20–30 nm) particles of Fe, Ni, and Fe–Ni alloys in a large scale [9]. In this method, the metals are evaporated by arc discharge into a circulating gas mixture of H_2 and Ar, which carried away the generated particles

into a collector. It was observed that ultrafine Fe–Ni particles are more resistant to oxidation than Fe and Ni particles. A nanocomposite of iron oxide and silver was fabricated by inert gas condensation [10]. The procedure involved:

(i) co-evaporation of silver and iron into helium gas;
(ii) in-situ oxidation of iron particles;
(iii) in-situ compacting of the particles; and
(iv) post-annealing in an inert or an oxidizing atmosphere.

Variation of the helium gas pressure between 0.1 and 10 Torr enabled control of the size of the nanoparticles. Ten-nanometer particles were obtained at 0.1 Torr. The magnetic species was identified as γ-Fe_2O_3 after the post-annealing treatment, whereas Fe and Fe_3O_4 coexist in the as-prepared loose powder and the as-compacted pellet. The nanocomposite was superparamagnetic with blocking temperatures >150 K.

The laser vaporization of metal targets has been combined with controlled condensation in a diffusion cloud chamber to produce varieties of metal oxide and metal carbide nanoparticles, depending on the reactant gas present in the chamber [11]. In laser vaporization a high-energy pulse laser with an intensity flux of approximately 10^6–10^7 W cm^{-2} is focused on a metal target. The resulting plasma causes highly efficient vaporization so that the density of the local atomic vapor can exceed 10^{18} atoms cm^{-3} (equivalent to 100 Torr pressure) in the microseconds after the laser pulse. Nanoparticles of iron oxides (γ-Fe_2O_3, Fe_3O_4) with a mean diameter of approximately 6 nm have been prepared by laser vaporization of iron in a helium atmosphere containing different concentrations of oxygen. All were superparamagnetic with blocking temperature ranging from 50 K to above room temperature. The significant advantage of laser vaporization is the possibility producing high-density metal vapor in an extremely short time (10^{-8} s), and generating directional high-speed metal vapor from a metal target for direct deposition of the particles. Ultrafine particles (20–30 nm) of Fe, Ni, and Fe–Ni alloys have recently been prepared on a large scale by use of a modified method called the activated hydrogen plasma–metal reaction method. In this method, the metals were evaporated by arc discharge into a circulating gas mixture of H_2 and Ar. It was observed that ultrafine Fe–Ni particles were more resistant to oxidation than Fe and Ni particles.

1.2.2 Water-in-oil Microemulsion Method

Nanoparticle synthesis by use of the water-in-oil microemulsion technique was first reported by Boutonnet et al., who prepared 3–5 nm noble metal particles in 1982 [12]. Water-in-oil microemulsions, also known as reverse micelles, have been used to synthesize a variety of nanostructured materials, for example nanoparticles of silver halides, superconductors, and magnetic oxide [13]. Reverse micelles are nanodroplets of water sustained in an organic phase by a surfactant that can hold and dissolve inorganic salts. The inorganic salts are then converted to an insoluble inorganic nanoparticle after chemical reaction and removal of water. The chemical

reactions that occur in the reverse micelles can be precipitation or reduction reactions, depending on the products desired.

In the precipitation reaction, two reverse micelles containing the constituent ions of a precipitate come in contact to each other upon mixing; this results in the formation of the precipitate. On the other hand metal cations in the aqueous phase of the reverse micelles can be reduced to metallic nanoparticles by adding a reducing agent such as hydrazine or sodium borohydride. The most frequently employed surfactants are sodium bis(2-ethylhexyl)sulfosuccinate (NaAOT), cetyltrimethylammonium bromide (CTAB), and didodecyldimethylammonium bromide (DDAB). The advantage of this method is that control of the physical and chemical properties of the reverse micelle and microemulsion systems enables great control over particle size with a narrow size distribution and shape.

Precipitation reactions with reverse micelles as templates are suitable for the synthesis of nanoparticles of magnetic oxides. Several groups have synthesized nanoparticles of hexagonal barium ferrite ($BaFe_{12}O_{19}$) by use of different microemulsion systems. Synthesis of barium ferrite involves two steps, preparation of nanoparticles of a precursor then calcination of the precursor to barium ferrite. Pillai et al. [13] employed a water–CTAB–*n*-butanol–*n*-octane system in which the aqueous cores (typically 5–25 nm in size) were used as constrained microreactors for the coprecipitation of precursor carbonates (typically 5–15 nm in size). The carbonates thus formed were separated, dried, and calcined at or above 950 °C to form nanoparticles of barium ferrite. Nanoparticles of barium ferrite with a narrow size distribution were also synthesized from an alcohol-in-oil microemulsion system [14], in which the metal ions were supplied in the form of the surfactants $Fe(AOT)_2$ and $Ba(AOT)_2$. A monodisperse, fine-gained Ba–Fe oxalate precursor was ensured by the reverse micelle structure, while the non-aqueous environment promoted stoichiometric coprecipitation. Pure barium ferrite particles were obtained by calcining the oxalate precursor at or above 950 °C.

A series of nanoparticles of spinel ferrites, γ-Fe_2O_3 and MFe_2O_4 (M = Fe, Co, Ni, and Mn), has been prepared by use of the reversed micelle method. Pileni et al. synthesized 2–5 nm cobalt ferrite particles by controlling the reactant concentrations in the water–CH_3NH_3OH–Co(II) dodecyl sulfate-Fe(II) dodecyl sulfate system [15, 16]. By use of this method it was possible to obtain the particles either suspended in the solvent to form a ferrofluid or as a dry powder. The particle size decreased as the total reactant concentration was reduced. The magnetic behavior of cobalt ferrite nanoparticles as the dry powder differed strongly from those as a ferrofluid, because of strong interaction between the particles. Magnetic measurement revealed that the reduced remanence, M_r/M_s, and the coercivity, H_c, increased with increasing annealing temperature. This was attributed to the increase in particle size and to the release of the adsorbed surfactant to the particle interface. O'Connor's group has synthesized nanoparticles of Fe_3O_4, $CoFe_2O_4$, and $MnFe_2O_4$ with an average size of 5 nm by use of metal aqueous solution–AOT–isooctane reverse micelle systems [17, 18]. In a typical preparation, NH_4OH–AOT solution was added into the reverse micelle system while stirring; Mn^{2+}, Fe^{2+}–AOT–isooctane systems, for example, were used to prepare $MnFe_2O_4$. The metal hydroxides were precipitated and oxidized to the ferrite within the nanosized micelles. Adding either H_2O_2 solution or excess aqueous

ammonia solution (NH_4OH) facilitated the oxidation. It was observed [18] that the processing conditions affected the distribution of manganese cation at the octahedral and tetrahedral sites. The presence of H_2O_2 or a surplus of NH_4OH resulted in an increase in the concentration of manganese, whereas the use of a stoichiometric amount of NH_4OH produced the stoichiometric manganese ferrite. In all Mn-ferrite nanoparticles, however, the manganese cation had a preference for octahedral site occupancy compared with bulk Mn ferrite.

In an attempt to improve the crystallinity of ferrites, John et al. developed a self-assembling organohydrogel containing the water–AOT–lecithin–isooctane reverse micelle system to synthesize 15–25 nm γ-Fe_2O_3 and $CoFe_2O_4$ particles [19]. Because of the slower diffusion of ion species through the gel medium during crystal growth, the nanoparticles were more crystalline, and thus their coercivity was higher than that of particles of the same size but prepared in regular reverse micelle systems.

Nanoparticles of metals and alloys have been synthesized by ion reduction in the reverse micelles. Pileni et al. synthesized nanoparticles of Cu, Co, and Fe–Cu alloy by reduction of the so-called functionalized surfactants $Fe(AOT)_2$, $Co(AOT)_2$, and $Cu(AOT)_2$ [20]. Cu particles (2–12 nm) were synthesized by use of the quaternary system $Cu(AOT)_2$–Na(AOT)–water–isooctane and hydrazine as a reducing agent. The size and shape of pure Cu particles were strongly correlated with the structure of the mesophase in the surfactant system. The size of the spherical Cu particles increased with increasing water-to-surfactant ratio, w (= $[H_2O]/[AOT]$). Further study has shown [21] that the shape of copper particles could be controlled by changing the $[H_2O]/[AOT]$ ratio during reduction with hydrazine of the $Cu(AOT)_2$ in water–isooctane solution. Spherical particles were formed when the $[H_2O]/[AOT]$ ratio was very low or high, because of the formation of reverse micelles, whereas cylindrical particles tended to be formed at some intermediate ratios, because of the formation of bi-continuous phases.

When the quaternary system $Co(AOT)_2$–Na(AOT)–water–isooctane with $NaBH_4$ as reducing agent was used to prepare Co nanoparticles the size decreased with increasing water content as a consequence of the formation of an oxide shell which prevented particle growth [20]. Nanoparticles of Fe–Cu alloys have been formed by a reaction between $Fe(AOT)_2$–Cu(AOT)–isooctane reverse micelle solution and $NaBH_4$ aqueous solution [20]. Particles of bcc α-Fe (10–100 nm) coated by an amorphous $Fe_{1-x}B_x$ alloy have been formed by a reaction between $Fe(AOT)_2$–isooctane reverse micelles and $NaBH_4$ aqueous solution [22].

In addition to the functionalized surfactants that act both as surfactants and as sources of metal in metal and alloy syntheses, other surfactants, for example didodecyldimethylammonium bromide (DDAB) and cetyltrimethylammonium bromide (CTAB), have also successfully been used to synthesize nanoparticles of metals such as cobalt. Lin et al. fabricated cobalt nanoparticles by $NaBH_4$ reduction of cobalt chloride in DDAB–toluene solution, and studied the effect of reaction temperature on particle size and morphology [23]. Low reaction temperatures yielded small spherical particles whereas high reaction temperatures resulted in clusters. In an attempt to control the size and size distribution of cobalt nanoparticles precisely, without formation of clusters, the germ-growth method in DDAB–toluene–$CoCl_2$ system

with $NaBH_4$ as reductant was developed. In this synthesis sequence uniform seed particles with a mean size of 3.8 nm in the form of a colloid were first synthesized at low temperature. Further Co^{2+} solution was slowly added into the reverse micelle system, followed by addition of $NaBH_4$ solution to enable the particles to grow [24]. O'Connor et al. used water–CTAB–1-butanol–octane reverse micelle solution and $NaBH_4$ as reductant to synthesize nanoparticles (15 nm) of Co, CoPt, and $CoPt_5$ [25].

Nanoparticles of iron and cobalt are very active and readily oxidized. To prevent oxidation they can be coated with inert metals to form the so-called core–shell structure. Synthesis of core-shell nanoparticles by use of the reverse micelle microemulsion method is conducted in a two-stage process. First, the core particles are synthesized in the reverse micelle medium by reduction of the metal ion with $NaBH_4$. This is followed by addition of an aqueous solution containing silver or gold ion to effect the coating. Iron particles (40–50 nm) coated with Ag have been prepared by use of this method [26] and O'Connor's group has synthesized Fe/Au core–shell nanoparticles with precisely controlled core size (8 nm) and coating thickness (2–3 nm) [27]. The magnetic core materials were synthesized in the reverse micelle medium by reduction of $FeSO_4$ with $NaBH_4$; this was followed by addition of an aqueous solution of $HAuCl_4$ to effect the gold coating of the nanoparticles. Magnetic measurements revealed superparamagnetic behavior with blocking temperature of 50 K, for uncoated 8-nm iron particles. The blocking temperatures were not affected by a subsequent gold coating 2–3 nm thick [27].

Synthesis of nanoparticles of antiferromagnets such as NH_4MnF_3, $KMnF_3$, and $NaMnF_3$ by the reverse micelle microemulsion method has attracted the interest of those wishing to study nano-antiferromagnetism. All these fluoromanganates are well known antiferromagnets with Neel temperatures of 80–88 K. Nanoparticles of NH_4MnF_3 were prepared by mixing the water–NH_4F–NH_4AOT–*n*-heptane microemulsion system with the water–$Mn(CH_3COO)_2$–NH_4AOT–*n*-heptane microemulsion system, then coagulation with acetone [28]. The mean crystallite sizes of NH_4MnF_3 particles were in the range 10–60 nm, depending on the reaction condition – i. e. water/oil ratio, salt concentration, temperature, and the period of time taken to mix the two microemulsions. O'Connor et al. has synthesized cubic shaped crystalline nanoparticles of $KMnF_3$ with average particle sizes of 13–35 nm and very narrow size distributions (confirmed by TEM). All samples were superparamagnetic below the ordering temperature, and the blocking temperature increased as the average size increased; hysteresis was observed below the blocking temperature [29].

Reverse micelle medium is also suitable for synthesis of polymer–ferrite nanocomposites. Recently, John et al. successfully developed a simple method for encapsulating nanometer-sized iron oxide crystals into micron-sized phenolic polymer particles to form superparamagnetic microspheres of ferrite–polymer composite [30, 31]. This method was a two-step process. In the first step, nanoparticles of ferrite were prepared using a normal reverse micelle system as described above. In the second step, a pre-synthesized polymer (poly(4-ethylphenol) was dissolved in a polar solvent (acetone), and re-precipitated using a large excess of the reverse micelle solution containing ferrite nanoparticles as a non-solvent solution. The polymer precipitated

with spherical morphology and during precipitation ferrite nanocrystals were incorporated, and uniformly distributed in the polymer matrix.

1.2.3 Organic/Polymeric Precursor Method

The organic/polymeric precursor approach to nanosize magnetic oxides is of great interest, because of the overall simplicity of the technique. Varieties of precursor methods have been developed mainly in the ceramic community. In general, these methods involve the preparation of a precursor using an organic acid in aqueous solution which contains all necessary cations in the desired product and combustible anions. After dehydration at mild temperatures the precursor becomes a dry gel that is amorphous in nature. The dry gel directly yields the required materials upon calcination in the presence of air or oxygen. Because the starting materials are homogeneously mixed on an atomic scale in the solution during precursor preparation, all the ions in the dry gel are homogeneously fixed in the polymeric matrix with very short diffusion paths to each other. The formation of a new phase occurs at a lower calcination temperature, in comparison with conventional solid-state reaction. The other advantage over other chemical methods such as co-precipitation is that it is not restricted by the stoichiometry of the product. Thus it is highly suitable for preparation of highly dispersed mixed oxides and oxide solid solutions. By use of these methods, ultrafine powders of a large number of spinel, garnet, and perovskite oxides have been synthesized.

The citrate precursor method, first introduced by Pechini [32], uses citric acid and ethylene glycol as complexing agents in the formation of precursor. Recently, Uekawa et al. have demonstrated that the citrate method with alkaline metal ion doping can be applied to the preparation of thin oxide film [33, 34]. Alkali metal ions were used to regulate the thermal decomposition process of the cation–citrate complex. Controlling the concentration of alkaline ion in the precursor and the reduction atmosphere enabled control of the nanostructure of the spinel iron oxide films [34]. With citric acid as the only complexing agent in the solution, a gelatinous precursor does not precipitate from the solution. The solution containing metal nitrate or acetate and citrate acid is, therefore, dehydrated in a rotary evaporator at temperatures below 100 °C until a dry and transparent gel is formed [35]. Because all the ions are in the gel, including anions such as nitrate ions or acetate ions, the calcination of the gel is a complex redox reaction. Study has showed that both the nature of the anions in the metal salts and the amount of citric acid affect the nanostructure of particle [36]. By using mixed Ni and Fe tartrates as precursor, Yang et al. synthesized 10-nm nickel ferrite particles [37]. In a detailed study of the thermal decomposition process by use of DTA/TG and XRD it was found that nickel ferrite was formed in the temperature range 280–420 °C, depending on solution pH in the preparation of the tartrate precursor from metal salts, tartaric acid, and NH_4OH. The higher the pH used for tartrate treatment the higher was the temperature at which the nickel ferrite was formed; nickel ferrite formed at the higher temperatures had fewer defects and was more thermally stable [37].

In a manner similar to the citrate precursor method, polyacrylic acid can also be used as a gelating agent to form an amorphous and gelatinous precursor, as described by Micheli [38]. The polyacrylate precursor method has been employed to synthesize nanocrystalline Cu ferrite, $Cu_{0.5}Fe_{2.5}O_4$; attempts have been made to obtain the material with all the copper in the monovalent state and occupying tetrahedral sites, to achieve high saturation magnetization [39]. It was observed that 10 nm particles of pure phase were formed from the polyacrylate precursor precipitated out of solutions at higher pH and with higher carboxylic group to cation ratio. The calcination temperature was below 400 °C. It was also observed that the saturation magnetization was significantly affected by the solution pH used to stabilize the precursor. Nanoparticles of LiZn ferrite, $Li_{0.3}Zn_{0.4}Fe_{2.3}O_4$ with a size of approximately 15 nm were also synthesized with polyacrylate as a precursor and after calcination at 450 °C [40]. All organic or polymeric precursor techniques are the same in principle in the sense that the starting materials are mixed in a solution, and the cations are disperse homogeneously in the precursor matrix. Another example is the use of a water-soluble polymer, poly(vinyl alcohol) (PVA), as matrix medium [41]. Two chemical routes were developed for synthesis of the amorphous precursors. The first route involved co-precipitation of the desired metal nitrates from their aqueous solution by use of triethylammonium carbonate solution in the presence of polyvinyl alcohol. Upon combustion in air, the precipitates generated nanoparticles of spinel ferrites (MFe_2O_4 where M = Ni, Co, or Zn), rare-earth orthoferrites ($RFeO_3$ where R = Sm, Nd, or Gd), and rare-earth garnets ($R_3Fe_3O_{12}$ where R = Sm, Nd, or Gd); the products were of high purity and chemical homogeneity. The other process involved complete evaporation of a mixture of optimum amounts of poly(vinyl alcohol) and the desired aqueous metal nitrate solutions, with and without addition of optimum amounts of urea. The mixture was evaporated to a pasty mass, then heated further to furnish the final ferrites and garnets [41].

1.2.4 Sonochemical Synthesis

Sonochemical synthesis of nanostructured materials, developed by Suslick and coworkers, involves the irradiation of a volatile organometallic compound (usually a metal carbonyl complex) in a non-aqueous and high-boiling solvent with high intensity ultrasound. Sonochemistry arises from acoustic cavitation – the formation, growth, and implosive collapse of bubbles within a liquid [42]. The collapsing bubbles generate localized hot spots in which the temperature and pressure can be as high as ca 5000 K and 1800 atm, respectively, and the cooling rate is greater than $10^{10}\,K\,s^{-1}$ [43, 44]. Under these extreme conditions, volatile organometallic compounds decompose inside collapsing bubbles to form solids consisting of agglomerates of nanometer clusters, which are often amorphous, because of rapid quenching. Suslick et al. have used this chemical approach to produce a variety of nanostructured catalysts including silica-supported Fe, Fe–Co alloy, and carbides [45].

Amorphous nanoclusters of Ni in the size range 10–15 nm have been deposited on submicrospheres of silica by sonication of a suspension containing $Ni(CO)_4$ and silica gel in decalin [46]. The as-deposited amorphous clusters were transformed to poly-

crystalline fcc Ni particles by heating in argon at 400 °C. As-deposited amorphous Ni had superparamagnetic behavior, whereas the polycrystalline Ni on silica was found to be ferromagnetic. Amorphous nanoclusters of Fe in the size range 5–10 nm deposited on silica microspheres have also prepared by use of the sonochemical method [47]. It was observed that the as-deposited amorphous iron clusters were very active, and reacted instantaneously with the active species on the silica surface to form amorphous oxyhydroxide precursors, which yielded nanocrystalline Fe_3O_4 on heating in argon. Nanoclusters of amorphous Fe could be only deposited on silica thermally treated in argon or under vacuum above 750 °C. The sonochemical approach to spinel ferrites involves preparation of the amorphous precursor powders, then thermal treatment at very low temperatures. For $CoFe_2O_4$, the precursor was prepared by sonochemical decomposition of $Fe(CO)_5$ and $Co(NO)(CO)_3$ in decalin at 273 K. Subsequent thermal treatment at 450 °C in air resulted in the formation of crystalline particles of $CoFe_2O_4$ (<5 nm) [48]. Amorphous nanoparticles of Fe_2O_3 (<25 nm) have also been synthesized by sonication of $Fe(CO)_5$ in decalin as solvent [49].

Sonochemical synthesis of nanoparticles of transition metal oxides in aqueous solutions has also been exploited. Ultrafine powders of Cr_2O_3 and Mn_2O_3 have been prepared at ambient temperature by the sonochemical reduction of ammonium dichromate and potassium permanganate, respectively, in aqueous solutions. The amorphous powders were converted into crystalline materials by thermal treatment at 320–600 °C [50].

1.2.5 Hydrothermal Synthesis

Hydrothermal synthesis of magnetic oxides offers mild reaction condition, production of high-quality particles, and elimination of the final high temperature calcination process common to many chemical routes. Hydrothermal synthesis is also realizable in a continuous flow-through powder synthesis process and on a large scale. Scientists at the Pacific Northwest National Laboratory (PNNL) have developed such a method, and called it the rapid thermal decomposition of precursors in solution (RTDS) method [51]. The engineering-scale unit operates in the temperature range 100–400 °C and the pressure range 4–8 kpsig; the solution residence time in the reactor is 5–30 s. By use of this method a large amount of nanoparticles (<20 nm) of iron-based oxides has been produced. So far most of the laboratory's efforts have been directed towards understanding the effects of reaction conditions such as the form of the starting materials, solution pH, temperature, pressure, and reaction time on particle size and morphology and magnetic properties.

Using a suspension of nanocrystalline goethite (3–5 nm) and barium hydroxide as a starting materials, Penn et al. synthesized nanocrystalline barium hexaferrite ($BaFe_{12}O_{19}$) below 50 nm by hydrothermal reaction at 250 °C in an autoclave [52]. The equilibrium morphology of crystals was truncated hexagonal. They studied the effect of precursor concentration, solution pH, and heating time on particle size and particle growth rate and suggested a topotactic transformation mechanism for barium hexaferrite formation from the nanocrystalline goethite. Remanent and satura-

tion magnetization, and hysteresis measurements, suggested the superparamagnetic threshold size for barium hexaferrite was approximately 7 nm; this was consistent with theoretical prediction [53]. In an attempt to reduce the reaction temperature, Dogan et al. studied the synthesis of 50 nm $BaTiO_3$ and $BaFe_{12}O_{19}$ particles under hydrothermal conditions below 100 °C, using barium hydroxide and titanium oxide, and barium hydroxide and ferric chloride, respectively, as starting materials [54]. While crystalline $BaTiO_3$ was formed relatively quickly (within a couple of days) formation of fully crystalline $BaFe_{12}O_{19}$ required longer (up to several weeks). Detailed analysis indicated that the $BaFe_{12}O_{19}$ particles started forming at low temperatures, and were fully converted from the amorphous phase to the crystalline phase over a long time period. It was found that a temperature exceeding 200 °C was necessary for efficient growth of nanocrystalline $BaFe_{12}O_{19}$.

Hydrothermal reaction has also been used to synthesize nanoparticles of soft ferrites such as NiZn ferrite and MnZn ferrite, commercially important magnetic and electronic materials. Early study [55] of the synthesis of MnZn ferrite indicated that the pH of the starting mixture had a decisive influence on the composition of the product, whereas the heating temperature and time determined the size of the particles. The effects of reaction conditions on the formation of mixed ferrites were more complex than the effects on simple spinel ferrites. Dias et al. have systematically investigated the effects of the starting materials, temperature, and reaction time on lattice parameters, particle size, density, and size and total volume of pores on the surface of the particles [56]. It was observed that the combination of metal sulfates and sodium hydroxide gave the best results under the same conditions of reaction temperature and time. Hydrothermal reaction of metal sulfates and sodium hydroxide solution at 110–190 °C generated nanocrystalline $Mn_{0.5}Zn_{0.5}Fe_2O_4$ (10–40 nm) [57] and $Ni_{0.5}Zn_{0.5}Fe_2O_4$ (52 ± 6 nm) [58]. These powders gave high-density and surface homogeneous ceramic components after high-temperature sintering. It was observed that small differences between hydrothermal powder morphology gave rise to sintered components with rather different microstructures [58]. With hydrothermal powders excellent magnetic properties could be achieved by sintering at considerably lower temperatures. For example, the initial permeability resulting from sintering under the same conditions was approximately 20% higher for the hydrothermal powder-based core of $Mn_{0.5}Zn_{0.5}Fe_2O_4$ than for the conventionally produced core, because the homogeneous microstructure was almost free from pores [59].

1.2.6 Pyrolysis

Laser pyrolysis is a technique used to synthesize ultrafine powders by heating a mixture of reactant vapor and inert gas with a laser. The rapid decomposition of reactant vapor as a result of heating produces a saturated vapor of the desired constituent atoms, which forms clusters upon collision with inert gas molecules. Varieties of nanoparticles of oxides, nitrides, and carbides have been prepared by use of this technique. Nanoparticles of α-Fe, Fe_3C, and Fe_7C_3 were produced by carbon dioxide laser pyrolysis of a $Fe(CO)_5$–C_2H_4 vapor mixture [60]. Nanoparticles (<35 nm) of

γ-Fe_4N and ε-Fe_3N were prepared by vapor-phase pyrolysis of $Fe(CO)_5$–NH_3 with a carbon dioxide laser in an Ar and N_2 atmosphere [61].

Aerosol spray pyrolysis is a technique in which aqueous metal salts are sprayed as a fine mist, dried, and then passed into a hot flow tube where pyrolysis converts the salts to the final products. In general, aerosol spray pyrolysis involves dissolution of precursor salts, nebulization of the solution, aerosol formation, drying, reaction in a reactor, and particle collection [62]. Nebulization is an important step in the control of particle size. A vibrating orifice, an ultrasonic nebulizer, or an electrospray nebulizer can be used in this step. Occasionally post-aerosol thermal treatment might be needed to achieve the homogeneous product desired.

Aerosol spray pyrolysis is an attractive means of producing high-purity oxide nanoparticles, for example barium ferrite ($BaFe_{12}O_{19}$), gadolinium garnet ($Gd_3Fe_5O_{12}$), manganese ferrite ($MnFe_2O_4$), and Fe_3O_4 [62], and is extensively used in industry to prepare metal oxides and ceramics. Several research groups have made efforts to prepare barium ferrite nanoparticles with crystalline size less than 50 nm and a narrow size distribution, which are required for high-density data storage applications in magnetic recording. Lee et al. sprayed a homogeneous aqueous solution with the targeted molar ratio of 0.313 BaO–0.215 B_2O_3–0.100 Na_2O-0.330 Fe_2O_3 on to the surface of a hot plate at 250 °C, and obtained pure and defect-free barium ferrite nanoparticles (50–70 nm) upon crystallization at temperatures below 600 °C [63]. The soluble precursor salts most often used are nitrates that decompose at relatively high temperatures (>600 °C). Choice of the proper precursors can, however, reduce the decomposition temperature. For example, nanoparticles of $BaFe_{12}O_{19}$ (10–20 nm) were prepared at the notably low temperature of 425 °C by use of a citrate precursor. The precursor decomposed at 425 °C to form a metastable spinel-like structure which underwent time- and temperature-dependent transformation to the final hexagonal spinel structure [64]. Use of ferric nitrate and barium nitrate as precursors with $ZnCl_2$ and $TiCl_4$ as additives in ultrasonic spray pyrolysis in which an ultrasonic nebulizer was employed enabled synthesis of spherical fine particles of pure and ZnTi-doped barium ferrites [65, 66]. Because of the short residence time, the precursors collected were amorphous and paramagnetic. Subsequent thermal treatment up to 1000 °C indicated that amorphous Ba–Fe–O was transformed directly into spherical barium ferrite particles whereas Ba–Fe–Zn–Ti–O was converted indirectly into doped barium ferrite particles through an intermediate α-Fe_2O_3 phase [66].

1.2.7 Arc Discharge Technique

In the short time since the discovery of spherical [67] and tubular fullerenes [68], much effort has been devoted to the study of particle confinement within their structures. Carbon-arc techniques are used to synthesize fullerenes, and the magnetic species can be incorporated concurrently with this preparation or into fullerene products on subsequent manipulation. In the former method the carbon rods that are burned contain a magnetically active component. The fullerene cage or tube produced will then contain the magnetic species. Guerrer-Piécourt et al. [69] and

others [70, 71] have reported the routine, direct preparation of magnetically important transition metals and/or their carbides inside both cages and nanotubes. This route has also been effective in the preparation of carbon-coated magnetic species, and researchers have made several finely divided materials including hard magnetic materials such as samarium–cobalt and neodymium–iron–boron alloys [72, 73]. The insertion of magnetic species into fullerenes subsequent to their synthesis has primarily been in the field of nanotubes. Methods have been developed that enable the removal of tube end-caps and placement of species inside [74]. Some metals in the molten state were placed directly in tubes by capillary action [75], but the most effective method for magnetic components was based on solution routes [74]. Nickel species, for example, have been inserted into tubes via aqueous solutions. Subsequent treatment under oxidizing conditions can produce metal oxides in the tubes, and in some instances on the tube surface also [76]. Similar chemistry under reducing conditions has resulted in tubes that contain ferromagnetic nickel particles [77]. Techniques have also been developed that enable the removal of the carbon structures after formation of the desired nanoparticle [76]. A modified tungsten arc technique, instead of conventional graphite–graphite arc techniques, has recently been used for the synthesis of carbon-encapsulated ferromagnetic nanoparticles of Ni, Co, and Fe [78]. In this technique a tungsten rod was used as a cathode and molten metal supported by a graphite crucible was used as the anode of the material to be encapsulated. Carbon-encapsulated Ni particles with an average size of approximately 18.2 nm were obtained by use of this arc discharge technique, which were highly environmentally and thermally stable [79].

1.2.8 Electrodeposition

Electrodeposition has mainly been used to prepare nano-processed soft magnetic materials such as pure iron, nickel, and cobalt, and binary nickel–iron and ternary nickel–iron–chromium alloys [80]. Nanoprocessing can be considered a distinct form of grain boundary engineering by means of which property enhancements are achieved by deliberately increasing the volume fraction of grain boundaries and triple junctions. The bulk materials or thin films nanoprocessed by electrodeposition have a grain size on the nanometer scale; they are also called nanocrystalline materials [81]. Nano-processing by electrodeposition has improved the overall performance characteristics of the soft magnetic materials used in recording heads [82]. Permalloy containing 15–25% (w/w) Fe and 0.05% (w/w) Cr was nano-processed by electrodeposition, using a metal chloride solution at 23 °C and 0.05 A cm^{-2}, to produce electrodeposits with a grain size of 7–16 nm and enhance properties such as coercivity, electric resistivity, hardness, and corrosion behavior for recording-head applications [83].

Recently, a new technique called pulsed electrodeposition has been developed for the production of metal nanoparticles. This technique is based on the use of a pulsed electrical current and a pulsed pressure caused by an ultrasound generator, their irradiation periods being out-of-phase. The combination of the pulsed current and vigorous electrolyte stirring enables the use of a higher current density. As a

result higher nucleation rates and smaller nucleus sizes can be achieved. Use of this technique has produced particles of Fe, Co, Ni, and their binary and ternary alloys with a mean size of 100 nm [84].

1.2.9 Mechanical Alloying

Mechanical attrition or mechanical alloying is a versatile approach to the production of nanostructured materials in large quantities. Since the first application of mechanical alloying by Benjamin [85] for the synthesis of oxide dispersion strengthened materials, this technique has been used to produce a broad range of alloys, intermetallic compounds, supersaturated solid solutions, and composites in the amorphous and nanocrystalline state. By use of high-energy ball milling the grain size of pure metal, and intermetallic compounds can be reduced to the nanometer scale. The high-energy ball milling technique is also suitable for synthesis of magnetic oxide and nanocomposite powders by solid-state reactions at ambient temperature – called mechanochemical synthesis. These solid-state reactions for bulk phases normally occur at very high temperatures.

Since the discovery of giant magnetoresistance (GMR) in granular structures in which metallic ferromagnetic nanoparticles are dispersed in a non-magnetic matrix, several investigators have prepared nanostructured Cu–Fe [86] and Cu–Co alloys [87, 88], by mechanical alloying, for study of magnetotransport properties. The alloy $Cu_{85}Fe_{15}$ was prepared by grinding fine powders of copper and iron in a high-energy ball mill. It was found that its magnetoresistance reached 5.5% at 4.5 K in a field of 5 Tesla; this was increased to 7.6% upon annealing at 300 °C for 20 min [86]. Nanostructured $Cu_{80}Co_{20}$ was prepared by repeated forging. The correlation between Co-substitution into the Cu-lattice and reduction of Co magnetization was studied using XRD and VMS [87]. It was shown by the recovery of Co magnetization that Co nanoparticles were precipitated in the Cu matrix as a result of annealing. The maximum magnetoresistance ratio under 1.0 MA m^{-1} at room temperature was 4.9% for $Cu_{80}Co_{20}$ with a mean Co particle size of 6 nm [88]. Study of the thermal stability of the nanocrystalline materials prepared by ball milling is of interest, because greater thermal stability of the nanocrystalline materials would be beneficial during subsequent thermal–mechanical consolidation or sintering in the fabrication of dense nanocrystalline solids. Jiang et al. investigated the thermal stability of the Fe–Al (Al <10% w/w) nanocrystalline alloys by ball milling [89] and observed that addition of 10% Al to Fe significantly enhanced the thermal stability of nanocrystalline Fe–Al alloys annealed at temperatures between 600 °C and 1000 °C, although addition of 4–10% Al had little effect on the thermal stability. Besides preparation of amorphous or nanocrystalline alloys from elemental components, ball milling has also used to synthesize nanocomposites composed of metal nanoparticles embedded in a non-metallic medium such as silica or alumina via displacement reactions. One recent example was synthesis of iron–silica and nickel–silica nanocomposites by exchange reactions between Fe_2O_3 and Si, and NiO and Si, respectively [90].

Great efforts have been made to apply the mechanical alloying technique to the preparation of high-performance nanostructured permanent magnets from rare

earth–transition metal compounds. Two systems that have been most studied are $Nd_2Fe_{14}B$ and $Sm_2Fe_{17-x}(C,N)_x$. The nanocrystalline structure developed by mechanical alloying and subsequent thermal treatment resulted in high coercivity and isotropic behavior associated with random grain alignment. The nanocrystalline powders of $Sm_2Fe_{15}Ga_2C_2$ prepared by ball milling of elemental powders had an average grain size of 5–10 nm in the as-milled state and 30–50 nm after annealing [91]. The hot compacted magnets made from ball milled powders had higher coercivity values up to 1.5 T and a nearly full density of 7.6 g cm^{-3}. Of these nanocrystalline magnets, a new class of magnets called "exchange spring magnets" has attracted considerable research interest. They are nanocomposites consisting of exchange-coupled hard and soft magnetic phases on the nanometer scale. The hard magnetic phases are rare earth transition metal materials such as $Nd_2Fe_{14}B$, and Sm_2Fe_{17} and their carbide and nitride. The soft magnetic phases are α-Fe, or α-(Fe, Co). Such exchange coupling across interface of grains helps give these magnets a high coercive force and enhanced remanence. Modeling studies and experimental work have shown that a crystallite size below 20 nm is generally necessary for effective coupling. A recent development in this respect was a review by McCormick et al. [92]. As expected, the application of mechanical alloying techniques to the synthesis of permanent magnet nanocomposites was very versatile. For example, mechanical alloying of Sm, Co, and Fe powders gave a mixture of amorphous Sm–Co–Fe and nanocrystalline bcc Fe–Co phase of composition $Sm_{10}Co_{49.5}Fe_{40}$. Thermal treatment of the mixture resulted in the formation of a metastable phase, which was transformed into a nanocrystalline phase $Sm_2(CoFe)_{17}$–Co–Fe at temperatures >650 °C [93]. The nanocomposites formed had single-phase magnetic hysteresis behavior and significantly enhanced remanence. The nanocomposite $Nd_2Fe_{14}B$–α-Fe obtained by mechanically alloying a mixture of $Nd_2Fe_{14}B$ and iron powder had enhanced remanence [94, 95].

Nanocrystalline spinel ferrites have been prepared at ambient temperature by high-energy ball milling from varieties of precursors. Vallet-Regi et al. prepared the nanocrystalline Zn ferrite, Mn ferrite, and ZnMn ferrite by mechanical milling of different precursors: (i) oxides and carbonates, (ii) ceramic products, and (iii) hydroxides and oxides [96]. It was observed that the precursors affected the magnetic properties of the products. The milling process led to distortion of the anion sublattice and redistribution of the cation between tetrahedral and octahedral sites. The chemical homogeneity of nanocrystalline ZnMn mixed ferrites (10–13 nm) obtained by high-energy ball milling of different precursors has been studied in detail [97]. The MnZn ferrite prepared from oxides and carbonates was a metastable structure and was highly inhomogeneous, because of the deficient dissolution of the larger cations such as Mn^{2+} into the structure. Use of hydroxides and acidic oxides as precursors reduced this inhomogeneity, because an acid–base reaction assisted the dissolution of Mn^{2+}. Mechanically induced structural disorder was also studied in the nanocrystalline Zn ferrite obtained by ball milling of the Fe_2O_3–ZnO mixture in a planetary mill [98]. The metastable structure was characterized by substantial displacement of Fe^{3+} cations into tetrahedral sites and Zn^{2+} cations into octahedral sites, and by deformation of the octahedral geometry. Crystallization of the mechanically synthesized Zn ferrite occurred at temperatures significantly lower than those synthesized by the conventional high-temperature method. Study of structural and

magnetic evolution in Cu ferrite ($CuFe_2O_4$) during long-term ball milling has established three sequential processes [99]: (i) the formation of partially inverted Cu ferrite nanoparticles with a non-collinear spin structure, (ii) decomposition of the Cu ferrite into α-Fe and other related phases, and (iii) reduction of α-Fe to Fe_3O_4.

1.2.10 Matrix-mediated Synthesis

By matrix-mediated or confined synthesis it is meant that a rigid structure is provided to act as a host or a matrix for the confined growth of the nanoscale magnetic particles. Several such host materials have been explored, including those based on organic resins, polymers, zeolite, and mesoporous solids. The host or matrix not only provides spatially localized sites for nucleation but also imposes an upper limit on the size of the nanoparticles. As a result, this method will produce nanoparticles with uniform dimensions.

Ion-exchange resins have rigid pore structures and are a suitable host material for synthesis of nanoparticles. Ziolo et al. [100] have synthesized nanocrystalline γ-Fe_2O_3-polymer composites using an ion exchange resin as the host structure. The resin was sulfonated polystyrene cross-linked with divinylbenzene to form a three-dimensional, porous polymer network. During the synthesis the resin was exchanged with $FeCl_2$ or $FeCl_3$ solution then treated chemically and heated to form the γ-Fe_2O_3–polymer nanocomposite. The nanocomposite had superparamagnetic behavior and appreciable optical transparency in the visible region. A superparamagnetic form of goethite, α-[FeO(OH)], has been prepared within macroporous poly(divinylbenzene) microspheres of 50–200 nm pore size by a chemical process [101]. The synthesis involved sulfonation of the microspheres, treatment with ferrous chloride solution, and oxidation with hydrogen at pH 14 and 70 °C. It was observed that there were two forms of goethite within the polymer – 25 nm diameter disks and 25 × 80 nm needles. Cohen et al. synthesized optically transparent block copolymer films of $[NORCOOH]_{30}[MTD]_{300}$ (NORCOOH = 2-norbornene dicarboxylic acid; MTD = methyltetracyclododecene) containing superparamagnetic γ-Fe_2O_3 nanoparticles by static casting [102]. The nanoparticles (approx. 5 nm) of γ-Fe_2O_3 were located within interconnected cylindrical microdomains and uniformly distributed throughout the film. Magnetic gels are of considerable interest for potential applications in medical diagnostic technologies. Winnik et al. reported a new approach to the synthesis of nanocrystalline γ-Fe_2O_3 in iron(II) cross-linked alginate gels, i. e. γ-Fe_2O_3-alginate nanocomposite [103]. In their preparation, the cross-linking ion was used as the reaction center for in-situ formation of nanocrystalline iron oxides. The resulting gel was isolated in the form of spherical beads that were superparamagnetic with a blocking temperature below 50 K.

Microporous solids such as zeolites and mesoporous solids also have rigid pore structures. Although use of these materials for the growth of semiconductor nanoparticles (quantum particles) is known [104], the growth of magnetic particles in these systems has been much less studied and, interestingly, often motivated by particle properties other than magnetism (e. g. catalytic activity). Of the investigations reported, most have concentrated on the use of zeolite hosts; some researchers have,

for example, examined the preparation of iron [105] and cobalt [106] metal and iron oxide [107]. Very few reports have extended to the study of mesoporous materials. One of the few examples found that iron oxide particles could be readily prepared in the silicate MCM-41 [108]. MCM-41 is one of a new family of molecular sieves with a regular hexagonal array of uniform pore openings and pore sizes in the range 2–10 nm. It has been found that the nanoparticles of Fe_2O_3 encapsulated in the uniform pores of MCM-41 have a uniform size of approximately 4 nm, and the bandgap of the resulting Fe_2O_3 particles is widened from 2.1 to 4.1 eV. The magnetic properties of this system remain undetermined.

A typical preparation of magnetic nanoparticles using zeolite as a host structure can be illustrated with the synthesis of iron clusters embedded in the Faujasite-type zeolite NaX [109]. The crystal structure of NaX consists of SiO_4 and AlO_4 tetrahedra forming cubo-octahedra which are interconnected by six-membered rings. The overall frame contains supercages which provide enough space to host molecular units of sizable dimensions (<1.3 nm). The NaX solids are saturated with $Fe(CO)_5$, and this is followed by thermal decomposition. The size of the iron nanoparticles depends on the conditions used for thermal decomposition of the system $Fe(CO)_5$-NaX. Thermal decomposition under continuous vacuum and temperatures up to 453 K leads to iron particles larger than 10 nm whereas thermal decomposition up to 723 K under argon leads to 3–4-nm clusters. In contrast, clusters in the 2-nm range could be obtained by thermal decomposition up to 453 K under static vacuum and subsequent heating up to 823 K under continuous vacuum. Microporous alumina has also been used as templates in the growth of magnetic nanostructures. Fig. 1 shows a scanning electron micrograph of an Fe network grown on 100-nm pore size, 50-nm wall width nanochannel alumina. The light connected regions correspond to the Fe network and the dark regions are the nanochannels (pores) in the alumina substrate [110].

1.3 Structure-Property Overview

Nanocrystalline and nanocomposite materials are polycrystalline materials with grain sizes of up to ca 100 nm. Because of the extremely small dimensions, a large volume fraction of the atoms is located at the grain boundaries and surfaces. Nanostructured materials are thus a special state of solid matter that consists primarily of incoherent interfaces (grain or interphase boundaries) formed between nanometer-sized crystallites with different crystallographic orientation. The atomic arrangement in the incoherent interfaces is characterized by reduced density and nearest neighbor coordination number relative to the glassy or crystalline state, because of the misfit between crystallites of different crystallographic orientation that are joined at the interfaces. The reduced density and nearest neighbor coordination number lead to a new type of atomic structure which has properties that differ (sometimes by many orders of magnitude) from those of crystals and glasses with the same chemical composition [111]. A clear picture of the structure of nanoscaled materials is only now

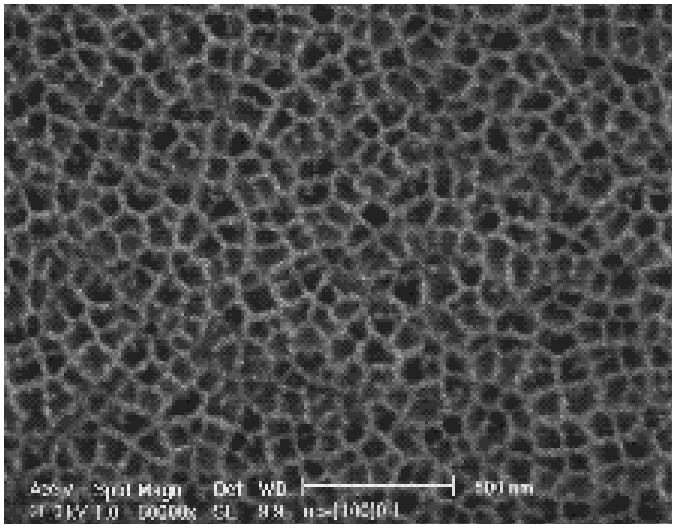

Fig. 1. Scanning electron micrograph of an Fe network grown on 100-nm pore size, 50-nm wall width nanochannel alumina. The light connected regions correspond to the Fe network and the dark regions are the nanochannels (pores) in the alumina substrate [110].

emerging. The properties of nanocrystalline materials are very often superior to those of conventional polycrystalline coarse-grained materials. Nanoscaled materials often have higher electrical resistivity, specific heat, and coefficient of thermal expansion, and lower thermal conductivity than conventional coarse-grained materials; they also often have superior magnetic properties. Nanostructured alloys enable the alloying of components that are immiscible in the crystalline and/or glassy states. New concepts of nanocomposites and nanoglasses are being intensively investigated. Although discovered several decades ago, nanostructured materials have started to enter the regime of technology applications. There is a great potential for future applications of nanoscaled materials. Extensive investigation of structure-property correlations in nanocrystalline materials in recent years have begun to unravel the complexities of these materials, and pave the way for successful exploitation of nanoscaled design principles to synthesize better materials than have hitherto been available.

When materials with long-range magnetic order, e. g. ferromagnetism and antiferromagnetism, are reduced in size, the magnetic order can be replaced by other magnetic states. One way of reducing the dimensions of the ordered magnetic regions is to isolate them inside non-magnetic matrices by precipitation from solid solution. Another way is to form a composite of nanometer-sized magnetic and non-magnetic species. The magnetic behavior of these nanocomposites becomes either paramagnetic or superparamagnetic [112]. Because of the ease with which the magnetic behavior can be controlled by controlling the processing parameters, such materials present great possibilities for the atomic engineering of materials with specific magnetic properties.

1.3.1 Quantum Tunneling

Quantum tunneling effects have recently been reported in several nanoscale magnetic materials and molecular magnets [113–116]. Fig. 2 shows one such nanoscale magnet, Fe_{10}, which consists of ten Fe^{3+} ions (large symbol) bound in a ring structure with chlorine, oxygen, and carbon [117].

Observation of quantum tunneling effects in nanostructured materials is possible partly because of significant advances both in the ability to obtain magnetic systems of almost any desirable size, shape, and composition, and in the development of instrumentation for detection of extremely weak magnetic signals. The observation of steps at regular intervals of magnetic field in hysteresis loops was interpreted as evidence of thermally assisted, field-tuned resonant tunneling between quantum spin states in a large number of identical high-spin molecules. Because the magnetization is a classical vector, this effect is also referred to as macroscopic quantum tunneling. Study of low-temperature magnetic relaxation, single particle measurements, and domain wall junction, quantum coherence, and quantum resonance measurements in nanostructured materials has provided the opportunity to observe the occurrence of quantum tunneling of magnetization. Quantum resonance measurements have shown unambiguously the occurrence of quantum tunneling of magnetization on the one-nanometer scale [118]. It has been shown that a staircase structure in the magnetization curve results from Landau–Zener tunneling between different pairs of nearly-degenerate energy levels for a uniaxial magnet [119]. Clusters of metal ions are a class of compounds actively investigated for their magnetic properties, which

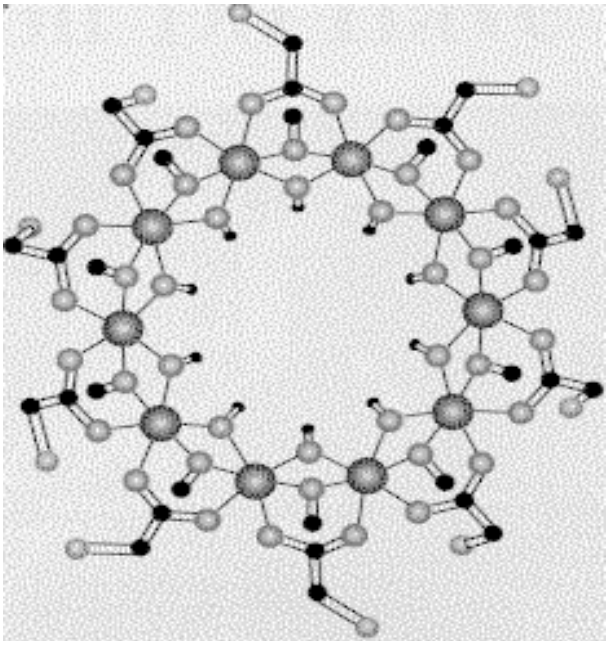

Fig. 2. Nanoscale magnet Fe_{10}, which consists of ten Fe^{3+} ions (large symbol) bound in a ring structure with chlorine, oxygen, and carbon [117].

changes from those of simple paramagnets to those of bulk magnets. In addition to the coexistence of classical and quantum behavior, these systems might help reveal the link between simple paramagnetism and bulk magnetic behavior [117].

1.3.2 Anisotropy

The most common types of anisotropy are crystalline anisotropy, shape anisotropy, stress anisotropy, and exchange anisotropy, of which crystalline anisotropy and shape anisotropy are most important in nanostructured materials. Magneto-crystalline anisotropy arises from spin–orbit coupling and energetically favors alignment of the magnetization along a specific crystallographic direction. Shape anisotropy is the result of departure of magnetic particles from sphericity and is predicted to produce the largest coercivity. El-Shall et al. found that magnetic anisotropy constants for iron oxide nanoparticles were one order of magnitude higher than known bulk values [11]. Study of the magnetic properties of nanocomposites of silver and iron oxide synthesized by sputtering, gas condensation, and in-situ oxidation have indicated that these composites were superparamagnetic above ~100 K [120, 121]. At lower temperatures hysteresis measurement provides evidence of the occurrence of unidirectional anisotropy; this is believed to be caused by interactions between the magnetic phases coexisting in the composites [122]. Induced magnetic anisotropy was found to increase with the field annealing time in nanocrystalline Fe–Cu–Nb–Si–B alloys. A high relative initial permeability, a flat B–H loop, and low remanence were obtained by transverse-field annealing for a short time [123]. Exchange-coupled ferromagnetic–antiferromagnetic thin films are known to have unidirectional anisotropy and an antiferromagnetic bias layer is used to enable selective alteration of the coercivity of a neighboring ferromagnetic layer in magnetic device structures. Fig. 3 shows such an exchange-coupled ferromagnetic-antiferromagnetic

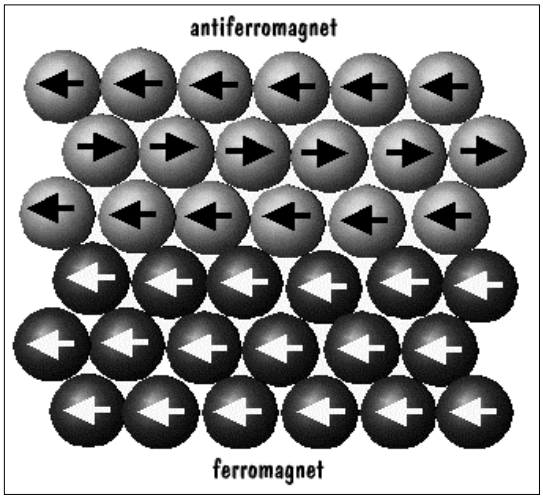

Fig. 3. Exchange-coupled ferromagnetic–antiferromagnetic thin film in which the moments of the ferromagnetic layer (bottom) are pinned by the antiferromagnetic layer (top).

thin film in which the moments of the ferromagnetic layer (bottom) are pinned by the antiferromagnetic layer (top). Exchange coupling in so-called "core-shell structures", in which magnetic nanoparticles are coated with an antiferromagnetic shell layer, is also being studied [124].

1.3.3 Analytical Instrumentation

Typical instruments used for analysis of magnetic nanostructured materials include transmission electron microscopy, scanning electron microscopy, X-ray diffraction, atomic-force microscopy, magnetic force microscopy, magneto-optical Kerr rotation, small-angle neutron scattering, nuclear magnetic resonance, electron spin resonance, Raman spectroscopy and IR spectroscopy, low-energy electron diffraction, and electron energy loss spectroscopy. Coherent Lorentz imaging using TEM, scanning electron microscopy with polarization analysis (SEMPA), spin polarized scanning tunneling microscopy, spin polarized low energy electron microscopy (SPLEEM), X-ray magnetic circular dichroism spectroscopy, and spin polarized photoemission studies are increasingly being used to characterize nanostructured magnetic materials. Fig. 4

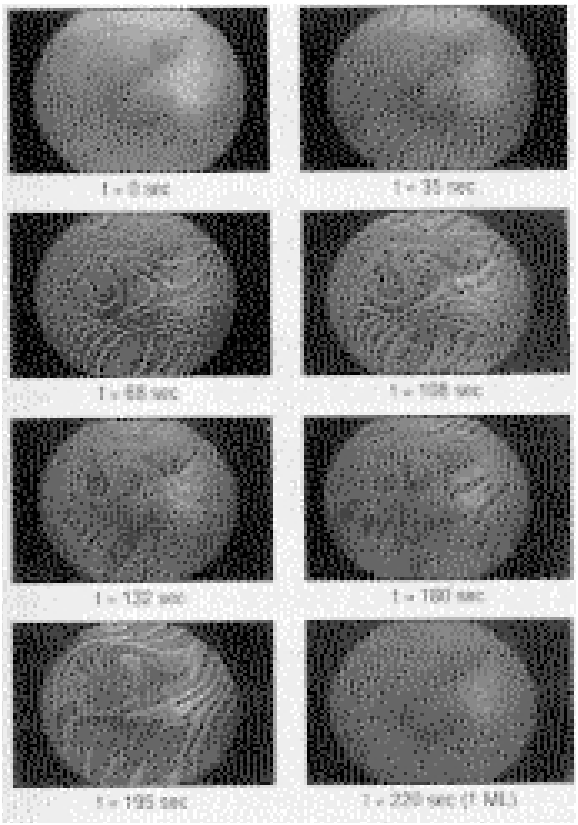

Fig. 4. An in situ-determined image of exact monolayer coverage of W (110) by Co at 650 K by use of SPLEEM [125].

shows an in-situ-determined image of exact monolayer coverage of W (110) by Co at 650 K by use of SPLEEM [125].

Mössbauer spectroscopy continues to be a very powerful tool for characterization of nanostructured materials containing iron and selected groups of elements. A new design of Mössbauer in-situ cell for studies of catalysts and nanometer-sized particles has been reported [126]. Non-linear magneto-optical phenomena such as magnetization-induced second-harmonic generation (MSHG) can only be observed in materials in which both space-inversion and time-reversal symmetry are simultaneously broken. This makes non-linear magneto-optical effects particularly attractive for the study of magnetic multilayers and nanostructures [127]. A hybrid magneto-optical magnetometer and optical microscope has been designed and constructed for probing the magnetic properties of submicron nanomagnets [128]. Near-field techniques have increasingly been applied, because they can surpass the resolution limit set by the wavelengths used [129].

Atomic-force microscopy and magnetic-force microscopy, AFM and MFM, are important and widely used versatile tools for characterization of magnetic materials. These techniques are increasingly being used, in industry and academia, to probe morphological information of nanostructured materials down to the atomic level and determine the orientation and stability of magnetic domains in the materials. Recent advances in magnetic resonance force microscopy (MRFM) have enabled the detection of the magnetic force exerted by electrons and nuclei in microscopic samples, and it might become possible to detect single-electron magnetic moments [130].

1.4 Theory and Modeling

1.4.1 Single-domain Particles

Magnetic particles of nanometer sizes are mostly single-domain, because the formation of domain walls becomes energetically unfavorable [131]. As particle size further decreases below the single-domain value, the magnetic moment of the particles will be gradually affected by thermal fluctuation and they will behave paramagnetically with giant moments. This superparamagnetism has zero coercivity and readily occurs above; the blocking temperature at which thermal energy is sufficient for the moment to relax during the time of the measurement. The evolution of intrinsic coercivity, H_{CI}, as a function of particle size is illustrated in Fig. 5. Above a critical particle size, D_S, the particles are multi-domain. The coercivity increases as the particle size decreases. Below, D_S, the particles are single-domain. When the average particle size decreases further below D_P the particles become superparamagnetic with unstable magnetic moments and vanishing coercivity. Stoner–Wohlfarth theory was developed to describe the behavior of an assembly of single-domain particles [132]. A more recent theory by Holz and Scherer addresses the coupling between

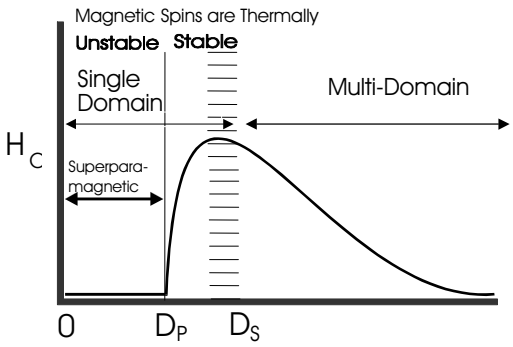

Fig. 5. Schematic representation of the change of intrinsic coercivity as a function of the size of a magnetic particle.

magnetic particles in nanostructured materials [133]. The issue of exchange coupling between magnetic nanoparticles has drawn much attention in recent years, because it will have significant impact on both the understanding and application of nanostructured magnetic materials.

1.4.2 Modeling

Combining classical micromagnetic theory with the Landau–Lifshitz–Gilbert gyromagnetic equations, recent modeling studies have led to much improved understanding of fundamental magnetization processes in magnetic thin films. For example, magnetic domain states of a permalloy prism are calculated by means of three-dimensional finite element modeling. Both the four-domain Landau structure and the seven-domain "diamond" structure are observed by using different starting conditions. Both domain patterns are sheared on the surfaces. This shearing is attributed to bulk effects of the magnetic structure [134]. Fig. 6 shows the simulated static magnetization configuration for a $1 \times 0.5\,\mu$m sized, 10 nm thick, Permalloy thin film element with the field applied along the element width direction. The gray scale pictured in the top and middle rows represents the magnetization component in the length and width directions, respectively. The gray scale in the bottom row represents the normal component of the magnetization curl $\nabla \times M$ [135].

Hysteresis properties and transition noise behavior of longitudinal thin film recording media with advanced microstructures have been studied by micromagnetic modeling. High coercive squarenesses can be achieved for films with a weak exchange coupling through the normal boundary. The high coercive squareness and extremely low noise make nanocrystalline films suitable for ultra-high density recording applications [136]. Chui and Tian have recently studied the finite temperature magnetization reversal of single domain nanostructures (particles and wires) of different materials with Monte Carlo and analytical techniques. For large structure diameters there are different reversal mechanisms at different orientations of the external field. For small structure diameters growth usually starts with the nucleation and subsequent depinning of domain walls at the end(s) of the structure. The nucleation energy of the domain wall in a magnetic field approaches zero near the

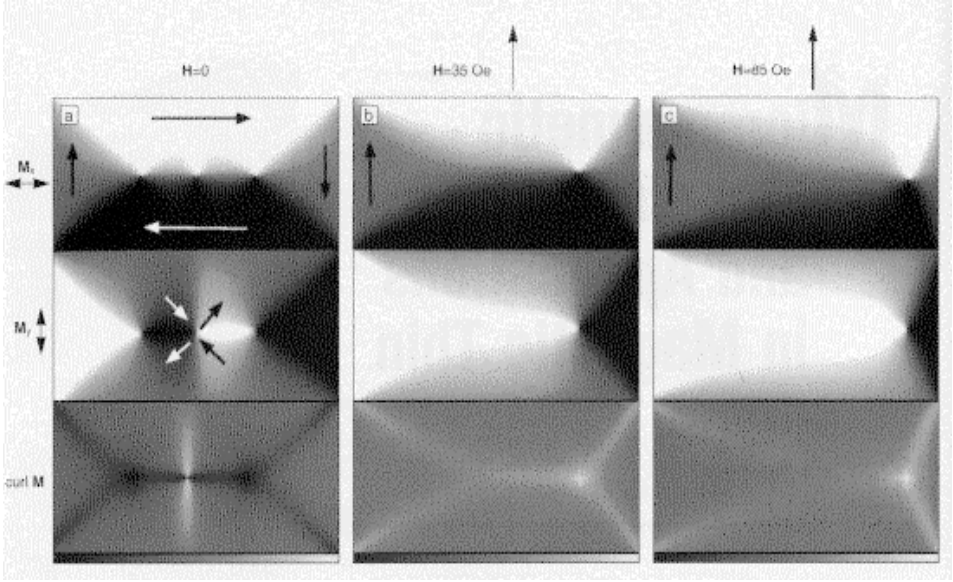

Fig. 6. Simulated static magnetization configuration for a $1 \times 0.5\ \mu$m sized, 10 nm thick, Permalloy thin-film element with the field applied along the element width direction. The gray scale pictured in the top and middle rows represents the magnetization component in the length and width directions, respectively. The gray scale in the bottom row represents the normal component of the magnetization curl $\nabla \times M$ [135].

coherent rotation limit at small aspect ratios and at fields less than the coherent rotation limit at large aspect ratios. As the domain wall energy approaches zero the domain wall width can remain finite. For small diameters the coercive field is significantly temperature-dependent [137].

1.5 Applications

1.5.1 Magneto-optical Recording

High density re-writable magneto-optical Kerr effect recording is now a reality. Future development includes application of shorter wavelength diode lasers for higher recording density and preparation of films with sufficiently small grain size for the reduction of media noise. Studies have found that nanoscaled transition metal multilayers, in particular Co–Pt multilayers, compare favorably with amorphous rare earth–transition metal alloys such as GdTbFe at short wavelengths. The Co–Pt multilayers have a Kerr rotation which is larger by, approximately, a factor of 3 in comparison to GdTbFe in the 400-nm region [138]. One of the deficiencies of Co–Pt mul-

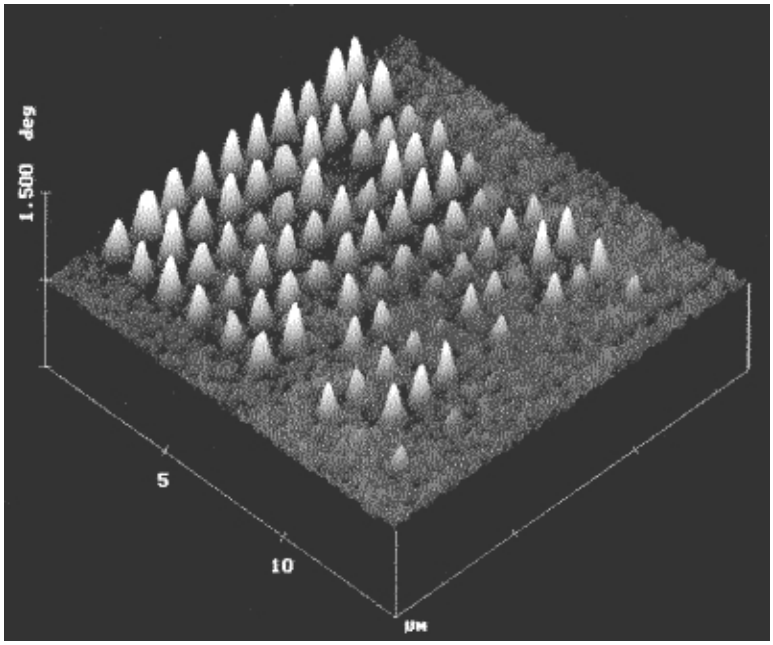

Fig. 7. The magnetic force image of rows of bits on TbGdFeCo magneto-optical medium produced by 3M Corporation [Courtesy of Digital Instruments].

tilayers is that they are polycrystalline rather than amorphous, although their grain size is quite small. Fig. 7 is the magnetic force image of rows of bits on TbGdFeCo magneto-optical medium produced by 3M Corporation [Courtesy of Digital Instruments].

Although MnBi-based compounds have rather large Kerr rotation compared with amorphous alloys and Co–Pt multilayers, the polycrystalline nature of the material and its relatively large grain size makes it unsuitable for practical recording film, because of high media noise. It also has a structural instability near its Curie temperature, which causes difficulties in the writing process. Although it was recently reported [139] that Al doping increases the Kerr rotation of MnBi, reduces the grain size, and improves the thermal stability; Sellmeyer et al. found that Al doping neither enhances the Kerr rotation nor eliminates the high temperature structural instability but does promote small grain sizes which are required for a low-noise recording medium [140].

MnBi-based compounds and garnets are both polycrystalline materials with large Kerr rotations at blue wavelengths. They have high potential as practical recording media. Synthesis of nanocrystalline materials with grain sizes less than 30 nm is desirable for low media noise.

1.5.2 Magnetic Sensors and Giant Magnetoresistance

Typical applications include magnetic field probes, magnetic read heads, contactless switches, position sensors in brushless motors, which might eliminate contact noise, a significant noise contribution in electronic devices, and pattern recognition, in which a magnetically printed pattern is scanned using a highly sensitive magnetic sensor made of giant magnetoresistance (GMR) materials. Bridge magnetic sensors made of GMR materials give signals 3–20 times larger than those of a traditional magnetoresistive sensor. They are linear over most of their operating range and have superior temperature stability [141].

Most studies on GMR materials have involved metal–metal systems in which magnetic metal particles are dispersed in a non-magnetic metal matrix, or magnetic metal layers are separated by non-magnetic metallic spacers. Recently, large magnetoresistance has been observed in metal–insulator–metal trilayers in which two magnetic layers are separated by a thin insulator film [142, 143]. The results support the claim that large magnetoresistance is a result of the spin-polarized tunneling of electrons between two magnetic metals through a thin Al_2O_3 insulator. These findings have attracted much attention because of the interesting problem of "spin tunneling" involved in such systems and their potential applications. GMR in granular materials employing an insulating matrix has also been reported recently [144]. One issue concerning tunneling magnetoresistance is the preparation of pinhole-free barriers [145]. One way of avoiding this problem is to make discontinuous tunnel junctions that consist of granular magnetic nanoparticles. Discontinuous junctions are not susceptible to metallic bridging by pinholes because of the multiple junction nature of the structure [146].

1.5.3 High-density Magnetic Memory

The areal density in longitudinal magnetic recording has surpassed the $1\,\mathrm{Gbit\,in^{-2}}$ level and reached $10\,\mathrm{Gbit\,in^{-2}}$ density [147, 148]. A further increase will require major improvements in head, media, and channel technologies [149]. Of particular interest are low-noise high-coercivity media. Currently, CoPtCr-based continuous media are used. These consist of exchange-coupled grains several tens of nanometers in size. Reduction of grain size and control of inter-grain exchange coupling would be highly desirable for further noise reduction, which is required in ultrahigh-density media, i. e. beyond $10\,\mathrm{Gbit\,in^{-2}}$. Reduction of grain size, however, will eventually lead to superparamagnetic particles, unsuitable for recording. Such limitations can be overcome by the design of novel nanocomposite materials with larger intrinsic magnetic anisotropies [150, 151]. For example, a nanocomposite structure consisting of CoPt nanoparticles with a highly anisotropic hard fct phase embedded in a fcc Ag matrix has been reported [152]. A Ni–Al nitride nanocomposite has been shown to have potential applications as a high density recording medium, as have other finely divided dispersions of ferromagnetic metals in insulating matrixes [153]. An especially interesting approach is the fabrication of completely exchange-decoupled magnetic nanoparticles which would enable the production of media in which the

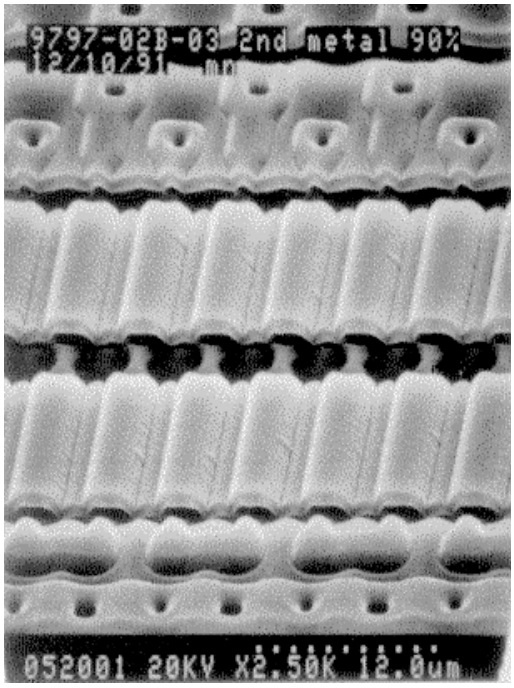

Fig. 8. The micrograph of section of magnetoresistive random-access memory developed by Honeywell Corporation, showing 2-μm $\times$ 12-μm MRAM bits [Courtesy of G.B. Granley, Honeywell Corporation].

transition between adjacent bits is controlled by the physical location of the particle, rather than by the demagnetization zone, as in continuous media. Development of a process enabling fabrication of regular arrays of such particles might eliminate transition noise completely [154]. Such processes could include nanolithography, as suggested by Chou et al. [155, 156], who have prepared patterned media by means of an injection-molding process for patterning and subsequent electrodeposition of Ni. Isolated and interactive arrays of magnetic Ni pillars were fabricated. Unique magnetic properties were obtained by controlling size, aspect ratio, and spacing of the pillar array. Particles as small as 15 nm in diameter have been reported and nominal areal densities of approximately 250 Gbit in^{-2} were suggested. Addressability (write, read, data rate, etc.) remains an open issue.

Magnetoresistive random-access memory (MRAM), an integrated magnetic memory technology that uses magnetic storage and magnetoresistive reading with semiconductor support circuits [157], has been developed using GMR materials. Fig. 8 is the micrograph of section of magnetoresistive random-access memory developed by Honeywell Corporation, showing 2-μm $\times$ 12-μm MRAM bits [Courtesy of G.B. Granley, Honeywell Corporation].

1.5.4 Optically Transparent Materials

A magnetic material with appreciable optical transmission in the visible region at room temperature has been found in a γ-Fe_2O_3–polymer nanocomposite. Optical studies show that the small-particle form of γ-Fe_2O_3 is considerably more transparent to visible light than is the single crystal form. The magnetization of the nanocomposite is greater by more than an order of magnitude than those of the strongest room-temperature-transparent magnets $FeBO_3$ and FeF_3 [100, 158].

Real time transitions from metallic (YH_2 or LaH_2) to semiconducting (YH_3 or LaH_3) behavior was recently found to occur in the coated films during continuous absorption of hydrogen; it was accompanied by pronounced changes in their optical properties – for example, it changes from a shiny mirror to a yellow, transparent window [159]. Although the time scale on which this transition occurs is currently rather slow, there seems to be considerable scope for improvement by appropriate choice of rare-earth element and by adopting electrochemical means for driving the transition. This switchable optical property might find important technological applications.

1.5.5 Soft Ferrites

Ferrites have many advantages in rf applications where the complex permeability can be modified by application of an external field or by changes in composition. The complex permeability of a ferrite of the YIG family was measured as a function of magnetic field to characterize control of the permeability at different temperatures [160]. It has been shown that there is a gradual increase in the real permeability of polycrystalline thin films of YIG with increasing frequency, as opposed to a decrease observed in bulk ferrite toroids of the same composition. These films seem to be useful in the construction of rf microstructures [161].

The demand for soft ferrites has been growing and ferrites will expand markedly in both quantity and the extent of application as the need for ferrites of higher quality increases. The electromagnetic properties of ferrites depend on the production process and on their micro and nanostructures. MnZn ferrite is a principal ferrite for high permeability and power uses. Spray roasting to produce the Mn–Zn–Fe ternary system has been developed recently [162]. Precise control of the production process to prevent the occurrence of defects is the key to producing high-performance ferrites. New applications of ferrites, for example ferrite carriers and toners for electrophotocopy and biochemical applications, is expanding.

The noise filter characteristics of a common-mode choke coil fabricated from a nanocrystalline Fe84Nb7B9 alloy have been studied with the aim of clarifying its potential for application as a core material [163]. The impulse attenuation characteristics of the choke coil with the nanocrystalline alloy core were superior to those of a coil with an Mn–Zn ferrite core. Choke coils made from the nanocrystalline alloy and amorphous alloy cores resulted in higher attenuation in the frequency range >1 MHz. The common-mode attenuation of the choke coil with the nanocrystalline alloy core resulted in attenuation values higher than those of coils with the other two

cores in the frequency range >4 MHz. The conducted radio noise characteristics of the choke coil with the nanocrystalline alloy core were superior to those of the coil with the amorphous alloy core. The attenuation of the former was 5 dB higher than that of the latter.

1.5.6 Nanocomposite Magnets

Recently developed nanocomposite magnets are composed of magnetically soft and hard ultra-fine grains the magnetization of which are coupled by the inter-grain exchange interaction. Because of the presence of soft grains and the coupling of the magnetization, nanocomposite magnets are expected to have superior hard magnetic properties, for example high remanence, large energy product, small temperature coefficient of the remanence, and high coercivity [164]. The nanocomposites have been predicted to offer a maximum energy product, $(BH)_{\max}$, in excess of 100 MGOe [165], because of the exchange coupling between the hard and soft magnetic grains [166]. The hard magnetic phase provides the high anisotropy and coercive fields and the soft phase enhances the magnetic moments. The moments in the soft grains near the interfaces are pinned to the hard grains by the exchange coupling and the centers of the soft grains can rotate in a reverse field. This configuration results in enhanced remanent magnetization and reversible demagnetization curves, because the moments of the soft grains will rotate back to align with the neighboring hard grains when the applied field is removed. An added advantage of such nanocomposite magnets is that they require less of the expensive rare earths and thus are potentially more competitive than the magnets currently available. The major problem with such magnets is the relatively low coercivity obtained in systems studied so far. The coercivity is found to decrease drastically as the soft phase is added. This might be mainly because of the experimental difficulties of obtaining an ideal nanostructure. A recent surge in the research interest in this field has shown that the nitride of the rare earth–iron compound has good magnetic properties. Also, application of mechanical alloying for the synthesis of the rare earth–iron compound is more versatile [167].

1.5.7 Magnetic Refrigerant

Upon application of an external magnetic field, the magnetic spins in a material partially align with the field, thereby reducing the magnetic entropy of the spin system. When this is performed adiabatically, the temperature of the specimen will increase. This temperature rise, which is related to the entropy change by the heat capacity, is known as the magnetocaloric effect. Upon cycling the magnetic field, this effect can be used to transfer heat from one thermal reservoir to another, forming the basis for a magnetic refrigerator. Composite magnetic materials containing nanometer-size magnetic species might have enhanced magnetocaloric effects especially at high temperatures or low magnetic fields over a large temperature range [168]. Enhanced magnetocaloric effects have been reported for a series of iron-substituted gadolinium garnets (GGIG) $Gd_3Ga_{5-x}Fe_xO_{12}$; this was consistent

with superparamagnetic behavior at low Fe concentrations and was in qualitative agreement with calculation [169]. A giant magnetocaloric effect has recently been discovered in the $Gd_5(Si_xGe_{1-x})_4$ pseudobinary alloys. Its ordering temperature is tunable between 30 and ~276 K and it exceeds the reversible (with respect to alternating magnetic field) magnetocaloric effect for any known magnetic refrigerant material at the corresponding Curie temperature by a factor of 2–10 [170].

1.5.8 High-T_C Superconductor

Because of their small coherence lengths, the high-T_c cuprates can be used as superconducting interconnects with widths of a few tens of nanometers, or as Josephson junctions with a surface area of a few hundred square nanometers. Nanopatterning of these materials has, therefore, become an attractive research undertaking [171].

1.5.9 Ferrofluids

Applications of ferrofluids include lubrication, sealing, air-moisture absorption, medical application, and electrically conducting fluids for electromechanical systems [172]. Ferrofluid seals, ferrofluids sustained by a magnetic field in the desired position, have the advantages of both contact and hydrodynamic seals. They have low friction moments and a high degree of sealing and can be used to seal vacuum systems and high pressure chambers, and to separate different media. Ferrofluid lubricants can be easily positioned, by means of a magnetic field, to the exact friction zone; this might be difficult to achieve with traditional lubricants. Ferrofluids can also find applications for damping oscillations and as shock absorbers. Shock absorbers made with ferrofluids have high supporting power and good amplitude–frequency characteristics.

The use of ferrofluids for cooling devices where magnetic fields are present is particularly promising. The possibility of intensifying convection at the expanse of a magnetic field converts a magnetic fluid into a highly effective heat carrier. It can also be used as a tool to control heat transfer.

Ferrofluid-based devices include sensors and actuators. Ferrofluids have, for example, been used in densimeters, accelerometers, pressure transducers, displacement transducers, and slope angle-data transmitters. By applying a magnetic field to a ferrofluid it is possible not only to position it easily, but to displace it easily or to change its shape. The basic advantages of such a mechanism lies in the absence of movable mechanical parts and, hence, in improved reliability. Typical examples of an actuator using ferrofluids are electromechanical converters, electrical contacts, displays, and level-detectors.

Because a magnetic fluids are either black or brown, they might be used as inks in a printer controlled by a magnetic field. Despite of their relatively slow printing speed, advanced design might enable printing at higher speeds [173]. They can also be used as magnetic toners in xerography.

Methods of preparing nanometer-sized γ-Fe_2O_3, Fe, other transition metal, or rare earth magnetic particles coated with carbon or organic layers have been reported [174–176]. It has been suggested that such coated magnetic particles might extend the applications of stabilizing ferrofluids or be used as contract agents in magnetic resonance imaging.

1.5.10 Biological Applications

Ferritin is a natural participant in the metabolic processes of most animals. It consists of a segmented protein shell and an inner space filled with a hydrated iron oxide similar to ferrihydrite. It is one of the ways an organism stores Fe^{3+} for physiological needs. It has been recently shown that after removal of the ferrihydrite core, it is possible to reconstitute the empty protein shell under controlled oxidative conditions, tailored to the synthesis of magnetite rather than ferrihydrite [177]. In addition to the potential for the production of novel nanophase materials derived from biological materials, nanoscaled magnets are also potentially useful in magnetic resonance imaging and controlled drug delivery as a biocompatible ferrofluid. The synthesis and understanding of artificial (and natural) ferritin proteins has been advancing rapidly. New technology in molecular chemistry is now realizing the possibility of creating true molecular magnets, in which the magnetic ions are added one at a time and the resulting magnet has precisely defined atomic weight and magnetic properties, and so might, for example, be able to target specific tissues [117].

Other examples of interest and importance are magnetotactic bacteria. There is evidence of a magnetic direction-finding ability in many species and this suggests some interesting biomimicking possibilities in relation to both magnetic sensors and the transducers. Currently our understanding in this area is limited to a group known as magnetotactic bacteria, which use the earth's magnetic field to orientate themselves and move in the direction of nutritional or chemical gradients [178]. The permanent magnetic dipole moment of each magnetotactic cell arises as a result of the presence of intracellular membrane-bound single-domain inorganic particles, which are arranged in chains. Most of the particles, known as magnetosomes, contain magnetite Fe_3O_4 or greigite Fe_3S_4 in the 40 nm to 100 nm size range [179].

Methods for the large-scale preparation of biodegradable and biocompatible magnetic nanospheres have been developed [180]. The nanospheres can be used for cell labeling in magnetic cell-separation techniques. The nanospheres have proved to be immunospecific, biodegradable, and biocompatible. These immunospecific magnetic nanospheres are expected to have many applications as biopharmaceutical reagents in biology and medicine.

References

[1] *Nanomaterials: Synthesis, Properties, and Applications*, (Eds. A.S. Edelstein, R.C. Cammarata), Institute of Physics Publishing, Bristol and Philadelphia, **1996**.
[2] *Advanced Catalysts and Nanostructured Materials: Modern Synthetic Methods*, (Ed. R.W. Moser), Academic Press, San Diego, **1996**.
[3] *Nanoparticles in Solids and Solutions*, (Eds. J.H. Fendler, I. Dekany), Kluwer Academic Publishers, Netherlands, **1996**.
[4] *Handbook of Nanophase Materials*, (Ed. A.N. Goldstein), Marcel Dekker, Inc., New York, **1997**.
[5] *Nanoparticles and Nanostructured Films: Preparation, Characterization and Applications*, (Ed. J.H. Fendler), Wiley–VCH, New York, **1998**.
[6] D. Leslie–Pelecky, R.D. Rieke, *Chem. Mater*. **1996**, *8*, 1770–83.
[7] J.F. Loffler, J.P. Meier, B. Doudin, J.-P. Ansermet, W. Wagner, *Physical Review B*. **1998**, *57*, 2915–24.
[8] C. Prados, M. Multigner, A. Hernando, J.C. Sanchez, A. Fernandez, C.F. Conde, A. Conde, *J. Appl. Phys*. **1998**, *85,* 6118–20.
[9] X.L. Dong, Z.D. Zhang, X.G. Zhao, Y.C. Chuang, S.R. Jin, W.M. Sun, *J. Mater. Res*. **1999**, *14*, 398–406.
[10] T. Nakayama, T.A. Yamamoto, Y.H. Choa, K. Niihara, *Key Eng. Mater. (Sci. of Eng. Ceram. II)*. **1999**, *161–163*, 497–500.
[11] M.S. El–Shall, S. Li, D. Graiver, U. Pernisz, *ACS Symp. Ser. 622, (Nanotechnology)*, **1996**, 79–99, and references therein.
[12] M. Boutonnet, J. Kizling, P. Stenius, G. Maire G., *Colloids Surfaces*. **1982**, *5*, 209.
[13] V. Pillai, P. Kumar, M.J. Hou, P. Ayyub, D.O. Shah, *Adv. Colloid Interface Sci*. **1995**, *55*, 241–69, and references therein.
[14] V. Bhabra, M. Lal, A.N. Maitra, P. Ayyub, *J. Mater. Res*. **1995**, *10*, 2689–92.
[15] N. Moumen, M.P. Pileni, *Chem. Mater*. **1996**, *8*, 1128–34.
[16] M.P. Pileni, N. Moumen, I. Lisiecki, P. Bonville, P. Veillet, *Nanoparticles in Solids and Solutions*, (Eds. J.H. Fendler, I. Dekany), Kluwer Academic Publishers, Netherlands, **1996**, pp. 325–358.
[17] C.T. Seip, E.E. Carpenter, C.J. O'Connor, V.T. John, S. Li, *IEEE Transactions on Magnetics*. **1998**, *34*, 1111–1113.
[18] E.E. Carpenter, C.J. O'Connor, V.G. Harris, *J. Appl. Phys*. **1999**, *85*, 5175–5177.
[19] S. Li, V.T. John, S.H. Rachakonda, G.C. Irvin, G.L. McPherson, C.J. O'Connor, *J. Appl. Phys*. **1999**, *85*, 5178–5180.
[20] J. Tanori, N. Duxin, C. Petit, I. Lisiecki, P. Veillet, M.P. Pileni, *Colloid Polym. Sci*., **1995**, *273*, 886–992.
[21] J. Tanori, M.P. Pileni, *Langmuir*. **1997**, *13*, 639–646.
[22] N. Duxin, O. Stephan, C. Petit, P. Bonville, C. Colliex, M.P. Pileni, *Chem. Mater*. **1997**, *9*, 2096–2100.
[23] X.M. Lin, C.M. Sorebsen, K.J. Klabunde, G.C. Hajipanayis, *Langmuir*. **1998**, *14*, 7140.
[24] X.M. Lin, C.M. Sorebsen, K.J. Klabunde, G.C. Hajipanayis, *J. Mater. Research*. **1999**, *4*, 1542.
[25] E.E. Carpenter, C.T. Seip, C.J. O'Connor, *J. Appl. Phys*. **1999**, *85*, 5184–5186.
[26] I. Lado–Tourino, A. Gonzalez–Penedo, M.A. Lopez–Quintela, J. Garcia–Otero, A.J. Garcia–Bastida, C. Izco, D. Baldomir, R.D. Sanchez, J. Rivas, J.M. Greneche, *Nanostruct. Non–Cryst. Mater. Proc. Int. Workshop Non–Cryst. Solids*, 4th, **1995**.

[27] E.E. Carpenter, C.J. O'Connor, C. Sangregorio, *IEEE Transactions on Magnetics*, **1999**, *35*(*5*), 3496–3498.
[28] M. Roth, R. Hempelmann, *Chem. Mater*. **1998**, *10*, 78–82.
[29] E.E. Carpenter, C.J. O'Connor, C. Sangregorio, *Mater. Res. Soc. Symp. Proc*. **1999**, *577*, 435–441.
[30] N.S. Kommareddi, M. Tata, V.T. John, G.L. McPherson, M.F. Herman, Y.S. Lee, C.J. O'Connor, J.A. Akkara, D.L. Kaplan, *Chem. Mater*. **1996**, *8*, 801–809.
[31] S. Banerjee, V.T. John, G.L. McPherson, Y.S.L. Buisson, C.J. O'Connor, J.A. Akkara, D.L. Kaplan, *Colloid Polym. Sci*. **1997**, *275*, 930–937.
[32] M. Pechini, U.S. Patent No. 3,330,697 (11 July **1967**).
[33] N. Uekawa, K. Kaneko, *J. Phys. Chem*. **1996**, *100*, 4193–4198.
[34] N. Uekawa, K. Kaneko, *J. Mater. Res*. **1999**, *14*, 2002–2006.
[35] C. Marcilly, P. Courty, B. Delmon, *J. Am. Ceram. Soc*. **1970**, *53*, 56–57.
[36] S. Roy, W. Sigmund, F. Aldinger, *J. Mater. Res*. **1999**, *14*, 1524–1531.
[37] J.M. Yang, W.J. Tsuo, F.S. Yen, *J. Solid State Chem*. **1999**, *145*, 50–57.
[38] A.L. Micheli, U.S. Patent No. 4,627,966 (9 December **1986**).
[39] D. Sriram, R.L. Snyder, V.R.W. Amarakoon, *Mat. Res. Soc. Symp. Proc., Vol. 457*, **1997**, pp. 81–87.
[40] Y.S. Cho, V.L. Burdick, V.R.W. Amarakoon, E. Underhill, L. Brissette, *Mat. Res. Soc. Symp. Proc., Vol. 494*, **1998**, pp. 27–32.
[41] P. Pramanik, *Bull. Mater. Sci*, **1995**, *18*, 819–829.
[42] K.S. Suslick, in *Ultrasound: Its Chemical, Physical, and Biological Effects* (Ed. K.S. Suslick), VCH Press, New York, **1988**, pp. 123–163.
[43] K.S. Suslick, *Science*, **1990**, *247*, 1439.
[44] E.B. Flint, K.S. Suslick, *Science*, **1991**, *253*, 1397.
[45] K.S. Suslick, T. Hyeon, M. Fang, *Chem. Mater*. **1996**, *8*, 2172–2179.
[46] S. Ramesh, Y. Koltypin, R. Prozorov, A. Gedanken, *Chem. Mater*. **1997**, *9*, 546–551.
[47] S. Ramesh, R. Prozorov, A. Gedanken, *Chem. Mater*. **1997**, *9*, 2996–3004.
[48] K.V. Shafi, A. Gedanken, R. Prozorov, J. Balogh, *J. Chem. Mater*. **1998**, *10*, 3445–3450.
[49] X. Cao, R. Prozorov, Y. Koltypin, G. Kataby, I. Felner, A. Gedanken, *J. Mater. Res*. **1997**, *12*, 402–406.
[50] N.A. Dhas, Y. Koltypin, A. Gedanken, *Chem. Mater*. **1997**, *9*, 3159–3163.
[51] D.W. Matson, J.C. Linehan, J.G. Darab, M.F. Buehler, M.R. Phelps, G.G. Neuenschwander, in *Advanced Catalysts and Nanostructured Materials* (Ed. W.R. Moser), Academic Press, Inc. USA, **1996**, pp. 259–284.
[52] R.L. Penn, J.F. Banfield, J. Voigt, *Mat. Res. Soc. Symp. Proc., Vol. 432*, **1997**, pp. 175–181.
[53] V. Sankaranarayanan, Q. Pankhurst, D. Kickson, C. Johnson, *J. Magn. Magn. Mater*. **1993**, *125*, 199–208.
[54] F. Dogan, S. O'Rourke, M.-X. Qian, M. Sarikaya, *Mat. Res. Soc. Symp. Proc., Vol. 457*, **1997**, pp. 69–74.
[55] M. Rozman, M. Drofenik, *J. Am. Ceram. Soc*. **1995**, *78*, 2449–2455.
[56] A. Bias, V.T.L. Buono, *J. Mater. Res*. **1997**, *12*, 3278–83.
[57] A. Bias, V.T.L. Buono, J.M.C. Vilela, M.S. Andrade, T.M. Lima, *J. Mater. Sci*. **1997**, *32*(*17*), 4715–4718.
[58] A. Bias, R.L. Moreira, N.D.S. Mohallem, J.M.C. Vilela, M.S. Andrade, *J. Mater. Res*. **1998**, *13*, 223–227.
[59] R. Lucke, E. Schlegel, R. Strienitz, *J. Phys. IV*. **1997**, *7*, C1/63–C1/64, 1155.
[60] X.X. Bi, B. Ganguly, G.P. Huffman, F.E. Huggins, M. Endo, P.C. Eklund, *J. Mater. Res*. **1993**, *8*, 1666–1674.

[61] X.Q. Zhao, Y. Liang, F. Zheng, Z.Q. Hu, G.B. Zhang, K.C. Bai, *Mater. Res Soc. Symp. Proc*. **1995**, *368*, 39–43.
[62] C.M. Sorensen, Q. Li, H.K. Xu, Z.X. Tang, K.J. Klabunde, G.C. Hadjipanayis, in *Nanophase Materials* (Eds. G.C. Hadjipanayis, R.W. Siegel), Kluwer Academic Publishers, Netherlands, **1994**, pp. 109–116.
[63] C.K. Lee, R.F. Speyer, G.W.D. Spratt, *J. Appl. Phys*.**1993**, *73*, 6266–6268.
[64] V.K. Sankaranarayanan, D.C. Khan, *J. Magn. Magn. Mater*. **1996**, *153*, 337–346.
[65] Y. Ikeda, C. Hara, T. Fujii, M. Sato, M. Inoue, *Jpn. J. Appl. Phys*. **1998**, Part 1, *22*, 249.
[66] Y.K. Hong, H.S. Jung, *J. Appl. Phys*. **1999**, *85*, 5549–5551.
[67] W. Krätchmer, K. Fostiropoulos, D.R. Huffman, *Chem. Phys. Lett*. **1990**, *170*, 167.
[68] S. Iijima, *Nature* **1991**, *354*, 56–58.
[69] C. Guerrer–Piécourt, Y. Bouar, A. Loiseau, H. Pascard, *Nature*. **1994**, *372*, 761–765.
[70] M. Terrones, J.P. Hare, K. Hsu, H.W. Kroto, A. Lappas, W.K. Maser, A.J. Pierik, K. Prassicles, R. Taylor, D.R.M. Walton, *Proc. Electrochem. Soc.*(*Proc. of the Symp. on Recent Advances in Fullerenes and Related Mater*.) **1995**, *95–10*, 599–620.
[71] E.M. Brunsmen, S. Anna, S. Majetic, M.E. McHenry, *Mater. Res. Soc. Symp. Proc.*. **1995**, *359*, 35–40.
[72] S.A. Majetich, J.H. Scott, E.M. Brunsman, S. Kirkpatrick, M.E. McHenry, D.C. Winkler, *Proc. Electrochem. Soc*. **1995**, *95–10*, 584–598.
[73] Y.S. Grushko, S.G. Kolesnik, T.M. Pershikova, A.E. Sovestnov, V.V. Voronin, V.F. Materov, V. K. Sobolevskii, *Proc. Electrochem. Soc*. **1995**, *95–10*, 648–653.
[74] S.C. Tsang, Y.K. Chem, P.J.F. Harris, M.L.H. Green, *Nature* **1994**, *372*, 159–162.
[75] a) P.M. Ajayan, S. Iijima, *Nature*. **1993**, *361*, 333–334; b) P.M. Ajayan, T.W. Ebbeseu, T. Ichihashi, S. Iijima, K. Tanigaki, H. Hiura, *Nature* **1993** *362*, 522–525.
[76] P.M. Ajayan, O. Stephan, P. Redlich, C. Colliex, *Nature* **1995**, *375*, 564–567.
[77] K. Parvin, S.P. Weathersby, S. Awadallah, R. LaDuca, R.S. Ruoff, S. Subramoney, P. Van Kavelaar, P.E. Nolan, J. Jiao, *Proc. Electrochem. Soc*. **1995**, *95–10*, 570–83.
[78] V.P. Dravid, J.J. Host, M.H. Teng, B.R. Elliott, J.H. Hwang, D.L. Johnson, T.O. Mason, J.R. Weertman, *Nature*. **1995**, *374*, 602.
[79] J.H. Hwang, V.P. Dravid, M.H. Teng, J.J. Host, B.R. Elliott, D.L. Johnson, T.O. Mason, *J. Mater. Res*. **1997**, *12*, 1076–1082.
[80] C. Cheung, U. Erb, *Novel Tech. Synth. Process. Adv. Mater. Proc. Symp*. (Eds. J. Singh, S.M. Copley), Minerals, Metals & Materials Society Publishers, Warrendale, **1994**, 455–463.
[81] U. Erb, *Can. Metall. Q*. **1995**, *34*, 275–280.
[82] C. Cheung, P. Nolan, U. Erb, *Mater. Lett*. **1994**, *20*, 135–138.
[83] C. Cheung, P. Nolan, U. Erb, *Scr. Metall. Mater*. **1994**, *31*, 735–740.
[84] J.L. Delplancke, O. Bouesnard, J. Reisse, R. Winand, *Mat. Res. Soc. Symp. Proc. Vol. 451*, **1997**, 383–388.
[85] J.S. Benjamin, *Metall. Trans. A*. **1970**, *1*, 217.
[86] S.S. Saxena, J. Tang, Y.-S. Lee, C.J. O'Connor, *J Appl. Phys*. **1994**, *76*, 6820–6822.
[87] T. Aizawa, Z. Cheng, K. Tokumitsu, J. Kihara, *Ceram. Eng. Sci. Proc*. **1997**, *18*, 593–600.
[88] Z. Cheng, T. Aizawa, K. Tokumitsu, K. Tatsuzawa, J. Kihara, *Mater. Sci. Forum*. **1998**, *269–272*, 913–918.
[89] H.G. Jiang, H.M. Hu, E.J. Lavernia, *J. Mater. Res*. **1999**, *14*, 1760–1770.
[90] A. Corris, G. Ennas, A. Musinu, G. Paschina, D. Zedda, *J. Mater. Res*. **1997**, *12*, 2767–2772.
[91] L. Cao, A. Handstein, W. Gruenberger, H.-D. Bauer, K.-H. Mueller, L. Schultz, *Rare–Earth Magnets Their Appl., Proc. Int. Workshop*, 14^{th} (Ed. F.P. Missell), World Scientific, Singapore, **1996**, pp. 57–66.

[92] P.G. McCormick, W.F. Miao, P.A.I. Smith, J. Ding, R. Street, *J. Appl. Phys*. **1998**, *83*, 6256–6261.
[93] P.A.I. Smith, P.G. McCormick, R. Street, *Mater. Sci. Forum*. **1995**, *179–181*, 527–532.
[94] K. Raviprasad, S. Kakoo, K. Makita, M. Umemoto, *Funtai oyobi Funmatsu Yakin*. **1996**, *43*, 634–639.
[95] W.F. Miao, P.G. McCormick, R. Street, J. Appl. Phys., **1996**, *79*, 2079.
[96] D. Arcos, N. Rangavittal, M. Vazquez, M. Vallet–Regi, *Mater. Sci. Forum*. **1998**, *269–272*, 87–92.
[97] D. Arcos, R. Valenzuela, M. Vazquez, M. Vallet–Regi, *J. Solid State Chem*. **1998**, *141*, 10–16.
[98] V. Sepelak, U. Steinike, D.C. Uecker, S. Wibmann, K.D. Becker, *J. Solid State Chem*. **1998**, *135*, 52–58.
[99] G.F. Goya, H.R. Rechenberg, J.Z. Jiang, *J. Appl. Phys*. **1998**, *84*, 1101–1108.
[100] R.F. Ziolo, E.P. Giannelis, B.A. Weistein, M.P. O'Horo, B.N. Ganguly, V. Mehrotra, M.W. Russell, D.R. Huffman, *Science* **1992**, *257*, 219–223.
[101] F.M. Winnik, A. Morneau, R.F. Ziolo, H.D.H. Stover, W.H. Li, *Langmuir* **1995**, *11*, 3660–3666.
[102] B.H. Sohn, R.E. Cohen, *Chem. Meter*. **1997**, *9*, 264–269.
[103] E. Kroll, F.M. Winnik, *Chem. Mater*.**1996**, *8*, 1594–1596.
[104] T. Bein, in *Supramolecular Architecture in Two and Three Dimensions* (Ed. T. Bein), American Chemical Society, Washington, D.C., **1992**, *499*, 274–293, and references therein.
[105] H.M. Ziethen, H. Winkler, A. Schiller, V. Schuenemann, A.X. Trautwein, A. Quazi, F. Schmidt, *Catal. Today* **1991**, *8*, 427–438.
[106] I. Hussain, I. Gameson, P.A. Anderson, M. Slaski, P.P. Edwards, A. Dyer, *J. Chem. Soc., Dalton Trans*. **1996**, *5*, 775–81.
[107] J.L. Garcia, F.J. Lazaro, C. Martinez, A. Corma, *J. Magn. Magn. Mater*. **1995**, *140–144*, 363–364.
[108] T. Abe, Y. Tachibana, T. Uematsu, M. Iwamoto, *J. Chem. Soc. Chem. Commun*. **1995**, 1617–1618.
[109] V. Schunemann, H. Winkler, H.M. Ziethen, A. Schiller, A.X. Trautwein, in *Studies of Magnetic Properties of Fine Particles and Their Relevance to Materials Science* (Eds. J.L. Dormann, D. Fiorani), Elsevier Science Publishers, The Netherlands, **1992**, 371–380.
[110] A. Butera, J.L. Weston, J.A. Barnard, *J. Appl. Phys*. **1997**, *81*, 7432.
[111] H. Gleiter, *Mater. Sci. Forum*. **1995**, *189/190*, 67.
[112] D.L. Leslie–Pelecky, R.D. Rieke, *Chem. Mater*. **1996**, *8*, 1770.
[113] D.D. Awschalom, D.P. DiVincenzo, J.F. Smyth, *Science* **1992**, *258*, 414.
[114] X.X. Zhang, J.M. Hernandez, J. Tejada, R.F. Ziolo, *Phys. Rev. B*. **1996**, *54*, 4101.
[115] J. Zhang, R. Ziolo, E.C. Kroll, X. Bohigas, J. Tejada, *J. Magn. Magn. Mater*. **1995**, *140/144*, 1853.
[116] M. Friedman, P. Sarachik, J. Tejada, R. Ziolo, *Phys. Rev. Lett*. **1996**, *76*, 3830.
[117] D. Gatteschi, A. Caneschi, L. Pardi, R. Sessoli, *Science* **1994**, *265*, 1054.
[118] B. Barbara, W. Wernsdorfer, *Curr. Opin. Solid State Mater. Sci*. **1997**, *2*, 220.
[119] H. De Raedt, S. Miyashita, K. Saito, D. García–Pablos, N. García, *Phys. Rev. B*. **1997**, *56*, 11761.
[120] R.D. Shull, U. Atzmony, A.J. Shapiro, L.J. Swartzendruber, L.H. Bennett, W.J. Green and K. Moorjani, *J. Appl. Phys*. **1988**, *63*, 4261.
[121] T.A. Yamamoto, R.D. Shull, P.R. Bandaru, F. Cosandey, H.W. Hahn, *Jpn. J. Appl. Phys*. **1994**, *33*, L1301.

[122] T.A. Yamamoto, R.D. Shull, H.W. Hahn, *Nanostruct Mater*. **1997**, *9*, 539.
[123] Y. Yoshizawa, H. Mori, S. Arakawa, K. Yamauchi, *Nippon Oyo Jiki Gakkaishi*. **1995**, *19*, 457.
[124] E.E. Carpenter, C. Sangregorio, C.J. O'Connor, *IEEE Transactions on Magnetics*. **1999**, *35*, 3496–3498.
[125] H. Poppa, E. Bauer, H. Pinkvos, *MRS Bull*. **1995**, *20*, 38.
[126] F. Bodker, S. Morup, *Nucl. Instrum. Methods Phys. Res., Sect. B*. **1996**, *108*, 413.
[127] T. Rasing, *J. Magn. Magn. Mater*. **1997**, *175*, 35.
[128] R.P. Cowburn, D.K. Koltsov, A.O. Adeyeye, M.E. Welland, *Appl. Phys. Lett*. **1998**, *73*, 3947.
[129] R. Schad, S.M. Jordan, M.J.P. Stoelinga, M.W.J. Prins, R.H.M. Groeneveld, H. van Kempen, H.W. van Kesteren, *Appl. Phys. Lett*. **1998**, *73*, 2669.
[130] J.A. Sidles, J.L. Garbini, K.J. Bruland, D. Rugar, O. Züger, S. Hoen, C.S. Yannoni, *Rev. Modern Phys*. **1995**, *67*, 249.
[131] J. Frenkel, J. Dorfman, *Nature*. **1930**, *126*, 274.
[132] E.C. Stoner, E.P. Wohlfarth, *Proc. Phys. Soc. A*, **1948**, *240*, 599.
[133] A. Holz, C. Scherer, *Phys. Rev. B*, **1994**, *50*, 6209.
[134] R. Hertel, H. Kronmuller, *J. Appl. Phys*. **1999**, *85*, 6190.
[135] J.G. Zhu, *MRS Bull*. **1995**, *20*, 49.
[136] J. Zhu, X. Ye, *Trans. Mater. Res. Soc. Jpn*. **1994**, *15B*, 881.
[137] S.T. Chui, D.C. Tian, *J. Appl. Phys*. **1995**, *78*, 3965.
[138] D.J. Sellmeyer, *Nanophase Materials*, (Eds. G.C. Hadjipanayis, R.W. Siegel) Kluwer Academic Publishers, Netherlands, **1994**, p. 537.
[139] Y.J. Wang, *J. Magn. Soc. Jpn*., **1993**, *17*, Suppl. S1, 294.
[140] D.J. Sellmeyer, R.D. Kirby, J. Chen, K.W. Wierman, J.X. Shen, Y. Liu, B.W. Robertson, S.S. Jaswal, *J. Phys. Chem. Solids*. **1995**, *56*, 1549.
[141] J. Brown, *Sensors*, **1994** (September), 42.
[142] J.S. Moodera, L.R. Kinder, T.M. Wong, R. Meservey, *Phys. Rev. Lett*. **1995**, *74*, 3273.
[143] T. Miyazaki, N. Tezuka, *J. Magn. Magn. Mater*. **1995**, *139*, L231.
[144] H. Fujimori, S. Mitani,*J. Appl. Phys*. **1996**, *79*, 4733.
[145] C.L. Platt, B. Dieny, A.E. Berkowitz, *J. Appl. Phys*. **1997**, *81*, 5523.
[146] S. Sankar, A.E. Berkowitz, D.J. Smith, *Appl. Phys. Lett*. **1998**, *73*, 535.
[147] T. Yogi, T.A. Nguyen, *IEEE Trans. Mag*. **1993**, *29*, 307.
[148] J. Li, M. Mirzamaani, X. Bian, M. Doerner, D. Duan, K. Tang, M. Toney, T. Arnoldussen, M. Madison, *J. Appl. Phys.*, **1999**,*85*, 4286.
[149] C. Tsang,*Proc. IEEE*. **1993**, *81*, 1344, and references therein.
[150] R. Coffey, M.A. Parker, J. K. Howard, *IEEE Trans. Mag*. **1995**, *31*, 2737.
[151] R.F.C. Farrow, D. Weller, R.F. Marks, M.F. Toney, A. Cebollada, G.R. Harp, *J. Appl. Phys*. **1996**, *79*, 5967.
[152] S. Stavroyiannis, I. Panagiotopoulos, D. Niarchos, J.A. Christodoulides, Y. Zhang, G.C. Hadjipanayis, *Appl. Phys. Lett*. **1998**, *73*, 3453.
[153] L. Maya, T. Thundat, J.R. Thompson, R.J. Stevenson, *Appl. Phys. Lett*. **1995**, *67*, 3034.
[154] D.N. Lambeth, E.M.T. Velu, G.H. Bellesis, L.L. Lee, D.E. Laughlin, *J. Appl. Phys*. **1996**, *79*, 4496.
[155] S.Y. Chou, P.R. Krauss, L. Kong, *J. Appl. Phys*. **1996**, *79*, 6101.
[156] S.Y. Chou, P.R. Krauss, *J. Appl. Phys*. **1996**, *79*, 5066.
[157] J.M. Daughton, *Thin Solid Films*,**1992**, *216*, 162.
[158] E.P. Giannelis, V. Mehrotra, J.K. Vassiliou, R.D. Shull, R.D. MacMichael, R.F. Ziolo, R.F., *Nanophase Materials, NATO ASI Series E, Vol 260*, (Eds. S.C. Hadjipanayis, R.W. Siegel), Kluwer Academic Publishers, Netherlands, **1994**, pp. 617–623.

[159] J.N. Huiberts, R. Griessen, J.H. Rector, R.J. Wijngaarden, J.P. Dekker, D.G. de Groot, N.J. Koeman, *Nature*. **1996**, *380*, 231.
[160] G.G. Bush, *J Appl. Phys*. **1993**, *73*, 6307.
[161] G.G. Bush, *J. Appl. Phys*., **1993**, *73*, 6310.
[162] H. Yoshimatsu, T. Narutani, *Jpn. Patent*, 83819, **1991**.
[163] Y. Kimura, A. Makino, A. Inoue, T. Masumoto, *Nippon Oyo Jiki Gakkaishi*. **1994**, *18*, 805.
[164] H. Fukunaga, *Nippon Oyo Jiki Gakkaishi*. **1995**, *19*, 791.
[165] R. Skomski, J.M. Coey, *Phys. Rev. B*, **1993**, *48*, 15812.
[166] E.F. Kneller, R. Hawig, *IEEE Trans. Magn*. **1991**, *27*, 3588.
[167] M. Umemoto, J. Yien, S. Kakoo, K. Raviprasad, I. Okane, S. Hirosawa, *Funtai oyobi Funmatsu Yakin*, **1995**, *42*, 16.
[168] R.D. Shull, R.D. McMichael, J.J. Ritter, L.H. Bennett, *Mater. Res. Soc. Symp. Proc*. **1993**, *286*, 449.
[169] R.D. McMichael, J.J. Ritter and R. D. Shull, *J. Appl. Phys*. **1993**, *73*, 6946.
[170] V.K. Pecharsky, K.A. Gschneidner, Jr., *Appl. Phys. Lett*. **1997**, *70*, 3299.
[171] J. Mannhart, J; *Phil. Trans. R. Soc. Lond. A*. **1995**, *353*, 377.
[172] B.M. Berkovsky, V.F. Medvedev, M.S. Krakov, *Magnetic Fluids, Engineering Applications*, Vol 1, Oxford University Press, New York, **1993**.
[173] S. Maruno, K. Yubakami, N. Soga, *J. Magn. Magn. Mater*. **1987**, *39*, 187.
[174] Q. Liu, Z. Xu, *J. Appl. Phys*. **1996**, *79*, 4702.
[175] M.E. McHenry, S.A. Majetich, E.M. Kirkpatrick, *Mater. Sci. Eng. A*. **1995**, *204*, 19.
[176] N.T. Nuhfer, M. DeGraef, M.E. McHenry, S.A. Majetich, J.O. Artman, S.W. Staley, *Electron Microsc. Proc. Int. Congr. Electron Microsc*., Vol 2A, 13th, (Eds. B. Jouffrey, C. Colliex), Editions de Physique, Les Ulis, France, **1994**, pp. 313.
[177] F.C. Meldrum, B.R. Heywood, S. Mann, *Science*. **1992**, *257*, 522.
[178] D.P.E. Dickson, *Nanophase Materials, NATO ASI Series E, Vol 260*, (Eds. S.C. Hadjipanayis, R.W. Siegel), Kluwer Academic Publishers, Netherlands, **1994**, p. 729.
[179] R.B. Frankel, R.P. Blakemore, *Bioelectromagnetics*. **1989**, *10*, 223.
[180] S. Winoto–Morbach, W. Mueller–Ruchholtz, *Eur. J. Pharm. Biopharm*. **1995**, *41*, 55.

Magnetism: Molecules to Materials III. Edited by J.S. Miller and M. Drillon

ISBNs: 3-527-30302-2 (Hardback); 3-527-60014-0 (Electronic)

2 Magnetism and Magnetotransport Properties of Transition Metal Zintl Isotypes

Susan M. Kauzlarich, Amy C. Payne, and David J. Webb

2.1 Introduction

Novel magnetic and electronic properties discovered in transition metal Zintl compounds crystallizing in the $Ca_{14}AlSb_{11}$ structure [1] will be the topic of this chapter. Zintl phases are made up of electropositive elements, typically alkali or alkaline earth elements, that donate electrons to more electronegative elements, typically group 13, 14, and 15 elements [2]. In this definition, the cations function as simple electron donors to the anionic substructure.

Motivated by the intriguing structures of this type of compound, we sought to discover new compounds that could be prepared at the metal–insulator boundary [2–4]. With this approach to synthesizing new compounds, $Ca_{14}MnBi_{11}$ was discovered [5]. It is isostructural with $Ca_{14}AlSb_{11}$, crystallizing in the tetragonal crystal system with space group $I4_1/acd$, and has ferromagnetic ordering at 56 K. The structure of this compound consists of isolated Ca^{2+} cations, discrete $MnBi_4^{9-}$ tetrahedra, Bi_3^{7-} linear anions, and isolated Bi^{3-} anions. A similar description had already been provided for $Ca_{14}AlSb_{11}$ [1]. Theoretical calculations are in agreement with the Zintl interpretation of the structure [6]. Much of our work has focussed on Mn analogs of the $Ca_{14}AlSb_{11}$ phase because of the unexpected ferromagnetic ordering observed in these phases. Mn containing compounds prepared to date are of the formula, $A_{14}MnPn_{11}$ (A = Ca, Sr, Ba, Eu, Yb; Pn = P, As, Sb, Bi) [2, 3, 5, 7–18]. The reason that magnetic ordering is surprising is that in this type of structure the Mn atoms are approximately 10 Å apart.

With the Zintl description of the structure, one expects localized d electrons and no possibility of magnetic ordering through orbital superexchange. In these phases, however, all the Sb and Bi compounds and $Eu_{14}MnAs_{11}$ and $Eu_{14}MnP_{11}$ have long-range magnetic order. The highest transition temperature has been observed for $Eu_{14}MnSb_{11}$ which has ferromagnetic ordering at approximately 92 K. Because of the large distances between Mn atoms and the absence of any covalent bonds between them, the magnetic coupling has been attributed to a Ruderman–Kittel–Kasuya–Yosida (RKKY) interaction between localized moments via conduction electrons [2, 15, 17, 19]. In addition, large magnetoresistance has been discovered in some of these compounds [13, 14, 16], and they can be classified as colossal magnetoresistance (CMR) materials because they have a large magnetoresistance effect coincident with the magnetic ordering temperature [20, 21].

2.2 Structure

The structure of $Ca_{14}AlSb_{11}$ has been discussed in detail [1]. We have also recently reviewed the Mn analogs of this structure type [2]. One formula unit of $Ca_{14}AlSb_{11}$ is best described as consisting of 14 Ca^{2+} + $AlSb_4^{9-}$ + Sb_3^{7-} + four Sb^{3-}. The Ca^{2+} cations and the Sb^{3-} anions are isolated – that is, these ions are not covalently bonded to any other atom in the structure. Many compounds have been synthesized with this type of structure (see Table 1).

Figure 1 shows the relative orientation of the two polyatomic units. Briefly, the MPn_4^{9-} tetrahedra (M = Al, Ga, Mn; Pn = pnictogen) and the Pn_3^{7-} linear chains alternate along the *c* axis. The chains are rotated by 90° relative to one another along the *c* axis. The chains and tetrahedra also alternate along the *a* and *b* axes, but are translated by a full unit-cell dimension along these directions (Fig. 2). This

Table 1. Compounds of the $Ca_{14}AlSb_{11}$ structure type with important distances and angles.

Compound	M–Pn distance (Å)	Pn–M–Pn angle (°)	Mn···Mn distance (Å)	Ref.
$Ba_{14}MnP_{11}$	–	–	–	–
$Ba_{14}MnAs_{11}$	–	–	–	–
$Ba_{14}MnSb_{11}$	2.872	118.7, 105.1	10.991	19
$Ba_{14}MnBi_{11}$	2.935	119.9, 104.5	11.128	19
$Sr_{14}MnP_{11}$	–	–	–	–
$Sr_{14}MnAs_{11}$	2.683	114.7, 106.9	9.970	19
$Sr_{14}MnSb_{11}$	2.838	115.9, 106.4	10.519	19
$Sr_{14}MnBi_{11}$	2.889	118.7, 105.0	10.658	19
$Eu_{14}MnP_{11}$ -	–	–	–	
$Eu_{14}MnAs_{11}$ -	–	–	–	
$Eu_{14}MnSb_{11}$	2.790	118.6, 105.1	10.352	10
$Eu_{14}MnBi_{11}$	2.862	119.5, 104.7	10.532	15
$Ca_{14}MnP_{11}$	–	–	–	–
$Ca_{14}MnAs_{11}$	2.603	113.4, 107.5	9.471	19
$Ca_{14}MnSb_{11}$	2.759	115.3, 106.6	10.030	19
$Ca_{14}MnBi_{11}$	2.814	118.0, 105.4	10.183	8
$Yb_{14}MnP_{11}$	–	–	–	–
$Yb_{14}MnAs_{11}$	–	–	–	–
$Yb_{14}MnSb_{11}$	2.750	117.5, 105.6	9.954	17
$Yb_{14}MnBi_{11}$	2.803	119.4, 104.7	10.155	17
$Ba_{14}InP_{11}$ *	2.71	114.2, 107.1	–	22
$Sr_{14}GaAs_{11}$	2.613	114.7, 106.9	–	23
$Ca_{14}GaAs_{11}$	2.546	113.0, 107.8	–	24
$Ca_{14}AlSb_{11}$ *	2.718	114.0, 107.3	–	25
$Sr_{14}AlSb_{11}$	2.833	114.6, 107.0	–	25
$Ba_{14}AlSb_{11}$	2.799	117.9, 105.4	–	25

All the data are from low-temperature single-crystal X-ray diffraction except those compounds marked *, which were obtained from room-temperature single-crystal diffraction data.

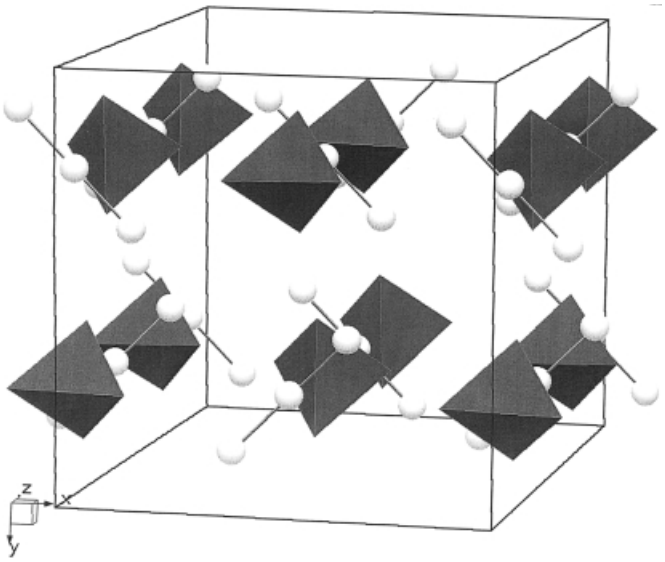

Fig. 1. A view of the unit cell along the *c* axis of $A_{14}MnPn_{11}$ (A = alkaline earth, Pn = pnictogen) with only the $MnPn_4$ tetrahedra and the Pn_3 units indicated.

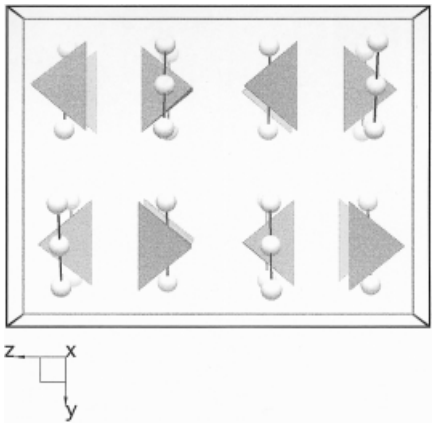

Fig. 2. A view of the unit cell along the *a* axis of $A_{14}MnPn_{11}$ (A = alkaline earth, Pn = pnictogen) with only the $MnPn_4$ tetrahedra and the Pn_3 units indicated.

figure shows the Pn_3^{7-} unit as being symmetric, but many of the As and P analogs are asymmetric [22–24, 26]. This effect is strongly related to the size of the atoms, in particular the radius of the cation and, therefore, the size of the cation cage that envelops the Pn_3^{7-} unit controls the symmetry of the linear unit.

The isolated Pn^{3-} anions are situated between the Pn_3^{7-} linear anion and the MPn_4^{9-} tetrahedron. These anions are located along fourfold screw axes and form spirals coincident with the *c* axis in the unit cell. These atoms seem to form loosely associated pairs within the spiral. The Pn···Pn distances within the spiral are considerably longer than any bonding interactions observed in other compounds; they are,

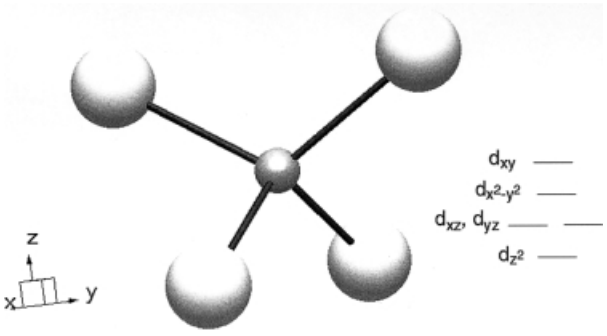

Fig. 3. A view of the tetrahedral unit showing the compression along the z axis with the proposed crystal-field splitting diagram.

therefore, not considered to be bonded. The isolated Pn^{3-} anion has seven cations in a distorted deltahedron.

The $MnPn_4^{9-}$ tetrahedron is compressed along the a–b plane compared with the main group analogs. This statement is true irrespective of the nature of the A^{2+} cation or the identity of the main group element (M = Al, Ga, In) in the tetrahedron, MPn_4^{9-}. The larger distortion found in the $MnSb_4^{9-}$ tetrahedra is attributed to Jahn-Teller distortion, because the Mn is formally a d^4 ion; a possible crystal-field splitting diagram is shown in Fig. 3. Depending upon the amount of crystal-field splitting expected from an Sb^{3-} anion, the relative energies of the degenerate d_{xz} and d_{yz} orbitals might be higher than that of the $d_{x^2-y^2}$ orbital. In any case, high-spin behavior is expected, because ligand-field splittings for tetrahedral complexes are small.

This type of structure has also been described as hierarchically related to that of Cu_2O, with two interpenetrating frameworks [22]. In this view the O and Cu atoms are replaced by the metal-centered tetrahedra fused to A^{2+} cation-centered octahedra. The nearest neighbor Mn tetrahedra are linked through an A^{2+} cation. Figs. 4 and 5 show one of the interpenetrating networks, Fig. 4 with only the cation that join the tetrahedra via their corners and Fig. 5 with the octahedra joining the tetrahedra. Fig. 6 shows the spatial relationship of the Mn centered tetrahedra, the A^{2+} octahedra, and the Pn_3^{7-} linear units.

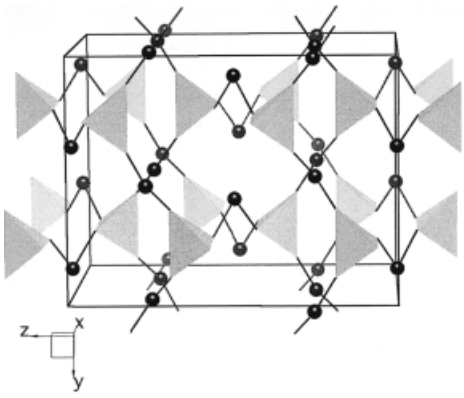

Fig. 4. A view showing the $MnPn_4^{9-}$ tetrahedra linked with A^{2+} cations.

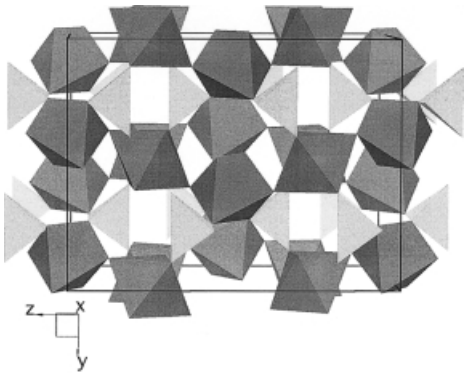

Fig. 5. A view showing the $MnPn_4^{9-}$ tetrahedra linked with APn_6 octahedra.

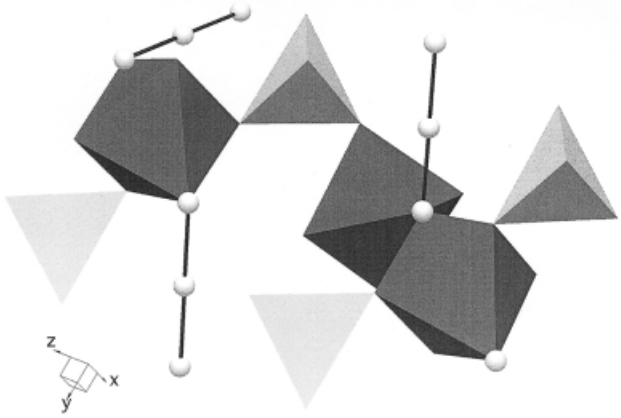

Fig. 6. A view of the spatial relationship between the A^{2+} octahedra, the tetrahedra, and the linear units.

The Eu series of compounds are the only compounds with two magnetic ions, Eu^{2+} and Mn^{3+}. In Figs. 7 and 8 the Eu^{2+} cation packing is shown in a zero-perspective view along the *c* axis and along the *b* axis. There is no simple description of the Eu^{2+} packing and one might expect fairly complex magnetic interactions.

2.3 Magnetism

Many of the magnetic properties of powder and polycrystalline samples of alkaline earth compounds have been reviewed elsewhere [2]; data relating to the high-temperature paramagnetic states and the low-temperature ordered states of these compounds were presented and discussed. Since that review, single-crystal samples of these alkaline earth compounds and single crystals of the newer rare earth analogs have been studied [13, 14, 18]. This chapter briefly summarizes the results presented in the past review for powder and polycrystalline material, and magnetism and elec-

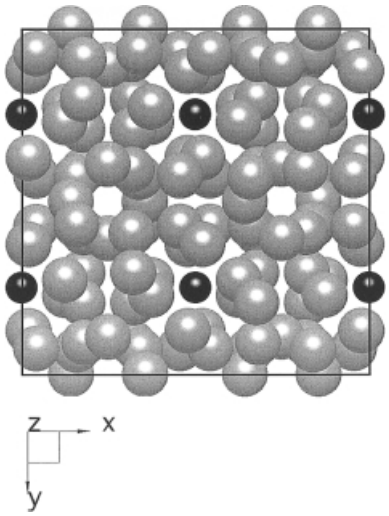

Fig. 7. A zero perspective along the a axis of the packing of the Eu^{2+} and Mn^{3+} cations (gray and black, respectively) in the unit cell.

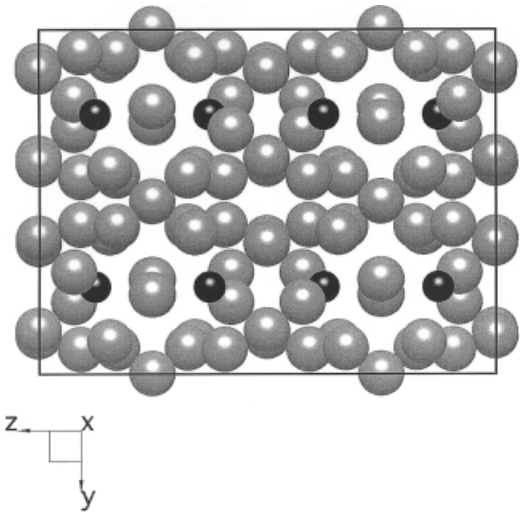

Fig. 8. A zero perspective along the *c* axis of the packing of the Eu^{2+} and Mn^{3+} cations (gray and black, respectively) in the unit cell.

tron transport for single crystals of the alkaline earth compounds and all the measurements for the rare earth compounds are presented and discussed in detail. Finally, some general conclusions about the microscopic mechanism of the colossal magnetoresistance (CMR) observed in these Zintl compounds will be presented, and the compounds will be compared with other CMR compounds.

2.3.1 Alkaline Earth Compounds

2.3.2 High-temperature Paramagnetic Susceptibility

Early magnetic measurements [8, 12, 19] on powders of $A_{14}MnPn_{11}$ materials (A = Ca, Sr, or Ba and Pn = As, Sb, or Bi) gave a clear picture of the general properties of the alkaline earth compounds. The molar susceptibilities at high temperature (generally $T > 100$–$150\,\mathrm{K}$) can be fit by the form $\chi(T) = \chi_0 + C/(T - \theta)$ which is the Curie–Weiss law plus a temperature-independent background. The values for the fitting parameters are given in Table 2.

The Curie constant can be used to identify the valence of the Mn ion by using the standard form [27] of the Curie constant for molar susceptibility:

$$C = \frac{N_A \mu_B^2 \mu_{eff}^2}{3k_B}$$

where N_A is Avogadro's number, μ_B is the Bohr magneton, k_B is Boltzmann's constant, and μ_{eff} is termed the "effective Bohr magneton number" of the ion and is given by $\mu_{eff}^2 = g^2 J(J+1)$, where g is the Lande g-factor and J is the total effective angular momentum of the ion. Examination of Table 2 shows that all these compounds have a value of μ_{eff} consistent with 4.9, which is appropriate for a high-spin Mn^{3+} ion with quenched orbital angular momentum. The values of μ_{eff} for Mn^{4+} and Mn^{2+}, for instance, are approximately 3.9 and 5.9, respectively, and are inconsistent with the experimental data. The second important property determined by the above fit for the molar susceptibility is the Weiss constant, θ. The Weiss constant is a measure of the strength of the exchange coupling [27] between pairs of Mn^{3+} local magnetic moments. The Weiss constant is nearly zero for the As compounds,

Table 2. Magnetic properties.

Compound	Ref.	C (emu K mol^{-1})	$\mu_{eff}(\mu_B)$	$\mu_{sat}(\mu_B)$	$\theta(K)$	Transition temperature (K)
$Sr_{14}MnAs_{11}$	19	3.5	5.1	–	–	–
$Ca_{14}MnAs_{11}$	19	3.3	5.2	–	–	–
$Ba_{14}MnSb_{11}$	19	3.0	4.9	2.2	18	20
$Sr_{14}MnSb_{11}$	19	3.6	5.4	3.3	40	45
$Ca_{14}MnSb_{11}$	19	3.3	5.2	2.7	62	65
$Yb_{14}MnSb_{11}$	17	3.04	4.92	–	48	56
$Eu_{14}MnSb_{11}$	15	88.9	27	102	95	92
$Ba_{14}MnBi_{11}$	8	2.9	4.8	2.9	17	15
$Sr_{14}MnBi_{11}$	8	3.1	5.0	2.7	38	33
$Ca_{14}MnBi_{11}$	8	2.9	4.8	2.5	50	55
$Yb_{14}MnBi_{11}$	17	3.1	4.9	–	51	60
$Eu_{14}MnBi_{11}$	15	85.3	26.1	–	45	32
$Eu_{14}InSb_{11}$	15	112	30	–	0.3	15
$Eu_{14}InBi_{11}$	15	114	30	–	-14	10

suggesting that these materials are simple Curie paramagnets with local magnetic moments that are not strongly coupled. On the other hand, Table 2 shows that for the Sb and Bi compounds the Weiss constant is relatively large (10–70 K) which implies that the Mn moments in these compounds are relatively strongly ferromagnetically coupled. This suggests that each of these compounds should become ferromagnetic at low temperature.

2.3.2.1 Low-temperature Magnetization

Ordered States and Transition Temperatures

Magnetization measurements [8, 12, 19] at low temperatures confirm that, with one exception, all of the alkaline earth analogs order ferromagnetically with the Curie temperature, T_C, near the Weiss constant, θ, as expected. The Curie temperatures are listed in Table 2. The exception is $Ba_{14}MnBi_{11}$ for which the peak in the low field susceptibility is interpreted as a transition to an antiferromagnetic ground state at a Néel temperature, T_N [12]. Figure 9 shows the dependence of magnetic susceptibility on temperature. There have been no magnetic structure determinations yet to verify this identification. A positive Weiss constant implies ferromagnetic coupling of the local moments. The existence of antiferromagnetic ordering in a material with a positive Weiss constant suggests there must be at least two sublattices of Mn ions and

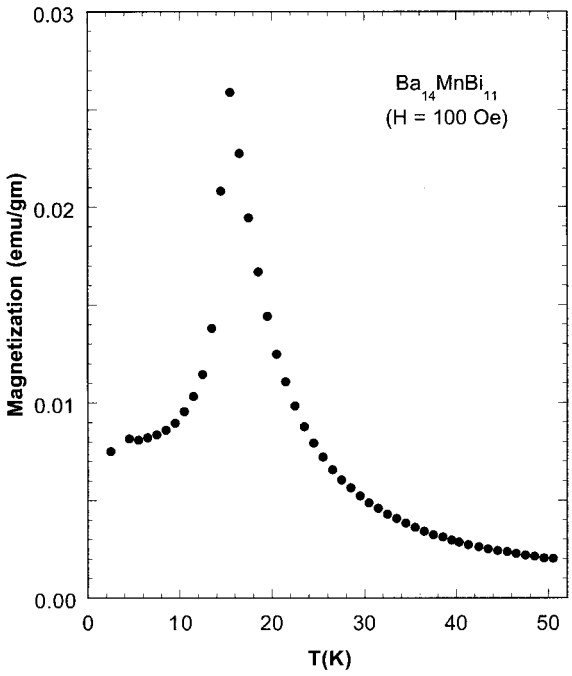

Fig. 9. Plot of magnetic susceptibility against temperature for $Ba_{14}MnBi_{11}$.

that there is strong ferromagnetic coupling between near-neighbor intrasublattice moments but that intersublattice moments are coupled antiferromagnetically [27]. Because the structures of all these compounds are the same, this would also imply that the intersublattice coupling in all alkaline earth Sb and Bi compounds of this structure type (except $Ba_{14}MnBi_{11}$) is ferromagnetic.

Ordered Magnetic Moments

For powdered samples of the ferromagnetic alkaline earth compounds, at $T = 5\,\mathrm{K}$, the magnetic field dependence of the magnetization, as seen elsewhere [7, 12, 19] and reviewed in Ref. [2], resembles that of a simple ferromagnet, except that the magnetization of these powder samples is difficult to saturate completely. The magnetization seems to be near saturation at a magnetic field, $H = 5\,\mathrm{T}$, however, and the ordered saturation moment corresponds to approximately $4\,\mu_\mathrm{B}$ for each Mn atom. This is the magnetic moment expected, $\mu_\mathrm{Mn} = gJ\mu_\mathrm{B}$, from a Mn^{3+} ion with four unpaired spins with their orbital angular momentum quenched, $g = 2$ and $J = 2$.

Magnetic Coupling

The Mn ions are very far apart (approximately 10 Å) and the electrons in these materials are all expected to have localized (bonding or atomic) filled orbitals. Magnetic exchange coupling depends on the overlap of wavefunctions, and the orbitals in these compounds should not overlap significantly. The Mn magnetic moments in the As compounds are weakly coupled. Measurement of the resistivity (to be discussed below) of the As compounds shows that they are semiconductors. How can this data be reconciled with the relatively strong ferromagnetic coupling of Mn moments in the Sb and Bi compounds? We will see that the Sb compounds are semimetals and the Bi compounds are poor metals so one looks to the spatially-extended wavefunctions of the conduction electrons in these materials to provide the magnetic exchange coupling.

The theory of magnetic exchange coupling mediated by conduction electrons [28–30] was worked out forty years ago by Ruderman, Kittel, Kasuya, and Yosida and is commonly called RKKY theory. The wavefunction of a conduction electron (generically an s-electron) overlaps that of the local unpaired electrons (generically a d-electron) so there will be an energy associated with the exchange of these two electrons. This exchange energy between the conduction electron and the local electron(s) is usually termed J_sd. This coupling causes magnetic polarization of the conduction electrons near a local moment that decays away as the distance from the local moment increases. The characteristic decay of the conduction electron polarization, assuming a spherical Fermi surface with Fermi wavevector, k_F, features a sinusoidal oscillation within an envelope function which is a power law decay [28]. The length scale over which the polarization oscillates is k_F^{-1}, and k_F also controls the power law decay. The neighbors of the local magnetic moment that causes the polarization experience the polarization through the same J_sd and so there is indirect coupling between each pair of local magnetic moments in a metal. This indirect

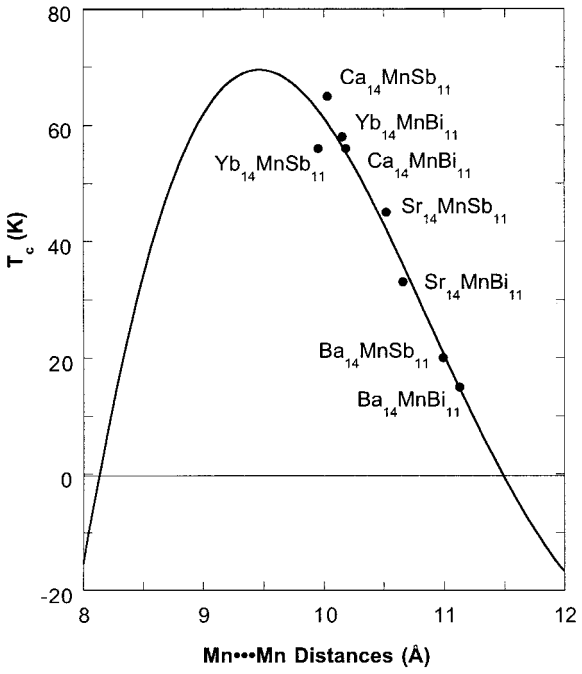

Fig. 10. T_C as a function of Mn–Mn distance for the $A_{14}MnPn_{11}$ compounds. The solid line is the calculated curve based on RKKY theory.

coupling [31] is given by:

$$J_{\mathrm{RKKY}}(r) = \frac{9\pi n^2 J_{\mathrm{sd}}^2}{E_{\mathrm{F}}} \left[\frac{(2k_{\mathrm{F}}r\ \cos(2k_{\mathrm{F}}r) - \sin(2k_{\mathrm{F}}r))}{(2k_{\mathrm{F}}r)^4} \right]$$

where n is the number density of conduction electrons, k_{F} is the Fermi wavevector, and E_{F} is the Fermi energy. The Fermi sea is isotropic in simple metals and, even though that is probably not true in these complex materials, an isotropic Fermi wavevector was used by Rehr et al. in their analysis of the magnetic exchange coupling [19]. Using the measured Mn–Mn distances and assuming that each Mn ion has ten Mn near-neighbors [19], the equation $\theta = 2zS(S+1)J_{\mathrm{RKKY}}(r = r_{\mathrm{nn}})/3k_{\mathrm{B}}$ was used for the Weiss constant where $S = 2$ is the Mn spin, z is the number of Mn near neighbors (10), r_{nn} is the near neighbor Mn–Mn distance, and $J_{\mathrm{RKKY}}(r)$ is given above. This function fits the data as shown in Fig. 10. The best fit is found with $k_{\mathrm{F}} \approx 5\,\mathrm{nm}^{-1}$, which means the conduction electron density is $n \approx 5 \times 10^{27}\,\mathrm{m}^{-3}$. It is interesting that this is very close to one charge carrier per Mn atom, but is also consistent with a small band overlap leading to a semimetal. If one uses $z = 10$ and the above estimate of the conduction electron density then the fit gives us a value for $3\pi S(S+1)J_{\mathrm{sd}}^2/E_{\mathrm{F}}$ of $5.5 \times 10^{-75}\,\mathrm{J\,m}^6$, which will be useful in quantitative discussion of the high-temperature resistivity.

Magnetic Anisotropy

Needle-like single crystals of $Sr_{14}MnSb_{11}$ have been grown, and the anisotropy of the magnetic state has been discussed [16]. In Fig. 11 the magnetic field-dependence of the magnetization of a single crystal of $Sr_{14}MnSb_{11}$ is shown in each of two orientations – with H applied parallel and perpendicular to the c-axis. The magnetic shape effect [32], because of the demagnetizing dipole field of a needle, would lead to the expectation that these crystals would be extremely easy to magnetize along the axis of the needle (the c-axis) and difficult to magnetize when the applied field is perpendicular to the axis of the needle. Exactly the opposite situation is found.

It is clear from Fig. 11 that $Sr_{14}MnSb_{11}$ has a magnetically hard axis along the c-axis; it is, therefore, referred to as an easy plane material. The magnetic anisotropy is large enough to override the shape effect in this instance. $Sr_{14}MnSb_{11}$ is difficult to categorize because it cannot be considered a soft ferromagnet where the shape anisotropy would dominate the field dependence of the magnetization, and it is not a useful candidate for a permanent magnet, because it saturates in relatively small (ca several T) magnetic fields and has an easy plane rather than an easy direction so the remanent magnetization (the magnetization remaining when the field is removed after saturation) is small. Similarly, $Ca_{14}MnSb_{11}$ has an easy plane perpendicular to the c-axis. The easy plane anisotropy of these compounds helps us understand the early work [7, 8] on hysteresis loops for powder samples. A powder material with random crystallite orientations will be very hard to saturate fully, because some crystals have their hard axis along the magnetic field. A powder sample will, on the

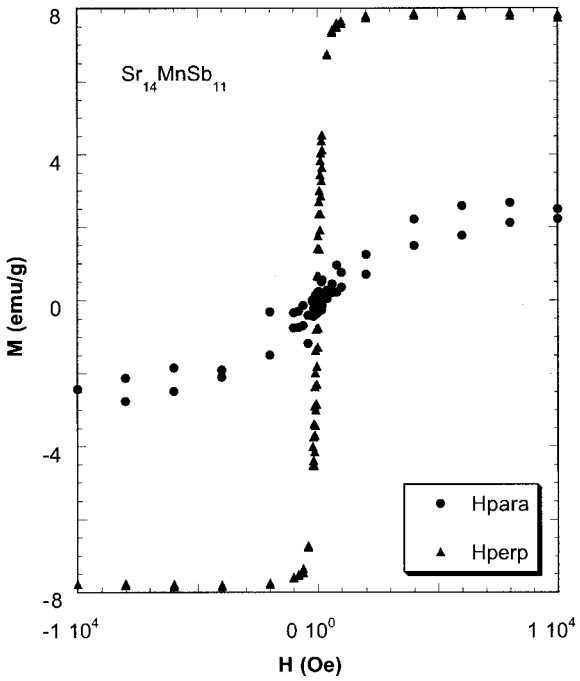

Fig. 11. Magnetization as a function of field at 5 K for $Sr_{14}MnSb_{11}$.

other hand, have a small coercive field, because the switching of the magnetization near zero field can always occur in a continuous fashion through the easy plane instead of the discontinuous change one sees in an easy axis (permanent magnet) material. In contrast with this result, we will see below that the Eu compounds are easy axis materials, with the easy axis along the c-axis, and that one of the Yb compounds seems to have a magnetic phase transition, where the c-axis changes from hard to easy as a function of temperature.

2.3.3 Ytterbium Compounds

2.3.3.1 High-temperature Paramagnetic Susceptibility

The Yb compounds made with Sb or Bi are quite similar [17] to the corresponding alkaline earth compounds. Fig. 12 shows the inverse magnetic susceptibility [17], χ^{-1}, as a function of temperature for $Yb_{14}MnSb_{11}$ and $Yb_{14}MnBi_{11}$. The high-temperature data are almost linear and can be fit to the equation $\chi(T) = \chi_0 + C/(T-\theta)$, furnishing the data listed in Table 2. The values of μ_{eff} derived from the Curie constants are, as for the alkaline earth compounds, consistent with one Mn^{3+} per formula unit. This result is consistent with the Yb ion having a valence of +2 which is also consistent both with structural analysis and with the result predicted by simple electron-counting considerations. The Weiss constants again imply ferromagnetic coupling and the values fall almost directly on the RKKY fit in Fig. 10, suggesting that the Yb does not significantly change the magnetic coupling or the underlying electronic state that gives rise to the indirect RKKY coupling. The inset to Fig. 12 shows the magnetization (at $H = 500$ Oe) for the two Yb compounds. A ferromagnetic transition occurs, and the Curie temperatures (T_C is marked by the inflection point in the plot of M against T) are given in Table 2. There is also an unusual discontinuity at approximately 28 K in the M–T data for $Yb_{14}MnBi_{11}$. The details of this anomaly will be discussed below in the section on single crystal magnetic anisotropy measurements.

2.3.3.2 Low-temperature Magnetization

Ordered States and Transition Temperatures

Magnetic field-dependent magnetization measurements for powder and single crystal samples of these two compounds have been reported [17]. The saturation magnetization measured for the powder sample was approximately 6 μ_B/Mn. This value is too large for Mn^{3+} alone but, because of the small concentration of Mn in these materials, it only takes a very small amount (approx. 2%) of an impurity phase containing Yb^{3+} to give this excess moment. This supposition was later supported by the results of Fisher et al. [18], who showed that large single crystals of $Yb_{14}MnSb_{11}$ had an ordered moment of approximately 4 μ_B (μ_{sat}) which is more consistent with Mn^{3+} and Yb^{2+}. This leads to the idea that the Yb compounds are magnetically similar to the alkaline earth compounds (except the antiferromagnetic $Ba_{14}MnBi_{11}$). The only distinct difference is in magnetic anisotropy.

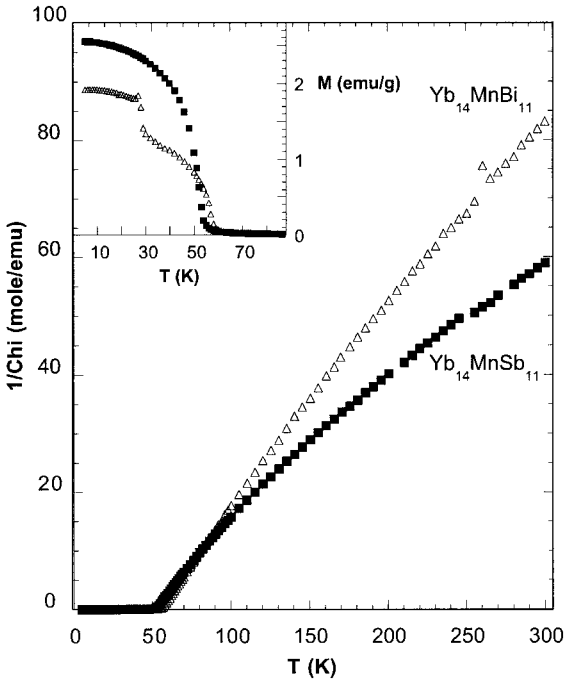

Fig. 12. Inverse susceptibility as a function of temperature for $Yb_{14}MnPn_{11}$ (Pn = Sb, Bi), $H = 1000$ Oe. The inset shows the low-temperature susceptibility as a function of temperature for $Yb_{14}MnPn_{11}$ (Pn = Sb, Bi).

Magnetic Anisotropy

Needle-shaped single crystals of $Yb_{14}MnSb_{11}$ and $Yb_{14}MnBi_{11}$ were grown in a temperature gradient from stoichiometric compositions [17], and much larger single crystals of $Yb_{14}MnSb_{11}$ have been grown from a Sn flux [18]. For the single crystals of Sb compound, the easy axis is along the *c*-axis. This is in contrast with the magnetically hard *c*-axis found in $Ca_{14}MnSb_{11}$ and $Sr_{14}MnSb_{11}$. The magnetic anisotropy of the Bi compound [17] is more complex, as shown in Fig. 13. At high temperatures ($T >$ 25 K) $Yb_{14}MnBi_{11}$ has a magnetically easy *c*-axis, similar to $Yb_{14}MnSb_{11}$, but at lower temperatures the *c*-axis becomes the hard direction with the *a*–*b* plane becoming a relatively easy plane, as one finds in $Ca_{14}MnSb_{11}$ and $Sr_{14}MnSb_{11}$. For this reason $Yb_{14}MnBi_{11}$ can be regarded as intermediate between the alkaline earth compounds and the other rare earth compounds (see Eu compounds below).

2.3.4 Europium Compounds

2.3.4.1 High-temperature Paramagnetic Susceptibility

The high-temperature paramagnetic behavior of $Eu_{14}MnSb_{11}$ and $Eu_{14}MnBi_{11}$ is also consistent with Eu^{2+} ions and Mn^{3+} ions [15]. Magnetization measurements [15] show that the Eu ions have the expected valence +2, so the f-shell is half filled – leading to an $S = 7/2$ spin state. This means that in these compounds

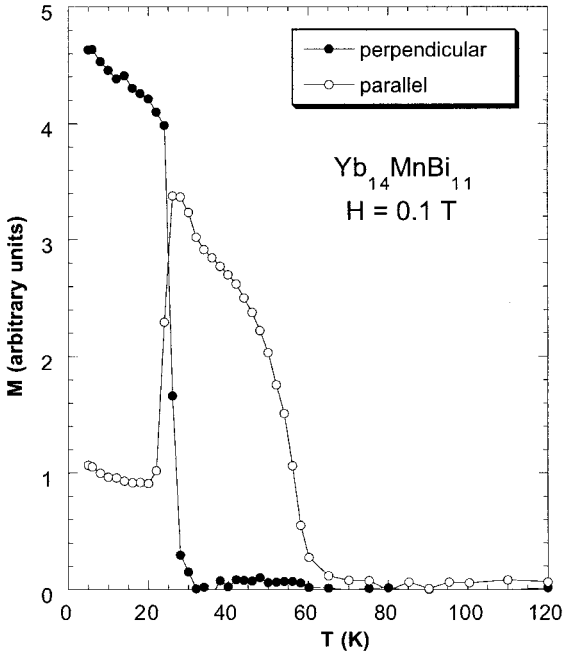

Fig. 13. Magnetization as a function of temperature for a single crystal of $Yb_{14}MnBi_{11}$ oriented with the c axis perpendicular and parallel to the applied magnetic field ($H = 1000\,\mathrm{Oe}$).

the 14 Eu atoms per formula unit are the major contributors to the bulk magnetic moment of the sample (see the effective moments in Table 2). Despite this large increase in the effective magnetic moment of the sample there is only a small increase in the magnetic coupling – implied by the θ values shown in the same table.

2.3.4.2 Antimony Compound

Ferromagnetic State

The temperature-dependence of the magnetization (Fig. 14) shows that $Eu_{14}MnSb_{11}$ orders ferromagnetically at approximately 92 K [10, 15]. This is close to the θ value obtained from the Curie–Weiss fit to the high-temperature data. This transition temperature is approximately 60 and 30° higher than the T_C values of $Sr_{14}MnSb_{11}$ and $Ca_{14}MnSb_{11}$, respectively [19]. Because this T_C is of the same order of magnitude as for the alkaline earth compounds, even though $Eu_{14}MnSb_{11}$ contains many more magnetic moments, it still seems reasonable, however, to suggest that the transition temperature is largely determined by the energy associated with Mn–Mn coupling. The increase in T_C as a result of the Eu can be explained as the effect of the (somewhat less dominant) energy associated with the Eu–Mn coupling. Single crystals of $Eu_{14}MnSb_{11}$ show that the c-axis is the easy magnetic direction [14]. This is similar to $Yb_{14}MnSb_{11}$ and $Yb_{14}MnBi_{11}$ (with $T > 25\,\mathrm{K}$), as discussed above.

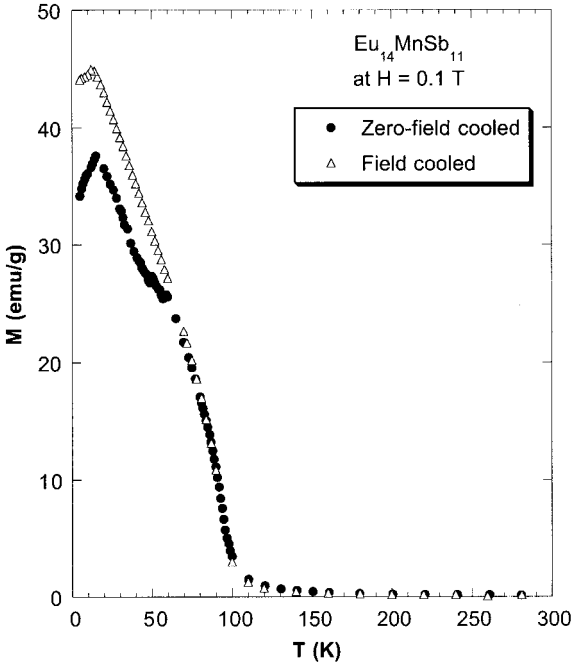

Fig. 14. Dependence of magnetic susceptibility on temperature for $Eu_{14}MnSb_{11}$.

The low-temperature ordered magnetic moment of $Eu_{14}MnSb_{11}$ is somewhat complicated because this low-T state apparently does not have simple ferromagnetic order [15] (see next section). Nevertheless a hysteresis loop at 5 K (Fig. 15) does show that, at the highest fields, the sample magnetization approaches saturation [15] with a net moment per formula unit of slightly more than 100 μ_B. This value is reasonable, because fully aligned lattices of Eu and Mn would lead to a magnetic moment of approximately 102 μ_B, assuming a g factor of 2.

Low-temperature Phase Transition and High-field Susceptibility

In addition to the ferromagnetic phase transition at 92 K, there is an anomaly [15], seen in Fig. 14 at approximately 15 K, which is suggestive of another magnetic phase transition. Measuring the magnetization at high magnetic fields reduces the ferromagnetic transition but leaves this low-T anomaly intact so that it is even more distinct. In addition, the temperature of the peak in the magnetization clearly drops with increasing magnetic field and extrapolates to zero temperature at approximately 15 Tesla. Both the peak in the magnetization and the temperature-dependence of the peak suggest there is underlying antiferromagnetic coupling in the Eu sublattice leading, perhaps, to a canted ferromagnetic state for $T < 15$ K which is difficult to saturate in a magnetic field (Fig. 15). The magnetic states for compounds such as $Eu_{14}InBi_{11}$ and $Eu_{14}InSb_{11}$ were studied and compared with their respective $Eu_{14}MnPn_{11}$ analogs, to determine the role of the underlying Eu–Eu sublattice [15].

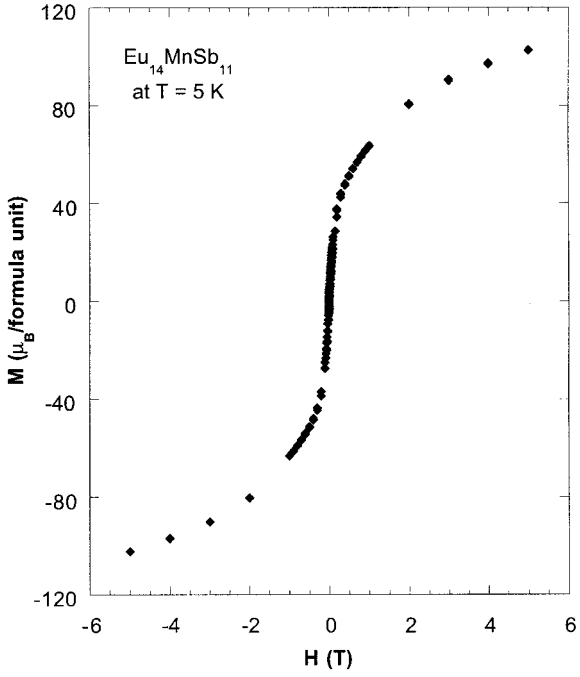

Fig. 15. Magnetic hysteresis loop for $Eu_{14}MnSb_{11}$ at 5 K.

In each of the $Eu_{14}MnPn_{11}$ compounds there is an apparent antiferromagnetic transition in the temperature range around 15 K, suggesting that the Eu–Eu sublattice in $Eu_{14}MnSb_{11}$ might, indeed, be forced to align ferromagnetically only because of the Eu-Mn coupling and the underlying Mn–Mn ferromagnetic state. Details of the spin alignment in $Eu_{14}MnSb_{11}$ will have to await direct measurement of the magnetic structure.

2.3.4.3 Bi Compound

There is apparently only one magnetic phase transition in $Eu_{14}MnBi_{11}$ [15] so one expects that both the Eu spins and the Mn spins take part in the order. Figure 16 [15] shows the magnetization for this compound as a function of temperature in several different magnetic fields. There is an apparent antiferromagnetic transition with the Neel temperature, T_N, equal to 32 K in zero magnetic field. The transition temperature decreases with applied magnetic field. This compound has the same general characteristics as $Ba_{14}MnBi_{11}$ discussed above – i. e. the Weiss constant suggests that the sample has strong ferromagnetic coupling but, instead of finding a ferromagnetic ground state, one finds a ground state that is apparently antiferromagnetic. One can argue [15] that the underlying Mn sublattice is antiferromagnetic in $Eu_{14}MnBi_{11}$ and $Ba_{14}MnBi_{11}$ and that in the Eu compound the Eu spins order at the same temperature, because the lowest energy state of the Eu sub-

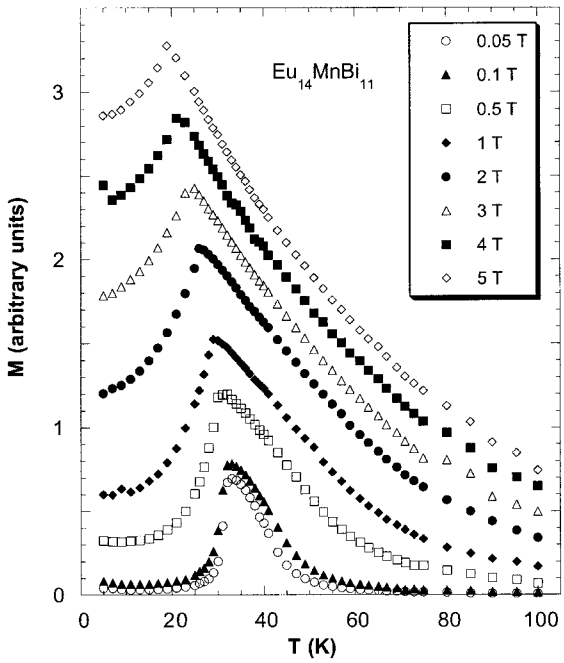

Fig. 16. Plot of magnetic susceptibility against temperature as a function of applied field for a single crystal of $Eu_{14}MnBi_{11}$ with the c axis of the crystal oriented parallel to the applied magnetic field.

lattice is apparently antiferromagnetic in all the Zintl compounds that have been studied.

2.4 Heat Capacity

Some heat-capacity measurements have been made on powder samples (pressed pellets) of $Sr_{14}MnBi_{11}$ and $Ba_{14}MnBi_{11}$ [11] and single crystals of $Yb_{14}MnSb_{11}$ [18] at low temperatures and at zero applied magnetic field. Each of the measurements can be fit with a model which includes conduction electrons, phonons, and the magnetic transition. These measurements yield an electron effective mass between $20\,m_e$ and $40\,m_e$ (the spread in values depends mostly on the fitting procedure used) and a Debye temperature of approximately 120–160 K. The conduction electrons are, therefore, somewhat heavy (the effective mass of the conduction electrons in pure Mn is also somewhat high, approximately $10\,m_e$) but certainly not on the scale of the heavy Fermion compounds which can have effective masses of approximately $1000\,m_e$.

2.5 Magnetotransport

2.5.1 Alkaline Earth and Ytterbium Compounds

2.5.1.1 Resistivity in Zero Magnetic Field

In the discussion of magnetic coupling conduction electrons were proposed as the most likely intermediary between the Mn magnetic local moments. The question of the presence of conduction electrons can, of course, only be definitively answered by more direct means, for example measuring the resistivity and extrapolating to lowest temperatures. Figure 17 shows data from Refs [7], [8], [18], and [19] for the temperature-dependence of the resistivity, ρ, of all of the alkaline earth and Yb compounds.

These data have several distinctive features. Firstly, the resistivity of all the As compounds diverges at low-T, showing they are semiconductors. Secondly, all the other compounds apparently have conduction electrons because the low-temperature resistivity always extrapolates to a finite value. Some of these compounds, however,

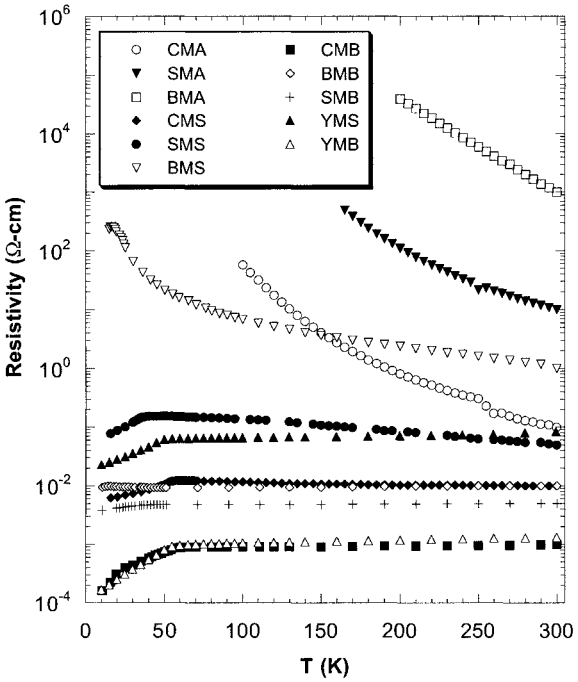

Fig. 17. Temperature dependent resistivity of the alkaline earth compounds and for Yb compounds. CMA = $Ca_{14}MnAs_{11}$, SMA = $Sr_{14}MnAs_{11}$, BMA = $Ba_{14}MnAs_{11}$, CMS = $Ca_{14}MnSb_{11}$, SMS = $Sr_{14}MnSb_{11}$, BMS = $Ba_{14}MnSb_{11}$, CMB = $Ca_{14}MnBi_{11}$, BMB = $Ba_{14}MnBi_{11}$, SMB = $Sr_{14}MnBi_{11}$, YMS = $Yb_{14}MnSb_{11}$, YMB = $Yb_{14}MnBi_{11}$.

have low-T regions in the data in which $d\rho/dT$ is positive and high-T regions in which $d\rho/dT$ is negative. For the purposes of this discussion we will usually refer to the material as metallic when $d\rho/dT$ is positive, as it is in most metals, and semiconducting (or semimetallic) when $d\rho/dT$ is negative as it is in any insulator as the resistivity diverges at $T = 0$. $Yb_{14}MnBi_{11}$, $Yb_{14}MnSb_{11}$, $Sr_{14}MnBi_{11}$, and $Ca_{14}MnBi_{11}$ are, therefore, all metallic over the entire range of T below 300 K. The high-temperature ($T > T_C$) resistivity of each of these compounds is almost independent of T and the low-temperature ($T < T_C$) resistivity decreases as T is reduced. $Ba_{14}MnBi_{11}$, $Sr_{14}MnSb_{11}$, $Ca_{14}MnSb_{11}$, and $Ba_{14}MnSb_{11}$, on the other hand, are semiconducting (or semimetallic) at high T and their resistivities change to metallic when $T < T_C$. In general, in each case in which there is magnetic order, the resistivity is smallest and $d\rho/dT$ is positive in the most ordered state at lowest T whereas the resistivity is largest and $d\rho/dT$ is small or negative at highest T in the magnetically disordered state. The scattering from phonons is expected to be strongly temperature-dependent in this temperature range; therefore, phonon scattering is not particularly important in most of these materials and magnetic disorder scattering is probably the predominant high-T term determining the scattering time. This conjecture is examined quantitatively below.

2.5.1.2 Magnetoresistance (MR)

It was pointed out above that the effect of magnetic order is to reduce the resistivity. We also know that the effect of an applied magnetic field on the magnetic order (at least for ferromagnets near T_C) is to increase the order. These materials should, therefore, have very large magnetoresistance. Specifically, there should be a large decrease in resistivity on application of a magnetic field. The magnetoresistance of single crystals of three of the compounds has been measured [16, 18] (Figs. 18–20), and each has a fairly large negative magnetoresistance (when compared with normal ferromagnetic metals). For example, application of a 5-T magnetic field reduces the resistivity of $Sr_{14}MnSb_{11}$ by approximately 30% near $T = T_C$ (Fig. 18). $Sr_{14}MnSb_{11}$ is phenomenologically quite similar to CMR materials such as $La_{1-x}Sr_xMnO_3$ (for a recent review see Ref. [20]). The underlying physics is, however, probably not the same. The $Yb_{14}MnPn_{11}$ compounds are distinctly different, being metallic at high temperatures (Figs. 19, 20).

2.5.1.3 Spin Disorder Scattering

The scattering of conduction electrons by a disordered set of spins was calculated over thirty years ago by Kasuya [29]. So, given the published experimental data (Weiss constants, high-T resistivity, and an estimated conduction electron effective mass from heat capacity) can one find a relationship between the conduction electrons and the magnetic spins? The RKKY fit to the Weiss constants of alkaline earth- and Yb-containing compounds provides a Fermi wavevector (and therefore, an estimate of the conduction electron density) setting the length scale of the interaction and

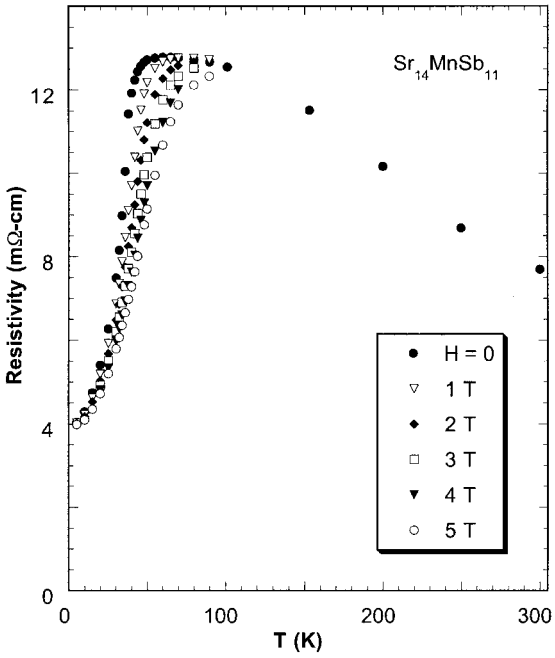

Fig. 18. Magnetoresistance as a function of temperature for a single crystal of $Sr_{14}MnSb_{11}$.

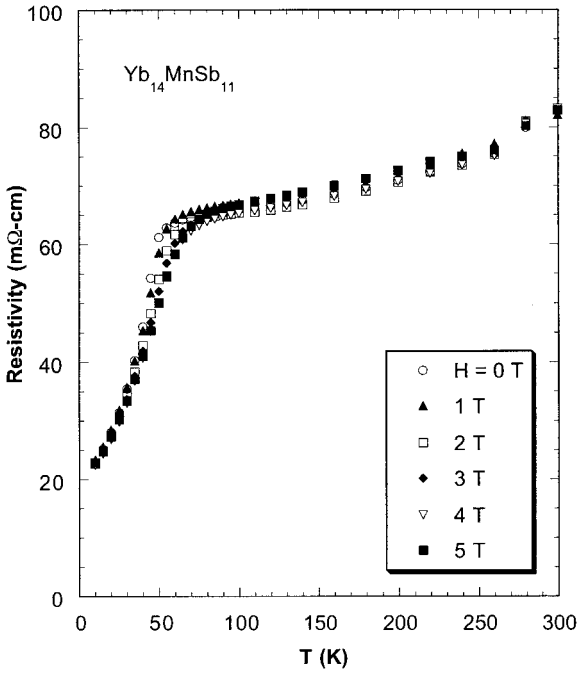

Fig. 19. Magnetoresistance as a function of temperature for a single crystal of $Yb_{14}MnSb_{11}$. The resistivity is measured along the *c* axis and the applied field is parallel.

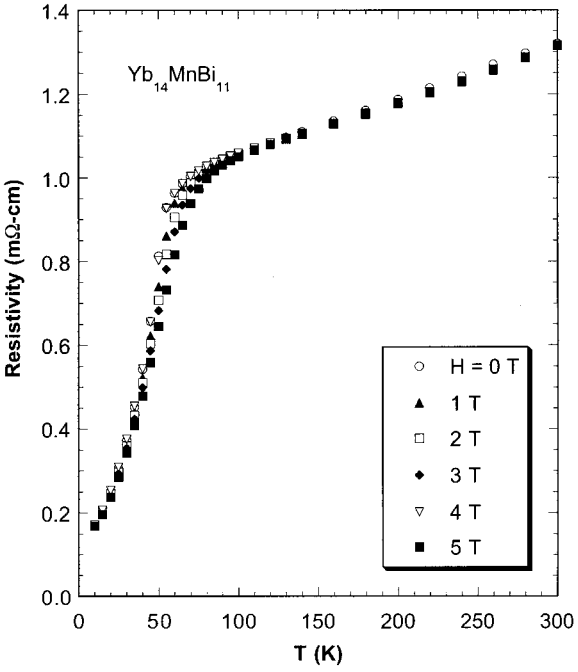

Fig. 20. Magnetoresistance as a function of temperature for a single crystal of $Yb_{14}MnBi_{11}$. The resistivity is measured along the c axis and the applied field is parallel.

providing a coupling constant which controls the magnitude of the interaction. The equation for the high-temperature spin disorder resistivity is [31]:

$$\rho_\infty = \left[\frac{3\pi S(S+1)J_{\mathrm{sd}}^2}{E_{\mathrm{F}}}\right]\frac{mN}{2\hbar e^2}$$

where we have estimates of m, the effective mass of a conduction electron, N, the density of magnetic scatterers (only the Mn ions are magnetic), and the expression in the brackets which was found by fitting the experimental values of T_{C} and Mn$\cdots$Mn distances to the RKKY function above. Using these estimates we predict that the high-temperature resistivity is between 1 and 4 mΩ cm and roughly independent of temperature. Although there are rather large errors in this value, most of the data fall within this range. It seems that the magnetic coupling and the high-temperature spin-disorder resistivity can be explained consistently in terms of the coupling between essentially local Mn magnetic moments and an independent conduction band.

2.5.2 Resistivity and Magnetoresistance of the Europium Compounds

Figures 21 and 22 show the resistivities of $Eu_{14}MnSb_{11}$ and $Eu_{14}MnBi_{11}$ as functions of temperature for several magnetic fields [13, 14]. The resistivity of these compounds in the high-temperature region ($T >$ ordering temperature) is very similar to that of

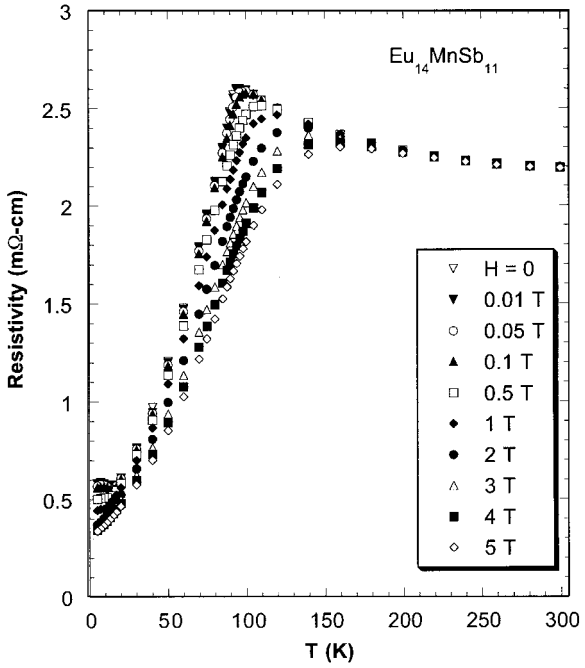

Fig. 21. Magnetoresistance as a function of temperature for a single crystal of $Eu_{14}MnSb_{11}$. The resistivity is measured along the *c* axis and the applied field is parallel.

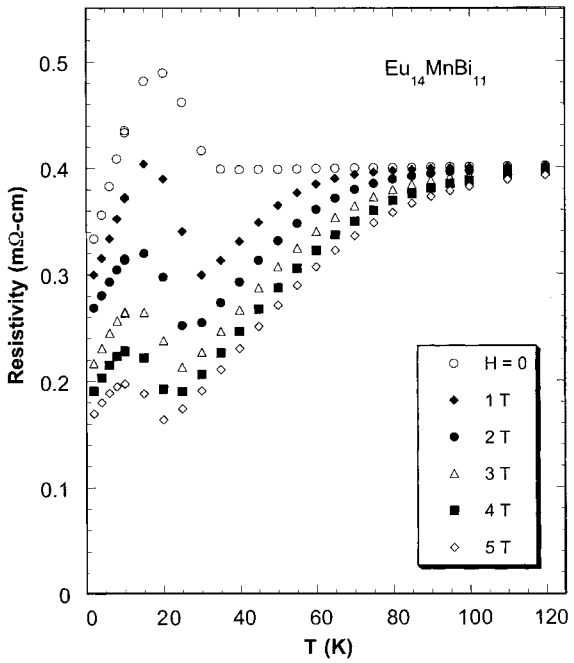

Fig. 22. Magnetoresistance as a function of temperature for a single crystal of $Eu_{14}MnBi_{11}$. The resistivity is measured along the *c* axis and the applied field is parallel.

the alkaline earth compounds. In particular, $Eu_{14}MnSb_{11}$ seems to be a semimetal (its temperature-dependent resistivity is similar to that of a semiconductor and yet the magnitude of the resistivity is similar to that of a poor metal) and $Eu_{14}MnBi_{11}$ has the temperature-dependence of a metal. The sublattice of magnetic Eu ions complicates quantitative discussion of the high-temperature zero-field resistivity for the same reasons that made it unreasonable to estimate the magnetic coupling constants. The substitution of alkaline earth or Yb ions by Eu ions does not, however, change the qualitative behavior of the high-temperature resistivity so it seems likely that the physics is not changed significantly, i. e. we still expect that the resistivity for temperatures above the ordering temperature is determined almost entirely by spin disorder scattering.

At low temperatures the effects of magnetic order are, again, quite clearly displayed in the resistivity. For $Eu_{14}MnSb_{11}$ the resistivity at zero magnetic field begins to decrease near the Curie temperature as the Mn spins (and presumably the Eu spins) develop short-range fluctuating order in the form of ferromagnetic spin fluctuations. The resistivity changes fastest with temperature at the Curie temperature and then continues to decrease as the temperature is further reduced and the ferromagnetic order parameter (the Weiss constant) increases. The zero-field resistivity also signals the change in magnetic order at about 15 K with an abrupt change in its temperature-dependence. The resistivity increases abruptly at the Neel temperature for $Eu_{14}MnBi_{11}$ [13], as is seen at many magnetic transitions into states in which the unit cell has been changed [33, 34]. A simple ferromagnetic transition does not change the unit cell of a material but an antiferromagnetic transition often increases the unit cell, leading to a change in the Fermi surface of the conduction electrons which can lead to an increase in the resistivity just below the Neel temperature. At sufficiently low temperatures, the development of antiferromagnetic order in a metal will still lead to a resistivity which decreases as the temperature is decreased. These two competing temperature dependencies lead to a peak in the resistivity, for example that seen for $Eu_{14}MnBi_{11}$.

The magnetoresistance [14] of $Eu_{14}MnSb_{11}$ classifies it as a colossal magnetoresistance material. It is largest when the applied magnetic field is used to induce magnetic order. This happens at T_C, because the change in magnetic susceptibility is largest at T_C, and also at $T < 15$ K, when the Eu sublattice seems to induce some spin disorder (perhaps spin canting) in the Mn magnetic lattice so that an applied magnetic field can rotate the Mn spins toward the ordered state and reduce the resistivity.

Interestingly, the magnetoresistance of $Eu_{14}MnBi_{11}$ is quite large even for T of the order of $3 \times T_N$ [13]. By analogy with essentially all other CMR materials it has been is proposed that this large magnetoresistance is because of the existence of ferromagnetic spin fluctuations in this temperature range, even though the ordered state is not ferromagnetic [13]. This idea is supported by the sign of the Weiss constant obtained from fitting the high-temperature paramagnetic susceptibility. This Weiss constant suggests that the strongest magnetic coupling is ferromagnetic, even when the ordered state of the compound is antiferromagnetic, so ferromagnetic spin fluctuations would be expected to develop as the crystal is cooled.

2.5.3 Comparison with other Magnetoresistive Materials

The CMR materials that have received the most attention recently are the perovskite $LaMnO_3$ where a divalent cation (Ca, Sr, Ba, etc.) is substituted for La, at a concentration x [20, 35–37]. The magnetic and transport phenomena of these perovskite materials are very similar to those of the Zintl compounds, but the mechanisms responsible for these phenomena seem to be quite different. The undoped $LaMnO_3$ compound has Mn^{3+} ions and is an antiferromagnetic insulator. Doping on the La site with a divalent ion results in a change of some Mn^{3+} (with three unpaired spins in t_{2g} states and one in an e_g state) into Mn^{4+} (with only the three t_{2g} spins). For each e_g electron there is strong "Hund's Rule" coupling with the three spin-aligned t_{2g} electrons on the same site, so e_g electrons can easily hop to nearby Mn^{4+} sites only when the t_{2g} electrons on the initial Mn^{3+} and final Mn^{4+} sites have the same spin alignment. This leads to a low-temperature spin-aligned (ferromagnetic) state in which all Mn d-electrons are ordered and the spin-aligned e_g electrons form a conduction band. The indirect exchange interaction between the local t_{2g} electrons, because of the hopping of delocalized e_g electrons, is called double exchange [38, 39]. Detailed measurements and calculations of both the conductivity and its temperature-dependence show that in addition to the double exchange another very important electron interaction in these compounds is between the electrons and the lattice [40, 41]. This interaction leads to a (Jahn–Teller) lattice distortion coupled to the conduction electrons (i. e. a polaron) and so tends to localize a conduction electron. The inclusion of this strongly localizing interaction is necessary in any theory to account for the magnitude of magnetoresistance in the doped $LaMnO_3$.

In contrast with doped $LaMnO_3$, most other CMR materials, for example $Tl_2Mn_2O_7$ (with the pyrochlore structure) [42, 43], doped EuSe [44, 45], amorphous Gd_xSi_{1-x} [46], and the transition metal Zintl compounds discussed in this review, are near a metal insulator transition and are proposed to have localized magnetic electrons which are distinct from the conduction electrons. In amorphous Gd_xSi_{1-x}, the metal insulator transition is driven by localization of conduction electrons, because of the disordered structure. The conduction electron concentration is quite low in the other three materials and is controlled either by doping (EuSe) or by the small overlap between the conduction and valence bands ($Tl_2Mn_2O_7$ and Zintl compounds). The magnetic coupling between the localized magnetic spins is because of either superexchange ($Tl_2Mn_2O_7$, EuSe, and possibly Gd_xSi_{1-x}) or RKKY-type coupling (possibly Gd_xSi_{1-x} and the Zintl compounds). Each of these materials has properties similar to those of the Zintl compounds discussed above. In general they have colossal magnetoresistance, either near a Curie temperature or at low-T, that increases as the material moves toward the insulating state. Unfortunately, as these materials move toward the insulating state, the region of T in which the magnetoresistance is large also moves to lower T. In other words, as the CMR effect becomes stronger the materials become less technologically useful because the effect is only at very low T. The current challenge in materials science is to find a material that has room-temperature magnetism and an arbitrarily large CMR effect.

2.6 Summary and Outlook

The incorporation of magnetic transition metals into Zintl phases has produced intriguing magnetic and magnetoresistive materials. The $A_{14}MnPn_{11}$ phases have many interesting magnetic and electronic properties. Within one crystallographic structure type they span the range from localized magnetic insulators to long-range magnetically ordered metals. Many of the properties have only been studied in a highly cursory fashion, and the results to date warrant a more detailed examination. This structure type has features that make it similar to molecular structures and it therefore provides insight into the design of high-temperature molecular magnets. Many Zintl phases have discrete units, such as those found in $A_{14}MnPn_{11}$, and further explorations in synthesis will produce new transition metal Zintl phases with similarly unexpected magnetic properties. The field is rich with possibilities.

Acknowledgments

We would like to thank the many students, undergraduates, graduates, and post-doctoral fellows in the Kauzlarich and Webb groups that have made this research possible. We are indebted to a P. Klavins and R.N. Shelton for useful discussion.

References

[1] G. Cordier, H. Schäfer, M. Stelter, *Z. anorg. allg. Chem. 519* (**1984**) 183–188.
[2] S. M. Kauzlarich, in S. M. Kauzlarich (Ed.): *Chemistry, Structure, and Bonding of Zintl Phases and Ions*, VCH Publishers, New York **1996**, p. 245–274.
[3] S. M. Kauzlarich, *Comments Inorg. Chem. 10* (**1990**) 75.
[4] S. M. Kauzlarich, J. Y. Chan, B. R. Taylor, in C. H. Winter, D. M. Hoffman (Eds.): *Inorganic Materials Synthesis, Vol. 727*, ACS, Washington D.C. **1999**, p. 15–27.
[5] S. M. Kauzlarich, T. Y. Kuromoto, M. M. Olmstead, *J. Am. Chem. Soc. 111* (**1989**) 8041–8042.
[6] R. F. Gallup, C. Y. Fong, S. M. Kauzlarich, *Inorg. Chem. 31* (**1992**) 115–118.
[7] T. Y. Kuromoto, S. M. Kauzlarich, D. J. Webb, *Mol. Cryst. Liq. Cryst. 181* (**1990**) 349–357.
[8] T. Y. Kuromoto, S. M. Kauzlarich, D. J. Webb, *Chem. Mater. 4* (**1992**) 435–440.
[9] J. Del Castillo, D. J. Webb, S. M. Kauzlarich, T. Y. Kuromoto, *Phys. Rev. B 47* (**1993**) 4849–4852.
[10] A. Rehr, S. M. Kauzlarich, *J. Alloys and Compounds 207/208* (**1994**) 424–426.
[11] D. P. Siemens, J. Del Castillo, W. Potter, D. J. Webb, T. Y. Kuromoto, S. M. Kauzlarich, *Solid State Commun. 84* (**1992**) 1029–1031.
[12] D. J. Webb, T. Y. Kuromoto, S. M. Kauzlarich, *J. Magn. Magn. Mater. 98* (**1991**) 71–75.
[13] J. Y. Chan, S. M. Kauzlarich, P. Klavins, R. N. Shelton, D. J. Webb, *Phys. Rev. B 57* (**1998**) R8103–R8106.
[14] J. Y. Chan, S. M. Kauzlarich, P. Klavins, R. N. Shelton, D. J. Webb, *Chem. Mater. 9* (**1997**) 3132–3135.

[15] J. Y. Chan, M. E. Wang, A. Rehr, D. J. Webb, S. M. Kauzlarich, *Chem. Mater. 9* (**1997**) 2132–2138.
[16] D. J. Webb, R. Cohen, P. Klavins, R. N. Shelton, J. Y. Chan, S. M. Kauzlarich, *J. Appl. Phys. 83* (**1998**) 7193.
[17] J. Y. Chan, M. M. Olmstead, S. M. Kauzlarich, D. J. Webb, *Chem. Mater. 10* (**1998**) 3583–3588.
[18] I. R. Fisher, T. A. Wiener, S. L. Bud'ko, P. C. Canfield, J. Y. Chan, S. M. Kauzlarich, *Phys. Rev. B 59* (**1999**) 13829.
[19] A. Rehr, T. Y. Kuromoto, S. M. Kauzlarich, J. Del Castillo, D. J. Webb, *Chem. Mater. 6* (**1994**) 93–99.
[20] A. P. Ramirez, *Journal of Physics–Condensed Matter 9* (**1997**) 8171–8199.
[21] A. R. Bishop, H. Roder, *Curr. Opin. in Solid State Mat. Sci. 2* (**1997**) 244–251.
[22] W. Carrillo–Cabrera, M. Somer, K. Peters, H. G. von Schnering, *Chem. Ber. 129* (**1996**) 1015–1023.
[23] S. M. Kauzlarich, T. Y. Kuromoto, *Croat. Chim. Acta 64* (**1991**) 343–352.
[24] S. M. Kauzlarich, M. M. Thomas, D. A. Odink, M. M. Olmstead, *J. Am. Chem. Soc. 113* (**1991**) 7205–7208.
[25] S. L. Brock, L. J. Weston, M. M. Olmstead, S. M. Kauzlarich, *J. Solid State Chem. 107* (**1993**) 513–523.
[26] J. T. Vaughey, J. D. Corbett, *Chem. Mater. 8* (**1996**) 671–675.
[27] C. Kittel, *Introduction to Solid State Physics*, John Wiley & Sons, New York **1986**.
[28] M. A. Ruderman, C. Kittel, *Phys. Rev. 96* (**1954**) 99.
[29] T. Kasuya, *Prog. Theor. Phys. 16* (**1956**) 45, 58.
[30] K. Yosida, *Phys. Rev. 106* (**1957**) 893.
[31] A. J. Decker, *J. Appl. Phys. 36* (**1965**) 906.
[32] D. J. Craik, *Magnetism: principles and applications*, John Wiley & Sons, New York **1995**.
[33] H. Miwa, *Prog. Theor. Phys. 28* (**1962**) **1962**.
[34] R. J. Elliot, F. A. Wedgewood, *Proc. Phys. Soc. 81* (**1963**) 846.
[35] S. Jin, M. McCormack, T. H. Tiefel, R. Ramesh, *J. Appl. Phys. 76* (**1994**) 6929–6933.
[36] R. von Helmolt, J. Wecker, B. Holzapfel, L. Schultz, *Phys. Rev. Lett. 71* (**1993**) 2331–2333.
[37] R. von Helmolt, J. Wecker, *J. Appl. Phys. 76* (**1994**) 6925–6928.
[38] C. Zener, *Phys. Rev. 81* (**1951**) 440.
[39] C. Zener, *Phys. Rev. 82* (**1951**) 403.
[40] A. J. Millis, B. I. Shraiman, R. Mueller, *Phys. Rev. Lett 74* (**1995**) 5144.
[41] A. J. Millis, B. I. Shraiman, R. Mueller, *Phys. Rev. Lett. 77* (**1996**) 175.
[42] M. A. Subramanian, B. H. Toby, A. P. Ramirez, W. J. Marshall, A. W. Sleight, G. H. Kwei, *Science 273* (**1996**) 81–83.
[43] M. A. Subramanian, J. E. Greedan, N. P. Raju, A. P. Ramirez, A. W. Sleight, *J. Phys. IV 7* (**1997**) 625–628.
[44] S. von Molnar, S. Methfessel, *J. Appl. Phys. 38* (**1967**) 959–964.
[45] S. von Molnar, A. Briggs, J. Glouquet, G. Remenyi, *Phys. Rev. Lett. 51* (**1983**) 706.
[46] F. Hellman, M. Q. Tran, A. E. Gebala, E. M. Wilcox, R. C. Dynes, *Phys. Rev. Lett. 77* (**1996**) 4652–4655.

Magnetism: Molecules to Materials III. Edited by J.S. Miller and M. Drillon

ISBNs: 3-527-30302-2 (Hardback); 3-527-60014-0 (Electronic)

3 Magnetic Properties of Large Clusters

Dante Gatteschi and Roberta Sessoli

3.1 Introduction

Molecular clusters are unique objects used to investigate the magnetic properties of organized matter a few nanometers in size. They are all identical, can be structurally characterized and their structure be perfectly known, and they can be investigated in single crystals, in polycrystalline powders, in solution, in polymer films, in Langmuir–Blodgett films, etc. Because they are all identical measurements can be performed on large assemblies and the response of the individual molecules can be monitored. Being finite objects they are expected to obey the laws of quantum mechanics, but at the same time they are large enough that some of their properties resemble those of bulk magnets more than those of simple paramagnets [1, 2]. This aspect of their behavior has been widely exploited in recent years after the discovery [3] that a cluster comprising twelve manganese ions, $[Mn_{12}O_{12}(CH_3OO)_{16}(H_2O)_4]$, Mn12Ac, the structure of which [4] is shown in Fig. 1, is characterized by slow relaxation of magnetization and hysteresis effects of molecular origin at low temperature. Other clusters were later found to have the same properties [5–12], although, in general, at lower temperature than Mn12Ac. For these molecules the term "single molecule magnets" is now used [13], even if, of course, it is not certainly proper. A magnet is characterized by divergence of the spin correlation length that is impossible in a cluster containing a finite number of coupled spins. The term is, however, certainly evocative and can be used with the above caveat.

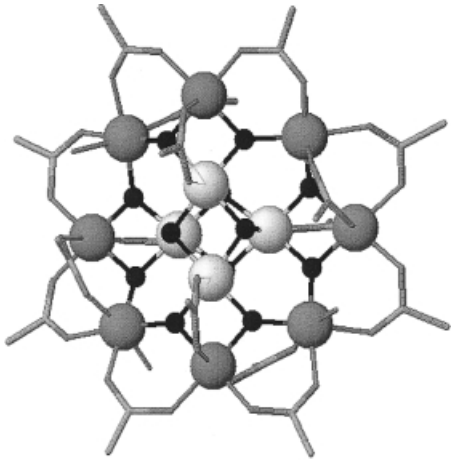

Fig. 1. Sketch of the structure of $[Mn_{12}O_{12}(CH_3COO)_{16}(H_2O)_4]$, Mn12Ac. The large light gray and dark gray spheres represent Mn^{4+} and Mn^{3+} ions respectively. The μ-oxo bridges are represented by black spheres and the acetate ligands are drawn as sticks.

Slow relaxation of the magnetization is certainly a feature in which the quantum nature of the cluster merges into a quasi-classical behavior. There are, however, several quantum features that can be observed in clusters, and these can be used to understand the conditions under which similar effects can be observed in macroscopic objects. This is the field of macroscopic quantum phenomena, MQP, which is now intensively investigated both for fundamental reasons [1, 2, 14] and to enable the design of new types of device and computers exploiting quantum phenomena [15]. MQP are numerous, and range from quantum tunneling of the magnetization [16], first proved in Mn12Ac [17, 18], and tunneling of the Neel vector in antiferromagnetic rings [19], to the periodic quenching of the tunnel splitting [20] (Berry phase) [21–23].

Investigation of the structural and magnetic properties of large molecular clusters is complex and requires the use of many different techniques. The number of levels which must be considered to calculate the thermodynamic properties of the clusters increases rapidly with the number, N, of metal ions of spin S, being $(2S+1)^N$. Because the clusters comprise a finite number of spins it is not possible to use translational symmetry to simplify the problems, as can be done for infinite lattices. These limitations require that as much experimental information as possible is collected to obtain a minimum understanding of the magnetic properties of the clusters.

The simplest possible approach for the description of the thermodynamic and spectroscopic properties of clusters is given by a spin Hamiltonian of the type [24]:

$$H = \Sigma_{i<k} J_{ik} \mathbf{S_i} \cdot \mathbf{S_k} + \Sigma_{i<j} \mathbf{S_i} \cdot \mathbf{D_{ik}} \cdot \mathbf{S_k} + \Sigma_i \mathbf{S_i} \cdot \mathbf{D_i} \cdot \mathbf{S}_i + \ldots \quad (1)$$

The sums are extended to all the magnetic centers of the clusters. The first term corresponds to the isotropic exchange interaction, the second to the exchange-determined anisotropy, and the third to the anisotropy of the individual centers. Other terms that can be included are biquadratic exchange, $H = \Sigma_{i<k} j_{ik} \mathbf{S}_i^2 \cdot \mathbf{S}_k^2$, higher-order anisotropy terms, of the type $H = \mathbf{S}_i^{2n} \cdot \mathbf{D}_{ik}^{2n} \cdot S_k^{2n}$, where $n = 2, 3$, etc., an antisymmetric exchange or Dzialoshinsky–Moriya term, $H = \Sigma_{i<k} \mathbf{G}_{ik} \cdot (\mathbf{S}_i \times \mathbf{S}_k)$, where $\mathbf{G}_{ik}$ is a vector whose components depend on the symmetry of the interacting pair, and higher-order anisotropic terms. The Zeeman term is also needed to describe the interaction with an applied magnetic field. Calculation of the energy levels is very difficult, even for reasonably small numbers of variables, and at the lowest level of approximation, i. e. including only the isotropic part of the Hamiltonian Eq. (1). In fact, for Mn12Ac, where eight ions are manganese(III) with spin $S_1 = 2$ and four are manganese(IV) with spin $S_2 = 3/2$, the total number of states is $(2S_1 + 1)^8 (2S_2 + 1)^4 = 100\,000\,000$! It is possible to reduce the size of the matrixes by using the total spin, $S = \Sigma_k S_k$, which ranges from $S = 0$ to $S = 22$. In fact the non-zero matrix elements are between functions with the same total spin, S, but the size of many matrixes is still intractably high, as is shown in Table 1. The largest block is that for $S = 4$, which is $1\,111\,696 \times 1\,111\,696$.

It is apparent that calculation of the energy levels for large clusters is currently beyond reach; a large number of different techniques is, therefore, needed to describe at least the low-lying energy levels responsible of the magnetic properties of the clusters. The goal of this contribution is to review the most important techniques

Table 1. Size of the matrixes of the total spin states of Mn12Ac.

S	$N(S)$	S	$N(S)$	S	$N(S)$
0	190 860	8	654 476	16	7 656
1	548 370	9	428 450	17	2 951
2	838 126	10	333 032	18	997
3	1 029 896	11	214 996	19	286
4	1 111 696	12	129 476	20	66
5	1 090 176	13	72 456	21	11
7	831 276	15	17 776	22	1

which have so far been used to investigate the low-lying energy levels of the clusters. We will first describe the best available techniques for calculation of the energy levels of the clusters, at the spin Hamiltonian level, and now also at the ab-initio level. Neutron techniques, both experiments polarized neutrons for determination of the spin density and inelastic neutron scattering for determination of the energy of the levels close to the ground state, will be reported to show how experimental techniques can be used to improve the theoretical description of the clusters. The third section will be devoted to magnetic measurements, both susceptibility and magnetization, under DC and AC conditions. New techniques allowing the measurement of magnetic anisotropy, even of very small crystals, will be taken into consideration. Magnetic resonance techniques, treated in the next section, will start with EPR, with particular emphasis on new developments in high-frequency–high-field techniques, HF-EPR. This will be followed by a treatment of NMR, and μSR, in which the nuclei or the muons are used as local probes of the magnetization of the clusters. All these results will be combined in Sections 5 and 6, where we will try to review conditions for the design and synthesis of new types of single molecule magnet and work out in detail the properties of an octanuclear iron cluster which has so far provided most evidences of tunneling of magnetization. A final section will be devoted to conclusions and to an outlook of this new field of research.

3.2 Calculation of the Energy Levels and Experimental Confirmations

3.2.1 Calculations

Calculation of the energy levels of the clusters is particularly simple for some high-symmetry cases where the isotropic exchange term is the only one needed. This can be done via the so-called generalized Kambe approach [25], which is possible whenever the individual spins can be factored into groups, under some conditions. The best way to show the potential of the Kambe approach is to work out a simple example. Let us consider a nonanuclear cluster as represented schematically [26] in Fig. 2.

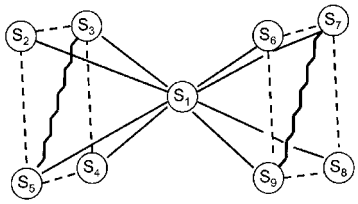

Fig. 2. Schematic diagram of the structure of a nonanuclear manganese cluster the energy levels of which can be described by the Kambe approach.

The S_1 spin corresponds to manganese(II) ($S_1 = 5/2$), all the others to manganese(III) ($S = 2$). The coupling within the two sets of spins, S_2–S_5 and S_6–S_9, can be described by the Hamiltonian:

$$H = J_2(\mathbf{S}_2 \cdot \mathbf{S}_3 + \mathbf{S}_3 \cdot \mathbf{S}_4 + \mathbf{S}_4 \cdot \mathbf{S}_5 + \mathbf{S}_5 \cdot \mathbf{S}_2) + J_2(\mathbf{S}_6 \cdot \mathbf{S}_7 + \mathbf{S}_7 \cdot \mathbf{S}_8 + \mathbf{S}_8 \cdot \mathbf{S}_9 + \mathbf{S}_9 \cdot \mathbf{S}_6) + J_3(\mathbf{S}_3 \cdot \mathbf{S}_5 + \mathbf{S}_7 \cdot \mathbf{S}_9) \quad (2)$$

Assuming the central S_1 spin is equally coupled to all the other eight spins the corresponding Hamiltonian is:

$$H = J_1 \Sigma_{k=2.9} \mathbf{S}_1 \cdot \mathbf{S}_k \quad (3)$$

If the individual spins are coupled as:

$$S_A = S_2 + S_4;\ S_B = S_3 + S_5;\ S_C = S_6 + S_8;\ S_D = S_7 + S_9;$$
$$S_E = S_A + S_B;\ S_F = S_C + S_D;\ S_G = S_E + S_F;\ S_T = S_G + S_1 \quad (4)$$

the energies of the states are given by:

$$E(S_T, S_G, S_F, S_E, S_D, S_C, S_B, S_A, S_1)$$
$$= J_1/2[S_T(S_T+1) - S_G(S_G+1) - S_1(S_1+1)] + J_2/2[SE(S_E+1) + S_F(S_F+1) - S_A(S_A+1) - S_B(S_B+1) - S_C(S_C+1) - S_D(S_D+1)] + J_3/2[S_B(S_B+1) + S_D(S_D+1) - 8S_2(S_2+1)] \quad (5)$$

This relatively simple expression for the energies of the levels arises because the four spins S_2–S_5 are coupled by one constant J_2, as are S_6–S_9, and S_1 is equally coupled to all the other spins. If these conditions are relaxed the Kambe approach breaks down. Exactly solvable cases using the Kambe formalism have been reported for clusters containing up to nine metal ions [27].

Unfortunately such examples are very rare and, in general, matrix-diagonalization techniques must be used. To reduce the size of the matrixes the best approach is that of irreducible tensor operators, ITO [28]. This fully exploits the symmetry of the total spin S. The eigenfunctions of the total spin are simply indicated as a set of numbers that identify the individual and intermediate spins. For example, for a cluster of eight spins, e. g. the octanuclear iron(III) cluster of formula $[Fe_8O_2(OH)_{12}(tacn)_6]^{8+}$, Fe8, where tacn is triazacyclononane [29], depicted in Fig. 3, many different schemes can be adopted to couple the individual spins to give the total spin S. The core of the cluster is given by the so-called butterfly arrangement [30] with Fe1 and Fe2 forming the body and Fe3 and Fe4 forming the wings. A convenient scheme, which has been used

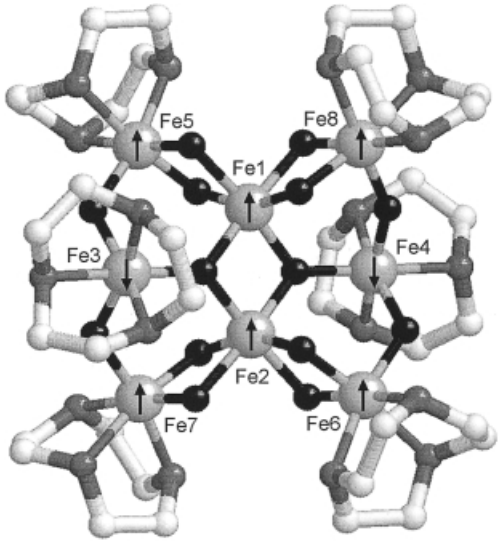

Fig. 3. Sketch of the structure of $[Fe_8O_2(OH)_{12}(tacn)_6]^{8+}$, Fe8. The large spheres represent the iron ions, oxygen are drawn in black, nitrogen in gray, and carbon in light gray.

to describe the wavefunction of the ground state [31], couples S_3 to S_4 to give S_{34}, S_1 to S_2 to give a resulting spin S_{12}, S_{12} to S_5 to give S_{125}, S_{125} to S_6 to give S_{1256}, S_{1256} to S_7 to give S_{12567}, S_{12567} to S_8 to give S_{125678}, and the latter to S_{34} to give S. The wavefunction can therefore be written as $|S_1 S_2 S_{12} S_5 S_{125} S_6 S_{1256} S_7 S_{12567} S_8 S_{125678} S_3 S_4 S_{34} SM\rangle$, where $-S \leq \mathrm{M} \leq S$. This is the only information needed for calculation of the matrix elements for the isotropic term using explicit formulas which have been reported elsewhere [28]. More recently the explicit forms of the matrix elements have also been reported [32] for the lower-symmetry components of the spin Hamiltonian Eq. (1). The possibility of electron delocalization was also taken into consideration [33]. The introduction of the lower symmetry terms, however, results in a dramatic increase in the size of the matrices to be diagonalized. In fact, in the limit of isotropic exchange interactions the energies are independent of the M component of the total spin, therefore only one component needs to be calculated for the energy of a given S multiplet. For lower symmetry all the M components must be calculated separately.

Occasionally the individual spins have been treated as classical spins, i. e. they have been considered as vectors, and the thermodynamic properties have been calculated classically [34]. Of course this approach has many limitations. The first is that it can only be used with individual spins as large as possible, typically for $S = 5/2$ or 2. The second is that the calculations become rapidly very complicated when the number of interactions for a given ion becomes larger than two. In fact the method is best suited for the calculation of the thermodynamic properties of rings, where each ion has only two nearest neighbors. The third is that the approach cannot be used at low temperature, when quantum effects become predominant.

Monte-Carlo simulations have recently been used to overcome some of these problems. It is now possible, in principle, to use both classic and quantum spins, but calculations with the latter are still very cumbersome. In general the Metropolis algorithm [35] is used. It has, for example, recently been possible to fit the temperature-

dependence of the magnetic susceptibility of a ring comprising eighteen iron(III) ions, allowing for two different coupling constants [36].

The levels obtained from the diagonalization of the matrixes can be used to calculate thermodynamic properties of the clusters – namely magnetic susceptibility, magnetization, specific heat. It should be remembered that use of the spin Hamiltonian is a parametric approach, i. e. the energy levels must be calculated for each set of parameters, which might mean many tens of calculations to reach an acceptable fit with the experimental data. Calculation of the magnetic susceptibility requires diagonalization of the matrixes in the presence of a field, which again complicates matters. It is certainly simpler to use the van Vleck equation, although its validity in the limit of many quasi-degenerate levels can be questioned.

The relative energies of the levels can be verified by the satisfactory fit of the thermodynamic properties, but certainly this is an indirect method, which leaves some margin of ambiguity. In general the number of parameters required for best fitting of the temperature-dependence of the magnetic susceptibility is large, and in the presence of a large correlation it is possible that several sets of parameters are acceptable. There is no general spectroscopic tool enabling direct insight into the energy levels, although EPR, inelastic neutron scattering, and high-field magnetization studies have sometimes provided excellent information. EPR, which will treated at some length in Section 4, usually provides information on the zero-field splitting of the lowest, and occasionally the first, excited states. In particular in some instances EPR has been able to provide unequivocal evidence for the S value of the ground state, which was not conclusively indicated by magnetic susceptibility and magnetization data [37]. Its range is, however, limited to thermally populated levels and, in general, the allowed transitions are those within a given S multiplet.

3.2.2 Inelastic Neutron Scattering

Inelastic neutron scattering, INS, can not only provide similar information, it can also be used for direct measurement of transitions between different multiplets [38, 39]. Neutrons are characterized by spin $S = 1/2$, which enables them to interact with magnetic materials. Because neutrons thermalized at room temperature have a wavelength $\lambda = 1.81$ Å, they can be scattered by crystal lattices. They can also be scattered both elastically, in this way enabling probing of the static structure of the sample, and inelastically, enabling probing of dynamic excitations within the sample. Hot neutrons have an energy range 800–4000 cm^{-1}, thermal neutrons 80–800 cm^{-1}, and cold neutrons 0.8–80 cm^{-1}, and resolution can be of the order of 0.05 cm^{-1}. The problem with neutrons is that they are strongly absorbed from some nuclei, for instance hydrogen nuclei, which make the measurement of samples containing many protons rather problematic.

In a neutron-scattering experiment the key variables are the change in neutron energy and wave vector. A neutron of wave vector $\mathbf{k}$ and energy E strikes a target in a state $|\xi\rangle$ and energy E_ξ and leaves the system with a wave vector $\mathbf{k}'$ and energy E', while the target is in the new state $|\xi'\rangle$, and energy $E_{\xi'}$. The energy transfer requires $E - E' = h\nu$ and momentum transfer $\mathbf{Q} = \mathbf{k} - \mathbf{k}'$. $\mathbf{Q}$ is the scattering vector.

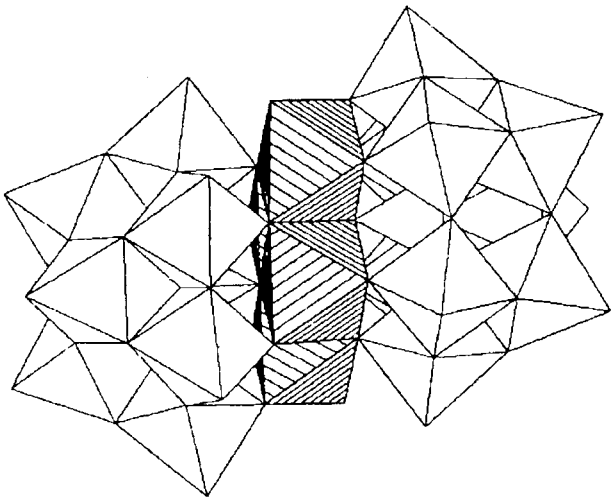

Fig. 4. Sketch of the structure of $[Ni_4(H_2O)_2(PW_9O_{34})_2]^{10-}$, Ni4 [40]. The nickel octahedra are hatched.

A recent example is provided by the cluster $[Ni_4(H_2O)_2(PW_9O_{34})_2]^{10-}$, the structure of which [40] is sketched in Fig. 4.

The magnetic moiety of the cluster is provided by the four nickel(II) ions that define a rhombus. A possible spin Hamiltonian is:

$$H = J(\mathbf{S}_1 \cdot \mathbf{S}_3 + \mathbf{S}_1 \cdot \mathbf{S}_4 + \mathbf{S}_2 \cdot \mathbf{S}_3 + \mathbf{S}_3 \cdot \mathbf{S}_4) + J'(\mathbf{S}_1 \cdot \mathbf{S}_2) + D(S_{1z}^2 + S_{2z}^2) + D'(S_{3z}^2 + S_{4z}^2) \quad (6)$$

The magnetic properties of the tetranuclear cluster are indicative of ferromagnetic coupling and yield the ground state $S = 4$. The lowest lying excited state has $S = 3$. Because the single nickel(II) ions are anisotropic all the multiplets have sizeable zero-field splitting. In an INS experiment the transitions observed follow the selection rule ($S = \pm 1, 0$; $\Delta M = \pm 1$. In this way it was possible to obtain the energy separations of the different M states belonging to the ground $S = 4$ multiplet [41]. It was also possible to measure directly the energies of the M components of the excited $S = 3$ states.

The $M = 0$ component of the ground $S = 4$ multiplet lies lowest, indicating positive zero-field splitting; the anisotropy of the cluster is, therefore, of the XY type. The energies of the excited M states follow to a good approximation the expected DM^2 dependence with $D = 0.66\,\mathrm{cm}^{-1}$.

A further advantage of INS is that by measuring the $\mathbf{Q}$ dependence of the spectra it is also possible to obtain first-hand information about the nature of the eigenvectors, not only the eigenvalues of the spin Hamiltonian. This, in general, produces an additional piece of information to be used in meaningfully estimation of the best-fit values of the parameters. In this case the best fit parameters, $J = -1.66\,\mathrm{cm}^{-1}$,

$J' = -0.78\,\mathrm{cm}^{-1}$, $D = 0.47\,\mathrm{cm}^{-1}$, and $D' = 0.60\,\mathrm{cm}^{-1}$, correspond to an overall splitting of the ground $S = 4$ state of ca $10.6\,\mathrm{cm}^{-1}$, with axial symmetry. If the basis functions are written using the intermediate spins $S_{12} = S_1 + S_2$, $S_{123} = S_{12} + S_3$ as $|S_{12}, S_{123}, SM\rangle$, the ground-state function is essentially the pure $|2, 3, 4M\rangle$. Some small admixture of excited states is possible for the low M values because the conditions for strong exchange are not exactly met; M states belonging to different S multiplets can be admixed.

3.2.3 Polarized Neutron Scattering

More important information can be obtained from polarized neutron scattering data [39]. On the one hand they can be used to measure microscopic distributions of spin densities as opposed, for example, to macroscopic measurements such as the magnetic susceptibility. On the other hand, unlike resonance techniques, which measure microscopic quantities at certain points of the molecule, neutrons are itinerant probes, giving information on spin density at every point in the crystal.

Neutrons are scattered via nuclear interactions with the nuclei and via magnetic interactions with the magnetization density. Under the experimental conditions used the nuclear spins are not polarized and nuclear scattering is independent of neutron spin. In contrast, the interaction of the neutron with the magnetization density is spin-dependent. This enables separation of the magnetic and nuclear contributions by using a polarized neutron beam and performing measurements for different beam polarizations.

Polarized neutron diffraction studies of a paramagnetic single crystal are possible by inducing a magnetization density by means of a strong magnetic field at low temperature. The induced magnetization density is periodic, as is the nuclear density. For this reason, all the coherent elastic scattering occurs at the Bragg positions (hkl).

The magnetic structure factor is the Fourier component of the magnetization density in the crystal:

$$\vec{F}_{\mathrm{M}}(\vec{k}) = r_0 \int \vec{M}(\vec{k}) e^{i(\vec{k},\vec{r})} \mathrm{d}^3 r \tag{7}$$

where $r_0 = 0.2696 \times 10^{-12}\,\mathrm{cm}\,\mu_{\mathrm{B}}$. The total scattered intensity of a Bragg reflection for a polarized neutron incident beam is given by the expression:

$$\begin{aligned} I(\vec{k}, \vec{\sigma}) &= |F_{\mathrm{N}}|^2 + |\vec{F}_{\mathrm{M}_\perp}|^2 + F_{\mathrm{N}}(\vec{\sigma}.F^*_{\mathrm{M}_\perp}) + F^*_{\mathrm{N}}(\vec{\sigma}.\vec{F}_{\mathrm{M}_\perp}) \\ \vec{F}_{\mathrm{M}_\perp} &= \hat{k} \times \vec{F}_{\mathrm{M}} \times \hat{k}, \text{ with } \hat{k} = \frac{\vec{k}}{|\vec{k}|} \end{aligned} \tag{8}$$

where the F_{N} values are the nuclear structure factors and $\vec{k}$ is the direction of polarization.

For an isotropic paramagnet the induced magnetization density is parallel to the applied field: $\vec{F}_{\mathrm{M}}(\vec{k}) = \vec{z}F_{\mathrm{M}}(\vec{k})$, where $\vec{z}$ is a unit vector along the applied field. If, furthermore, the crystal structure is centrosymmetric, both F_{M} and F_{N} are real quantities. In practice one measures the "flipping ratio", R, of Bragg reflections, that is the ratio of scattered intensities for "up" (parallel to the applied field) and "down" (antiparallel) polarizations of the incident beam. Using the general formula Eq. (8) the expression for R is given by:

$$R_{(\mathrm{h,k,l})} = \frac{I\uparrow}{I\downarrow} = \frac{F_{\mathrm{N}}^2 + F_{\mathrm{M}_\perp}^2 + 2F_{\mathrm{N}}F_{\mathrm{M}_{\perp z}}}{F_{\mathrm{N}}^2 + F_{\mathrm{M}_\perp}^2 - 2F_{\mathrm{N}}F_{\mathrm{M}_{\perp z}}} \tag{9}$$

where $\vec{F}_{\mathrm{M}} = \vec{z}F_{\mathrm{M}}$, $F_{\mathrm{M}_\perp} = F_{\mathrm{M}} \sin\alpha$, $F_{\mathrm{M}_{\perp z}} = F_{\mathrm{M}} \sin^2\alpha$, and α is the angle between the scattering vector (hkl) and $\vec{z}$.

If the crystal structure is known, the F_{N} values are known and the magnetic structure factors can be extracted from Eq. (9). The experiment usually includes two steps. In the first, the precise structure of the crystal at low temperature, including the location of the hydrogen atoms and the thermal parameters, is determined using conventional unpolarized neutron diffraction techniques. The second step consists in measuring the flipping ratios with polarized neutrons at low temperature to maximize the amount of ordered spin density induced by the applied field.

An elegant example of the kind of information which can be extracted from the analysis of polarized neutron diffraction of clusters has recently been provided by $[Fe_8O_2(OH)_{12}(tacn)_6]^{8+}$, Fe8 [42]. The ground state of the cluster has $S = 10$, which suggests that there are six spins up and two down. It must be stressed that this is not unambiguous, because the spin topology is complex, with many triangles which for antiferromagnetically coupled spins can yield spin-frustration effects [43]. This means that it is difficult, or impossible, to describe the ground state with simple up-down-spin arguments.

Assuming that the coupling mechanisms are dominated by the μ-oxo bridges connecting the butterfly ions, the coupling constant connecting the body ions Fe1 and Fe2, which corresponds to a double bridge with Fe–O–Fe angles of 96.8° on average, is expected to be much smaller than those defining the wings, in which the single μ-oxo bridges form, on average, an Fe–O–Fe angle of 128.8°. Such a trend in the strength of the interaction is in agreement with the angular dependence of the coupling constants in iron(III) pairs, recently well established both experimentally and theoretically [44, 45]. The average $\mathrm{Fe–O_{bridge}}$ distance is, moreover, significantly shorter for the wing-core pairs. The fit of the temperature dependence of the magnetic susceptibility was made on this assumption, suggesting that the down spins are Fe3 and Fe4. The temperature-dependence of χ_{T} has been successfully reproduced [31, 46], assuming D_2 symmetry for the cluster to reduce the matrices to a tractable size, using $J_{12} = 17\,\mathrm{cm}^{-1}$, $J_{27} = 42\,\mathrm{cm}^{-1}$, $J_{18} = 25\,\mathrm{cm}^{-1}$, and $J_{13} = 140\,\mathrm{cm}^{-1}$.

The reconstructed magnetization density map confirmed this view, thus providing visual access to the exchange pathways of the cluster. The magnetization density, MD, map shows also that the spins of the four peripheral iron atoms are aligned parallel to Fe1 and Fe2, suggesting that the antiferromagnetic interactions between them are weaker than that with Fe3 and Fe4. In this case the $\mathrm{Fe–O_{bridge}}$ distances are

similar but the Fe–O–Fe angles are significantly smaller for the first type of bridge.

Looking in more detail at the experimental MD we see that it deviates substantially from the assumed D_2 symmetry, and there are, in fact, marked asymmetries in the moment on the Fe1 and Fe2 and on the Fe3 and Fe4 pairs. The asymmetry is much less marked on the Fe5, Fe6, Fe7, and Fe8 ions. From the point of view of the crystal symmetry this is not surprising, because the cluster lacks a center of symmetry, but no large differences are observed in the exchange pathways. It is possible that, given the presence of eight triangles, spin frustration effects finely determine the MD. Unfortunately it is not possible to calculate the spin levels without using symmetry, because the size of the matrixes to diagonalize would become too large, and letting 13 coupling constants vary independently would probably be not meaningful.

3.2.4 High-field Magnetization

Beyond inelastic neutron scattering it is possible to explore the energies of the excited levels using high-field magnetization techniques, but this is only possible for antiferromagnetic and ferrimagnetic clusters. In fact, in these cases the zero-field ground state has not the maximum possible value of S, which means that it is not the ground state in the presence of strong fields. This is easily understood by looking at the energy-level diagram for a pair of $S = 1/2$ spins, in which the singlet lies lowest. If an external field is applied parallel to the z axis, the levels, the energy separation between the $S = 0$ and the $M = -1$ component of $S = -1$, is given by:

$$\Delta = J - g\mu_B H \tag{10}$$

Equation (10) suggests that at $H = J/g\mu_B$ the two levels are degenerate, and for higher fields the triplet becomes the ground state. At sufficiently low temperature the magnetization rapidly increases from zero, as requested by the $S = 0$ state, to the saturation value for $S = 1$, $M_{sat} = gN\mu_B S$. In principle this is a good method, but it might require high magnetic fields. A field of approximately 1 T is required for a system with $g = 2$, with two levels differing by unity in the value of S, separated by 1 cm^{-1}. Static fields can reach approximately 30 T, whereas with pulsed fields it is relatively easy to go up to ca. 50–60 T. Pulsed fields reaching 700–800 T have recently become available [47]! These techniques have been applied both to antiferromagnetic rings and to ferrimagnetic clusters. Among the antiferromagnetic rings those which have been better investigated are iron(III) rings with six and ten members. The coupling between the metal ions is antiferromagnetic and the ground state for the cluster is $S = 0$. In zero field the energies of the lowest lying excited multiplets are, to a good approximation, given by:

$$E(S) = J_{eff} S(S + 1) \tag{11}$$

where $J_{eff} = 2J/N$. J is the nearest-neighbor exchange interaction and N is the number of ions in the ring. The Lande interval rule in Eq. (11) originates from the fact that the lowest lying levels of the ring can be approximated by coupling the ions on the odd-number sites with those on the even-number sites to give the maximum

spin multiplicity. For instance in a ring of ten iron(III) ions, each with $S = 5/2$, the five odd-site spins are coupled to give $S_{\text{odd}} = 5 \times 5/2 = 25/2$ and the five-even site spins $S_{\text{even}} = 25/2$. These two spins are then coupled to give the total spin S, $S_{\text{odd}} - S_{\text{even}} \leq S \leq S_{\text{odd}} + S_{\text{even}}$. For a given S there are many more states, but those found with the above procedure are of lowest energy with that spin multiplicity.

Experimentally the best determination of excited energy levels in antiferromagnetic rings has been performed on $[Fe_{10}(OMe)_{20}(CH_2ClCOO)_{10}]$ [48], the so called ferric wheel [49], the structure of which is shown in Fig. 5. In this instance a pulsed magnetic field experiment up to 50 T has provided a magnetization curve with regular pattern of peaks separated by ca. 4 T, as shown in Fig. 6. In a pulsed experiment the

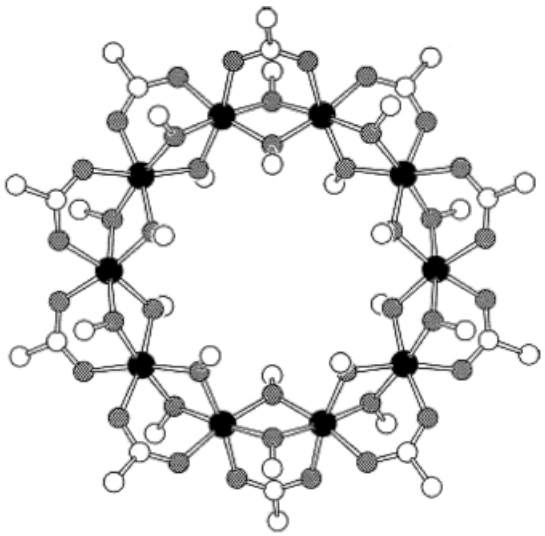

Fig. 5. Sketch of the structure of the "ferric wheel", $[Fe_{10}(OMe)_{20}(CH_2ClCOO)_{10}]$. The iron, carbon and oxygen atoms are represented by full, empty, and hatched circles, respectively. The chlorine atoms of the ligands are omitted for clarity.

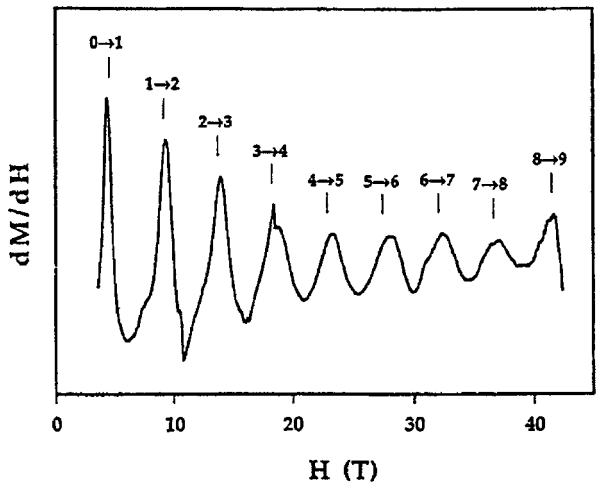

Fig. 6. Differential magnetization of the "ferric wheel" in a pulsed magnetic field measured at 0.65 K. The crossover between the S and $(S + 1)$ states is noted above each maximum.

derivative of the magnetization, dM/dH, is recorded; the peaks therefore correspond to points of inflection of the integral curve.

The magnetization of the ferric wheel increases in steps from 0 to the saturation value for $S = 9$. The regular pattern of peaks is a clear confirmation of the Lande interval rule predicted by Eq. (11). In fact it requires that the field separation for the crossover from a spin S to the nearest $S + 1$ is $\Delta H = 2(S + 1)J_{\text{eff}}/g\mu_{\text{B}}$ and the separation between two neighboring peaks is:

$$\Delta H = 2J_{\text{eff}}/g\mu_{\text{B}} \tag{12}$$

From this $J = 10.6\,\text{cm}^{-1}$ is obtained. A rigorous fit of the magnetic susceptibility of the ferric wheel could not be achieved, because ten iron(III) ions require matrixes which are too large. By using classical spins, however, a fit with the value $J = 9\,\text{cm}^{-1}$ was obtained, in reasonable agreement with experimental data. Similar results ($J = 9.6\,\text{cm}^{-1}$) were obtained by fitting the susceptibility per iron with the energy levels for a ring of eight iron(III) ions. In fact it is well known that the susceptibility of antiferromagnetic rings rapidly converges on increasing the number of members. This procedure has long been used to calculate the thermodynamic functions of infinite chains by extrapolating from rings [50].

High-field magnetization data were also reported for smaller rings comprising six iron(III) ions [51]. In this instance the energy levels can be calculated exactly by direct diagonalization of the isotropic part of the Hamiltonian Eq. (1); agreement with the observed energy differences is excellent. Because in this instance it was also possible to measure the magnetic anisotropy, a detailed description of these results will be deferred to the magnetic anisotropy section.

It must also be stressed that in a pulsed experiment the sample might not be in thermal equilibrium with the bath. Rapid transfer of heat to and from the spin system is required to maintain the spin system at a constant temperature when the magnetic field is rapidly changed. The spin temperature T_{S} will remain equal to the bath temperature T_{bath} only if heat can also be exchanged rapidly between the lattice and the bath. If this is not so, because the time of the pulse is too short, T_{S} varies significantly during the pulse. In fact the spin systems tends to cool at the crossing fields, because of magnetocaloric effects. This has been clearly observed in experiments performed on the antiferromagnetic dimer $[\text{Fe(salen)Cl}]_2$ [52]. Satellite peaks were observed at the crossover fields to $S = 1$ and $S = 2$, respectively. An acceptable fit to the experimental data was made assuming that for T_{S} the rate of change is:

$$\frac{dT_{\text{S}}}{dt} = -\frac{T_{\text{S}}}{C_{\text{H}}}\left(\frac{\partial M}{\partial T}\right)_{\text{H}}\left(\frac{dM}{dT}\right) + \frac{1}{C_{\text{H}}}\left(\frac{dQ}{dT}\right) \tag{13}$$

where C_{H} is the specific heat at constant H and dQ/dT is the rate of heat flow from the bath to the spin–lattice system.

Recently extremely high fields have become available through a technique that generates fields up to 800 T [47]. The sample, which can be a polycrystalline powder or an oriented single crystal, is placed in one of two inductive coils of diameter of 1.6 mm and length 8 mm. The coils are accurately checked to ensure that only the

sample magnetization voltage is present, and the sample is cooled to the desired temperature by means of a plastic cryostat. Magnetic fields are created by the explosive compression of initial magnetic flux as developed in special generators, usually indicated as MC–1. The field rise time in the pulse is 15 μs, and the measurements are single shot, because the measuring coils, the cryostat, and the samples are destroyed as a result of each experiment. A laser that follows the Faraday rotation measures the differential magnetization of the sample.

When the technique was applied to bulk ferrimagnets the magnetization increased gradually. In contrast, when it was applied to molecular ferrimagnets the magnetization showed a stepped behavior indicating the quantum nature of the energy levels. Megagauss magnetization experiments were performed on Mn12Ac, the structure of which is shown schematically in Fig. 1 [4]. The Mn12Ac molecules have tetragonal symmetry and the $S = 10$ ground state arises from the antiferromagnetic coupling between the eight manganese(III) ($S = 3/2$) and the four manganese(IV) ($S = 2$) spins [53]. The quantum nature of the low-lying states has been confirmed by several experiments [54, 55], but essentially nothing is known of the excited states.

Figure 7 shows the measured differential magnetization of a single crystal of the cluster. The external magnetic field is parallel to the tetragonal axis of the cluster. The curve shows several well resolved spikes, with the middle spike, centered at ca 520 T, of huge amplitude. The four low-field spikes can be located at 382, 416, 448, and 475 T. There are spikes also in the high-field region, but they are less well characterized, and are more difficult to locate. No spikes are, however, observed above 690 T.

Although quantitative analysis is complicated, as will be better shown below, the overall appearance of the high-field differential magnetization of Mn12Ac provides some useful information. The lowest field spike must arise from the transition from the ground $S = 10$ to the lowest $S = 11$ state, whereas the next three correspond to the crossing over of the $S = 12$, 13, and 14 states, respectively. The large spike must be assigned to a bunch of levels, presumably $S = 15$, 16, 17, and 18, which crossover

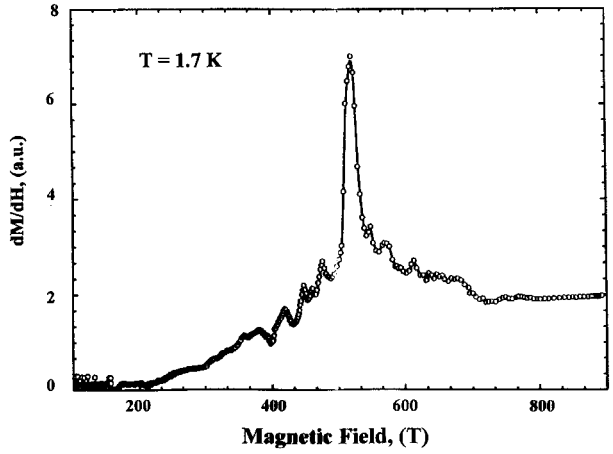

Fig. 7. Megagauss pulsed-field magnetic susceptibility of a single crystal of Mn12Ac. The field is applied parallel to the tetragonal axis.

in a narrow field range, whereas the remaining states, $S = 19, 20, 21$, and 22 crossover in the high field region up to 690 T.

It is, in principle, possible to calculate at the simplest possible level of approximation the fields at which the spin crossovers occur by using the spin Hamiltonian:

$$H = g\mu_B H \Sigma_i S_{i(z)} + \Sigma_{i<j} J_{ij} \mathbf{S}_i \cdot \mathbf{S}_j \tag{14}$$

where g has been assumed to be isotropic and close to 2. The sizes of the matrices to be diagonalized are shown in Table 1. Exact calculations could be performed in zero field for S ranging from 16, which corresponds to a 7656×7656 matrix, to $S = 22$, which corresponds to a 1×1 matrix. The crossover fields were calculated under the simplified conditions:

$$H_{S \to S+1} = [E(S+1) - E(S)]/(g\mu_B) \tag{15}$$

This equation holds for a regular pattern of levels, i. e. for a system in which the energy of the lowest $S + 1$ level is higher than that of the lowest S level, and the energy $E(S+2) > 2E(S+1) - E(S)$. The advantage of this approach is that it is as accurate as possible; it is, however, only applicable to the high field spikes, which are the least resolved.

An alternative approach has been also developed, assuming a perturbative treatment [56]. The basis for this is the consideration that the coupling constant J_1, which corresponds to a double oxo bridge between a manganese(III) and a manganese(IV) ion should provide the most efficient antiferromagnetic pathway in the cluster. Under these conditions it is possible to assume that the lowest lying states, comprising the ground $S = 10$ state, derive from the configuration in which the four pairs of manganese(III)–manganese(IV) ions are in the ground $S = 1/2$ state. The energies of the excited states were then obtained by second-order perturbation theory in the small parameters $\varepsilon_i = J_i/J_1$. Although the quantitative agreement of this approach is not totally satisfactory, as shown by comparison of the energies calculated by diagonalization of the matrixes, it shows a general pattern of levels that agrees well with experimental data. If, in fact, the values of ε_i are kept small, the crossover fields can be grouped in three sets. The crossovers corresponding to $S = 11$, 12, 13, and 14 occur at regular spacing, the crossovers corresponding to $S = 15$, 16, 17, and 18 occur in a narrow range of fields, and the others occur at higher fields. The calculated differential susceptibilities yielded the best-fit parameters, $J_1 = -65\,\mathrm{cm}^{-1}$, $J_2 = -32\,\mathrm{cm}^{-1}$, $J_3 = 6\,\mathrm{cm}^{-1}$, $J_4 = -16\,\mathrm{cm}^{-1}$.

3.3 Magnetic Measurements

3.3.1 Introduction

The standard magnetic measurements performed on clusters are the DC susceptibility and magnetization, which are of fundamental importance for the description

of the low-lying levels and for the determination of the nature of the ground state and of its zero-field splitting. We will not spend additional time on these, because their role is well known and readily available in many laboratories. We will outline here additional techniques which are well suited to the determination of the dynamic susceptibility (AC magnetic measurement), or to the direct measurement of the magnetic anisotropy in small single crystals (cantilever magnetometry), or to the investigation of very small crystals (microSQUID arrays), and which are becoming increasingly important.

3.3.2 AC Susceptibility Measurements

Slow relaxation of magnetization is one of the exciting features of the magnetic behavior of large molecular clusters. This was first discovered in Mn12Ac by performing AC susceptibility measurements [3]. The inductive response of a specimen might be measured in the presence of an oscillating magnetic field, and in this case it depends on the frequency ω of the field. It can, in general, be expressed as the sum of an in-phase component, χ', and an out-of-phase component, χ'', of the susceptibility $-\chi(\omega) = \chi'(\omega) - i\chi''(\omega)$. If the change of the external field is slow compared with the relaxation time of the magnetization, τ, (i. e. $\omega \ll \tau^{-1}$) then the magnetization is always in equilibrium over the time-scale of the experiment. The measured susceptibility is the same as the static susceptibility and is called the isothermal susceptibility, χ_T. If the frequency is much faster than the reorientation of the magnetization (i. e. $\omega \gg \tau^{-1}$) then the magnetic system is effectively isolated from the surroundings and an adiabatic susceptibility, χ_S, is measured, which is smaller than χ_T. The dynamic susceptibility can be expressed as:

$$\chi' = \chi_S + \frac{\chi_T - \chi_S}{1 + \omega^2\tau^2};\ \chi'' = \frac{(\chi_T - \chi_S)\omega\tau}{1 + \omega^2\tau^2} \tag{16}$$

The real part of the susceptibility is in dispersion, and the imaginary is in absorption, as shown in Fig. 8. If the relaxation process is single-exponential, i. e. if it is dominated by one relaxation time, then when $\chi''(\omega)$ is plotted against $\chi'(\omega)$, the so-called Argand

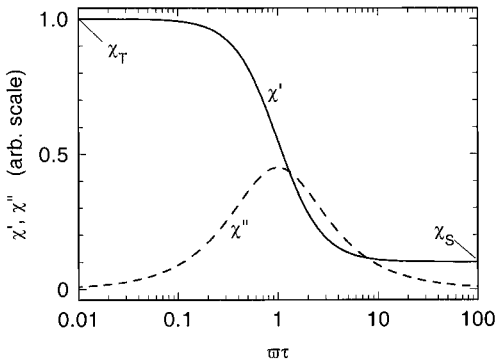

Fig. 8. Real (solid line) and imaginary (dashed line) components of the AC magnetic susceptibility as a function of the product of the AC frequency ω with the relaxation time τ. χ_S and χ_T denote the adiabatic and isothermal susceptibility, respectively.

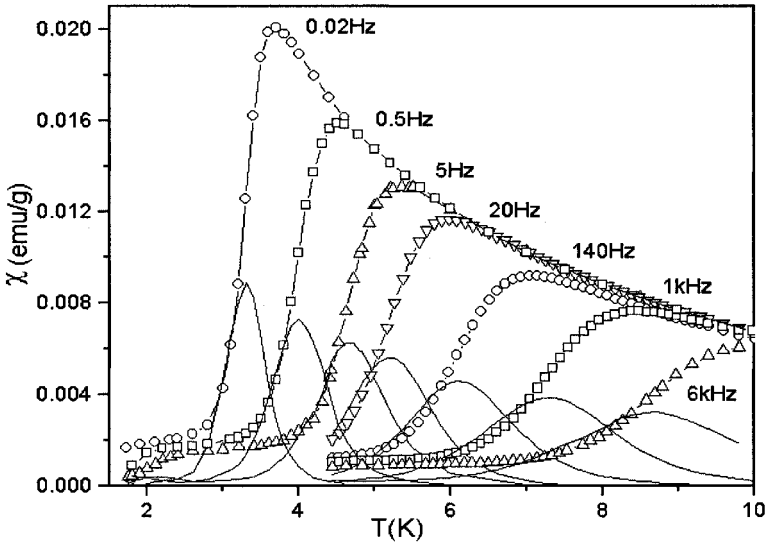

Fig. 9. Real (symbols) and imaginary (solid line) components of the AC magnetic susceptibility of Mn12Ac at several frequencies ranging from 0.02 Hz to 6 kHz. (Courtesy of M. Novak.)

diagram, a semicircle is obtained. The intersections of the curve with the x axis give χ_T and χ_S and the frequency at which the maximum value of χ'' is observed gives the relaxation rate.

Mn12Ac shows peaks in the out-of-phase components of the susceptibility below 10 K, clear indication of slow magnetic relaxation, as shown in Fig. 9.

The position of the peaks is temperature-dependent, ruling out the possibility of slow relaxation determined by the transition to magnetic order. An Argand plot shows a semicircle, indicating that single-exponential relaxation behavior is being monitored. If the relaxation time, obtained from the maximum value of χ'' at any given temperature is plotted against temperature between 2 K and 10 K the exponential dependence of the Arrhenius law is observed:

$$\tau = \tau_0 \exp(\Delta/kT) \tag{17}$$

where Δ is a barrier for the reorientation of the magnetization and τ_0 is the attempt time, the time the magnetization spends in a potential well before jumping to the other orientation. The best fit values are $\tau_0 = 2.1 \times 10^{-7}$ s and $\Delta/k = 62$ K. At ca 4.0 K the relaxation time is approximately 1 s; at 2.3 K it is approximately 1 day and at 2.0 K it is approximately 1 month. The Arrhenius behavior is analogous with that of classical superparamagnets [57]. These are single-domain magnets the size of which is so small that the barrier to reorientation of the magnetization, Δ, is comparable with the thermal energy. The pre-exponential factor in classical superparamagnets is much shorter than the value observed here ($\tau_0 \approx 10^{-10}$–10^{-13} s).

The origin of the barrier in Mn12Ac is associated with the zero-field splitting of the ground $S = 10$ state of the cluster [58–60], as determined by many other different

techniques. All the data concur, and show that the lowest components of $S = 10$ are those with $M = \pm 10$, the $M = 0$ state lying ca 70 K higher. This energy separation compares well with the experimentally determined barrier. The zero-field splitting of Mn12Ac is determined by the zero-field splitting of the individual manganese(III) ions [59], which deviate substantially from octahedral symmetry because of crystal-field effects.

Another feature of the AC susceptibility data shown in Fig. 9 is that a second, much smaller, peak in χ'' is observed at lower temperatures. This peak is generally observed also in other derivatives of Mn12 [5, 13]. There has been some controversy in the literature, but it seems now established that this is because of defective clusters present in the lattice of Mn12Ac [61]. In other words, there are some defective molecules in which the barrier to reorientation of the magnetization is smaller than in the bulk of Mn12Ac. This might be because one or more manganese(III) ions have elongation axes which are not parallel to those of the other manganese(III) ions of the cluster.

3.3.3 Cantilever Magnetometry

This technique is a recent extension of the old method of measuring the magnetic anisotropy of a single crystal through the torque exerted on the wire holding it in a magnetic field. The problem of this technique was that the sensitivity was low, and large single crystals were required. Now the use of high-sensitivity cantilevers enables measurements to be performed on tiny crystals, of approximately a few micrograms. The method is sensitive to the couple $\mathbf{T} = \mathbf{M} \times \mathbf{B}$ experienced by a magnetically anisotropic substance in a uniform magnetic field $\mathbf{B}$. $\mathbf{M}$ is the magnetization of the sample. $\mathbf{T}$ vanishes when the magnetic field is applied along one of the principal directions of the susceptibility tensor χ of the sample, because now $\mathbf{M}$ and $\mathbf{B}$ are collinear. The experimental apparatus is shown schematically in Fig. 10.

The crystal is laid on the cantilever. The magnetic field is applied in the xz plane and the apparatus measures the y component of the torque vector (T_y) acting on the sample. The crystal can be rotated around the y axis by means of a goniometer. The deflection of the cantilever from the zero field position, d, is detected by measuring the capacitance of the torquemeter (C), assuming $C \propto 1/d$. Capacitance variations (ΔC) during the experiments are typically less than 0.5% of the zero-field capacitance (approx. 1 pF), so that simple proportionality between ΔC and T_y can be assumed. The y axis of the torquemeter is usually aligned parallel to one of the principal

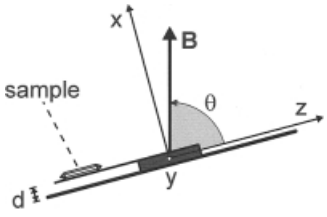

Fig. 10. Schematic diagram of a cantilever magnetometer. The component of the torque along the y axis is measured as a function of the field and of the angle θ.

directions of the susceptibility. In this case the y component of the torque vector is given by:

$$T_y = B^2(\chi_{zz} - \chi_{xx}) \sin\theta \cos\theta \tag{18}$$

where θ is defined in Fig. 10. Because the torque signal is proportional to the in-plane anisotropy and to the square of the magnetic field modulus, the sensitivity increases dramatically in high magnetic fields.

An important application of this technique has been performed on single crystals of antiferromagnetic rings [51, 62]. We have already reported in Section 2 how high-field magnetization studies can be used to obtain information about the energies of the excited states of iron(III) rings. Here we show how cantilever magnetometry can also provide the magnetic anisotropy of the excited levels.

The most elegant cantilever results were obtained on the Fe6 rings [51], because they have trigonal symmetry. In $[NaFe_6(OCH_3)_{12}(dbm)_6]PF_6$, where dbm = 1,3-dibenzoylmethane, the structure of which [63] is shown in Fig. 11. The six membered ring of iron(III) ions hosts an alkali ion in the center of the ring. The crystals were mounted with the y axis in the plane of the ring. The maximum torque was measured at $\theta = 45^\circ$. It varies rapidly with field at ca. 10 T, as shown in Fig. 12, because this is the crossover field B_c for passing from the $S = 0$ to the $S = 1$ ground state. In Fig. 12 the orientation dependence of B_c is also reported. This clearly shows that z, the trigonal axis, is the hard axis, and that the anisotropy is fairly large, B_c varying from ca. 10.75 T when the field is parallel to the trigonal axis to ca. 10.15 T when the field is in the ring plane.

The origin of the observed anisotropy must be in the $S = 1$ state, and because the g tensor for an iron(III) ion is expected to be very isotropic [64], the origin must be

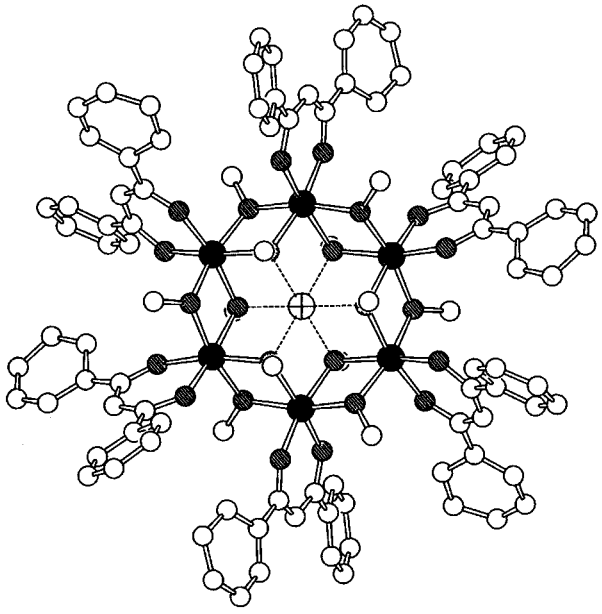

Fig. 11. Sketch of the structure of $[NaFe_6(OCH_3)_{12}(dbm)_6]^+$, NaFe6. The iron atoms are represented by large black circles and oxygen by small black circles.

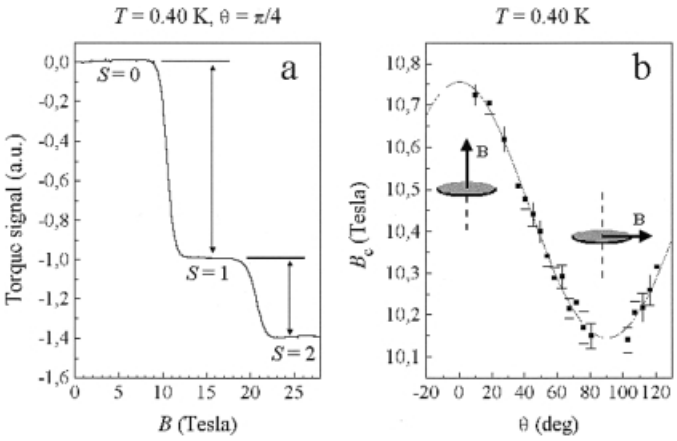

Fig. 12. (a) Field dependence of the torque signal showing the level crossing from $S = 0$ to $S = 1$ and from $S = 1$ to $S = 2$. (b) Orientation dependence of the crossover field B_c for NaFe6. If $\theta = 0^\circ$ the field is perpendicular to the ring; if $\theta = 90^\circ$ the field is parallel to the ring.

the zero-field splitting. The experimental data were satisfactorily analyzed to give a zero-field splitting axial parameter $D_1 = 4.32\,cm^{-1}$. In Table 2 this is compared with the corresponding value for the ferric wheel and for another Fe6 derivative, Fe6Li, in which the central alkali metal ion is lithium instead of sodium. The number of observed states depends on the value of the exchange coupling constant and on the maximum available field. In Fe6Li $J = 14\,cm^{-1}$, which, according to Eqs. (11) and (12) gives crossovers with a step of ca. 7 T. With a maximum field of 20 T, therefore, only two crossovers were observed. For Fe6Na $J = 22\,cm^{-1}$ and the step separation is 11 T, whereas for the ferric wheel it is 4 T. The experimental determination of the zero-field splitting for so many excited states is very rare. In principle HF-EPR can also provide information for excited multiplets.

The data in Table 2 enable checking of the validity of the rules that relate the zero-field splitting tensors of the S states, $\mathbf{D_S}$, with the corresponding tensors of the individual ions, $\mathbf{D_k}$, plus the interaction-determined contributions, $\mathbf{D_{jk}}$, as defined by the Hamiltonian Eq. (1). Assuming that the separation between multiplets is large

Table 2. Zero-field splitting data for three iron(II) antiferromagnetic rings (cm^{-1}).

	Fe6Li	Fe6Na	Fe10
$S = 1$	1.16(1)	4.32(3)	2.24(2)
$S = 2$	0.295(2)	–	0.599(3)
$S = 3$	–	–	0.291(1)
$S = 4$	–	–	0.180(1)
$S = 5$	–	–	0.123(1)

Table 3. Calculated coefficients for the zero-field splitting of the low lying multiplets of antiferromagnetic iron(III) rings.

S	$N = 6$			$N = 10$		
	d_1	d_{12}	d_{13}	d_1	d_{12}	d_{13}
1	−2.4000	2.85556	−3.00000	−2.24000	2.70800	−2.80000
2	−0.54422	0.69048	−0.68027	−0.52381	0.64857	−0.65476
3	−0.23492	0.32963	−0.29365	−0.23778	0.30533	−0.29722
4	−0.12245	0.19841	−0.15306	−0.13377	0.18052	−0.16721
5	−0.06838	0.13533	−0.08547	−0.08376	0.12051	−0.10471

compared with the splitting of the multiplets, the zero-field splitting tensors of the S multiplets are given by [24]:

$$\mathbf{D_S} = \Sigma_j d_j \mathbf{D_j} + \Sigma_{j<k} d_{jk} \mathbf{D_{jk}} \tag{19}$$

where d_j and d_{jk} are symmetry-determined coefficients which can be calculated with standard rules [24]. The $\mathbf{D_{jk}}$ tensors are expected to be given for iron(III) ions by the magnetic dipolar interaction only. In Table 3 we show the calculated coefficients relating the individual parameters to those of the cluster for the low-lying S multiplets of rings with six and ten iron(III) ions. We assume C_N symmetry for the rings, where N is the number of iron ions in the ring. Only the coefficients d_{12} and d_{13} are reported because all the other coefficients d_{12n} are identical with d_{12} and the d_{12n+1} are identical with d_{13}. All the other coefficients can be obtained from these by applying symmetry operations within the rings.

The analysis is relatively simple for the dipolar contribution. Let us assume completely planar, regular rings. In this case the $\mathbf{D_{ij}}$ tensor has a principal component, which is negative, parallel to the i–j direction. All the tensors must, therefore, have the same component perpendicular to the ring; this is given by:

$$D_{ij,zz} = 0.433 g^2 / r_{ij}^3 \tag{20}$$

where $D_{ij,zz}$ is in cm^{-1} and r_{ij} in Å. For example, for $N = 10$ the dipolar contribution to $D_{S,zz}$ is given by:

$$D_{S,zz} = 10(D_{12,zz} + D_{13,zz} + D_{14,zz} + D_{15,zz} + D_{16,zz}/2) \tag{21}$$

In a regular ring the ij distances can be expressed as a function of the nearest-neighbor distance $r_{12} = r$, so that the $D_{S,zz}$ components can be calculated with one variable r. Because the symmetry of the regular rings is axial, z is the unique axis, and the zero-field splitting parameter is given [64] by $DS = 1.5 D_{S,zz}$. The calculated coefficients are given in Table 4 and must be multiplied by r^{-3} (in Å) to give the zero-field splitting in cm^{-1}.

It is apparent that the calculated zero-field splitting is positive, corresponding to an XY type anisotropy. Further, the zero-field splitting roughly increases in proportion to N. The relative data for Fe10 and Fe6Li are not too far from this limit (the ratio of the D values is ca. 2 instead of 1.66), whereas that for Fe6Na is much larger than

Table 4. Dipolar zero-field splitting for low-lying S multiplets of antiferromagnetic rings comprising N iron(III) ions.

	$N = 6$	$N = 10$
$S = 1$	38.2955	62.2468
$S = 2$	9.3953	14.9821
$S = 3$	4.5786	7.1046
$S = 4$	2.8270	4.2402
$S = 5$	1.9850	2.8629

expected. If an average distance of 3.25 Å for the nearest-neighbor distance is taken for Fe6Li and Fe10, in agreement with the X-ray crystal structure data, the calculated and experimental values are in good agreement, suggesting that for these rings the dipolar interaction is dominant. The large value for Fe6Na must arise from a sizeable single-ion contribution. This shows how subtle changes in the structure of the rings, for example the substitution of one alkali ion for another in the center of the ring, can drastically alter not only the magnetic coupling but also the magnetic anisotropy.

3.3.4 MicroSQUID Arrays

The microSQUID (Super-Conducting Quantum Inference Device) technique is very similar to the traditional SQUID technique to amplify the variation of the magnetic flux. The essential difference is that the pick-up coil is replaced by direct coupling of the sample with the SQUID loop. When a small sample is placed directly on the wire of the SQUID loop, the sensitivity of the microSQUID technique is nine orders of magnitude better than that for traditional SQUID. This result is only achieved when the size of the sample is smaller than that of the SQUID. In a practical realization implemented [65] at the CNRS Laboratories in Grenoble the magnetometer is a chip with an array of micro-SQUIDs, as shown in Fig. 13. The sample is positioned by means of a piezoelectric quartz tool. If the sample is very close to a SQUID the response will be sensitive to the local environment, whereas if the sample is removed farther away the response will be mediated over all the sample. The high sensitivity of the techniques enables the measurement of single crystals of 10–500 μm. The magnetometer works in the range 35 mK to 6 K and in fields of up to 1.4 T. Another interesting feature of the magnetometer is that the field can be swept at very high speed-in fact the sweeping rate can be as high as 1 T s^{-1}. The stability of the field is also

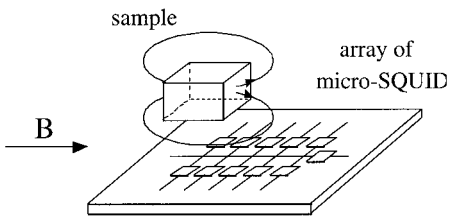

Fig. 13. Schematic diagram of a microSQUID array for measurement of the magnetization of small samples. (Courtesy of W. Wernsdorfer.)

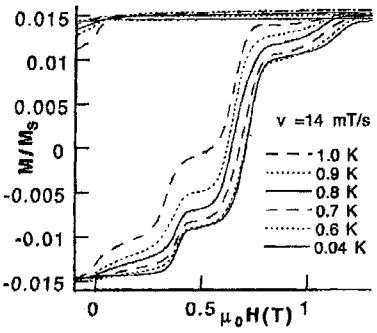

Fig. 14. Stepped magnetic hysteresis at different temperatures of the minority species present in a tiny single crystal of Mn12Ac.

very high, better than 1 μT s^{-1}. Finally the time resolution is also high, approximately 1 ms, enabling short-term measurements.

All these unique features have been recently exploited in the analysis of the dynamics of the relaxation of Fe8 [66] and Mn12Ac [61] at very low temperatures. In particular we want to show how the technique has been used to characterize the defective species present in Mn12Ac, mentioned in Section 3.2. The defective species, which is present at a concentration of 1–2%, has a tunneling relaxation time much faster than that of the major species; measurements for the former are, therefore, easier, because it is not necessary to wait for years as is the case for the latter. Both the major and the minor species are characterized by means of stepped hysteresis, which arises as a result of resonant quantum tunneling. The stepped hysteresis of the minor species measured with the microSQUID array between 40 mK and 1.0 K is shown in Fig. 14. The steps correspond to the fields at which the tunneling is enhanced by the degeneracy of pairs of M levels. Before the measurements the major species was demagnetized and, because of the long relaxation time at $T < 1$ K, this practically does not affect the measurements. The hysteresis curve becomes almost independent of temperature below 600 mK. This seems to be good evidence for quantum tunneling between the lowest $M = \pm 10$ levels. No such evidence could be obtained for the major species, because of its extremely long relaxation times in this temperature range. Matters are different for the minor species, which has lower barrier for the reorientation of the magnetization and faster quantum tunneling relaxation.

By comparison of the signal from a SQUID placed close to the edges of the crystals and from those close to the center of the crystal it could be concluded that the defective species is homogeneously distributed throughout the crystal and not located on the surface. This possibility of performing a sort of magnetic imaging is one advantage of the microSQUID technique.

3.4 Magnetic Resonance Techniques

3.4.1 Introduction

Magnetic resonance techniques, especially EPR, have been very important in the development of the field of molecular magnetic clusters. EPR can provide information about the spin of the ground state, and occasionally about that of lower excited states also. It also provides information about the zero-field splitting of the states; this is, in turn, of fundamental importance for understanding the magnetic anisotropy of the clusters. NMR is used to obtain information on the spin dynamics of the clusters, because the shifts and the relaxation of the nuclei, which act as local probes, are affected by electron relaxation. In this respect muon spin resonance, μSR, can also be used to obtain information similar to that of NMR, but using muons instead of protons.

In the following sections we will first discuss high-frequency-high-field EPR spectra, then zero-field and low-frequency-high-field spectroscopy applications. Subsequent sections will cover NMR and μSR spectroscopy.

3.4.2 HF-EPR

High-frequency–high-field EPR (HF-EPR) spectroscopy has developed rapidly in the last few years [37, 67–72]. The definition of HF-EPR is not exactly established, but it can reasonably be regarded as EPR spectroscopy performed with exciting frequencies no lower than 95 GHz. This frequency, which corresponds to a W band, is the only one implemented on a commercial instrument – higher frequencies are available on laboratory-developed instruments only. The exciting frequencies can be generated either by FIR Lasers or by Gunn diodes with frequency multipliers. The former are better for very high frequencies (>350 GHz), because at lower frequencies the laser lines tend to have low power and to be unstable, but, of course, they require very high fields. For $g = 2$ the resonance field for a frequency of 350 GHz is 11.7 T. Further high frequencies require quasi-optical approaches which are difficult to implement. Gunn diodes are much easier to handle, but have limited power, and with a frequency multiplier this is even lower.

HF spectrometers differ from the conventional X- and Q-band (9, 35 GHz) spectrometers, firstly because they do not use a cavity for recording the spectra. The loss in sensitivity is partially compensated because the sensitivity of the instrumentation increases as the frequency is increased, although sensitivity is, certainly, still one of the problems of HF spectrometers. This might not be a very serious problem for the investigation of clusters, because magnetically concentrated samples are usually used.

The main reason for using HF-EPR, rather than the conventional and less expensive X or Q band spectroscopy, with magnetic molecular clusters is that they often have large spin states. The spectra of an S spin state comprise at least $2S$ spin-allowed transitions spread over a wide field range. High fields are, therefore, needed just to observe all the expected transitions. Matters can be dramatic with integer spin val-

ues, because in this case when the zero-field splitting is larger than the microwave frequency no spectrum is observed when moderate fields are used. Another important point is that the HF-EPR spectra not only enable simplified determination of the zero-field splitting of a multiplet, but also of the sign. This is of paramount importance in the determination of the nature of magnetic anisotropy.

These points are very well illustrated by the X band and 350 GHz spectra of $[N(CH_3)_4]_4[Mn_{10}O_4(biphen)_4Cl_{12}]$ (biphen = 2,2′-biphenoxide) the structure of which is shown in Fig. 15 [73]. The cluster comprises four manganese(III) ions, with $S = 2$, and six manganese(II) ions, with $S = 5/2$, arranged in a complex three-dimensional structure determined by the presence of four μ_4-oxo groups [74]. The nature of the ground state was not unambiguously determined by low-temperature magnetization measurements, because of the presence of moderate zero-field splitting. They suggested, however, that the ground state has $S \geq 12$. X-band EPR spectra showed a pattern of parallel transitions above 0.3 T with an average separation of ca. 0.09 T, which suggested a zero-field splitting of ca. 0.045 cm^{-1}. These did not, however, provide any clear indication on the nature of the ground state, because the available field did not enable observation of all the $2S$ transitions. The HF-EPR spectra at 245 GHz are shown in Fig. 16. The $g = 2$ resonance is at ca. 8.2 T and clearly all the expected transitions are now observed. It is, therefore, only necessary to count the transitions for the field parallel or perpendicular to the unique axis of

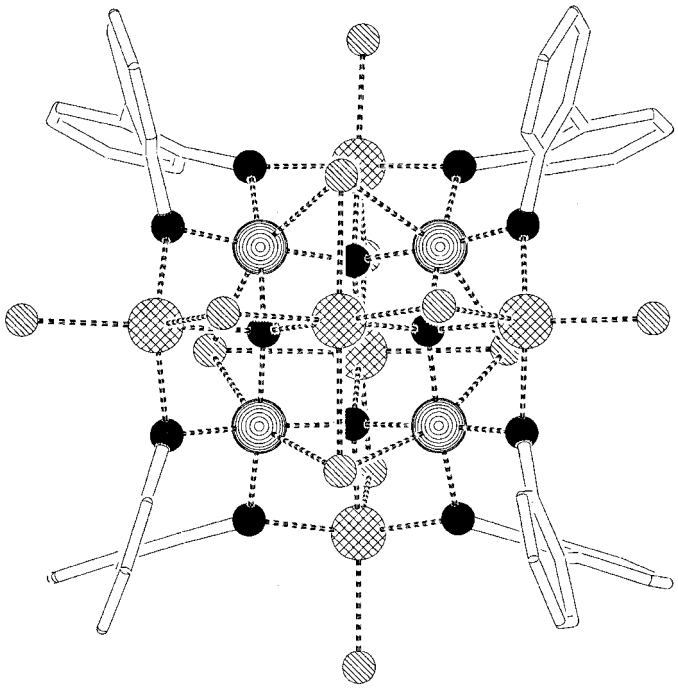

Fig. 15. Sketch of the structure of $[Mn_{10}O_4(biphen)_4Cl_{12}]^{4+}$, Mn10. Manganese(III) ions are drawn in large contoured spheres, manganese (II) in cross-hatched spheres, oxygen as small black ones, and nitrogen as hatched small spheres.

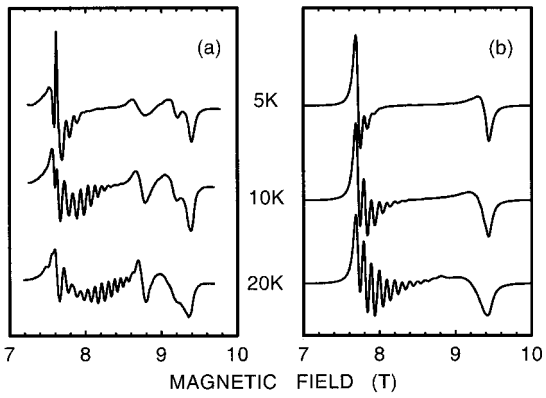

Fig. 16. HF-EPR spectra (245 GHz) of Mn10 recorded from partially oriented microcrystalline powder at different temperatures (left). On the right are the simulated spectra obtained with $S = 12$, $g_{\parallel} = 1.974$, $g_{\perp} = 1.983$, $D = -0.047\,\mathrm{cm}^{-1}$, and $E = 0$.

the cluster to determine unambiguously the nature of the ground state. In this case it turned out that 24 transitions are observed, corresponding to $S = 12$. The zero-field splitting was found to be $D = -0.047\,\mathrm{cm}^{-1}$. The negative sign, which corresponds to Ising type anisotropy, is because at low temperature at and low field the parallel transitions become intense. The fine-structure transitions correspond to excitations from the M to the $M + 1$ level. The lowest field transition might correspond to the $-S \rightarrow -S + 1$ or $S - 1 \rightarrow S$ excitation, depending on the sign of the zero-field splitting. The former is the correct for negative zero-field splitting, the latter for positive. In a high magnetic field the Zeeman energy is comparable with or larger than the thermal energy, so depopulation effects will be relevant, and the $-S \rightarrow -S + 1$ transition is of greater intensity than the $S - 1 \rightarrow S$ transition.

3.4.3 Zero-field EPR

In complete contrast with HF-EPR spectroscopy, it is now possible to measure the zero-field splitting of large spin multiplets directly, without applying an external magnetic field. The best results so far reported [75] have been obtained for Mn12Ac; these are shown in Fig. 17.

These spectra are, perhaps, more difficult to obtain than HF-EPR spectra, because the sensitivity of the technique is low, but they are certainly more easily read by non-experts than are EPR spectra. The absorption corresponds to direct transitions between the M components of the S multiplet. At 2.56 K only one absorption is observed at $10.02\,\mathrm{cm}^{-1}$, corresponding to the $\pm 10 \rightarrow \pm 9$ transition. At 5.3 K a second absorption at $8.50\,\mathrm{cm}^{-1}$ corresponding to the $\pm 9 \rightarrow \pm 8$ transition is observed. At 17.8 K a third absorption at $7.20\,\mathrm{cm}^{-1}$, corresponding to the $\pm 8 \rightarrow \pm 7$ transition is observed. The zero-field splitting of Mn12Ac at the simplest level of approximation can be described by the spin Hamiltonian:

$$H = DS_z^2 \tag{22}$$

which requires that the relative energies of the $\pm 10 \rightarrow \pm 9$, $\pm 9 \rightarrow \pm 8$, and $\pm 8 \rightarrow \pm 7$

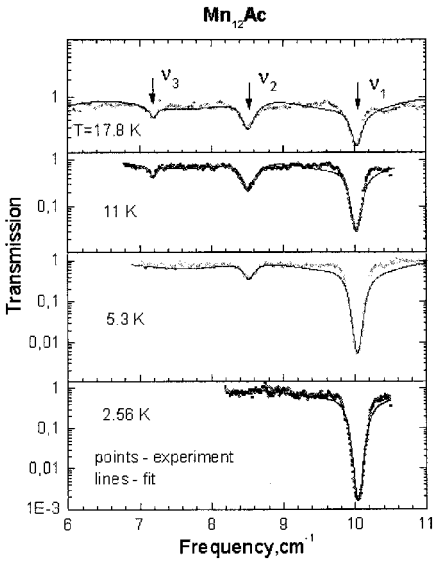

Fig. 17. Zero-field EPR spectra of Mn12Ac. The data used for the simulations are given in the text.

transitions are at anergies which follow the ratio 19:17:15. The experimental data yield the ratio 19:16:13.5, showing that Eq. (22) is not adequate. This had, indeed, been previously observed in the analysis of the HF-EPR spectra, which required a spin Hamiltonian including fourth order terms:

$$H = DS_z^2 + D'S_z^4 + C(S_+^4 + S_-^4) \tag{23}$$

The best-fit data obtained from the zero field experiment are $D = -0.389\,\mathrm{cm}^{-1}$, $D' = -7.65 \times 10^{-4}\,\mathrm{cm}^{-1}$; these can be compared with the values obtained from HF-EPR spectroscopy [76], $D = -0.388\,\mathrm{cm}^{-1}$, $D' = -7.7 \times 10^{-4}\,\mathrm{cm}^{-1}$. The value of C cannot be meaningfully obtained from the zero-field experiment.

3.4.4 Low-frequency EPR

Low-frequency EPR can be very important in the detection of the splitting of the lowest-lying levels in the presence of strong transverse fields. For instance, with an $S = 10$ ground state, as observed in Mn12Ac and Fe8, it is important to understand the mechanism of tunneling within the lowest $M = \pm 10$ levels to measure the so-called tunnel splitting. This is the separation of the two components determined by an applied transverse magnetic field. Experiments were performed on Fe8 [77], by using a loop-gap resonator operating at 680 MHz. Please notice that the exciting frequency is almost three orders of magnitude smaller than that in the highest frequency HF-EPR spectra, 550 GHz. The sample was a bunch of oriented microcrystallites, total weight 80 mg, buried in an epoxy slab. Fig. 18 shows the field dependence of the out-of-phase component of the susceptibility measured at 25 mK. Two peaks are clearly

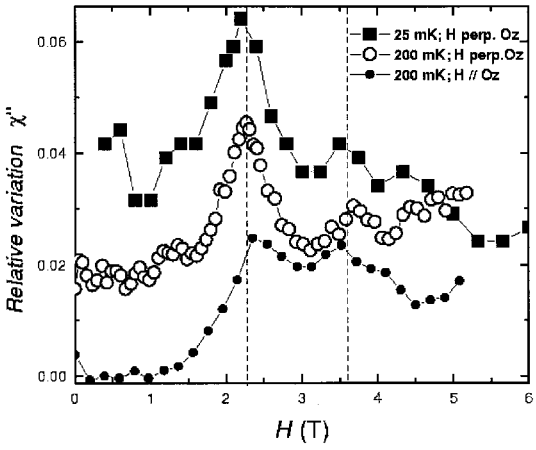

Fig. 18. Field-dependence of the out-of-phase component of the susceptibility of Fe8 at 25 mK. The sample was a bunch of crystals oriented by the magnetic field [78].

apparent, the first at $H_1 = 2.25 \pm 0.05\,\mathrm{T}$ and the second at $H_2 = 3.60 \pm 0.05\,\mathrm{T}$; these are associated to the transitions within the ground doublet when the external field is applied along the intermediate and hard axis, respectively.

3.4.5 NMR

NMR experiments on clusters have usually been performed in the low-resolution broad-band mode, because the presence of paramagnetic centers dramatically broadens the lines of the nuclear resonances in such a way that the paramagnetically shifted lines of different nuclei are observed only very rarely. We want to show, however, that even at low resolution it is possible to obtain important information about the spin dynamics of the clusters. This is best achieved by measuring the relaxation times, both spin–lattice and spin–spin, because for the reasons mentioned above the spectra are usually not very informative.

The most common technique used in NMR experiments is the Hahn-echo technique [78]. A $\pi/2$ pulse is applied and this is followed, after a delay time τ, by a π pulse. The first pulse moves the magnetization parallel to x, z being the field direction. After the pulse the magnetization starts to dephase in the xy plane. The second pulse re-phases the magnetization parallel to $-x$ and a signal is recorded (the spin-echo). The $\pi/2$ pulses are typically of a few microseconds. The spin–lattice relaxation times can be measured by the inversion recovery method or by use of the saturation recovery pulse sequence at low temperatures. Protons are, of course, the most widely investigated nuclei, but work on deuterons and others has also been reported.

The advantage of using NMR is that of having available a probe, the nuclear spin, which is sensitive to local fields [79, 80]. Collecting information on nuclear spin relaxation thus provides information about the relaxation of the magnetization of the system. In simple terms, the nuclear relaxation is strongly influenced by the much faster electron relaxation. Therefore by measuring the nuclear relaxation rates

as a function of exciting frequency, field, and temperature it is possible to obtain indirect information about electron relaxation. The theoretical expression relating the nuclear relaxation to the electron-spin dynamics [78] is:

$$T_1^{-1} = \frac{(\hbar\gamma_N\gamma_e)^2}{4\pi g^2 \mu_B k_B T}\left[\frac{1}{4}\sum_q A^{\pm}(q)\chi^{\pm}(q) f_q^{\pm}(\omega_e) + \sum_q A^z(q)\chi^z(q) f_q^z(\omega_N)\right] \tag{24}$$

where the coefficients $A^{\pm}(q)$ and $A^z(q)$ are the Fourier transforms of the spherical components of the product of two dipole interaction tensors describing the hyperfine coupling of a given nucleus to the electrons. The symbols $\pm$ and z refer to the components of the electron spins transverse and longitudinal relative to the direction of quantization, parallel to the external field. $\chi(q)$ is the wave vector-dependent magnetic susceptibility, and $f_q(\omega)$ is the normalized relaxation function at the indicated frequency. The first term in Eq. (24) corresponds to the relaxation at the electron resonance frequency, ω_e, and the second to the nuclear resonance frequency, ω_N.

The $A(q)$ coefficients can, in principle, be calculated if the structure is known and if it is reasonable to assume where the electrons are localized. For metal ion clusters it is usually assumed that the unpaired electrons are located on the metal ions, neglecting ligand delocalization effects. $\chi(q, T)$ and $f_q^{\alpha}(\omega)$ are, however, much more difficult to calculate, and no general treatment is yet available. An example of the full exploitation of Eq. (24) for calculation of proton relaxation rates in antiferromagnetic clusters will be given below.

At the simplest level of approximation Eq. (24) reduces to:

$$T_1^{-1} = A\frac{\tau_c}{1+\omega_N^2\tau_c^2} \tag{25}$$

where τ_c is a correlation time which can be identified with the relaxation time of the electron spin. In Fig. 19 we show the calculated relaxation times for a range of values of τ_c. The region of interest is that when $\omega_N\tau_c \approx 1$, because the longitudinal nuclear relaxation rate goes through a maximum. It can, therefore, be useful to measure the nuclear relaxation rate as a function of temperature and frequency. If, in the investigated (ω_N, T) range, τ_c becomes of the same order of magnitude as ω_N, then a maximum in the relaxation rate is observed. This behavior has been observed [81], for instance, in the proton relaxation rate of Mn12Ac, as shown in Fig. 20. In experiments performed at 14.1 and 31 MHz the proton relaxation rate steadily increases as the temperature is reduced, but below 40 K the relaxation rate becomes too fast and cannot be measured further. This indicates that in this temperature range τ_c is faster than 5×10^{-9} s. When the experiments are performed at higher frequencies (87 and 200 MHz) distinct maxima in the proton relaxation rate are observed at ca. 60–70 K. These data indicate that in this range of temperature τ_c is ca. 8×10^{-10} s. This value should be compared with the value of the relaxation rate of the magnetization calculated using Eq. (17) – $\tau_0 = 2.1 \times 10^{-7}$ s and $\Delta/k = 62$ K are the values estimated at low temperature from the AC magnetic susceptibility. At 60 K Eq. (17) yields $\tau = 8 \times 10^{-7}$ s which is almost three orders of magnitude

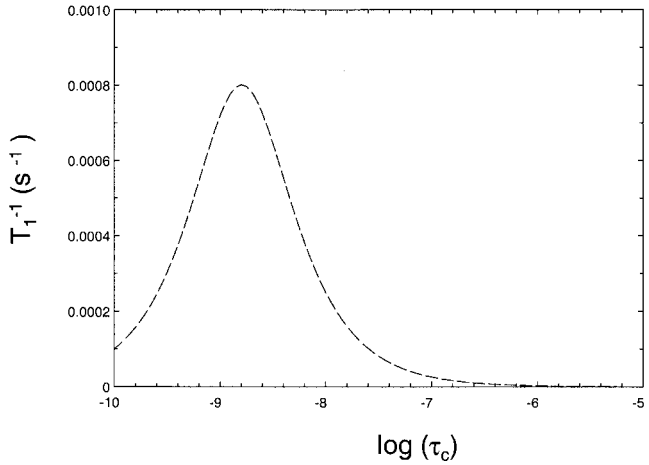

Fig. 19. Proton relaxation times calculated by use of Eq. (24). $\omega_N = 6.28 \times 10^8$ rad s^{-1}, $A = 1 \times 10^5$ s^{-2}.

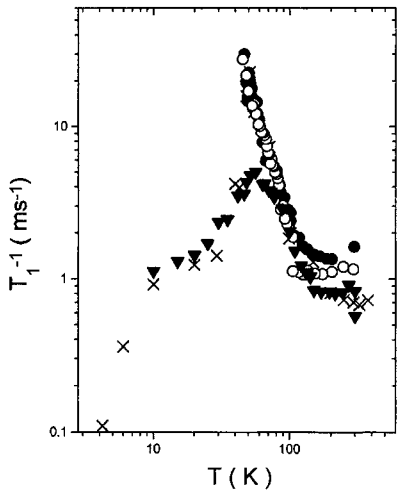

Fig. 20. Temperature-dependence of the proton spin-lattice relaxation rate of Mn12Ac. •, 14.1 MHz; ○, 31 MHz; × 87 MHz; ▼ 200 MHz.

longer than the value estimated by use of NMR. This is not an unexpected result because Eq. (17) is valid at low temperature when only the M levels of the ground state $S = 10$ manifold are populated; on increasing the temperature higher energy S levels become populated, thus increasing the electron relaxation rate.

Similar results were obtained for Fe8 [82]. For this compound relaxation rates obtained by NMR are in agreement with those obtained by Mössbauer techniques which explore essentially the same time window [7]. Additional data are available through μSR spectroscopy; these are discussed in the Section 4.6.

NMR experiments have also been performed on antiferromagnetic rings [83]. A nice example is provided by clusters comprising six and ten high-spin iron(III), al-

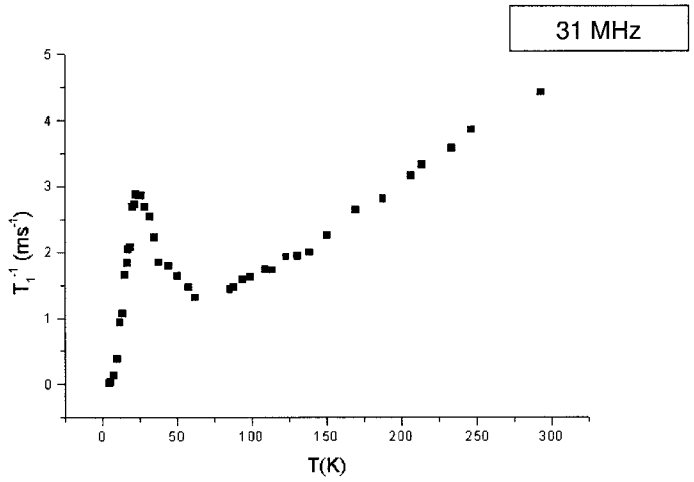

Fig. 21. Temperature-dependence of the proton spin-lattice relaxation rate of NaFe6 at 31 MHz.

ready described in Section 3.3. The temperature-dependence of the proton relaxation rate of NaFe6 measured at 31 MHz is shown in Fig. 21.

It is apparent that a sharp maximum is present at ca. 20 K. At low temperatures the relaxation rate is slow in agreement with the fact that the ground state is non-magnetic. On increasing the temperature the excited $S \neq 0$ levels become populated. In particular the first excited level which is 19 K above the ground state has $S = 1$. The experimental data have been fitted assuming a model in which the relaxation rate is given by the sum of two terms, corresponding to the contribution from the first excited triplet and to all the other levels, obtained by use of the equation:

$$T_1^{-1} = \left\{ A \exp(-E_T/kT) + B \int_d^\infty D(E) \exp(-E/kT) \mathrm{d}E \right\} Z^{-1} \qquad (26)$$

where E_T is the energy of the first excited triplet. The second term in curly brackets is based on the assumption that the levels above the triplet can be approximated by a continuum of levels $D(E)$, as shown in Fig. 22. Z is the partition function and A, B, and d are parameters. The best fit values are $A = 7.3\,\mathrm{ms}^{-1}$, $B = 5\,\mathrm{ms}^{-1}$, $d = 200\,\mathrm{K}$.

One interesting feature of magnetic rings is that they have long been used to extrapolate the thermodynamic functions of infinite chains. One of the fingerprints of one-dimensional magnetic behavior is the $\nu^{-1/2}$ dependence of the nuclear relaxation rates at high temperature [24]. One possible question which can, therefore, be asked is at which stage the one-dimensional spin dynamics sets in for antiferromagnetic rings. The field-dependence of the nuclear relaxation rate of the Fe6 cluster has shown that this is, indeed, not so for such small rings. The experimental behavior has been well justified by a mode-coupling approach assuming that after a long time the electron-spin correlation function decays, because of some cut-off mechanism. Similar results were obtained from analysis of the proton relaxation rate in a ferromagnetic ring comprising six copper(II) ions which has a ground $S = 3$ state [84].

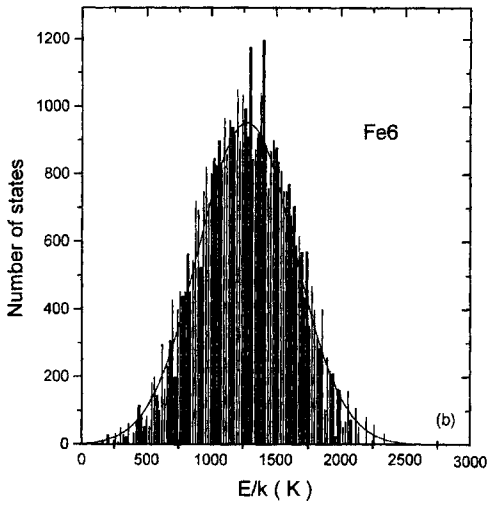

Fig. 22. Calculated spin energy levels for NaFe6. The curve is a Gaussian fit to the histogram of the distribution of levels.

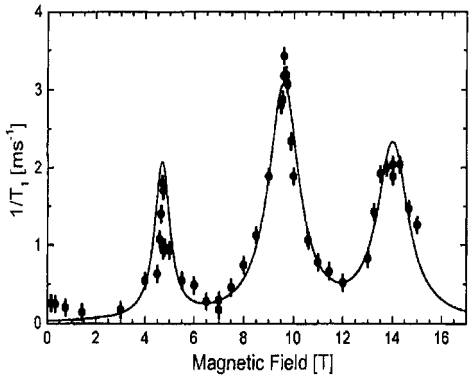

Fig. 23. Field-dependence of the proton relaxation rate of the ferric wheel at 1 K.

It is, in general, a good approximation that nuclear spin–lattice relaxation is induced by the dipolar fields of the electrons, and in principle it can be calculated. The best evidence for this has been obtained from analysis of the proton relaxation rate in the ferric wheel, to be discussed below. We have already mentioned that in the ferric wheel the ground state has $S = 0$, with the lowest lying S states at $E(S) = JS(S+1)/5$, with $J/k = 15.8\,\mathrm{K}$ [48]. The ground state can be changed by an external field, which stabilizes the higher spin states. In fact the $S \rightarrow S+1$ crossover fields in Tesla are given by Eq. (12). Proton NMR experiments have been performed at 2 K, in fields ranging from 2 to 16 T and the maxima of the spin–lattice relaxation rates have been found to correspond to the crossing fields as shown in Fig. 23 [85].

Like the stepped magnetization shown in Fig. 6, the peaks in the proton relaxation rate are a manifestation of quantum effects. The origin of the peaks can be understood by considering that when the separation between the electronic levels becomes close to zero the nuclei can easily relax by exchanging a quantum with the electron spin corresponding to the nuclear frequency. In the simplest approximation

the coupling between the electron and the nuclear spin is provided by the dipolar hyperfine interaction:

$$T_1^{-1} = \frac{1}{2N^2}(\gamma_e\gamma_N\hbar)^2\Bigg[2\pi\delta(\omega_N)\frac{1}{1+e^{\beta\hbar\omega_{eg}}}\left[S^2+e^{\beta\hbar\omega_{eg}}(S+1)^2\right]G_\alpha + \pi\left[\delta(\omega_N+\omega_{eg})-\delta(\omega_N-\omega_{eg})\right]\frac{(S+1)\left[(Ns+1)^2-(S+1)^2\right]}{2(2S+3)}G_\beta\Bigg] \tag{27}$$

where is N the number of spins in the ring, S is the total spin, ω_{eg} is the frequency corresponding to the energy difference between the ground and the first excited electron spin state, ω_N is the nuclear frequency, and $\beta = kT$. Eq. (27) is valid at low temperature, when it is a good assumption to consider only the lowest and the first excited levels. G_α and G_β are the average values of the hyperfine dipolar fields on the protons exerted by the electron spins. In the actual calculation the Dirac deltas are substituted by Lorentzian functions $2\pi\delta(\omega) = 2\Gamma/(\omega^2+\Gamma^2)$, where Γ is inversely proportional to the natural lifetime of the level. This has been used to fit the experimental data, with good agreement. It must be mentioned that this cross-relaxation behavior can be also interpreted as evidence for quantum tunneling of the electron magnetization. The splitting of the S and $S+1$ levels can, in fact, be considered as tunnel splitting which, when quenched, results in less efficient electron spin relaxation and enhancement of nuclear relaxation.

3.4.6 μSR

Muons are charged particles with rest mass approximately 1/14 that of the protons. There are both positive and negative muons, with charge $\pm e$. In general, positively charged muons, also called muonium, are used. They have spin $S = 1/2$, a magnetic moment $\mu_\mu = 4.84\times10^{-3}\,\mu_B$, and a gyromagnetic ratio $\gamma_\mu/2\pi = 135.5$ MHz/T. The average lifetime of the muons is $\tau_\mu = 2.2\times10^{-6}$ s. A muon can, therefore, be regarded as a light proton, and it can be used as a probe analogous to the latter to measure many properties of condensed matter [86]. In particular muons are widely used to investigate the magnetic properties of materials, and investigation of molecular materials [87–89] and clusters [81] has begun.

Muons are obtained through the weak decay of pions, which have an average lifetime of 26 ns according to the reaction:

$$\pi^+ \rightarrow \mu^+ + \nu_\mu \tag{28}$$

The pions are produced when protons with energy >180 MeV hit beryllium or graphite targets. In a typical experiment the muons are selected such that their spins are 100% polarized. This is a definite advantage over NMR experiments in which spin polarization is very low. The sensitivity of measurements with muons is, therefore, very high.

The muons are injected into the sample and they thermalize in a time less than 1 ps, principally by interaction with electrons. After this time the thermalized muons usually become localized in a well defined site in the sample. The muon spin will precess around the local field B_μ which in general can be expressed as:

$$B_\mu = B_{\text{ext}} - B_{\text{demag}} + B_{\text{Lor}} + B_{\text{hyp}} + B_{\text{dip}} \tag{29}$$

where B_{ext} is the external field, B_{demag} is the demagnetizing field of the sample, B_{Lor} is the field of the Lorentz cavity in which the muon is hosted, B_{hyp} is the hyperfine field of the electron, and B_{dip} is the dipolar field generated by magnetic nuclei. After a time of the order of τ_μ the muon decays emitting a positron, a neutrino, and an antineutrino. The probability of emission of a positron at an angle θ from the muon spin is:

$$W(\theta) = 1 + A\,\cos\theta \tag{30}$$

The time-dependence of the precession of the muons can be monitored by measuring the emitted positrons. Typical μSR experiments can be performed with a transverse field, with a longitudinal field, and in zero field. In all the experiments what is measured is the depolarization of the muons while they are reaching thermal equilibrium by interacting with the local fields of the sample in the neighborhood of the site where the muon has become localized. If the transverse field is parallel to z, the muon polarization will precess in the xy plane and the time-dependence of the polarization will be given by:

$$N(t) = A P_x(0) G_x(t)\,\cos(\omega_\mu t + \varphi) \tag{31}$$

where $P_x(0)$ is the initial polarization of the muon, $G_x(t)$ is the depolarization function, $\omega_\mu = 2\pi\gamma_\mu B$, and φ is the initial phase factor of the polarization when the muons enter the magnetic field. The depolarization function depends on correlation times of the local fields experienced by the muons. In the limit of slow motion, when $\tau_c \gg (\Delta\omega)^{-1}$, the depolarization function is Gaussian, whereas in the limit of fast motion the function is exponential. The Fourier transform in the slow limit is Gaussian, whereas in the fast limit it is Lorentzian. The analogy with the NMR experiment is apparent.

If the field is applied parallel to the direction of the muon beam, the muon spins will remain polarized parallel to that direction without precessing. Under these conditions also two limiting situations can be considered – that in which the local fields which cause the depolarization are much stronger than the applied field, and that in which the local fields are much weaker. The latter limit is achieved when no field is applied. The depolarization function then takes the form:

$$G(t) = 1/3 + 2/3(1 - \Delta^2 t^2)\,\exp(-\Delta^2 t^2/2) \tag{32}$$

where Δ is the second moment of the field distribution at the muon. The decay of the polarization is initially Gaussian, but after a long time there is recovery of the polarization along z. The polarization tail, which levels off at 1/3, is sensitive to very

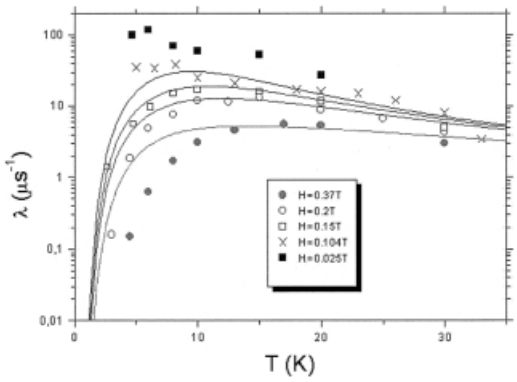

Fig. 24. Temperature-dependence of the muon longitudinal relaxation rate of Mn12Ac in different fields.

slow fluctuations of the local fields. When the external field is larger than the internal fields muon polarization remains almost constant. Under intermediate conditions, however, when dynamic internal fields are present, the system of muons thermalizes towards the temperature of the lattice with a characteristic time, λ^{-1}, which is the equivalent of the spin–lattice relaxation time T_1 of the NMR experiment.

μSR experiments have been performed on Mn12Ac [81], in conjunction with the NMR described in the previous section. The experiments were performed either in zero field or in a longitudinal field. The decay of muon polarization was fitted with a stretched exponential, $\exp[-(\lambda t)^{\beta}]$, indicating that the muons become distributed among several different sites. The muon relaxation rates were measured for fields ranging from 0 to 0.37 T. The relaxation rates vs. temperature go through maxima which shift to higher temperature as the field is increased, as shown in Fig. 24.

The relaxation rate was expressed as:

$$T_1^{-1} = \frac{A}{Z} \sum_{m=+10}^{-10} \frac{\mathrm{e}^{-E_m/kT\tau_m}}{1+\omega_{\mathrm{L}}^2\tau_m^2} \tag{33}$$

where A is an adjustable parameter, the sum is on all the M states of the $S = 10$ ground state of Mn12Ac, E_m is the corresponding energy, τ_m is the lifetime of the level, and ω_{L} is the Larmor frequency. The lifetime τ_m is expressed as:

$$\tau_m^{-1} = p_{m\to m-1} + p_{m\to m+1} \tag{34}$$

where $p_{m\to m-1}$ is the transition probability from m to $m-1$. These can be expressed as:

$$p_{m\to m-1} = C\frac{(E_{m-1}-E_m)^3}{\mathrm{e}^{[(E_{m-1}-E_m)/kT]}-1}, \quad p_{m\to m+1} = C\frac{(E_m-E_{m+1})^3}{1-\mathrm{e}^{[(E_m-E_{m+1})/kT]}} \tag{35}$$

The equation is valid for $m > 0$. For $m < 0$, $m-1$ must be replaced by $m+1$ in the first equation, and $m+1$ by $m-1$ in the second equation. C is a parameter which takes into account the phonon coupling responsible of the relaxation. The data of Fig. 24 were solid lines correspond to the fit with $A = 6 \times 10^{15}\,\mathrm{rad\,s^{-2}}$ and $C = 0.9 \times 10^5\,\mathrm{Hz\,K^{-3}}$.

3.5 Control of the Nature of the Ground State and of the Anisotropy

Although the magnetic properties of antiferromagnetic clusters can be of some interest, it is apparent that one of the main reasons for interest in the synthesis of molecular magnetic clusters is that of obtaining single-molecule magnets with higher blocking temperatures. To achieve this one possible strategy is that of designing molecules with a high value of S in the ground state. This is best achieved by using building blocks with large spin – it is clearly easier to reach large S numbers by assembling $S = 5/2$ spins rather than $S = 1/2$. A high spin state can be obtained by ferromagnetic coupling, of course. This approach has been successful, for instance, in a ring containing twelve ferromagnetically coupled $S = 1$ nickel(II) ions [90] and in another with six $S = 2$ manganese(III) ions [91]. In both examples the ground state has $S = 12$. The conditions for establishing nearest neighbor ferromagnetic interactions are, however, rather stringent, because the magnetic orbitals on the two ions must be orthogonal to each other. For this reason the ferrimagnetic approach, in which the couplings are antiferromagnetic, is, in general, easier to achieve.

A high spin ground state can be achieved either by assembling two sets, each containing the same number of different spins, or by assembling two sets of identical spins, but with different number in each. An example of the former strategy is a ring containing six $S = 5/2$ manganese(II) ions and six $S = 1/2$ nitronyl-nitroxide radicals [92], which has a ground $S = 12$ spin; an example of the latter is a planar cluster with nineteen $S = 5/2$ iron(III) ions, Fe19 [93], which has the structure sketched in Fig. 25 [94]. The spin topology of the clusters is such that many triangles of antiferromagnetically coupled iron(III) ions are present. Under these conditions the nature of the ground state is very difficult to predict with simple hand waving arguments. In particular, it might turn out to be impossible to predict the ground state by trying to put the spins of the various metal ions either up or down. In the limit of all identical coupling constants the situation referred to as spin frustration is achieved. The characteristic result of this is that the ground state is highly degenerate. The ground state of Fe19 turns out to be $S = 33/2$, one of the highest so far observed in molecular clusters.

Another example of non-compensation of antiferromagnetically spins yielding a high spin ground state is shown by a CrMn6 cluster [12] containing a central $Cr^{III}(CN)_6$ moiety with $S = 3/2$, connected to six $S = 5/2$ Mn^{II}(TrispicMeen) moieties – TrispicMeen = N,N,N′-(tris(2-pyridylmethyl)-N′-methylethane)1,2-diamine) – which gives a ground $S = 27/2$ state. This compound has also recently been investigated by X-MCD experiments which confirmed the antiferromagnetic nature of the magnetic coupling [95].

The conditions for slow relaxation of the magnetization of clusters have so far been met by systems with a large spin in the ground state, reasonably well separated from the nearest excited states, but the role of the magnetic anisotropy is by no means secondary. A fundamental point is that to observe slow relaxation of the magnetization the anisotropy must be of the Ising type. This condition is met when the zero-field splitting is negative, i. e. when the $M = \pm S$ levels of the ground S multiplet lie lowest. Another important point to be controlled is the transverse anisotropy,

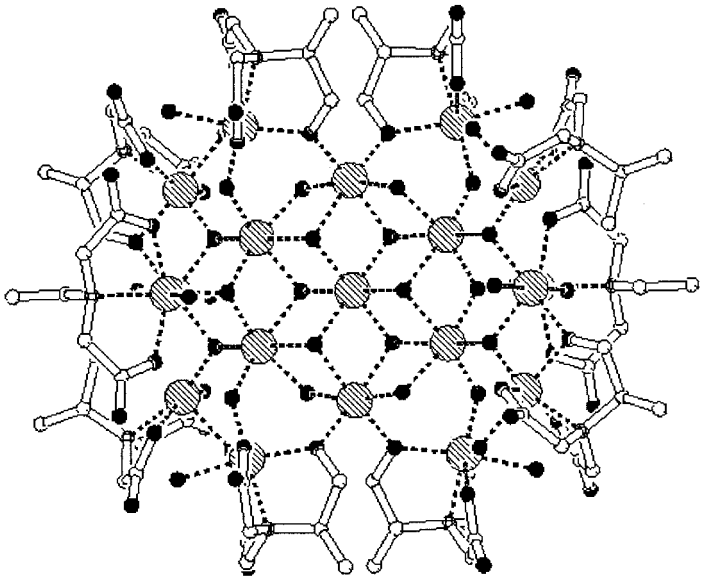

Fig. 25. Sketch of the structure of Fe19. Iron atoms are represented by hatched large circles and oxygen by filled circles.

which can considerably reduce the height of the barrier. This is all of paramount importance in the successful design of new molecules and we will spend some time on it.

In general the concept of a barrier for slow-relaxing paramagnets has been extended from the theory worked out for superparamagnets. For these the magnetization can have two different orientations, say up and down, and these correspond to minima in a potential curve, with the maximum, which gives the height of the barrier, corresponding to the orthogonal orientation of the magnetization vector [57]. Because a superparamagnet is a classical particle, the potential well is represented by a continuum of levels. As the volume of the particle is reduced the height of the barrier decreases linearly, and the density of levels in the potential wells gradually decreases. Eventually the discontinuities typical of quantum systems begin to be observed, and the overall relaxation behavior of the magnetic particles will acquire a quantum nature. In particular, it will become possible to observe reversal of the magnetization without reaching the top of the barrier. In the quantum regime the barrier concept itself becomes fuzzy [46].

For strict Ising anisotropy, i. e. with axial symmetry, at the lowest level of approximation the reversal of the magnetization at low temperature, i. e. the change from the $M = -S$ state to the degenerate $M = +S$ state, can occur through thermally activated behavior. In this case the spin passes from $M = -S$ to $-S+1$, then to $-S+2$, up to $S = 0$, and then goes down to $M = +S$ [58]. For this simplified model the energy barrier is defined as the energy difference between the lowest lying $M = \pm S$ level to the highest lying $M = 0$ level. The height of the barrier is, therefore, given by $|D|S_2$

for integer spins and $|D|(S_2 - 1/4)$ for half-integer spins. It must be stressed that this is true only if the transverse anisotropy, represented by E, is zero. If E is different from zero the pairs of $\pm M$ levels of integer spin states are no longer degenerate. In fact M is no longer a good quantum number, and extensive admixture of states can occur. Because the E term admixes states with M differing by ± 2, its effect is large on the states with small M, whereas it has a small effect only on the states with large M. For the latter the approximation of the two potential wells is, therefore, still acceptable. If, for instance, we consider an $S = 10$ state, with moderate transverse anisotropy given by $E/D = 0.16$, the pairs are quasi degenerate up to $M = \pm 5$, but the higher levels are heavily admixed. In particular there are three reasonably well separated levels, and higher there are two more quasi-degenerate pairs. There is, therefore, no $M = 0$ top level. In fact the two highest, quasi degenerate levels are admixtures of various levels. One is the admixture of $M = 0$ with $M = \pm 2$ and other even M values and the other is the admixture of $M = \pm 1$ with other odd M values. The assumption of the height of the barrier no longer holds, therefore, and the distinction between levels with positive and negative M also fails. In fact the transition probability from one state on the right of the barrier to that which is higher on the same side of the double well might become smaller than the transition to the corresponding level on the other side of the well. This is, for instance, the situation which occurs in Fe8. Indeed this cluster has provided the best evidence for quantum tunneling of the magnetization [96], because it has a reasonably long relaxation time at low temperature which enabled very sophisticated measurements which provided evidence for unique quantum behavior predicted by several theories [20]. In the following section we will review the main results observed for this cluster, which can be taken as a case history of the potential observation of quantum effects in mesoscopic matter.

3.6 Fe8 – A Case History

The structure of Fe8 has been shown in Fig. 3 [29]. The analysis of the temperature dependence of the magnetic susceptibility [31], and the data obtained from the polarized neutron experiments [42], provided the values of the coupling constants, and the overall spin distribution in the ground state, characterized by $S = 10$. The ground wavevector, with the basis functions written as indicated in Section 2.1 as $|S_1 S_2 S_{12} S_5 S_{125} S_6 S_{1256} S_7 S_{12567} S_8 S_{125678} S_3 S_4 S_{34} S M\rangle$, is ca. 70% $|2.5, 2.5, 5, 2.5, 7.5, 2.5, 10, 2.5, 12.5, 2.5, 15, 2.5, 2.5, 5, 10 M\rangle$. The ground state in split in zero field, as evidenced by HF-EPR [7] and INS experiments [97]. The latter, shown in Fig. 26, are particularly rich, in transitions, which enabled the determination of the energies of the split components of the ground $S = 10$ state.

Results from both sets of measurements, HF-EPR and INS, agree that the spin Hamiltonian for describing the zero-field splitting requires the inclusion of the fourth order terms:

$$H = \mu_B \mathbf{S} \cdot \mathbf{g} \cdot \mathbf{B} + D S_z^2 + E(S_x^2 - S_y^2) + B_4^0 O_4^0 + B_4^2 O_4^2 + B_4^4 O_4^4 \qquad (36)$$

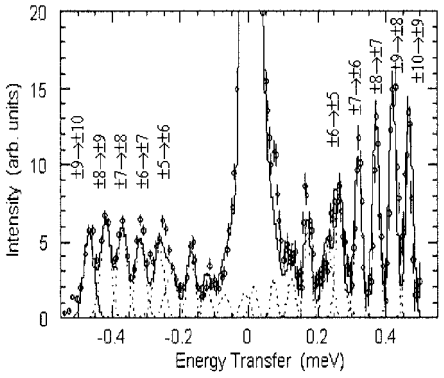

Fig. 26. INS spectra of Fe8 at 10 K. 1 meV corresponds to 8.065 cm^{-1} and the transitions have been assigned as indicated on the spectrum.

where:

$$
\begin{aligned}
O_4^0 &= 35S_z^4 - 30S(S+1)S_z^2 + 25S_z^2; \\
O_4^2 &= [(7S_z^2 - S(S+1) - 5)(S_+^2 + S_-^2) \\
&\quad + (S_+^2 + S_-^2)(7S_z^2 - S(S+1) - 5]/4; \text{ and} \\
O_4^4 &= 1/2(S_+^4 + S_-^4)
\end{aligned}
\tag{37}
$$

The zero-field splitting leaves the $M = \pm 10$ levels as the lowest, and slow relaxation of the magnetization is observed. Mössbauer experiments [7], which have a time-scale of 10^{-8}–10^{-9} s, enable monitoring of slow relaxation below 20 K, whereas AC susceptibility measurements enable observation of that below 3 K only [7]. As a consequence of the presence of sizeable transverse anisotropy terms (E, B_4^2, B_4^4) the height of the barrier for Fe8 is not well defined and, in fact, the Arrhenius type relaxation described by Eq. (17) is never rigorously obeyed by Fe8. The relaxation time of the magnetization becomes so slow below 1 K that hysteresis loops of molecular origin can be observed, as shown in Fig. 27. The hysteresis has the stepped appearance first reported for Mn12Ac [17, 18]. The flat regions correspond to fields at which the relaxation is slow and the steps correspond to fields at which a rapid increase of the relaxation rate is observed. This behavior has been attributed to resonant quantum tunneling [60]. Beyond the relaxation activated by absorption and emission of phonons it is possible to relax by tunneling between two degenerate levels. At zero field the condition is met by the lowest lying pairs of M levels, and the relaxation is comparatively fast. In the presence of an external field the energy of the $+M$ level increases and that of the $-M$ level decreases, making quantum tunneling impossible. The conditions for tunneling are, however, restored for fields at which the $+M$ level has the same energy as the $-M + 1$ level. The fields where these conditions are met can be calculated by use of Eqs. (36) and (37). The calculated fields correspond to the fields where steps are observed in the hysteresis.

Direct measurements of the relaxation time of Fe8 can be achieved at low temperature by first saturating the magnetization and then monitoring its time decay. In this way it is observed that below 350 mK the relaxation becomes temperature-

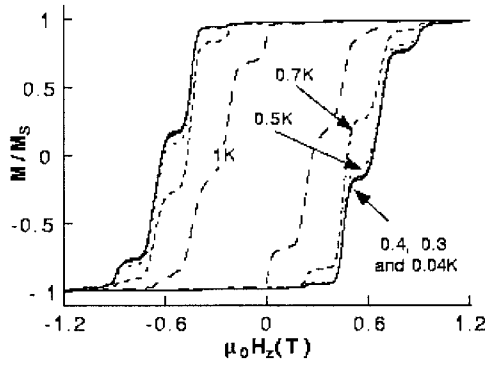

Fig. 27. Stepped magnetic hysteresis measured by use of microSQUID on a small single crystal of Fe8 with the magnetic field parallel to the easy axis. Below 0.4 K the curves no longer depend on temperature.

independent, thus confirming the quantum tunneling effects. Under these conditions only the lowest $M = \pm 10$ levels are populated, and tunneling occurs between them. The tunnel matrix element is of the order of 10^{-9} K [46]. In an ideal system resonant tunneling requires that the magnetic field (local to the S spin) is smaller than the field associated with the tunnel splitting. This makes it difficult, in principle, to observe tunneling. Justification of the observed behavior can, however, be found if the dipolar interactions with the neighboring cluster and the hyperfine interaction with the magnetic nuclei are taken into consideration. In fact, rapidly fluctuating hyperfine fields bring molecules into resonance. The molecules which relax modify the dipolar internal field and remove from resonance a large number of neighboring spins. This same effect might, however, bring into resonance molecules which are farther away from the relaxed center, and enable continuous relaxation. One therefore expects rapid relaxation on a short time-scale and a slow logarithmic relaxation on a long time-scale [98].

The first particularly interesting evidence obtained for Fe8 was that in the quantum regime the relaxation of the magnetization on the short time-scale must follow a square-root time dependence [20, 99]:

$$M(H,t) = M_{\text{in}} + (M_{\text{eq}}(H) - M_{\text{in}})(\Gamma_{\text{sq}}(H)t)^{1/2} \tag{38}$$

where M_{in} is the initial magnetization at $t = 0$ and $M_{\text{eq}}(H)$ is the equilibrium magnetization. The rate function Γ_{sq} is proportional to the normalized distribution $P(H)$ of molecules which are in resonance with the applied field and to the square of the energy difference, Δ_{qt}, between the $M = \pm 10$ states:

$$\Gamma_{\text{sq}}(H) \propto \Delta_{\text{qt}}^2 P(H) \tag{39}$$

Starting from a well defined magnetization state it is possible to obtain Γ_{sq} as a function of field, and this can be used to follow the time evolution of molecular states in the sample during tunneling relaxation.

These results show that it is possible to control the number of relaxing molecules by using additional fields. This can be achieved properly by use of the microSQUID arrays described in Section 3.4, because this magnetometer enables rapid variation

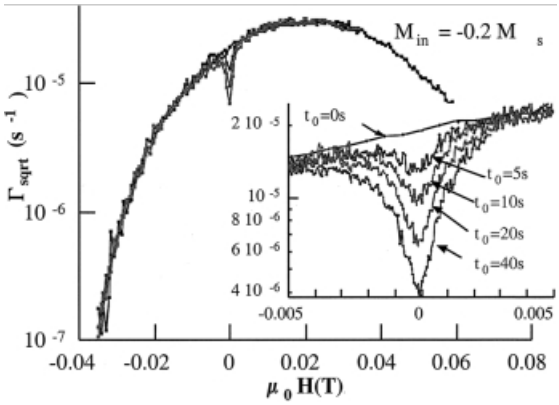

Fig. 28. Field dependence of the square root of relaxation rate as function of the time of digging at $H = 0$. In the inset the holes dug in the rate distribution are shown at an enlarged scale.

of the applied field. Starting from a well defined magnetization state, a field $H_{\rm dig}$ is applied and the molecules are left to relax for a time $t_{\rm dig}$ ('dig' stands for digging as will be explained below). Finally a field H is applied and $\Gamma_{\rm sq}$ is measured. Under these conditions $\Gamma_{\rm sq}$, which, we remember, is proportional to the number of molecules which relax in a given field H, is a function of H, $H_{\rm dig}$, and $t_{\rm dig}$. The number of molecules which can relax in a given field H depends on previous treatment. The application of $H_{\rm dig}$ effectively digs a hole in the total number of molecules which can relax, because some of them have already been relaxed. This is shown in Fig. 28 for different digging times $t_{\rm dig}$. It is apparent that a hole is dug in the curve at $H = 0\,\mathrm{T}$, and the longer the digging time the deeper the hole. The hole width has an intrinsic broadening which depends on the magnetic moments of the nuclei which are present in the cluster. It has, in fact, been experimentally observed that the hole broadens if the non-magnetic iron nuclei are substituted by the magnetic ^{57}Fe ($I = 1/2$), and it becomes narrower if the less magnetic deuterium is substituted for a proton. These experiments therefore point to a strong isotope effect on the quantum relaxation of the magnetization. In general, isotope effects are associated with phonon coupling, but in this instance they point out the assistance of relaxation by nuclear spin.

A different experimental procedure, in which the longitudinal field (parallel to the easy axis) is swept rapidly over the entire resonance, has been used to measure the tunnel splitting, and its dependence on a transverse field applied parallel to the hard axis of the cluster. On each sweep a certain number of clusters reverse their magnetization according to the tunnel probability, P, that is given by:

$$P = 1 - \exp\left[\frac{\Delta^2}{4\hbar g \mu_{\rm B} S(\mathrm{d}H/\mathrm{d}t)}\right] \tag{40}$$

where $\mathrm{d}H/\mathrm{d}t$ is the constant field sweeping rate. Eq. (40) thus enables calculation of the tunnel splitting. The experiments are performed by sweeping the longitudinal field around $H = 0$, after having saturated the magnetization, and in this case the tunnel splitting between the $M = \pm 10$ states is monitored. When the longitudinal field oscillates around the value for which the $M = 10$ state equals the energy of

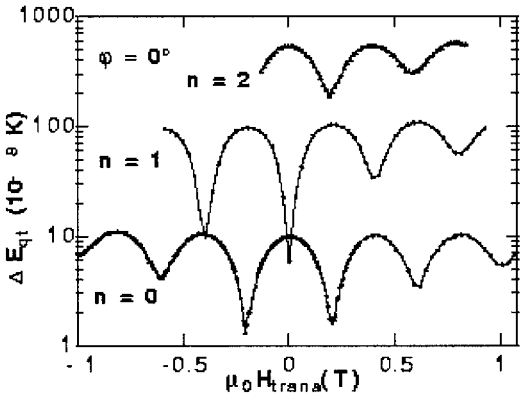

Fig. 29. Field-dependence of tunnel splitting when the field is applied along the hard axis. For $n = 0$ the splitting between $M = \pm 10$ states is monitored; the other curves correspond to the tunnel splitting of the $M = -10$ and $M = 10 - n$ states of the ground $S = 10$ multiplets. A parity effect of n on the phase of the oscillations is evident.

the $-M + n$ state, the tunnel splitting between these two states is monitored. The oscillating behavior obtained by adding a variable transverse field, H_x, is clearly visible in Fig. 29, although different phases are observed, depending on whether n is odd or even.

In fact for $n = 0$ and $n = 2$ at $H_x = 0$ the tunnel splitting is in a maximum; minima are observed for $H_x = (k + 1/2)\Delta H_0$, whereas for $n = 1$ the minima are observed for $H_x = k\Delta H_0$ where $k = 0, 1, 2 \ldots$ and $\Delta H_0 = 0.41$ T. If the magnetic anisotropy is described by the second-order spin Hamiltonian of Eq. (36) the periodicity, ΔH_0, is simply given by:

$$\Delta H_0 = \frac{2k_\mathrm{b}}{g\mu_\mathrm{B}}\sqrt{2E(E+D)} \tag{41}$$

but higher-order terms in the spin Hamiltonian contribute strongly to ΔH_0, making this technique very powerful for the evaluation of small higher-order corrections to the spin Hamiltonian. In a semi-classic picture these oscillations can be seen as interferences, because of the two possible paths that the spin can follow in the plane perpendicular to the hard axis in the reversal of the magnetization. This result had long been sought in magnets, under the term 'Berry phase' [23], and is a good demonstration that molecular clusters might really provide much new physics. They also suggest the possibility of controlling the magnetic hysteresis loop (cohercitivity, remanent magnetization, etc.) by adding a transverse field.

3.7 Conclusions and Outlook

Molecular clusters are a challenge for many different disciplines, but primarily for chemists who want to learn how to make larger molecules, and to give them predefined properties. In this field some important success has already been achieved, but much remains to be done. Most efforts have so far been concentrated on metal ions

of the first transition series and on rare earth ions, but it can be expected that important results might be obtained by using heavier transition metal ions and organic radicals also.

The contributions of molecular clusters to the development of mesoscopic physics cannot be overlooked. Important effects have already been discovered and understanding of mesoscopic quantum phenomena has certainly advanced greatly after the discovery of magnetic molecules.

Biology is interested in these systems because magnetic clusters are present in many different metallo-enzymes and metallo-proteins. Other large inorganic clusters are present in ferritin, in magnetosomes, etc., so the development of large synthetic analogs might shed light on the mechanism of biomineralization and on the magnetic properties of biological clusters.

Finally it must be remembered that these large systems, in which quantum size effects are still so important, might be considered for use as hardware in quantum computing devices. There is no doubt that this will be an important area of research for many years to come.

Acknowledgments

The results reported in this chapter have been obtained by collaboration with many colleagues whose name are given in the references. Particular thanks are due to Andrea Caneschi, who has contributed to the synthesis of many of the compounds described in the text, and to Andrea Cornia, who has unique capabilities in synthetic chemistry, physical measurements, and theoretical investigations.

Financial support from MURST, CNR, and PFMSTAII is gratefully acknowledged.

References

[1] Gatteschi, D.; Caneschi, A.; Pardi, L.; Sessoli, R. *Science* **1994**, *265*, 1054.
[2] Barbara, B.; Gunther, L. *Physics World* **1999**, *12*, 35–39.
[3] Sessoli, R.; Gatteschi, D.; Caneschi, A.; Novak, M. A. *Nature (London)* **1993**, *365*, 141–3.
[4] Lis, T. *Acta Crystallographica* **1980**, *B36*, 2042–2046.
[5] Aubin, S. M. J.; Sun, Z. M.; Guzei, I. A.; Rheingold, A. L.; Christou, G.; Hendrickson, D. N. *Journal of the Chemical Society*, *Chemical Communications* **1997**, 2239–2240.
[6] Barra, A. L.; Caneschi, A.; Cornia, A.; De Biani, F. F.; Gatteschi, D.; Sangregorio, C.; Sessoli, R.; Sorace, L. *Journal of the American Chemical Society* **1999**, *121*, 5302–5310.
[7] Barra, A. L.; Debrunner, P.; Gatteschi, D.; Schulz, Ch. E.; Sessoli, R. *Europhys. Lett.* **1996**, *35*133–138.
[8] Brechin, E. K.; Yoo, J.; Nakano, M.; Huffman, J. C.; Hendrickson, D. N.; Christou, G. *Journal of the Chemical Society*, *Chemical Communications* **1999**, 783–784.

[9] Castro, S. L.; Sun, Z. M.; Grant, C. M.; Bollinger, J. C.; Hendrickson, D. N.; Christou, G. *Journal of the American Chemical Society* **1998**, *120*, 2365–2375.
[10] Sun, Z. M.; Grant, C. M.; Castro, S. L.; Hendrickson, D. N.; Christou, G. *Journal of the Chemical Society*, *Chemical Communications* **1998**, 721–722.
[11] Mallah, T.; Auberger, C.; Verdaguer M.; Veillet, P. *Journal of the Chemical Society*, *Chemical Communications* **1995**, 61.
[12] Scuiller, A.; Mallah, T.; Verdaguer, M.; Nivorozkhin, A.; et al. *New Journal of Chemistry* **1996**, *20*, 1.
[13] Aromi, G.; Aubin, S. M. J.; Bolcar, M. A.; Christou, G.; Eppley, H. J.; Folting, K.; Hendrickson, D. N.; Huffman, J. C.; Squire, R. C.; Tsai, H. L.; Wang, S.; Wemple, M. W. *Polyhedron* **1998**, *17*, 3005–3020.
[14] Chudnovsky, E. M.; Tejada, J. *Macroscopic Quantum Tunneling of the Magnetic Moments*; Cambridge University Press: Cambridge, 1998.
[15] Deutsch, D.; Jozsa, R. *Proceedings of the Royal Society London Series A* **1985**, *239*, 553.
[16] *Quantum Tunneling of Magnetization–QTM '94;* Kluwer: Dordrecht, 1995.
[17] Friedman, J. R.; Sarachik, M. P.; Tejada, J.; Ziolo, R. *Physical Review Letters* **1996**, *76*, 3830.
[18] Thomas, L.; Lionti, F.; Ballou, R.; Gatteschi, D.; Sessoli, R.; Barbara, B. *Nature (London)* **1996**, *383*, 145–147.
[19] Chiolero, A.; Loss, D. *Phys. Rev. Lett.* **1998**, *80*, 169.
[20] Wernsdorfer, W.; Sessoli, R. *Science* **1999**, *284*, 133–135.
[21] Garg, A. *Europhys. Lett.* **1993**, *22*, 205.
[22] Garg, A. *Phys. Rev. B* **1995**, *51*, 15161.
[23] Berry, M. V. *Proc. Roy. Soc. London A* **1984**, *392*, 45.
[24] Bencini, A.; Gatteschi, D. *EPR of Exchange Coupled Systems*; Springer, Berlin, 1990.
[25] Kambe, K. *Journal of the Physical Society Japan* **1950**, *5*, 48.
[26] Christmas, C.; Vincent, J. B.; Chang, H.-R.; Huffman, J. C.; Christou, G.; Hendrickson, D. N. *Journal of the American Chemical Society* **1988**, *110*, 823–830.
[27] Belorizky, E.; Fries, P. *J. Chim. Phys.* **1993**, *90*, 1077.
[28] Gatteschi, D.; Pardi, L. *Gazz. Chim. Ital.* **1993**, *123*, 231–40.
[29] Wieghardt, K.; Pohl, K.; Jibril, I.; Huttner, G. *Angewandte Chemie*, *International Edition in English* **1984**, *23*, 77–78.
[30] Vincent, J. B.; Christmas, C.; Chang, H.-R.; Li, Q.; Boyd, P. D. W.; Huffman, J. C.; Hendrickson, D. N.; Christou, G. *J. A. Chem. Soc.* **1989**, *111*, 2086.
[31] Delfs, C.; Gatteschi, D.; Pardi, L.; Sessoli, R.; Wieghardt, K.; Hanke, D. *Inorganic Chemistry* **1993**, *32*, 3099–103.
[32] Borras–Almenar, J. J.; Clemente–Juan, J. M.; Coronado, E.; Tsukerblat, B. S. *Inorganic Chemistry* **1999**, *38*, 6081–6088.
[33] Borras–Almenar, J. J.; Clemente–Juan, J. J.; Coronado, E.; Georges, R.; Palii, A. V.; Tsukerblat, B. S. *J. Chem. Phys.* **1996**, *105*, 6892–6909.
[34] Goodyear, G.; Stratt, R. M. *J. Am. Chem. Soc.* **1993**, *115*, 10452–10453.
[35] Metropolis, A. W.; Rosenbluth, A. W.; Rosenbluth, M. N.; Teller, A. H.; Teller, E. *J. Chem. Phys.* **1953**, *21*, 1087.
[36] Cano Boquera, J.; Journaux, Y. *Molecular Crystals and Liquid Crystals* **1999**, *335*, 1397–1407.
[37] Barra, A. L.; Brunel, L. C.; Gatteschi, D.; Pardi, L.; Sessoli, R. *Accounts of Chemical Research* **1998**, *31*, 460–466.
[38] Güdel, H. U. *Molecular Magnetism: From Molecular Assemblies to the Devices*; Coronado, E.; Delhaes, P.; Gatteschi, D.; Miller, J. S., Kluwer: Dordrecht, 1996; Vol. NATO ASI Series E 321, pp 229–242.

[39] Schweizer, J. *Molecular Magnetism: From Molecular Assemblies to the Devices*; Coronado, E.; Delhaes, P.; Gatteschi, D.; Miller, J. S., Kluwer: Dordrecht, 1996; Vol. NATO ASI Series E 321, pp 199–228.
[40] Galan–Mascaros, J. R.; Gomez–Garcia, J. R.; Borras–Almenar, J. J.; Coronado, E. *Advanced Materials* **1994**, *6*, 221.
[41] Clemente–Juan, J. M.; Andres, H.; Borras–Almenar, J. J.; Coronado, E.; Güdel, H. U.; Aebersold, M.; Kearly, G.; Büttner, H.; Zolliker, M. *Journal of the American Chemical Society* **1999**, *121*, 10021–10027.
[42] Pontillon, Y.; Caneschi, A.; Gatteschi, D.; Sessoli, R.; Ressouche, E.; Schweizer, J.; Lelievre–Berna, E. *Journal of the American Chemical Society* **1999**, *121*, 5342–5343.
[43] Vannimenous, J.; Toulouse, G. *J. Phys. C* **1977**, *10*, 537.
[44] Weihe, H.; Güdel, H. U. *Journal of the American Chemical Society* **1998**, *120*, 2870–2879.
[45] Le Gall, F.; Fabrizi de Biani, F.; Caneschi, A.; Cinelli, P.; Cornia, A.; Fabretti, A. C.; Gatteschi, D. *Inorg. Chim. Acta* **1997**, *262*, 123–132.
[46] Barra, A.-L.; Gatteschi, D.; Sessoli, R. *Chemistry a European Journal* **2000**, *6*, 1608–1614.
[47] Bykov, A. I.; Dolotenko, M. I.; Kolokol'chikov; Tatsenko, O. M. *Physica B* **1996**, *216*, 215.
[48] Taft, K. L.; Delfs, C. D.; Papaefthymiou, G. C.; Foner, S.; Gatteschi, D.; Lippard, S. J. *J. Am. Chem. Soc.* **1994**, *116*, 823–32.
[49] Taft, K. L.; Lippard, S. J. *Journal of the American Chemical Society* **1990**, *112*, 9629.
[50] Bonner, J. C.; Fisher, M. E. *Physical Reviews A* **1964**, *135*, 640.
[51] Cornia, A.; Affronte, M.; Jansen, A. G. M.; Abbati, G. L.; Gatteschi, D. *Angewandte Chemie*, *International Edition in English* **1999**, *38*, 2264–2266.
[52] Shapira, Y.; Liu, M. T.; Foner, S.; Dube, C. E.; Bonitatebus, P. J. *Physical Review B-Condensed Matter* **1999**, *59*, 1046–1054.
[53] Sessoli, R.; Tsai, H. L.; Schake, A. R.; Wang, S.; Vincent, J. B.; Folting, K.; Gatteschi, D.; Christou, G.; Hendrickson, D. N. *J. Am. Chem. Soc.* **1993**, *115*, 1804–1816.
[54] Hennion, M.; Pardi, L.; Mirebeau, I.; Suard, E.; Sessoli, R.; Caneschi, A. *Physical Review B–Condensed Matter* **1997**, *56*, 8819–8827.
[55] Barra, A. L.; Caneschi, A.; Gatteschi, D.; Sessoli, R. *Journal of Magnetism and Magnetic Materials* **1998**, *177*, 709–710.
[56] Zvezdin, A. K.; Popov, A. I. *JETP* **1996**, *82*, 1140.
[57] Morrish, R. *The Physical Principles of Magnetism*; Wiley: New York, 1966.
[58] Villain, J.; Hartman–Boutron, F.; Sessoli, R.; Rettori, A. *Europhysics Letters* **1994**, *27*, 159–194.
[59] Hartmann–Boutron, F.; Politi, P.; Villain, J. *Int. J. Mod. Phys. B* **1996**, *10*, 2577.
[60] Fort, A.; Rettori, A.; Villain, J.; Gatteschi, D.; Sessoli, R. *Physical Review Letters* **1998**, *80*, 612–615.
[61] Wernsdorfer, W.; Sessoli, R.; Gatteschi, D. *Europhysics Letters* **1999**, *47*, 254–259.
[62] Cornia, A.; Jansen, A. G. M.; Affronte, M. *Molecular Crystals and Liquid Crystals* **1999**, *334*, 1113–1123.
[63] Abbati, G. L.; Cornia, A.; Fabretti, A. C.; Malavasi, W.; Schenetti, L.; Caneschi, A.; Gatteschi, D. *Inorg. Chem.* **1997**, *36*, 6443–6446.
[64] McGarvey, B. R. *Transition Metal Chemistry*, Marcel Dekker Inc. New York, 1966; Vol. 3, p 89.
[65] Wernsdorfer, W.; Dovin, B.; Mailly, D.; Hasselbach, K.; Benoit, A.; Maier, J.; Ansermet, J.-Ph.; Barbara, B. *Phys. Rev. Lett.* **1996**, *76*, 1873–1876.
[66] Wernsdorfer, W.; Ohm, T.; Sangregorio, C.; Sessoli, R.; Mailly, D.; Paulsen, C. *Physical Review Letters* **1999**, *82*, 3903–3906.

[67] Muller, F.; Hopkins, M. A.; Coron, N.; Grynberg, M.; Brunel, L. C.; Martinez, G. *Review of Scientific Instruments* **1989**, *60*, 3681.
[68] Bloess, A.; Möbius, K.; Prisner, T. F. *Journal of Magnetic Resonance* **1998**, *134*, 30.
[69] Earle, K. A.; Freed, J. H. *Applied Magnetic Resonance* **1999**, *16*, 247.
[70] Eaton, G. R.; Eaton, S. S. *Applied Magnetic Resonance* **1999**, *16*, 161.
[71] Hassan, A. K.; Maniero, A. L.; van Tol, H.; Saylor, C.; Brunel, L. C. *Applied Magnetic Resonance* **1999**, *16*, 299.
[72] Smith, G. M.; Lesurf, J. C. G.; Mitchell, R. H.; Riedi, P. C. *Review of Scientific Instruments* **1998**, *70*, 1787.
[73] Barra, A. L.; Caneschi, A.; Gatteschi, D.; Sessoli, R. *J. Am. Chem. Soc.* **1995**, *117*, 8855–8856.
[74] Goldberg, D. P.; Caneschi, A.; Sessoli, R.; Delfs, C. D.; Lippard, J. S. *J. Am. Chem. Soc.* **1995**, *115*, 5789.
[75] Mukhin, A. A.; Travkin, V. D.; Zvezdin, A. K.; Lebedev, S. P.; Caneschi, A.; Gatteschi, D. *Europhys. Lett.* **1998**, *44*, 778–782.
[76] Barra, A. L.; Gatteschi, D.; Sessoli, R. *Physical Review B–Condensed Matter* **1997**, *56*, 8192–8198.
[77] Del Barco, E.; Vernier, N.; Hernandez, J. M.; Tejada, J.; Chudnovsky, E. M.; Molins, E.; Bellessa, G. *Europhysics Letters* **1999**, *47*, 722–728.
[78] Abragam, A. *The Principles of Nuclear Magnetism*; Clarendon: Oxford, 1961.
[79] Borsa, F.; Mali, M. *Phys. Rev. B* **1974**, *9*, 2215.
[80] Borsa, F.; Rigamonti, A. *Magnetic Resonance of Phase Transitions*; Owens, F. J.; Poole, C. P. Jr.; Farach, H. A., Academic Press: New York, 1979; p 79.
[81] Lascialfari, A.; Gatteschi, D.; Borsa, F.; Shastri, A.; Jang, Z. H.; Carretta, P. *Physical Review B–Condensed Matter* **1998**, *57*, 514–520.
[82] Lascialfari, A.; Gatteschi, D.; Borsa, F.; Cornia, A. *Phys. Rev. B: Condens. Matter* **1997**, *56*, 8434.
[83] Lascialfari, A.; Jang, Z. H.; Borsa, F.; Gatteschi, D.; Cornia, A. *Journal of Applied Physics* **1998**, *83*, 6946–6948.
[84] Zucchi, C.; Shchegolikhina, O. I.; Borsari, M.; Cornia, A.; Gavioli, G.; Fabretti, A. C.; Rentschler, E.; Gatteschi, D.; Ugo, R.; et al. *J. Mol. Catal. A: Chem.* **1996**, *107*, 313–321.
[85] Julien, M. H.; Jang, Z. H.; Lascialfari, A.; Borsa, F.; Horvatic, M.; Caneschi, A.; Gatteschi, D. *Physical Review Letters* **1999**, *83*, 227–230.
[86] Schenck, A. *Muon Spin Rotation Spectroscopy: Principles and Applications in Solid State Physics*; Hilger: Bristol, 1986.
[87] Blundell, S. J.; Pattenden, P. A.; Pratt, F. L.; Valladares, R. M.; Sugano, T.; Hayes, W. *Europhysics Letters* **1995**, *31*, 573–578.
[88] Lappas, A.; Prassides, K.; Vavekis, K.; Arcon, D.; Blinc, R.; Cevc, P.; Amato, A.; Feyerherm, R.; Gygax, F. N.; Schenk, A. *Science* **1995**, *267*, 1799–1802.
[89] Garcia–Munoz, J. L.; Cirujeda, J.; Veciana, J.; Cox, S. F. J. *Chemical Physics Letters* **1998**, *293*, 160–166.
[90] Blake, A. J.; Grant, C. M.; Parsons, S.; Rawson, J. M.; Winpenny, R. E. P. *Journal of the Chemical Society, Chemical Communications* **1994**, 2363–2364.
[91] Abbati, G. L.; Cornia, A.; Fabretti, A. C.; Caneschi, A.; Gatteschi, D. *Inorganic Chemistry* **1998**, *37*, 1430–1431.
[92] Caneschi, A.; Gatteschi, D.; Laugier, J.; Rey, P.; Sessoli, R.; Zanchini, C. *Journal of the American Chemical Society* **1988**, *110*, 2795.
[93] Powell, A. K.; Heath, S. L.; Gatteschi, D.; Pardi, L.; Sessoli, R.; Spina, G.; Del Giallo, F.; Pieralli, F. *J. Am. Chem. Soc.* **1995**, *117*, 2491–502.

[94] Heath, S. L.; Powell, A. K. *Angewandte Chemie International Edition in English* **1992**, *31*, 191.
[95] Arrio, M. A.; Sciuller, A.; Sainctavit, P.; Moulin, C. C. D.; Mallah, T.; Verdaguer, M. *Journal of the American Chemical Society* **1999**, *121*, 6414–6420.
[96] Sangregorio, C.; Ohm, T.; Paulsen, C.; Sessoli, R.; Gatteschi, D. *Phys. Rev. Lett.* **1997**, *78* 4645–4648.
[97] Caciuffo, R.; Amoretti, G.; Murani, A.; Sessoli, R.; Caneschi, A.; Gatteschi, D. *Physical Review Letters* **1998**, *81*, 4744–4747.
[98] Ohm, T.; Sangregorio, C.; Paulsen, C. *Journal of Low Temperature Physics* **1998**, *113*, 1141–1146.
[99] Prokof'ev, N. V.; Stamp, P. C. E. *Physical Review Letters* **1998**, *80*, 5794–5797.

Magnetism: Molecules to Materials III. Edited by J.S. Miller and M. Drillon

ISBNs: 3-527-30302-2 (Hardback); 3-527-60014-0 (Electronic)

4 Quantum Tunneling of Magnetization in Molecular Complexes with Large Spins – Effect of the Environment

Igor Tupitsyn and Bernard Barbara

4.1 Introduction

Can quantum mechanics, which determines behavior on the atomic and sub-atomic scale, be manifest on a macroscopic scale? This question, which was posed when the foundations of quantum theory were first laid, has fascinated physicists for more than seventy years.

The phenomena of superconductivity and superfluidity in helium are quantum manifestations on a macroscopic scale. In both there is a macroscopic non-dissipative current of particles. More recently, quantum manifestations have been observed on scales well above atomic scale – for example, quantum tunneling of the phase in a Josephson junction, permanent currents in small conductor rings, and, more recently, Bose condensates. These systems, the sizes of which vary from 10 to 10^5 nm, are relatively complex; their properties can, nevertheless, be described using a small number of degrees of freedom defined as a "macroscopic order parameter".

In magnetism, since the discovery of superparamagnetism by Néel, it has been known that a ferromagnetic or ferrimagnetic particle a few nanometers in size can also be described with a small number of degrees of freedom, those of the magnetic moment of the single domain particle, which behaves as a small magnet (the exchange energy dominates by orienting all the moments in one direction).

The search for quantum effects on the "macroscopic scale" in magnetism started in the early seventies after it was shown that single crystals of rare-earth intermetallics (Dy_3Al_2, $SmCo_{3.5}Cu_{1.5}$) have fast magnetic relaxation in the Kelvin range. This phenomenon was interpreted in terms of magnetization reversal by quantum tunneling, below a certain crossover temperature. The reversal of magnetization of the bulk crystals was the sum of the elementary reversals of single domain blocks (nucleation of the so-called Barkhausen jumps); this type of study is equivalent to the study of single nanoparticles, but with many complications (size, energy barrier and switching field distributions, effects of domain walls, various dissipation effects...).

More recently there have been developments in various disciplines that have led to great progress in obtaining different types of nanoparticle. In material science magnetic materials have been produced as isolated aggregates, as deposits of aggregates, as carbon nanotubes and nanocages filled with magnetic material, as electrodeposits of magnetic material in nanoporous polycarbonate membranes, and as dispersals in polymers. Molecular chemistry has produced molecules with giant spins and colloidal chemistry has used micelles as microreactors to make all sorts

of new magnetic nanoparticle. Naturally occurring biological systems have given us ferritin, and biochemistry has provided us with their artificial analogs.

Among all these systems, an exciting type of material – molecular crystals with identical magnetic molecules – has emerged for the study of macroscopic tunneling in magnetism. Despite their relatively large size and the dipolar interactions between their magnetic moments, these molecules clearly exhibit quantum tunneling of magnetization. The focus of this article is on two of these materials: (i) the spin cluster system called "Mn_{12}-ac", a manganese acetate, the first system to exhibit what is referred to as "resonant tunneling of magnetization"; and (ii) an analogous system, the so-called "Fe_8", in which the same phenomenon was subsequently observed, but at lower temperatures, which enables easier experimental studies.

4.2 Mn_{12}-acetate

4.2.1 Experimental Results

In recent years much experimental and theoretical work has been performed on molecules of $[Mn_{12}O_{12}(CH_3COO)_{16}(H_2O)_4]$. This molecule has tetragonal symmetry [1] and contains a cluster of twelve Mn ions divided into two shells (four Mn^{4+}ions with spin $S = 3/2$ in an inner shell surrounded by eight Mn^{3+}ions with spin $S = 22$ in an outer shell) with strong antiferromagnetic coupling (frustrated triangles; Fig. 1). They form a collective ground state spin $S = 10$ with magnetic moment $M = gS\mu_B \approx 20\mu_B$ ($g \approx 2$ is the Lande factor) [2]. These molecules are chemically identical and form a crystal with an average distance between Mn_{12} molecules of the order of 15 Å [1]. Intermolecular exchange interactions are negligible and dipolar interactions are approximately 0.01-0.02 K. This is much smaller than the anisotropy barrier, U_0, of each molecule (which is approximately 61–65 K [6a, 7, 9, 10]).

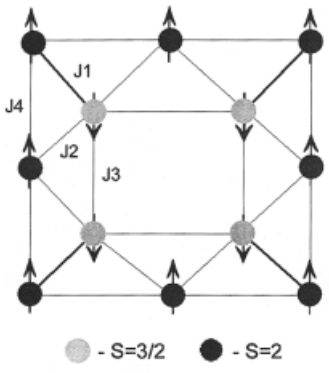

Fig. 1. Interaction scheme of Mn_{12} molecule.

The AC susceptibility measurements of Sessoli et al. [2] and the magnetization experiments of Paulsen et al. [6a, 7] reveal superparamagnetic behavior with a relaxation time that obeys the Arrhenius law $\tau = \tau_0 \exp(U_0/k_B T)$ (see Néel [3]) with $\tau_0 = 2 \times 10^{-7}$s at high temperatures ($T > 2.5$ K) and a blocking temperature T_B close to 3 K ($T_B \approx k_B U_0/\ln(t/\tau_0) \approx 3.3$ K for $t \approx 1$ h). Above the blocking temperature this superparamagnetic behavior is characterized by a Curie–Weiss law with a very small positive paramagnetic temperature $\theta \approx 70$ mK. This indicates the existence of weak dipole–dipole interactions between molecules. As the temperature decreases from ~3 K the magnetization evolves from relatively rapid roughly exponential relaxation (approx. 10^3s) to very slow non-exponential relaxation (approximately 10^7s at $T \approx 2.1$ K; non-exponential behavior, discovered later, will be discussed below) [6a, 7, 9] (experimental results [8] have even suggested the occurrence of logarithmic relaxation below 1 K, but this has not been confirmed by the more recent results of Chiorescu et al. [85]). It was also found that the relaxation time $\tau(H)$ has a deep minimum in zero field at $T < 2$ K [7, 9–11] whereas above this temperature $\tau(H)$ has a maximum at 0.2 T (Fig. 2) observed, for the first time, by Paulsen et al. [7] (see also the review paper by Barbara et al. [9]). This picture (strongly supported by dips observed in AC-susceptibility measurements by Novak et al. [10]) was interpreted as quantum tunneling of magnetization (QTM) of the collective spin $S = 10$ with a crossover temperature $T_C \approx 2$ K, because of resonant energy-level crossing in a two-well potential in a longitudinal magnetic field [6a, 7, 9–11, 4].

The reported experiments [6a, 9] were thoroughly repeated and confirmed [7]. More detailed measurements performed later [4, 11], showed steps in the isothermal hysteresis loop (Friedman et al. [4] and Thomas et al. [11]) when the field is increased

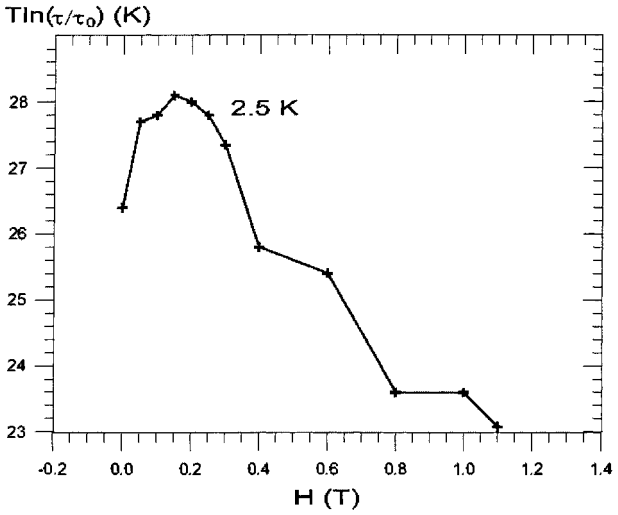

Fig. 2. Variation of $\tau(H_z)$ [7, 9] at $T > T_C$. Note that in this figure [9] the value of $T \ln(\tau(H_z)/\tau_0)$ is plotted to show also that $U_0(H_z)$ (effective barrier height) deviates from $\sim DS_2(1 + H_z/2DS)^2$.

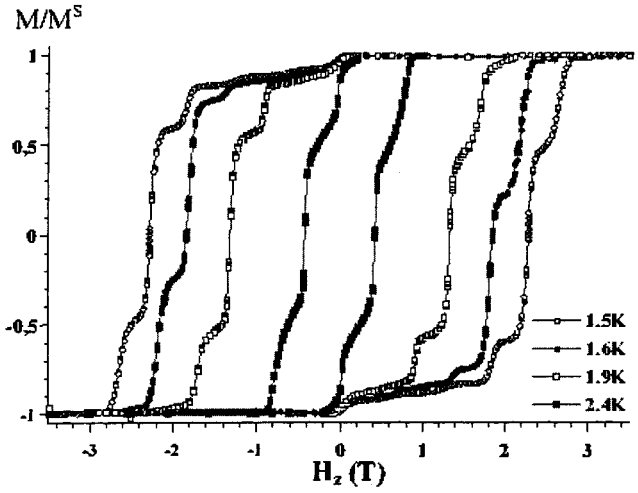

Fig. 3. Hysteresis loops of Mn_{12} with the field along z-axis [11].

in the direction opposite to the magnetization at $T < T_B$ (Fig. 3, see also Ref. [6b]). In the flat regions of the hysteresis loop the relaxation times were found to be much longer than the experimental time window (∼600 s [11]) whereas in the steep regions magnetization relaxes much more rapidly and the relaxation times can be of the order of (or even less than) the experimental time window. The plot of $\partial M_Z/\partial H_Z$ against longitudinal field H_Z (Fig. 4) gives a series of peaks (with Lorentzian shape). The maxima of these peaks enable definition of the values of magnetic field, H_n,

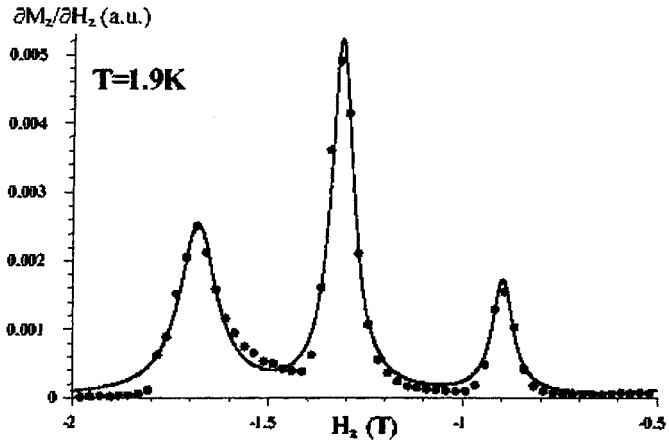

Fig. 4. Field variation of the derivative $\partial M_Z/\partial H_Z$ taken at 1.9 K along the hysteresis loop of the single monocrystal [12]. The sharp peaks correspond to the magnetization jumps, and the flat regions correspond to the plateaus located between the jumps. The continuous line is a fit to the Lorentzian peaks centered at H_n.

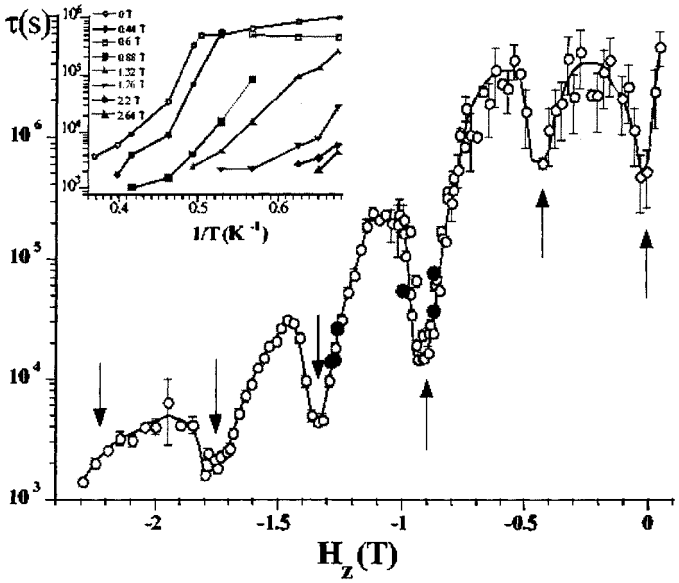

Fig. 5. Dependence of relaxation times at 1.9 K on H_z obtained by Thomas et al. [11] from repeated measurements for given H_z and T on the hysteresis loop. The insert shows the dependence of relaxation-time drops on inverse temperature.

at which the magnetization steps occur, i. e. the fields H_n such that $H_n \approx 0.44n$ $T (n = 0, 1, 2, \ldots)$. The relaxation measurements of Thomas et al. [11] show that the relaxation time oscillates with the magnetic field (Fig. 5) and has deep minima (resonances) at the same values of field where the steps are observed in the hysteresis loop. These new experimental results clarify the problem of the maximum previously observed at $H = 0.2$ T [7, 9, 10]. As suggested by Barbara et al. [9], it is effectively the first maximum of the $\tau(H)$ curve. In addition, the blocking temperature T_B also has strong minima approximately at the fields H_n (extracted from the temperature behavior of magnetization at different values of the field [4]).

All these results, interpreted as strong evidence of QTM, were obtained at $T < T_B \approx 3.3$ K (in a longitudinal field). At the higher temperatures the magnetization relaxes too rapidly for quasi-static measurements and AC-susceptibility ($\chi(\omega) = \chi'(\omega) - i\chi''(\omega)$) measurements are necessary. The relaxation times can then be determined, either from the position of the maxima of the imaginary susceptibility ($\chi(\omega)''$ is maximum at $\omega\tau = 1$) or from the relationship $\tau = \chi''(\omega)/\omega(\chi'(\omega) - i\chi'(\infty))$, where ω is the frequency of the AC field. The higher temperature relaxation times also oscillate with minima at nearly the same field as in the low-temperatures example, but the amplitude of the oscillations decreases. At 10 K, for example, this amplitude is 25 times smaller than at the low- temperature [12] (Fig. 6). These measurements show that, together with the regular decrease of the relaxation time with the applied field (the usual field-dependence of the barrier), there is, even at temperatures well above the quasi-static blocking temperature, a fraction of molecules with

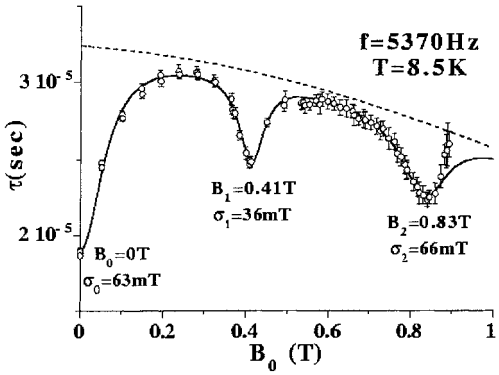

Fig. 6. Field dependence of the relaxation time $\tau = \chi''(\omega)/\omega(\chi'(\omega) - i\chi'(\infty))$ from AC susceptibility measurements [12]. The dashed line represents the fit of the thermal activation background and the continuous curve is a fit of thermally activated resonance dips.

tunneling channels, as in the low-temperature regime. This means that at high temperature the mechanism of relaxation is intermediate between that of the quantum regime (where the ratio of the relaxation times at resonance and out of resonance are much smaller than unity) and that of the classical regime (where this ratio tends to unity).

It has also been found experimentally [4, 11] that the transition rate decreases rapidly with temperature. If, therefore, the QTM mechanism is relevant for all these experiments, it can be understood only by thermally assisted QTM (introduced by Novak and Sessoli [10] and Barbara et al. [9]), where tunneling occurs from excited levels. As the temperature decreases, the higher levels (close to the top of the barrier) become increasingly less populated and the tunneling occurs between the lower levels with smaller probability, explaining the extremely long relaxation time observed below 1 K [6a, 7, 9].

In the presence of increasing longitudinal or transverse magnetic field, however, relaxation is faster and can be easily measured in the main bulk phase of Mn_{12} (see very recent experiments [85]). As an example we show in Fig. 7(a) some hysteresis loops obtained from torque experiments in fields up to 6 T. As in Fig. 3, where measurements were performed in lower fields and at higher temperatures, the loops depend on temperature, but here this is true only above 0.8 K. Below this temperature the loops are independent of temperature, showing that tunneling takes place from the ground state, $S = 10$.

Similar results were obtained in a transverse magnetic field of approximately 4 T. As an example we give in the insert of Fig. 7b the temperature-dependence of the relaxation times measured on a short time-scale. They are clearly independent of temperature below 0.8 K (this temperature is, by accident, nearly the same as in the longitudinal field). This result shows that tunneling occurs here between the ground states $S = 10$ and $S = -10$ of the two symmetrical wells. The main part of Fig. 7b gives also an example of relaxation curves measured in the plateaus. On a short time-scale the relaxation follows a square-root law, but on long time-scales it is exponential

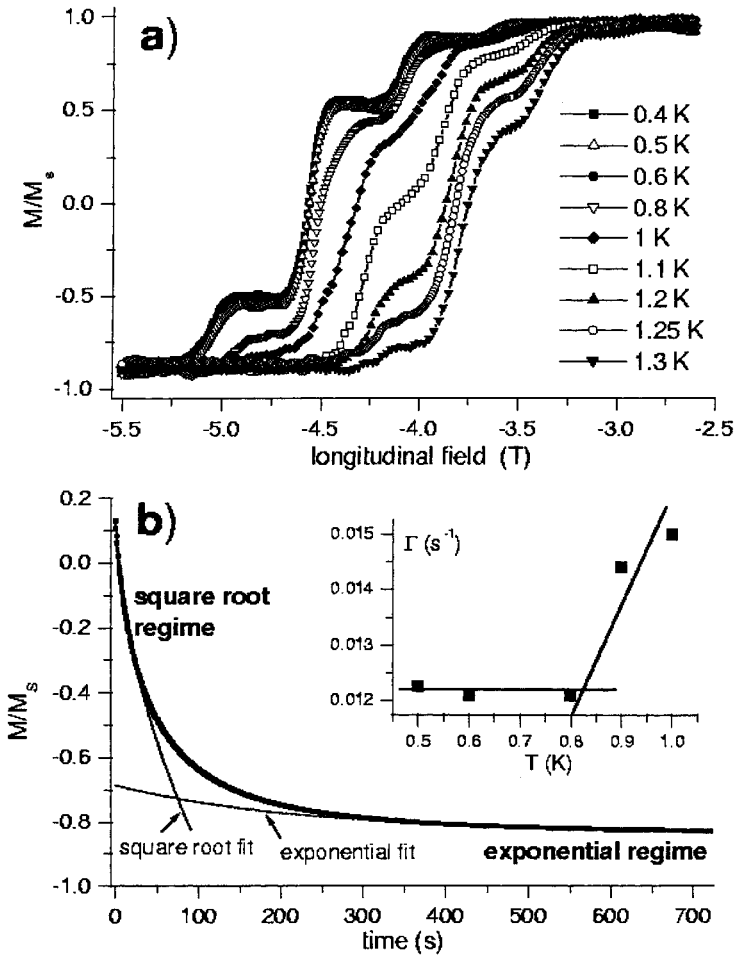

Fig. 7. (a) Hysteresis loops obtained from torque experiments on a single crystal of Mn_{12} (main phase) [85] performed at temperatures between 1.3 and 0.4 K. The magnetization was first saturated in a large positive field. The field was then reduced to zero and reversed. Data points were obtained between −2.5 and 5.5 T. The sweeping field velocity was equal to 10.8 mT s^{-1}. The amplitude of the steps depends on temperature, but only above 0.5–0.8 K. Below this temperature the hysteresis loops are independent of temperature, suggesting tunneling from the ground-state, $S = 10$. (b) An example of magnetic relaxation experiments performed near the maximum of the first resonance in the presence of a transverse field of approximately 4 T, on a single crystal of Mn_{12}. The data were obtained after saturation in a positive field and fast application of the field to the top of the resonance. This curve shows that the relaxation follows a square-root law on short time-scales and an exponential law on long time-scales. The insert shows the temperature-dependence of the square root of relaxation time. Below 0.8 K the relaxation time is independent of temperature, showing the existence of ground-state tunneling between $S = 10$ and $S = -10$ in this bulk phase of Mn_{12}.

(we should note that, although the two third of the relaxation curves could be fit by $\ln(t)$, on the short time-scale the relaxation always follows the square-root law). Such a crossover between square root and exponential relaxation occurs in all the experiments of Chiorescu et al. [85] in both longitudinal and transverse fields. Note that it was also observed in the low-field and high-temperature regime [57].

4.2.2 Basic Model

To proceed with some theoretical interpretations and conclusions one should, first of all, establish a basic model describing the Mn_{12} spin structure. Early experimental work by Sessoli et al. [2, 13] resulted in observation of the $S = 10$ collective spin ground state, and the high-frequency EPR experiments of Barra et al. [5] enabled fitting of its results to a "giant spin" $S = 10$ Hamiltonian which includes fourth order anisotropy in the form:

$$H_{\mathrm{G}} = -DS_z^2 - K_{\parallel}S_z^4 + K_{\perp}(S_+^4 + S_-^4) - g\mu_{\mathrm{B}}\mathbf{HS} \tag{1}$$

neglecting higher-order terms, with $D/k_{\mathrm{B}} \approx 0.56\,\mathrm{K}$, $K_{\parallel}/k_{\mathrm{B}} \approx 1.11 \times 10^{-3}\,\mathrm{K}$ and $K_{\perp}/k_{\mathrm{B}} \approx 2.9 \times 10^{-5}\,\mathrm{K}$. Recently, a new experimental technique, the "submillimeter spectroscopy', was applied to the Mn_{12} magnetic clusters [14]. This technique can measure directly the energy levels which, in principle, give full information about the Hamiltonian of the system. The information can be used to tune Hamiltonian Eq. (1) in respect of higher-order anisotropy terms.

In this model, described by Eq. (1), the fourth-order terms contribute to tunneling and, therefore, play a crucial role (the importance of the higher-order terms neglected in Eq. (1) is discussed in Section 4.3.2.). Before using this Hamiltonian, however, it is necessary to understand how the model of the collective spin $S = 10$ ground state is stable with increasing temperature. To succeed in this task one can try to calculate the energy levels of the entire problem (with all the couplings between 12 Mn ions, as shown in Fig. 1). The dimension of the Hilbert space of such a problem is 10^8 and, because of the obvious uncertainty in the experimental determination of the anisotropy constants, any such attempts will be rather useless. To achieve a solution of the problem at least in the temperature region below 150 K, Tupitsyn et al. [15] suggested application of the idea of a "reduced" Hamiltonian. It was assumed that the largest coupling constant J_1 (Fig. 1), which is of the order of 200 K, locks two Mn ions with $S_1 = 2$ and $S_2 = 3/2$ into a spin state of $S_{12} = 1/2$ up to temperatures of the order of J_1 (similar tactics – "dimerization" – have been exploited [16, 17] after an earlier suggestion [13]). Using this assumption, one can apply an effective eight-spin Hamiltonian, Eq. (2), to check the temperature stability of the $S = 10$ ground state:

$$\begin{aligned} H = {} & \frac{1}{2}\left[\sum_{\langle\mu,\nu\rangle}^{4}\left(C_1\mathbf{S}_\mu\sigma_\nu + C_{\parallel}\mathbf{S}_\mu^z\sigma_\nu^z\right) + C_2\sum_{\langle\alpha,\beta\rangle}^{4}\sigma_\alpha\sigma_\beta\right] \\ & + g\mu_{\mathrm{B}}\mathbf{H}\left(\sum_{\mu=1}^{4}\mathbf{S}_\mu + \sum_{\nu=1}^{4}\sigma_\nu\right) \end{aligned} \tag{2}$$

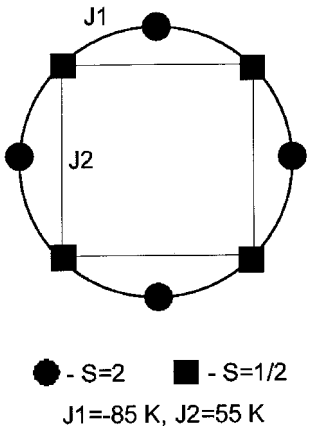

Fig. 8. Simplified coupling scheme for the Mn_{12} molecule.

where S and σ distinguish four $S = 2$ spins from the outer shell and four combined $\sigma = \frac{1}{2}$ spins (Fig. 8). The Hilbert space of this Hamiltonian is 10^4 and it is now possible to use the method of exact diagonalization to obtain the structure of the energy levels. Even though this Hamiltonian is "reduced" (or "truncated") it includes both exchange and anisotropy, because of the second term with $C_{\|}\}$ and simulates the whole Mn12 molecule up to temperatures of approximately 150 K, at least. Note that Eq. (2) ignores Dzyaloshinskii–Moria (DM) interactions which might also be important in Mn_{12} [18], because, in antiferromagnetic systems with strong couplings, this term can produce single-ion anisotropy which can affect the tunneling (but this type of anisotropy can be "simulated" by the exchange anisotropy). In general, this is a time-reversal symmetry- breaking term which can remove the Kramer's degeneracy of the energy levels (if any). Recent theoretical work (see Ref. [16] and references cited therein) suggests rather strong DM interaction in the Mn_{12} clusters.

Because we do not know the constants C_1, C_2, and $C_{\|}$, we should use experimental results to determine them. Firstly, we calculated the magnetization $M_z(T, H_z)$ and the susceptibility $\chi_{\|}(T, H_z)$ for different T and H_z. Comparing these calculated values with the experimental results we tuned our coupling constants to obtain agreement with experiment. As can be seen from Fig. 9, we found very good agreement for $C_1 = -85$ K, $C_2 = 55$ K and $C_{\|} = -7.5$ K. We then used these constants to predict the magnetization, $M_x(T, H_x)$, and the susceptibility, $\chi_{\perp}(T, H_x)$, in a transverse field.

Figure 10 shows there is good agreement with experimental results up to 150 K. Above this temperature our model is no longer valid, because the pairs of spins $S = 2$ and $S = 3/2$ become unlocked. These calculations enable, in particular, conclusions about the temperature range of validity of the collective spin $S = 10$ model. As is apparent from Fig. 11, the multiplet $S = 9$ becomes occupied above approximately 40 K and the "giant spin" model with $S = 10$ becomes invalid. Another calculation, made in the simple limit of a spin $S = 10$, enabled very good fitting of the magnetization curves, but only up to 30–40 K, showing also that the giant spin $S = 10$ cannot be valid above this temperature [18, 21]; interestingly, the measured (and fitted) magnetization curves could not be distinguished from an hyperbolic tangent with $S = 10$, showing the Ising-like character of the ground state $S = 10$, which is

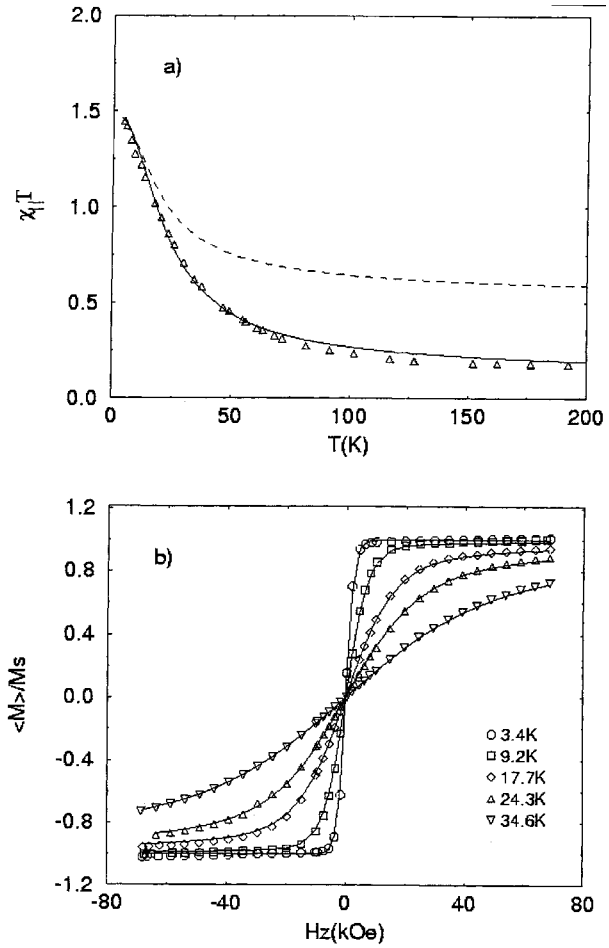

Fig. 9. (a) Temperature-dependence of longitudinal susceptibility $\chi_{\parallel}$. Triangles are experimental results [59]. The dashed line is $\chi_{\parallel}T$ calculated from Eq. (2) with the contribution from the energy levels up to 100 K only, starting from the ground state (85 levels). The solid line is $\chi_{\parallel}T$ calculated from Eq. (2) with the contribution from all the energy levels (10^4 levels). (b) Dots are magnetization curves, plots of $\langle M_z \rangle / M_s$ against longitudinal field measured by Thomas at different temperatures [59]. Solid curves are the same curves calculated from Eq. (2).

occupied at temperatures below 10 K. This does not mean that the upper levels are not occupied (the phenomenon of thermally activated tunneling developed below, will show that), but simply that the weight of the ground state $S = 10$ dominates magnetization curves below 10 K.

We can conclude that the tunneling in the $S = 10$ multiplet at temperatures above 30–40 K should be faster than in the $S = 9$ multiplet (for example), because higher multiplets have broader and higher energy barriers. Experimentally this conclusion is confirmed by the observation of well-defined and equally spaced resonances at

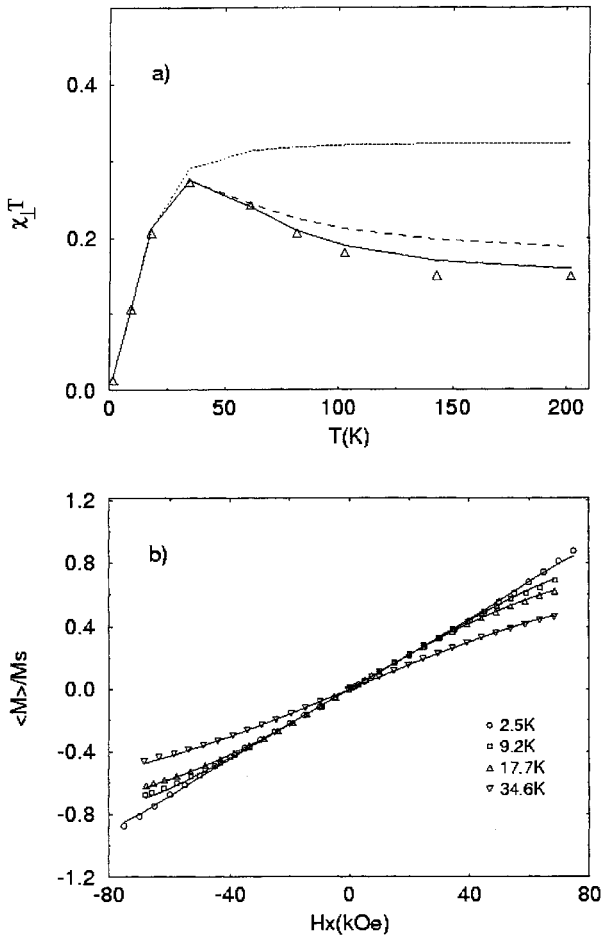

Fig. 10. (a) Temperature-dependence of transverse susceptibility $\chi_\perp$. Triangles are experimental results [59]. The dotted line is $\chi_\perp T$ calculated from Eq. (2) with the contribution only from the energy levels up to 100 K. The dashed line is the same but with the contribution from energy levels up to 500 K (2982 levels). The solid line is $\chi_\perp T$ calculated from Eq. (2) with the contribution from the energy levels up to 1000 K (8362 levels). (b) Dots are magnetization curves, plots of $\langle M_x \rangle / M_s$ against transverse field measured by Thomas [59] at different temperatures. Solid curves are the same curves calculated from Eq. (2).

temperatures above 30 K [18, 21] (instead of randomly spaced resonances). It is also interesting to note that neutron scattering experiments performed on Mn_{12}-ac reported the same temperature of approximately 40 K [19] for the transition from the $S = 10$ ground state to $S = 9$. This means that the "reduced" Hamiltonian model works well in the temperature region not higher than 120–150 K. In the framework of almost the same model it was also shown by Zvezdin et al. [20] that the susceptibility measured along a transverse field $\chi_\perp(T, H_x)$ has a peak in a transverse magnetic field

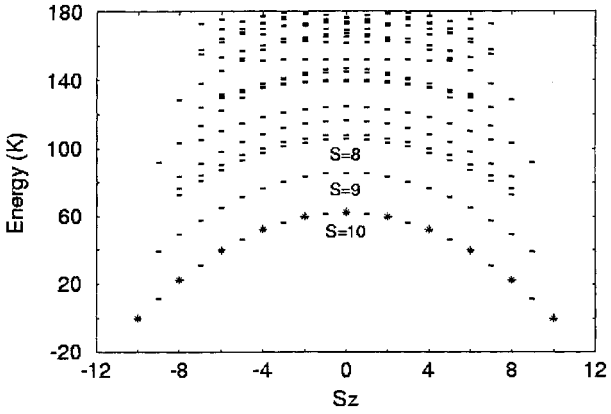

Fig. 11. Energy spectrum, calculated from Eq. (2) up to 180 K. The stars show the parabolic behavior ($A(S_2 - S_z^2)$ where $-S \leq S_z \leq S$ and A =0.627 K) of the $S = 10$ multiplet.

at approximately 7–8 T. This peak can be interpreted in terms of a "resonance" between two states which are symmetrical relative to the applied field. Experimentally this transition can easily be hidden by the effect of fourth-order anisotropy terms on the magnetization curve, and to avoid thermal resonance, the temperature should be at least 0.2 K.

Now, after the temperature range of validity of the "giant spin" model is established, it is easy to estimate from Eq. (1) the critical values of the longitudinal magnetic field H_n at which the intersection of energy levels occurs. The condition for the intersection of the two levels $S_z = m > 0$ and $S_z = (n - m) < 0$ [9, 10], simply reads [4, 11]:

$$H_n \approx nD/g\mu_B \tag{3}$$

(for simplicity we neglect here all the other terms in Eq. (1), but can take them into account in a more detailed analytical expression or numerically). Note that, because the steps in the hysteresis loop were discovered only when the field is increased in the direction opposite to the magnetization, we have changed a sign before the H_z term. When the field is reduced, being parallel to the magnetization, there is no steps, because the system is in its true ground state and there is no possibility of tunneling to another well until the field passes through zero. The value $D/k_B \approx 0.56$ K gives with Eq. (3) $H_n \approx 0.42n$ T, whereas the experimental value is $H_n \approx 0.44n$ T, as is apparent from Fig. 5. At these values of the magnetic field H_z the levels $m > 0$ and $(n - m) < 0$ come into resonance and the tunneling channels open.

Experimental measurements of the "effective barrier" height [21] enable us to identify the lowest energy level ($S_z = m_t$) where tunneling is fast enough to be recorded in a magnetization experiment. All the levels above this level have larger tunnel splitting and, therefore, tunnel much more rapidly. They effectively short-circuit the top of the barrier. This means that the "effective" height of the barrier in zero magnetic field is $E_{\text{eff}}(0) = D(S_2 - m_t^2)$ whereas in a non-zero longitudinal

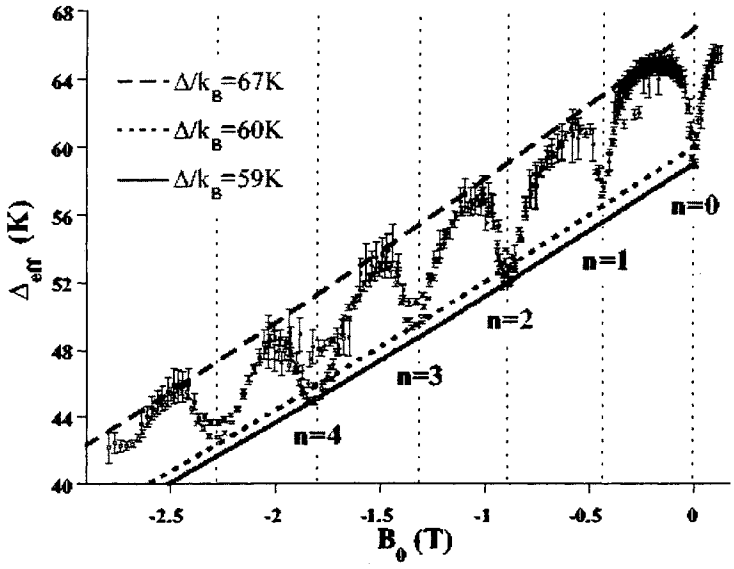

Fig. 12. Dependence of the effective energy barrier of the Mn12 molecule on longitudinal field [21]. The solid, dashed, and dotted curves represent the law $E_{\rm eff}(H) = \Delta_{\rm eff} = -\Delta(1 + H_z/2DS)^2$ for different values of the barrier height $U_0 = \Delta$.

magnetic field we have $E_{\rm eff}(H) = -E_{\rm eff}(0) \times (1 + H_z/2DS)^2$ (we neglected all other terms in Eq. (1) and assumed $S \gg 1$). In the high-temperature regime ($T \approx 2.6{-}3$ K), the relaxation time behaves approximately exponentially and follows the Arrhenius law, with $E_{\rm eff}(H) = T \ln(\tau(T, H)/\tau_0)$. By measuring the relative size of dips on the curve $E_{\rm eff}(H)$ one can estimate $m_{\rm t}$. As is apparent from Fig. 12 [21], the height of the barrier in dips is reduced by approximately 10%; this corresponds to tunneling from the levels $m_{\rm t} \approx$ 3-4.

If, however, $H_z = 0$, all the levels are in resonance, and tunneling can, in principle, occur simultaneously from all the thermally excited levels. The tunneling rate $\Gamma_0(m)$ between levels m and $-m$ at zero temperature (and with no bias field between the levels) is approximately:

$$\Gamma_0(m) \approx \Delta_{\rm m}^2/G_0 \tag{4}$$

(see also Ref. [22]) where $\Delta_{\rm m}$ is a tunneling splitting, G_0 is a level-broadening (we assume $G_0 > \Delta_{\rm m}$). At non-zero temperatures one must include the thermal population of the excited levels, which gives for the tunneling rate:

$$\tau^{-1} \approx \sum_m \Gamma_0(m) \exp(-E_m/k_{\rm B}T) \tag{5}$$

where E_m is the energy of level with $S_z = m$. Without a transverse field in Eq. (5) there are only five terms which correspond to the tunneling between the levels linked by the fourth-order term in Eq. (1) (i. e., only even values of m). From this "toy" model

we can estimate the crossover temperature, T_C, at which thermal activation over the barrier is replaced by tunneling through the bottom of the barrier. At $T < T_C$ the function $F_m = -E_m/k_B T + 2\ln(\Delta_m)$ has a maximum at $m = 10$ whereas at $T > T_C$ the maximum is at $m = 2$. Then, for crossover temperatures between these two regimes, we can take $T_C \approx (E_2 - E_{10})/2\ln(\Delta_2/\Delta_{10})$. Using the method of the exact diagonalization we have calculated from Eq. (1) the energy spectrum and the values of tunneling splitting $\Delta_{m,-m}$. Assuming that G_0 is independent of m (actually there is a weak dependence but we neglected it in this "toy" model), we obtain the crossover temperature $T_C \approx 1.3\,\mathrm{K}$ for $H_z = 0$.

This simplified model is far from reality, because it ignores correct description of interactions with the environment and involves only transitions $\Delta m = \pm 4$, whereas experimentally almost all transitions with $\Delta m = -1$ are observed (see Thomas et al. [11]). This model cannot, therefore, be used to explain, e. g., the field dependence of the relaxation time. Even from this model, however, it is clear that the tunneling between the lowest levels at temperatures of approximately 2 K is already unfavorable. Therefore, at this temperature, the relaxation process should involve at least three steps:

1. thermal activation (by phonons) to excited levels (for example $S \rightarrow m_t$);
2. tunneling across the barrier ($m_t \rightarrow -m_t$); and
3. transition to the true ground state with phonon emission ($-m_t \rightarrow -S$). This is thermally assisted QTM suggested for the first time [9, 10].

This was in zero transverse field. In the presence of a transverse field the situation is completely different. The splitting $\Delta m = S$ increases in proportion to the power $2S = 20$ of the ratio of the transverse to the anisotropy field (see Ref. [71a], for example), the rate of relaxation should increase very rapidly as soon as the transverse field is a sizable fraction of the anisotropy field. The results of Barbara et al. [18] are highly indicative of ground-state tunneling in Mn_{12} if the transverse field reaches 3–4 T. Chiorescu et al. [85] showed that in such a field, relaxation is fast enough to be easily and completely measured. This relaxation results, furthermore, from tunneling through the barrier between the ground states $S_z = \pm 10$ and becomes faster than relaxation by thermal activation above the barrier at the crossover temperature $T_C \approx 0.8\,\mathrm{K}$. In these circumstances, when the transverse component of the applied field, is much larger than all the other transverse matrix elements, Eq. (1), in principle, can give quite satisfactory explanations of magnetic relaxation.

This is no longer so in low transverse fields, because then, even small transverse matrix elements can be relevant, in particular those resulting from the environment which is not taken into account in this section (see Section 4.4). Using this equation one can, nevertheless, still predict very interesting effects which can be experimentally observed at low temperatures and in a low transverse field. The tunneling splitting depends on the Haldane topological phase [32] originating from the quantum interference of possible paths (around the hard axis) between two potential minima (S and $-S$). This topological phase can be changed by an external magnetic field, causing oscillations of the tunneling splitting [23, 24, 31, 33, 36]. These oscillations have already been observed experimentally in the similar system Fe_8 [25], but we will discuss this system later. The easiest way to see the oscillations of the tunneling splitting analytically is to truncate the Hamiltonian in Eq. (1) to a simple low-energy

two-level Hamiltonian. Because of the presence of fourth-order terms, however, this task becomes rather complicated and as far as we are aware the form of such a truncated Hamiltonian has not yet been established. Because higher-order anisotropy terms (up to 20th order with $S = 10$) can, moreover, contribute importantly to the value of the tunneling splitting (Section 4.3.2), any attempt to calculate the tunneling splitting precisely becomes rather pointless, because higher-order anisotropy terms cannot be measured with current experimental techniques. Because we just want to show the principle effects, we proceed, nevertheless, with the simple biaxial Hamiltonian which includes an easy axis/easy plane anisotropy in the following way:

$$H = -DS_z^2 + ES_x^2 - g\mu_B H_x S_x \tag{6}$$

The calculation of tunneling splitting for an isolated tunneling spin in the instanton technique began with the work of Enz and Shilling [71b]. For interaction of spin tunneling with background spins, results were first obtained by Prokof'ev and Stamp [28], with much more detailed work appearing later (see Tupitsyn et al. [23, 31]). Different aspects of this problem have been discussed elsewhere [27, 28, 34–36, 71, 72]. The two-level effective Hamiltonian obtained reads simply:

$$H_{\text{eff}} = 2\Delta_0 \tau_x \cos[\pi S - \Psi] \tag{7}$$

where Δ_0 is the tunneling splitting in zero external field [23, 29–31], τ_x is the Pauli matrix, and Ψ is the Haldane topological phase:

$$\Psi = \pi g\mu_B H_x/2[E(E + D)]^{1/2} \tag{8}$$

This expression of Ψ was given by Garg [24] for the particular Hamiltonian where the quantization z-axis is chosen along the hard axis and the field is applied along this axis. Note that the result relative to the Haldane phase [23] was given in the limit $|E| \gg |D|$, i. e. $\Psi = \pi g\mu_B H_x/2E$. This limit does not, however, affect the physics of the problem in general. For integer S, we obtain from Eq. (7):

$$\Delta_H = \langle\downarrow |H_{\text{eff}}| \uparrow\rangle = \Delta_0 |\cos(\Psi)| \tag{9}$$

whereas for half-integer S:

$$\Delta_H = \Delta_0 |\sin(\Psi)| \tag{10}$$

Eqs. (9) and (10) clearly show the oscillations of the tunnel splitting as a function of the transverse magnetic field, together with the parity effect [23, 31, 35–38]. This last effect shows that half- integer spin does not tunnel in zero transverse field. Note that a magnetic field along the easy axis (or along the medium axis, which is y-axis in this example) does not produce any oscillations and this can be seen mathematically, because the effective tunneling splitting Δ_H in this instance behaves like $\Delta_0 |\cosh(\Psi)|$ (for details see Tupitsyn et al. [23, 31]). Eq. (7) gives the general effective two-level Hamiltonian describing tunneling with a transverse magnetic field ($\Psi = \Psi_H + i\Psi_M$

is complex; the contributions from hard and medium axes are denoted Ψ_{H} and Ψ_M, respectively).

For Mn_{12}, where the lowest-order transverse anisotropy term is of the fourth-order (higher-order terms have not yet been determined), we can write instead of Eq. (8), (for $H_y = 0$):

$$\Psi = \pi g \mu_{\mathrm{B}} H_x / T_x(D, K_{\parallel}, K_{\perp}, S) \tag{11}$$

where $T_x(D, K_{\parallel}, K_{\perp}, S)$, the period of the oscillations along the x-axis, can be calculated numerically from Eq. (1). Note that this equation has two hard axes (x and y) which are equivalent. This means that oscillations with the same period should be seen along both directions. By use of the exact diagonalization method we have calculated the tunnel splitting $\Delta_{m,-m}$ for different m; the results can be seen in Fig. 13.

Firstly, it is easy to understand that the tunneling splitting has a non-zero value in zero transverse magnetic field, only for levels with even values of m (which is related to the fourth-order anisotropy term). For all the other levels (with odd m)

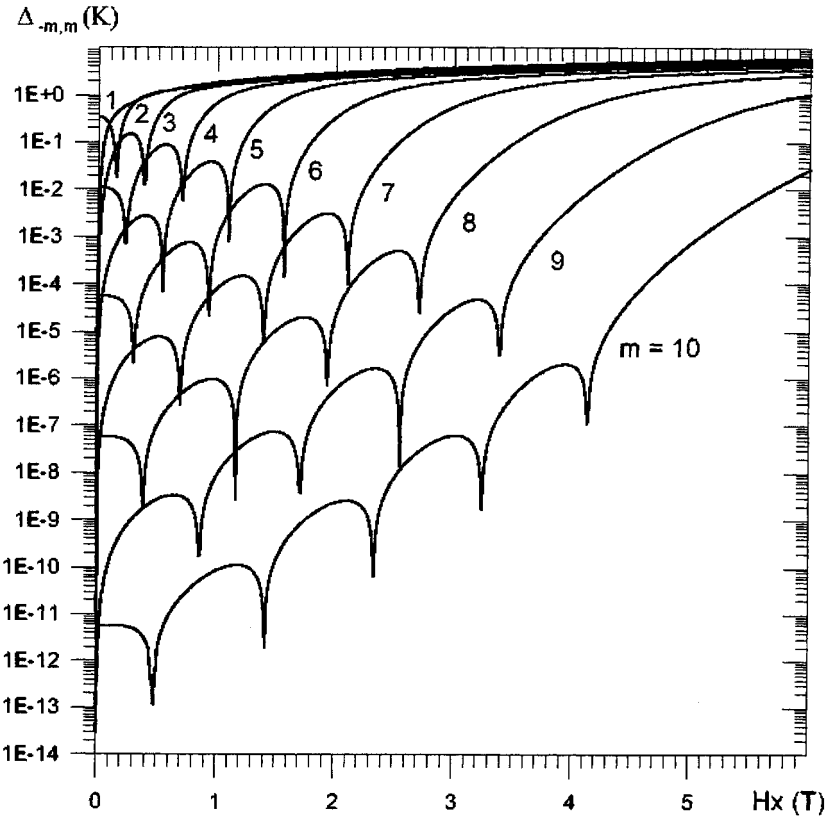

Fig. 13. Dependence of the tunneling splitting $\Delta_{-m,m}$ (Mn_{12}), calculated from Eq. (1) for different values of m, on transverse magnetic field.

the tunneling splitting is non-zero only if the magnetic field is finite (which also produces transitions because of S_+ and S_-). To see easily why the oscillations can be seen only in a finite region of transverse magnetic field (from $-H_c$ to H_c), let us again forget for a moment about the fourth-order term and return to Eq. (6). Combining two non-diagonal terms we obtain the function $A(\theta, \varphi) = (\sin(\theta)\cos(\varphi) - H_x/2ES)^2$. When $H_x < H_c = 2ES$, $A(\theta, \varphi)$ as a function of φ has two local minima at non-zero φ. Because the Haldane phase is nothing else but the area on a unit sphere enclosed by two possible paths between two minima $S_z = S$ and $S_z = -S$, when $H_x < H_c$ the topological phase (which is an imaginary part of the instanton action) has a non-zero value and changes in H_x results in oscillations of Δ. For $H_x > H_c = 2ES$, however, the function $A(\theta, \varphi)$ has only one local minimum at $\varphi = 0$, meaning that both paths joining the states S and $-S$ coincide (up to the φ fluctuations of trajectories which re-normalize the value of H_c to $[2E(E + D)]^{1/2}S$). The area enclosed by these two paths, i. e. the imaginary part of the instanton action is zero and, therefore, there are no more oscillations of the tunneling splitting (see also Garg [24]).

It is important to note that the number of zeros of the $\Delta_{m,-m}(H_\perp)$ function is highly dependent on the symmetry of the anisotropy terms. For the Hamiltonian of Eq. (1) (for Mn_{12}) where the lowest transverse anisotropy term is of fourth order, the number of zeros for even values of m (along the positive or negative direction of the field) should not exceed the number of times ($\nu = 1, \ldots, 5$) the operator S_-^4 has to be applied to the state $S_z = m$ to reach the state $S_z = -m$. (This is, however, valid for $K_\perp > 0$ only; if $K_\perp < 0$, the x and y axes are no longer the hard axes and $\Delta(H_\perp)$ would obviously not show oscillations along these directions.) The tunneling splitting for odd m has an additional zero at zero magnetic field. In these circumstances the chain of operators S_-^4 or S_+^4 which should be applied to the state $|m\rangle$ to reach the state $|-m\rangle$ must be completed by additional operators S_- (or S_+) which come from the magnetic field term (i. e. $|-m\rangle = (S_-)^2(S_-^4)^\nu|m\rangle$ with $\nu = 0, \ldots, 4$). The same situation should occur for tunneling between the levels involved in the resonance by applying a non-zero longitudinal magnetic field (for example, levels $S_z = -m$ and $S_z = m - n$). Only the levels linked by $(S_+^4)^\nu$ or $(S_-^4)^\nu$ ($\nu = 0, \ldots, 4$) can have non zero tunneling splitting in zero transverse field (Fig. 14). It is, moreover, easy to see from this figure how the period of the first oscillation decreases when n increases inside the group of curves $(-10, 9)/(-10, 7)$ (or $(-10, 5)/(-10, 3)$). To reach the states $S_z = 9, 8, 7$ from the state $S_z = -10$ we should apply S_-^4 four times and then, to complete the chain linking the mentioned states, apply S_- three times, twice, or once.

If, in addition, we apply the transverse magnetic field at different azimuth angles φ and increase φ from 0, the amplitude of the oscillations becomes smaller and vanishes at $\varphi = \pi/4$, because for fourth-order anisotropy the $\pi/4$-axis is an easy axis. When φ is increased from $\pi/4$ to $\pi/2$, however, one can see the same curves. This is quite obvious from the symmetry of the problem (Fig. 15). This is so when $K_\perp > 0$. If $K_\perp < 0$, as noted already the x and y axes are no longer the hard axes. Two axes along the directions $\varphi = \pm\pi/4$ become harder for the system. Some oscillations along these directions should be observed.

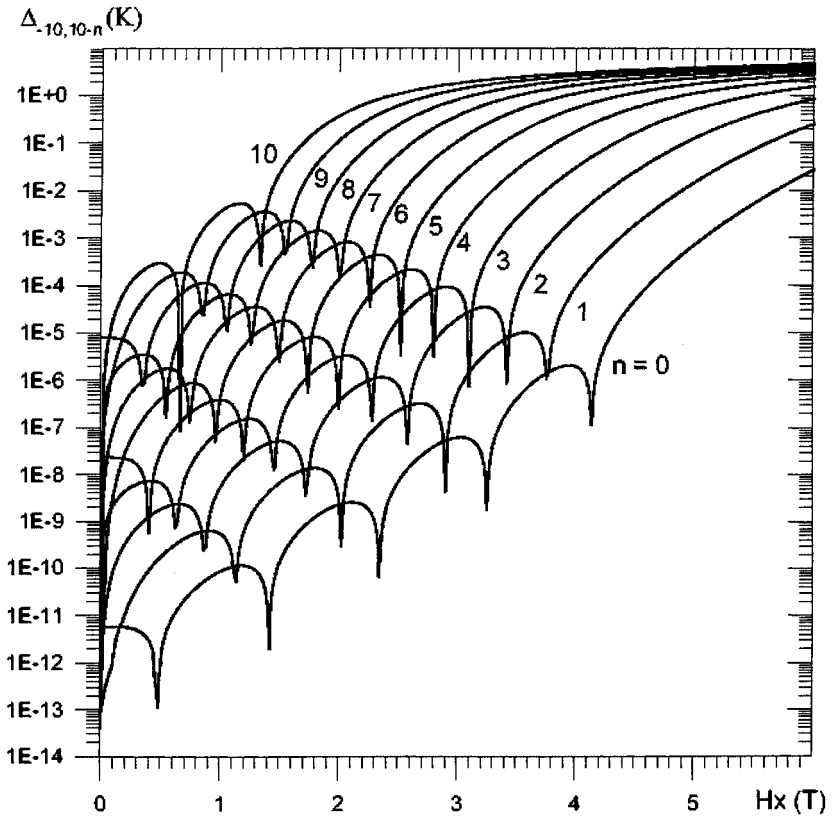

Fig. 14. Dependence of tunneling splitting $\Delta_{-10,10-n}$ (Mn_{12}), calculated from Eq. (1) for different values of n, on transverse magnetic field.

4.3 Fe_8 Octanuclear Iron(III) Complexes

4.3.1 Experimental Results

Another molecule, the so-called Fe_8, with the chemical formula $[Fe_8O_2(OH)_{12}(tacn)_6]^{8+}$, where tacn represents the organic ligand triazacyclononane, is currently under intensive investigation. It contains eight iron(III) ions ($S = 5/2$) with strong antiferromagnetic coupling between the ions [39] (Fig. 16). Similarly to Mn_{12} they form an uncompensated $S = 10$ collective ground state. Four Fe_8 ions in the middle of the molecule are in the so-called "butterfly arrangement". This system is nearly orthorhombic with strong Ising-like anisotropy and an energy barrier of approximately 24 K (approximately one-third of that for Mn_{12}) [39, 40]. Analysis of the dependence of magnetic susceptibility on temperature shows that only the levels $S > 8$ are populated near 10 K [39]. (As for Mn_{12} – see above – one

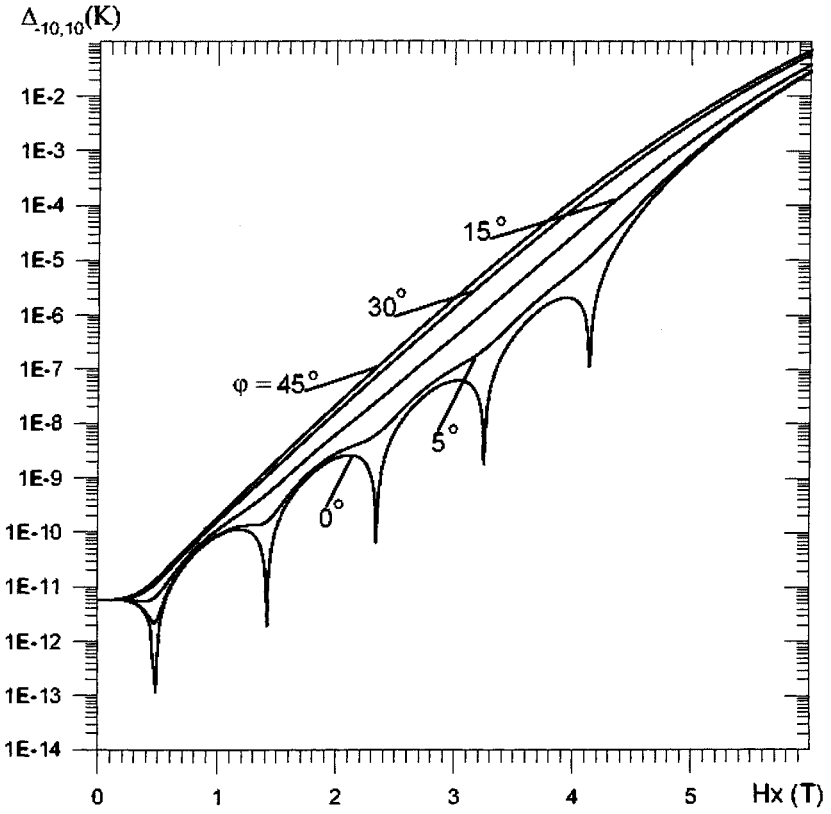

Fig. 15. Dependence of tunneling splitting $\Delta_{10,-10}$ (Mn_{12}), calculated from Eq. (1) for different values of the azimuth angle φ, on transverse magnetic field.

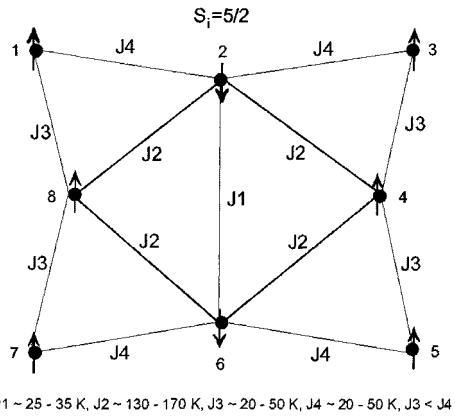

Fig. 16. Interaction scheme for the Fe8 molecule.

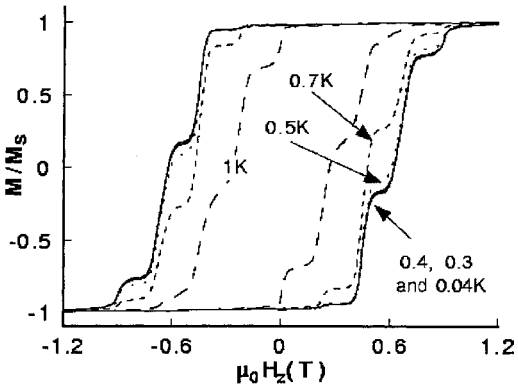

Fig. 17. Hysteresis loops recorded on a single crystal of Fe_8 molecules [42] at different temperatures and at a constant sweep rate, $\partial H/\partial t$, of $0.14\,\mathrm{T\,s^{-1}}$.

must say that upper levels are also occupied, but the weight of the ground state, $S = 10$, dominates the susceptibility.)

Magnetic relaxation experiments have been performed on Fe8, by following the same procedure as described above for Mn_{12}. The relaxation rate becomes temperature-independent below 0.35 K, as was shown by Sangregorio et al. [41]. This can also be seen in the hysteresis loop recently shown for a single crystal (Fig. 17) [42].

As in Mn_{12}, equally-spaced steps were observed, but with smaller spacing – $\Delta H \approx 0.22\,\mathrm{T}$ instead of 0.44 T. It has been found that at these values of the field ($H_n \approx 0.22n\,\mathrm{T}$), the relaxation becomes much faster than that in the plateaus [41]. These observations give a second example of tunneling across the anisotropy energy barrier, when the levels from the opposite sides of the barrier come into resonance. At low temperature, and without a transverse field, the ratio of the relaxation time measured at resonance and out of resonance is larger than in Mn_{12} by one or two orders of magnitude, showing that under these conditions the relaxation in Fe_8 is faster than that in Mn_12, by the same factor (one or two orders of magnitude). (As mentioned above, however, in the presence of a transverse field of a few Tesla the relaxation of Mn_12 becomes much faster; if the transverse field is 3–4 T, ground-state tunneling between $S = +10$ and $S = -10$ is observed below the crossover temperature $T_C \approx 0.8\,\mathrm{K}$ [85].) In Fe_8 ground-state tunneling occurs below $T_C \approx 0.35\,\mathrm{K}$, but for Fe_8 it is not necessary to apply a transverse field. To fit the relaxation data, a stretched exponential law $M(t) = M(0)\exp[-(t/\tau)^{\beta(T)}]$ was used (with $\beta(T)$ increasing from approximately 0.4–0.5 (below 0.4 K) to nearly 1 at $T \approx 1\,\mathrm{K}$) [41]. This law was also observed for measurements on an oriented crystal by Ohm et al. [43, 56]. At temperatures below 0.35 K and after short times, the best fit of the data is square root behavior $M(t) = M(0)[1 - (t/\tau_{\mathrm{short}})]^{1/2}$) (Fig. 18). This law was, in fact, predicted by the theory of Prokof'ev and Stamp [44] for relaxation as a result of tunneling at the bottom of the barrier, after short times and at low temperatures, with initial magnetization near saturation. These measurements were later repeated at lower temperatures ($T = 40\,\mathrm{mK}$) by Wernsdorfer et al. and the square root law was confirmed [45]. Note, however, that this law was also observed by a zero-field

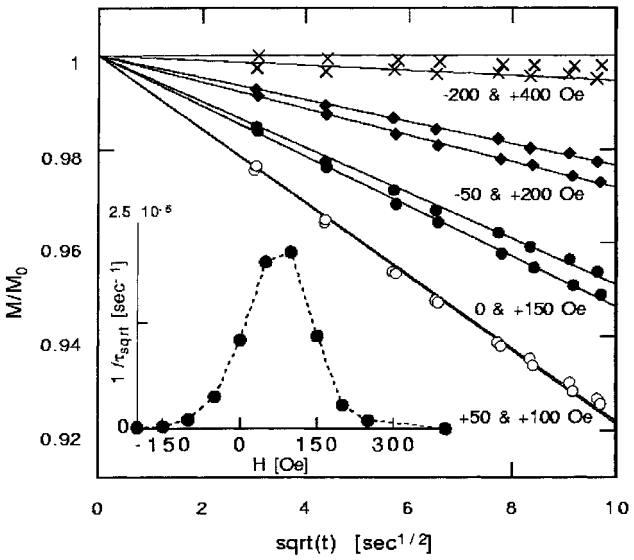

Fig. 18. Square root of time relaxation curves for a single crystal of Fe_8, as measured by Ohm et al. [43] (see also Ref. [56]) at 150 mK for $M_{in} = M_s$. The insert shows the distribution of τ_{sqrt}^{-1} extracted from the above data as a function of field.

cooled annealed sample which was then left to relax in a finite field, i. e. near zero magnetization. A similar effect was also observed for Mn_{12} [85] (see below). This needs further theoretical investigation [91].

In conclusion, in Fe_8 relaxation occurs in the pure quantum regime by tunneling through the barrier between the states $S_z = \pm 10$ at temperatures $T \leq T_C \approx 0.35\,K$ and zero transverse field. Similarly, ground-state tunneling was also observed in Mn_{12}, although a transverse field of 3–4 T must be applied to achieve this result; the crossover temperature is then larger than in Fe_8 ($T_C \approx 0.8\,K$ for Mn_{12}). The application of such a transverse field to Fe_8 would makes the relaxation so fast it would be impossible to measure it (unless by EPR). At higher temperatures the AC-susceptibility experiments of Caneschi et al. [42] show peaks similar to those observed in Mn_{12} [12, 21], but they are more pronounced than in Mn_{12}, from which we may conclude that m_t (m value for the barrier short-cut) is larger for Fe_8. One should, however, keep in mind that the collective spin $S = 10$ of this molecule breaks down near 10 K, suggesting that the peaks observed at high temperature (7 K) come, to a large extent, from multi-spins tunneling. This is corroborated by the observation that the peaks are not regularly separated and that their mean separation looks closer to 0.14 T than to the 0.22 T of the spin $S = 10$.

4.3.2 Basic Model

High-frequency EPR was applied by Barra et al. [40] to investigate the magnetic anisotropy of Fe_8 molecules. They found biaxial anisotropy described by the Hamiltonian $H = -DS_z^2 + E(S_x^2 + S_y^2)$. More recent neutron spectroscopy experiments (Caciuffo et al. [46]) have discovered the presence of a fourth-order term. According to these experimental data, the Hamiltonian for the Fe_8 molecule can be written:

$$H_G = -D_0 S_z^2 + E_0(S_x^2 - S_y^2) + K_\perp(S_+^4 + S_-^4) - g\mu_B \mathbf{HS} \tag{12a}$$

which is equivalent to:

$$H_G = -DS_z^2 + ES_x^2 + K_\perp(S_+^4 + S_-^4) - g\mu_B \mathbf{HS} \tag{12b}$$

where $D/k_B = (D_0 - E_0)/k_B \approx 0.23\,K$, $E/k_B = 2E_0/k_B \approx 0.094\,K$, and $K_\perp/k_B \approx -3.28\times10^{-5}\,K$ ($g \approx 2$; [40, 46]). Eqs. (12a) and (12b) are valid only in the temperature range where the collective spin $S = 10$ can be defined, i. e. at temperatures below 10 K [39] (this temperature is 40 K in Mn_{12}).

In the same way as for the Mn_{12} molecule we can estimate the value of the longitudinal magnetic fields at which the levels from the opposite sides of the barrier (say, $S_z = m$ and $S_z = n - m$) come into resonance. Eq. (12b) gives:

$$H_n = (nD/g\mu_B)[1 + E/2D] \tag{13}$$

(we again neglected the fourth-order term). The contribution $E/2D$ compensates for the difference between D and D_0 (compare with Eq. 3) and one must, therefore, have $D_0 = D[1 + E/2D]$, which is true and identical with $D = D_0 - E_0$ (see above). Eq. (13) gives $H_n \approx 0.205n$ (in Tesla), whereas the experimental value is $0.22n$ T.

These considerations show there can be some uncertainty in both the actual values of the constants and in the types of the anisotropy terms included in the Hamiltonians. As was pointed out elsewhere [44, 47], higher-order transverse anisotropy terms (even with very small constants) can make an important contribution to the value of the tunneling splitting. This can be seen easily from perturbation theory (for the lowest-order perturbation approach for the tunneling splitting [48, 49, 71]. A simple form of the tunnel splitting, $\Delta_{-m,m} \approx D(K_{\perp p}/D)^{2m/p}$ (where p is the order of the anisotropy term in the Hamiltonian), can be written [21] by following Ref. [71] (we omit here the dependence on the value of S). As an example, Eq. (12b) gives for $m = S = 10$ and $p = 2$ or $p = 4$, $\Delta_{10,-10} \approx D(E/D)^{10}$ or $\Delta_{10,-10} \approx D(K_\perp/D)^5$. The contribution of, e. g., the 10th-order term already gives $D(K_{\perp 10}/D)^2$. Unless there is a quasi-exponential increase of Δ with p, divergence of higher orders of the tunneling splitting is forbidden, because of the rapid decrease of the constants $K_{\perp p}$ (these constants are directly connected to the crystal- field parameters, which we know decrease very rapidly with the expansion order p). Δ depends, nevertheless, on the value of $K_{\perp p}$ in a such a crucial way that all the terms up to 20th order can be important. Values of $K_{\perp p}$ for the higher orders (except $p = 4$) cannot, however, currently

be measured experimentally. This makes very problematic any quantitative calculations of the tunneling splitting from Eq. (12b). The actual behavior of $\Delta_{m,n-m}(H_x)$ is highly dependent on the values of the anisotropy constant. Any uncertainties in these constants cause changes in the period and amplitude of the oscillations in the transverse magnetic field (Figs 13–15, 22–23). The number of the oscillations (which are confined in a given field interval) itself also depends on the relative values of the constants. In the simplest example of biaxial anisotropy (Eq. 6) the field interval for oscillations is $[-H_c, H_c]$, where $H_c \approx [2 \cdot E \cdot (E + D)]^{1/2} \cdot S$. Consider the tunnel state where $|-10\rangle$ and $|10\rangle$ are admixed, with splitting $\Delta_{10,-10}$. To reach the state $|-10\rangle$, starting from the state $|10\rangle$, the operator S_+^p must be applied $20/p$ times (for even p). The main consequence is that the number of oscillations depends directly on the symmetry of the anisotropy – $\nu(p = 2) = 10$ oscillations for second-order anisotropy or $\nu(p = 4) = 5$ oscillations for fourth-order anisotropy. It is clear that if $K_\perp$ increases from zero the transition from $\nu(p = 2) = 10$ to $\nu(p = 4) = 5$ will not be discontinuous, because both periodicity will be involved in the interference. If $K_\perp$ is negligible (in Eq. (12), only the second order term contributes to the splitting. As $K_\perp$ increases above some critical value $K_{\perp c} \approx 2E/S^2$, however, (with $K_\perp > 0$) its contribution becomes dominant and $\nu(p = 2) = 10$ decreases progressively to the value $\nu(p = 2) = 4$ (as in Eq. 1). Simultaneously, the period and amplitude of oscillations increase. One must note that the changes in anisotropy constants are not small–the transition between $\nu(p = 2)$ and $\nu(p = 4)$ occurs when the values of consecutive orders in Eq. (12b) are nearly identical. In the above example $K_{\perp c} \approx 2E/S^2 \approx 1.8 \times 10^{-3}$ K is approximately 10^2 times the real value of $K_\perp$! Except for very unusual values of the crystal field parameters, such a transition could not be observed. In any case, this situation is not stable, because the splitting resulting from such large $K_\perp$ is itself very large – $\Delta_c \approx 7 \times 10^{-3}$ K, i. e. nine orders of magnitude larger than the actual splitting given above; (let us note, in passing, the huge effect of $K_\perp$ on Δ). If the value of Δ_c is compared with the splitting given (e. g. Fig. 22), it is not difficult to imagine that the energy spectrum will changes dramatically and all the levels with definite S_z will be completely admixed (S_z will not be conserved). In the opposite case ($K_\perp < 0$), increasing $|K_\perp|$ above $K_{\perp c}$ leads to disappearance of the oscillations, because the x-axis is no longer the hard axis of the system. (This is also true for the y-axis, because of the tetragonal symmetry of Eq. 12b).

Any other anisotropy terms of order higher than four could, in principle, change the number, the period, and the amplitude of the oscillations. These oscillations have recently been observed in the Fe_8 system by Wernsdorfer et al. [25]. Figure 19 shows the measured tunneling splitting as a function of transverse magnetic field at different azimuth angles φ.

Using the Hamiltonian Eq. (12b) we have calculated the tunnel splitting in a transverse field by simple diagonalization of the 21×21 matrix. We obtain similar oscillations as in Ref. [25] with the values $D/k_B = 0.23$ K, $E/k_B = 0.094$ K, and $K_\perp/k_B = -3.28 \times 10^{-5}$ K. There are some differences between the curve calculated for $\varphi = 0^\circ$ and the measured curve (the calculated curve is sharper near the nodes, and the experimental curve shows some increase of the value of $\Delta_{-10,10}(H_x)$ in the nodes). The curve calculated for $\varphi = 1^\circ$ (shown in Fig. 20) is, however, more similar to the experimental curve.

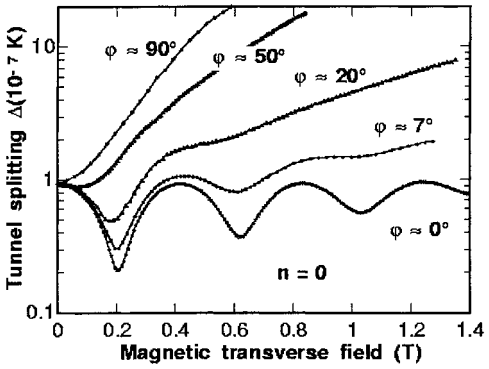

Fig. 19. Dependence of ground-state tunneling splitting $\Delta_{10,-10}$, measured for several azimuth angles φ, on transverse magnetic field [25].

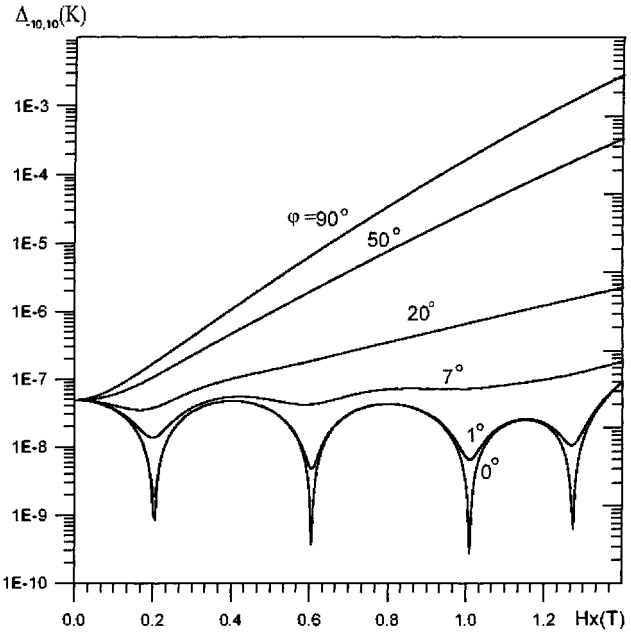

Fig. 20. Dependence of the ground-state tunneling splitting $\Delta_{10,-10}$, calculated from Eq. (12b) for several azimuth angles φ, on transverse magnetic field.

This suggests misorientation in the experiments. The reason for this suggestion is connected with the observation that increasing the magnetic field along the medium axis (which is the y-axis in this instance) increases the tunneling splitting which obeys the relation $\Delta_0|\cosh(\Phi_y)|$ (where Φ_y is the Haldane phase for the magnetic field H_y and Δ_0 is the tunneling splitting in zero field). The simplest (although not unique) way to simulate this non-zero component of the H_y field is to introduce a "misalignment" angle between the x-axis and the direction of the applied magnetic field. One cause could be the mosaic which is always present in molecular crystals of this type, which is also of the order of 1°. This, however, leads to random misorientation be-

tween, say, $+0.5^\circ$ and -0.5°. Such a mosaic should modify the curve $\Delta_{-10,10}(H_x)$, but in a distributed way, and this could contribute to the observed broadening of the nodes. Another origin of misorientation is the triclinic symmetry of the Fe_8 molecule; reducing the symmetry should induce new crystal-field parameters and new contributions to the tunneling splitting, which are, to a first approximation, taken into account by field H_y. In what follows, we will use the value $\theta_m = 1^\circ$ for this "misalignment" angle.

The calculated $\Delta_{-10,10}(H_x)$) with zero longitudinal field (but $\theta_m = 1^\circ$), can be seen in Fig. 20. The period of the oscillations is approximately 0.41 T, in agreement with the experimental value. The curves with the larger value of φ (up to $\pi/2$) clearly show that the oscillations disappear (in agreement with the experimental behavior) when the direction of the applied field approaches the medium axis (y). The agreement is not very good for the absolute value of $\Delta_{-10,10}(H_x)$ and the shape of the last oscillation. These discrepancies might indicate that the Hamiltonian Eq. (12b) is not quite satisfactory in respect of the unknown higher-anisotropy terms. It would always be possible to choose values of these terms up to highest order (20) to get the best fit. One might also consider the effects of couplings to the environment. To give an idea of the influence of high-order terms, we show Fig. 21, the effect of the fourth-order term added to the second order term. Starting from Eq. (12b), we have calculated numerically the period of oscillations T_H, for different values of $K_\perp$. When this term is null i. e. when the period is given by Eq. (8), the value of T_H is about one half the measured value. The value of the fourth-order term $K_\perp = -2.9 \times 10^{-5}$ K, enables recovery of the measured period. One could also take another value of $K_\perp$, determined independently, and fit the period on the eighth-order term (for example). This type of activity is currently unproductive and we stop this discussion here.

At higher values of $K_\perp$ the period depends on $K_\perp$ almost linearly but the value of interest ($|K_\perp| \approx 3/4 \times 10^{-5}$ K) is in the non-linear region. In the absence of longitudinal field, ($\Delta_{-m,m-n}$ with $m = 10$ and $n = 0$), it is easy to interpolate T_H by some simple formula, even in this region, but all the other anisotropy constants also have uncertainty in their values. To tabulate T_H as a function of all available anisotropy constants, we have used the combination of the method of exact diagonalization with the method of polynomial interpolations. The final formulas are valid in quite a wide region of the values of the anisotropy constants (in Kelvins):

$$D/k_B \in [-0.06, -0.45];\ E/k_B \in [0.5, 0.13];$$
$$K_\perp/k_B \in [-0.8 \times 10^{-5}, -5.2 \times 10^{-5}] \tag{14}$$

and can be written:

$$T_H = (2k_B/g\mu_B)[E(E+D)]^{1/2} \sum_{\mu,\nu=1}^{3} X_\mu^K G_{\mu\nu} X_\nu^E \tag{15}$$

$$\text{where } G_{\mu,\nu} = \sum_{\alpha,\beta=1}^{3} X_\alpha^\nu \Omega_{\alpha,\beta}^\mu X_\beta^D \tag{16}$$

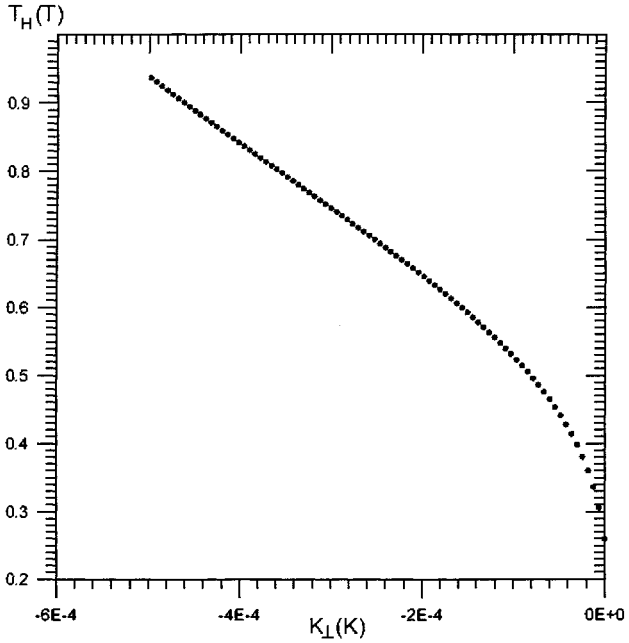

Fig. 21. The period of the oscillations of the ground-state tunneling splitting $\Delta_{10,-10}$, calculated from Eq. (12b), as a function of the fourth-order anisotropy constant, $K_\perp$.

$$\mathbf{X}^1 = \begin{pmatrix} 1 \\ 0 \\ 0 \end{pmatrix};\ \mathbf{X}^2 = \begin{pmatrix} 0 \\ 1 \\ 0 \end{pmatrix};\ \mathbf{X}^3 = \begin{pmatrix} 0 \\ 0 \\ 1 \end{pmatrix};\ \mathbf{X}^{\mathrm{D}} = \begin{pmatrix} D^2S^2 \\ DS \\ 1 \end{pmatrix};$$
$$\mathbf{X}^{\mathrm{E}} = \begin{pmatrix} E^2S^2 \\ ES \\ 1 \end{pmatrix};\ \mathbf{X}^{\mathrm{K}} = \begin{pmatrix} K_\perp^2 S^8 \\ K_\perp S^4 \\ 1 \end{pmatrix} \tag{17}$$

$$\Omega^1 = \begin{pmatrix} -0.2027 & -0.7838 & -1.6242 \\ 0.3877 & 1.3462 & 4.0468 \\ -0.1251 & -0.0644 & -2.6684 \end{pmatrix}$$
$$\Omega^2 = \begin{pmatrix} -0.1790 & -0.5550 & -1.6797 \\ 0.3449 & 1.8759 & 4.4967 \\ -0.1031 & 0.2321 & -3.6051 \end{pmatrix} \tag{18}$$
$$\Omega^3 = \begin{pmatrix} -0.0498 & -0.2483 & -0.0030 \\ 0.1155 & 0.6170 & 0.0108 \\ -0.0653 & -0.3996 & -2.9928 \end{pmatrix}$$

For the general case ($n > 0$), one must return to full numerical calculations. The period depends on the values of n and m (Figs. 22 and 23a,b). Figure 22 shows the tunneling splitting $\Delta_{m,-m}$ (in Kelvins) as function of H_x (in Tesla) in zero longitudinal

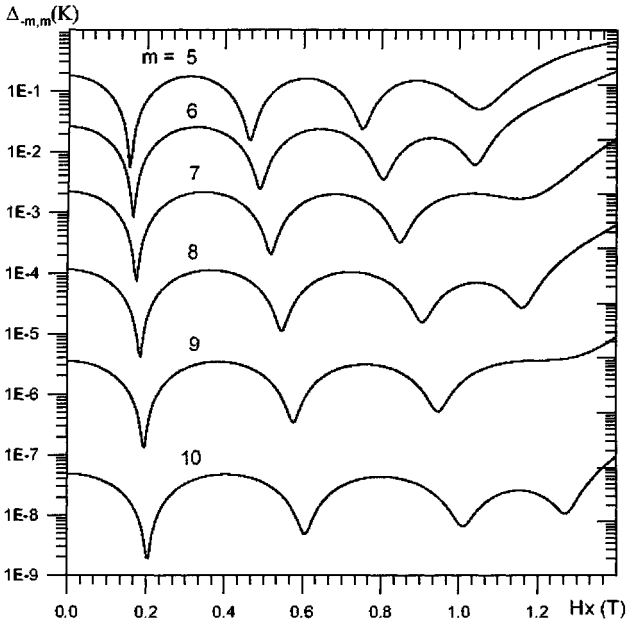

Fig. 22. Dependence of tunneling splitting $\Delta_{-m,m}$ (Fe_8), calculated from Eq. (12b) for different values of m, on transverse magnetic field.

magnetic field for the azimuth angle $\varphi = 0$ (with "misalignment" angle $\theta_{\rm m} = 1^\circ$). Because of the presence of the second-order term in Eq. (12b) all the $\Delta_{m,-m}$ have non-zero values in zero transverse field. As discussed above, negative $K_\perp$ tends to reduce the number of the oscillations along the hard x-axis because it makes x-direction easier for quasi-classical motion of the giant spin. This effect leads to the decrease of the imaginary part of the instanton action (by reducing the area on the unit sphere enclosed by two possible paths joining quasi-classical minima $-S$ and S). In these circumstances it is difficult to calculate the exact number of oscillation. Firstly, analytical solution of the problem in the presence of the fourth-order term is not easy; perturbation theory, in particular, cannot be applied to large transverse magnetic fields. The instanton technique and WKB approximations give non-analytical solutions which require numerical calculations (there is no reason to apply this, because we already have an answer given by the method of exact diagonalization). As mentioned above, the only conclusion we can make here is that the number of oscillations is determined by the exponents α, β and γ in the chain of operators $(S_\pm^1)^\alpha (S_\pm^2)^\beta (S_\pm^4)^\gamma$ which should be applied to the state $|m\rangle$ to reach the state $|n-m\rangle$. The operator $S_\pm$ comes from the transverse magnetic field term and $S_\pm^2$ and $S_\pm^4$ come from the second- and fourth-order anisotropy terms, respectively. It is clear that the whole picture is defined by the combined symmetries of the anisotropy terms. This is apparent in Fig. 22, with the change of the period with m and the shape of the last oscillation. Note, in particular, that the quantities $\Delta_{10,-10}$, $\Delta_{8,-8}$, and $\Delta_{6,-6}$ (with the difference $\delta S_z = 4$ in the lengths of the chains connecting $|m\rangle$ and $|-m\rangle$

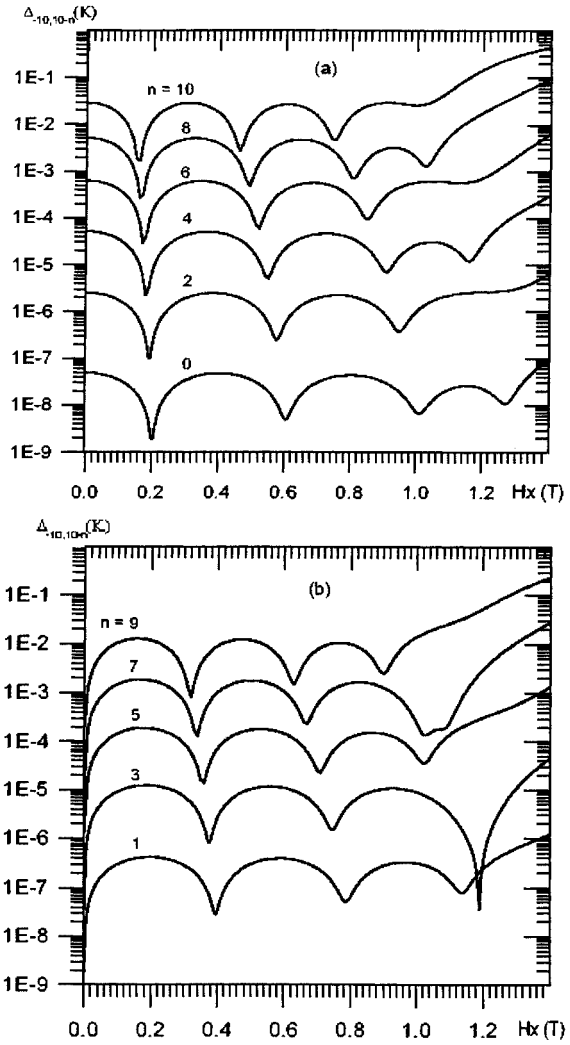

Fig. 23. Tunneling splitting $\Delta_{-10,10-n}$ (Fe_8), calculated from Eq. (12b) for different even (a) and odd (b) values of n, as a function of transverse magnetic field.

states) behave similarly. The situation is the same for $\Delta_{9,-9}$, $\Delta_{7,-7}$ and $\Delta_{5,-5}$. For smaller m the structure of the interference is also affected by the admixing of states with different m (S_z is not a good quantum number for the Hamiltonian Eq. 12b).

The same conclusions can be drawn, in the presence of a longitudinal field. The functions $\Delta_{-10,10-n}(H_x)$ calculated for $\varphi = 0$, are plotted in Fig. 23 (with n even (a) or odd (b)). The resonant longitudinal field for particular n is defined by Eq. (13) (it was, of course, necessary to tune the value of the field around these H_n). The levels $S_z = -10$ and $S_z = 10 - n$ with odd values of n cannot be linked in zero transverse

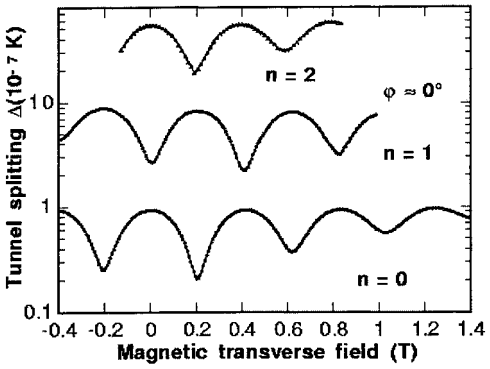

Fig. 24. Tunneling splitting $\Delta_{-10,10-n}$ (Fe_8) measured for $n = 0, 1, 2$ [25].

field (there are no matrix elements between them) and, therefore, they have a zero tunneling splitting at $H_x = 0$. The levels $S_z = -10$ and $S_z = 10 - n$ with even values of n can be linked, even in zero transverse field, and tunnel splitting is finite. (As an example, for $n = 1$ and $n = 2$ one must apply $S_\pm$ and $S_\pm^2$, respectively.) The curves calculated in Fig. 23 can be compared with those measured for Fe_8 [25] and plotted in Fig. 24. The absolute value of the tunneling splitting is, again, not in the best possible agreement with experimental results. These authors [25] did not, unfortunately, show the behavior of the curves with $n = 1, 2$ (and larger n) at higher values of transverse magnetic fields. Comparison of measured and calculated curves in the region of high fields can help determine which types of anisotropy are important in the "giant spin" Hamiltonian. In other words, measurement of the tunnel splitting as a function of a magnetic field can be used to determine the crystal field parameters of the "giant spin" Hamiltonian. This method should be quite sensitive to higher-order anisotropy.

In addition, we would like to stress that the actual behavior of the tunneling splitting in the region of the nodes is very sensitive to the environment. This point will be discussed below in the part of this review related to the low-temperature limit of the relaxation of the magnetization (Environmental Effects).

4.4 Environmental Effects

Current theories are unable to explain results from relaxation experiments in all temperature ranges. It is, therefore, reasonable to consider low temperatures (ground-state tunneling regime) and higher temperatures (thermally assisted tunneling regime) separately. The first is better understood by the theory of Prokof'ev and Stamp [44, 47, 72, 73, 77], while progress in the understanding of the second is being made by Luis et al. [50], Fort et al. [51], and Leuenberger et al. [52]. Because the barrier height for Fe_8 is approximately one third that for Mn_{12}, the amount of tunneling splitting is larger for all states. In particular, one expects a barrier cut-off at larger m_t in the high-temperature range, and faster relaxation in the low-temperature range.

These circumstances make Fe8 molecules very attractive for the study of ground-state tunneling (i. e. the pure quantum regime). The thermally assisted regime is usually (historically) the main subject of investigations on Mn_{12} molecules.

4.4.1 Experimental Picture

To deal with relaxation one must take into account environmental effects. The environment of a molecule essentially comprises ensembles of bosons and fermions coupled to the spin of the molecule. In real molecular systems the most important environmental effects come from phonons, nuclear spins, and dipolar fields. The environment can absorb finite variations of energy and angular momentum. This is extremely important because the non-conservation of these quantities can forbid tunneling. The environment is also responsible for the broadening of resonance lines. The shape of these lines is usually obtained from a plot of dM_z/dH_z against H_z, as this was first defined by Thomas et al. [11]; for Mn_{12} resonance line-shapes were nearly Lorentzian and of width 40 to 100 mT. Furthermore, as mentioned by Barbara et al. [18, 11], tunneling resonance could not have been detected with the poor field resolution of conventional SQUID magnetometers, if resonance lines were not substantially broadened, and, because pure phonon broadening is too small by a factor of 100 [65], broadening of magnetic origin must play the major role (the line-width in the absence of environment is approximately equal to tunnel splitting, Δ). This is true at low temperature only, because the effect of phonons is obviously dominant in the thermally assisted regime. Very similar broadening of transitions was observed for Fe_8 by Ohm et al.; at low temperatures they were approximately 12–15 mT [43].

We now describe the origin of the resonance line-width in molecular crystals, in the two limits of high and low temperatures (see also Barbara et al. [21] for qualitative description from experiments). In the thermally activated regime (where Δ at the bottom of barrier can reach values of the order of 0.5 K) the line-width is at least equal to the value of the tunneling splitting. The resonance line in this regime must be homogeneously broadened with Lorentzian shape, because of equilibrated spin–phonon transitions, and was observed for Mn_{12} [11, 12, 60]. Note that line-shape can deviate from Lorentzian, depending on the magnetic history of the sample, because the width of distributions of dipolar and hyperfine fields are of the same order as tunneling splitting. It might be surprising to see that magnetic history can be important in a basic effect such as tunneling. In fact the magnetic history is always important when irreversible processes are involved, and this is so here.

It is well known that frozen distributions of hyperfine and dipolar fields (quenched from the super- paramagnetic state) have Gaussian distributions if the temperature is low enough to prevent fast spin reorganizations. In these circumstances resonance lines will be inhomogeneously broadened, with no Lorentzian and, eventually, Gaussian line-shapes. In the low temperature regime, where thermal fluctuations are essentially frozen, tunneling will only be possible through internal field fluctuations, of amplitude H_f. These fluctuations are because of nuclear spins in weak dipole–dipole interactions, and because of strong hyperfine interactions with electronic spins. Internal field fluctuations involve spin–spin quantum dynamics of the considered sys-

tem, which can be tested on either electronic or nuclear spins. In Mn12 each ion has a nuclear spin, whereas in Fe_8 this is so for only 2% of the ions (^{57}Fe). Each Fe_8 molecule contains 120 hydrogen, 18 nitrogen, and 8 bromine atoms, however, all of which have non-zero nuclear magnetic moments. They produce (together with the dipole moment of each molecule) the fluctuating internal field acting on each molecule. The amplitudes, H_f, of these fluctuating fields are extremely small (they can be evaluated from NMR experiments [86]; e. g., for the protons in Fe_8 $H_f \approx 1.4$mT [21]). Because quantum tunneling is possible only within this range of fluctuating fields, spin reversals from S to $-S$ will occur only in a narrow energy window of width H_f, "digging a hole" in the initial distribution of internal fields. The frozen distribution of internal fields (resulting from electronic and nuclear spins which are not affected by the quantum dynamics) could be obtained from measurements of dM_z/dH_z against H_z, by sweeping the longitudinal field, as discussed above. In contrast with the high-temperature situation, however, the distribution which is probed here for each value of H_z is inhomogeneous, and it will be possible to probe this distribution as long as H_f remains much smaller than its width. This will be so unless the temperature increases to the point where H_f becomes of the order of the total local field distribution. The cross-over between inhomogeneous Gaussian-like to homogeneous Lorentzian-like distributions occurs when the temperature becomes large enough to equilibrate the spin system. In Mn_{12}, the tunneling window H_f was evaluated assuming oscillations of the mean dipolar and hyperfine field with $\Delta m = \Delta I = \pm 1$ [21, 87].

Low-temperature (0.04-0.3 K) experiments by Wernsdorfer et al. [53], using the "hole digging" technique'[45], based on the theory of Prokof'ev and Stamp'[44], have recently enabled measurement of the tunneling window. In this theory the rate of relaxation of the magnetization, $\Gamma_{sqrt}(H)$, is proportional to the distribution of internal bias field $P(\xi_H)$. In the experiment, during the digging time t_{dig} a small fraction of the molecules (those in resonance with the applied external digging field, H_{dig}) tunnel, reversing the direction of their magnetization. This causes rapid transitions of molecules close to resonance around H_{dig}. Such transitions are effectively "digging a hole" in an initial distribution of the internal fields (Fig. 25). The hole widens in time, depending on the digging time, t_{dig}. The hole-width (which is obtained by linear interpolation to $t_{dig} = 0$) results in intrinsic broadening of the nuclear fields σ_{hyp} (Fig. 26). It has been found [53] that the width of the Gaussian distribution of hyperfine fields, σ_{hyp}, is $\sim$12 mT, which is orders of magnitude larger than the value of the tunneling splitting $\Delta_{10,-10}$. σ_{hyp} is temperature-independent up to approximately 0.4 K and then starts to increase (Fig. 27). (This last observation needs further theoretical investigation, because the square-root theory [44] does not work at such high temperatures.) We should note, however, that these "hole digging" experiments were performed on the minority phase of Mn_{12}, and that in the presence of a magnetic field this system can have a lower crossover temperature. Low-temperature studies of main phase of Mn_{12} have recently become possible. A large magnetic field was applied to get rid of the minority phase [85].

Similarly to Mn_{12}, it was observed for Fe8 that the first maximum in the relaxation rate is not in zero applied field, but at 8 mT. As in Mn_{12} this was attributed to the effect of internal fields [41]. This was for a powder sample; for a single crystal it was found that the resonance width (approximately 12- 15 mT) is as in Mn_{12} and,

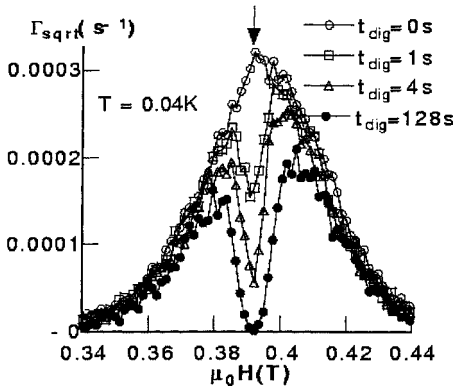

Fig. 25. Quantum-hole digging in the initial distribution of internal fields [53]. Note that these measurements were performed on a minor species of Mn_{12}. (For details about the different species of Mn_{12}, see Refs [42] and [53] and references cited therein.)

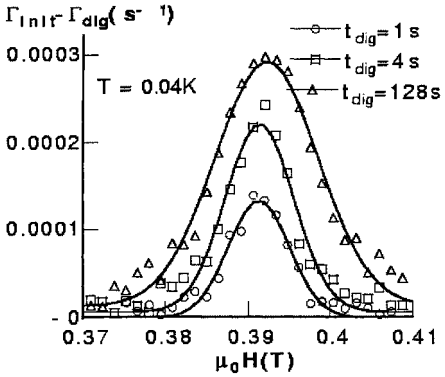

Fig. 26. The dependence on digging-time of hole-shape in Mn_{12} [53].

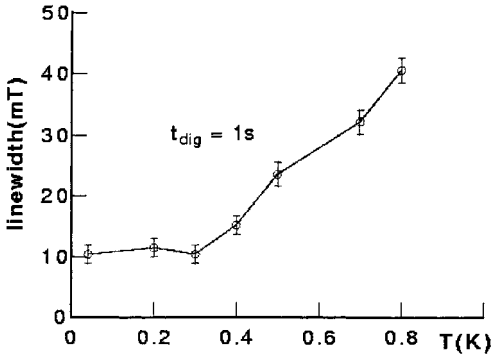

Fig. 27. Temperature-dependence of hyperfine line-width (σ_{hyp}) in the Mn_{12} crystal [79].

for the same reason (intermolecular dipolar interaction), orders of magnitude larger than expected without environment or with phonons only [11, 18, 65]. A difference between these two systems is that the first resonance is observed in a negative field in Mn_{12} and in a positive field in Fe_8. This was interpreted as a consequence of the competition between the demagnetizing field $-NM$ (shape-dependent, where N is the demagnetizing factor) and the local Lorentz field $+(4\pi/3)M$ [21]. Because the Mn_{12} crystals are elongated, the demagnetizing field (which is antiparallel to M) is smaller than the Lorentz field and the internal field is parallel to the magnetization, M – it is necessary to apply a negative field to cancel the internal field.

The situation is just opposite with Fe_8. This discussion was with reference to the most probable values of internal fields; we now know that the internal fields are widely distributed in both systems (see above). Hole-digging experiments similar to those described above for the impurity phase of Mn_{12} were performed for Fe_8 [45], also at low temperature. It was found that, for thermally annealed sample (down to values of magnetization of approximately $-0.2M_s$, where M_s is the saturated magnetization), the distribution $P(\xi_H)$ of the internal bias field ξ_H is very accurately described by a Gaussian function (Fig. 28). As a matter of fact such a distribution is expected from theoretical models, but only in the limit of high spin concentrations (dipolar field distribution of a dense set of randomly oriented spins [88, 54]. In the other limit, of dilute static dipoles, the distribution must be Lorentzian, as was shown by Anderson [55]. A study for different concentrations was performed and showed that more complicated and sometimes bi-modal distributions could occur between these two limits [89]. Interestingly, in Fig. 28 the maximum of $P(\xi_H)$ is shifted from $H = 0$. The shift is even larger than in Ref. [41], because the experiment was performed at a lower temperature - the magnetization, and thus the local field, are larger (the sample was not absolutely annealed). The width of this distribution (σ_{dip}) was found to be of the order of 50 mT).

The relaxation of the molecules, as for Mn_{12}, digs a hole in $P(\xi_H)$ at the value of the applied field. The width and depth of the hole change with waiting time, i. e. with

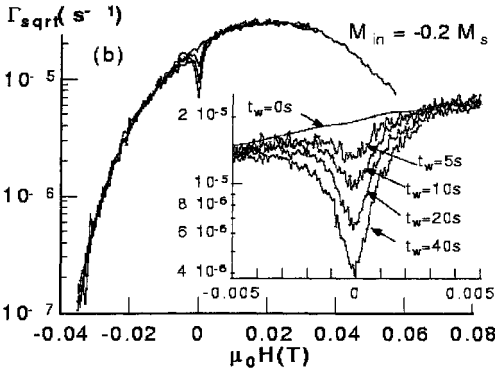

Fig. 28. Tunneling distribution in Fe_8 (which, according to Prokof'ev and Stamp [44], is proportional to the distribution of $P(\xi_H)$ of the internal bias field, ξ_H) for and annealed sample [45]. The insert enlarges the region of the fields around the hole.

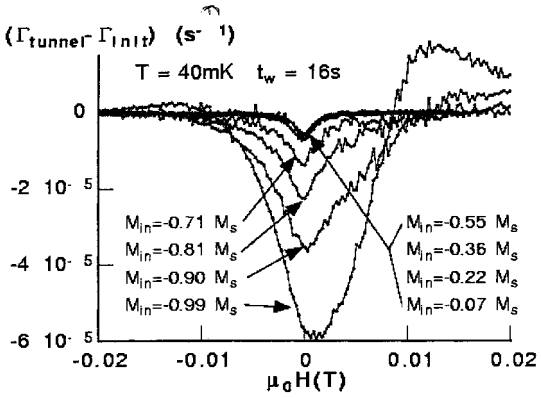

Fig. 29. Dependence of hole shape (in initial distribution of the dipolar fields in Fe_8) on the amount of annealing [45]. At initial magnetization $M_{in} < |0.5M_s|$ the hole becomes independent of future annealing and gives the line-width $\sigma_{hyp} \approx 1.2$–1.6 mT.

the time during which the field is applied (insert in Fig. 28). For initial magnetizations close to saturation the hole is large and asymmetric, whereas for initial magnetization less than $|0.5M_s$ it becomes symmetric, independent of further annealing (on initial magnetization), and has a width of approximately 1.2–1.6 mT (Fig. 29). Similarly to Mn_{12} this line-width is temperature-independent up to 0.4 K and then starts to increase (Fig. 30). Before these experiments were performed values of the hole width at 0 K were predicted by Prokof'ev and Stamp [44], from the nuclear spins, by use of in their theory; the values obtained, 0.3 mT for Fe_8 and 25 mT for Mn_{12}, are close to the measured values. It was shown that the dipolar fields produce the bias, ξ_H, which is a few orders of magnitude larger than the value of the tunneling splitting and, therefore, can block the tunneling. The fast nuclear dynamics (transverse relaxation in nuclear subsystem or, in other words, T_2 processes) broaden the resonance line, however, and open a channel for tunneling. This explains the origin of the hole (its width is defined by the width of the distribution of the hyperfine fields) in the field-dependent relaxation rate (which is proportional to the total distribution of internal fields).

All these low-T experiments performed on Fe_8 [41, 43, 45, 53, 56] demonstrate the square-root relaxation law after short times (approximately the first 100 s; see, e. g., Fig. 17). According to the theory of Prokof'ev and Stamp this law comes from the time-dependent distribution of fluctuating internal dipolar fields in a sample. Fast initial transitions change the total distribution of internal fields across the sample that can push some molecules out of resonance but bring other molecules into the resonance everywhere in the sample and allow continuous relaxation. When times are longer times the experimental relaxation data are better fitted by the stretched exponential law with $\beta \approx 0.4$ [41, 43].

Thomas and Barbara [21, 57–59] have shown that in Mn_{12} relaxation behaves non-exponentially, even at relatively high temperatures (up to 2.8 K); this can be understood as a consequence of intermolecular dipolar coupling. (At low temper-

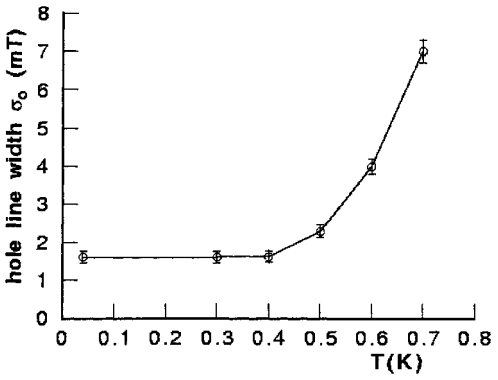

Fig. 30. Temperature-dependence of the hyperfine line-width width (σ_{hyp}) in a crystal of Fe_8 [80].

atures non-exponential relaxation was seen in many experiments [4, 6, 7, 11, 53, 62]). The exponential relaxation can occur only in the limit of non-interacting (with each other and with the nuclear thermostat) molecules when we can simply write $dM(t)/dt = -\tau^{-1}M(t)$. For interacting molecules the right-hand side of this equation contains a different term, $M^*(t), = f(M(t))$, which results in deviation from the exponential law (note that simple distribution of relaxation times also results in non-exponential behavior). As was reported elsewhere [57], below approximately 1.7 K the relaxation follows a square-root law with characteristic time, τ, weakly dependent on temperature, whereas at temperatures above 2.5 K the characteristic time follows the Arrhenius law, but the relaxation is still non-exponential, because of the dipolar interaction between molecules. To fit the experimental relaxation curves it was necessary to use the stretched exponential law with $\beta(T) < 1$. Below 1.9 K $\beta(T)$ is approximately constant near 0.5. At low temperatures, however, the stretched exponential law was not really satisfactory. As is apparent from Fig. 31, the square-root law fits all the experiments up to ~1.7–1.8 K (see also Thomas and Barbara [58]).

At higher temperatures, between 2 K and 2.8 K, dipolar interactions play a less fundamental role, but their influence can still be observed, e. g. from the observation that the relaxation is clearly non- exponential (the exponent of a stretch exponential fit increases from 0.5 to 1 [21, 57–59]) and also from the shift of the maximum of the relaxation curve in magnetic field. This shift, found by Thomas and Barbara for Mn_{12} at different temperatures [21, 57–59], is because of the evolution of the internal field with temperature. It was suggested [21, 57] that this shift can produce square root-like relaxation laws of origin different from the Prokof'ev and Stamp law. Instead of being at zero Kelvin, this law, with temperature-dependent relaxation times, is valid at high temperature, even if the system is equilibrated. This suggests that quantitative description of the thermally assisted regime for Mn_{12} should take into account interactions with the spins' environment (not only with the spin–phonon interaction). This also explains [21] why the resonance lines have Lorentzian shape [11, 12] although the relaxation is not exponential.

Note that even if the observed resonances can be well fitted to Lorentzian law [11, 12] (and not to the Gaussian law associated with hyperfine and dipolar fields [60]) this does not mean that hyperfine and dipolar interactions are not relevant. The widths

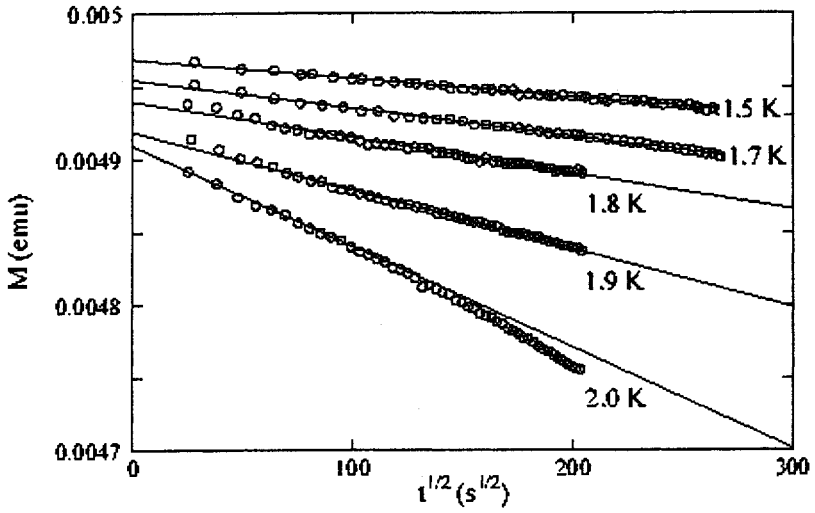

Fig. 31. Time decay of magnetization in Mn_{12}, plotted as a function of the square root of time [58]. Lines show linear fits.

of the dipolar fields and the distribution of hyperfine fields in Mn_{12} are comparable, and although these fields can participate in the resonance broadening their non-Lorentzian character is hidden by the long Lorentzian tails (and experimental error bars). It has been shown that the observed Lorentzian line-shape does not prove that the system of molecules is equilibrated - the shape of the resonance depends on the history of the sample (field cooled or zero-field cooled, quenched or not quenched) [21]. Finally, it should be mentioned that the published line-widths depend on the authors; they vary from 20 mT [60] to 30 mT [53] or 35 mT [12].

A continuous increase of the resonance line-width was observed with the index of the resonance at temperatures close to 3 K [21]. Because this effect was not symmetrical with the magnetization state $M = 0$, one cannot infer dipolar field distribution. It might, instead, be because of the intrinsic line-width, Δ, which, at the higher temperatures (when the tunneling occurs at the top of the barrier) is of the order of 0.5 K (which is larger than the other contributions [21]) and which increases, on average, with applied field. This observation confirms that even if dipolar interactions and hyperfine interactions (with longitudinal T_1 relaxation processes, driven by the fast dipolar processes [44, 47, 61]) are essential in the range 2 to 2.8 K, at the higher temperatures (e. g. between 2.8 and 3 K) the intrinsic line-width, Δ, plays the most important role. Under these conditions, i. e. at temperatures rather close to the blocking temperature (3 K), the transitions are homogeneously broadened and the observed Lorentzian line-shapes really attest to thermal recovery of the spin–phonons system. (Note that fast dipolar flip–flop processes are also able to provide thermal quasi-equilibrium on each side of the barrier, producing, simultaneously, rapidly fluctuating fields acting on each molecule.) In this limit the spin–phonon interaction becomes predominant leading to the thermally assisted tunneling regime.

The observation of history-dependent peak shapes for Mn12 at a relatively low temperature (1.6 K) [21], leads us to question the validity of experimental determinations of Lorentzian line- shapes. To extract this distribution from the plot of measured relaxation against field it is necessary to assume an analytical law to fit the data. As an example, Friedman et al. [60] fitted the experimental curve to $\exp(-t/\tau)$. As shown above [21, 53, 57–59], however, the relaxation clearly deviates from exponential even at these high temperatures (2–2.6 K). This must lead to large errors in the relaxation time (obtained at each field) and, therefore, in the resonance line-width. Note that even in the exponential regime, error bars on the equilibrium magnetization, M_{eq}, in $M(t) = M_{\mathrm{eq}} + (M_{\mathrm{in}} - M_{\mathrm{eq}})\exp(-t/\tau)$ lead to uncertainties in the line-shape. The value of M_{eq} can be obtained accurately only when relaxation is very fast, i. e. either very close to the blocking temperature of 3 K (and under these conditions there is no doubt about the Lorentzian form) or in the presence of a large transverse magnetic field which increases the tunneling gap [85].

In conclusion, each molecule can tunnel under the effect of rapidly fluctuating fields originating from dipolar and hyperfine interactions, and also under the effect of spins–phonon interactions at higher temperatures. Only in this last circumstance (where the transition width is intrinsic) are the spins and phonons is equilibrated (no hole in the spin energy distribution).

4.4.2 Thermally Assisted Tunneling Regime

The first attempt to apply phonon-based mechanisms was made by Villain et al. [63] and Politi et al. [64] before the resonant tunneling in Mn_{12} was confirmed experimentally. Politi et al. [64] considered the giant spin model for single Mn_{12} molecule in a longitudinal magnetic field (Eq. (1) with no S_z^4 term) with coupling to the acoustic phonons in the form:

$$H_{\mathrm{sp-ph}} = \sum_g \left(\hbar/2N_u M_u \omega_q\right)^{1/2} \left[iqV_q(\mathbf{S})C_q^+ - iqV_q^+(\mathbf{S})C_q\right] \tag{19}$$

where $V_q(\mathbf{S}) \approx D(S_x Sz + S_z S_x)$, N_u is the number of unit cells, M_u is the mass per unit cell and C_q is the phonon annihilation operator. They ignored the possibility of the tunneling (because of the fourth-order anisotropy term) at the top of the barrier (and at the bottom) and obtained the result $\tau^{-1} \approx (SH_z)^3$ for the relaxation rate, in contradiction with the experiments which demonstrated the existence of a minimum of relaxation time near $H_z = 0$, rather than a maximum (Fig. 5). Later, this theory was extended by including the interactions with nuclear spins (the possibility of tunneling was again ignored and only the longitudinal part of hyperfine interaction was considered) [65]. It was found that combination of these two mechanisms (strictly speaking, the sum of two different curves) can give a minimum of the relaxation time at zero field. This theory was also unable to describe the resonant behavior of the relaxation curve.

Phonon-mediated tunneling relaxation was considered in the theory of Garanin and Chudnovsky [26], which also involved random hyperfine fields. They ignored

higher-order anisotropy terms in the Hamiltonian, however, and based their calculations on perturbation theory for a small transverse field, H_x.

All these models are qualitatively or quantitatively in contradiction with experimental results. They are, nevertheless, not incorrect and they show (directly or indirectly) the importance of the hyperfine interaction and of intermolecular dipolar coupling (see, for example, Burin et al. [67]). The problem is that to obtain a quantitatively correct answer it is necessary to remember that (even at temperatures of approximately 2 K) the tunneling effect involves all the interactions of the spin of each molecule with the environment of spins and phonons. This is very difficult task. For example, Dobrovitski and Zvezdin [68] concluded that correct description of the jump width of the hysteresis loop (Fig. 3) required consideration of fluctuating internal fields, because they found for pure giant spin Hamiltonian a huge discrepancy with the experimental results. They limited themselves to the suggestion that the origin of this field could be dipole–dipole in nature, however. They estimated an average value for jump width by using a Gaussian distribution of the fluctuating field. Similar calculations were made by Gunther [69] who calculated the width of the jump in the hysteresis loop and concluded that it is necessary to involve dynamical transverse magnetic fields to avoid discrepancies with experimental results.

The first theory to accommodate fourth-order anisotropy terms was that of Luis et al. [50]. They presented a theory of resonant quantum tunneling of large spins through thermally activated states which includes: phonon-mediated transitions between the states m and m' with $m - m' = \delta m = \pm 1$ (in the simplest form $S_x S_z + S_z S_x$), resonant tunneling as a result of fourth-order anisotropy terms, and a transverse magnetic field. They assumed that the transverse magnetic field originates from the combined action of dipolar and hyperfine fields. They concluded, of course, that internal fields alone cannot explain the minima on the relaxation curve but, together with fourth-order terms, these fields can account for the experimentally observed behavior of relaxation in Mn_{12}. To obtain the lifetime of the excited levels (because of phonon-mediated transitions) they applied a standard master equation. Finally, the spin-relaxation rate was averaged over a Gaussian distribution of longitudinal dipolar fields (together with hyperfine fields). Despite the inequivalent treatment of tunneling between the resonance states and phonon-mediated transitions, this model was the first which described (qualitatively) the hysteresis loop of Mn_{12} [11], and other experimental results obtained at high temperatures ($T > 2.5$ K). It is important to note, however, that in this model the magnetization always relaxes exponentially "after a brief non-exponential relaxation" (see also Fernandez et al. [78]). As we have seen above, however, the magnetization relaxes non-exponentially, unless the temperature is very close to the blocking temperature (approximately 3 K).

Fort et al. [51] recently improved the calculations of Villain et al. [63–65] by adding tunneling through the top of the barrier. They derived the master equation:

$$\begin{aligned} \mathrm{d}N_\mathrm{m}/\mathrm{d}t \;=\; & \sum_{p=1}^{2} N_{m-p}\gamma_{m-p}^{m} + \sum_{p=1}^{2} N_{m+p}\gamma_{m+p}^{m} \\ & -N_m \sum_{p=1}^{2}(y_m^{m-p} + \gamma_m^{m+p}) - (N_{-m} - N_m)\Gamma_m \end{aligned} \tag{20}$$

where nm is the number of molecules in spin state $|m\rangle$, $\gamma_m p$ is the spin–phonon relaxation rate from state $|m\rangle$ to state $|p\rangle$, and Γ_m is the tunneling relaxation rate from state $|m\rangle$ to state $|-m\rangle$. This equation includes phonon mediated transitions with $\delta m = \pm 1, \pm 2$ and tunneling between the states $|m\rangle$ and $|-m\rangle$. Using Eq. (20) the authors concentrated on investigation of the first resonance ($H_z = 0$) on the relaxation curve (Fig. 5). They noted that in the region of the validity of their theory ($H_z < 3\,\mathrm{kOe}$) the relaxation rate calculated at the temperatures $T = 2.8\,\mathrm{K}$ and $T = 2.97\,\mathrm{K}$ are in good agreement with the experimental temperature, and that this agreement between the theory and experiment becomes better at higher temperatures. They also noted that a general treatment of this problem requires incorporation of other interactions (dipolar, random fields, etc.), because the model with fourth-order anisotropy term gives only transitions with $\delta m = \pm 4$. It was suggested that the theory was modified by inclusion of transverse fields (of any nature) which obey selection rule $\delta m = \pm 1$ (i. e. which contain terms like S_x or S_y).

Very recently Leuenberger and Loss [52] presented a theory of the relaxation in Mn_{12} at high temperatures (2 K and higher) based on thermally assisted spin tunneling in a weak transverse magnetic field. They solved the standard master equation (for the reduced density matrix $\rho(t)$) which includes both resonance tunneling as a result of the fourth-order anisotropy term (and transverse fields) and phonon-induced transitions with $\delta m = \pm 1, \pm 2$. The origin of the transverse field was attributed to misalignment of $\theta_m = 1^\circ$ between the field direction and easy axis, extracted from the experiment of Friedman et al. [60] (see also Ref. [4]). As is noted by the authors, this model is in "reasonably good agreement with all the experimental parameter values known so far". Differences from the work of Fort et al. [51] are:

1. a more general spin–phonon interaction was considered;
2. transitions induced by a transverse magnetic field were included; and
3. longitudinal fields were not limited to the resonance near $H_z = 0$.

All this enabled them to obtain an independent description for each resonance in the experimental curve of Fig. 5. To obtain a continuous description of the dependence of relaxation time on H_z the authors applied Kirchhoff's rules by associating each independent path from $|-10\rangle$ to $|10\rangle$ with the probability current $J_n = \mathrm{d}\rho_n/\mathrm{d}t$, where ρ_n is the reduced density matrix $\rho(t)$ for a particular path n. This theory can be applied to Mn_{12}, but after some correction, given below. The theory, given in [52], allows to recover the observed Lorentzian line-shape for the resonance peaks, but the procedure used to obtain the experimentally observed line-width was, however, "confusing". The authors cut off the calculated Lorentzians to the appropriate values, because these Lorentzians were found to be extremely high and narrow. This procedure was, of course, supported by mathematical arguments, but the problem is that the authors (and Fort et al. [51]) missed from their theory the most important contribution – the value of the tunneling splitting in the denominator of their formula for the tunneling rate. As we will discuss below, this missed term makes the most important contribution to the width of the resonance line.

It was also shown [52], that even and odd resonances should have different sizes, because even resonances are induced by S_+^4 or S_-^4, whereas odd resonances are induced by combinations such as $S_x S_+^4$ or $S_x S_-^4$ (a similar effect was found experimentally by Thomas and Barbara [11, 21]). In addition, on the basis of experiments

by Caneschi et al. on dilute samples [70] (compared with the same measurements on powder samples), the authors completely ignored dipolar fields and hyperfine coupling, because these contributions should give rise to the Gaussian distribution, whereas the peaks of relaxation rate, observed experimentally, are Lorentzian in shape. We have, however, already noted (see the penultimate paragraph of Section 4.4.1), that it is not easy to draw conclusions from experiments at $T < T_B \approx 3\,K$ about the real shape of these peaks (even if they are the Lorentzians) close to tails. Even if the phonons dominate in the relaxation mechanism at $T > 2\,K$ (about which there is no doubt), the influence of dipolar and hyperfine couplings cannot be negligible because (at least) the relaxation behaves non-exponentially at these temperatures [21, 53, 57–59, 62].

In the following text we would like to present a qualitative picture of the thermally assisted tunneling phenomenon including coupling to the environment (in respect of resonance line-width). We do not state that our calculations are complete; we merely wish to show how this works. (N.B. similar calculations were performed by Prokof'ev and Stamp several years ago but were not published.)

The Hamiltonian of interest for the Mn_{12} molecule can be written:

$$H = H_G + H_{sp-ph} + H_{hyp} + H_{dip} \tag{21}$$

where H_G is given by Eq. (1) and we take the spin–phonon Hamiltonian in the simplest form of Eq. (19) with $V(\mathbf{q}) = D(S_xS_z + S_zS_x) = (D/2)[(S_+ + S_-)S_z + S_z(S_+ + S_-)]$. The third term in Eq. (21) describes the hyperfine interaction of central spin S with the nuclear spins σ_k of each Mn ion (i. e. $N = 12$ nuclear spins):

$$H_{hyp} = 1/S \sum_{k=1}^{12} (\hbar\omega_k/2)\mathbf{S}\sigma_k \tag{22}$$

And, finally, the last term gives the dipolar intermolecular interaction:

$$H_{dip} = 1/2 \sum_{i \neq j} V_{i,j}\mathbf{S}_i\mathbf{S}_j \tag{23}$$

where $V_{i,j}$ depends on the cube of the inverse distance between the molecules. Let us now assume that the system is close to the characteristic magnetic field H_n (Eq. 3) when some pairs of levels from the two opposite sides of the barrier come into resonance. Because this pair of levels is well separated from the others, we can truncate the giant spin Hamiltonian H_G to a two-level Hamiltonian $H_{m,n-m}$ and consider the pair of levels $|m\rangle$ and $|n-m\rangle$ with the corresponding energies E_m^0 and E_{n-m}^0 ($E_m^0 = -Dm^2 - K_\parallel m^4$):

$$H_{m,n-m} = \Delta_{m,n-m}\tau_x + \xi_{m,n-m}\tau_z \tag{24}$$

where $\Delta_{m,n-m}$ is the tunneling splitting (because of fourth-order anisotropy terms, transverse components of dipolar and hyperfine interactions, and transverse components of external magnetic field which can originate from the experimental mis-

alignment of the crystal), $\xi_{m,n-m}$ is longitudinal bias:

$$\xi_{m,n-m} = (2m-n)\Bigg[(E_m^0 - E_{n-m}^0)/(2m-n) + 1/S\sum_{k=1}^{12}(\hbar\omega_{\mathrm{k}}/2)\sigma_{\mathrm{k}}^z + \sum_{j\neq 0}(V_{0,j}/2)m_j^* - g\mu_{\mathrm{B}}H_{\mathrm{z}}\Bigg]/2 \tag{25}$$

and τ_x, τ_z are the Pauli matrixes. In Eq. (25) the third term comes from the longitudinal part of the dipolar interaction, where m_j^* is the spin state of the jth molecule. In these circumstances can obtain, for the maximum value of the tunneling probability with no phonons:

$$P_{m,n-m}(0) = \Delta_{m,n-m}^2/(\xi_{m,n-m}^2 + \Delta_{m,n-m}^2) \tag{26}$$

The longitudinal hyperfine couplings give a Gaussian spread to each giant spin energy level, E_m. This means that each energy level E_m is actually split into a Gaussian multiplet with $N+1$ different polarization groups of $N = 12$ nuclear spins. In reality one should consider tunneling between sublevels from opposite sides of the barrier, which are in the resonance for a given field. In the simplest example (zero approximation), however, we will consider the longitudinal internal bias (which comes from the hyperfine coupling) just as some "mute" variable ε with Gaussian distribution:

$$G(\varepsilon) = (2\pi\sigma_o^2)^{-1/2}\exp(-\varepsilon^2/2\sigma_o^2) \tag{27}$$

In this example the half-width $\sigma_o \approx N^{1/2}\omega_0$ with $\omega_0 = \langle\omega_{\mathrm{k}}\rangle$ and, according to the experimental results given above [21, 53, 87], $\sigma_o \approx 6\,\mathrm{mT}$ (i. e. $\omega_0 \approx 1.75\,\mathrm{mT}$). As for the dipolar coupling, we do not know it reliably except from some preliminary measurements which give $E_{\mathrm{D}} = 2\sigma_o \approx 20\,\mathrm{mT}$) and, therefore, for the distribution of dipolar fields we take the same value $\sigma_o \approx 6\,\mathrm{mT}$. A remark should be made here. The distribution of dipolar fields is highly dependent on the value of the magnetization (e. g. $M \approx 0$ after zero-field cooling or $M \approx M_{\mathrm{s}}$ after field cooling, where M_{s} is the saturated magnetization) and on the shape of the sample. Only after sufficiently strong annealing $M < 0.5|M_{\mathrm{s}}|$ one can observe the Gaussian distribution for dipolar fields. In the following discussion we assume zero-field cooling (an annealed sample). Thus, we can rewrite Eq. (25) in a more transparent form (ε includes contributions from both hyperfine and dipolar fields):

$$\xi_{m,n-m} = (2m-n)[g\mu_{\mathrm{B}}(H_n - H_{\mathrm{z}}) + \varepsilon]/2 \tag{28}$$

where H_n is the characteristic field from Eq. (3) (values of H_n are calculated using Eq. 1). Choosing Gaussian distributions for both dipolar and hyperfine fields, and with the same σ_o, is a great simplification which leads to the belief that dipolar fields are more or less ignored, because they behave as "non-interacting" hyperfine fields. Strictly speaking we are not far from this suggestion in our simple model, but here we do not see the reason to play with the form of distributions. In reality, however, one should also include the flip–flop transitions between molecules which come from the

transverse part of dipolar interaction. When system relaxes, moreover, the total bias field (internal plus external) changes in time. The flipping of the molecules produces time-dependent fluctuations of dipolar fields which also cause the transitions in the nuclear subsystem. Each molecule therefore feels a rapidly fluctuating field $\xi = \xi(t)$ [44, 47, 61, 72, 73]. This means that the Boltzmann distribution is time- dependent and additional time-dependence produces deviations from the exponential law (and these deviations increase with decreasing temperature). Ignoring that, we assume here that all these processes are fast enough to keep the thermal quasi-equilibrium at each side of the barrier with the "static" Boltzmann distribution. This leads, of course, to exponential relaxation, but the above simplification is sufficient for our purpose, which consists in estimating the width of the resonance line for an annealed sample.

The transverse part of the hyperfine interactions contributes to the Berry phase of a central spin in producing a random complex phase (for a details see Tupitsyn et al. [23, 31] and Prokof'ev and Stamp [47, 72, 73]). For our current purposes we can say that the transverse hyperfine interaction will act as a transverse field, and therefore change the tunnel splitting into effective splitting:

$$\Delta_{m,n-m} = \Delta_{m,n-m}(\Phi) \tag{29}$$

where $\Delta_{m,n-m}(0)$ is the tunneling splitting in zero external transverse magnetic field with no hyperfine interactions and Φ is an additional phase from hyperfine interactions. It would be wrong to say that the distributions of internal transverse and longitudinal fields are always the same. In zero approximation, however (and for a strongly annealed sample) we can use this suggestion and consider the Gaussian distributions with the same width, σ_0, for both transverse and longitudinal fields (it is, of course, easy to take different σ_0 for these fields).

Next, we should take into account the magneto–acoustic interaction. It was shown by Kagan and Maksimov [74] that the correct contribution (to all orders in Δ) from inelastic phonon processes to the transition rate can be written as:

$$\Gamma_{m,n-m} = \Delta^2_{m,n-m} W_{\mathrm{m}} / (\xi^2_{m,n-m} + \Delta^2_{m,n-m} + \hbar^2 W^2_{\mathrm{m}}) \tag{30}$$

where $\hbar W_{\mathrm{m}}$ is the phonon line-broadening (see, for example, Blum [66]):

$$W_{\mathrm{m}} = 1/4 \left(\sum_{K=m-p}^{m+p} W_{K,m} + \sum_{K=n-m-p}^{n-m+p} W_{K,n-m} \right) \tag{30a}$$

and p is an integer number which describes inter-level transitions, allowed by the particular form of spin–phonon interaction $V(\mathbf{q})$. Note that Eq. (30) clearly shows the expected dependence of the Lorentzian form on longitudinal fields for a system at quasi-equilibrium (see Eq. 28). The most important transition here is that to the next upper level (from $|m\rangle$ to $|m-1\rangle$) with phonon absorption. From Eq. (19) with $V(\mathbf{q}) = D(S_x S_z + S_z S_x)$ we obtain [63–65, 90]:

$$W_{m-1,m} = (3D^2(S+m)(S-m+1)(2m-1)^2 E_{m-1,m}^3) \cdot \left(8\pi\rho c^5\hbar^4\left[\exp(E_{m-1,m}/T)-1\right]\right)^{-1} \quad (31)$$

where $\rho = M/a^3$ is the mass density (a is the lattice constant), $c = (k_B/\hbar)\theta_D(V_o/6\pi^2)^{1/3}$ [75], is the velocity of sound, θ_D is the Debye temperature, V_o is the unit cell volume, and $E_{m-1,m} = E_{m-1} - E_m$. According to recent measurements of the specific heat of Mn_{12} by Gomes et al. [76] $\theta_D = 38 \pm 4$ K; from Ref. [1] we can take $V_o = 3716$ Å^3 and $\rho = 1.83 \times 10^3$ kg m^{-3}.

To see the dominant contribution to the Lorentzian line-width (Eq. 30) one must compare $\xi_{m,n-m}$, $\Delta_{m,n-m}$ and $\hbar W_m$. As already noted, the estimated width of the Gaussian distribution of internal fields is approximately $2\sigma_0 = 12$ mT (for hyperfine interaction, at least). Let us concentrate for the moment on the high-temperature regime, with thermally activated tunneling from levels m smaller or equal to 4. In zero external field $\Delta_{m,-m}(0)$ gives 1.1×10^{-2} K and 0.34 K, for $m = 4$ and $m = 2$, respectively, whereas $\hbar W_{3,4} \approx 1.02 \times 10^{-5}$ K and $\hbar W_{1,2} \approx 6.08 \times 10^{-7}$ K (for $T = 2.6$ K and $c = 1.4 \times 10^3$ m s^{-1}). It is only in the region of $m = 6$ (or larger) that values of $\hbar W_{m-1,m}$ and $\Delta_{m,-m}(0)$ become more or less comparable. To take into account odd values of m (and non-zero n), we have to include internal transverse fields (as discussed above Eq. 29).

We can also consider phonon-assisted transitions with $\delta m = \pm 2$. For simplicity we take $V(\mathbf{q}) = D(S_x^2 - S_y^2) = D(S_+^2 + S_-^2)/2$. For the transition from $|m\rangle$ to $|m-2\rangle$, this yields 52]:

$$W_{m-2,m} = (3D^2(S+m)(S+m-1)(S-m+2)(S-m+1)E_{m-2,m}^3) \cdot (8\pi\rho c^5\hbar^4[\exp(E_{m-2,m}/T)-1])^{-1} \quad (32)$$

This equation gives $\hbar W_{2,4} \approx 2.99 \times 10^{-5}$ K and $\hbar W_{0,2} \approx 1.16 \times 10^{-5}$ K (for $T = 2.6$ K also). These numbers show that transitions with $\delta m = \pm 2$ cannot change the relative contributions of the values $\hbar W_m$ and $\Delta_{m,-m}(0)$ to the Lorentzian line-width. For definition of W_m in Eq. (30a), however, we use the contribution from both transitions ($|m\rangle \to |m-1\rangle$ and $|m\rangle \to |m-2\rangle$ simultaneously). Of course, spin–phonon interaction contains other terms but it is unlikely that this contribution will be larger in magnitude than the value already calculated for W_m. Although it also possible to include the transitions from $|m\rangle$ to $|m+1\rangle$ or to $|m+2\rangle$ in the definition of W_m, these transitions are important to the kinetics only in the sense that they are important in establishing equilibrium on each side of the barrier. Because we merely want to estimate the width of the resonance line, we do not include these processes in our qualitative model.

All this means that in the thermally activated regime (near the top of the barrier) the line-width is defined mainly by the tunneling splitting of the resonant levels and by the internal longitudinal fields (see Eq. 28), but not by the phonon line-broadening. Note, however, that the phonons play an essential role in "linking" the states on the same side of the barrier (otherwise only the ground state would be occupied, unless one admits that *all* the bias is dynamic). The dipolar flip–flop processes also can cause transitions between the energy levels providing thermal equilibrium.

We should note that Villain and Fort et al. [51] and Leuenberger and Loss [52] have slightly different definitions of the tunneling rate. Both definitions can, however, be written:

$$\Gamma_{m,n-m} = \Delta^2_{m,n-m} W_{\mathrm{m}} / \left(\xi^2_{m,n-m} + \hbar^2 W^2_{\mathrm{m}} \right) \tag{33}$$

where m and $n-m$ are the levels in the resonance and $\xi_{m,n-m} = \xi_{\mathrm{m}} - \xi_{n-m}$ with $\xi_{\mathrm{m}} = E^0_m - g\mu_{\mathrm{B}} m H_{\mathrm{z}}$ (where $E^0_m = -Dm^2 - K_{\|} m^4$), i. e. $\xi_{m,n-m}$ is the bias of Eq. (25) (or Eq. 28) with no internal bias fields. According to this formula, the half- width of the resonance peak should be of the order of $\hbar W_{\mathrm{m}}$ (see Eq. 30a) which is actually very small in comparison with $\Delta_{m,-m}$ in zero field for upper levels where the tunneling occurs at $T > 2\,\mathrm{K}$. (see above, just after Eq. 32). The reason for this problem is that Eq. (33) misses the term relative to the intrinsic width $\Delta_{m,n-m}$ (Eqs. 30 and 33). This term is definitely not negligible for thermally activated tunneling. The problem with the tunneling rate calculations in both papers is the same – instead of inserting the *stationary* solution for the *non-diagonal part* of the density matrix in the equation for the *diagonal part* of the density matrix, one should apply the Laplace transformation to these equations and find the smallest real root of the equation for the Laplace variable "s". This root gives $\Gamma_{m,n-m}$ as in Eq. (30) with $\Delta^2_{m,n-m}$ in the denominator. The approximation with *stationary* solution of the equation for the non-diagonal part of the density matrix gives Eq. (33) without $\Delta^2_{m,n-m}$. Apparently, this approximation does not work well and leads to very narrow and high Lorentzians. This problem has been "eliminated" by an analytical truncation procedure [52] leading to an effective half- width of the peaks (relative to external field, H_{z}) of $\omega' \approx \Delta_{m,m'}/\eta_{m,m'}$ (where $\eta_{m,m'} = |m - m'| g\mu_{\mathrm{B}}$). This result, however, comes directly from Eq. (30) if we ignore the contribution from dipolar and nuclear fields (Eq. 28). In addition we should mention that the equation for the diagonal part of the density matrix was solved numerically, by exact diagonalization, by use of Eq. (33) *without truncation procedure* (i. e., with $\omega' \approx \hbar W_{\mathrm{m}}/\eta_{m,m'}$) [52]. It was claimed that numerical calculations give results very similar to those obtained analytically with the tunneling rate given by Eq. (33) *with the truncation procedure* (i. e. with effective line-width of the order of $\Delta_{m,m'}$). Because we do not know the details of these numerical calculations, the origin of this similarity is not clear to us.

Note also that, together with the tunneling rate $\Gamma_{m,n-m}$ between resonant levels, one can include an incoherent tunneling rate $\Gamma^{\mathrm{in}}_{m,m'}$ which involves (when $H_{\mathrm{z}} = 0$) direct transitions between levels $|m\rangle$ and $|-m-1\rangle$ (or $|-m-2\rangle$) because of phonon emission. Let us assume that Eq. (33) (in the transition between $|m\rangle$ and $|m\rangle = -m-1, -m-2, \ldots\rangle$) would give such an incoherent tunneling rate. Then, because $\xi_{m,m'} = \xi_{\mathrm{m}} - \xi_{m'}$, the incoherent rate $\Gamma^{\mathrm{in}}_{m,m'}$ (relative to H_{z}) is a Lorentzian with a half-width of the order of $\hbar W_{\mathrm{m}}/\eta_{m,m'}$, centered at the field $H^0 = (E^0_m - E^0_{m'})/\eta_{m,m'}$ even for the first resonance ($n = 0$, $H_{\mathrm{z}} < 0.44\,\mathrm{T}$). It is easy to see that, even at the top of the barrier, H^0 is quite large, because $E^{(0)}_m - E^{(0)}_{m'}$ for $m = 2$ and $m' = -3$ is approximately 2 K. Of course, the resonance peak (for definite n) is the combination of all possible $\Gamma_{m,m'}$ (coherent and incoherent), but this does not sufficiently improve the above mentioned problem, because the experimentally measured resonance peak for $n = 0$ is centered at $H_{\mathrm{z}} = 0$.

Bearing in mind the kinetics of the relaxation processes in this system, we suppose, however, that the contribution from the correct incoherent tunneling rate does not change the resonance line-width by much in comparison with the contribution from the coherent tunneling rate of Eq. (30). The reason for this suggestion is quite simple. The above mentioned transition ($|m\rangle \rightarrow |-m-1\rangle$) can be realized also by the consecutive transitions (i) $|m\rangle \rightarrow |-m\rangle$ (described by the tunneling rate $\Gamma_{m,-m}$) and (ii) $|-m\rangle \rightarrow |-m-1\rangle$ (described by the phonon probability $W_{-m-1,-m}$). These consecutive transitions do not, however, change the resonance line-width seriously in comparison with the coherent tunneling transition alone, because the dependence of $W_{-m-1,-m}$ on H_z is much slower than that of $\Gamma_{m,-m}$. We omit, therefore, incoherent transitions from our simplified (qualitative) consideration. (Note that at the top of the barrier (for $m = 4, 3, 2, 1$), both probabilities ($\Gamma_{m,-m}$ and $W_{-m-1,-m}$) have the same order of magnitude (which is easy to check). This means also, that molecules can return from the level $|-m\rangle$ to the level $|m\rangle$ ($\Gamma_{m,-m} = \Gamma_{-m,m}$) or deactivate to the level $|-m-1\rangle$ with equal probabilities.)

In the thermally activated regime, the value of the tunneling rate can be evaluated for each resonance (i. e. each value of n) by taking the product of the Boltzmann factor and the rate $\Gamma_{m,n-m}$. This must be summed for all the contributions from different $|m\rangle$:

$$\tau_n^{-1}(H_z) = Z^{-1}(H_z) \sum_{\mathrm{m}} \Gamma_{m,n-m} \exp[(-E_m^0 - g\mu_B H_z m)/k_B T] \tag{34}$$

where $Z(H_z)$ is the partition function. (For simplicity we omit here the time-dependence of the Boltzmann factor, i. e. we still assume quasi-equilibrium.) The plot of $\tau_n^{-1}(H_z)$ gives the expected Lorentzian line-shape of the resonance peaks. The width is rather sensitive to conditions such as the distribution of internal fields or the velocity of sound, although realistic values for these enable experimentally measured line-widths to be obtained. To give some numbers, we obtained a width (for $n = 0$) of approximately 25 mT [60] with $\sigma_0 = 6$ mT at $T = 2.6$ K. To get the same height it was necessary to change only one value from all the set. We put the velocity of sound equal to $c = 1.4 \times 10^3$ m s^{-1}; the other values are the same as given above (Eqs. 1 and 31). Our curves show slightly faster decay near the tails (which is the consequence of averaging over a Gaussian distribution of fluctuating internal fields). If, however, we neglected these internal fields, Eq. (34) would give too narrow and sharp resonance lines.

Before concluding, a few remarks should be made. We have limited ourselves by taking an average of Eq. (30) over fluctuating internal fields (longitudinal in bias $\xi_{m,n-m}$ and transverse in $\Delta_{m,n-m}$) but this is just zero approximation, to show that even this approximation can lead to correct resonance line-width. As already noted, in reality the interaction with the nuclear subsystem spreads each giant spin energy level into a Gaussian multiplet and one should consider all possible transitions between the resonant levels from the opposite sides of the barrier inside such multiplets. The internal bias field $\varepsilon(t)$ is, moreover, actually, time-dependent (i. e. it varies both in space and time) and produces a time-dependent Boltzmann factor ($\exp[(-E_m^0 + mH_t(t))/k_B T]Z^{-1}(H_t(t))$, where $H_t(t) = g\mu_B(H_z - \varepsilon(t))$ and, as a consequence, deviation from exponential relaxation occurs. As has already been

mentioned, however, we do not give here the exact theory of the relaxation. *The actual relaxation law can be extracted only by solving the kinetics of the problem, which includes the effect of the environment.* Such an analysis will be published elsewhere.

To conclude our discussion of the high-T behavior of the relaxation in Mn12-acetate, we should emphasize the following main results:

1. At relatively high temperatures ($T > 2\,\mathrm{K}$) the relaxation is dominated by the phonon-assisted tunneling mechanism;
2. The Lorentzian shape of the resonance peaks is determined by Eq. (30), which describes the tunneling between levels which are in resonance in a given magnetic field;
3. Despite the dominant role of phonons the resonance line-width is determined mainly by the value of the tunneling splitting $\Delta_{m,n-m}$ together with the internal bias ε (Eq. 28) which originates from the hyperfine and dipolar interactions;
4. All the theories mentioned predict exponential relaxation of the magnetization while the experiments reveal non-exponential behavior at these temperatures [4, 6, 7, 21, 53, 57-59, 62]. This clearly shows the important role played by intermolecular interactions and by interactions with nuclear spins, both of which produce a time-dependent bias field which causes the non-exponential behavior of relaxation.

4.4.3 Ground-state Tunneling

Let us now concentrate on the low-temperature limit of $T \ll T_C$ where tunneling occurs in the ground state only. In the instanton approach (see below) we assume that $k_B T \ll \Omega_0$, where Ω_0 is the "bounce frequency" of the instanton transition (which is roughly the distance from the ground-state level to the first excited level. Under these conditions only the lowest levels are thermally populated and we can truncate the "giant spin" Hamiltonian (Eqs. 1 or 12b) to an effective Hamiltonian (which is valid only at energies $\ll \Omega_0$) describing two states $|S_z\rangle = \pm S$ and their mixture, separated by the tunneling splitting $\Delta \ll \Omega_0$. We should, moreover, couple the "giant spin" S of each molecule to the nuclear "spin-bath" $\{\sigma_k\}$ with $k = 1, 2, \ldots, N$. For hyperfine coupling the latter can be described by Eq. (22) with $\omega_k \ll \Omega_0$ ($\omega_k \gg \Delta$, usually) and with N equal to actual number of nuclear spins inside molecule (one can take $N = 12$ for Mn_{12}, neglecting the effect of hydrogen ..., and $N = 146$ for Fe_8, including 120 hydrogen, 18 nitrogen and 8 bromine atoms, neglecting the few percent of ^{57}Fe).

Without hyperfine interactions the total nuclear spectrum, containing 2^N states, is almost completely degenerated, with only a tiny spreading, $\sim T_2^{-1}$, of levels caused by the inter-nuclear dipolar interactions. With the hyperfine interaction, the nuclear levels spread into a Gaussian multiplet of $N + 1$ polarization groups around each giant spin level [12, 44, 47,61,72]. The half-width of this distribution σ_0 is of the order of $\omega_0 N^{1/2}$ (where $\omega_0 = (1/N)\sum_k^N \omega_k$). Note that in each polarization group the hyperfine levels are also distributed according to a Gaussian half- width of approximately T_2^{-1}. Typically, the different polarization groups completely overlap within of the Gaussian envelope of Eq. (27). The nuclear T_2 processes (transverse relaxation)

are responsible for transitions inside each polarization group, whereas the nuclear T_1 processes (longitudinal relaxation) enable transitions between different polarization groups. According to Wernsdorfer et al. [45], the half-width of the hyperfine distribution in Fe_8 is of the order of 0.6 mT, yielding $\omega_0 \approx 0.05$ mT (for the estimate we take only hydrogen atoms with $\sigma = 1/2$, i. e., $N = 120$). Because $\omega_0 \gg T_2^{-1}$ (typically $T_2^{-1} \approx 10^{-7}$ K), the nuclear spin dynamics is slaved by dynamics of **S**. We also suggest that the T_1 processes are long and therefore not relevant, at these temperatures. The reason is that the T_1 processes are driven by the dipolar flip–flop transitions, which are essentially frozen at $T \ll T_C$. In general, we should consider two effects: (i) the effect of nuclear spins on giant spin dynamics during tunneling, and (ii) the effect of the motion of S on the nuclear spins. Both effects have to be handled self-consistently.

Using the instanton technique, we can write the effective Hamiltonian for a single molecule [23]:

$$H_{\text{eff}}^{(1)} = \left[2\Delta_0 \tau \cos\left(\pi S - \beta_0 \mathbf{n}\mathbf{H} + \sum_{\text{k}}^{N} \alpha_{\text{k}} \mathbf{n}\sigma_{\text{k}} \right) + h.c. \right] + 1/2 \left[\tau_z \sum_{\text{k}}^{N} \omega_{\text{k}}^{||} \mathbf{l}_{\text{k}} \sigma_{\text{k}} + \sum_{\text{k}}^{N} \omega_{\text{k}}^{\perp} \mathbf{m}_{\text{k}} \sigma_{\text{k}} \right] + \sum_{k \neq 1}^{N} V_{kl}^{\alpha\beta} \sigma_{\text{k}}^{\alpha} \sigma_l^{\beta} \tag{35}$$

where τ describes the "giant spin" of the molecule (τ and σ are both the Pauli matrices). The first term in Eq. (35) is a non-diagonal term (because of $\tau_{\pm}$) which operates during transition of **S**. It produces a time-dependent field $\gamma_{\text{k}} = (\omega_{\text{k}} \mathbf{S}/S)$, acting on each σ_{k}, and this causes σ_{k} to flip. If we expand out the cosines, we see that we have a whole series of terms like $\sim \tau_{\pm} \Gamma_{\alpha\beta\gamma\delta} \sigma_{k1}^{\alpha} \sigma_{k2}^{\beta} \sigma_{k3}^{\gamma} \sigma_{k4}^{\delta} \ldots$ in which an instanton flip of the giant spin couples to many different nuclear spins simultaneously, i. e., a single instanton can simulate multiple transitions in the nuclear bath. The probability that σ_{k} will flip during a single instanton passage between two quasi-classical minima $|S_1\rangle$ and $|S_2\rangle$ is $|\alpha_{\text{k}}|^2/2$. Thus, the average number of nuclear spins that will flip each time S flips (the so-called "co-flipping" amplitude) is approximately:

$$\lambda = 1/2 \sum_{\text{k}}^{N} |a_{\text{k}}|^2 \tag{36}$$

which, can in principle, be > 1. One can easily calculate the dimensionless constants α_{k} and β_0 in the simple bi-axial Hamiltonian of Eq. (6) with H_{hyp} given by Eq. (22). The answer is [23, 31]:

$$\alpha_{\text{k}} \mathbf{n} \cdot \sigma_{\text{k}} \approx (\pi \omega_{\text{k}} / 2\Omega_0)[-i\sigma_y + (D/(E+D))^{1/2} \sigma_x] \tag{37}$$

$$\beta_0 \mathbf{n} \cdot \mathbf{H} \approx (\pi g \mu_{\text{B}} S / \Omega_0)[-i H_y + (D/(E+D))^{1/2} H_x] \tag{38}$$

where **n** is a unit vector in the (xy) plane and the "bounce frequency" Ω_0 is:

$$\Omega_0 \approx 2S(E \cdot D)^{1/2} \tag{39}$$

(For non-zero values of $K_\perp$, see Eqs. 14–18). Eq. (37) tells us that $\lambda < 1$ in the particular case of E and D as in Fe_8 or Mn_{12} (note that non-diagonal fourth-order terms re-normalize Eqs. (37) and (38) but for $K_\perp/k_B = -3.28 \times 10^{-5}$ K it gives $\alpha_k \approx (\omega_k/\Omega_0 C_\perp$ with $C_\perp \approx 1.56$). The second term in Eq. (35) is diagonal, which operates when S is in one of its two quasi-classical minima. Let us introduce two corresponding fields $\gamma_k^{(1)}$ and $\gamma_k^{(2)}$. In general (any non-zero external and internal magnetic field) S_1 and S_2 are not antiparallel. It is easy to see that the sum and the difference between these two vectors define $\omega_k^\parallel$ and $\omega_k^\perp$ i. e.:

$$\omega_k^\parallel \mathbf{l}_k = \gamma_k^{(1)} - \gamma_k^{(2)} \tag{40}$$

$$\omega_k^\perp \overline{\mathbf{m}}_k = \gamma_k^{(1)} + \gamma_k^{(2)} \tag{41}$$

where $\mathbf{l}_k$ and $\mathbf{m}_k$ are mutually perpendicular unit vectors. The longitudinal coupling $\omega_k^\parallel$ gives the change in energy of σ_k before and after S flips (i. e. the difference between the effective fields acting on σ_k before and after transition of **S**). The transverse coupling $\omega_k^\perp$ defines the deviation of initial and final orientations of S from the $\pm z$-direction (which is the easy-axis for the Hamiltonian of Eq. 12b). For the biaxial Hamiltonian for small values of $H_x (g\mu_B H_x \ll S(E + D))$ we obtain:

$$\omega_k^\parallel \mathbf{l}_k \sigma_k \approx \omega_k \sigma_z \tag{42}$$

$$\omega_k^\perp \mathbf{m}_k \cdot \sigma_k \approx (\omega_k g\mu_B H_x/(2S(E + D)))\sigma_x \tag{43}$$

Finally, the third term in Eq. (35) describes very weak internuclear dipolar coupling ($|V_{kl}^{\alpha\beta}| \approx T_2^{-1}$). To complete our Hamiltonian, we should also include the dipolar–dipolar interactions between molecules. Ignoring the transverse part of this interaction (which leads to flip–flop processes), we obtain:

$$H_D = 1/2 \sum_{\mu \neq \nu} V_{\mu,\nu}^{(D)} \tau_z^\mu \tau_z^\nu \tag{44}$$

where $|V_{\mu,\nu}^{(D)}| \approx 1$ mK. Thus, to work in the low-T quantum regime, one can use the effective Hamiltonian:

$$H_{eff} = H_{eff}^{(1)} + H_D \tag{45}$$

We do not include the spin–phonon interaction in this Hamiltonian because the phonons can play no role at $T < T_C$.

Now, after the effective low-T Hamiltonian has been established, we would like to discuss briefly some effects which follow from the coupling of the central spin to the spin bath (a detailed explanation is given in the original papers [47, 72] and in reviews [61, 73]).

Let us start from the non-diagonal term in Eq. (35) (the first term). Because α_k is a complex quantity, two effects can be expected. The imaginary part of α_k gives a renormalization of the effective tunneling splitting, depending on the coupling constants ω_k. One can expect an increase (decrease) of the effective tunneling splitting with ω_k. The width of the distribution of hyperfine fields also depends on ω_k. It should also increase with ω_k. The real part of α_k adds an extra random phase to the Haldane phase $\beta_0 \mathbf{nH}$. As we have seen already, the average number of nuclear spins that flip together with S is proportional to $|\alpha_k|^2$. These flips modify the total phase of the bath state and, consequently, randomize the phase of the giant spin (between the instanton and anti-instanton) producing phase decoherence of the tunneling process that can completely block the latter (this is called, *"topological decoherence"*). Indeed, we know that a half-integer spin cannot tunnel in zero transverse field. We can imagine that in different molecules the transition of S is accompanied by a different number of the nuclear spins. If the total flipping spin ($\mathbf{S}$ and the nuclear spins σ_k) is integer, tunneling is allowed. Otherwise, the tunneling is blocked. Thus, the possibility of tunneling depends on the particular environment inside of each molecule (nuclear spins), and over the entire sample the transition of S can happen at random.

The second term in Eq. (35) produces an internal bias field (we put here $\omega_k^{\perp} = 0$) $\varepsilon = 1/2 \sum_k \omega_k^{\parallel} \sigma_k^z$ acting on $\mathbf{S}$. Together with the first term it gives the Hamiltonian of the biased two-level system (see Eq. 24) with an effective tunneling splitting $2\Delta_\Phi = 2\Delta_0 \cos(\Phi)$, where Φ is the complex phase (we assume here that there is no nuclear spin dynamics itself, i. e. $|V_{kl}^{\alpha\beta}| = 0$). In this case the tunneling probability is given by:

$$P^{(0)}(t) = (4\Delta_\Phi^2/E^2)\sin^2(Et) \tag{46}$$

$$E = \pm(\varepsilon^2 + 4\Delta_\Phi^2)^{1/2} \tag{47}$$

Because $\varepsilon \gg \Delta_{-10,10}$ (in our example $\omega_0 \gg \Delta_{-10,10}$), only a small fraction of molecules is not pushed away from resonance by the additional longitudinal field ε (ε depends, of course, on the particular environment state) and, therefore, are able to tunnel. To estimate this small number of molecules that are close to the resonance, we should take the average of $P^{(0)}(t)$ over the ensemble of the molecules with different ε weighted by the Gaussian distribution of Eq. (27). This gives (in what follows, for nuclear spins we use notation ξ_0 instead of σ_0) for $\xi_0 \gg \Delta_0$ (see Chapter in Ref. [72]):

$$P^{(0)}(t) \approx \rho \sum_{k=0}^{\infty} J_{2k+1}(4\Delta_\Phi t) \tag{48}$$

which oscillates as the Bessel function $J_{2k+1}(z)$ with the amplitude equal to:

$$\rho = (2\pi)^{1/2}\Delta_\Phi/\xi_0 \tag{49}$$

The value of ρ estimates the fraction of molecules that are able to tunnel. It is easy to see that $\rho \ll 1$. This mechanism (called "degeneracy blocking") can very

effectively block the tunneling. If, however, we include the dynamics of the nuclear bath ($|V_{kl}^{\alpha\beta}| \neq 0$), the situation changes dramatically. Because of the interaction between the nuclear spins, the bias energy ε becomes time-dependent – within each polarization group $\varepsilon(t) = \varepsilon + \delta\varepsilon(t)$ passes over all the energy range $\sim T_2^{-1}$ and this gives to the system a resonance window. Inside this window the total bias field fulfils the condition $\xi = \xi_{\rm H} + \varepsilon(t) < \Delta$ (where $\xi_{\rm H}$ is external bias field) and central spin can tunnel. (The same mechanism can also destroy coherence by pushing molecules away from the resonance window.) Note that tunneling can occur only between the polarization states M and $-M$ ($M = S_z$) because the energy of the final state $E_{\rm f}$ should be in resonance with the energy of the initial state E_i ($|E_{\rm f} - E_i|$ should not exceed Δ_0, at least). This means that if the initial polarization state of the molecule is M, $2M$ nuclear spins flip when S flips. As discussed above, the *average* number of nuclear spins that will flip together with S is $\lambda \ll 1$ (for Fe_8 and Mn_{12}). In fact, a better possibility of tunneling is realized for molecules with initial polarization state $M = 0$. Molecules with $M_{\rm in} \neq 0$ also can tunnel (with $\delta M = 2M$) but the contribution of these events to the statistics falls very rapidly with increasing M. Actually $\Delta_\Phi(M)$ falls as $\sim (\lambda^M/M!)^{1/2}$ for $M \gg \lambda$ (see Chapter 4 in Ref. [47]).

If $\omega_{\rm k}^{\perp} \neq 0$, there is a transverse magnetic field acting on environmental spins. Because of this field the initial and final directions of the nuclear spins are not parallel (or antiparallel) to each other. Assume that all nuclear spins are initially aligned in $\gamma^{(1)}$ (before S flips). After S flips, nuclear spins $\sigma_{\rm k}$ are not parallel (antiparallel) to the new field $\gamma^{(2)}$) acting on them (note that the instanton flip of S is a sudden perturbation for nuclear spins, which undergo a non- adiabatic transition). This new state is not an eigenstate of the Hamiltonian and nuclear spins must relax in making transitions to avoid misalignment with $\gamma^{(2)}$ (this transitions transform their wavefunction to the exact eigenstate). Thus, the tunneling of S can be suppressed (depending on how slow are the transitions in the particular environment state), because the initial and the final states of the nuclear bath are not exactly orthogonal. This mechanism is known as the *"orthogonality blocking"* mechanism [47, 72].

All these effects can be handled by three different kinds of averaging procedure and the final answer can be obtained by combining them, depending on its importance in each particular case (analytical expressions are given elsewhere [47, 61, 72, 73]). We have seen also that the dynamics of the nuclear bath are extremely important, because, producing a rapidly fluctuating hyperfine field, it can help the system to find a resonance window by "scanning" over the entire range of the bias energy (which for a single molecule is of the order of T_2^{-1}). For the particular case of Fe_8 or Mn_{12} we have $\lambda \ll 1$ which means that, in general, molecules in the resonance window relax incoherently (only molecules in a nuclear polarization state with $M = 0$ can relax coherently in this example). The relaxation rate for such incoherent process is given by [47]:

$$\tau_N^{-1}(\xi) \approx \tau_0^{-1} \exp(-|\xi|/\xi_0) \tag{50}$$

$$\tau_0^{-1} \approx 2\Delta_{-10,10}^2/\pi^{1/2}\xi_0 \tag{51}$$

These equations describe merely the initial stage of the relaxation, however. Continuous relaxation requires more and more molecules to be brought into; this can be achieved by fluctuations of the dipolar field across the sample [44]. When the spin of a given molecule flips, it produces a time-dependent magnetic field (long-range) which can push some molecules away from resonance and bring others into the resonance window, depending on the nuclear bath state of each molecule.

To investigate the problem of the relaxation in quantum regime (ground-state tunneling), Prokof'ev and Stamp [44] introduced a kinetic equation for the distribution function $P_\alpha(\xi, \mathbf{r}, t)$ which gives the probability of find a molecule at a position $\mathbf{r}$ with polarization $\alpha = \pm 1$ (i. e. $|S_z\rangle = \pm S$) having a bias energy ξ at time t. This equation reads:

$$\begin{aligned} \mathrm{d}P_\alpha(\xi, \mathbf{r})/\mathrm{d}t \;=\; & -\tau_N^{-1}(\xi)[P_\alpha(\xi, \mathbf{r}) - P_{-\alpha}(\xi, \mathbf{r})] \\ & - \sum_{\alpha'} \int \mathrm{d}\mathbf{r}' \Omega_0^{-1} \int \mathrm{d}\xi' \tau_N^{-1}(\xi') \\ & \times [P^{(2)}_{\alpha\alpha'}(\xi, \xi', \mathbf{r}, \mathbf{r}') - P^{(2)}_{\alpha\alpha'}(\xi - \alpha\alpha' V^{(D)}(\mathbf{r} - \mathbf{r}'), \xi', \mathbf{r}, \mathbf{r}')] \quad (52) \end{aligned}$$

where $P^{(2)}_{\alpha\alpha'}(\xi, \xi', \mathbf{r}, \mathbf{r}')$ is a two-molecule distribution which gives the probability of finding a second molecule with polarization α' and bias ξ' if the first molecule is with α and bias ξ. The quantity Ω_0 is the volume of the unit molecular cell, $V^{(D)}(\mathbf{r})$ is the longitudinal part of the dipole–dipole interaction (see Eq. 44), and the integration $\int \mathrm{d}\mathbf{r}'$ is performed over the sample volume. The first term of this equation describes the local tunneling relaxation whereas the second (which is analogous to a collision integral) describes the influence of the dipolar field produced by the spin flip of a molecule at site $\mathbf{r}'$. Solution of Eq. (52) (analytical or numerical) gives the magnetization $M(t)$ as a function of time, in the form of this obvious equation:

$$M(t) = \int \mathrm{d}\xi' \int \mathrm{d}\mathbf{r}' \Omega_0^{-1} [P_+(\xi, \mathbf{r}) - P_-(\xi, \mathbf{r})] \quad (53)$$

If at $t = 0$ the sample is fully polarized. For short times Eq. (52) can be solved analytically (for ellipsoidal shape, at least). At the beginning of the relaxation the number of flipped molecules is small ($M(t)/M_\mathrm{s} \ll 1$, where M_s is the saturated magnetization) and, according to Anderson [55], the field distribution of the randomly placed *dilute* static dipoles can be described by the Lorentzian:

$$P_\alpha(\xi) = [(1 + \alpha M(t))/2]/[(\Gamma_d(t)/\pi)/\{(\xi\alpha E(t))^2 + \Gamma_d^2(t)\}] \quad (54)$$

$$\Gamma_d(t) = (4\pi^2 E_\mathrm{D}/3^{5/2})[1 - M(t)] \quad (55)$$

$$E(t) = \eta E_\mathrm{D}(1 - M(t)) \quad (56)$$

where η is a sample-shape-dependent constant and E_D is the strength of the dipolar interaction ($E^{(D)}(\mathbf{r}) = V_\mathrm{D}\Omega_0[1 - 3\cos(\theta)]/r^3$. Under these conditions (short times,

the Lorentzian distribution) the two-molecule distribution function becomes factorizable (i. e., $P^{(2)}(1,2) = P(1)P(2)$) and Eq. (52) gives the square-root relaxation law [44]:

$$M(t)/M_{\mathrm{s}} = 1 - (\tau_{\mathrm{short}}^{-1} t)^{1/2} \tag{57}$$

where $\tau_{\mathrm{short}}^{-1}$ is the rate of relaxation:

$$\tau_{\mathrm{short}}^{-1} = \chi \Delta_{10,-10}^{2} P(\xi_{\mathrm{D}})/\hbar \tag{58}$$

with normalized distribution of the dipolar fields in a sample $P(\xi_{\mathrm{D}})$. When the number of the flipped molecules becomes large enough (larger than 10–15%), the field distribution of the flipped spins becomes non-Lorentzian and Eq. (52) should be solved numerically, because Eqs. (54)–(56) are no longer valid. This equation also can be solved numerically for non-saturated sample (i. e. $M_{\mathrm{in}}/M_{\mathrm{s}} < 1$, where M_{in} is the initial magnetization) and for samples of different geometry with $M_{\mathrm{in}} = M_{\mathrm{s}}$. The latter was achieved by means of kinetic Monte Carlo simulations [44]. The main result of these simulations is that the short-time relaxation still obeys the square-root law with a sample-geometry-dependent constant η (very recently Cuccoli et al. confirmed this result with numerical calculations [81]). With regard to relaxation in non-saturated samples, very interesting results were obtained experimentally by Wernsdorfer et al. [45] for Fe_8 and by Chiorescu et al. [85] for Mn_{12}. They found that the short-time square-root law is accurately obeyed for both saturated and non-saturated samples and, moreover, that the square-root law for a strongly annealed sample or in the presence of strong transverse field is even more pronounced, as is apparent from comparison of Fig. 18 ($M_{\mathrm{in}} = M_{\mathrm{s}}$) with Fig. 32 ($M_{\mathrm{in}} = 0$).

In the original letter [44], Prokof'ev and Stamp only give an explicit answer for the long-time relaxation of annealed samples (using the same kinetic equation, but now expanding in $M(t)$ rather than $(1 - M(t))$). Their kinetic equation does, however, in this instance, also give $\sqrt{t}$ relaxation [92], and this can also be verified in MC simulations [91]. Among other possible suggestions one could say that the distribution function $P^{(2)}_{\alpha\alpha'}(\xi, \xi', \mathbf{r}, \mathbf{r}'))$ is also factorizable if M_{in} is small, and any difference

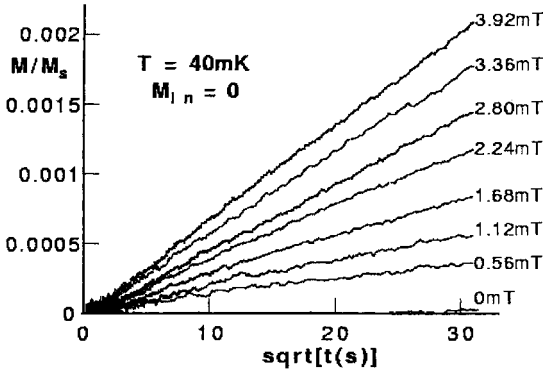

Fig. 32. Square root of time relaxation curves for Fe_8 crystal measured at 40 mK for $M_{\mathrm{in}} = 0$ [45].

from the saturated sample is in numerical constant χ. The square-root law for an annealed sample was confirmed elsewhere [25] by comparison of the tunneling rates extracted from the relaxation experiments using Eqs. (57) and (58) and from experiments based on the Landau–Zener model [68, 69, 82]. These experimental results require further theoretical investigation. One should nevertheless mention that this square-root relaxation is necessarily a short-time regime and a cross-over to another relaxation regime must be observed after long times and/or at high temperatures. Such cross-over has been observed in Mn_{12} for both $M \to M_s$ [57] and $M \to 0$ [85]. The new regime is exponential and corresponds to phonons recovery.

As we understand now, at low T the short-time square-root relaxation law is explained by dynamic dipolar interactions (but, to find a resonance window at the beginning of the relaxation, the system needs dynamic hyperfine interactions). The influence of dipolar fields can also be investigated by measurement of the dependence of tunnel splitting Δ/H_x on a transverse magnetic field. In Fe_8 at low T this quantity is highly dependent (near the nodes) on the value of the initial magnetization (as was found experimentally by use of the Landau–Zener method [83]), i. e. it depends strongly on the strength of dipolar interactions between molecules (Fig. 33). In the following text we would like to show how to analyze this dependence using very simple language [84].

The tunneling probability in the Landau–Zener model depends on the sweep rate of the longitudinal field, H_z, in the following way [82]:

$$P_{m,m'} = 1 - \exp(\pi \Delta^2_{m,m'}(\xi_\parallel, \xi_\perp)/\hbar\upsilon) \tag{59}$$

where $\upsilon = g\mu_B(m \cdot m')^{1/2} dH_z/dt, dH_z/dt$ is the constant sweep rate and, $\Delta_{m,m'}$ depends on dipolar bias fields $(\xi_\parallel, \xi_\perp)$. At large sweep rates $P_{m,m'} \approx \pi \Delta^2_{m,m'}/\hbar\upsilon$. Thus, the average probability over the distribution of the dipolar fields is:

$$P_{m,m'}(t) \approx (\pi/\hbar\upsilon) \int d\xi_\parallel \int d\xi_\perp G(\xi_\parallel, \xi_\perp, t_0) |\Delta_{m,m'}(\xi_\parallel, \xi_\perp)|^2 \tag{60}$$

where $G(\xi_\parallel, \xi_\perp, t_0)$ is the distribution of the dipolar fields in a sample. We have calculated $G(\xi_\parallel, \xi_\perp, t_0)$ numerically for different sample geometries (sphere, cube,

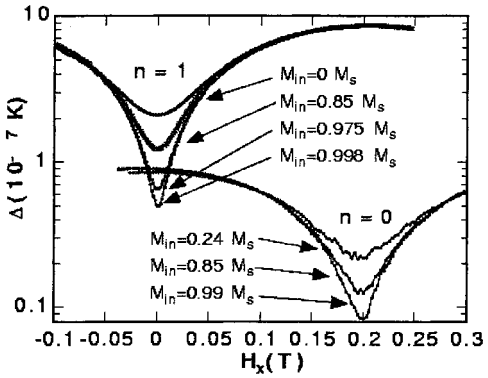

Fig. 33. Dependence of the tunneling splitting $\Delta_{S,n-S}$ on the transverse magnetic field, H_x ($\varphi = 0°$), around the first node for different values of the initial magnetization M_{in} [83].

parallelepiped) and for different initial magnetizations ($M(t_0) = M_{\rm in}$). When $M_{\rm in} \ll M_{\rm s}$ (e. g. zero-field cooled sample) the distributions are the Gaussians along all the axes (x, y, z). Then, for $\mathrm{d}H_{\rm z}/\mathrm{d}t \gg 1$, Eq. (60) can be simplified to (for $m = S$ and $m' = -S$):

$$P_{S,-S}(t_0) \approx (\pi/\hbar\upsilon) G_{\parallel}(H_{\rm z}) \int \mathrm{d}\xi_x \int \mathrm{d}\xi_y |\Delta_{S,-S}(\xi_{\parallel} = H_{\rm z}, \xi_x, \xi_y)|^2 G_{\perp}(\xi_x, \xi_y) \tag{61}$$

$$G_{\perp}(\xi_x, \xi_y) \approx (2\pi E_{DX} E_{DY})^{-1} \cdot \exp[-\{(\xi_x - H_x)^2/(2E_{DX}^2) + (\xi_y - H_y)^2/(2E_{DY}^2\}] \tag{62}$$

$$G_{\parallel}(H_{\rm z}) \approx (2\pi E_{DZ}^2)^{-1/2} \exp[H_{\rm z}^2/2E_{DZ}^2] \tag{63}$$

Note that a molecule can tunnel only if the total bias field $\xi_{\parallel} - H_{\rm z} < \xi_0/g\mu_{\rm B}S$. Using this condition we put (approximately) $\xi_{\parallel} \approx H_{\rm z}$. Next we would like to calculate $P_{S,-S}(t_0)$ near the nodes of $\Delta_{S,-S}(H_x, H_y)$. Let us replace the integral in Eq. (61) by γ. Eq. (35) gives the effective tunnel splitting:

$$\Delta_{S,-S} = \Delta_0 \cosh[\pi H_y/T_y + i\pi H_x/T_x] \tag{64}$$

where T_x is the oscillation period along the x-axis and T_y is the "related" period along the y-axis. For Eq. (12b) we obtain:

$$T_x/T_y = [(D + E)/D]^{1/2} \tag{65}$$

Near the node (the first node, to be precise) we can put:

$$H_x = H_x^0 + \delta H_x + H_x^{\rm dip},\ H_y = H_y^0 + \delta H_y + H_y^{\rm dip} \tag{66}$$

where (H_x^0, H_y^0) is the position of the node in the (H_x, H_y) plane, $\delta H_{x,y}$ is the distance from the node, and $H_{x,y}^{\rm dip}$ is the contribution from the dipolar fields ($\xi_{x,y}$). At the first node ($m = S, m' = -S$) $H_y^0 = H_{\rm z} = 0$ and $H_{\rm x}^0/T_x = \pi(n + 1/2)$. If $\delta H_{x,y}$ is small, it is easy to calculate γ analytically:

$$\gamma \approx \Delta_0^2[\Psi_x^2 + \Psi_y^2 + (\pi^2)(E_{DX}^2 + E_{DY}^2)] \tag{67}$$

$$\Psi_x = \pi\delta H_x/T_x,\ \Psi_y = \pi\delta H_y/T_y \tag{68}$$

Thus, for $E_{DX} = E_{DY} = E_{\rm D}$ (zero-field cooled after annealing at high temperature) exactly at the node ($\Psi_{x,y} = 0$) we obtain:

$$\gamma \approx 2\pi^2 \Delta_0^2 E_{\rm D}^2 \tag{69}$$

When M_{in} decreases, the width of the dipolar fields distribution increases. With increasing E_{D} the value of γ in the nodes also increases. This result explains the experimental behavior of the tunneling splitting at the nodes (because $\Delta_{S,-S}$ is proportional to $\gamma^{1/2}$). To check these formulas we have calculated γ numerically by use of Eq. (12b). Fig. 34 shows that: (i) for different values of E_{D} (i. e., depending on annealing) γ in the nodes really behaves like E_{D}^2 (see Fig. 34c); (ii) around the nodes γ has parabolic dependence on applied transverse magnetic field in accordance with Eq. (67) (see Fig. 34b). Figure 35 shows the same γ as in Fig. 34a but calculated with

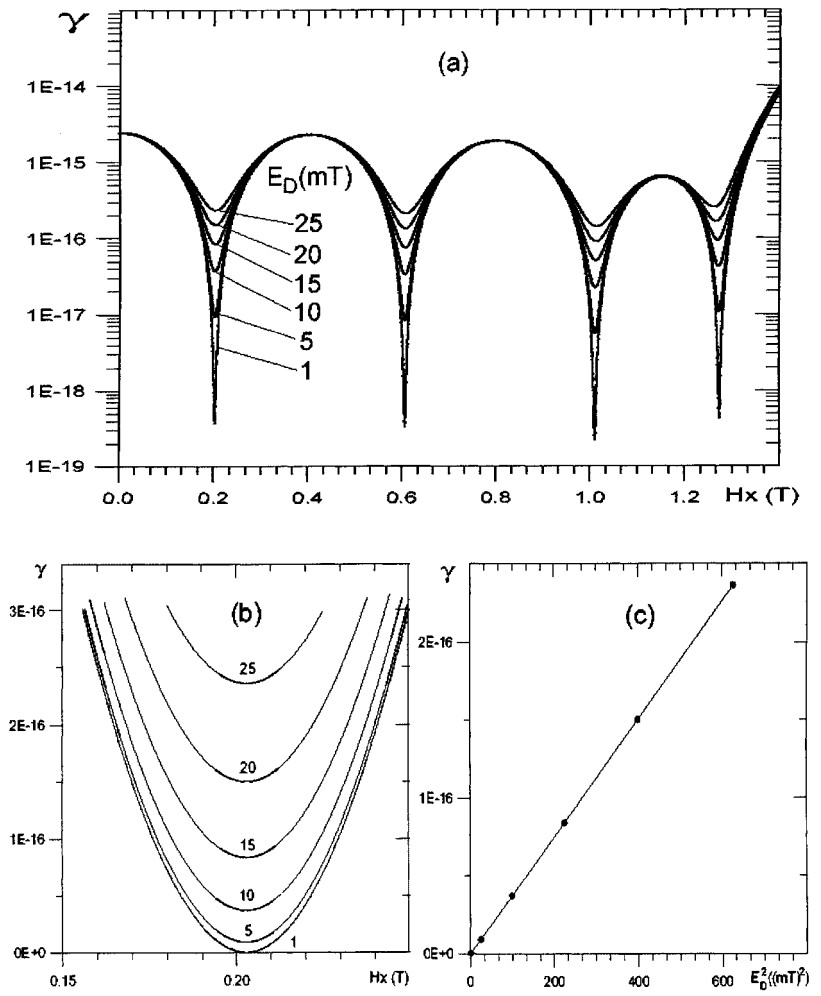

Fig. 34. The value of γ calculated from Eqs. (12b) and (61) for a strongly annealed sample (Gaussian distribution of the dipolar fields). (a) γ as a function of transverse magnetic field at different values of Gaussian half-width E_{D}; (b) enlarged region of transverse magnetic field around the first node; (c) the dependence on E_{D}^2 of the value of γ at the node.

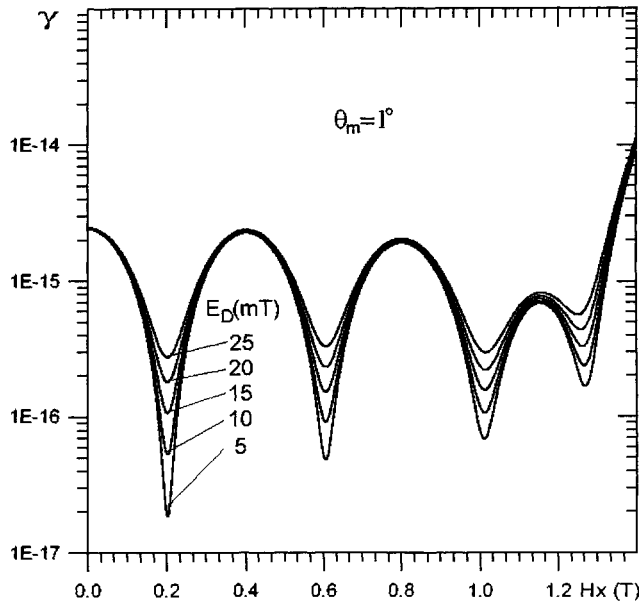

Fig. 35. The dependence of γ on transverse magnetic field calculated with small "misalignment" angle $\theta_{\mathrm{m}} = 1^{\circ}$ at different values of E_{D}.

a small "misalignment" angle $\theta_{\mathrm{m}} = 1^{\circ}$. The curves in Fig. 35 behave more similarly to the experimental curves in respect of relative value of γ in different nodes.

These considerations conclude our discussion of the quantum regime of relaxation (low-T ground-state tunneling) in Fe_8 and Mn_{12}. Strictly speaking, all these effects are not restricted to these systems but are valid for all mesoscopic systems in which quantum tunneling is associated with extremely small tunneling splitting, i. e. $\Delta \approx 10^{-n}$ with n much larger than unity ($n \approx 7$ and $n \approx 11$ in Fe_8 and Mn_{12}, respectively). Because the number of phonons available at these temperatures is negligible, phonons are not really relevant. In contrast, other types of fluctuation are numerous in this regime, and this is so for fluctuations of the spin bath. The main result, which we would like to emphasize here, looks very simple and straightforward. All the physics in this limit depends on hyperfine and dipolar interactions. Any particular result is solely a consequence of these interactions. Finally we would like to say that the molecules Fe_8 and Mn_{12} discussed in this paper are ferrimagnetic with a large non-compensated moment, i. e. their physics is dominated by the ferromagnetic order parameter. They have large spins and, therefore, important energy barriers and small tunneling splittings. In other systems with small non-compensated spins (eventually zero in antiferromagnetic molecules), energy barriers are much smaller leading to much larger tunnel splitting. In these circumstances mesoscopic physics is not limited to the spin bath, the phonons bath is also very relevant.

Acknowledgments

We are very grateful to P.C.E. Stamp, N. Prokof'ev, and W. Wernsdorfer for numerous helpful and motivating discussions. We thank L. Thomas, F. Lionti, I. Chiorescu, R. Giraud, A. Sulpice, C. Paulsen, A. Caneschi and D. Gatteschi for enjoyable collaboration. We thank C. Paulsen and W. Wernsdorfer for providing us with originals of experimental figures. We are indebted to Ch. Barbara, A. Mishchenko, and S. Burmistrov for their assistance in the preparation of this manuscript. One of us (IT) is very grateful to the J. Fourier University of Grenoble (France) for an invitation to stay in Grenoble and for financial support. IT is also grateful to Laboratoire de Magnétisme Louis Néel (CNRS, Grenoble, France) and to the Max-Plank Institute fur Festkorperforschung (CNRS, Grenoble, France) for its hospitality (and, personally, to I. Vagner and P. Wyder for everything that is absolutely impossible to list here, because of the lack of space). This work was also supported by INTAS-97-12124 (European Community) and, partially, by RFBR-97-02-16548 (Russia).

References

[1] T. Lis, *Acta Crystallogr. B 36*, 2042 (**1980**).
[2] R. Sessoli, D. Gatteschi, A. Caneschi, and M. A. Novak, *Nature 365*, 141 (**1993**).
[3] L. Néel, *Ann. Geophys. 5*, 99 (**1949**).
[4] J. R. Friedman, M. P. Sarachik, J. Tejada, and R. Ziolo, *Phys. Rev. Lett. 76*, 20 (**1996**).
[5] A. L. Barra, D. Gatteschi, and R. Sessoli, *Phys. Rev. B 56*, 8192 (**1996**).
[6] (a) C. Paulsen, J. G. Park, B. Barbara, R. Sessoli, and A. Caneschi, *J. Magn. Magn. Mater. 140-144*, 379 (**1995**); (b) C. Paulsen, J. G. Park, B. Barbara, R. Sessoli, and A. Caneschi, *J. Magn. Magn. Mater. 140-144*, 1891 (**1995**).
[7] C. Paulsen and J. P. Park, in L. Gunter, B. Barbara (Eds), *Quantum Tunneling of Magnetization – QTM'94*, NATO ASI Series E: Applied Science, Vol. 301, Kluwer, Dordrecht, 189 (**1995**).
[8] J. A. A. J. Perenboom, J. S. Brooks, S. Hill, T. Hathaway, and N. S. Dalal, *Phys. Rev. B 58*, 333 (**1998**).
[9] B. Barbara, W. Wernsdorfer, L. C. Sampaio, J. G. Park, C. Puulsen, M. A. Novak, R. Ferre, D. Mailly, R. Sessoli, A. Caneschi, K. Hasselbach, A. Benoit, and L. Thomas, *J. Magn. Magn. Mater. 140-144*, 1825 (**1995**).
[10] M. A. Novak, R. Sessoli, in L. Gunter, B. Barbara (Eds), *Quantum Tunneling of Magnetization – QTM'94*, NATO ASI Series E: Applied Science, Vol. 301, Kluwer, Dordrecht, 171 (**1995**).
[11] L. Thomas, F. Lionti, R. Ballou, D. Gatteschi, R. Sessoli, and B. Barbara, *Nature 383*, 145 (**1996**).
[12] F. Lionti, L. Thomas, R. Ballou, B. Barbara, R. Sessoli, and D. Gatteschi *J. Appl. Phys. 81 (8)*, 4608 (**1997**).
[13] R. Sessoli, H. L. Tsai, A. R. Shake, S. Wang, J. B. Vincent, K. Folting, D. Gatteschi, G. Christou, and D. N. Hendrickson, *J. Am. Chem. Soc. 115*, 1804 (**1993**).
[14] A. A. Mukhin, V. D. Travkin, A. K. Zvezdin, S. P. Lebedev, A. Caneschi and D. Gatteschi, *Europhys. Lett. 44 (6)*, 778 (**1998**).

[15] I. Tupitsyn, P. C. E. Stamp, B. Barbara, L. Thomas, (preprint **1996**).
[16] M. I. Katsnelson, V. V. Dobrovitski, B. N. Harmon, cond-mat/9807176.
[17] A. K. Zvezdin, A. I. Popov, Sov. *Phys. JETP 82*, 1140 (**1996**).
[18] B. Barbara, L. Thomas, F. Lionti, I. Chiorescu, A. Sulpice, *J. Mang. Magn. Mater. 177–181*, 1324 (**1998**).
[19] M. Hennion, L. Pardi, I. Mirebeau, E. Suard, R. Sessoli, and A. Caneschi, *Phys. Rev. B 56*, 8819 (**1997**).
[20] A. K. Zvezdin, V. V. Dobrovitski, B. N. Harmon, and M. I. Katsnelson, *Phys. Rev. B 58*, R14723 (**1998**).
[21] B. Barbara, L. Thomas, F. Lionti, I. Chiorescu, A. Sulpice, *J. Magn. Magn. Mater.* (accepted for publication).
[22] L. D. Landau and E. M. Lifshits, *"Quantum mechanics"*, **1965** (Oxford, Pergamon).
[23] I. S. Tupitsyn, N. V. Prokof'ev, and P. C. E. Stamp, *Int. J. Mod. Phys. B 11*, 2901 (**1997**).
[24] A. Garg, *Europhys. Lett. 22*, 205 (**1993**); cond-mat/9906203.
[25] W. Wernsdorfer and R. Sessoli, *Science 284*, 133 (**1999**).
[26] D. A. Garanin, E. M. Chudnovsky, *Phys. Rev. B 56*, 11102 (**1997**).
[27] I. Y. Korenblit, E. F. Shender, *Sov. Phys. JETP 48*, 937 (**1978**).
[28] N. V. Prokof'ev and P. C. E. Stamp, *J. Phys. Cond. Mat. 5*, L663 (**1993**).
[29] A. I. Vainshetejn, V. I. Zakharov, V. N. Novikov, and M. A. Shifman. *Usp. Fiz. Nauk*, 136, 553 (**1982**); *Sov. Phys. Usp. 25*, 195 (**1982**).
[30] S. N. Burmistrov and L. B. Dubovski, *Preprint IAE-3881/1 (in Russian)*, Kurchatov Institute of Atomic Energy, Moscow (**1984**).
[31] I. Tupitsyn, *JETP Lett.*, *67*, 28 (**1998**). (cond-mat/9712302).
[32] F. D. M. Haldane, *Phys. Rev. Lett. 50*, 1153 (**1983**).
[33] E. N. Bogachek and I. V. Krive, *Phys. Rev. B 46*, 14559 (**1992**).
[34] A. S. Ioselevich, *JETP Lett. 45*, 69, 3232 (**1987**).
[35] J. von Delf and C. Henley, *Phys. Rev. Lett. 69*, 3236 (**1992**).
[36] D. Loss, D. P. di Vinchenzo, and G. Grinstein, *Phys. Rev. Lett.*, *69*, 3232 (**1992**).
[37] H. B. Braun and D. Loss, *Phys. Rev. B 53*, 3237 (**1996**).
[38] A. Garg, *Phys. Rev. Lett. 74*, 1458 (**1995**).
[39] C. Delfs, D. Gatteschi, L. Pardi, R. Sessoli, K. Wieghardt, and D. Hanke, *Inorg. Chem. 32*, 3099 (**1993**).
[40] A. L. Barra, P. Debrunner, D. Gatteshi, Ch. E. Shultz, and R. Sessoli, *Europhys Lett.*, *35 (2)*, 133 (**1996**).
[41] C. Sangregorio, T. Ohm, C. Paulsen, R. Sessoli, and D. Gatteschi, *Phys. Rev. Lett.*, *78*, 4645 (**1997**).
[42] A. Caneschi, D. Gatteschi, C. Sangregorio, R. Sessoli, L. Sorace, A., Cornia, M. N. Novak, C. Paulsen, and W. Wernsdorfer, *J. Mang. Magn. Mater. 200*, (accepted for publication, **1999**).
[43] T. Ohm, C. Sangregorio, and C. Paulsen, *Eur. Phys. J. B 6*, 195 (**1998**).
[44] N. V. Prokof'ev and P. C. E. Stamp, *Phys. Rev. Lett.*, *80*, 5794 (**1998**).
[45] W. Wernsdorfer, T. Ohm, C. Sangregorio, R. Sessoli, D. Mailly, and C. Paulsen, *Phys. Rev. Lett. 82*, 3903 (**1999**).
[46] R. Caciuffo, G. Amoretti, and A. Murani, *Phys. Rev. Lett.*, *81*, 4744 (**1998**).
[47] N. V. Prokof'ev and P. C. E. Stamp, *J. Low. Temp. Phys.*, *104*, 143 (**1996**).
[48] D. A. Garanin, *J. Phys. A: Math. Gen. 24*, L61 (**1991**).
[49] F. Hartmann-Boutron, *J. Phys. I France 5*, 1281 (**1995**).
[50] F. Luis, J. Bartolome, and J. Fernandez, *Phys. Rev. B 57*, 505 (**1998**).
[51] A. Fort, A. Rettori, J. Villain, D. Gatteschi, and R. Sessoli, *Phys. Rev. Lett.*, *80*, 612 (**1998**).
[52] M. N. Leuenberger and D. Loss, *Europhys Lett.*, *46 (5)*, 692 (**1999**); cond- mat/9907154.

[53] W. Wernsdorfer, R. Sessoli, and D. Gatteschi, *Europhys. Lett.*, *47 (2)*, 254 (**1999**).
[54] D. V. Berkov, *Phys. Rev. B 53*, 731, (**1996**).
[55] P. W. Anderson, *Phys. Rev. 82*, 342 (**1951**).
[56] T. Ohm, C. Sangregorio, and C. Paulsen, *J. Low. Temp. Phys.*, *113*, 1141 (**1998**).
[57] L. Thomas and B. Barbara, *Phys. Rev. Lett.*, *83*, 2398 (**1999**).
[58] L. Thomas and B. Barbara, *J. Low. Temp. Phys. 113*, 1055 (**1998**).
[59] L. Thomas, Ph. D. *Thesis*, Université Joseph Fourier, Grenoble, France, **1997**.
[60] J. R. Friedman, M. P. Sarachik, R. Ziolo, Phys. Rev. B 58, R14729 (**1998**). Note that in their determination of the line-width, the authors have mentioned that the procedure of the preparation of the sample (powder of the crystallites oriented in a field) is equivalent to that used in [4]. However, according to [4] (see Figure 1 of this paper), the magnetization at zero field is less than 0.25 of its saturated value. It is quite clear that the crystallites in this powder are not so well oriented. In fact this result is very strange because this fraction of 0.25 is even smaller than the 0.5 value which is expected for a completely disordered ensemble of uniaxial spins. This will of course, and at least, increases the experimental errors on the line-width.
[61] P. C. E. Stamp, in S. Tomsovic (Ed.), *'Tunneling in Complex Systems"*, Word Scientific Publishing, Singapore, 101 (**1998**).
[62] J. M. Hernandez, X. X. Zhang, F. Luis, J. Tejada, J. R. Friedman, M. P. Sarachak, and R. Ziolo, *Phys. Rev. B 55*, 5858 (**1997**).
[63] J. Villain, F. Hartmann-Bourtron, R. Sessoli, and A. Rettori, *Europhys. Lett.*, *27*, 159 (**1994**).
[64] P. Politi, A. Rettori, F. Hartmann-Bourtron, and J. Villain, *Phys. Rev. Lett. 75*, 537 (**1995**).
[65] F. Hartmann-Bourtron, P. Politi, and J. Villain, *Int. J. Mod. Phys. 10*, 2577 (**1996**).
[66] K. Blum, Density Matrix Theory and Applications, *Plenum Press*, *New York*, **1996**.
[67] A. L. Burin, N. V. Prokof'ev, and P. C. E. Stamp, *Phys. Rev. Lett. 76*, 3040 (**1996**).
[68] V. V. Dobrovitski and A. K. Zvezdin, *Europhys. Lett.*, *38 (5)*, 377 (**1997**).
[69] L. Gunter, *Europhys. Lett.*, *39*, 1 (**1997**).
[70] A. Caneschi, T. Ohm, C. Paulsen, D. Rovai, C. Sangregorio, and R. Sessoli, *J. Magn. Magn. Mater. 177-181*, 1330 (**1998**).
[71] (a) J. L. van Hemmen and S. Suto, in L. Gunter, B. Barbara (Eds), *Quantum tunneling of Magnetization – QTM'94*, NATO ASI Series E: Applied Science, Vol. 301, Kluwer, Dordrecht, 189 (**1995**). *Europhys. Lett.*, *1*, 481 (**1986**); *Physics B 141*, 37 (**1986**); (b) M. Enz and R. Shilling, *J. Phys. C 19*, L711 (**1986**); (c) E. M. Chudnovsky and L. Gunther. *Phys. Rev. Lett. 60*, 661 (**1988**); (d) P. C. E. Stamp, E. M. Chudnovsky, and B. Barbara, *Int. J. Mod. Phys. B 6*, 1355 (**1992**).
[72] N. V. Prokof'ev and P. C. E. Stamp, *cond-mat/9511011*.
[73] N. V. Prokof'ev and P. C. E. Stamp, in L. Gunter, B. Barbara (Eds), *Quantum tunneling of Magnetization – QTM'94*, NATO ASI Series E: Applied Science, Vol. 301, Kluwer, Dordrecht, 347 (**1995**).
[74] Yu. Kagan, L. A. Maksimov, Sov. *Phys. JETP 52 (4)*, 688 (**1980**).
[75] L. D. Landau and E. M. Lifshits, *"Statistical physics"*, **1965** (Oxford, Pergamon).
[76] A. M. Gomes, M. N. Novak, R. Sessoli, A. Caneschi, and D. Gatteschi, *Phys. Rev. B 57*, 5021 (**1998**).
[77] N. V. Prokofev and P. C. E. Stamp, *J. Low. Temp. Phys. 113*, 1147 (**1998**).
[78] J. F. Fernandez, F. Luis, and J. Bartolome, *Phys. Rev. Lett.*, *80*, 5659 (**1998**).
[79] W. Wernsdorfer, unpublished.
[80] W. Wernsdorfer, T. Ohm, C. Sangregorio, R. Sessoli, D. Gatteschi, and C. Paulsen, (to appear in *Physica B*).
[81] A. Cuccoli, A. Fort, A. Rettori, E. Adam, and J. Villain, *cond-mat/9905273*.

[82] C. Zener, Proc. R. Soc. *London A 137*, 696 (**1932**); S. Miyashita, *J. Phys. Soc. Jpn. 64*, 3207 (**1995**).
[83] W. Wernsdorfer, R. Sessoli, A. Caneshi, D. Gatteshi, and A. Cornia, (to appear in *J. Appl. Phys.*).
[84] G. Rose, P. C. E. Stamp, and I. S. Tupitsyn, (submitted to *Phys. Rev. Lett.*, **1999**).
[85] I. Chiorescu, R. Giraud, A. Canneschi, L. Jansen, and B. Barbara, (to be published).
[86] A. Lascialfari, Z. H. Jang, F. Borsa, P. Carretta, and D. Gatteschi, *Phys. Rev. Lett. 82*, 3773, (**1998**).
[87] T. Goto, T. Kubo, T. Koshiba, U. Fujii, A. Oyamada, J. Arai, T, Takeda, K. Awaga. (submitted to *Physica B*, *LT22*, 18 Sept. **1999**), and private communication.
[88] Zhang and Widom, *JMMM 122*, 119 (**1993**).
[89] R. Ferré and B. Barbara, (**1995**) not published.
[90] A. Wurger, J. Phys.: *Condens. Matter 10*, 10075, (**1998**).
[91] The Prokof'ev-Stamp kinetic equation [44] also gives $\sqrt{t}$ relaxation for annealed samples (as well as giving exponential relaxation at long times). Detailed MC simulations will be published elsewhere.
[92] N. V. Prokof'ev and P. C. E. Stamp, unpublished.

Magnetism: Molecules to Materials III. Edited by J.S. Miller and M. Drillon

ISBNs: 3-527-30302-2 (Hardback); 3-527-60014-0 (Electronic)

5 Studies of Quantum Relaxation and Quantum Coherence in Molecular Magnets by Means of Specific Heat Measurements

Fernando M. Luis, Fabian L. Mettes, and L. Jos de Jongh

5.1 Introduction

One hundred years after its discovery, the interpretation of quantum mechanics still continues to puzzle physicists. One of its most remarkable predictions, which is also against our daily perception of the macroscopic world, is that the wave-function of a particle can extend beyond classically allowed regions. In this way, the particle can escape from a metastable potential energy well by quantum tunneling (QT) through the energy barrier. A related effect is the phenomenon of quantum coherence (QC), in which a particle undergoes periodical oscillations by tunneling between two equivalent states, separated by a potential energy barrier (Fig. 1).

For a closed system, these coherent oscillations can be understood as a consequence of the principle of superposition of quantum mechanics. This principle states that the superpositions of two physical states of a particle are also possible states of the particle. If the energy barrier is finite, and the Hamiltonian contains a kinetic energy term, the wave-functions that describe the energy states of the particle are not localized in each of the wells, that is, they do not correspond to the "classical" states. The true energy states are the symmetric and antisymmetric linear combinations of the classical states, for which there is equal probability of finding the particle on the left or on the right of the energy barrier. These two states are not degenerate.

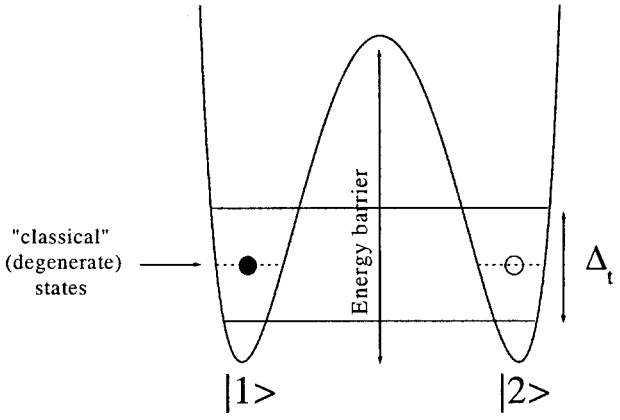

Fig. 1. Schematic diagram of a particle in a symmetric double-well potential in which two, initially degenerate, "classical" energy levels are tunnel-split by an amount Δ_t.

The energy difference between them is called the tunnel splitting, Δ_t, and is simply $\hbar$ times the angular frequency ω_t of the coherent oscillation. Consequently, the existence of QC can be detected by observation of this energy splitting, for instance by means of spectroscopic techniques, magnetic resonance, inelastic neutron scattering, or specific heat measurements.

There are many well-studied examples of QC in the microscopic world; one of the most famous is the ammonia molecule NH_3, in which the position of the plane of the three H atoms relative to the N atom oscillates coherently. One additional point is that some physical properties of the quantum superpositions of states, such as, e. g., the electrical polarizability of NH_3, are very different from the incoherent mixture of the two possible classical states and can, therefore, be distinguished experimentally.

It is evident that such superpositions of states are not observed in the macroscopic world. The most plausible explanation within the standard theory of quantum mechanics is that macroscopic objects can never be considered as isolated from the rest of the world, but are in strong interaction with the many microscopic degrees of freedom of the environment, which "measure" the state of the system [1–5]. This interaction very rapidly destroys the coherence between the different components of these superpositions, thus leading to the more robust "classical" states. This interpretation raises a new question – where, if it exists, is the border between quantum and classical descriptions? To investigate this point it is crucial to find pure quantum effects, such as QC, in two-level systems made of a large number of atoms and to be able to study and control the effect of decoherence induced by the interaction with the environment.

Molecular clusters made of some tens of atoms can be ideal systems for study of QT and QC at the mesoscopic scale (that is, in between the macroscopic and the atomic worlds) [6, 7]. These molecules, for example Mn_{12} [8, 9], Fe_8 [10, 11], or Mn_4 [12, 13], have a large net magnetic moment which results from the strong exchange interactions between the different magnetic atoms inside a cluster. The magnetic anisotropy favors a direction for the orientation of the magnetic moment. The two possible projections ("up" or "down") along the anisotropy axis are then two equivalent states of the system, separated by a potential energy barrier, because of the anisotropy. These molecular compounds, moreover form crystals, with the easy axes of all molecules in parallel [14]. The molecules are well separated from each other, which minimizes their mutual interaction. These properties enable the use of macroscopic experimental solid-state techniques to obtain information about the physical properties of a single cluster. A review of the extensive experimental and theoretical work that has been devoted to the study of these systems can be found in the chapters by D. Gatteschi, and by B. Barbara and I. Tupitsyn, in this book. The experiments show convincingly that incoherent tunneling plays an important role in the low-temperature spin–lattice relaxation of the magnetic moments towards thermal equilibrium. It was observed that the hysteresis loops of Mn_{12} contain steps at regular intervals of the applied magnetic field [15–17], which are accompanied by an increase in the spin–lattice relaxation rate [16–19]. This effect was attributed to the existence of phonon-assisted tunneling between different excited magnetic states. This process leads to a relaxation rate, Γ, that decreases exponentially as the temperature is reduced and becomes resonant when spin states on both sides

of the barrier become degenerate as a result of the action of the applied magnetic field. The magnetic relaxation of Fe_8 and Mn_4 becomes temperature-independent below approximately 0.4 K, and 0.6 K, respectively [20, 21]. A similar saturation of the relaxation time was observed for Mn_{12} below 2 K [17, 22], although the interpretation of these experiments is more difficult because they require extremely long experimental times ($\tau_e \approx 10^5$ s). The saturation of the relaxation time at these low temperatures suggests that when the population of the excited states becomes negligibly small incoherent tunneling proceeds between the two lowest lying $m = \pm S$ states.

The direct observation of Δ_t of the magnetic ground state of these molecular clusters is, however, a much more difficult experimental task. Δ_t is a very small quantity, of order 10^{-11}–10^{-7} K, and QC is thus completely destroyed by the much stronger interaction with the phonons and with the magnetic nuclei [2, 5]. It is, however, possible to increase the value of Δ_t, while keeping the symmetry of the double-well potential intact, by application of a magnetic field *perpendicular* to the anisotropy axis [23]. Such a field introduces a non-diagonal term in the spin–Hamiltonian and thus greatly enhances the tunneling probability. In this way, it is possible to make Δ_t large even with respect to the interactions mentioned above that induce decoherence. Following this idea, two groups have studied the resonant absorption of electromagnetic radiation by Fe_8 and Mn_{12} as a function of $B_\perp$ [24, 25]. They found that the imaginary part of the susceptibility measured at high frequencies has maxima at field values for which Δ_t is expected to become of the order of the energy of the photons, although interpretation of the experimental results as evidence of QC seems to be not straightforward [26].

In this chapter, we show that a large amount of information about these systems can be obtained from time-dependent specific heat measurements. By varying the temperature, the magnetic field, and the experimental time scale, it is possible to investigate the relaxation mechanism which brings the electronic spins into equilibrium with the lattice and study, in this way, incoherent tunneling processes. As shown in the next section, these experiments are an easy means of measuring the rate of relaxation of the magnetic moment for moderate and large transverse magnetic fields. In Section 3 we present the theoretical background necessary to give an account of the specific heat experiments, which are discussed in Section 4. We focus mainly on two topics – how QC can prevail at large magnetic fields and the role QT plays in the mechanism of spin–lattice relaxation. The data show that tunneling via progressively lower-lying excited spin states and ultimately through the ground-state doublet can be explored by applying large enough perpendicular magnetic fields. The spin–lattice relaxation rate that is obtained from these experiments depends only on transitions between different energy levels of the electronic spin in which energy is absorbed from, or released to, the phonon-bath. The fact that QT is observed not only for Fe_8 and Mn_{12}, which both have an integer spin value $S = 10$, but also for Mn_4 that has $S = 9/2$ is important, because an isolated half-integer spin should not flip by QT [27]. We think that the underlying reason is to be found in the hyperfine coupling of the nuclear spins. These data, therefore, provide valuable information that is complementary to the study of magnetic relaxation. Under thermal equilibrium conditions the specific heat of Mn_{12}, Fe_8, and Mn_4 clusters measured at low-T

and in large transverse magnetic fields gives clear evidence for the existence of a Δ_t [28, 29, 30]. It is very important in this respect that the data can be compared with theoretical calculations for both the coherent and the incoherent limits, which predict very different variation of the equilibrium specific heat with the magnetic field, thus enabling clear distinction between the two.

5.2 Experimental Techniques

The specific heat experiments described in this chapter are based on two different techniques. In both there is a characteristic time involved in the experiment (τ_e), or, similarly, a characteristic frequency $\omega_e = 2\pi/\tau_e$. In what follows the properties of both techniques will be described and compared.

In the method as described by Mettes et al. [30], the power, P, to heat the sample is applied in the form of rectangular pulses with typical time-periods of the order of seconds. The calorimeter is thermally connected with the mixing chamber through a weak, adjustable heat-link with thermal resistance R. As will be shown below, the ability to adjust the thermal heat-link (and thus the experimental time τ_e) has great advantages when studying equilibrium and non-equilibrium effects. When the heat is switched on and off, the calorimeter relaxes to the new thermal equilibrium. The heat capacity is obtained by fitting the temperature evolution of the calorimeter to a single exponent. After determining the characteristic relaxation time (τ_e) and the thermal resistance of the heat-link ($R = \Delta T/P$) for each temperature, the heat capacity is easily calculated according to $C = \tau_e/R$. The characteristic time of the experiment, τ_e, can be varied by changing the heat-link resistance. Typical relaxation constants vary between 1 and 10^2 s. Specific heat measurements in the temperature range 0.07–7 K and in magnetic fields of 0–12 T were performed using a commercial ^{3}He–^{4}He dilution refrigerator equipped with a superconducting magnet. A special calorimeter was designed, enabling specific heat measurements on samples with masses between approximately 0.1–100 mg and in a high magnetic field.

The calorimeter itself consists of a thin sapphire disk of thickness ~0.3 mm, diameter ~1 cm, that is suspended in a copper vacuum can by four thin nylon threads. Power is applied to the plate by resistive heating of a silver layer several nanometers thick (typically 100 Ω), which is sputtered on the plate. The heat-link is in the form of a 25 μm gold wire. The temperature evolution of the calorimeter is monitored by means of a Speer carbon resistor. Superconducting NbTi wires approximately 20 μm in diameter are used to connect to the heater and thermometer. The thermometer resistance is measured by means of a home made four-point ac resistance bridge operating at 25 Hz. During every temperature sweep the carbon resistor is calibrated against an RuO_2 thermometer attached to the mixing chamber. The sensitivity of the calorimeter, without sample, is approximately 20 nJ K^{-1} at 1 K and 2 nJ K^{-1} at 0.1 K. The measured specific heat is believed to be accurate to within at most 10 % of its absolute value in the temperature range of this work. The applied field was produced

by a superconducting magnet with a homogeneity at its centre of 0.07 % cm^{-1} over 1 cm.

For additional specific heat measurements in the temperature range 5–200 K, use was made of a commercial apparatus. In this temperature range samples of approximately 5 mg of Mn_{12} and Fe_8 mixed with Apiezon-N grease were measured in zero field to estimate the lattice contribution to the specific heat.

Fominaya et al. used an ac steady-state method [31]. The major advantage of the ac technique is the possibility of detecting very small changes in the heat capacity. When the ac heating current of frequency $\omega/2\pi$ is passed through a heater the ac temperature response of frequency ω can be observed, i. e. $T(t) = T_0 + \delta T(t)$. The main disadvantage of the ac steady state device is the requirement that the internal thermal relaxation (i. e. the response time of the sample and substrate to the heat input) should occur much faster than the applied modulation frequency (ω) and, furthermore, that thermal relaxation of the calorimeter to the bath occurs much slower than ω. When these conditions are met, the amplitude of the observed temperature modulation (ΔT) can be directly related to the total heat capacity according to: $C = P/(\Delta T\omega)$, where P is the ac heating power.

The sample-holder is a silicon frame (10 mm × 15 mm × 280 μm) which is fabricated by anisotropic etching of a (100) oriented monocrystalline silicon substrate. A square area (5 mm × 5 mm) of this silicon frame is subsequently etched by KOH until a membrane of thickness of 2–10 μm remains. To reduce further the thermal coupling of the membrane to the frame, holes are etched into the membrane so that a 3.3 mm × 3.3 mm membrane suspended by 12–40 μm wide bridges remained. The thermal link is defined by the geometry of the bridges. The suspended membrane itself defines an isothermal area. On the membrane, and on the frame, a 100-nm film thermometer of NbN and a 150-nm film heater of CuNi are deposited. The electrical connections are fabricated by depositing a 100-nm film of NbTi and were patterned by optical lithography, ion beam etching, and chemical etching. The silicon frame is anchored to a copper holder which has an accurately known thermal link to the bath. The NbN thermometer is calibrated against a germanium resistance attached to the copper holder. The whole is mounted in a conventional low-temperature device by means of which the temperature could be varied between 1.5 and 300 K. Magnetic fields up to 5 T could be applied. A dc measurement of the resistance of the thermometer gives the temperature of the membrane. Simultaneously, this resistance oscillates slightly at a frequency ω, because of the temperature modulation of the heat-capacity measurement. The voltage oscillation δV is amplified by a low-noise differential preamplifier. The sensitivity of the calorimeter without sample amounts to approximately 3 nJ K^{-1} at 4 K and 0.5 nJ K^{-1} at 1.5 K. In the actual experiments on Mn_{12}, monocrystals of masses of the order of μg are pasted on the reverse of the membrane by means of liquified Apiezon-N grease.

5.3 Theoretical Background

Since the discovery of resonant tunneling in Mn_{12}, several attempts have been made to explain the results theoretically. It is not our purpose to give here a full review of all the models proposed. The reader can find an extensive introduction to the theory of magnetic relaxation and tunneling in magnetic molecules in the chapter by B. Barbara and S. Tupitsyn in this book. We shall limit ourselves to explaining the theoretical framework needed to interpret time-dependent specific heat experiments. For this reason, we first introduce a spin-Hamiltonian from which the energy levels and the specific heat in equilibrium can be calculated. We pay special attention to the influence of the magnetic field on the scheme of energy levels and how it can counter the effect of decoherence induced by interaction with phonons and nuclear spins. The second section is devoted to the study of the spin–lattice relaxation of a spin system which can perform tunneling transitions between degenerate states. Finally, we will describe a way of predicting measurable quantities, in particular time-dependent specific heat.

5.3.1 Spin-Hamiltonian for Molecular Magnets – Field-dependent Quantum Tunneling

In what follows, we shall make use of the "giant-spin" model Hamiltonian, which is a good approximation when, as a consequence of the strong exchange interaction between the magnetic ions inside a molecular cluster, the magnetic ground state can be described by a well-defined total spin S. This is valid at low enough temperatures, when the excited levels of different S are weakly populated. The magnetic behavior of the molecule is then equivalent to that of a single-domain particle and the relevant energy levels correspond to different orientations of the total spin or linear combinations of these. For a system with dominant uniaxial anisotropy, the spin-Hamiltonian can be written:

$$\mathcal{H} = -DS_z^2 + \mathcal{H}' - g\mu_B \left[B_z S_z + B_\perp \left(\cos(\phi)S_x + \sin(\phi)S_y\right)\right] + \mathcal{H}_{\text{dip}} + \mathcal{H}_{hf} \quad (1)$$

The first two terms of $\mathcal{H}$ arise from crystal-field interactions. The first defines a direction (z) as the preferred axis for the magnetization. In the absence of other terms, that is, for pure rotational symmetry around z, the different projections m of the spin would be eigenstates of the Hamiltonian. The corresponding energy levels would then lie on a double-well landscape with two degenerate minima separated by a potential energy barrier, as sketched in Fig. 2.

The second term of the spin Hamiltonian includes higher-order perturbation terms, which arise from deviations from this pure uniaxial anisotropy. For the three compounds considered, $\mathcal{H}'$ can be written as

$$\begin{aligned}\mathcal{H}' = & -E\left(S_x^2 - S_y^2\right) + A_4 S_z^4 + E_2\left[S_z^2\left(S_x^2 - S_y^2\right) + \left(S_x^2 - S_y^2\right)S_z^2\right] \\ & + C\left(S_+^4 + S_-^4\right) \end{aligned} \quad (2)$$

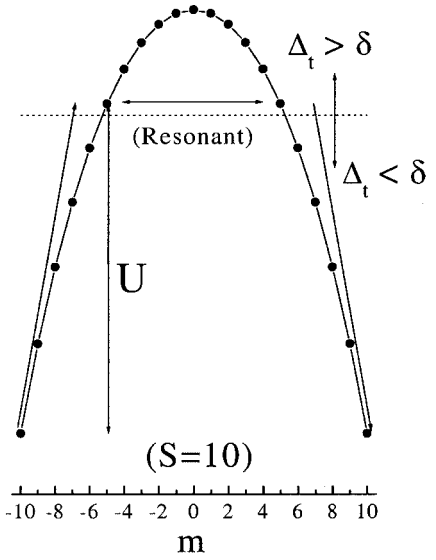

Fig. 2. Double-well potential for a spin $S = 10$ with uniaxial anisotropy at zero magnetic field. The horizontal dotted line marks the border between "classical" ($\Delta_t < \delta$) and "tunneling" ($\Delta_t > \delta$) energy levels. The activation barrier, U, is roughly given by $\Delta E_{l_1,2} \equiv E_{l_1} - E_2$, where l_1 is the first energy level which fulfills $\Delta_t \approx \delta$.

The crystal-field parameters, D, E, A_4, E_2, and C, of Fe_8, Mn_{12}, and Mn_4 have been obtained by several groups using different experimental techniques, such as Mössbauer spectroscopy [32], ESR [12, 32–35], inelastic neutron scattering [13, 36–38], and optical methods [39]. The approximate values are given in Table 1. It is important to stress that these data are obtained from experiments performed in the "classical" high temperature regime; this enables comparison with quantum tunneling experiments with almost no fitting data.

Because of the presence of off-diagonal terms in $\mathcal{H}'$ pure m states are no longer eigenstates of $\mathcal{H}$. The true eigenstates are their symmetric and antisymmetric combinations, each of different energy. The degeneracy of $\pm m$ spin levels is lifted by an amount, Δ_t, called the tunnel splitting, which is larger the lower the energy barrier and, therefore, increases exponentially as m decreases. It is then convenient to label the energy levels by a different index, l, in increasing order of energy. Using the data given above, Δ_t of the ground state is approximately 10^{-10}–10^{-11} K at zero field for Fe_8 and Mn_{12}, although recent relaxation experiments [40] give a larger estimate ($\Delta_t \approx 10^{-7}$ K) for Fe_8. As pointed out by Politi et al. [41], and by Prokof'ev and Stamp [42], however, the interaction of the magnetic moment with the environ-

Table 1. Parameters of the spin-Hamiltonian of four molecular magnets.

Sample	g	D(K)	E(K)	A_4(K)	C(K)	E_2(K)
Mn_{12} [34]	1.9	0.6	0	-1.0×10^{-3}	-3.06×10^{-5}	0
Fe_8 [32, 37]	2	0.294	4.65×10^{-2}	3.53×10^{-5}	4.26×10^{-6}	2×10^{-7}
Mn_4, X=Cl^- [13]	2	0.69	-3.15×10^{-2}	-3.25×10^{-3}	-9.95×10^{-5}	0
Mn_4, X=OAc^- [13]	2	0.59	-2.43×10^{-2}	-3.96×10^{-3}	-1.21×10^{-4}	0

ment, that is, with other degrees of freedom, or with stray magnetic fields, blocks the coherent tunneling process very effectively.

The Hamiltonian given above includes interaction terms with other molecules ($\mathcal{H}_{\rm dip}$) and with the nuclei of the atoms composing the molecule ($\mathcal{H}_{\rm hf}$). Because the direct exchange interaction between neighboring molecules is very small, the intermolecular interaction is mainly the direct dipole–dipole interaction between the magnetic moments. The term $\mathcal{H}_{\rm hf}$ results from the hyperfine interaction between the electronic spins and the nuclear magnetic moments. It is especially important for those molecules, such as Mn_{12} or Mn_4, in which the nuclei of the magnetic atoms posses a spin ($I = 5/2$ for Mn), thus leading to a strong contact hyperfine interaction. For clusters of magnetic atoms with no nuclear spin, as for the Fe_8 cluster, which contains the isotope ^{56}Fe, $\mathcal{H}_{\rm hf}$ represents the interaction with the magnetic nuclei located at the ligand molecules which surround the cluster. These ligand molecules always contain H atoms and sometimes other atoms like N, which carry nuclear spins. Also these weaker hyperfine couplings will thus have to be considered in principle, although we shall show below that they are weak enough to be neglected. Although the hyperfine and the dipole–dipole interactions are weak relative to the strength of the uniaxial anisotropy, they can induce a Zeeman splitting, δ, of the ground state of the molecule that is many orders of magnitude larger than $\Delta_{\rm t}$. The diagonal terms present in both $\mathcal{H}_{\rm dip}$ and $\mathcal{H}_{\rm hf}$ can be regarded as a sort of bias magnetic field, which produces an asymmetry of the two wells that blocks tunneling when $\delta \gg \Delta_{\rm t}$. The typical value of these bias fields has been found experimentally to be of order $\delta \approx 0.2\,{\rm K}$ for the ground states of both Fe_8 and Mn_{12} [43, 44]. Unassisted tunneling is thus prohibited for the vast majority of the molecules present in a given crystal.

The influence of the magnetic field on the tunneling experiments turns out to be essential. We shall, therefore, here give a detailed account of how the energy levels and the wave-functions are modified by the third term appearing in Eq. (1). If the field is parallel to z (B_z), it breaks the symmetry and thus the degeneracy of the states m and $-m$ by the amount $\Delta_Z = 2g\mu_{\rm B}mB_z$. The energy difference between the two levels of a tunnel-split doublet becomes $\Delta E_{l+1,l} \equiv E_{l+1} - E_l = \sqrt{\left(\Delta_{\rm t}^2 + \Delta_{\rm Z}^2\right)}$. When $\Delta_Z \gg \Delta_{\rm t}$, tunneling between these magnetic states is blocked. When, however, $B_z \approx D/g\mu_{\rm B}$, the magnetic field brings two other m levels, located on opposite sides of the energy barrier, into resonance, thus again restoring the possibility of quantum tunneling between the two wells. This situation is depicted in Fig. 3 for Fe_8.

This crossing of levels gives rise to the phenomenon of resonant tunneling. If, by contrast, the magnetic field is perpendicular to z ($B_\perp$), the symmetry of the double-well potential is maintained. Classically, the transverse field keeps the degeneracy of the energy minima intact. It just shifts the position of the bottom of the two wells towards the plane perpendicular to z, and thereby reduces the height of the energy barrier. In quantum mechanics, however, the situation is different. The transverse field introduces an off-diagonal term in the spin-Hamiltonian, that is, one which does not commute with S_z. This is crucial because, as we have seen, QC is completely washed out at zero field by the hyperfine and dipole–dipole interactions. The question is whether $\Delta_{\rm t}$ can be made large enough compared with both $k_{\rm B}T$ and δ. Fortunately, the application of a transverse field offers the possibility of significantly increasing $\Delta_{\rm t}$, and in a well-controlled way.

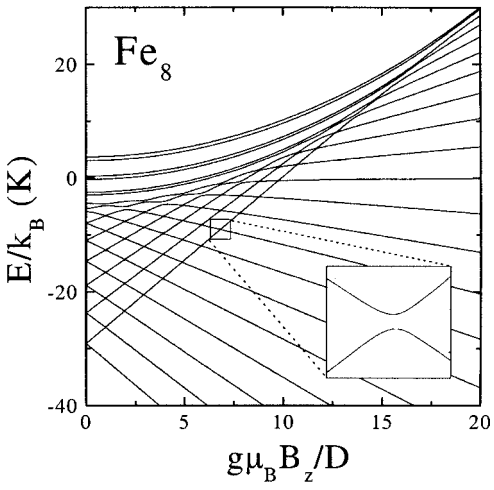

Fig. 3. Energy levels as a function of applied field parallel to the anisotropy axis (B_z) for Fe_8 as calculated from Eq. (1), with $\mathcal{H}_{dip} = \mathcal{H}_{hf} = 0$. Inset shows level repulsion, as present at all crossings.

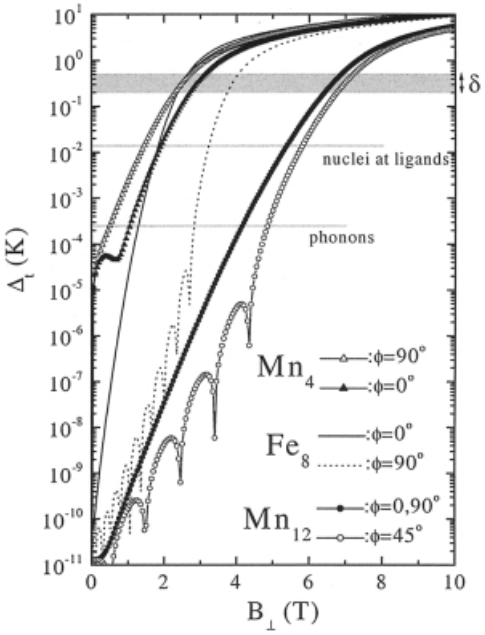

Fig. 4. Quantum tunnel splitting (Δ_t) as calculated from Eq. (1), with $\mathcal{H}_{dip} = \mathcal{H}_{hf} = 0$, as a function of applied field perpendicular to the anisotropy axis (z) for Mn_4, Fe_8, and Mn_{12}. ϕ is the angle that $B_\perp$ makes with the easy (x) axis within the hard (xy) plane. The orders of magnitude of interactions of the electronic spins with different microscopic degrees of freedom are also indicated.

We have plotted the calculated tunnel splitting of the ground state of Fe_8, Mn_{12}, and Mn_4 as a function of $B_\perp$ in Fig. 4.

The calculations shown are for non-interacting spins, that is, the latter two terms in $\mathcal{H}$ ($\mathcal{H}_{dip}$ and $\mathcal{H}_{hf}$) are neglected. At low magnetic fields the value of Δ_t is still mainly dominated by the off-diagonal terms of $\mathcal{H}'$. As a result, Δ_t depends strongly on ϕ, the angle that the magnetic field makes with the easy axis (x) of the hard xy plane. When the magnetic field is applied along a hard or intermediate axis it modifies the

quantum interference between different tunnel paths [27], which leads to maxima or minima of Δ_t if the interference is constructive or destructive, respectively. These effects can lead to oscillations of the rate of incoherent tunneling; these have been experimentally observed for Fe_8 [43]. An important application of these ideas is for a molecule with a half-integer spin, for example Mn_4, with $S = 9/2$. At zero field, interference effects are predicted to make $\Delta_t = 0$ [45, 46]. Therefore, quantum tunneling should not occur unless a magnetic field is applied. Here, the interaction with the nuclei can also have an important effect. The off-diagonal terms in $\mathcal{H}_{hf}$ enable tunneling and lift the degeneracy of the ground-state doublet and of the excited states. The tunneling process of the central spin is then accompanied by the flip of one or several nuclear spins [42]. Although the magnetic field or the interaction with the nuclear spins are needed to break the selection rule, because of the interference effect, the value of Δ_t will still be determined mainly by the anisotropy terms, and thus need not be much smaller than for molecules with an integer spin. For example, using the crystal field value, E, found experimentally for one of the varieties of Mn_4 [13], and taking $H_x = 300\,\text{Oe}$, we get $\Delta_t = 1 \times 10^{-5}\,\text{K}$, whereas for $E = 0$ a much larger magnetic field ($\sim$0.7 T) would be needed to obtain the same tunnel splitting.

For higher perpendicular magnetic fields, Δ_t increases in proportion to $B_\perp^{2S}$ [23]. In Fig. 4 we have indicated the order of magnitude of δ caused by dipole–dipole and hyperfine interactions and the homogeneous broadening of the levels arising from the interaction with the phonon-bath. Even for fields of relatively moderate strength (easily produced in the laboratory), Δ_t can be of the same order as, or larger than, δ caused by these perturbations, thus opening a possibility of observing QC. For the excited states, the splitting also increases, the relative effect being larger because the effective energy barrier is smaller for these states.

5.3.2 Resonant Tunneling via Thermally Activated States

We have seen in the previous section that tunneling between the two lowest magnetic states, $m = +S$ and $m = -S$ is suppressed by the environment when $\delta \gg \Delta_t$. For the excited states, however, Δ_t is much larger, because it increases as the level approaches the top of the classical energy barrier. For a given tunnel-split excited state it might thus happen that the condition $\Delta_t \geq \delta$ is fulfilled. Tunneling via these states is then not completely blocked because the wave-functions are not pure m states, as shown in Fig. 5.

To study spin–lattice relaxation, it is necessary to take into account the interaction of the electronic spins with the phonon-bath, which can induce transitions between different energy levels of the electronic spin. The bath is considered to be in internal thermal equilibrium. The Hamiltonian of the combined system is:

$$\mathcal{H}_{\text{s-ph}} = \mathcal{H} + \mathcal{H}_{\text{ph}} + \mathcal{H}_{\text{int}} \tag{3}$$

where the first term is the spin-Hamiltonian given by Eq. (1), the second is the Hamiltonian of the phonon-bath, and the third describes the interaction between both. For $T \geq 2\,\text{K}$, the population of the excited spin states is not negligibly small

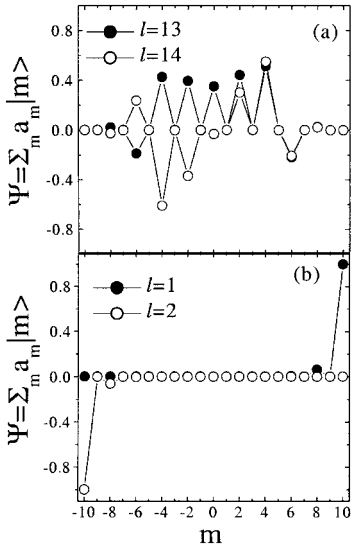

Fig. 5. Calculated wave-functions (Ψ), as expressed in amplitudes (a_m) of m states for two different pairs of energy levels: (a) tunnel-split excited levels $l = 13, 14$ (which correspond to the m states: $m = \pm 4$); (b) ground state doublet ($l = 1, 2$) which fulfills $\Delta_t \ll \delta$.

and the magnetic relaxation can proceed via a phonon-assisted tunneling process. This mechanism, illustrated in Figs. 2 and 6, involves a phonon-induced transition from the minimum of one of the two wells to the lowest of these "tunneling" levels, followed by a decay into the opposite well.

The relaxation rate, Γ, for this process decreases exponentially with T:

$$\Gamma = \Gamma_0 \exp\left(-\frac{U}{k_B T}\right) \tag{4}$$

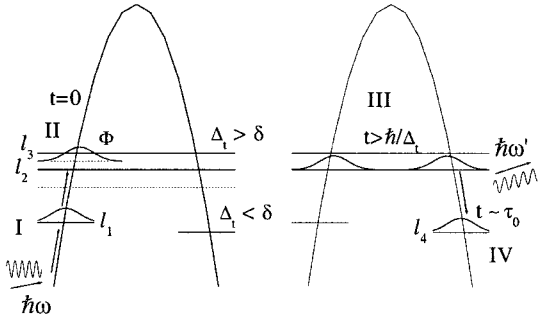

Fig. 6. Schematic diagram of tunneling via a thermally excited level. Initially (I), the system occupies the energy state l_1. In step II, a phonon of energy $\hbar\omega = \Delta E_{l_2,l_1}$ is absorbed and the system evolves to the localized wave-function $|\phi\rangle$, which is a linear combination of l_2 and l_3. After a decoherence time of the order of $\hbar/\Delta_t$, that is, less than the period of a coherent tunneling oscillation, the system evolves towards the symmetric wave-function l_2. After the much longer period τ_0 (step III), the system decays towards a lower-lying level on the opposite side of the barrier (IV), by emitting a phonon of energy $\hbar\omega'$.

and the activation barrier U is roughly given by $\Delta E_{l_2,2} \equiv E_{l_2} - E_2$, where l_1 is the first level which fulfils $\Delta_t \approx \delta$ (see Fig. 6) and Γ_0 is the inverse of the typical lifetime τ_0 of the excited levels. Experiments performed in the last few years give strong evidence for the occurrence of quantum tunneling via excited states at high enough temperatures (above 2 K for both Fe_8 and Mn_{12}) [15–17, 47]. This mechanism is in principle a resonant process, that is, it becomes faster whenever the longitudinal magnetic field brings levels on different sides of the energy barrier into resonance, whereas relaxation is much slower for intermediate field values.

We next show that the time evolution of the system is basically incoherent, because it occurs via the interaction with the phonon-bath, which brings the molecules to the excited states. Consider a spin that is initially in a state $|i\rangle$. To calculate the subsequent evolution with time of any physical quantity it is necessary to evaluate the reduced density matrix $\rho(t)$, with elements:

$$\langle l|\rho(t)|l'\rangle = \sum_{r,r'} P_r \langle \varepsilon_{r'}|\langle l|U(t)|i\rangle|\varepsilon_r\rangle\langle\varepsilon_r|\langle i|U^{\dagger}(t)|l'\rangle|\varepsilon_{r'}\rangle \tag{5}$$

where $U(t)$ is the time evolution operator for the system, that is, of the spin plus the phonon-bath, and $|\varepsilon_r\rangle$ represents energy states for the phonon-bath alone (defined by the number of excited phonons of each energy). In general, the density matrix defined in Eq. (5) is not diagonal. The diagonal elements $P_l = \langle l|\rho|l\rangle$ give the populations of the electronic energy states, whereas the off-diagonal elements represent the occurrence of coherent superpositions of different energy states. We first write the time evolution of a state $|i\rangle|\varepsilon_r\rangle$ as:

$$U(t)|i\rangle|\varepsilon_r\rangle = \sum_{j,r''} b_{i,r}^{j,r''}(t) \exp\left(\frac{-iE_{j,r''}^0 t}{\hbar}\right)|j\rangle|\varepsilon_{r''}\rangle \tag{6}$$

where $E_{j,r''}^0 = E_j + \varepsilon_{r''}$ is the unperturbed energy and the coefficients $b_{i,r}^{j,r''}(t)$ depend on time because of the interaction between the spins and the phonon-bath.

In what follows we investigate a particular case of interest in the study of molecular clusters, where these states are "long-lived" [48–50]. By this we mean that the homogeneous broadening of the levels induced by the interaction with the bath is much smaller than the energy difference $\Delta E_{l+1,l} = E_{l+1} - E_l$ between neighboring energy levels. If we denote a typical lifetime of an electronic energy level by $\tau_0 = 1/\Gamma_0$, this condition reads $\hbar/\tau_0 \ll \Delta E_{l+1,l}$. Fulfilment of this inequality guarantees that we can apply standard methods of first-order time-dependent perturbation theory to the calculation of the density matrix. In that case, the coefficients $b_{i,r}^{j,r''}(t)$ can be expanded up to terms which are linear in $\mathcal{H}_{\rm int}$, giving:

$$b_{i,r}^{j,r''}(t) \simeq \delta_{i,j}\delta_{r,r''} + \frac{1}{i\hbar}\int_0^t \exp\left[\frac{i\left(E_{j,r''}^0 - E_{i,r''}^0\right)t'}{\hbar}\right]\langle\varepsilon_{r''}|\langle j|\mathcal{H}_{\rm int}|i\rangle|\varepsilon_r\rangle dt'. \tag{7}$$

After integration of Eq. (7) and substitution in Eq. (5), it follows that:

$$\langle l|\rho(t)|l'\rangle \simeq \sum_{r,r'} P_r \langle \varepsilon_{r'}|\langle l|\mathcal{H}_{\rm int}|i\rangle|\varepsilon_r\rangle\langle\varepsilon_r|\langle i|\mathcal{H}_{\rm int}|l'\rangle|\varepsilon_{r'}\rangle \exp\left[\frac{-i\,(E_l - E_{l'})\,t}{\hbar}\right] \times \frac{\exp[\frac{i\left(E^0_{l',r'}-E^0_{i,r}\right)t}{\hbar}]-1}{E^0_{l',r'}-E^0_{i,r}} \frac{\exp[\frac{-i\left(E^0_{l,r'}-E^0_{i,r}\right)t}{\hbar}]-1}{E^0_{l,r'}-E^0_{i,r}}. \quad (8)$$

The terms in Eq. (8) which contribute most are resonant terms for which $E^0_{j,r'} - E^0_{i,r} \simeq 0$ with $j = l$ or l'. As a consequence, the diagonal elements of $\rho(t)$ increase with t, whereas the off-diagonal elements cease to increase when $t \approx \hbar/(E_l - E_{l'})$, thus ρ becomes diagonal for still longer times. It is important to note here that the time interval during which off-diagonal matrix elements exist is much shorter than the average lifetime of the excited electronic levels. The coherent evolution is thus destroyed for times longer than the tunneling time, that is, long before the spin decays (by emitting a phonon) to a lower-lying energy level. The process is sketched in Fig. 6. The long-term dynamics of the system mainly driven by incoherent transitions between different energy eigenstates, with either localized or delocalized wave-functions.

In the next section, we will give a more quantitative account, and describe a way of predicting measurable physical quantities. Before we do so, it is convenient to check the extent to which the above model is applicable to the description of quantum tunneling in molecular magnets. The criterion of validity is $\Delta E_{l+1,l} \gg \hbar/\tau_0$ for any two energy levels $l+1$ and l. For levels located on the same side of the energy barrier, $\Delta E_{l+1,l} \geq D$. For two tunnel-split levels near resonance, $\Delta E_{l+1,l} \approx \sqrt{(\delta^2 + \Delta_{\rm t}^2)}$. Because $D > \delta$, it is therefore sufficient to show that $\delta \gg \hbar/\tau_0$. The value of τ_0 was estimated from the prefactor of the Arrhenius law, which describes the temperature-dependence of Γ [9, 15–17, 34, 51], to be of order of 10^{-8}–10^{-7} s for Fe_8 and Mn_{12}. Similar values were obtained from measurements of T_1 of the protons of Mn_{12} molecules [52]. The width of the distribution of bias fields associated with the dipole–dipole and hyperfine interactions has, on the other hand, been estimated experimentally to amount to about 200–500 Oe [43, 44]. Using the values given above gives $\delta \approx 0.05$–1 K, depending on the level, whereas the homogeneous broadening $\hbar/\tau_0 \approx 8 \times 10^{-5}$–$8 \times 10^{-4}$ K, i. e., two to four orders of magnitude smaller. In other words, the condition of validity of the model described above is fulfilled by most of the molecules of a sample which have a large enough δ. If the condition is not fulfilled, i. e., if the homogeneous broadening is large, it is necessary to consider the effect of the off-diagonal matrix elements of ρ, and the master equation that we will introduce in the next section is not applicable. To solve this problem some authors have used another approach in which the tunneling is taken as a perturbation [53–55]. A very similar theoretical problem was considered in the description of proton tunneling in hydrogen bonds [56]. Tunneling then gives rise to an extra term in a generalized master equation that involves transitions between magnetic states, m, instead of true energy states, l. In the common range of validity of the two approaches (for weak transverse magnetic fields and $\Delta_{\rm t} \gg \hbar/\tau_0$), it is possible to show that both give the same result for the shape of the resonances in $\Gamma(B_z)$ [57]. We choose here the

first model because it is applicable to the experimental situation in which a large transverse field is applied, as in the specific heat experiments described later in this chapter.

5.3.3 Master Equation – Calculation of Γ

We have shown in the previous section that when the spin–phonon interaction is weak, the density matrix, expressed in the basis of true energy states l of the molecule, becomes diagonal after a time that is much shorter than τ_0. To calculate the long-term evolution of the system we might therefore, make use of a standard Pauli master equation for the populations P_l

$$\frac{dP_l}{dt} = \sum_{l'} (w_{l\leftarrow l'} P_{l'} - w_{l'\leftarrow l} P_l) \tag{9}$$

which involves transition rates $w_{l\leftarrow l'}$ induced by phonons only. These probabilities can be calculated with Fermi's golden rule, using the appropiate $\mathcal{H}_{\text{int}}$. Hartmann-Boutron et al. [58] obtained:

$$w_{l'\leftarrow l} = q|E_l - E_{l'}|^3 |\langle l'|V(\mathbf{S})|l\rangle|^2 A_{l,l'} \tag{10}$$

where $A_{l,l'} = n_{l,l'}$ and $A_{l,l'} = 1 + n_{l,l'}$ for transitions upward and downward, respectively, in energy, $n_{l,l'}$ is the number of available thermal phonons for a transition with $\Delta E_{l',l} = E_{l'} - E_l \geq 0$, q is a constant that depends on the elastic properties of the lattice, and $V(\mathbf{S})$ is an operator acting on the spin variables. In the calculations that follow, the lowest order hermitian spin operator that is compatible with uniaxial anisotropy was used $B = [S_x, S_z]_+ + [S_y, S_z]_+$ [58]. For this case, q is given by [55, 58, 59]:

$$q \equiv \frac{D^2}{6\pi\rho_m c_s^5 \hbar^4}. \tag{11}$$

This parameter sets the scale to all transition rates. Here ρ_m is the mass density and c_s the average speed of sound of the two transverse acoustic modes in the medium. It is of interest to note here that q can be obtained experimentally by measuring Γ, e. g. from the frequency-dependent susceptibility at a given temperature. Because the crystal-field parameter D is known, we can extract from q the average speed of sound in the medium and compare it with the value obtained from the phonon contributions to the specific heat as measured in our experiments. To a first approximation, the value for c_s can be calculated from the obtained Debye temperature Θ_D, which is deduced in the low temperature limit $T \ll \Theta_D$, where the phonon specific heat follows the well-known Debye T^3 law. The relation between c_s and Θ_D is:

$$c_s = \frac{k_B \Theta_D}{\hbar} \left(\frac{6\pi^2 N}{V}\right)^{-\frac{1}{3}} \tag{12}$$

where N is the number of molecules per unit cell with volume V. From the above it is clear that we can, in principle, obtain estimates of the magnitude of all variables involved in the physical description of the problem at hand.

Let us define P as a column vector with components P_1, P_2, ... The master equation for all levels can be written:

$$\frac{dP}{dt} = WP \tag{13}$$

where W is a matrix of transition rates with elements $(W)_{l,l'} = w_{l \leftarrow l'}$ for $l \neq l'$ and $(W)_{l,l} = -\sum_{l' \neq l} w_{l' \leftarrow l}$. The relaxation rate, Γ, is the smallest non-zero eigenvalue of W. The other eigenvalues, of order $1/\tau_0$, are associated with fast relaxation modes. At zero magnetic field, these modes are related to transitions between levels inside each of the two potential wells, whereas Γ gives the rate at which the relative populations of both wells reach mutual equilibrium. At higher transverse magnetic fields, as applied in the specific heat measurements described below, or when the deviation from pure uniaxial anisotropy is important, the wave-functions of an increasing number of energy levels become delocalized. The separation between *intra*-well and *inter*-well transitions then becomes artificial. Still, by using the master equation it is possible to calculate the response of the system to an external perturbation and to separate the fast and slow components of this response.

Calculated data for the rate of relaxation of Mn_{12} at $T = 5\,K$ are shown as a function of the longitudinal field in Fig. 7.

Resonant tunneling gives rise to Lorentzian shaped peaks at the crossing fields. The width of the peaks ΔB_z is determined by Δ_t of the lowest delocalized levels. The reason is that tunneling becomes blocked via a given excited doublet when $\Delta_Z \geq \Delta_t$, where $\Delta_Z = g\mu_B(2m + n)\left|B_z - B_{n,m}\right|$ is the Zeeman splitting between the states m and $-m - n$, which are in resonance when $B_z = B_{n,m}$. At zero field, all levels are

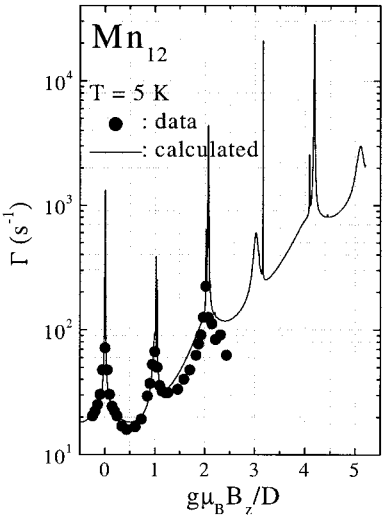

Fig. 7. Calculated spin–lattice relaxation rate for Mn_{12} (line) compared with the experimental relaxation rate of a single-crystal of Mn_{12} (full dots), as a function of the applied field parallel to the easy axes. The calculated behavior for Γ is obtained by using the master equation (Eq. (9)), as explained in Section 3.3.

in resonance. The peak of Γ consists, then, of two superimposed peaks of different width and amplitude. The narrowest peak corresponds to the tunnel-split $m = \pm 4$ ($\Delta_t = 2.3 \times 10^{-2}$ K), where $\Delta B_z \approx 23$ Oe and the broader peak corresponds to $m = \pm 2$ ($\Delta_t = 0.7$ K), for which $\Delta B_z \approx 1.4$ kOe. For non-zero bias field, the peaks have "satellites" because of tunneling through different resonant levels. The difference between Γ for odd and even values of n is because quantum tunneling is mainly induced by the (strong) perturbation $\mathcal{H}'$ at zero field, whereas a linear term (arising from the dipole–dipole or hyperfine interactions) is necessary to induce tunneling when n is odd. This effect would be smeared out by the distribution of dipolar fields (here not yet taken into account) and especially, under the usual experimental conditions, by any misalignment of the sample relative to the applied field, which induces a component $B_\perp$. In the same figure, we compare the calculations with the experimental data obtained from frequency-dependent susceptibility measured on a single crystal of Mn_{12} [60]. The calculations reproduce the measured results fairly well. We emphasize that the calculated Γ (full line) has not yet been broadened by the distribution of dipolar fields. This inhomogeneous broadening could explain why the width of the measured resonances is larger than calculated and why the experiments show no "satellites" near the resonant fields.

In the picture given above for the magnetic relaxation of magnetic molecules, the effect of a transverse field is solely to reduce gradually the threshold energy above which $\Delta_t \geq \delta$ is fulfilled (dotted line in Figs. 2 and 6). As a result, U decreases, as can be inferred from the decreasing slope of the calculated $\log(\Gamma)$ against T curves (shown in Fig. 8).

Below a given cross-over temperature T_Q the population of these excited states becomes negligible and incoherent tunneling via the ground state becomes favorable

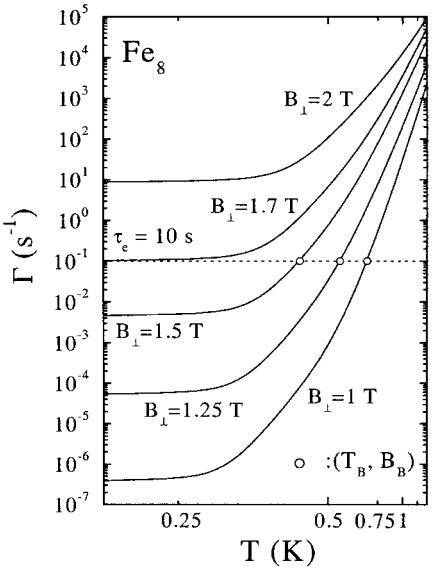

Fig. 8. The effect of a perpendicular field on the temperature-dependence of the spin–lattice relaxation rate in Fe_8 (solid lines). Typical time in the specific heat experiment ($\tau_e = 10$ s) is marked by the dotted line. Intersection points between the experimental time curve and the calculated spin–lattice relaxation rate curves are denoted by an open circle. The presence of an intersection point will lead to a blocking feature in the experiment. For $\tau_e = 10$ s, no blocking feature is expected for $B_\perp \geq 1.7$ T in Fe_8.

[41], leading to a temperature-independent relaxation rate $\Gamma \approx \Gamma_{\rm dir}$ for $T \to 0$ (cf. Fig. 8). Note, as can be seen from Fig. 8, that $T_{\rm Q}$ depends only weakly on $B_\perp$ and the experimental time. At low field $\Gamma_{\rm dir}$ is very small because, for most of the molecules, $\delta > \Delta_{\rm t}$ and the overlap of the initial and final wave-functions is negligible. This phonon-assisted tunneling process is, furthermore, not resonant, because the density of states of the phonons with $\hbar\omega = \Delta E_{2,1}$ becomes very small near zero field. The spin-lattice relaxation associated with this mechanism thus becomes extremely slow in this temperature regime. By contrast, when $B_\perp$ increases, $\Delta_{\rm t}$ and the overlap of the wave-functions associated with the two lowest energy levels increases. Under these conditions, tunneling through the ground state doublet can dominate the spin–lattice relaxation and proceed at rates that can be experimentally observed.

5.3.4 Calculation of Time-dependent Specific Heat and Susceptibility

We mentioned in the previous section that the populations of the levels in the same well reach mutual equilibrium very quickly, time approximately τ_0, but the equilibrium between the populations of the two wells can take much longer, $1/\Gamma$. We, therefore, expect that the low-temperature specific heat can show interesting time-dependent effects in molecular clusters when the experimental time, $\tau_{\rm e}$, becomes of the order of $1/\Gamma$. To obtain predictions for time-dependent quantities, we must first obtain the "slow" and "fast" contributions from the master equation. The method was indicated for the specific heat in Ref. [49] and also can be applied to the magnetic susceptibility. The result is that, for fixed δ and a given magnitude and orientation of the magnetic field, the time-dependent specific heat $C_{\rm m}$ follows exponential relaxation for $t \gg \tau_0$,

$$C_{\rm m} = C_{\rm eq} - \left(C_{\rm eq} - C_0\right) \exp(-\Gamma t), \tag{14}$$

where C_0 is the contribution to the specific heat of all these fast processes (at zero magnetic field, C_0 just equals the specific heat for one of the two potential wells) and $C_{\rm eq}$ is the specific heat measured under thermal equilibrium conditions.

If the temperature or the magnetic field has low-amplitude periodical variation with time (so that the master equation can be expanded in such perturbations, and terms other than linear can safely be disregarded), then the frequency-dependent specific heat and the ac susceptibility are given by the Debye equations

$$C'_{\rm m} = C_0 + \frac{C_{\rm eq} - C_0}{1 + (\omega/\Gamma)^2} \tag{15}$$

$$C''_{\rm m} = \frac{\omega}{\Gamma}\left(C_{\rm m} - C_0\right) \tag{16}$$

$$\chi' = \chi_0 + \frac{\chi_{\rm eq} - \chi_0}{1 + (\omega/\Gamma)^2} \tag{17}$$

$$\chi'' = \frac{\omega}{\Gamma}\left(\chi' - \chi_0\right) \tag{18}$$

where again C_0 and χ_0 are "fast" contributions and $C'_{\rm m}$ (or χ') and $C''_{\rm m}$ (or χ'') give

the responses of the system that are in-phase and shifted by 90°, respectively, with the external perturbation. C_0 can be calculated using the values for the fast eigenvalues and eigenvectors of W and its derivatives with respect to temperature. The method was illustrated by Fernández et al. [49] for the specific heat and is valid for the susceptibility also, although we prefer to skip here the details of the calculation. We define a new matrix $Y = \mathrm{d}W/\mathrm{d}T$ and denote by P_{eq} and W_{eq}, respectively, the vector of populations and the matrix of transition rates in thermal equilibrium. We can write $Y P_{\mathrm{eq}} = \sum_\nu a_\nu \phi_\nu$, where ϕ_ν is an eigenvector of W_{eq}. The slow component of the specific heat (that is, the contribution that decays with a relaxation rate Γ) is given by

$$C_{\mathrm{eq}} - C_0 = \frac{a_1 \mathcal{E}_1}{\Gamma}, \tag{19}$$

where $\mathcal{E}_1 = \sum_l E_l f_l^{(1)}$ is the average energy in the eigenstate ϕ_1, which corresponds to Γ, and $f_l^{(1)}$ are the populations of the energy levels, l, in this state. Because the equilibrium specific heat can be easily calculated when the energy levels of the Hamiltonian are known, Eq. (19) can be used to calculate C_0. Using a fully analogous method, and taking $Y = \mathrm{d}W/\mathrm{d}B$, it is possible to write the slow component of the susceptibility as:

$$\chi_{\mathrm{eq}} - \chi_0 = \frac{a_1 \mathcal{M}_1}{\Gamma} \tag{20}$$

where $\mathcal{M}_1 = \sum_l \mu_l f_l^{(1)}$ is now the average magnetic moment (projected along the direction of the applied field) in the state l.

To obtain numerical results that can be compared with the measured quantities, it is still necessary to average Eqs. (14)–(18) over a distribution of bias fields and, in case the experiments are performed on powder samples, over a distribution of orientations of the anisotropy axes with respect to the magnetic field. In what follows we shall use a Gaussian distribution of bias fields, and the width, σ, of the distribution found experimentally in Refs [43] and [44] – $\sigma = 250\,\mathrm{Oe}$ for Fe_8 and $\sigma = 200\,\mathrm{Oe}$ for Mn_{12}. Very similar results, although in slightly better agreement with the experimental specific heat and susceptibility data, are obtained if the average is taken over a Lorentzian distribution [49]. In the next section we use this model to simulate numerically the experimental results obtained for the three molecular clusters.

5.4 Experimental Results and Discussion

To estimate the magnetic specific heat C_{m}, the contribution of the lattice to the total specific heat must first be determined. This contribution is extracted from the T^3 contribution to the specific heat as measured at zero field between $T = 3$ and $T = 11\,\mathrm{K}$. The Debye temperatures obtained in this way are $\Theta_{\mathrm{D}} = 35$–$41\,\mathrm{K}$ [30, 31,

61] for Mn_{12}, $\Theta_D = 35$ K [30] for Fe_8, and $\Theta_D = 41$ K [30] for Mn_4. Using Eq. (12), these values give $c_s = 1.4$–1.6×10^3 m/s, $c_s = 1.5 \times 10^3$ m/s, and $c_s = 1.5 \times 10^3$ m/s, respectively.

5.4.1 Superparamagnetic Blocking in Zero Applied Field

The relaxation rate of Mn_{12}, Fe_8, and Mn_4 follows the Arrhenius law, at least above the crossover temperature T_Q, that is, Γ decreases exponentially with T. At a given temperature, usually called the blocking temperature T_B, the relaxation rate becomes of order τ_e^{-1}, where τ_e is the typical time in a particular measurement. Using this condition and Eq. (4) for Γ, it follows that

$$T_B = \frac{U}{k_B \ln(\Gamma_0 \tau_e)} \tag{21}$$

Below T_B, the reversal of the spin cannot be completed within the experimental time, τ_e, thus the response of the system decreases. The phenomenon of superparamagnetic blocking can easily be studied by means of frequency-dependent ac susceptibility experiments. For this technique, $\tau_e = 1/\omega$, where ω is the angular frequency of the ac magnetic field. As an example, we show in Fig. 9 ac susceptibility data for Fe_8 measured as a function of temperature for different values of ω.

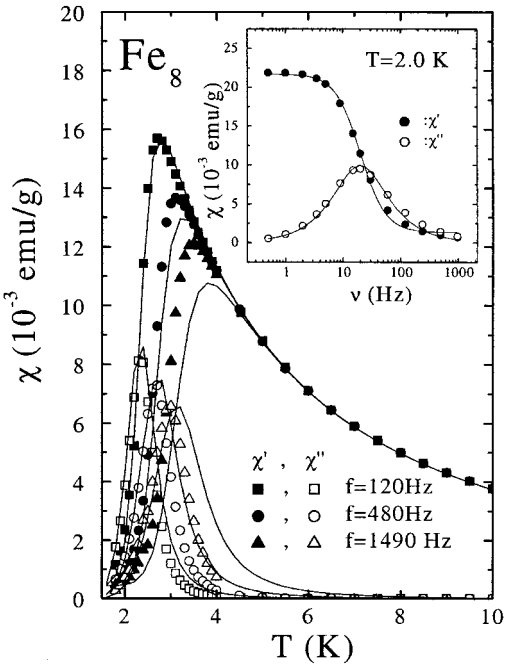

Fig. 9. Real and imaginary components of the ac susceptibility of Fe_8 measured at zero field for different frequencies as a function of temperature. The lines are calculated results that follow from Eq. (17). The inset shows the frequency-dependence of χ measured at $T = 2.0$ K, together with the calculated results (lines).

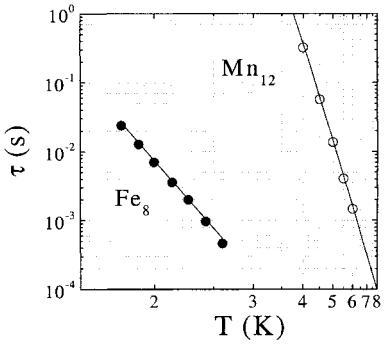

Fig. 10. Temperature-dependence of the spin–lattice relaxation time of Fe_8 and Mn_{12} as derived from zero-field frequency-dependent susceptibility ($\chi(\omega)$) data. The lines are calculated results that follow from Eq. (17).

For $T > 4\,\mathrm{K}$ the susceptibility is real (in the frequency range covered) and equals the equilibrium susceptibility, $\chi_{\mathrm{eq}} \propto 1/T$. Below 4 K the real component $\chi'(T)$ has a maximum at a blocking temperature T_{B}, and then decreases to a value much smaller than χ_{eq}. T_{B} decreases with ω, in full agreement with Eq. (21). The observed behavior is characteristic of a superparamagnetic system. Just below T_{B} a peak in the imaginary component χ'' is also observed. As shown in the inset of the figure, the frequency dependence of χ' and χ'' can be well fitted to the Debye function, Eqs (17) and (18). From this fit the spin–lattice relaxation rate, Γ, can be obtained. In Fig. 10 we show the temperature-dependence of τ measured for Fe_8 and Mn_{12} and compare it with the calculations.

The relaxation time is seen to follow the Arrhenius law at zero and finite parallel fields. In this way, the value of q, the strength of the spin–phonon interaction, which gives the best agreement with the experiments can be estimated. From q the average speed of sound is obtained by use of Eq. (11). The results are $c_{\mathrm{s}} = 0.7 \times 10^3$ m/s for Fe_8 and $c_{\mathrm{s}} = 0.8 \times 10^3$ m/s for Mn_{12}. These values are a factor of two smaller than those found from the specific heat. The reason for the observed difference might be because only specific modes contribute to the spin–lattice relaxation, whereas all modes contribute to the specific heat.

Next we show that, under the appropriate conditions, the blocking of the magnetic moment of the molecular clusters can also be observed by means of specific heat measurements. Below T_{B}, the population of the levels cannot reach equilibrium during the measurement time and the measured C_{m} will approach C_0. At low temperatures C_0, which arises mainly as a result of transitions to excited states from the ground state doublet, decreases exponentially. In general, $C_{\mathrm{eq}} > C_0$, even at zero applied field, because the ground doublet of the molecule is split by an average amount δ due to hyperfine and dipole–dipole interactions. Actually, $C_{\mathrm{eq}} - C_0$ is approximately given by the two-level Schottky anomaly associated with (slow) transitions within the ground state doublet, although much broadened by the distribution of dipolar fields. This is illustrated in Fig. 11, where the two components of the specific heat are plotted as a function of T.

In Fig. 12 we show the magnetic specific heat of Fe_8 measured at zero field.

The data show a shoulder-like anomaly at approximately $T = 1.3\,\mathrm{K}$. This anomaly occurs at about the same temperature range in which the superparamagnetic

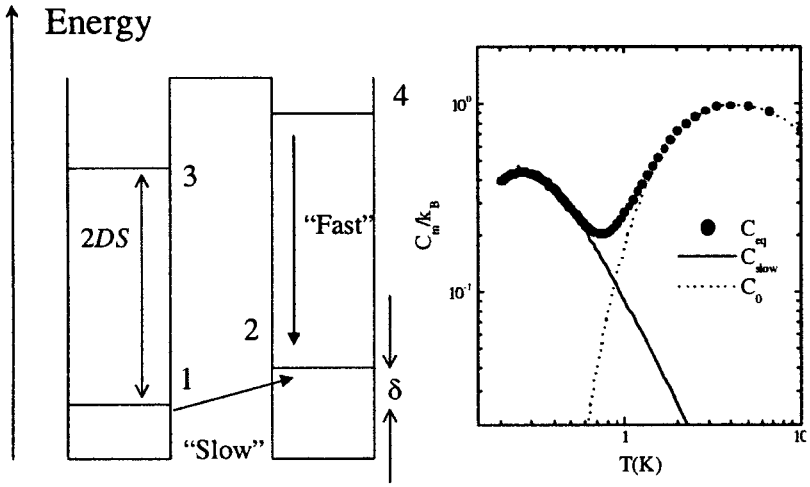

Fig. 11. Left: Schematic picture of a double-well potential where some of the lowest-lying energy levels and the possible transitions between them are indicated. Right: fast intra-well transitions give rise to the high temperature contribution to C_{m} (dotted line), whereas slow transitions between the two wells are responsible for the low-temperature Schottky anomaly (full line).

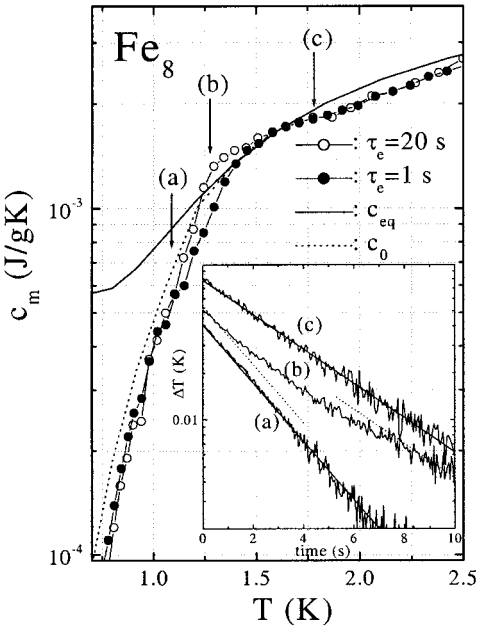

Fig. 12. Zero field magnetic specific heat for an oriented sample [30] of Fe_8 as a function of temperature for two different experimental times: $\tau_{\mathrm{e}} = 20\,\mathrm{s}$ for open circles, $\tau_{\mathrm{e}} = 1\,\mathrm{s}$ for closed circles. Included are the calculations following Eq. (14): full line denotes C_{eq}, dotted line C_0. The inset shows the temperature variation (on a log-scale) with time at three different temperatures: $T = 1.09\,\mathrm{K}$ at (a), $T = 1.27\,\mathrm{K}$ at (b), $T = 1.78\,\mathrm{K}$ at (c). In this scale, a straight line means that there is a single relaxation time dominating. The heat capacity is proportional to the slope of the straight line.

blocking is observed from susceptibility measurements with long experiment times ($\tau_e \approx 100\,s$). To ascertain whether the anomaly is indeed because of superparamagnetic blocking, measurements with different values of τ_e were performed. As mentioned in Section2, τ_e corresponds to the length of the power pulse applied to the sample; this can be modified by changing the thermal resistance of the thermal link from the sample to the bath. The results show that the anomaly shifts towards lower temperatures as τ_e increases, in agreement with the interpretation based on superparamagnetic blocking. The inset of the figure shows the relaxation of the temperature of the sample on a semi-logarithmic scale at three different temperatures, below, near, and above T_B. The slope of these curves is proportional to C_m. The relaxation is clearly non-exponential near T_B, which indicates that C_m increases with time during the time-interval the power pulse is applied. In contrast, the temperature of the calorimeter decays exponentially when T is distinctly below or above T_B. In the figure we have plotted the calculated "fast" specific heat and the equilibrium specific heat, obtained for a Gaussian distribution of bias fields with a mean width $\sigma = 250\,Oe$. We emphasize that the blocking temperature can only be observed because the inhomogeneous broadening makes $C_{eq} > C_0$ near the corresponding blocking temperature T_B. The value of σ obtained from specific heat data corresponds well with previous estimates. For Mn_{12} the specific heat does not have any anomaly near $T_B \approx 3\,K$ [28, 61, 31]. This probably because $C_{eq} - C_0$ decreases in porportion T^{-2} and must thus be approximately one order of magnitude smaller than for Fe_8.

5.4.2 Phonon-assisted Quantum Tunneling in Parallel Fields

It is by now well established that the mechanism of resonant tunneling between nearly degenerate states of Mn_{12}, Fe_8, Mn_4 and other molecules promotes the reversal of the spin when B_z is near a field value at which two energy levels cross (cf. Fig. 3). This phenomenon has been studied by several groups using different experimental techniques, such as hysteresis loops, magnetic relaxation, and ac susceptibility. In this section, we will show that the existence of resonant tunneling also leads to an unusual variation of C_m with the longitudinal magnetic field when the temperature is below T_B.

In Fig. 13 we show frequency-dependent specific heat data measured by Fominaya et al. [31] at different temperatures on a very small single-crystal of Mn_{12}. It is important to note that for the frequencies used in the experiment (4 to 20 Hz), T_B is expected to be above 4.75 K at zero field. The measured C_m is, therefore, not an equilibrium quantity and, indeed, it is observed that the data lie below the calculated C_{eq}, also shown in the figure, at low fields ($B_z \leq 3B_1$, approximately). Moreover, C_m approaches C_{eq} when the frequency ω decreases (not shown) [31], in agreement with Eq. (15). The most remarkable feature is that the specific heat has maxima near the crossing fields. These data were interpreted qualitatively by Fominaya et al. [31]. It follows from Fig. 7 that $\Gamma \ll \omega$ away from the resonant fields, but it can become of the same order when $B_z \approx B_{n,m}$. Therefore, the field-dependence of C_m at a given frequency just reflects the resonant behavior of the relaxation rate, caused by the

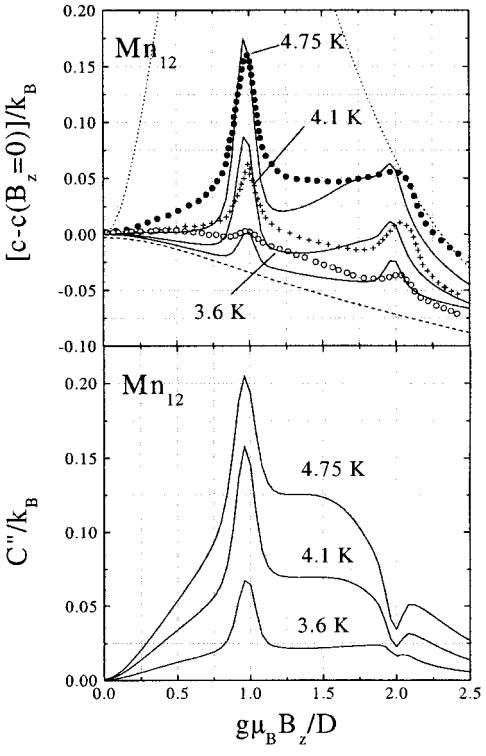

Fig. 13. Frequency-dependent magnetic specific heat of Mn_{12} measured for $\omega/2\pi = 4\,\mathrm{Hz}$ and three different temperatures below T_B: $T = 3.6$, 4.1, and 4.75 K; top plot: amplitude $c = \sqrt{\left[(C'_m)^2 + (C''_m)^2\right]}$, bottom plot: imaginary part. The lines represent the calculated specific heat that follows from Eqs (15) and (19) averaged over a Gaussian distribution of bias fields.

existence of quantum tunneling. The first resonance, at zero field, is not observed. As argued in the preceding section, the reason is probably that $C_{eq} \approx C_0$ at these temperatures because $k_B T \gg \delta$. The data show that C_m approaches equilibrium when T increases, indicating that the relaxation is thermally activated, as expected. It can also be seen in the figure that the model, described in the previous section, reproduces the experimental results reasonably well. The calculated results follow from Eq. (15), averaged over a Gaussian distribution of bias fields with $\sigma = 200\,\mathrm{Oe}$. Similar results were obtained for Mn_{12} using a power-pulse method [62], instead of a frequency modulation.

In Fig. 14 we have plotted the specific heat of a sample of oriented powder of Fe_8.

The data were recorded at a few temperatures around the zero-field blocking temperature, $T_B \approx 1.3\,\mathrm{K}$. The numerical simulation of the data is more difficult, because the orientation of the sample is only partly known from magnetization measurements [30]. We can, however, obtain a reasonable fit of the data by introducing a misalignment of a few degrees relative to the easy axis. For the highest temperature shown ($T = 1.57\,\mathrm{K}$), i. e. just above the zero-field blocking temperature (see Fig. 12), the field dependence of C_m mimics the well-known multi-level Schottky anomaly. The calculations show no difference between the equilibrium and non-equilibrium specific heat at $T = 1.57\,\mathrm{K}$, which confirms that the system remains in thermal equilibrium at this temperature for heat pulses of approximately 15 s. For

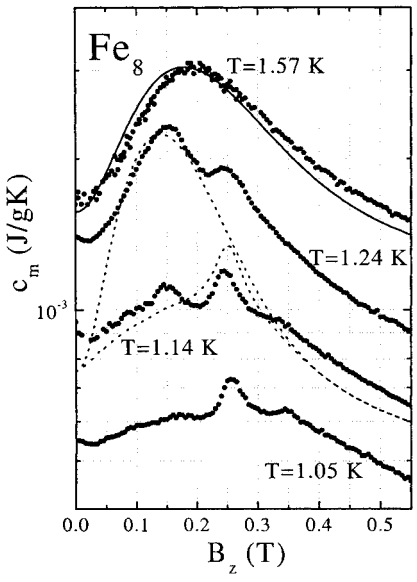

Fig. 14. Dependence of measured specific heat on B_z (black dots) at various temperatures around T_B for an oriented sample [30] of Fe_8. The full lines represent calculations for the data at $T = 1.57\,K$ (equilibrium and non-equilibrium curves fall on top of each other). The dotted lines are calculated for the data at $T = 1.14\,K$, lower line: non-equilibrium; upper line: equilibrium. The calculations are based on the model described in Section 3.

temperatures very close to or just below the zero-field T_B of approximately 1.3 K the measured specific heat lies below the expected equilibrium value (for most of the field range) and also shows clear increases in C_m at specific field values, i. e. at $B_z = 0\,T$, 0.15 T, 0.25 T, and 0.35 T, approximately (see the curve for $T = 1.14\,K$). The value $B_z = 0.25\,T$ is very close to that corresponding to the first level crossing for Fe_8, as obtained from the ac susceptibility measurements [47, 30]. We argue that the peaks at $B_z = 0\,T$ and 0.25 T are a result of the zeroth and first level crossing in Fe_8, whereas the origin of the other two peaks lies in the shape of the equilibrium specific heat. This argument is strengthened by the calculations for the data at $T = 1.14\,K$, included in Fig. 14. Initially the specific heat decreases, because at zero applied field the levels are in resonance. The effect can be detected under these condition because, for Fe_8, C_{eq} is large enough relative to C_0 at these lower temperatures. The maximum at $B_z = 0.15\,T$ arises because the system, although not fully in equilibrium, does reflect the field variation of the equilibrium specific heat curve which has its maximum at $B_z = 0.14\,T$ (solid curve). At $B_z = 0.25\,T$ the levels cross and the system is brought into resonance again, the spin–lattice relaxation rate increases, leading to the third peak. Finally, at some higher field value, the classical activation energy is reduced sufficiently for the system to come into equilibrium, which gives rise to the fourth peak near 0.35 T. Note that the calculation shows that, although the specific heat almost reaches the calculated equilibrium value at $B_z = 0.25\,T$, it departs once more, further from equilibrium, at higher fields. Only at approximately $B_z = 0.38\,T$ the system finally reaches equilibrium again. The calculations for the other two temperatures, $T = 1.05\,K$ and $T = 1.24\,K$, show similar behavior.

5.4.3 Phonon-assisted Quantum Tunneling in Perpendicular Fields

In this section we discuss the effect of a transverse field on resonant tunneling. It is important to realize first that, although the samples measured always contain a certain amount of misalignment, the specific heat data measured at low temperature and high fields ($B_\perp > 1\,\mathrm{T}$ for $S = 10$) are mainly dominated by those crystals having the easy axes nearly perpendicular to the applied field. The reason is that a relatively small B_z can induce a splitting Δ_Z of the ground state that is larger than $k_\mathrm{B}T$, thus exponentially suppressing C_m. For example, if $\theta < 86^\circ$ (here, $\theta = 90^\circ$ corresponds with the perpendicular orientation), $\Delta_Z > 2\,\mathrm{K}$ for a field $B \geq 1\,\mathrm{T}$. The peak of the Schottky anomaly associated with the two lowest magnetic energy levels is then already shifted towards $T > 1\,\mathrm{K}$. This unique property of the specific heat makes it possible to measure easily the relaxation rate as a function of $B_\perp$, *even in randomly oriented samples!*

In Figs. 15 and 16, we plot the temperature dependence of C_m of Fe_8 and Mn_{12} (oriented samples [30]) measured at different values of $B_\perp$ [28]. The kink-like anomaly that we associate with the equilibrium to non-equilibrium transition shifts towards progressively lower temperatures as $B_\perp$ increases and is no longer present for fields $B_\perp \geq 2\,\mathrm{T}$ and 5 T for, respectively, Fe_8 and Mn_{12}. The interpretation of these data is based on the effect that $B_\perp$ has on Δ_t and on Γ, which was illustrated in Figs. 4 and 8, respectively. The values of Δ_t of all tunnel-split levels increase as $B_\perp$ increases. As a result, resonant tunneling can proceed through progressively lower-lying excited states, as soon as Δ_t becomes of the order of, or larger than, δ and Δ_Z for these states. The energy barrier for the spin reversal is roughly given by $U = \Delta E_{l_2,2}$, with l_2 the first energy level that fulfils $\Delta_\mathrm{t} \approx \delta$. As $B_\perp$ increases, lower-lying excited states fulfil the above condition and as a result U decreases. For a fixed experimental time the blocking temperature must, according to Eq. (21), also decrease (see also Fig. 8). The values of $B_\perp$ which are necessary to reduce T_B below 1 K are larger for Mn_{12} than for Fe_8, in agreement with the larger anisotropy D of the former compound.

The activation energy can be estimated from the values of T_B and τ_e as $U = k_\mathrm{B}T_\mathrm{B}\ln(\Gamma_0\tau_\mathrm{e})$. This enables estimation of which levels contribute most to the relaxation path. At zero field, tunneling proceeds via the tunnel-split $m = \pm 4$ states for Mn_{12} and via $m = \pm 5$ for Fe_8 [30]. For finite fields, lower-lying levels contribute. As an example, we get $U \approx 9.5\,\mathrm{K}$ at $B_\perp = 1.5\,\mathrm{T}$ and $T_\mathrm{B} = 0.5\,\mathrm{K}$ for Fe_8, and $U \approx 22\,\mathrm{K}$ at $B_\perp = 4\,\mathrm{T}$ and $T_\mathrm{B} = 1.3\,\mathrm{K}$ for Mn_{12}. These values compare quite well with the calculated separation between the tunnel-split $m = \pm 10$ and $m' = \pm 8$ levels, suggesting that tunneling proceeds via these excited states ($m' = \pm 8$). To understand qualitatively why these states contribute most to tunneling, we can compare the splittings Δ_t and $\Delta_Z = 2g\mu_\mathrm{B}m'B_z$ induced by the two components of the applied field. We use as a typical value $\theta \geq 89^\circ$, because it gives a Schottky anomaly centered around and below T_B for these field values and therefore corresponds to the molecules which contribute most to C_m. The calculated Δ_t of the $m' = \pm 8$ levels is as large as 0.43 K for Fe_8 and 0.55 K for Mn_{12}, being larger than the average δ and of the order of $\Delta_Z \leq 0.5 - 1.4\,\mathrm{K}$. This qualitative interpretation is further confirmed by numerical calculations that follow from Eq. (14), and which are shown as lines in the same Figs. 15 and 16. They describe reasonably well the field dependence of T_B.

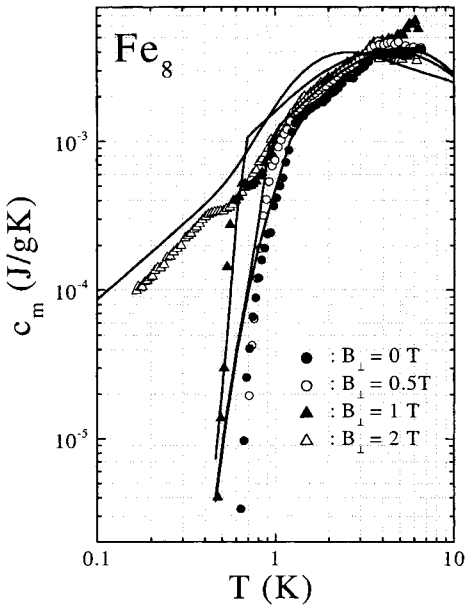

Fig. 15. Magnetic specific heat of an oriented sample [30] of Fe_8 measured for different values of $B_\perp$. The lines represent the calculated time-dependent specific heat that follow from Eq. (14) and averaging over a Gaussian distribution of bias fields with $\sigma = 250\,\mathrm{Oe}$.

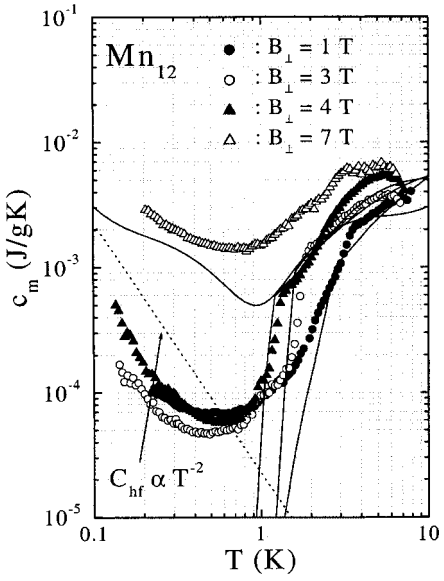

Fig. 16. Magnetic specific heat of a sample of oriented single crystals [30] of Mn_{12} measured for different values of $B_\perp$. The full lines give the calculated time-dependent specific heat that follows from Eq. (14) and averaging over a Gaussian distribution of bias fields with $\sigma = 200\,\mathrm{Oe}$. The dotted line represents the calculated hyperfine contribution under thermal equilibrium conditions.

At high enough fields we expect that $\Delta_t \geq \delta$ even for the ground state (see Fig. 4). Under this condition the wave-functions of the two lowest energy states can become delocalized. At temperatures low compared with the separation with the nearest excited level, the spin–lattice relaxation is then dominated by direct transitions between these two states, which results in a nearly temperature-independent

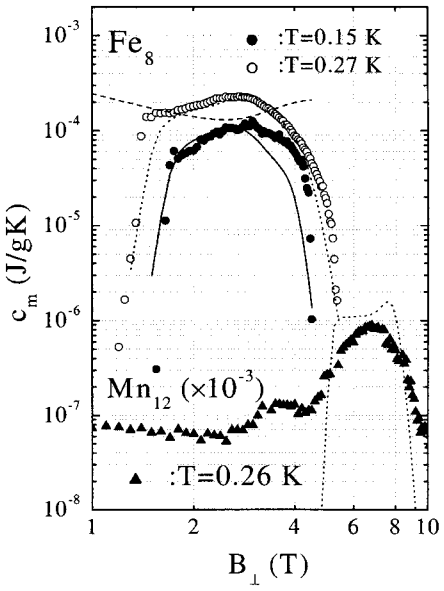

Fig. 17. Field dependence of the magnetic specific heat of oriented samples [30] of Fe_8 and Mn_{12} at low temperatures. The field is applied perpendicular to the easy axes. The lines represent calculations following the model described in Section 3: solid line lowest temperature, dotted line, higher temperature. The dashed line is the calculated behavior at $T = 0.15\,\mathrm{K}$ for Fe_8 in the absence of coherence, i. e., $\Delta_t = 0$.

rate Γ_{dir} (see Fig. 8). In agreement with this, it is observed in Figs. 15 and 16 that C_{m} measured for $B_\perp \geq 2\,\mathrm{T}$ for Fe_8 and $\geq 5\,\mathrm{T}$ for Mn_{12} *does not show any deviation from equilibrium down to the lowest temperatures*. We note here that the observation of a temperature-independent Γ does in itself not give sufficient evidence for QC, because it characterizes the relaxation of the energy of the system. It is, however, remarkable that, at these high transverse fields, direct incoherent processes occur at rates of the order of $1\,\mathrm{s}^{-1}$ or faster (compare with $\Gamma \leq 10^{-4}\,\mathrm{s}^{-1}$ measured at zero field [22, 43, 63]), indicating that the magnetic field induces considerable delocalization of the two lowest energy wave-functions.

To obtain further insight in the physics of these incoherent tunneling processes it is convenient to study the field-dependence of the specific heat in more detail. In Fig. 17 we show the magnetic specific heat of both compounds as a function of $B_\perp$ measured in the temperature range $T = 0.1 - 0.3\,\mathrm{K}$.

At low fields, C_{m} is very small, indicating again that the electronic spins are out of equilibrium at these temperatures. At finite fields $B_{\mathrm{B}} \approx 1.5\,\mathrm{T}$, C_{m} for Fe_8 rises a very steeply from a hardly observable value. C_{m} reaches a maximum at approximately $B_\perp = 2 - 2.5\,\mathrm{T}$ and then decreases abruptly at higher fields. The same qualitative behavior is seen for Mn_{12}, although the maximum is shifted to higher fields. Also the "background" specific heat for Mn_{12} is higher; this, we shall show below, is because of hyperfine contributions in this compound. Taking into consideration how T_{B} decreases with $B_\perp$, it makes sense to attribute the first jump to the transition from non-equilibrium to thermal equilibrium conditions. In fact, B_{B} decreases as τ_{e} increases, and is thus equivalent to the blocking phenomenon that occurs when T is reduced. For a fixed experimental time τ_{e}, the unblocking of the spins occurs at the values (T_{B},B_{B}), indicated as open circles in Fig. 8, when the spin–lattice relaxation

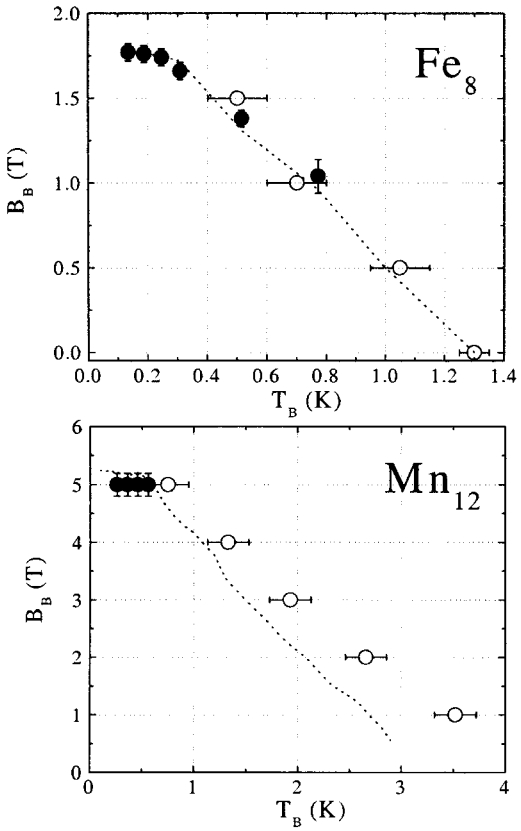

Fig. 18. Temperature-dependence of B_B for Fe_8 (upper plot) and Mn_{12} (lower plot). Open circles are obtained from $C_m(T)$, closed circles from $C_m(B)$ measurements. The dotted lines follow from calculations of C_m as a function of $B_\perp$, like those shown in Fig. 17. Below a "cross-over" temperature $T_Q \approx 0.2\,K$ for Fe_8 and $T_Q \approx 0.6\,K$ for Mn_{12}, B_B becomes effectively temperature-independent, marking the onset of predominant relaxation through the ground-state doublet.

becomes fast enough through the action of the applied magnetic field so that the condition $\Gamma\tau_e \approx 1$ is fulfilled.

As can be inferred from inspection of Fig. 8, the variation of B_B with T, shown in Fig. 18, enables direct mapping of the temperature-dependence of Γ, thus providing valuable information about the nature of the relaxation process. We observe that B_B first increases roughly linearly as T decreases and then reaches a constant value $B_{B,0} \approx 1.8\,T$ for Fe_8 and $B_{B,0} = 5\,T$ for Mn_{12}.

The saturation marks the "cross-over" from thermally activated relaxation to relaxation via the ground state. The application of $B_\perp$ makes it possible to study incoherent tunneling at high enough relaxation rates, so that very long experimental times are not required. In this way, it is possible to measure the cross-over temperature $T_Q \approx 0.2\,K$ for Fe_8 and $T_Q \approx 0.6\,K$ for Mn_{12}. The former value compares well with $T_Q \approx 0.4\,K$ obtained previously [20] from magnetic relaxation experiments recorded at low fields. The cross-over temperature found for Mn_{12} is smaller than $T_Q \approx 2\,K$ obtained from long-term magnetic relaxation experiments performed for $B_\perp \approx 0$ [17, 22]. It agrees well with the observation that the widths of the hysteresis loops only become independent of T below $0.595\,K \leq T_Q \leq 0.895\,K$ [64], however,

and with a more recent determination of T_Q performed also using large magnetic longitudinal and transverse fields [65].

We have found that T_Q, and the magnitude and temperature dependence of B_B (and therefore Γ), above and below T_Q are rather well reproduced by the numerical calculations that follow from Eq. (9). This is an important point because theoretical arguments [66, 67], and recent experimental evidence [63], support the idea that incoherent tunneling between the two lowest energy states is mainly induced by fluctuations of the spin-bath, whereas in the calculations shown in Fig. 18 only transitions induced by phonons were considered. There are, however, two possible arguments which might explain this apparent contradiction. The first is that the specific heat measurements shown here are performed in large transverse fields. As discussed in Section 3.3, the rate Γ_{dir} for a direct process from the state $l = 2$ to the ground state, accompanied by the emission of a phonon, can then become large enough to account for the observed relaxation rates. Using, for $\theta = 89^\circ$, Eq. (10) and the predictions of Ref. [67] we calculate that phonon-assisted tunneling becomes dominant above $B_\perp \approx 1\,\mathrm{T}$, in agreement with our observations.

There is a second argument against the interpretation in terms of the fluctuation model, which is rather general. Specific heat measurements are only sensitive to the rate at which the system approaches thermal equilibrium with the lattice at the new temperature. To reach equilibrium it is then necessary that the electronic spin and the lattice exchange energy. A relaxation mechanism for the electronic spins mediated by the nuclear spin bath will, therefore, be efficient only if the nuclei reach thermal equilibrium faster than the electrons. As we will see in the next section, this is actually not so for the molecular clusters studied here. Whether or not the presence of the nuclear-induced processes can explain the disagreement between the experimental T_Q values found for high and low fields $B_\perp$ is not clear and probably requires a more detailed theoretical treatment that includes the effect of both mechanisms.

5.4.4 Time-dependent Nuclear Specific Heat

In this section, we shall discuss the relationship between the electronic relaxation and the nuclear spin-lattice relaxation by which the nuclear spins approach thermal equilibrium. The low temperature C_m data of Mn_{12} shown in Fig. 16 increase below approximately $T = 0.5\,\mathrm{K}$ for all field values. This increase can be related to the existence of a nuclear contribution to the specific heat C_{nucl}. It arises because the hyperfine interaction with the electronic spins splits the nuclear magnetic levels. It is not observed for Fe_8, in agreement with the observation that only 2% of the Fe nuclei have a nuclear spin moment $I = 1/2$, whereas all Mn nuclei have a nuclear spin $I = 5/2$. The absence of a nuclear contribution to the specific heat in Fe_8 for $T > 0.1\,\mathrm{K}$ (and even up to 9 T) shows that in this temperature range the nuclear specific heat of the protons and N nuclei surrounding the Fe ions can be neglected. The underlying reason is that the hyperfine interaction with these nuclei is much weaker and thus the splitting of the nuclear levels is correspondingly smaller. Because the same is expected for the protons in Mn_{12} we have only to consider the Mn nuclei. Under equilibrium conditions, C_{nucl} should take the form of a multilevel Schottky

and thus be proportional to T^{-2} in the high-temperature limit. It should, moreover, depend on $B_\perp$ only slightly, in view of the low value of the nuclear moment. It can be calculated as $C_{\rm nucl} = [32A(\mathrm{Mn}^{3+}) + 9A(\mathrm{Mn}^{4+})]I(I+1)T^{-2}$, which is valid for a magnetically ordered cluster [59]. The two terms correspond to the eight Mn^{3+} ($S = 2$) and the four Mn^{4+} ($S = 3/2$) ions, respectively. The hyperfine constants can be taken as $A(\mathrm{Mn}^{3+}) = 6\,\mathrm{mK}$ and $A(\mathrm{Mn}^{4+}) = 9\,\mathrm{mK}$, as was used to explain the inhomogeneous broadening obtained from low-T relaxation experiments [44]. Below 5 T, the measured specific heat is actually much smaller than that calculated (indicated by the dotted line in Fig. 16). The experimental $C_{\rm nucl}$, moreover, strongly increases as the field is raised, and this variation is much larger than the expected effect caused by the Zeeman splitting of the nuclear energy levels.

In our interpretation of these data we consider the dynamics of the nuclear spins. To reach equilibrium, the nuclear spins must undergo fast transitions between their different magnetic states m_I. Because there is no direct coupling between the nuclear spins and the lattice, these transitions cannot be induced by direct coupling to the phonon-bath. For the nuclei of magnetic insulators the nuclear relaxation is mainly driven by the fluctuation of the electronic spins which, in turn, is induced by the spin-phonon interaction (see Fig. 19). Therefore the nuclei can only relax their energy to the lattice indirectly via the electronic spins [52, 68].

A rather general expression relates the relaxation time T_1 of the nuclei to the correlation function of the (time-dependent) transverse hyperfine field $\delta H(t)$ at the nucleus [68]:

$$\frac{1}{T_1} = \frac{1}{2}(\gamma_n)^2 \int_{-\infty}^{\infty} \langle\{\delta H^+(t)\delta H^-(0)\}\rangle \cos(\omega_0 t)dt \tag{22}$$

where γ_n is the nuclear gyromagnetic ratio, and $\omega_0 \approx As$ is the Larmor frequency of the nucleus. At low T, the main contribution to $\langle\{\delta H^+(t)\delta H^-(0)\}\rangle$ (where $\langle\rangle$ indicates a thermal average) is given by transitions between the lowest-lying energy levels of the electronic spin, which are schematically depicted in Fig. 19. We have seen in Section 3.3 that transitions between levels located in the same potential well occur at a rate Γ_0. At low $B_\perp$ these transitions must play the dominant role in the nuclear relaxation, but they become exponentially less probable as T decreases. As

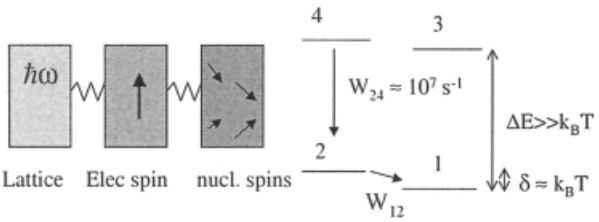

Fig. 19. Schematic diagram showing the interaction between the lattice and the nuclear spins mediated by the fluctuations of the electronic spin (left). The plot on the right shows the transitions between electronic levels which play a role in nuclear spin–lattice relaxation at low temperature.

a result, the nuclear spins remain at an effective spin temperature that is higher than the temperature of the lattice (the concept of spin temperature is well defined here, because the nuclear spin–spin relaxation time is quite fast, i. e. nuclear flip-flop transitions occur at a rate $T_2^{-1} \gg T_1^{-1}$, so that the nuclear spin system itself is in thermal equilibrium). This explains why the measured C_{nucl} lies below the calculated thermal equilibrium value. When $B_\perp \geq 5\,\mathrm{T}$, fast direct transitions between the two lowest lying levels take place down to very low T, thus "connecting" the nuclear spins to the phonon-bath. As a result the nuclear specific heat is "recovered" when Γ_{dir} becomes of the order of τ_{e}^{-1}. The observed increase of C_{nucl} with $B_\perp$ is in fact another piece of evidence for our interpretation that the transverse field induces fast direct transitions between the two lowest energy levels of the electronic spin.

5.4.5 Detection of the Tunnel Splitting for High Transverse Fields

The experimental data discussed above show that the rate of direct incoherent processes between the lowest-energy states becomes very fast at high enough $B_\perp$. According to Eq. (10), this indicates that the wave-functions of the ground state doublet have become delocalized through the action of the magnetic field $B_\perp$. The question whether full coherence is indeed established can best be answered by the observation of the ensuing quantum splitting of the ground state in the energy spectrum. At low temperatures, when only the two lowest energy levels contribute to the specific heat, the contribution of each of the molecules to C_{eq} is given by the well-known Schottky anomaly

$$C_{\mathrm{eq}}/k_{\mathrm{B}} \approx \left(\frac{\Delta E_{2,1}}{k_{\mathrm{B}}T}\right)^2 \frac{\exp\left(\Delta E_{2,1}/k_{\mathrm{B}}T\right)}{\left[1+\exp\left(\Delta E_{2,1}/k_{\mathrm{B}}T\right)\right]}, \tag{23}$$

where $\Delta E_{2,1} \approx \sqrt{\left(\Delta_{\mathrm{t}}^2 + \Delta_Z^2\right)}$. According to Eq. (23), C_{eq} should be maximum when $\Delta E_{2,1}$ becomes of the order of $2k_{\mathrm{B}}T$, which provides a way of directly detecting and measuring the energy splitting. We have seen that both Δ_{t} and Δ_Z depend on the orientation of the applied field relative to the anisotropy axis. To simulate the experiment, Eq. (23) must be averaged over the distribution of orientations of the different crystallites which form a sample. The existence of a tunnel splitting gives a minimum value for $\Delta E_{2,1}$ which, moreover, increases with the applied magnetic field much faster than Δ_Z. The existence of QC will thus give rise to a maximum of C_{eq} which is broadened on the high temperature (or energy) side by the effect of the misalignment and the other perturbations such as the hyperfine interaction with the nuclei.

The experimental results shown in Fig. 17 indicate that C_{m} does indeed go through such a maximum at exactly the field range for which Δ_{t} is expected to be of the order of $2k_{\mathrm{B}}T \approx 0.3 - 0.5\,\mathrm{K}$ (see Fig. 4). The different field values required for Fe_8 and Mn_{12} are again in full agreement with the different anisotropy of these compounds. The sharp decrease of C_{m} observed experimentally at higher fields is explained by the strong dependence of the energy splitting on $B_\perp$ [23]: $\Delta_{\mathrm{t}} \propto (B_\perp)^{2S}$, which can be seen in Fig. 4. We stress that an explanation in terms of the Zeeman splitting between

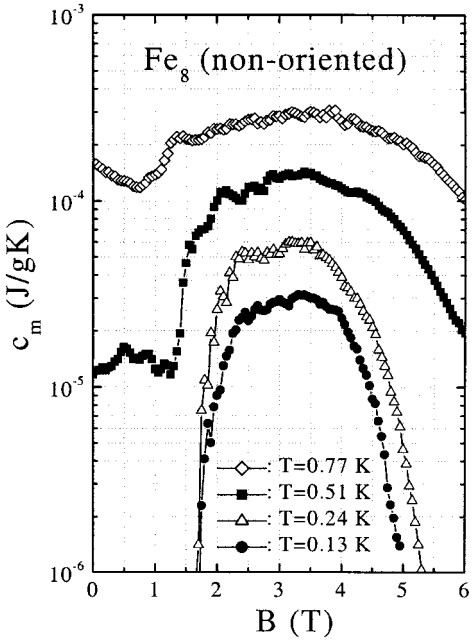

Fig. 20. Field dependence of the magnetic specific heat of a non-oriented (powder) sample of Fe_8 at different temperatures below 1 K. Note that the maxima are reduced by a factor of three compared with those in Fig. 17.

the lowest lying classical states $+S$ and $-S$ is excluded, since it will not depend on the D-value of the molecule, as is the case here, and the shape of the anomaly would be completely different (see Section 5). Included in Fig. 17 are our ab initio calculations. They compare remarkably well with experimental results, showing that the observed Schottky anomaly can only be because of tunnel splitting of the degenerate $S = \pm 10$ ground state levels.

Additional measurements performed on non-oriented samples of Fe_8 are depicted in Fig. 20. They show dependence on the magnetic field that is very close to that found for oriented samples. The reason, as we explained in the previous section, is that only those crystals with the easy axes nearly perpendicular to the field contribute to C_m at low temperatures.

In a powdered sample, for most of the molecules the values of Δ_Z are too large and thus the molecules make no significant contribution to C_{eq} in the measured temperature range. As can be seen by comparison of Figs 17 and 20, the only difference between the results for oriented and non-oriented samples is that the height of the peak, which is proportional to the the number of molecules that contribute, is substantially lower for the non-oriented samples, in agreement with numerical calculations and with the interpretation of the anomaly in terms of the tunnel splitting.

There is still more physical evidence that supports the existence of QC in Mn_{12}. We have already seen that the nuclear spins must interact with the electronic spins if they are to equilibrate to the temperature of the bath. We can now make use of this microscopic probe to decide if tunnel splitting exists at high transverse fields. In Fig. 21 we have plotted the specific heat of a very well oriented single-crystal of Mn_{12}

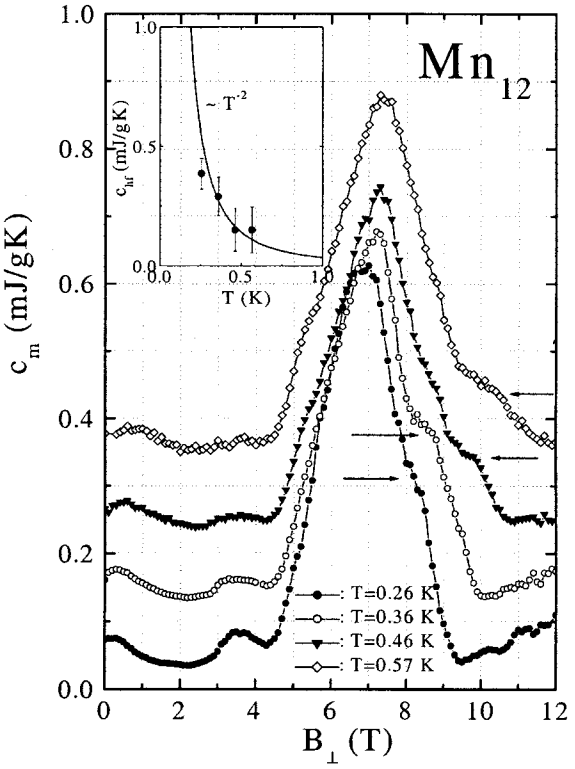

Fig. 21. Field-dependence of the specific heat of an oriented sample [30] of Mn_{12} measured at different temperatures. For clarity, the curves for $T = 0.36$, 0.46, and 0.57 K are shifted upwards by 0.1, 0.2, and $0.3\,\mathrm{mJ\,g^{-1}K}-1$, respectively. The shoulder at the high field side of the main maximum is indicated by the arrows. The inset shows the calculated hyperfine contribution (line) and the value of the specific heat at the observed shoulders.

(we estimate that $\theta \approx 89.3^\circ$ [30]) as a function of $B_\perp$ for different temperatures.

In principle, these data look very similar to those shown in Fig. 17. C_m first reaches equilibrium and then goes through a maximum at the field for which $\Delta_\mathrm{t} \approx 2k_\mathrm{B}T$. There is, however, a second anomaly at slightly higher fields, an anomaly which is more visible the higher the temperature. We recall now that, according to the model for nuclear spin–lattice relaxation (see Fig. 19), the fluctuations of the hyperfine field at nuclear sites depend on the rate of transitions between the lowest-lying energy levels of the electronic spin. If Δ_t becomes appreciably larger than $k_\mathrm{B}T$, the probability of transitions inside the ground state doublet of the electronic spin decreases exponentially, thus the nuclear spin should again start to deviate from equilibrium. In other words, it is now the thermal link between electrons and nuclei that is broken (and not, as before, the connection between the electronic spins and the phonon-bath). It seems therefore justified to attribute the second anomaly observed in the experimental curves $C_\mathrm{m}(B_\perp)$ to this effect. To ascertain this, we have plotted the excess specific heat value at the anomaly as a function of T. It is shown in the inset of Fig. 21. This excess specific heat follows very well the T^{-2} curve predicted for the equilibrium specific heat of the nuclear spins for this compound (see above). In our view, this remarkable result confirms indirectly the presence of an energy gap, the tunnel splitting, in the energy level spectrum for the electronic spin.

5.5 Effect of Decoherence

It is interesting to compare the experimental data with the specific heat $C_{\rm inc}$ predicted for complete incoherence, that is, for $\Delta_{\rm t} = 0$. To calculate $C_{\rm inc}$ while taking into account, at the same time, the classical effects of the transverse field it is possible to substitute the "true" energy states $|1\rangle$ and $|2\rangle$ by linear combinations $|\psi_r\rangle$ and $|\psi_l\rangle$ of these, which have wave-functions localized on each side of the energy barrier. $C_{\rm inc}$ is then given by Eq. (23) but with $|\langle E\,(\psi_r)\rangle - \langle E\,(\psi_l)\rangle|$ instead of $\Delta E_{2,1}$. This "incoherent" specific heat is shown as the dashed line in Fig. 17 (for Fe_8) and is in complete disagreement with experiment, thus showing the need for quantum splitting, $\Delta_{\rm t}$, to explain the abrupt vanishing of the specific heat measured for $B_\perp \geq 4$ T. This is an example of a measurable physical property which can help to distinguish between a coherent superposition and an incoherent mixture of states.

We finally comment on possible decoherence mechanisms arising from the coupling to the environment. Because the materials are insulators, Ohmic dissipation [2] obviously need not be considered. Interactions with phonons are very weak at these low temperatures. We calculate the associated broadening $\hbar/\Gamma_{\rm dir}$ of the electronic tunnel-split levels to be less than 1 mK in our field and temperature ranges. This is much smaller than the temperature at which the specific heat experiments were performed and, therefore, smaller than the tunnel splitting that was studied with this technique at high transverse fields (see also Fig. 4). The main source of decoherence is, therefore, hyperfine (hf) coupling to nuclear spins. Using the formalism of Ref. [5] we can estimate the ensuing level broadening from the expression $\delta = 2\omega_0 N^{1/2}$, where $2\omega_0$ is the splitting of the nuclear levels because of opposite polarization of the electron spin, and N is the number of nuclei involved. In both compounds H nuclei are present; N and Br nuclei also are present in Fe_8. Their hf couplings are, however, very small, leading to $\delta \approx 0.02$ K only. For Fe_8 only 2% of the Fe isotopes carry a nuclear spin. As already mentioned, no nuclear specific heat is expected for Fe_8, in agreement with experimental results. For Mn_{12}, however, a substantial hf contribution from the Mn nuclear spins is expected, and is, indeed, observed. The calculated broadening is $\delta \approx 0.2$ K, making this system a test-case to study the effect of the nuclei. As indicated in Fig. 4, by varying the ground state tunnel splitting, $\Delta_{\rm t}$, with $B_\perp$, we can tune between high and low dissipation limits. For zero and small $B_\perp$, the system is indeed incoherent ($\Delta_{\rm t} \ll \delta$), whereas for sufficiently large $B_\perp$ we have $\Delta_{\rm t} > \delta$ and QC is established.

5.6 Incoherent Tunneling and QC in Molecules with Half-integer Spin

The study of molecules with half-integer spin is interesting because quantum tunneling of the isolated system should be completely suppressed by the destructive interference of equivalent tunneling paths [45, 46]. Correspondingly, the tunnel splitting

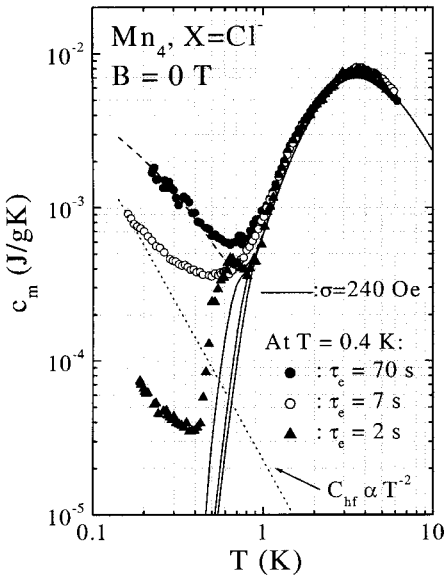

Fig. 22. Time-dependent magnetic specific heat of a sample of non-oriented Mn_4 ($X=Cl^-$) clusters measured at zero field and for three different values of the experimental time τ_e. The full lines are the calculated results using spin–phonon interactions only and averaging over a Gaussian distribution of bias fields of width $\sigma = 240$ Oe. The dashed line corresponds to the calculated specific heat under equilibrium conditions. The dotted line denotes the calculated hyperfine contribution to C_m.

vanishes at zero magnetic field. Under these conditions, the spin must interact with the environment to effect an incoherent transition from the state $-S$ to $+S$. The study of the time-dependent specific heat of such molecular magnets can, therefore, give very useful information on the role played by the nuclei in the mechanism of incoherent tunneling at very low temperatures.

A very interesting example of this kind is represented by a family of Mn_4 molecular magnets [13, 21]. The magnetic core of the molecules is a distorted cube with formula $[Mn_3^{III}Mn^{IV}O_3X]$, where X is a mono-anion. The magnetic moment of the molecules corresponds to a total spin $S = 9/2$. Neutron-scattering measurements [13] performed on different samples of Mn_4 show that the values of D and E can be tuned by changing the anion X. The specific heat at zero field of the compound with $X=Cl^-$ is shown in Fig. 22.

The high-temperature ($T > 1$ K) magnetic specific heat has a broad anomaly. In this temperature range C_m is adequately reproduced by a Schottky calculated for the zero-field splitting of the $S = 9/2$ multiplet caused by the magnetocrystalline anisotropy. At lower temperatures, C_m shows an extra contribution which probably arises from the splitting of the $\pm S$ electronic states by the dipole–dipole and hyperfine interactions together with the nuclear contribution C_{nucl}. The fast spin–lattice relaxation time of these compounds makes it possible to measure the equilibrium specific heat down to much lower temperatures than for Fe_8 and Mn_{12}. This enables us to study the "slow" contribution to C_m, which, as was explained in Fig. 11, arises from transitions between the two lowest energy levels split by the interaction with nuclei and neighboring molecules. The data can be fitted reasonably well by taking a distribution of bias fields with $\sigma = 240$ Oe for the $X = Cl^-$ compound and adding to it the expected C_{nucl} for the Mn nuclei, which is calculated using the same hyperfine data as for Mn_{12}. AC susceptibility measurements performed in this temperature

range [21] provide evidence for the occurrence of superparamagnetic blocking and give $U = 11.8\,\mathrm{K}$ and $\Gamma_0 = 2.8 \times 10^6\,\mathrm{s}^{-1}$ for X=Cl$^-$. Furthermore, the variation of both χ and Γ with B_z indicate the occurrence of resonant tunneling at the crossing fields for both compounds [21].

A salient feature of the specific heat data is that they show no deviation from equilibrium at low temperatures when τ_e is large enough (e. g. at $T = 0.4\,\mathrm{K}$, τ_e should be $\geq 70\,\mathrm{s}$). These data indicate that Γ becomes independent of T, because if Γ followed the Arrhenius law down to these temperatures, C_m would deviate from equilibrium, as is indeed observed for shorter experimental times. The situation is similar to when $B_\perp \approx 1.7\,\mathrm{T}$ for Fe_8 (Fig. 8), but now at zero applied field. In other words, we have $T_Q > T_B$ when $\tau_e \geq 70\,\mathrm{s}$ (at $T = 0.4\,\mathrm{K}$), but $T_Q < T_B$ for shorter times. This result also yields upper and lower bounds for the rate of the incoherent tunneling process $1.4 \times 10^{-2}\,\mathrm{s}^{-1} \leq \Gamma_{dir} \leq 1.4 \times 10^{-1}\,\mathrm{s}^{-1}$. These results are fully compatible with magnetic relaxation data performed in the cluster with X=Cl$^-$ [21]. It is observed that Γ measured at zero field saturates below approximately $T_Q = 0.6\,\mathrm{K}$ to a value of order $3 \times 10^{-2}\,\mathrm{s}^{-1}$.

In Fig. 22 we also plotted the specific heat calculated by use of the model outlined in Section 3, which only takes into account the interaction with phonons. The calculated time-dependent specific heat deviates from the equilibrium curve for all experimental times, in clear discrepancy with experiment. Taking $B_z = B_\perp \approx 100\,\mathrm{Oe}$ as typical values for the dipolar fields, Eq. (10) gives $\Gamma_{dir} \approx 10^{-9}\,\mathrm{s}^{-1}$, much smaller than the observed value. It seems, therefore, that there is a mechanism of QT that is able to drive the system towards thermal equilibrium and that it is much faster than the simple phonon-induced mechanism described in Section 3.2. As already mentioned (Section 4.3), relaxation of the magnetization observed for Fe_8 [63] near zero applied field and low temperatures ($T < 0.5\,\mathrm{K}$) strongly suggests that QT is then mediated by the fluctuation of the nuclear spins. This fluctuation, at rate T_2^{-1}, can cause modulation of the bias field at the electronic spin, thus giving a finite probability of tunneling when the total bias field crosses zero. It is not clear, however, how this tunneling process can bring the temperature of the spin toward the temperature of the lattice, because it does not involve any exchange of energy between them. We believe that explanation of these data requires more detailed theoretical treatment which takes into account both phonons and nuclear spins.

We next turn our attention to the experiments performed in applied magnetic fields. The data obtained for powder samples of both compounds are shown in Fig. 23. At low fields, the measured C_m lies below the equilibrium specific heat, which shows that the experimental time ($\tau_e \approx 12 - 30\,\mathrm{s}$) is shorter than Γ^{-1}. Above a given field, B_B, the magnetic moments can reach thermal equilibrium. B_B is found to become independent of T below $T_Q \approx 0.4\,\mathrm{K}$ and $0.3\,\mathrm{K}$, respectively, as shown in Fig. 24. This saturation confirms that incoherent QT, via the ground state, dominates the relaxation at low enough temperatures. The low-temperature limit of B_B is smaller for the cluster with X=OAc, in agreement with the fact that this compound has lower D and higher E/D values than the other [13].

For $B > B_B$ the equilibrium specific heat has an anomaly and then decreases abruptly. As for Mn_{12} and Fe_8, this anomaly appears at field values for which Δ_t becomes larger than δ and of the order of the thermal energy. As we argued be-

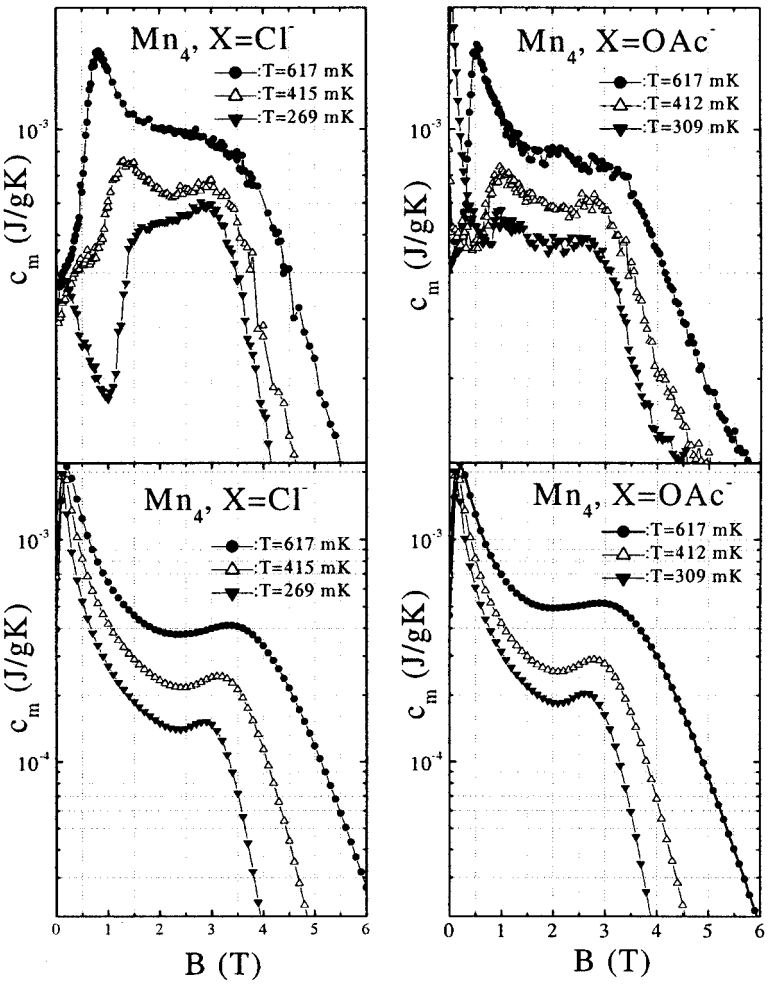

Fig. 23. The upper parts show the measured field-dependence of the specific heat of non-oriented samples of Mn_4 ($X=Cl^-$, OAc^-) at low temperatures. The lower part shows the calculated equilibrium specific heat curves for the same temperatures as in the experiments. For small field values ($B < B_B$), C_m lies below the calculated equilibrium specific heat.

fore, when we discussed the experiments on Mn_{12} and Fe_8, these two facts indicate there is a minimum value of $\Delta E_{2,1}$, which is in agreement with the occurrence of tunnel splitting of the ground state. The calculated specific heat, also shown in the same figure, is, furthermore, in qualitative agreement with the position and the field dependence of the observed anomaly only when a finite Δ_t is taken into account.

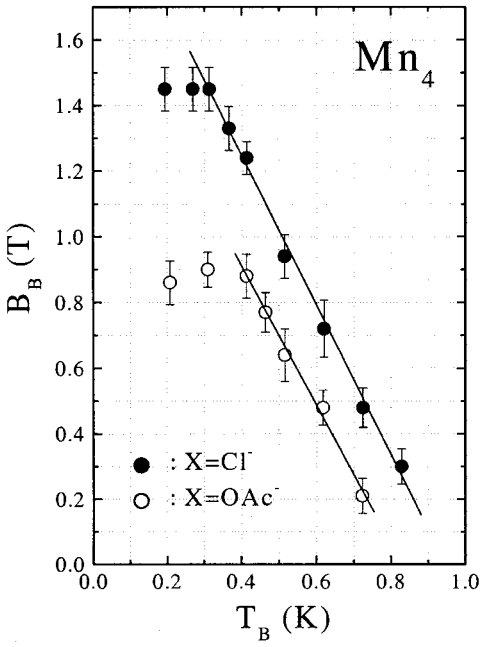

Fig. 24. Temperature dependence of B_B as obtained from field-dependent specific heat data for Mn_4, such as those shown in Fig. 23. Below a "cross-over" temperature $T_Q \approx 0.4\,K$ for X=OAc^- and $T_Q \approx 0.3\,K$ for X=Cl^-, B_B becomes effectively temperature-independent, marking the onset of predominant relaxation through the ground state doublet.

5.7 Conclusions

We have tried to illustrate how the spin–lattice relaxation of molecular magnets such as Fe_8, Mn_{12}, and Mn_4 can be studied by means of specific heat measurements. In particular, these experiments make it possible to study the phenomenon of resonant tunneling and how it is influenced by the application of a perpendicular magnetic field. The data show that resonant tunneling via excited states occurs via progressively lower-lying excited states as $B_\perp$ increases, which results in a decreasing the blocking temperature. For sufficiently large fields, the relaxation rate is observed to become nearly independent of temperature (cf. Figs 18 and 24). A plausible explanation of this is that when the wave-functions of the two lowest energy levels become delocalized, fast ($\geq 1\,s^{-1}$) phonon-induced transitions occur between these two states. A temperature-independent spin–lattice relaxation rate has also been observed for Mn_4, which has a half-integer spin $S = 9/2$, even at zero applied field. This is surprising because the tunnel splitting of this cluster is in principle quenched by Kramers degeneracy. The observed QT must, then, be enabled by interaction with nuclear spins, which can flip with the central electronic spin. The spin–lattice relaxation rate estimated at zero applied field is still much larger than predicted for spin–phonon direct transitions between the two lowest energy states. It is possible that the exchange of the energy between the lattice and the electronic spins is then induced by the interaction with the nuclear spins. We believe, however, that the nature of this mechanism remains unclear.

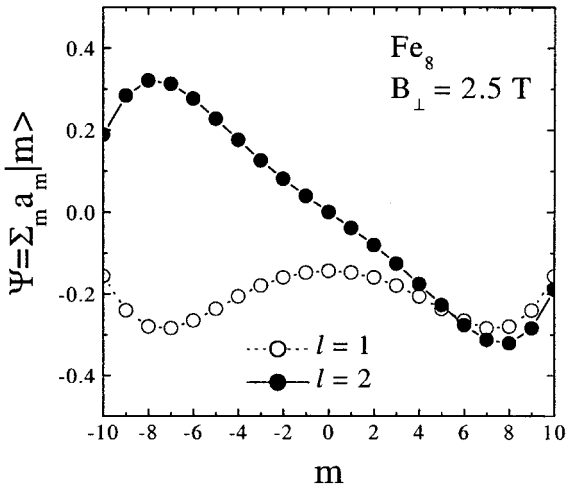

Fig. 25. Calculated wave-functions (Ψ), as expressed in amplitudes (a_m) of m states for the ground state doublet ($l = 1, 2$) of Fe_8 for $B_\perp = 2.5\,T$.

The specific heat data measured on Mn_{12} also have another interesting feature. The specific heat of the nuclei is much smaller than the calculated equilibrium value when the spin–lattice relaxation rate of the electronic spins is too slow. By the action of the magnetic field, however, the Mn nuclear spins present in Mn_{12} reach thermal equilibrium, simultaneously with the electronic spins. This experimental result indicates that the field induces rapid direct transitions between the two lowest-lying states of the electronic spins which, in turn, bring the nuclear spins into equilibrium. This observation confirms that the perpendicular field induces delocalization of the wave-functions of the electronic spins and shows the close relationship between the electronic and the nuclear spins.

Using the specific heat data measured under equilibrium conditions, evidence for the presence of a tunnel-split magnetic ground state in all compounds is obtained. The presence of large perturbations, because of hyperfine and dipolar interactions responsible for an energy splitting δ, does not destroy coherent tunneling as soon as Δ_t is made large enough by application of $B_\perp$. Our data show that, under these conditions, coherent linear superpositions of different projections of the spin, such as those shown in Fig. 25, occur and, moreover, that they are robust against decoherence.

We can now ask if these two states are actually different at the macroscopic or, rather, at the mesoscopic scale. The wave-function of the ground state of Fe_8 at $B_\perp = 2.5\,T$ can be seen as a symmetric linear combination of two functions having average moment $\pm 6\mu_B$ along z. When the field is not perfectly perpendicular to the easy axis, the wave-function still contains both components, but the amplitude of one increases relative to that of the other. The wave-function, moreover, actually represents the magnetic state of a large (> 100) number of electrons. These systems can, therefore, be considered as *mesoscopic*. It is an exciting prospect that systems of such size may indeed show QC under the right conditions.

Acknowledgements

We are indebted to J. Tejada, D. Gatteschi, and G. Aromi for kindly providing us with the Fe_8, Mn_{12}, and Mn_4 samples, respectively. Illuminating discussions with P.C.E. Stamp and J.F. Fernández are gratefully acknowledged. This work is part of the research program of the Stichting voor Fundamenteel Onderzoek der Materie (FOM), which is supported by the Nederlandse Organisatie voor Wetenschappelijk Onderzoek (NWO). J.T. acknowledges funding from CICYT and CIRIT. F.L. acknowledges a grant funded by the European Union in the framework of its TMR Marie Curie Program.

References

[1] A. J. Leggett, *J. Superconductivity* **12**, 683 (1999).
[2] A. J. Leggett, S. Chakravarty, A. T. Dorsey, M. P. A. Fisher, A. Garg, and W. Zwerger, *Rev. Mod. Phys.* **59**, 1 (1987).
[3] W. H. Zurek, *Phys. Today* **36**, October 1991.
[4] D. Giulini, E. Joos, C. Kiefer, J. Kupsch, I. O. Stamatescu, and H. D. Zeh, *Decoherence and the Appearence of a Classical World in Quantum Theory*, Springer-Verlag, Berlin Heidelberg (1996).
[5] N. V. Prokof'ev and P. C. E. Stamp, *Rep. Prog. Phys.* **63**, 669 (2000) and references therein.
[6] *Quantum Tunneling of Magnetization*, edited by L. Gunther and B. Barbara (Kluwer, Dordrecht, 1995).
[7] E. M. Chudnovsky and J. Tejada, *Macroscopic Quantum Tunneling of the Magnetic Moment*, Cambridge University Press, Cambridge (1998).
[8] T. Lis, *Acta Crystallogr. B.* **36**, 2042 (1980).
[9] R. Sessoli, D. Gatteschi, A. Caneschi, and A. Novak, *Nature (London)* **365**, 141 (1993).
[10] K. Wieghardt, K. Pohl, I. Jibril, and G. Huttner, *Angew. Chem. Int. Ed. Engl.* **23**, 77 (1984).
[11] C. Delfs, D. Gatteschi, L. Pardi, R. Sessoli, K. Wieghardt, and D. Hanke, *Inorg. Chem.* **32**, 3909 (1993).
[12] S. M. J. Aubin, M. W. Wemple, D. M. Adams, H-L. Tsai, G. Christou, and D. N. Hendrickson, *J. Am. Chem. Soc.* **118**, 7746 (1996).
[13] H. Andres, R. Basler, H-U. Güdel, G. Aromí, G. Christou, H. Büttner, and B. Rufflé, *J. Am. Chem. Soc.* **50**, 12469 (2000).
[14] An exception is Mn_4 – the four molecules within a unit cell are canted at angles of 8.97° to each other.
[15] J. R. Friedman, M. P. Sarachik, J. Tejada, and R. Ziolo, *Phys. Rev. Lett.* **76**, 3830 (1996).
[16] J. M. Hernández, X. X. Zhang, F. Luis, J. Bartolomé, J. Tejada, and R. Ziolo, *Europhys. Lett.* **35**, 301 (1996).
[17] L. Thomas, F. Lionti, R. Ballou, D. Gatteschi, R. Sessoli, and B. Barbara, *Nature (London)* **383**, 145 (1996).
[18] F. Luis, J. Bartolomé, J. F. Fernández, J. Tejada, J. M. Hernández, X. X. Zhang, and R. Ziolo, *Phys. Rev. B* **55**, 11448 (1997).
[19] J. M. Hernández, X. X. Zhang, F. Luis, J. Tejada, J. R. Friedman, M. P. Sarachik, and R. Ziolo, *Phys. Rev. B* **55**, 5858 (1997).

[20] C. Sangregorio, T. Ohm, C. Paulsen, R. Sessoli, and D. Gatteschi, *Phys. Rev. Lett.* **78**, 4645 (1997).
[21] S. M. J. Aubin, N. R. Dilley, L. Pardi, J. Krzystek, M. W. Wemple, L-C. Brunel, M. B. Maple, G. Christou, and D. N. Hendrickson, *J. Am. Chem. Soc.* **120**, 4991 (1998).
[22] L. Thomas, A. Caneschi, and B. Barbara, *Phys. Rev. Lett.* **83**, 2398 (1999).
[23] D. Garanin, *J. Phys. A.* **24**, L61 (1991).
[24] E. Del Barco, N. Vernier, J. M. Hernández, J. Tejada, E. M. Chudnovsky, E. Molins, and G. Bellessa, *Europhys. Lett.* **47**, 722 (1999).
[25] G. Bellessa, N. Vernier, B. Barbara, and D. Gatteschi, *Phys. Rev. Lett.* **83**, 416 (1999).
[26] The interpretation of the data of Bellessa et al. in terms of phonon-assisted tunneling has been criticized by E. Chudnovsky, *Phys. Rev. Lett.* **85**, 5259 (2000), see also the reply by Bellessa et al., *Phys Rev. Lett.* **85**, 5260 (2000). For arguments against the idea that resonance experiments give evidence for the existence of QC, see Ref. [5].
[27] A. Garg, *Europhys. Lett.* **22**, 205 (1993).
[28] F. Luis, F. L. Mettes, J. Tejada, D. Gatteschi, and L. J. de Jongh, *Phys. Rev. Lett.* **85**, 4377 (2000).
[29] F. L. Mettes, G. Aromí, F. Luis, M. Evangelisti, G. Christou, D. N. Hendrickson, and L. J. de Jongh, *Polyhedron*. **20**, 1459 (2001).
[30] F. L. Mettes, F. Luis, and L. J. de Jongh, *Phys. Rev. B* (2001), accepted for publication.
[31] F. Fominaya, J. Villain, P. Gandit, J. Chaussy, and A. Caneschi, *Phys. Rev. Lett.* **79**, 1126 (1997); F. Fominaya, J. Villain, T. Fournier, P. Gandit, J. Chaussy, A. Fort, and A. Caneschi, *Phys Rev. B* **59**, 519 (1999).
[32] A.-L. Barra, P. Debrunner, D. Gatteschi, Ch. E. Schulz, and R. Sessoli, *Europhys. Lett.* **35**, 133 (1996).
[33] R. Sessoli, H.-L. Tsai, A. R. Schake, S. Wang, J. B. Vincent, K. Folting, D. Gatteschi, G. Christou, and D. N. Hendrickson, *J. Am. Chem. Soc.* **115**, 1804 (1993).
[34] A.-L. Barra, D. Gatteschi, and R. Sessoli, *Phys. Rev. B* **56**, 8192 (1997).
[35] S. Hill, J. A. A. J. Perenboom, N. S. Dalal, T. Hathaway, T. Stalcup, and J. S. Brooks, *Phys. Rev. Lett.* **80**, 2453 (1998).
[36] M. Hennion, L. Pardi, I. Mirebeau, E. Suard, R. Sessoli, and A. Caneschi, *Phys. Rev. B* **56**, 8819 (1997).
[37] R. Caciuffo, G. Amoretti, A. Murani, R. Sessoli, A. Caneschi, and D. Gatteschi, *Phys. Rev. Lett.* **81**, 4744 (1998).
[38] I. Mirebeau, M. Hennion, H. Casalta, H. Andres, H. U. Güdel, A. V. Irodova, and A. Caneschi, *Phys. Rev. Lett.* **83**, 628 (1999).
[39] A. A. Mukhin, V. D. Travkin, A. K. Zvezdin, S. P. Lebedev, A. Caneschi, and D. Gatteschi, *Europhys. Lett.* **44**, 778 (1998).
[40] W. Wernsdorfer and R. Sessoli, *Science* **284**, 133 (1999).
[41] P. Politi, A. Rettori, F. Hartmann-Boutron, and J. Villain, *Phys. Rev. Lett.* **75**, 537 (1995).
[42] N. V. Prokof'ev and P. C. E. Stamp, *J. Phys. Cond. Matter* **5**, L663 (1993); P. C. E. Stamp, *Physica B* **197**, 133 (1994).
[43] W. Wernsdorfer, T. Ohm, C. Sangregorio, R. Sessoli, D. Mailly, and C. Paulsen, *Phys. Rev. Lett.* **82**, 3903 (1999).
[44] W. Wernsdorfer, R. Sessoli, and D. Gatteschi, *Europhys. Lett.* **47**, 254 (1999).
[45] D. Loss, D. P. DiVincenzo, and G. Grinstein, *Phys. Rev. Lett.* **69**, 3232 (1992).
[46] J. von Delft and C. L. Henley, *Phys. Rev. Lett.* **69**, 3236 (1992).
[47] X. X. Zhang, J. M. Hernández, E. del Barco, J. Tejada, A. Roig, E. Molins, and K. Wieghardt, *J. Appl. Phys.* **85**, 5633 (1999).
[48] F. Luis, J. Bartolomé, and J. F. Fernández, *Phys. Rev. B* **57**, 505 (1998).
[49] J. F. Fernández, F. Luis, and J. Bartolomé, *Phys. Rev. Lett.* **80**, 5659 (1998).

[50] J. F. Fernández, J. Bartolomé, and F. Luis, *J. Appl. Phys.* **83**, 6940 (1998).
[51] M. Novak and R. Sessoli, in Ref. [6], pp. 171–188.
[52] A. Lascialfari, Z. H. Jang, F. Borsa, P. Carretta, and D. Gatteschi, *Phys. Rev. Lett.* **81**, 3773 (1998).
[53] D. A. Garanin and E. M. Chudnovsky, *Phys. Rev. B* **56**, 11102 (1997).
[54] A. Fort, A. Rettori, J. Villain, D. Gatteschi, and R. Sessoli, *Phys. Rev. Lett.* **80**, 612 (1998).
[55] M. N. Leuenberger and D. Loss, *Europhys. Lett.* **46**, 692 (1999).
[56] R. Meyer and R. R. Ernst, *J. Chem. Phys.* **93**, 5518 (1990).
[57] J. F. Fernández, unpublished.
[58] F. Hartmann-Boutron, P. Politi, and J. Villain, *Int. J. Mod. Phys. B* **10**, 2577 (1996).
[59] A. Abragam and A. Bleaney, *Electron Paramagnetic Resonance of Transition Ions*, Clarendon Press, Oxford (1970).
[60] F. Luis, J. M. Hernández, J. Bartolomé, and J. Tejada, *Nanotechnology* **10**, 86 (1999).
[61] M. Novak, R. Sessoli, A. Caneschi, and D. Gatteschi, *J. Magn. Magn. Mater.* **146**, 211 (1995).
[62] E. del Barco, J. M. Hernández, M. Sales, J. Tejada, H. Rakoto, J. M. Broto, and E. M. Chudnovsky, *Phys Rev. B* **60**, 11898 (1999).
[63] W. Wernsdorfer, A. Caneschi, R. Sessoli, D. Gatteschi, A. Cornia, V. Villar, and C. Paulsen, *Phys. Rev. Lett.* **84**, 2965 (2000).
[64] J. A. A. J. Perenboom, J. S. Brooks, S. O. Hill, T. Hathaway, and N. S. Dalal, *Physica B* **246–247**, 294 (1998); *Phys. Rev. B* **58**, 330 (1998).
[65] A. D. Kent, Y. Zhong, L. Bokacheva, D. Ruiz, D. N. Hendrickson, and M. P. Sarachik, *Europhys. Lett.* **49**, 521 (2000).
[66] N. V. Prokof'ev and P. C. E. Stamp, *J. Low Temp. Phys.* **104**, 143 (1996).
[67] N. V. Prokof'ev and P. C. E. Stamp, *Phys. Rev. Lett.* **80**, 5794 (1998).
[68] T. Moriya, *Progr. Theoret. Phys.* **16**, 641 (1956).

Magnetism: Molecules to Materials III. Edited by J.S. Miller and M. Drillon

ISBNs: 3-527-30302-2 (Hardback); 3-527-60014-0 (Electronic)

6 Self-organized Clusters and Nanosize Islands on Metal Surfaces

Jean-Pierre Bucher and Fabrice Scheurer

6.1 Introduction

Small metal clusters have become the center of interest of a variety of interdisciplinary subjects such as catalysis, macroscopic quantum tunneling, and Coulomb blockade devices [1–4]. Clusters can be studied on their own, for example in molecular beams [5], but they also constitute the ultimate state of integration in electronic and optoelectronic devices, and as such are the subject of many interesting studies in the form of supported particles. In this review we are primarily interested in magnetic particles that form spontaneously on surfaces during deposition of metal vapor. Magnetic materials and devices made of well defined nanoscale particles are an important part of recent progress in spin electronics, magnetic data storage, and sensors for giant magnetoresistance applications [6, 7]. In this context, the controlled formation of ordered metal nanostructures on solid surfaces by self-organized growth [8–10] enables anticipation of new data-storage technologies based on nanoscale dots with tunable densities in excess of 1 Tbits in^{-2}.

The synthesis and magnetic properties of organized metal hetero-structures on surfaces will be reviewed and examples will be presented from recent research. We will not address the topic of magnetic particles in matrixes, which is a subject in itself and has its own specificity in the field of composite materials. Nanosize islands on metal surfaces spontaneously form as a result of condensation of metal vapor from the gas phase and subsequent nucleation and growth. By controlling the growth kinetics, nanostructures with particular properties can be synthesized [11, 12]. Islanding on surfaces is also the constrained pathway for the growth of thin films. Each time it is possible, therefore, reference will be made to ultrathin magnetic films for which a large amount of information exists [13]. In most current work, however, the initial stage of growth is only marginally addressed, although it is central to understanding the magnetic properties of assembled structures on surfaces, although there are a few exceptions [14–16, 50].

Because this paper is not devoted exclusively to self-organized systems, the issue of growth of nanostructures on surfaces will be placed in a more general context (Sections 6.2 and 6.3). In Section 6.2 we will first describe how well defined nanostructures can be built by controlling growth kinetics. Section 6.3 will be devoted to a description of thermodynamic growth modes and interconnects between elastic and structural aspects. The possibility of obtaining self-organized islands on surfaces will be addressed in Section 6.4, where the driving mechanisms will also be discussed.

The first part of Section 6.4, however, will be devoted to surface reconstruction and strain relaxation patterns, owing to their central role as atomic scale templates for the organization of small entities on the nanometer scale. The magnetic properties of low-dimension systems from isolated islands to the 2D limit, will be reviewed in Section 6.5 and experimental results will be presented in Section 6.6. The goal is to develop a good understanding of nanostructured magnetic materials in terms of their basic properties such as grain size and density. Ultimately, magnetism will be viewed as the result of interacting building blocks (spin blocks), a particularly fruitful approach for self-organized cobalt dots. In this part of the work, we will show how the interaction between dots develops towards the formation of magnetic domain structures.

6.2 First Stage of Growth Kinetics

Adsorption of atoms on a surface from the gas phase is a non-equilibrium process. A system comprising a two-dimensional adatom lattice gas is temporarily supersaturated and tries to restore equilibrium by condensing into islands. As a result, growth can be viewed as a non-equilibrium phenomenon governed by competition between kinetics and thermodynamics. An atomistic view of the processes involved in adatom diffusion and attachment can be found elsewhere [11, 12]. In this section, we will summarize ways of manipulating the growth kinetics to tune the density, size, and shape of nanostructures. This section does not imply any reference to self-organization. For simplicity we will follow the fate of metal atoms adsorbed on perfect, single-crystal, metal surfaces prepared under the best condition of ultrahigh vacuum (UHV). We will not, furthermore, go into the details of atomic exchange leading to unwanted alloy formation.

6.2.1 Island Density

The basics of nucleation and growth on surfaces will be presented with silver adatoms on Pt(111) as an example. Although it is not magnetic, this system has been studied more extensively than any other [11, 17, 18]. Figure 1 shows variable-temperature Scanning Tunneling Microscopy (STM) images of Ag islands on Pt(111) grown and imaged at different substrate temperatures between 80 and 110 K; the silver coverage is 0.12 ML (monolayer). The continuous diagonal lines in the images are monatomic steps of the Pt(111) substrate and the bright zones are the monoatom-thick silver structures. It is apparent that the density of the islands drops markedly, and the average size of the islands increases, when the temperature is increased. There is even a temperature (170 K in this example) at which islands are no longer nucleated on the terraces and silver condenses at the steps of the platinum substrate (step flow). Silver on Pt(111) is representative of islands formed by two-dimensional isotropic diffusion.

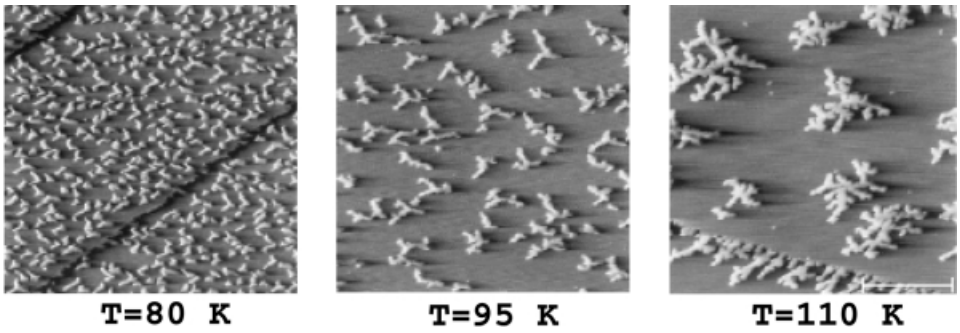

Fig. 1. STM topographs of low-coverage Ag submonolayer structures ($\Theta = 0.12$ ML) on a Pt(111) surface, grown and imaged at the temperatures indicated. The lateral scale is given by the white bar, which represents a length of 20 nm [17].

A possible scenario of island formation and growth is that when an incoming adatom is adsorbed on the surface from the gas phase it may have two distinct destinies – it can meet another adatom during its thermally activated random walk and form a stable nucleus (an immobile dimer), or it can be directly incorporated into an already existing island.

The latter alternative does not contribute to increasing the number of islands on the surface, it merely increases the size of an existing island. The first event is much more frequent in the first stage of the growth process, whereas incorporation into an already existing island will dominate after longer times. After very long time no new islands are formed and an incoming adatom diffuses to an existing island before it has the opportunity to meet another adatom. As a result, the island density saturates and we can define a capture area for each island. The average separation between islands then provides a good measure of the adatom diffusion length Λ_a. Nucleation in stages occurs when the average diffusion length before encounter of an island becomes larger than the extension of one terrace. An analytical expression of this saturation density of islands N_{sat} has been proposed by Venables [19]:

$$N_{\mathrm{sat}} = \eta(\Theta)\left(\frac{R}{v_0}\right)^{\frac{i}{(i+2)}} \exp\left(\frac{E_i + i\,E_d}{k_B T(i+2)}\right) \tag{1}$$

where η is a slowly varying function of the coverage Θ, R is the deposition rate and v_0 is the attempt frequency and is approximately 10^{13} to 10^{14} Hz. The size of the critical nucleus is i and E_i is its binding energy. $(i + 1)$ is the smallest island still stable at a given temperature. When the critical nucleus is unity, E_i becomes zero and we obtain the exponent $E_d/3$. The formula reflects the fact that the adatom diffusion is thermally activated with an energy barrier E_d. In this limit, the adatom migration barrier can be directly obtained by exploiting the results from variable-temperature STM. When the saturation density of islands is reported as a function of $1/T$ in an Arrhenius plot, the slope of the straight line directly provides E_d. It is of advantage to work at low temperature, in the regime where the critical nucleus is unity, because then we do not have to worry about the binding energy of dimers,

trimers, etc. The variable temperature STM approach is among the most precise methods of determination of E_d. An extensive review of this technique and a table of diffusion barriers are given elsewhere [20].

6.2.2 Island Shapes

Until now we have shown that the density of islands depends on the diffusion of adatoms on the bare surface. We show now that the shapes of these islands depend on the diffusion of adatoms along the edges of the islands. At low temperatures diffusing atoms stick where they hit; islands will, therefore, have fractal structures because diffusion is hindered along the perimeter of the island (Fig. 2). The fractal dimension of the islands is 1.78, which is very close to the value obtained from computer simulation within the diffusion-limited aggregation (DLA) model [21]. This ideal situation of frozen perimeter is realized in practice only at sufficiently low substrate temperatures. The influence of substrate temperature and the flux of incoming adatoms on the final shape has recently been analyzed in detail [18] and a transition from randomly divided to dendritic islands has been observed. At the higher temperatures at which diffusion of adatoms around the perimeter is activated [22], rearrangements occur and we can obtain compact structures which are close to a thermodynamic equilibrium.

For example hexagonal aggregates have been obtained by depositing Pt atoms on Pt(111) at 450 K and it was shown [23] (Fig. 3) that there is a transition from hexagonal to triangular islands as a function of growth temperature. The results were explained on the basis of a well known crystallographic fact – a compact island on a (111)-type substrate is limited by both, edges with a {111} face and edges with a

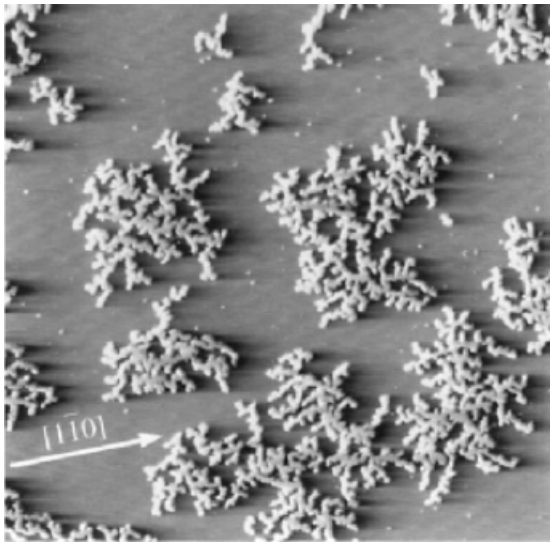

Fig. 2. STM image showing fractal aggregates grown on Pt(111) at 110 K and a deposition flux $R = 1.6 \times 10^{-5}\mathrm{MLs}^{-1}$ (image 120 nm × 120 nm) [11].

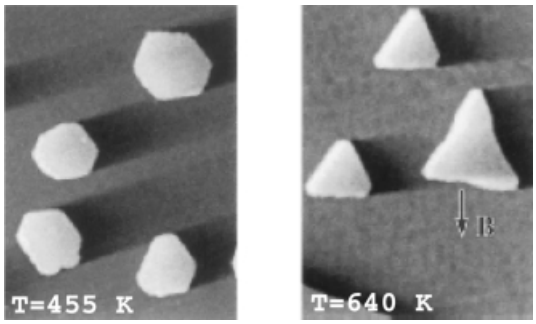

Fig. 3. Island shapes on Pt(111) after deposition at substrate temperatures of 455 and 640 K. (STM images 77 nm $\times$ 110 nm and 230 nm $\times$ 330 nm respectively and $\Theta = 0.15$ ML [23].

{100} face. The triangular shapes then appear as a result of temperature-dependent preferential diffusion along one type of edge and accumulation at the corners. Triangular cobalt islands are observed also when deposited at 300 K on Cu(111). Under these conditions, however, fcc and hcp stackings are nearly degenerate in energy and two orientations of the triangles, rotated by 60°, coexist [24].

In some circumstances (anisotropic diffusion or anisotropic bonding) [25–27] atomic chains and stripes can be grown, and then particular symmetries of the surface can play a leading role, for example by favoring the easy diffusion of adatoms along potential wells or grooves. Anisotropic diffusion can be exploited to tailor highly elongated metastable islands. The simplest example of an anisotropic substrate is a (110) surface of a fcc crystal (Fig. 4). Such a substrate is made of compact atomic rows, along the $[1\bar{1}0]$ direction, separated by channels. Under favorable conditions the adatoms will diffuse preferentially within the channels in a linear type of random motion, at least when temperatures are not too high. Linear chains form spontaneously by aggregation of adatoms diffusing along the channels.

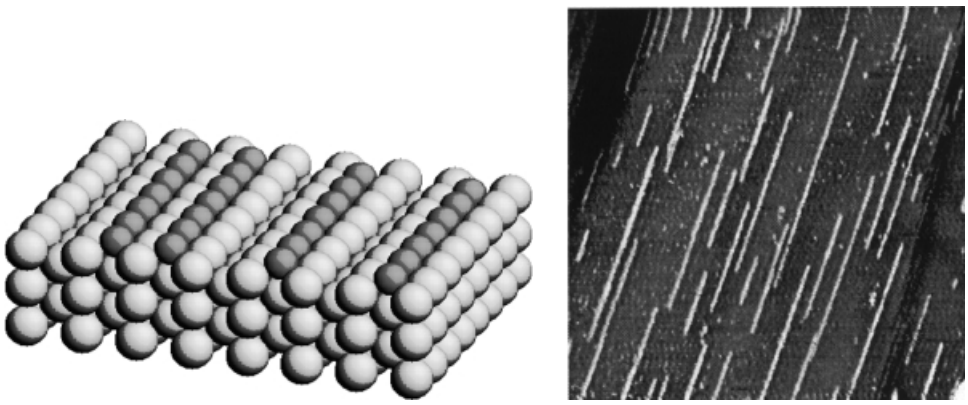

Fig. 4. (a) Schematic view of linear atomic chains formed in the grooves of the (110) face of an fcc crystal. (b) STM image with 0.1 ML copper deposited at 300 K on Pd(110). Images 120 nm $\times$ 120 nm [26].

An example of this simple picture has been observed in variable-temperature experiments with Cu (0.1 ML) adsorbed on Pd(110) in the temperature range from 265 to 350 K. At temperatures below 300 K linear chains several hundred Ångströms long, "monatomic" in width, grow spontaneously along the $[1\bar{1}0]$ direction. Above 300 K, 2D islands that are still elongated along the $[1\bar{1}0]$ direction start to form. Simultaneously, the surface density of islands drops markedly as a function of temperature. It has been shown by LEED experiments that these Cu islands grow pseudomorphically on Pd(110). Several examples of growth mechanisms of linear chains have been described in the literature [28, 29].

So far we have only addressed the question of the shapes of the first monolayer of adislands. The reasons clusters grow in the third dimension, and why particular shapes are favored as a consequence of strain relaxation, will be summarized in Section 6.3.

6.3 Growth Modes

Whereas growth kinetics were addressed in Section 6.2, this section deals with thermodynamic growth criteria. To synthesize metallic nanostructures (organized or not) on a surface, one must actually prevent the formation of flat, defect-free layers. The appropriate adsorbate and substrate elements can be chosen on the basis of simple thermodynamic and elasticity theory arguments.

6.3.1 Thermodynamic Growth Criterion

The growth of an adsorbate on a surface can occur in many different ways. Usually one distinguishes three main growth modes [30], depicted in Fig. 5.

1. The layer-by-layer growth mode (so-called Frank-van der Merwe mode) in which a layer, n, grows atomically flat and is completed before the next layer, $n + 1$, starts growing.
2. The Stranski-Krastanov mode in which growth occurs layer-by-layer for one or several layers during the first stage and is then followed by a 3D growth mode.
3. The three-dimensional (3D) growth mode (also called Volmer-Weber mode) in which crystallites grow vertically rather than expanding laterally on the surface, thus maintaining a small contact area with the substrate.

Several other growth modes have also been identified [31], for example the simultaneous layer growth mode, or "Poisson growth", obtained in the absence of mass transport between successive layers. The islands grow in height and in lateral size simultaneously. Another important phenomenon is the formation of a diffuse interface; this is often observed for both miscible and immiscible elements.

A thermodynamic macroscopic approach was developed to explain some general growth trends [30, 32]. It is a simplified theory of growth considering systems at thermodynamic equilibrium and neglects all the kinetic effects occurring during the nucleation processes mentioned previously. Let us consider two equilibrium

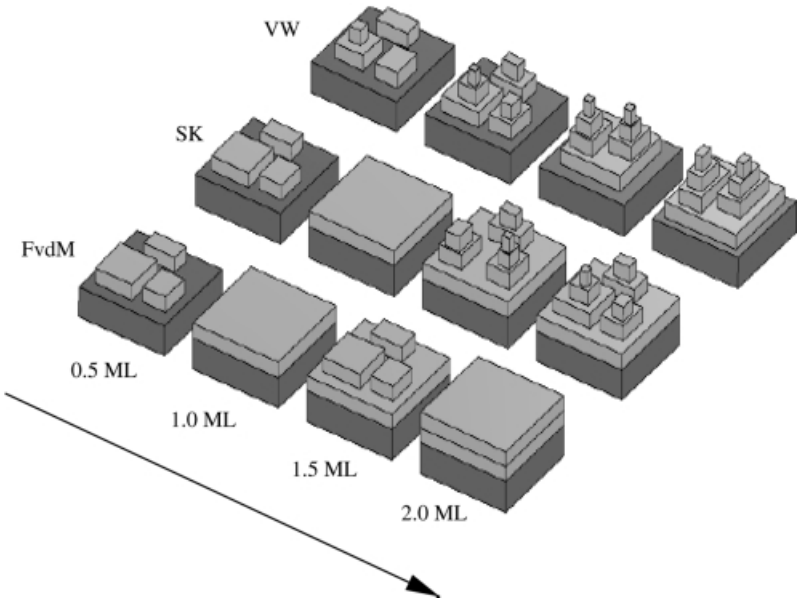

Fig. 5. The three usual growth modes. Frank-Van der Merve, Stranski-Krastanov, Volmer-Weber as a function of coverage.

situations – in the first the atoms, A, completely cover the surface of the substrate, S, and in the second they form a 3D crystallite of element A (bulk-like), leaving the major part of the substrate surface, S, free.

The energy difference per surface area of the two situations is given by:

$$\Delta\gamma_\infty = (\gamma_A + \gamma_{AS}) - \gamma_S \tag{2}$$

where γ_A, γ_S, and γ_{AS} are, respectively, the surface energies of the adsorbate and of the substrate, and the interfacial energy. (The surface of the 3D crystallite is neglected.) If $\Delta\gamma_\infty < 0$, energy is gained when layers cover the surface, hence layer-by-layer (Frank-van der Merwe) growth will occur. If $\Delta\gamma_\infty > 0$, the growth will be three-dimensional (Volmer-Weber).

Here we have neglected the surface tensions of the different facets that bind the crystallites (the surface tension depends on facet orientation) and might also determine the equilibrium shape of the adsorbate (Wulff theorem) [33–36]. Mezay and Giber calculated the surface energies for polycrystalline metals, using experimental data [37]. More recently, metal surface energies have been computed by use of ab initio methods, taking into account the crystallographic orientation of the surface [38].

The interfacial term γ_{AS} is more difficult to estimate and has often been neglected in the past [39]. For metal-on-metal growth it is a priori not possible to neglect the interfacial energy, particularly when γ_A and γ_S are similar. The sign of $\Delta\gamma_\infty$ is than determined by γ_{AS}. For metallic multilayer growth, in which the two elements A and

S alternate, the role of the interfacial energy γ_{AS} is very important. If flat interfaces are to be obtained A must wet S and S must also wet A. This is theoretically only possible when γ_{AS} is non-zero. Bauer and van der Merwe, although neglecting the interfacial energy, give the phenomenological criterion $2|(\gamma_A - \gamma_S)/(\gamma_A + \gamma_S| < 0.5$ for multilayer growth [40]. The validity of this criterion was demonstrated later within a microscopic model.

6.3.2 Microscopic Model

A microscopic approach to wetting, based on a tight-binding electronic structure calculations, has been developed by Gautier and Stoeffler [41]. Consider N_A adsorbate atoms and N_S substrate atoms of bulk energy E_A and E_S, and N surface adsorption sites. Assuming A builds n perfect layers of N atoms of element A, the energy of the system is:

$$E = N_A E_A + N_B E_B + N(\gamma_B + \Delta\gamma_n) \tag{3}$$

$\Delta\gamma_n$ is called the spreading energy and must not be confused with the previously introduced $\Delta\gamma_\infty$. In the macroscopic limit, as $n \to \infty$, we have $\Delta\gamma_n \to \Delta\gamma_\infty$. To obtain layer-by-layer growth mode, one must first have the necessary, but not sufficient, condition $\Delta\gamma_1 < 0$. This also requires that $\Delta\gamma_2 - \Delta\gamma_1 < \Delta\gamma_3 - \Delta\gamma_2 < \ldots < 0$, i. e. one must gain energy when depositing an additional layer (Fig. 6a). If the last condition is no longer fulfilled for a given n, Stranski-Krastanov growth will set in (Fig. 6b).

This model enables estimation of the spreading energy (hence the interfacial energy for large n) which contains a negative contribution from a repulsive Born-Meyer term and an attractive band contribution, calculated in the tight-binding approximation [41]. The model has been tested on several surface orientations for transition metals and the general trends are:

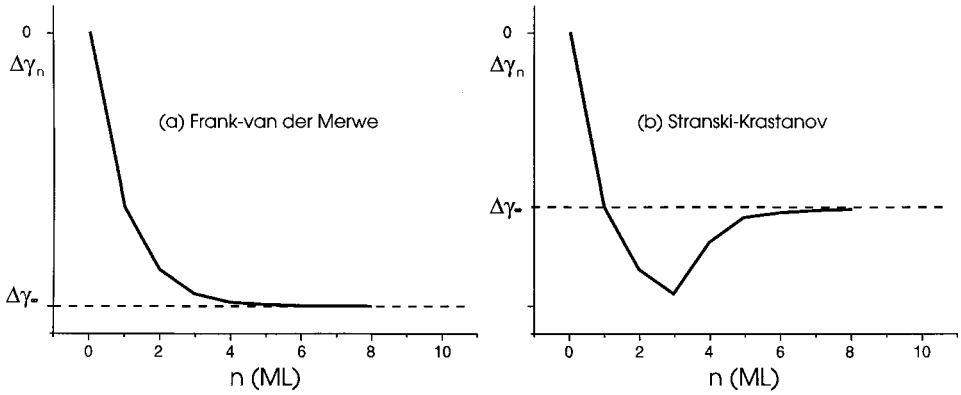

Fig. 6. Dependence of the spreading energy on the coverage n. (a) Frank-Van der Merve growth, (b) Stranski–Krastanov growth [41].

1. The phenomenological criterion of A wetting S, $\gamma_A < \gamma_S$, is approximately valid.
2. 4d metals wet most 5d (100) metal surfaces.
3. 3d metals wet most 4d and 5d (100) metal surfaces.
4. The phenomenological Bauer and van der Merwe criterion [40] is justified.

6.3.3 Elastic and Structural Considerations

In the previous model only pseudomorphic layers are considered. i. e. the adsorbate is forced to adopt the structure of the substrate. The elastic contribution in $\Delta\gamma_n$, arising from the misfit energy between the substrate and the adsorbate is, therefore, implicitly taken into account. The elastic contribution can also be introduced into the macroscopic thermodynamic model, as proposed by Kern et al. [35]. The elastic misfit energy was added explicitly and the spreading energy $\Delta\gamma(z)$ assumed to decay exponentially towards $\Delta\gamma_\infty$ (for metals). Recently, Müller et al. allowed successive layers to relax [42, 43] and showed that strain is the force driving the transition from layer-by-layer growth toward the Stranski-Krastanov mode, in agreement with earlier molecular dynamic simulations using the Lennard Jones potential [44]. After a certain critical number of filled pseudomorphic layers, the accumulated strain must be relaxed. Initially this is achieved by growing islands vertically instead of expanding laterally. The second stage is the introduction of dislocations, which modifies the shape of the growing 3D crystallites. The larger the elastic energy, the larger will be the shape ratio (height/lateral size) of the islands. The substrate is also affected by the strain release, because it is dragged by the relaxing island [45, 46]. To form nanostructures, i. e. well separated entities on a surface (obtained, e. g., for 3D growth), one should associate elements having a large misfit and a large substrate-to-adsorbate stiffness ratio [36].

Sometimes the adsorbate grows incoherently or even in a structure different from that of the substrate. A particular example, in which the elastic strain directly influences the structure of the adsorbate, occurs when bcc metals are associated with fcc or hcp metals. The epitaxial relationships for these systems favor crystallographic multi-domain states. Because such fcc/bcc associations might be potentially interesting for the fabrication of templates of dislocation lines or arrays for organized growth [47, 48], we briefly recall the epitaxial relationships one might expect in this class of systems. Geometrical criteria for the epitaxial relationships between fcc (or hcp) and bcc crystals are used [49].

1. The simplest example is the Bain orientation, for bcc(100)//fcc(100) epitaxy, in which there is a matching of the two in-plane directions.
2. The Pitsch orientation is obtained when bcc(110)//fcc(100). Here, there is only a matching in one in-plane direction. Because of rotational and mirror symmetries, four types of domains with different in-plane orientations coexist on the surface.
3. The Nishiyama–Wassermann and Kurdjumov–Sachs orientations occur for bcc(110)//fcc(111) or hcp(00.1). Both comprise uniaxial matching. Three or six, respectively, domains with different in-plane orientations are found, for reasons of symmetry.

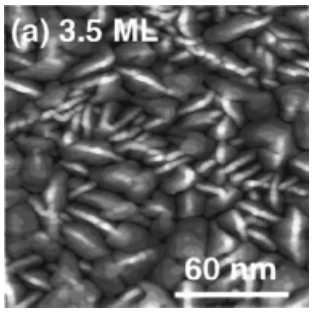

Fig. 7. STM topography of 3.5 ML Fe on Cu(111) with bcc ridge-like Fe structures which appear during a phase transition of Fe from fcc to bcc [50].

It should be noted that except for the Bain orientation it is not equivalent to deposit a bcc crystal on a fcc(111) substrate, or a fcc crystal on a bcc(110) substrate. In the latter the number of differently oriented domain types is lower because of the reduced symmetry of the substrate surface.

There is matching in the two in-plane directions (2D epitaxy) for the Bain orientation only. In all other cases there is a uniaxial alignment – the adsorbate matches the substrate well in one direction but there is poor coincidence in the other. Because there is preferential strain accumulation in one direction, rather large shape ratios, i. e. rather elongated islands, are expected along the matching direction. An illustration is given for Fe/Cu(111) in Fig. 7, in which the elongated islands take different orientations relative to the substrate [50]. Because of strain accumulation, transitions between different epitaxial relationships, implying very important mass transport and island shape modifications, have been predicted [51] and observed [52].

The geometrical criteria are confirmed by energy calculations either in rigid lattice models [53, 54] or in models taking into account the elastic deformation [40]. The influence of misfit strain on island size and height has also been studied within the same framework [55, 56]. These calculations enable determination of the stability of the different epitaxial relationships which are essentially dependent on the nearest-neighbor distances ratio of the fcc and bcc elements and on the stiffness coefficient [40].

6.4 Organized Growth

Two types of self-organized islanding can be distinguished. The first type proceeds through cooperative growth in which the atoms of two adjacent islands interact at a distance and rearrange during the growth process; this can be termed evolutionary, dynamic self-organization (very often occurring in the Stranski–Krastanov growth mode at thermal equilibrium; Section 6.3). This lateral exchange of information (mesoscopic correlation of elastic origin) between atoms enables the growth of hetero-structures that self-organize in the third dimension. A good example is

semiconductor growth [57, 58]. In the second type of growth the substrate behaves as if it were inert. Surface reconstructions and vicinal surfaces are used as templates. These two processes are not mutually exclusive, although for the metal structures of interest to us the second type is more frequent.

Surfaces can reconstruct spontaneously as a result of free energy minimization. This means that relative to their positions in the bulk crystal, surface atoms adopt new equilibrium positions. An example of such a reconstruction is the chevron reconstruction of the Au(111) surface. It induces rearrangement of surface atoms at the nanoscopic scale that can appear as a modulation of the topmost atomic layer (Section 6.4.2). Dislocation networks that are of interest for self-organized growth are, however, most easily induced by hetero-epitaxy where the lattice mismatch between two different materials is exploited.

6.4.1 Incommensurate Modulated Layers

Modulated phases can be studied within a simple one-dimensional model proposed in the thirties by Frenkel and Kontorova [59]. This model takes into account the competing interactions between a substrate potential and lateral adatom interactions. A chain of atoms coupled by harmonic springs is placed in a cosine substrate potential of amplitude V and periodicity a. The equilibrium separation of atoms in a chain is b and the force constant of the springs is K. The energy of the system is then given by:

$$H = \sum_n \frac{K}{2}(x_{n+1} - x_n - b)^2 + \sum_n V\left[1 - \cos\left(2\pi\frac{x_n}{a}\right)\right] \tag{4}$$

where x_n is the position of the nth atom. Frank and van der Merve solved this equation analytically within a continuum approximation [60]. They replaced the index n by a continuous variable and x_n by a continuous function $\varphi(n) = (2\pi x/a) - 2\pi n$. The problem contains three parameters, the misfit $\delta = (b - a)/a$ and the two constants K and V. The results show that for slightly differing lattice parameters of chain and substrate potentials (small δ), the lowest energy state is obtained for a system which consists of large commensurate domains separated by regularly spaced regions of bad fit (Fig. 8). The regions of bad fit are called misfit dislocations, solitons, or domain walls. They can be considered as collective long period lattice distortion waves, which are excitations of the commensurate ground state.

In the continuum limit the ground state satisfies the time-independent sine Gordon equation:

$$\frac{\mathrm{d}^2\varphi}{\mathrm{d}n^2} = pA\sin(p\varphi) \tag{5}$$

where $\sqrt{A} = 2\pi/b\left(\sqrt{V/K}\right)$, and p is the commensurability. One solution of this

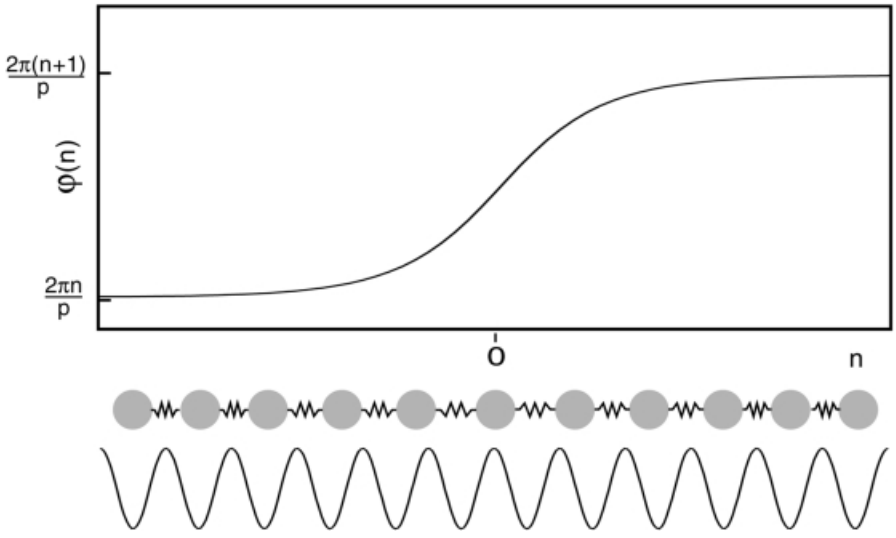

Fig. 8. Uniaxial soliton solution of the Frenkel-Kontorova model. It describes the domain wall located at $n = 0$ separating two adjacent commensurate regions. In this model, the width of the domain wall is $L = 1/\left(p\sqrt{A}\right)$.

equation is the solitary lattice distortion:

$$\varphi(n) = \frac{4}{p} \arctan\left[\exp\left(pn\sqrt{A}\right)\right] \tag{6}$$

the so-called soliton. This solution, shown in Fig. 8, describes the domain wall at $n = 0$ between two adjacent commensurate regions.

For small $\sin\varphi$, Eq. (5) can be linearized, yielding an exponential decay and therefore an exponential repulsive interaction between walls. In two-dimensional systems walls are lines of finite width. Because there are three equivalent directions in a compact crystallographic plane, the domain walls can cross. In a (111)-fcc crystal adjacent domains can correspond to different stackings of the topmost layer, which is either fcc of hcp (Fig. 9). The average period of the dislocation pattern is then given by $D = b/(b - a)$, as a function of the lattice constants b of the film and a of the substrate.

6.4.2 Atomic-scale Template

Self-organization of metal clusters and islands on surfaces relies heavily on the occurrence of surface reconstruction and strain relaxation patterns. Dislocation networks similar to those shown schematically in Fig. 9 have been obtained on hetero- and homo-epitaxial systems. Figure 10 shows the dislocation pattern formed by Ag bilayers on Pt(111). Another, widely studied example, is the surface reconstruction

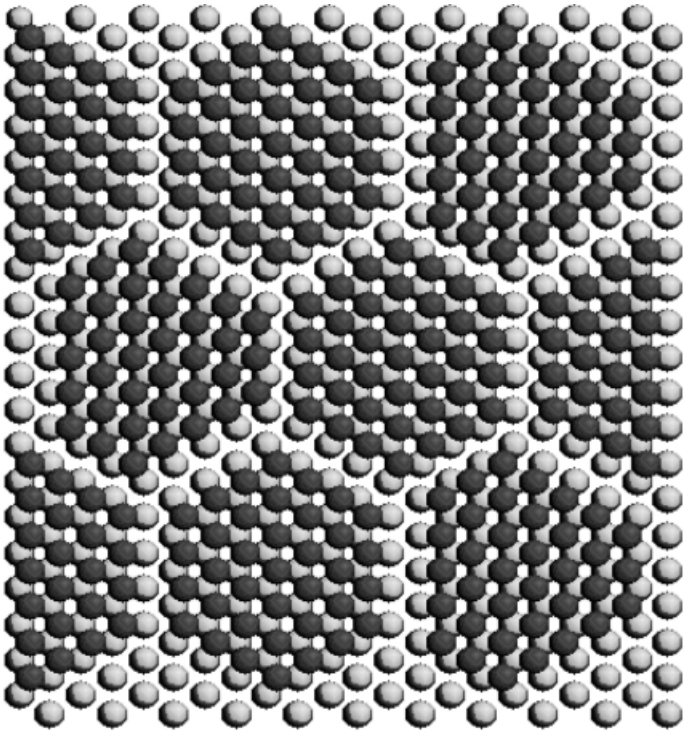

Fig. 9. Schematic diagram of the two-dimensional hard sphere model of fcc and hcp commensurate domains separated by domain walls.

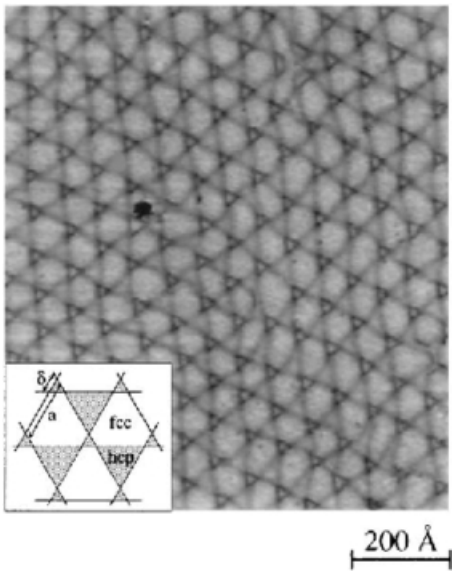

Fig. 10. STM image of the domain wall network obtained after annealing the Ag-bilayer on Pt(111). The inset shows a model for the trigonal domains [63].

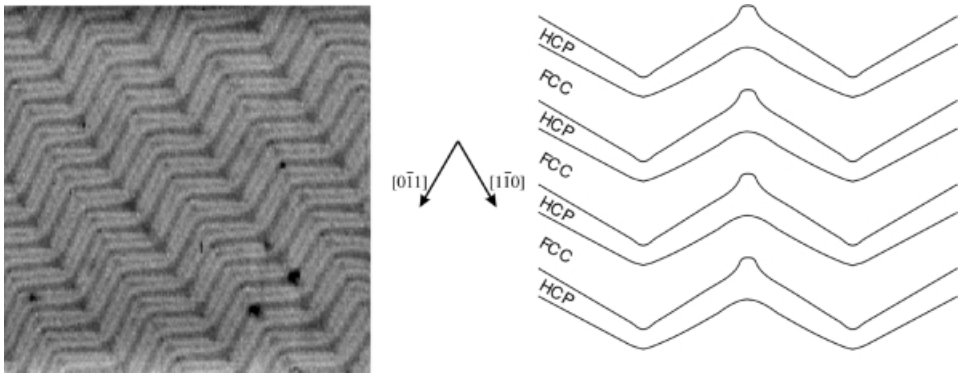

Fig. 11. Zigzag reconstruction of the Au(111) surface. Left: STM image 100 nm × 100 nm. Right: schematic view of the domains.

of Au(111) [61, 62]. Visible in Fig. 11 are the bright contrasts of the zigzag domain walls that produce corrugations in the STM images. These discommensuration walls are limiting fcc and hcp stacking domains of the topmost atomic layer which form spontaneously by strain relaxation. The locations of surface gold atoms vary from the hollow sites of the fcc stacking to the hollow sites of the hcp stacking (the fcc regions are wider than the hcp regions). The fcc to hcp transition (the discommensuration wall) appears as ridges in the STM images, because surface atoms near bridge sites rest about 0.2 Å higher than those in hollow sites.

Because of its particular conformation, the zigzag reconstruction of Au(111) leads to singularities that can best be illustrated as single atomic site dislocations (five nearest neighbors instead of six) located at the elbows of the chevron reconstruction [8]. The dislocations are distributed on a rectangular lattice of unit cell 75 Å × 140 Å. Although this reconstruction was first demonstrated experimentally, it is now fairly well understood as a result of, for example, molecular dynamics simulations [62].

Among other potentially interesting systems with stress relaxation patterns are Ag on Cu(111) [64], Cr on Pt(111) [65], and Au on Ni(111) [29], which have been investigated both experimentally and theoretically. Theoretical prediction for Pt on Co(111) has a similar outcome [66].

6.4.3 Self Organization

Two approaches have been exploited to achieve self-organization of metal clusters – nucleation on ordered point dislocations and nucleation by capture within cells limited by dislocation lines. Some attempts have been made to use these templates for the self-organization of magnetic systems, but as far as we are aware magnetic measurements have been performed on Co/Au(111) only. We will, therefore, focus on Co/Au(111) which has been studied in detail.

6.4.3.1 Nucleation on Ordered Dislocations

It has been observed that the Au(111) surface can be used as a template for growth of organized metal clusters of Ni [8], Co [9], and Fe [67]. The point dislocations at the elbows of the chevron reconstruction (Fig. 12) act as nucleation sites for adatoms adsorbed from the gas phase. For Ni as an example it has been suggested that in the initial stage the mechanism involves site exchange between one Ni and one Au atom [68]. This substituted atom will then act as a nucleation site for further incoming Ni atoms. Self-organized cobalt bilayer clusters containing 300 atoms each can be synthesized in the same way (Fig. 12). If it were possible to store information in these dots, the storage density would reach 10^{12} bits $\cdot$ cm^{-2}, 10^3 times higher than the highest storage densities reached today.

These clusters are stable in an UHV environment at temperatures up to 400 K. Above this temperature the clusters burrow into the gold substrate, simultaneously expelling gold atoms. This is because of the low surface energy of gold which tends to encapsulate the cobalt clusters [15]. Annealing below 600 K, does not significantly perturb the cobalt clusters, because the magnetic properties are preserved. For ex situ measurements and potential applications, Co clusters and films can easily be stabilized by a protective film of a few gold monolayers [15, 69].

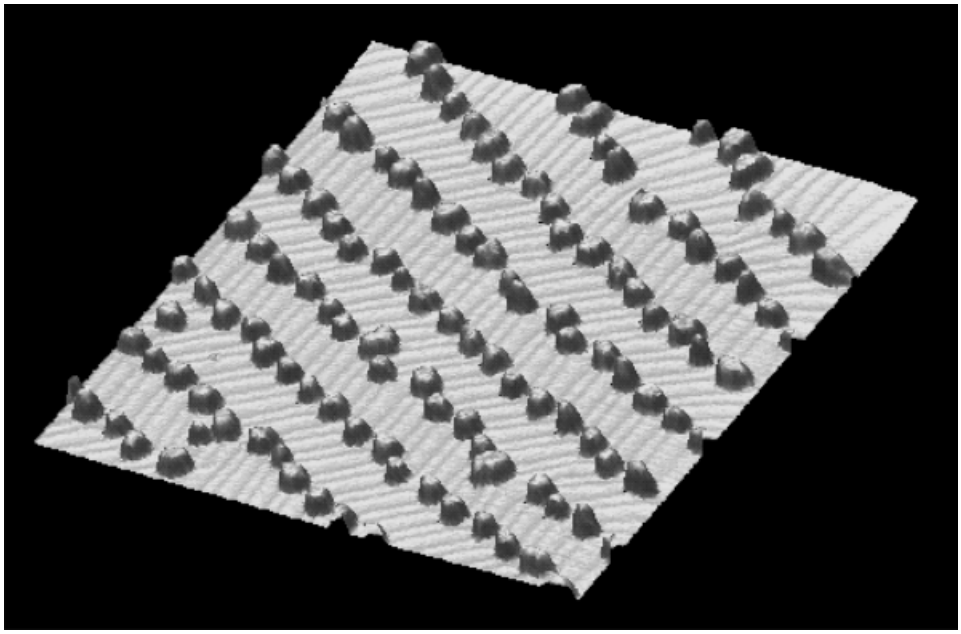

Fig. 12. Cobalt clusters made of two Co monolayers, approximately 300 atoms each, self-assembled on the zigzag reconstruction of the Au(111) surface. Image 100 nm $\times$ 100 nm.

6.4.3.2 Confined Nucleation

Confined nucleation was demonstrated recently [10] for submonolayer Ag structures grown on strain relaxation patterns of Ag/Pt(111) (Fig. 10). Because the dislocation lines repel diffusing silver atoms, the silver atoms are confined inside the unit cell in which they have landed (capture area). Because the Ag adatoms are sufficiently mobile they will form one, and only one, island per unit cell located at the center of the cell. Long-range repulsion at dislocations and the preferred binding to fcc areas creates in each unit cell a local adsorption minimum to which the atoms are guided. The island size distribution for this type of nucleation is binomial and, therefore, significantly sharper than for nucleation on isotropic substrates (Section 6.2). The feasibility of this approach has been demonstrated also for Fe on Cu/Pt(111) [10]. It should be mentioned, however, that this route of synthesizing nanostructures has been tested at low temperature only (below 300 K).

6.4.4 Periodic Patterning by Stress Relaxation

When growing adatom islands on a surface, we must consider that the islands are stressed because of possible lattice mismatch between the island material and the substrate. The stressed islands relax at the boundary and exert a force on the substrate which is elastically distorted and mediates the interaction between islands during growth. Using elastic theory of continuous media, Marchenko [70] and others [71-74] explained the spontaneous formation of periodic domain patterns in different systems. Mesoscopic domain ordering was observed on Si(100) [75], Au(111) [61], Cu(110) covered with oxygen [76], and Pd(110) covered with Cu [27]. The physical origin of these ordering phenomena is believed to be long-range elastic interactions.

Let us consider the uniaxial problem. For a surface comprising alternating stripes of two phases A and B of widths L_A and L_B, respectively, the extra free energy per unit length ΔF, because of the formation of domains is given by:

$$\Delta F = \frac{2F_s}{L_A + L_B} - \left(\frac{2C_{el}}{L_A + L_B}\right) \ln\left(\frac{L_A + L_B}{2\pi a} \sin(\pi\Theta)\right) \tag{7}$$

$$\Theta = L_A/(L_A + L_B),\ 0 < \Theta < 1 \tag{8}$$

ΔF is the sum of two terms, the first term is the free energy per unit length for the creation of a boundary, the second term describes the elastic relaxation. The logarithm becomes infinity for the limits $\Theta = 0$ or 1 and it goes through a minimum for $\Theta = 0.5$. C_{el} depends on elastic properties such as the shear modulus and the Poisson ratio of the substrate, and on the difference between the normal components of the surface stress for domains A and B; a is the lattice constant. The equilibrium periodicity D is obtained by minimizing ΔF relative to L_A, keeping Θ constant:

$$D(\Theta) = \frac{\varkappa}{\sin(\pi\Theta)} = L_A(\Theta) + L_B(\Theta) \tag{9}$$

$$L_A(\Theta) = \frac{\varkappa\Theta}{\sin(\pi\Theta)} \tag{10}$$

where $\varkappa = 2\pi a \exp(1 + F_S/C_{el})$. L_A does not vary much as a function of Θ for $0 < \Theta < 0.7$, and the D curve as a function of Θ is also rather flat around a central value of about half coverage. It has been shown that there should be a firm relationship between the periodicity D at an intermediate coverage Θ and the width of a single island L_A at low coverage [74]. The ratio D/L_A is between 0.25 and 0.33 for coverage of approximately 0.5. This ratio is roughly independent of C_{el} and the free energy for the formation of one boundary.

Several results have been analyzed in terms of this theory. Island ordering has been observed on Cu/Pd(110) above a critical coverage, somewhere between 0.15 and 0.25 ML. At a coverage of 0.2 ML the one-dimensional island-island correlation function in the [001] direction has a repeat distance of 40 Å. Because the average island width is 11 Å, the ratio D/L_{Cu} is 0.28, which is within the predicted interval [27]. This interpretation of island ordering is strictly valid only for systems at equilibrium.

6.4.5 Organization on Vicinal Surfaces

When the mean free path Λ_a of adatoms on a surface (Section 6.2.1) becomes larger than the typical width of a terrace Λ_t, the adatoms will reach the steps before they have the chance to meet another adatom on their path. As a result, in the so called "step flow" limit islands no longer form on the terraces. In favorable circumstances, when the adatoms wet the steps, this leads to the formation of stripes of adatoms oriented parallel to the steps. This approach was first attempted on vicinal surfaces (surfaces with slight miscuts away from a dense crystallographic plane) that develop regularly spaced steps [77, 78]. Results for Co/Cu(111) and Fe/Cu(111) are somewhat disappointing, because the stripes are irregular and sometimes segmented (Section 6.6.2.2). As a result, structures are much less perfect than, for example, the Cu-stripes of Fig. 4b obtained by anisotropic diffusion. Linear arrays of Fe particles have been obtained by the shading technique [79], in which the metal vapor is deposited at a grazing incidence on a SiO-coated NaCl grating.

6.4.6 Low-temperature Growth

As was mentioned in Section 6.2.1, low temperature deposition favors growth of small islands with a high surface density. This behavior manifests itself in a quite spectacular way in Co/Au(111), because of the large incidence of magnetism. As a matter of fact, Co/Au(111) is known to be a prototype of 3D growth, because cobalt forms ordered *bilayer* clusters when grown at 300 K (Fig. 13a). However, as was shown by variable-temperature STM [80], nucleation is completely different when Co is grown on Au(111) at 30 K (Fig. 13b). Small *monolayer*-thick islands with a high surface density form spontaneously [81], and a quasi layer-by-layer growth mode becomes apparent after completion of the first monolayer.

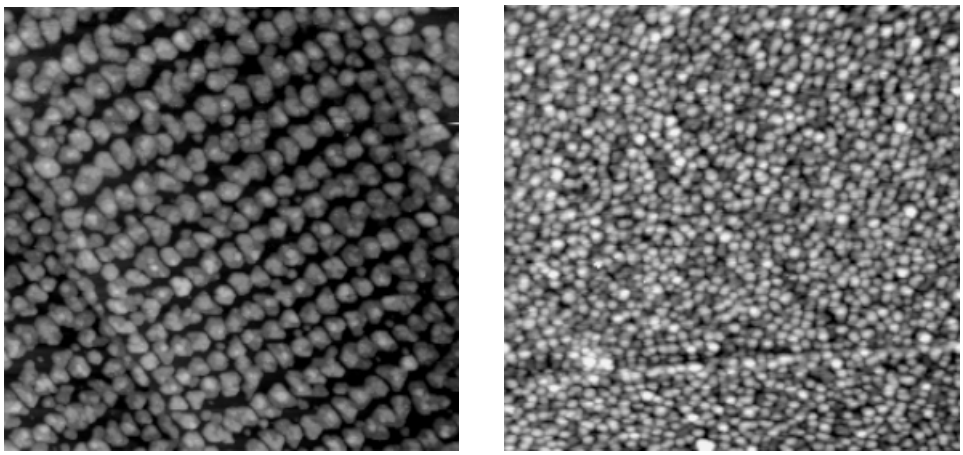

Fig. 13. Comparison of (a) 1.3 ML Co grown on Au(111) at 300 K (image 150 nm × 150 nm) and (b) 1.0 ML Co grown on Au(111) at 30 K (image 100 nm × 100 nm). In (b) compact stacking of monolayer clusters of diameter of 0.5 nm occurs while the 300 K growth in (a) leads to 7-nm bilayer clusters.

As was discussed previously, the growth of Co on Au(111) is normally governed by nucleation on point dislocations of the zigzag reconstruction. This particular mode of growth of bilayer-high islands is observed down to temperatures as low as 150 K. At some point during the reduction of substrate temperature the mean free path of adatom diffusion becomes small compared with the separation between point dislocations of the zigzag reconstruction. The new island density is then given by $N \approx R^{1/3} \exp(-E_{\mathrm{d}}/3kT)$, where R is the deposition rate and E_{d} the diffusion barrier for a cobalt adatom on the gold surface. A much higher density of islands than that expected from self-assembly is, therefore, achieved in the early growth stage at low temperature (Fig. 13). Growth first proceeds by random nucleation of monolayer-thick islands with lateral sizes of approximately 5 Å. The small monolayer-thick islands then coalesce well before a Schwoebel-Ehrlich barrier can form at the island edges [82, 83]. Quasi layer-by-layer 2D growth occurs, in contrast with the 3D growth observed at 300 K. As can be foreseen, the properties of films grown at low and high temperatures will be quite different as will be illustrated later with magnetism as an example.

6.5 Magnetic Properties

Magnetic nanostructures have become the subject of many interesting studies related to their reduced dimensionality. In the text below the important concepts of surface magnetism necessary for understanding the magnetic properties of small objects will be introduced briefly. More details on surface magnetism, ultrathin magnetic structures, and their magnetic properties can be found elsewhere [13, 84–86].

6.5.1 Magnetism in Low-dimensional Systems

In a small cluster, at a surface or in a very thin layer, the environment of most atoms does not have the same symmetry as in the bulk. Bonds are broken and, therefore, the coordination of the atoms is reduced; this results in substantial modifications of the electronic structure. For transition metals the electronic "d" bands, which are responsible for the itinerant magnetism are affected by this symmetry breaking. In a tight-binding scheme the band width, W_S, is directly related to the coordination number [87]:

$$W_S = W(1 - Z_{BB}/Z)^{1/2} \tag{11}$$

where W and Z are the bulk band width and coordination number respectively, and Z_{BB} is the number of broken bonds. In this picture the bandwidth is reduced at the surface and, therefore, the electronic density of states is enhanced (because the number of electronic states is unchanged). The Stoner criterion, (which results from the competition of the exchange energy, gained by transferring electrons from one spin band into the other, and the loss of band energy) tells us that a magnetic state is favored when:

$$Jn(E_F) > 1 \tag{12}$$

where J is the exchange integral and $n(E_F)$ the density of states at the Fermi level.

One expects enhanced magnetic moments at the surface for magnetic "d" metals [88], or in epitaxial film [89]. In epitaxial film, the magnetic moment can also be reduced because of hybridization with the substrate, as for example in Fe/W [90]. As a matter of fact, enhanced magnetic moments have been observed in Stern–Gerlach experiments for free Co [91], Fe [92], and Ni [93, 94] clusters. Rare earth clusters, on the other hand, have much lower global magnetic moment than in the bulk, probably because of spin canting [95].

Even more surprising, some metals that are non-magnetic in the bulk (e. g. V, Rh, Ru, Pd) are expected to be magnetic when the atomic coordination drops [96], as in free-standing or epitaxial films [97–100]. Indeed, free Rh clusters were found to be magnetic in Stern-Gerlach experiments [101], confirming theoretical calculations [102].

There is, however, currently no clear evidence of ferromagnetism in epitaxial layers or supported clusters of such metals. For V, Rh, or Ru clusters on Ag or Au the situation remains controversial, but nearly all experiments give negative results [103–107]. Recent anomalous Hall effect and weak localization experiments might indicate that Ru atoms have a small magnetic moment when deposited on Pd at a very low coverage [108]. These results should, however, be confirmed by other magnetic characterization techniques. As demonstrated theoretically [109], the magnetism of these metals is highly sensitive to the local environment. Diffusion or imperfections, which are found in real systems, lead to a complete extinction of the magnetic state.

Another difficulty is that an assembly of small ferromagnetic clusters often has an average magnetization of zero, because of thermal fluctuations. The clusters behave

like independent giant magnetic moments, fluctuating on a very short time scale. The fluctuations can be blocked only at very low temperatures (depending on cluster size). This is the so-called superparamagnetic behavior (Section 6.5.4).

6.5.2 Anisotropy in Ferromagnetic Nanostructures

In bulk magnetic materials, with no applied external magnetic field the magnetization lies in a preferential direction, the so-called easy magnetization axis, which often coincides with a high-symmetry crystallographic direction. This magnetocrystalline anisotropy arises from the spin–orbit coupling which forces the electron spin to couple with its orbital momentum (relative to the lattice) [110]. This mechanism applies for localized spin magnetism and for itinerant magnetism. For uniaxial perpendicular anisotropy, and neglecting higher order terms, the magnetocrystalline anisotropy energy is written phenomenologically as:

$$E_{\mathrm{mc}} = V\left[K_{2\mathrm{mcv}}\sin^2\theta + K_{4\mathrm{mcv}}\sin^4\theta\right] \tag{13}$$

where V is the volume, θ is the angle between the easy axis and the magnetization, and $K_{2\mathrm{mcv}}$ and $K_{4\mathrm{mcv}}$ are the first- and second-order anisotropy constants. Eq. (13) is not a general case – when in-plane anisotropies are present, one must add an anisotropy term taking into account the energy-dependence of the in-plane projection of the magnetization.

At surfaces or interfaces the broken symmetry modifies the coupling and specific surface anisotropy can appear, as suggested by Néel [111]. The surface anisotropy, which is actually also of magnetocrystalline origin, can favor an easy magnetization direction either parallel or perpendicular to the surface plane. Actually, the true surface/interface anisotropy is difficult to estimate experimentally. It often contains in a hidden way magneto-elastic effects occurring from the strain present inepitaxial films [112]. Its energy contribution is:

$$E_{\mathrm{s}} = SK_{\mathrm{s}} \tag{14}$$

where S is the surface area and K_{s} the surface anisotropy constant.

Another source of anisotropy is the shape anisotropy which arises from long-range dipolar interactions between magnetic moments. It is highly dependent on the shape of the object [113]. For a revolution ellipsoid the energy of the shape anisotropy contribution is:

$$E_{\mathrm{dip}} = \mu M_{\mathrm{s}}^2 V\left[(N_{\mathrm{para}} - N_{\mathrm{perp}})\sin^2\theta + N_{\mathrm{perp}}\right]/2 \tag{15}$$

where V is the volume, M_{s} the saturation magnetization, and θ the angle between the magnetization and the ellipsoid axis. N_{para} and N_{perp} are factors which depend on the shape of the magnetic object. One has $2N_{\mathrm{para}} + N_{\mathrm{perp}} = 1$. For a thin two-dimensional film $N_{\mathrm{perp}} = 1$, and taking $K_{\mathrm{dip}} = -\mu_0 M_{\mathrm{s}}^2/2$ one can write, dropping the constant term:

$$E_{\mathrm{dip}} = K_{\mathrm{dip}} V\sin^2\theta \tag{16}$$

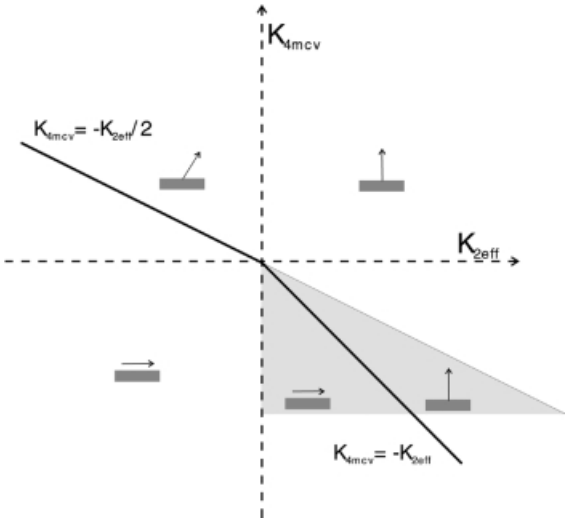

Fig. 14. Easy axis orientation as a function of $K_{2\mathrm{eff}}$ and $K_{4\mathrm{mcv}}$. The shaded area corresponds to a metastable zone where out-of-plane and in-plane domains can coexist [114].

Shape anisotropy favors in-plane anisotropy. It is zero for an in-plane uniform film ($\theta = \pi/2$). Shape anisotropy can, however, become important for nanostructures with finite lateral sizes and high aspect ratios. The total anisotropy energy is given by the sum of all contributions and can be written as:

$$E_{\mathrm{A}} = V\left[K_{2\mathrm{eff}}\sin^2\theta + K_{4\mathrm{mcv}}\sin^4\theta\right], \text{ where} \tag{17}$$
$$K_{2\mathrm{eff}} = K_{2\mathrm{mcv}} + K_{\mathrm{dip}} + K_{\mathrm{s}}/d$$

The equilibrium direction of the magnetization is obtained by minimizing the energy with respect to θ. A phase diagram providing the preferred directions is given in Fig. 14 as a function of $K_{2\mathrm{eff}}$ and $K_{4\mathrm{mcv}}$ [114]. Usually $K_{4\mathrm{mcv}}$ (and the higher-order terms), is neglected but it is this term which can produce a canted easy axis.

If $K_{2\mathrm{eff}} > 0$, there will be an out-of-plane magnetization. According to Eq. (17), because $K_{2\mathrm{mcv}} + K_{\mathrm{dip}} < 0$ there is a critical thickness, $d_c = -K_{\mathrm{S}}/(K_{2\mathrm{mcv}} + K_{\mathrm{dip}})$, below which an out-of-plane magnetization axis can be found, assuming $K_{\mathrm{s}} > 0$.

The anisotropy is extremely difficult to compute for real systems, because the theory relies on the ab initio resolution of the relativistic Dirac equation [115, 116], although perturbative theories have been attempted [117]. Many systems have been studied both theoretically and experimentally for their anisotropy properties. We mention only some theoretical work on ordered nanostructures, Co wires, either free standing or in epitaxy on Pd(110) [118]. Length effects are demonstrated for short chains (less than five atoms). Free standing Co chains (not too short) are shown to have an easy axis along the chain. When deposited on the Pd substrate the easy axis is perpendicular to the chain and to the substrate surface.

6.5.3 Magnetic Domains

In the absence of any magnetic field, the magnetization lies along an easy magnetization axis. It can, however, point in the two opposite directions of this axis, or even more if there is higher magnetocrystalline symmetry. Magnetic domains with opposite magnetization directions (denoted plus and minus) therefore coexist, separated by domain walls in which the magnetization rotates over a short length from plus to minus.

Magnetic domains appear because of a balance between short-range exchange coupling (J), which tends to align adjacent spins in ferromagnetic materials, and long-range magnetostatic (dipolar) coupling, favoring antiparallel alignment (which keeps stray fields small). The wall width, w, between two domains is roughly given by a micromagnetic model $w = \sqrt{J/K}$. In nanostructures, the sizes of the objects are comparable with, or even smaller than, the magnetic wall width. In these circumstances no walls can form inside the objects and a single domain state is expected (neglecting edge effects). For continuous films different domain structures may form (stripe domains, checkerboard, single domain states), depending on the relative strength of the anisotropy and the dipolar coupling [119–121].

Domains in ultrathin films are usually observed by secondary electron microscopy with polarization analysis (SEMPA), magnetic force microscopy (MFM), or Kerr microscopy. Magnetic imaging techniques are described in detail elsewhere [122]. An illustration is given in Fig. 15 for a Co wedge grown on Au(111) [123]. Dark and bright regions correspond to plus and minus magnetized zones. On the left of the figure the easy axis is out of plane, on the right the magnetization lies in plane. Other examples, and discussion of domains in thin films, can be found elsewhere [124].

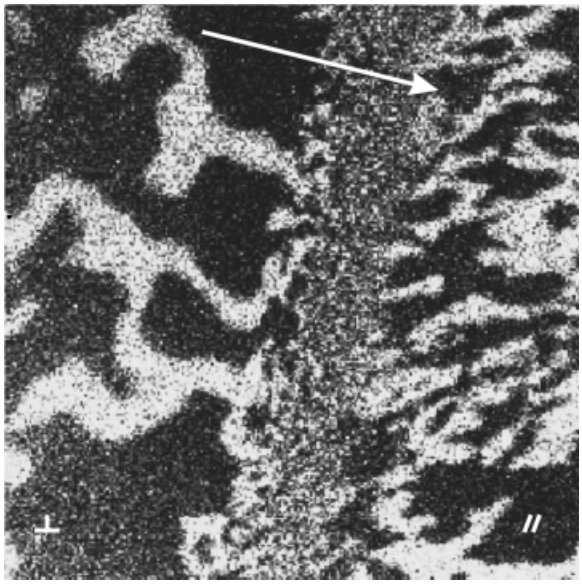

Fig. 15. Composite SEMPA image of a Co wedge on Au(111) showing magnetic domains. The wedge is along the arrow, from 3 ML (left) to 6 ML (right) Co. The magnetization is out-of-plane on the left, in-plane on the right. Image 112.5 nm × 112.5 nm [123].

6.5.4 Superparamagnetism

Small ferromagnetic particles, like those obtained in organized growth, can be in a magnetic single domain state as mentioned earlier. They have a macroscopic magnetic moment $m = n\mu$ (n is the number of atoms in a particle and μ the magnetic moment per atom). If K is the anisotropy constant (e. g., uniaxial) and V the particle volume, the magnetic energy of the system is $E = KV \sin^2\theta$. It can be regarded as a two-level system separated by a barrier KV.

For very low temperatures ($k_B T \ll KV$), m is locked in one state along the easy axis. For intermediate temperatures ($k_B T \approx KV$), the switching of m between the two states is thermally activated with a probability $\nu = \nu_0 \exp[-KV/(k_B T)]$ (ν_0 is of the order of $10^9\ s^{-1}$). The magnetic moment of the particles will fluctuate over a typical time scale $\tau = 1/\nu$. A sufficiently high applied field will align the individual giant moments m. When the field is turned off the moments will relax and the macroscopic magnetization of the assembly of particles (assumed non-interacting), $M(t)$, will decrease in accordance with $M(t) = M_s \exp(-t/\tau)$. In the high temperature regime, the fluctuations occur over a very short time-scale and a continuum of states in θ can be considered. High fields are needed to saturate the cluster assembly. The total magnetization in a field, $M(H)$ is given by the Langevin function:

$$M(H) = M_s L[\mu_0 M_s V H/(k_B T)], \text{ where } L(x) = \text{cotanh}(x) - 1/x \qquad (18)$$

Jacobs and Bean have arbitrarily defined a blocking temperature, $T_B = 25\,KV$ [125]. A system well above T_B is said to be superparamagnetic and will have anhysteretic magnetization loops (given by the Langevin function) in a cycling applied field. In the vicinity of, or below, T_B one observes hysteretic magnetization loops as soon as the sweeping rate is fast, because the system has a finite relaxation time. If the field is applied quasi-statically, allowing the system to relax, the hysteretic behavior disappears. One must, therefore, be careful when comparing experimental blocking temperatures obtained with different techniques, because the sampling times can differ by several orders of magnitude!

6.5.5 Dimensionality and Critical Phenomena

The presence of long-range magnetic order in a system of dimensionality D at a non-zero temperature depends on the model used to describe the interaction between the spins and, in particular, on their number of degrees of freedom, n. It is, for example, well known from the Mermin–Wagner theorem that magnetic long range order is not observed for an infinite isotropic two dimensional system at finite temperatures. At the ferromagnetic/paramagnetic transition, critical exponents are defined. The spontaneous magnetization, M_s, is proportional to t^β, where $t = (T - T_c)/T_c$ (where T_c is the critical temperature), and the susceptibility is proportional to $1/t^\gamma$. The values of the critical exponents depend on the model. Table 1 lists all the simple cases encountered, namely the Ising model ($n = 1$), the XY model ($n = 2$), and the Heisenberg model ($n = 3$) [86].

Table 1. Critical exponents, and presence or absence of long-range order for the different models [86].

	$D = 0$	$D = 1$	$D = 2$	$D = 3$
$n = 3$ (Heisenberg)		No long range order at $T \neq 0$		$\beta = 0.3647$ $\gamma = 1.3866$
$n = 2$ (XY)	Super-para-magnetism		$\gamma = \infty$ No long-range order	$\beta = 0.346$ $\gamma = 1.316$
$n = 1$			$\beta = 1/8$ $\gamma = 7/4$	$\beta = 0.3250$ $\gamma = 1.2402$

Organized clusters, stripes, and thin flat layers enable study how magnetic long-range order appears and how the critical exponents evolve [85]. Monte Carlo methods enable simulations of more realistic systems, by taking into account finite anisotropy terms [126, 127] and the dipolar interaction [127, 128] both of which can stabilize long-range order in 2D systems (Section 6.6). These stabilizing effects are of great importance in low-dimensional nanostructures. One should note that the "magnetic" dimensionality is not always connected with the real "topographic" dimension of the nanostructures.

6.6 Magnetic Nanostructures – Experimental Results

In the following text we will analyze several examples how ferromagnetism sets in as a function of coverage. We will see how the different ingredients, e. g. surface anisotropy and dipolar interactions, enable either true low-dimensional ferromagnetism to appear, or phases close to it. We will discuss the magnetic properties of nanostructures of non-interacting, well separated islands, of interconnected islands forming stripes, and of almost continuous films of two-dimensional character. Because of the amount of work available, it is not possible to give a review of all the systems studied and we will limit ourselves to structures which have been well defined and characterized both magnetically and topographically.

6.6.1 Isolated Islands

From the considerations in Section 6.5, one expects the formation of separated and magnetically non-interacting clusters in the early stage of growth. As coverage increases, these islands coalesce and can form fractal, linear, or film-like structures. At this stage magnetic interactions (exchange and dipolar coupling) set in. A typical illustration of this is given by the Fe/W(110) and Co/Au(111) systems.

6.6.1.1 Fe/W (110)

For room-temperature growth, Fe grows into epitaxial monolayer islands (Fig. 16). As long as the islands remain separated, i. e. up to a coverage of 0.58 ML, no ferromagnetic signal is observed (Fig. 17) [14]. There is an abrupt onset of ferromagnetism, measured by spin polarized low energy electron diffraction (SPLEED), as soon as the islands coalesce, at 0.6 ML.

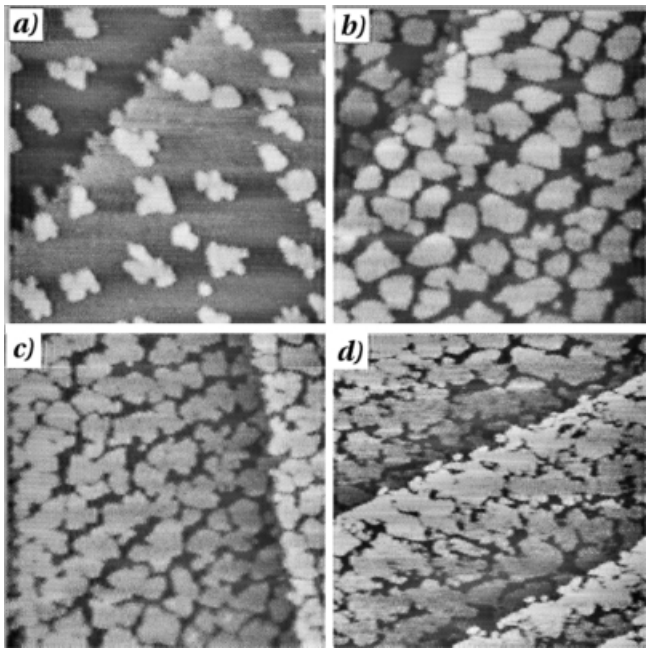

Fig. 16. STM image for (a) 0.23 ML Fe (b) 0.53 ML, (c) 0.66 ML, (d) 0.85 ML Fe grown on W(110) at room temperature. Images 70 nm × 70 nm [14].

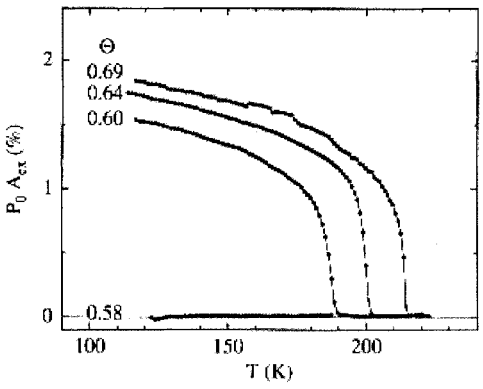

Fig. 17. SPLEED-polarization as a function of measurement temperature for different Fe coverage, at 300 K, of W(110) [14].

The ferromagnetic phase, in the 2D limit, will be discussed later, in Section 6.6.3. Below 0.6 ML the films are supposed to be in a superparamagnetic state. The islands are too small to have a blocked magnetic moment. This is a quite general behavior in the low coverage limit and it will be analyzed more precisely for Co/Au(111).

6.6.1.2 Co/Au(111)

As mentioned earlier, Co grows in well ordered, bilayer-high clusters on the surface zigzag reconstruction of Au(111) (see, e. g., Fig. 12) [9]. At room temperature Co clusters nucleate at the kinks of the gold reconstruction and expand laterally as a function of coverage, until they come close to contact at about 1.0 ML (because the clusters are bilayers the gold surface is half-covered with Co). Here we will consider only coverage below 1.0 ML, where the assumption of non- or weakly interacting clusters is valid.

Because the saturation fields needed to evidence the superparamagnetic state are so high, in situ Kerr-effect measurement on as-grown clusters is difficult. The samples must, therefore, be covered by a protective layer. When measured ex situ in high fields by the Kerr effect or SQUID, an anhysteretic magnetization curve, characteristic of a superparamagnetic state, is obtained (Fig. 18)[16, 129, 130]. The saturation fields are approximately 10 kOe.

Because the magnetization of superparamagnetic clusters is described by a Langevin function of argument $N\mu_B/k_BT$, the experimental curve enables, in principle, determination of the size of the clusters. One must assume that the clusters are all of the same size. This is, actually, true for self-organized Co clusters nucle-

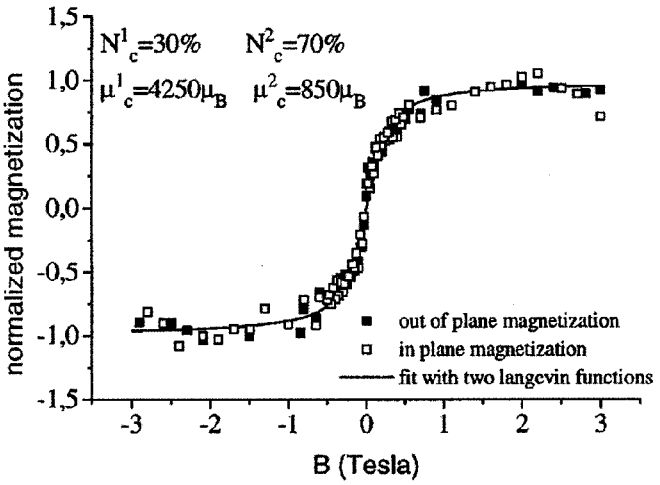

Fig. 18. SQUID magnetization curves recorded at 290 K for 0.4 ML Co on Au(111). The data points are fitted by a sum of two Langevin functions corresponding to two populations of clusters of different size (given in values of giant moments μ'_c). The fit gives the proportion of the two populations, N_c^i [16].

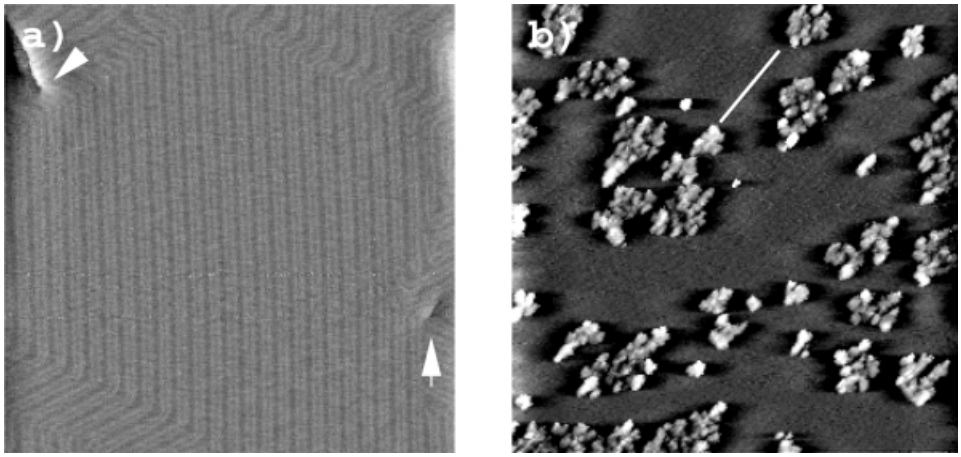

Fig. 19. (a) STM images of a clean Au(111)/mica surface with linear reconstructions, pinned by screw dislocations (arrows). (b) 0.3 ML Co grown on a linear reconstructed zone. The white line indicates the direction of the reconstruction. Images 150 nm × 150 nm [16].

ated on the herringbone reconstruction. The magnetization curves in Refs [16] and [129] are, however, measured on Co clusters deposited on thick gold films grown on mica substrates. The Au surface of such samples has many more defects than the well prepared Au(111) single crystalline surface. On Au/mica substrates regions with the usual herringbone reconstruction coexist with linearly reconstructed regions (Fig. 19a) where the Co atoms nucleate randomly and form clusters four to five times larger than those nucleated on the herringbone (Fig. 19b). Although they represent only 20 to 30 % of the total number of clusters, they contribute to the main part of the magnetic signal [16]. One must, therefore, be very careful when estimating cluster sizes from Langevin function fits.

Small and well calibrated clusters, like the Co clusters on Au(111), are suited to study electronic properties. As mentioned previously, modifications in the electronic structure can be expected in small clusters. Indeed, changes in the electronic structure are observed by Kerr spectroscopy for Co coverage below 2 ML [131]. The consequence is an enhanced orbital magnetic moment, as shown by X-ray magnetic circular dichroism (Fig. 20).

The enhanced orbital contribution leads to slightly larger anisotropy in the small clusters [132]. Similarly, a doubling of the orbital moment of Fe has been observed for small clusters deposited on graphite [133]. A spectacularly increased magnetic moment has also been observed for Co and Fe atoms on Cs for extremely low amounts of deposited material [134].

Presently, such small organized dots are of great interest in the study of fundamental aspects of magnetism. Because of their very low blocking temperature, however, (below 30 K at approximately 0.5 ML) they are not yet suitable for technological application in magnetic data storage. In the outlook of this review (Section 6.7) we will show how this inconvenience might be overcome.

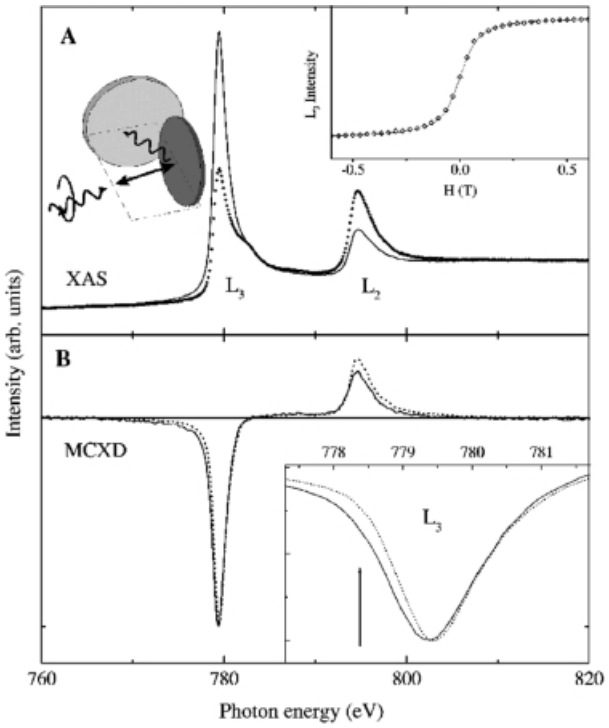

Fig. 20. (a) X-ray absorption spectra of the Co L edges for 1.5 ML Co on Au(111) for the two photon spins in a 4 T field at 20 K. (Inset: Langevin function fit of the magnetization curve). (b) XMCD difference spectra for 1.5 ML Co (dashed line) and ~0.2 ML (continuous line). The differences are because of modification of the orbital magnetic moment [132].

6.6.2 Interacting Islands and Chains

In this section four types of linear structures, obtained in various ways, are considered. They illustrate different magnetic regimes. The Co/Au(111) system in the 1 ML coverage range is briefly mentioned in this part and treated in detail in Section 6.6.3. The Fe/Cu(111) and Fe/W(110) systems are discussed because of their peculiar growth on vicinal surfaces.

6.6.2.1 Co/Au(111)

At 1 ML Co coverage, bilayer Co clusters grow laterally and come close to contact. They form more or less continuous bilayer chains approximately 8 nm wide and 100 nm long. The chains, separated by approximately 15 nm (Fig. 13b), remain superparamagnetic. If these chain structures are considered as a unidimensional arrangement of spins with perpendicular anisotropy (1D Ising model), magnetic long range order is not expected (Table 1) – indeed, the chains behave as large fluctuating spin blocks the sizes of which are larger than those of individual clusters [129, 132]. In these circumstances the magnetization curves are not supposed to fit a Langevin function, because the clusters interact with each other.

6.6.2.2 Fe/Cu(111)

As mentioned in Section 6.4.5, metallic stripes can be obtained upon deposition on vicinal surfaces. In the first growth stages there is preferential nucleation of the deposited atoms at the step edges. The aggregation in the steps produces stripes with width controlled by the total coverage. The miscut angle of the crystal determines the spacing between the steps (hence the spacing between adjacent stripes). For example, the Fe stripes in Fig. 21 are obtained on a Cu(111) vicinal surface (miscut 1.2°) for 273 K deposition [78]. The stripes are aligned along ⟨011⟩. They are monolayer high and have a width of approximately 10 nm (coverage 0.3 ML). As in the previous example the chains are not perfectly continuous – it is apparent that defects sometimes interrupt the stripes.

No magnetic longitudinal Kerr signal is obtained, irrespective of the field applied along or perpendicular to the stripes. Hysteretic polar Kerr loops are obtained at low temperatures, from 50 K for 0.3 ML to approximately 200 K for 0.8 ML (Fig. 22), suggesting a ferromagnetic phase for a quasi-1D system with out-of-plane anisotropy. The remanence of these Fe stripes is, however, time-dependent. After application of a field pulse the remanent magnetization decreases over a period of several seconds (Fig. 23). This demonstrates the presence of fluctuating spin blocks, which can be partially frozen at low temperatures. There is, therefore, only magnetic long-range order over a limited time-scale. The hysteretic behavior arises because, at a given temperature, the sweeping rate of the field is much higher than the fluctuation time of the spin blocks. The magnetization curves can be fitted in an Ising model description in which Glauber-type dynamics have been introduced [78]. In this model, for a given

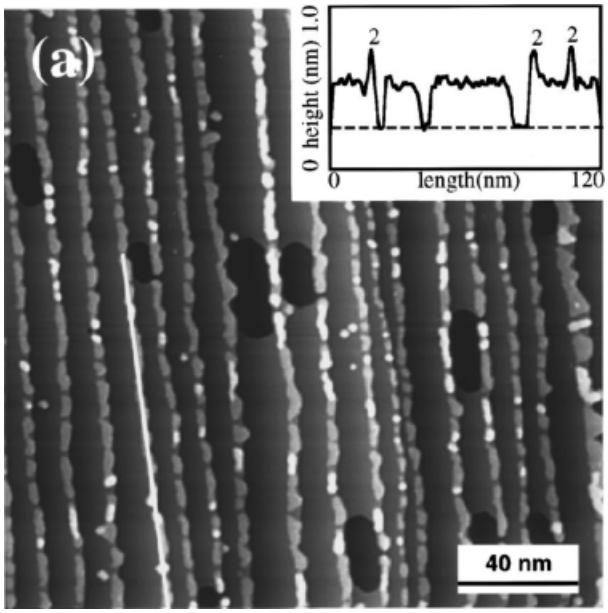

Fig. 21. Fe stripes on vicinal Cu(111) for 0.3 ML coverage A linescan is given along the white line [78].

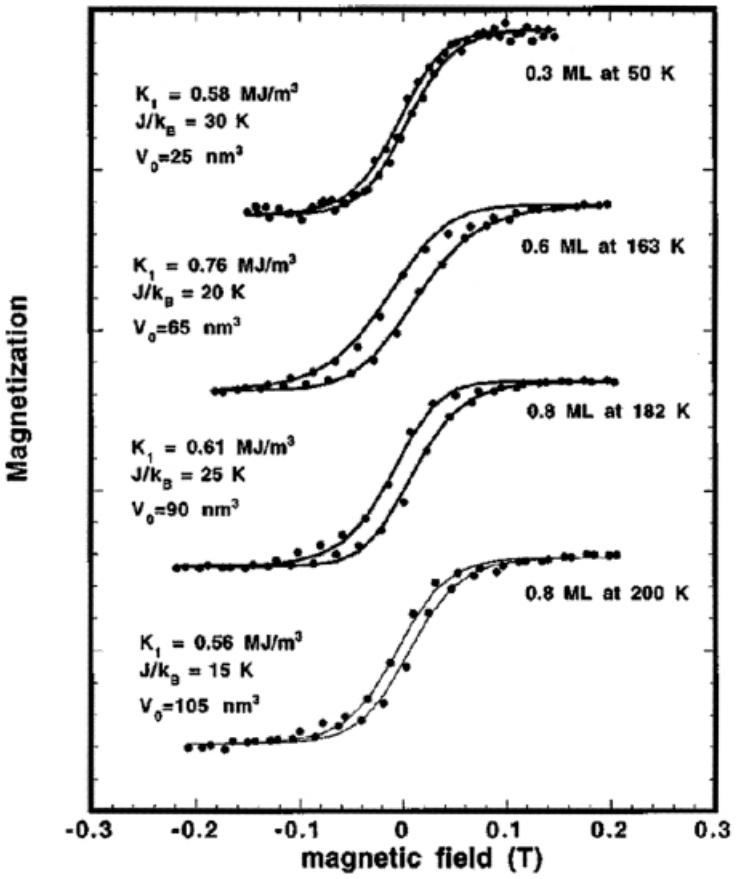

Fig. 22. Kerr loops of Fe on vicinal Cu(111) recorded for different temperatures and coverage. The solid lines are theoretical curves obtained in the Glauber-type model (see text) for the given anisotropies (K_1), exchange constant (J) and volume (V_0) [78].

field sweeping rate, the anisotropy, K_1, the volume, V_0, of the spin blocks, and the exchange coupling strength, J, between adjacent segments can be deduced from the fit.

6.6.2.3 Fe/W(110)

Similar Fe stripes were also obtained on a W(110) vicinal crystal (miscut 1.4°). In this instance, and in contrast with Fe/Cu(111), persistent remanent magnetization is observed [135], although long-range order should not be observed for non-interacting single stripes. The Fe stripes are, however, parallel to [001], whereas the easy magnetization axis of Fe/W(110) is along $[1\bar{1}0]$, i. e. perpendicular to the Fe stripes, because of a strong uniaxial in-plane surface anisotropy (despite the shape anisotropy). Because the spins are perpendicular to the stripes, the dipolar interaction across the

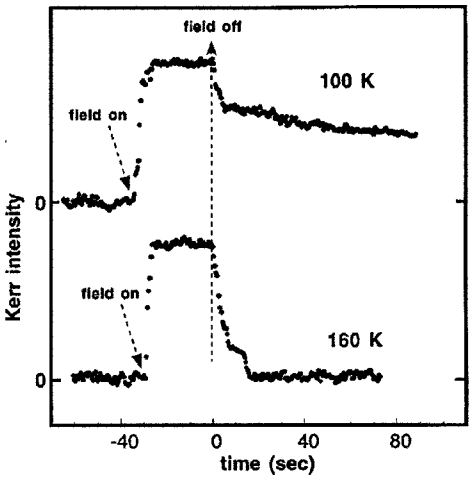

Fig. 23. Kerr signal as a function of time for an applied field pulse for a 0.8 ML Fe film on Cu(111) [78].

stripes favors alignment between spin blocks in two adjacent chains (to keep stray fields low). This additional dipolar interaction is expected to stabilize the long range ferromagnetic order.

6.6.2.4 Fe/SiO/NaCl(110)

Fe particles, arranged into linear arrays were obtained by deposition of Fe on a SiO-coated NaCl(110) crystal, which has natural facets forming grooves (Fig. 24, right) [79]. Because Fe is deposited on a SiO buffer, the clusters are not expected

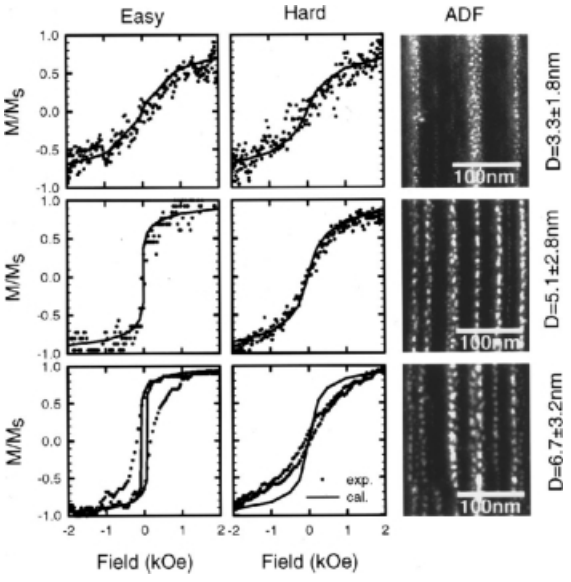

Fig. 24. Magnetic (Kerr) and structural (transmission electron microscopy) for Fe particles on SiO-coated NaCl. The average particle size is given on the right. The easy magnetization axis is along the wires. The continuous lines represent the Monte-Carlo simulated magnetization loops [79].

to have well defined crystallographic order. In contrast with Fe/W(110), therefore, the magnetic anisotropy should be weak. Above a given size, the clusters couple through the dipolar interaction and the magnetization aligns along the particle chains (Fig. 24, left and middle), for minimization of the stray field. The presence of long-range magnetic order in this system could be reproduced by Monte Carlo simulations.

6.6.3 The 2D Limit

By use of selected examples we illustrate the transition from non-, or weakly interacting structures, towards correlated, two-dimensional structures.

6.6.3.1 Co/Au(111)

We mentioned in Section 6.6.2.1 that at 1 ML coverage, the Co structures on Au(111) have no remanent magnetization. The first ferromagnetic signal is obtained at 1.6 ML. The two STM pictures in Fig. 25 are indicative of two slightly different coverages (1.4 ML and 1.6 ML); also shown are the corresponding in situ Kerr magnetization loops. The abrupt transition indicates a percolation threshold below which there is no ferromagnetic signal.

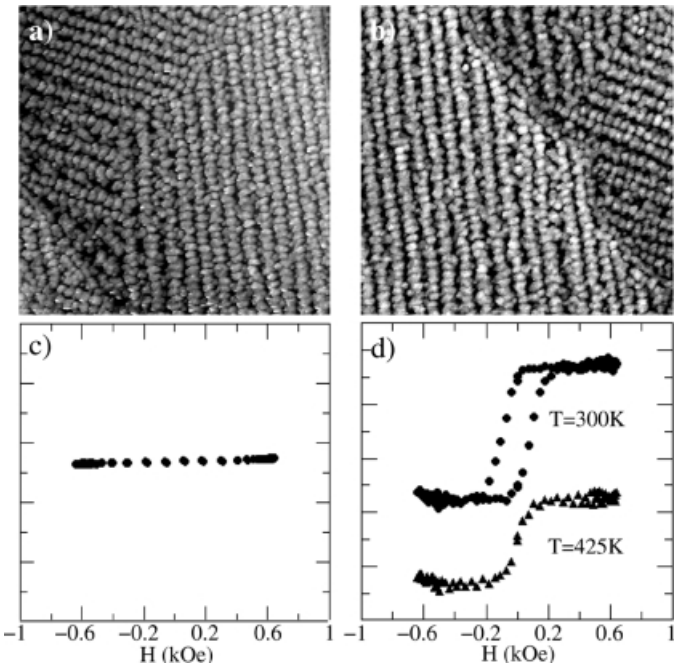

Fig. 25. STM images for (a) 1.4 ML and (b) 1.6 ML Co on Au(111) with the corresponding polar Kerr signals (c) and (d). Images 200 nm × 200 nm [16].

Monte Carlo simulations were performed to describe the onset of ferromagnetism as a function of Co coverage [16]. We assume an $N \times N$ hexagonal array of Co clusters of approximately 75 Å average diameter (2 ML thick) with a giant magnetic moment. The system is described in a 2D Heisenberg-like model. The Hamiltonian is:

$$H = S \sum_{i,j} \delta_{i,j} \sigma_i \varepsilon_i \sigma_j \varepsilon_j - KV \sum_i \left(\sigma_i^z \varepsilon_i\right)^2 - \mu_0 MH \sum_i \sigma_i^z \varepsilon_i \tag{19}$$

where σ_i is the normalized magnetization of the cluster at a site i (M is the saturation magnetization), $\varepsilon_i = 1$ or 0 if the site is occupied, or not, by a cluster, $\delta_{i,j} = 1$ for nearest neighbor clusters (0 otherwise), S is the contact surface between the clusters, V the individual cluster volume, K the perpendicular anisotropy constant, H the external field (applied in the z direction, perpendicular to the surface), and γ is the wall energy, for two opposite magnetizations in two adjacent clusters. The wall energy can be estimated from a micromagnetic model ($\gamma = 2\sqrt{JK}$). The dipolar coupling between chains is neglected (it can be neglected at room temperature, but dipolar effects can be observed at low temperature). The numerical values used for the simulation are reported in the caption of Fig. 26. We start from the situation of 1 ML coverage, i. e. from an array of chains separated by a line of unoccupied sites (white in Fig. 13). Then we start filling the unoccupied sites randomly with clusters. The σ^z-maps (there is nearly no in-plane component of σ) are shown for several coverages in the demagnetized state at $T = 300$ K.

Below 1.5 ML (Fig. 26a, b) the up and down domains are small and confined within the chains. There are not enough connections to the adjacent row to enable strong magnetic coupling. At about 1.5 ML, (Fig. 26c) the domain size increases and they start spreading over the whole surface. At 2 ML (Fig. 26d), the domain structure is very similar to that observed experimentally [136]. The corresponding simulated magnetization curves are represented. A drastic decrease of the saturation field is observed from 1 to 1.5 ML. Significant remanent magnetization appears above 1.2 ML. These simulations are in quantitative agreement with experimental results. Because of perpendicular anisotropy, there is a transition from a 1D Ising-like system with no ferromagnetic long-range order, towards a long-range ordered 2D Ising system.

6.6.3.2 Fe/W(110)

As mentioned in Section 6.6.2.1, the abrupt onset of ferromagnetic order at 0.6 ML coverage corresponds to the percolation of the Fe islands as observed by STM. The Fe/W(110) system is an ideal system to study critical phenomena, because it is possible to obtain a thermodynamically stable and flat monolayer film. The Curie temperature can be easily measured, as can critical exponents. It has been shown that an Fe monolayer on W(110) can be described as a two-dimensional anisotropic Heisenberg system (actually the critical phenomena were analyzed on a Fe monolayer deposited at high temperature, which is thermodynamically stable) [137].

It is worth mentioning that the room-temperature-deposited films have somewhat peculiar behavior in the 1.2 ML to 1.5 ML range. These Fe sesquilayers (i. e. one

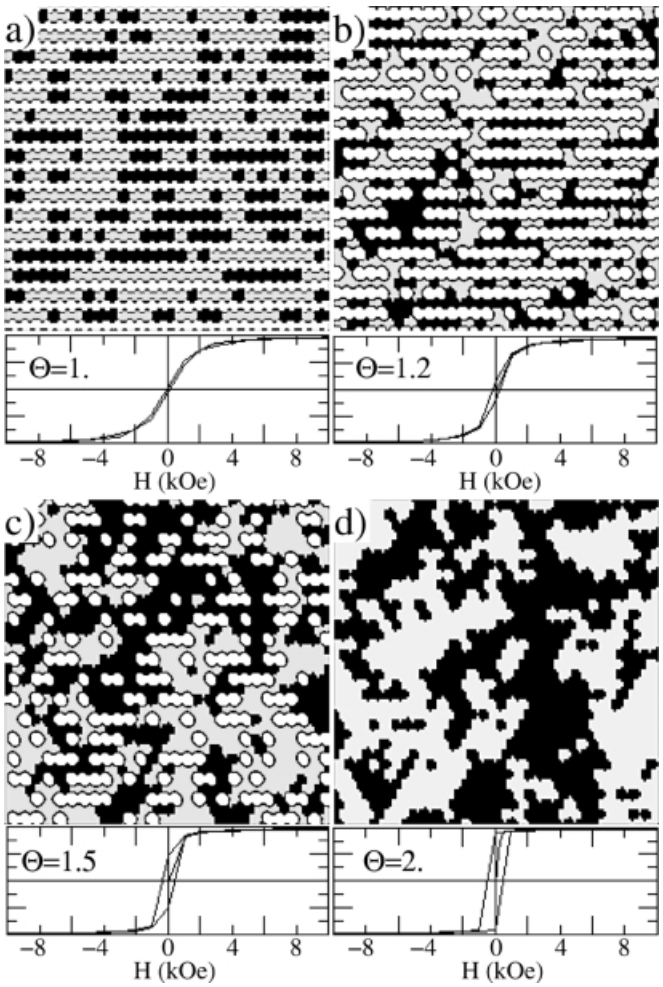

Fig. 26. Demagnetized σ^z maps of 30×30 sites for different coverages θ. Unoccupied sites are in white, occupied sites with up (down) magnetization in gray (black). Hysteresis loops and first magnetization loops are shown [16]. $\gamma S/k_B = 125\,\mathrm{K}$, $KV/k_B = 1000\,\mathrm{K}$, $M/k_B = 1000\,\mathrm{K/T}$.

monolayer and a half) on W(110) lose their remanent magnetization [138] (Fig. 27). STM pictures show that in this coverage range double-layer Fe islands are surrounded by an Fe monolayer sea (Fig. 28) [139].

Torsion oscillatory magnetometry coupled with Kerr effect measurements at different temperatures show that the Fe monolayer is ferromagnetic with in-plane anisotropy whereas the double layer islands are superparamagnetic with a perpendicular anisotropy; some of these are blocked, others are not. The coupling between the double-layer islands and the surrounding layer produces micromagnetic phenomena not yet very well understood. The perpendicular anisotropy of the double

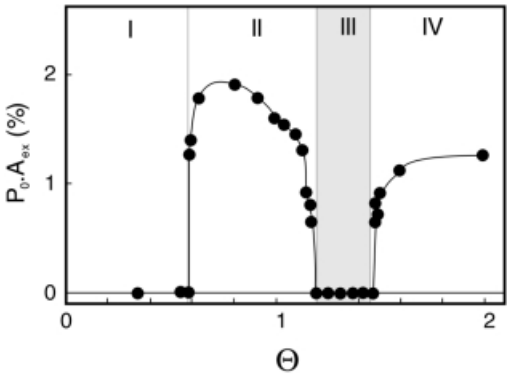

Fig. 27. SPLEED-polarization as a function of Fe thickness. Note the absence of magnetic signal in region III [138].

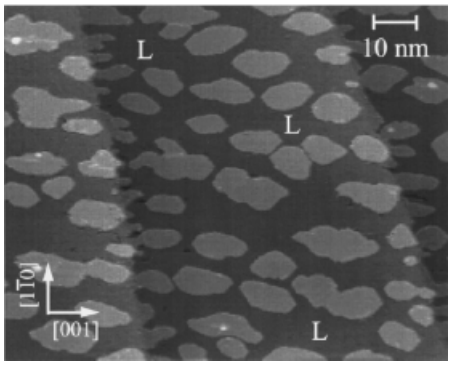

Fig. 28. STM picture of an Fe sesquilayer on W(110). L indicates the Fe monolayer [139].

layer islands is attributed to the high epitaxial strain in the Fe. Above 1.5 ML misfit dislocations enable strain release and the system returns to the normal situation of an in-plane magnetized film.

6.6.3.3 Co/Cu(100)

For low-dimensional structures interesting questions arise at the critical temperature above which long-range ferromagnetic order disappears. Is the critical temperature a true Curie temperature, at which the spontaneous magnetization vanishes, is it a superparamagnetic blocking temperature, or does the film just break into domains? These questions have been answered for the Co/Cu(100) system [140]. A Co film, between 1 and 2 ML thick is ferromagnetic with weak magnetocrystalline anisotropy; the magnetization is confined in-plane by the shape anisotropy. Kerr effect combined with SEMPA measurements showed that for such a thin Co film the spontaneous and remanent magnetization decrease in the same way with temperature. This demonstrates that the critical temperature is a true Curie temperature. Above the Curie temperature the system has a strong susceptibility in a weak external magnetic field, as a result of large fluctuating spin-blocks evidenced by SEMPA. The system behaves like a two-dimensional Heisenberg ferromagnet.

6.6.3.4 Influence of Growth Conditions

The magnetic properties of such structures are governed by their morphology and crystalline structure. Because the later depend on growth conditions, very different magnetic properties can be expected as a result of the use of different growth conditions. We will give two examples.

As mentioned in Section 6.4.6, when the density of island N_{sat} (Eq. (1) in Section 6.2.1) is increased by reducing the growth temperature, the morphology of Co clusters grown on Au(111) is modified. When Co is deposited at 30 K on Au(111) small monolayer grains nucleate and build rather compact Co layers (Fig. 13b). These layers are ferromagnetic above 1.5 ML and are magnetized in-plane [81], in contrast with to room-temperature-grown Co clusters, which are magnetized perpendicularly between 1.6 and 5 ML. Similarly, N_{sat} can be enhanced by increasing the rate of deposition, R. Because N_{sat} follows a power of R, however, whereas it is exponential with the temperature, R must be increased by several orders of magnitude to have the same effect as cooling the substrate from 300 K to 30 K.

Such elevated deposition rates are obtained by pulsed laser deposition (PLD), for which the instantaneous flux is of the order of 10^3 to 10^4 ML s^{-1}. PLD-deposited Fe on Cu(100) has been shown to grow in a perfect layer-by-layer growth mode. These PLD-Fe layers are magnetized in-plane for coverages at which the thermal deposited films have out-of-plane anisotropy [141]. The exact origin of the in-plane anisotropy of Co and Fe when grown under these particular conditions is not yet completely clear. It seems that both low-temperature deposited Co on Au(111) and PLD-Fe on Cu(100) have a smaller magnetocrystalline anisotropy than for usual growth conditions and therefore the shape anisotropy can force the magnetization in-plane.

In the systems addressed above, the magnetic properties can be understood quite well in terms of percolating superparamagnetic islands. They can be described by use of a few types of thermodynamic models, if the growth and morphology are known accurately and one takes proper account of the anisotropy term and the dipolar coupling.

6.7 Conclusion and Outlook

Simultaneous analysis of STM topographs and the magnetic properties of organized islands on surfaces has led to improved understanding of the relationship between the growth and magnetism of films and self-organized clusters. Particular properties of magnetic "films" increasingly seem to be a result of spontaneous nanostructuring during growth (interaction between spin block, pinning of magnetic walls on island boundaries, etc.) and not of intrinsic properties of monolithic, continuous films, as was sometimes assumed in the past. The recent development of variable-temperature STM equipment enables characterization of highly out of equilibrium materials with unexpected properties. This very fruitful approach also opens up new

ways of exploiting atomic diffusion to tailor, to a large extent, the density and shapes of nanostructures.

Although the feasibility of self-organization on dislocation networks has been demonstrated (Section 6.4.3), many problems remain to be addressed. A major challenge in future work will be tuning the periodicity of templates for self-organization purposes, because currently only a few combinations of lattice mismatch of heteroepitaxial systems (see Ag/Pt or Au(111)) are used. It should, ideally, be possible to adjust continuously the periodicity from one value to another. In this respect, the possibility of using alloys of continuously varying concentration should certainly be considered. Another important opening would be to use metal oxides as substrates, as suggested by recent work on MgO [142]. Finally, the possibility of growing the magnetic structures in the third dimension, in a fashion similar to that achieved on some semiconducting systems [143], should be investigated.

Until now, ordered, well separated structures could be synthesized on few systems. The magnetic blocking temperatures thus achieved on Co dots on gold amounts to a few tens of degrees Kelvin. Blocking temperatures in excess of 300 K are reached only when structures start to interact magnetically. To increase the blocking temperature of each dot separately, the volume of the dot must be increased, eventually its aspect ratio must be optimized. Along these lines, an attempt has been made to pile up self-organized cobalt dots on Au(111) [144]. Alternating gold and cobalt deposition under appropriate conditions leads to arrays of 8-nm-high columns (4 nm in diameter). Although the self-organized columns obtained in this way have blocking temperatures close to 300 K they nevertheless interact magnetically. Because of their strong magnetic anisotropy, small clusters of rare earth metals [95] or transition/rare earth metals [145] should also be considered for self-organization. Self-organized magnetic dots would provide a state of the art solution for large scale integration of very small particles for artificial atom devices, spin-polarized transport structures, and single-electron Kondo physics devices [2, 146, 147], which have so far been studied only as single elemental devices.

Finally, self-organized magnetic dots embedded in a free-electron-like matrix are, by construction, materials with very high density of interfaces. They are, therefore, particularly promising for giant magnetoresistance applications (GMR). Recent work on Co/Au/Co/Au(111) films [148] seems to confirm this prediction, although self-organization has not been verified in this work.

Acknowledgments

We gratefully acknowledge helpful discussion with H. Brune, H. Bulou, I. Chado, C. Demangeat, K. Dumesnil, O. Fruchart, C. Goyhenex, U. Gradmann, W. Hergert, C. Massobrio, T. Michely, S. Padovani, G. Pastor, and V. Stepaniuk. We would like to thank S. Ottogali and M. Romeo for their help in preparing the figures for this contribution.

References

[1] P.S. Bechthold et al. Zeit. Phys. Chem. Neue Folge **1990,** 169, 101.
[2] R.C. Ashoori, H.L. Stormer, J.S. Weiner, L.N. Pfeiffer, K.W. Baldwin, K.W. West, Surface Sci. **1994**, 305, 558–565.
[3] L. Thomas et al. Nature, **1996**, 383, 145.
[4] P.J.M. van Bentum, R.T.M. Smokers, and H. van Kempen, Phys. Rev. Lett. **1988**, 60, 2543.
[5] Clusters of Atoms and Molecules I, ed.: H. Haberland, Series in Chemical Physics, Vol. 52, Springer, **1994.**
[6] Physics Today, April **1995** special issue on "Magnetoelectronics".
[7] B. Doudin and J.P. Ansermet, Europhys. News **1997**, 28, 14.
[8] D.D. Chambliss, R.J. Wilson, and S. Chiang, J. Vac. Sci. Technol. B**1991**, 9, 993.
[9] B. Voigtländer, G. Meyer, N.M. Amer, Phys. Rev. B **1991**, 44, 10354.
[10] H. Brune, M. Giovannini, K. Bromann, and K. Kern, Nature **1998**, 394, 451.
[11] H. Roeder, E. Hahn, H. Brune, J.P. Bucher, and K. Kern, Nature, **1993**, 366, 141.
[12] Z.Y. Zhang and M.G. Lagally, Science **1997**, 276, 377.
[13] Ultrathin Magnetic Structures I and II (Eds.: J.A.C. Bland, B. Heinrich), Springer, Berlin, Heidelberg, **1994.**
[14] H.J. Elmers, J. Hauschild, H. Höche, U. Gradmann, H. Bethge, D. Heuer, U. Köhler, Phys. Rev. Lett. **1994**, 73, 898.
[15] S. Padovani, F. Scheurer and J.P. Bucher, Europhys. Lett. **1999**, 45, 327.
[16] S. Padovani, I. Chado, F. Scheurer and J.P. Bucher, Phys. Rev. B **1999**, 59, 11887.
[17] H. Roeder, H. Brune, J.P. Bucher and K. Kern, Surface Sci. **1993**, 298, 121.
[18] H. Brune et al. Surface Sci. **1996**, 349, L115–L122.
[19] J. Venables, G.D.T. Spiller and M. Hanbücken, Rep. Prog. Phys. **1984**, 47, 399.
[20] H. Brune, Surface Sci. Rep. **1998**, 31, 121.
[21] T.A. Witten and L.M. Sander, Phys. Rev. B **1983**, 27, 5686.
[22] M.C. Bartlett and J.W. Evans, Surface Sci. **1994**, 314, L829–L834.
[23] T. Michely, M. Hohage, M. Bott, and G. Comsa, Phys. Rev. Lett. **1993**, 70, 3943.
[24] J. de la Figuera, J.E. Prieto, C. Ocal, and R. Miranda, Surface Sci. **1994**, 307–309, 538–543 and Phys. Rev. B **1993**, 47, 13043.
[25] Y.W. Mo, J. Kleiner, M.B. Webb, M. Lagally, Phys. Rev. Lett. **1991**, 66, 1998.
[26] J.P. Bucher, E. Hahn, P. Fernandez, C. Massobrio and K. Kern, Europhys. Lett. **1994**, 27, 473.
[27] E. Hahn, E. Kampshoff, A. Fricke, J.P. Bucher and K. Kern, Surface Sci. **1994,** 319, 277.
[28] A.A. Baski, J. Nogami, and C.V.F. Quate, Phys. Rev. B **1991**, 43, 9316–9319.
[29] L.P. Nilsen et al. Phys. Rev. Lett. **1993**, 71, 754.
[30] E. Bauer, Z. Krist. **1958**, 110, 372.
[31] C. Argile and G.E. Rhead, Surface Sci. Rep. **1989**, 10, 277.
[32] E. Bauer and H. Poppa, Thin Solid films **1972**, 12, 167.
[33] J.M. Blakely Introduction to the Properties of Crystal Surfaces, Oxford: Pergamon **1973**.
[34] R. Kern, Bull. Miner. **1978**, 101, 202.
[35] R. Kern, G. Lelay and, J.J. Métois, Current Topics in Material Science Vol 3, ed. E. Kaldis, Amsterdam, North Holland **1979**.
[36] P. Müller and R. Kern, J. Cryst. Growth **1998**, 193, 257.
[37] L.Z. Mezay and J. Giber, Jpn J. Appl. Phys. **1982**, 21 1569.
[38] H.L. Skriver and N.M. Rosengaard, Phys. Rev. B **1992**, 46, 7157.
[39] E. Bauer, Applications of Surface Science **1982**, 11/12, 479.

[40] E. Bauer and J.H. van der Merwe, Phys. Rev. B **1986**, 33, 3657.
[41] F. Gautier and D. Stoeffler, Surface Sci. **1991**, 249 265.
[42] P. Müller and R. Kern, Appl. Surf. Sci. **1996**, 102, 6.
[43] P. Müller and R. Kern, Microsc. Microanal. Microstruct. **1997**, 8, 229.
[44] M.H. Grabow and G.H. Gilmer, Surface Sci. **1988**,194, 333.
[45] R. Kern and P. Müller, Surface Sci. **1997**, 392, 103.
[46] A. Bourret, Surf. Sci. **1999**, 432, 37.
[47] K. Restöft, C. Jensen, U. Köhler, Surface Sci. **1999**, 421, 320.
[48] L.P. Zhang, J. van Ek, U. Diebold, Phys. Rev. B **1999**, 59, 5837.
[49] M. Kato, Mat. Sci. Eng. **1991**, A146, 205.
[50] P. Ohresser, J. Shen, J. Barthel, M. Zheng, Ch. V. Mohan, M. Klaua and J. Kirschner, Phys. Rev. B **1999**, 59, 3696.
[51] I. Daruka, J. Tersoff and A.–L. Barabasi, Phys. Rev. Lett. **1999**, 82, 2753.
[52] O. Hellwig, K. Theis–Bröhl, G. Wilhelmi, A. Stierle, H. Zabel, Surface Sci. **1998**, 398, 379.
[53] Y. Gotoh, M. Uwaha, I. Arai, Appl. Surface Sci. **1988**, 33/34, 443.
[54] Y. Gotoh, and H. Fukura, Surface Sci. **1989**, 223, 315.
[55] J.H. van der Merwe and E. Bauer, Phys. Rev. B **1989**, 39, 3632.
[56] H. Fukura and Y. Gotoh, Thin Solid Films **1990**, 188, 193.
[57] R. Nötzel et al. Europhys. News, **1996**, 27, 148.
[58] J. Tersoff, C. Teichert, and M.G. Lagally, Phys. Rev. Lett. **1996**, 76, 1675.
[59] T. Kontorova and Y. I. Frenkel, Zh. Eksp. Teor. Fiz. **1938**, 89, 1340.
[60] F.C. Frank and J.H. van der Merve, J. Proc. Roy. Soc. A **1949**, 198, 205.
[61] J.V. Barth, H. Brune, G. Ertl, and R.J. Behm, Phys. Rev. B **1990**, 42, 9307–9318.
[62] S. Narasimhan and D. Vanderbilt, Phys. Rev. Lett. **1992**, 69, 1564.
[63] H. Brune, H. Roeder, C. Boragno, and K. Kern, Phys. Rev. B **1994**, 49, 2997.
[64] I. Meunier, G. Tréglia, J.M. Gay, B. Aufray, B. Legrand, Phys. Rev. B **1999**, 59, 10910.
[65] L. Zhang, J. van Elk, and U. Diebold, Phys. Rev. B **1998**, 57, R4285.
[66] C. Goyhenex, H. Bulou, J.P. Deville, and G. Tréglia, Phys. Rev. B **1999**,.60, 2781.
[67] J.A. Strocio, D.T. Pierce, R.A. Dragosset, P.N. First, J. Vac. Sci. Technol. A **1992**, 10, 1981.
[68] J. A. Meyer, I. D. Baike, E. Kopatzki, R. J. Behm, Surface Sci. **1996**, 365, L647.
[69] J. Wollschläger and N.M. Amer, Surface Sci. **1992**, 277, 1.
[70] V.I. Marchenko, JETP Lett. **1981**, 33, 381.
[71] O.L. Alerhand, D. Vanderbilt, R.D. Meade, and J.D. Joannopoulos, Phys. Rev. Lett. **1988,** 61 1973.
[72] D. Vanderbilt, in *Computations for the Nano–scale*, eds. P.E. Blöchl et al. (Kluwer, New York 1993) p.1.
[73] J. Tersoff and R.M. Tromp, Phys. Rev. Lett. **1993**, 70, 2782.
[74] P. Zeppenfeld et al. Phys. Rev. Lett. **1994**, 72, 2737.
[75] F.K. Men, W.E. Packard and M.B. Webb Phys. Rev. Lett. **1988,** 61, 2469.
[76] K. Kern et al. Phys. Rev. Lett. **1991**, 67, 855.
[77] J. Camarero et al. Mat. Res. Symp. Proc. **1995**, 384, 49.
[78] J. Shen, R. Skomski, M. Klaua, H. Jenniches, S. Sundar Manoharan, J. Kirschner, Phys. Rev. B **1997**, 56, 2340.
[79] A. Sugawara and M.R. Scheinfein, Phys. Rev. B **1997**, 56, R8499.
[80] S. Padovani, I Chado, F. Scheurer, and J.P. Bucher, Appl. Surf. Sci. **2000**, 164, 42 and Appl. Surf. Sci. **2001**, 172, 190.
[81] S. Padovani, F. Scheurer, I. Chado, and J.P. Bucher, Phys. Rev. B **2000**, 61, 72.
[82] R. Kunkel, B. Poelsma, L. K. Verheij, and G. Comsa, Phys. Rev. Lett. **1990**, 65, 733.
[83] J. Tersoff, A.W. Denier van der Gon, and R.M. Tromp, Phys. Rev. Lett. **1994**, 72, 266.

[84] H.C. Siegmann, J. Phys. Condens. Mat. **1992**, 4, 8385–8434.
[85] U. Gradmann in Handbook of Magnetic Materials vol. 7, (Ed.: K.H.J. Buschow), Elsevier, **1993**, pp.1–96.
[86] J.P. Renard in Magnetism and Synchrotron Radiation, (Eds.: E. Beaurepaire, B. CarriSre, J.–P. Kappler), Les Editions de Physique, Les Ulis, **1997**, pp.185–209.
[87] F. Gautier in Metallic Multilayers, Material Science Forum vol. 59, 60 (Eds. A. Chamberod, J. Hillairet),. Trans Tech Publications, Switzerland, **1990** pp.361–437.
[88] G. Allan, Surface Sci **1978**, 74, 79.
[89] C.L. Fu, A.J. Freeman and T. Oguchi, Phys. Rev. Lett. **1985**, 54, 2700.
[90] S.C. Hong, A.J. Freeman, C.L. Fu, Phys. Rev. B **1988**, 38, 12156.
[91] J.P. Bucher, D.C. Douglass, L.A. Bloomfield, Phys. Rev. Lett. **1991**, 66, 3052.
[92] I. Billas, A. Châtelain, W. de Herr, Science **1994**, 265, 1681.
[93] S.E. Apsel, J.W. Emmert, J. Deng, L.A. Bloomfield, Phys. Rev. Lett. **1996**, 76, 1441.
[94] I. Billas, J.A. Becker, A. Châtelain, W. de Herr, Phys. Rev. Lett. **1993**, 71, 4067.
[95] D.C. Douglass, J.P. Bucher, L.A. Bloomfield, Phys. Rev. Lett. **1992**, 68, 1774.
[96] G. Allan, Phys. Rev. B **1979**, 19, 4774.
[97] H. Dreyssé, A. Mokrani, S. Bouarab and C. Demangeat, Surface Sci. **1991**, 251, 41.
[98] S. Blügel, Phys. Rev. B **1995**, 51, 2025.
[99] K. Wildberg, V.S. Stepanyuk, P. Lang, R. Zeller, P.H. Dederichs, Phys. Rev. Lett. **1995**, 75 509.
[100] H. Dreyssé, C. Demangeat, Surface Sci. Rep. **1997**, 28, 65–122.
[101] A.J. Cox, J.G. Louderback and L.A. Bloomfield, Phys. Rev. Lett. **1993**, 71, 923.
[102] B.V. Reddy, S.N. Khanna and B.I. Dunlap, Phys. Rev. Lett **1993**, 70, 3323.
[103] M. Stampanoni, A. Vaterlaus, D. Pescia, M. Aeschlimann, F. Meier, W. Dürr, and S. Blügel, Phys. Rev. B **1988**, 37, 10380.
[104] H. Li, S.C. Wu, D. Tian, Y.S. Li, J. Quinn, and F. Jona, Phys. Rev. B **1991**, 44, 1438
[105] C. Liu and S.D. Bader, Phys. Rev. B **1991**, 44, 12062.
[106] H. Beckmann, Fei Ye, and G. Bergmann, Phys. Rev. Lett **1994**, 73, 1715.
[107] H. Beckmann and G. Bergmann, Phys. Rev. B **1997**, 55, 14350.
[108] H. Beckmann and Bergmann, Eur. Phys. J. B **1998**, 1, 229.
[109] I. Turek, J. Kudrnovsky, M. Sob, V. Drchal, and P. Weinberger, Phys. Rev. Lett. **1995**, 74, 2551
[110] J.H. Van Vleck, Phys. Rev. **1937**, 52, 1178.
[111] L. Néel, J. de Phys. Rad. **1954**, 15, 225.
[112] D. Sander, Rep. Prog. Phys. **1999**, 62, 809–858.
[113] D. Craik in Magnetism, Wiley, England, **1995**.
[114] Y. Millev and J. Kirschner, Phys. Rev. B **1996,** 54, 4137.
[115] J.G. Gay and R. Richter, Phys. Rev. Lett. **1986**, 56, 2728.
[116] G.H.O. Daalderop, P.J. Kelly and M.F.H. Schuurmans in Ultrathin Magnetic Structures I, (Eds.: J.A.C. Bland, B. Heinrich), Springer, Berlin, Heidelberg, **1994**, p. 40.
[117] P. Bruno, Phys. Rev. B **1989**, 39, 865.
[118] J. Dorantes–Dávila and G.M. Pastor, Phys. Rev. Lett. **1998**, 81, 208.
[119] C. Kittel, Phys. Rev. **1946**,70, 965.
[120] Y. Yafet and E.M. Gyorgy, Phys. Rev. B **1988**, 38, 9145.
[121] R. Czech and J. Villain, J. Phys. Cond. Mat. **1989**,1, 619.
[122] A. Hubert, Magnetic Domains, Springer Verlag, New York, **1998**.
[123] H.P. Oepen, M. Speckmann, Y. Millev and J. Kirschner, Phys. Rev. B **1997**, 55, 2752.
[124] R. Allenspach, J. Magn. Magn. Mat. **1994**, 129, 160.
[125] I.S. Jacobs and C.P. Bean in Magnetism, Vol.3 (Eds G.T. Rado, H. Suhl), Academic Press, New York, **1963**.

[126] R.P. Erickson and D.L. Mills, Phys. Rev. B **1991**, 43, 11527.
[127] S.T. Chui, Phys. Rev. B **1994**, 50, 12559.
[128] Y. Yafet J. Kwo and E.M. Gyorgy, Phys Rev. B **1986**, 33, 6519.
[129] H. Takeshita, Y. Suzuki, H. Akinaga, W. Mitzutani, K. Ando, T. Katayama, A. Itoh, K. Tanaka, J. Magn. Magn. Mat. **1997**, 165, 38.
[130] J. Xu, M.A. Howson, B.J. Hickey, D. Greig, E. Kolb, P. Veillet, N. Wiser, Phys. Rev. B **1997**, 55, 416.
[131] H. Takeshita, Y. Suzuki, H. Akinaga, W. Mitzutani, K. Tanaka, T. Katayama, A. Itoh, Appl. Phys. Lett. **1996**, 68, 3040.
[132] H.A. Dürr, S.S. Dhesi, E. Dudzik, D. Knabben, G. van der Laan, J.B. Goedkoop, F.U. Hillebrecht, Phys. Rev. B **1999**, 59, R701.
[133] K.W. Edmonds, C. Binns, S.H. Baker, S.C. Thornton, C. Norris, J.B. Goedkoop, M. Finazzi and N. Brookes, Phys. Rev. B **1999**, 60, 472.
[134] H. Beckmann and G. Bergmann, Phys. Rev. Lett. **1999**, 83, 2417.
[135] J. Hauschild, H.J. Elmers, U. Gradmann, Phys. Rev. B **1998**, 57, R677.
[136] R. Allenspach, M. Stampanoni, A. Bischof, Phys. Rev. Lett. **1990**, 65, 3344.
[137] H.J. Elmers, J. Hauschild and U. Gradmann, Phys. Rev. B. **1996**, 54, 15224.
[138] H.J. Elmers, J. Hauschild, H. Fritzsche, G. Liu and U. Gradmann, Phys. Rev. Lett. **1995**, 75, 2031.
[139] N. Weber, K. Wagner, H.J. Elmers, J. Hauschild, U. Gradmann, Phys. Rev. B **1997**, 55, 14121.
[140] D. Kerkmann, D. Pescia, R. Allenspach, Phys. Rev. Lett.**1992**, 68, 686
[141] H. Jenniches, J. Shen, Ch. V. Mohan, S. Sundar Manoharan, J. Barthel, P. Ohresser, M. Klaua, and J. Kirschner, Phys. Rev. B **1999**, 59, 1196.
[142] Noguera et al. in *Chemisorption and reactivity on Supported Clusters an Thin Films*. (Kluver Ed. 1997) pp: 455–478
[143] Q. Xie, A. Madhukar, P. Chen, and N. Kobayashi, Phys. Rev. Lett. **1995**, 75, 2542.
[144] O. Fruchart, M. Klaua, J. Barthel, and J. Kirschner, Phys. Rev. Lett **1999**,83, 2769. By alternating gold and cobalt deposition under appropriate conditions, arrays of 8 nm–high columns (4 nm in diameter) are obtained. The Co bilayer dots, are covered with 4 ML Au at 425 K. Because of the different step heights of Co and Au, troughs are formed on top of the Co dots. Subsequent deposition of Co (at 425 K) leads to preferential nucleation on top of the Co dots formed in the first place, an exchange between Co and Au is supposed to favor 3D growth of columns.
[145] A. Mougin, C. Dufour, K. Dumesnil, N. Maloufi, and Ph. Mangin, Phys. Rev. B **1999**, 59, 5950.
[146] B. Doudin, G. Redmond, S.E. Gilbert, J.–Ph. Ansermet, Phys. Rev. Lett. **1997**, 79, 933
[147] V. Madhavan, W. Chen, T. Jamneala, M.F. Crommie, N.S. Wingreen, Science, **1998**, 280, 567
[148] J. Corno, M. Galtier, D. Renard, J.P. Renard, and F. Trigui, Eur. Phys. J. B, Eur. Phys. J. B, **1999**, 10, 223.

Magnetism: Molecules to Materials III. Edited by J.S. Miller and M. Drillon

ISBNs: 3-527-30302-2 (Hardback); 3-527-60014-0 (Electronic)

7 Spin Electronics – An Overview

Ivan Petej and John Gregg

7.1 Introduction

The advances achieved in the semiconductor industry over the last fifty years have made an enormous impact on human life. The field of semiconductor electronics has expanded so rapidly (particularly since the cash injection as a result of the NASA 1960s space-race program) that it is difficult nowadays to imagine an area of technological development that does not use computer technology. Behind the success in this field lies a simple physical principle. In a semiconductor two different families of electric current carrier arise when electrons jump across a band gap in the allowed energy spectrum – the promoted electrons in the conduction band and the positively charged holes which they leave behind them in the valence band. The distinction between these two types of carrier lies at the core of all electronic devices – their manipulation by locally created electric fields and concentration gradients was the mechanism used in the very first Ge transistor which originated in Bell Laboratories and is still used in the modern Pentium microprocessors.

All these charge carriers also have another (inherently quantum) property, however – when electrons traverse a region in which there is a magnetic field, their angular momentum, known as spin, aligns itself either parallel or antiparallel to the magnetic field axis. This phenomenon, despite its having been known for over five decades, had been largely ignored until recently by the electronics community. The need for faster, more compact electronic devices has, however, prompted researchers to recognize that, just as charge can be used as a distinguishing label, so also can spin. So arose the birth of spin electronics. The newly emerging technology has the potential to change forever the way computer memories and processors work.

Spin electronic devices function by transferring magnetic information from one part of the device to another by using nanoscale magnetic elements (mesomagnets) to encode it on to (and subsequently read it from) the itinerant electron spin channels. This coding can be changed by re-magnetizing the mesomagnets thus enabling the creation of electronic components whose characteristics may be engineered to respond to applied magnetic fields.

The aim of this article is to introduce the field of spin electronics by giving a description of the relevant physical systems and length scales on which the spin effects become important. Early devices are described, some more recent developments are illustrated, and the authors conclude by outlining their own thoughts on the future potential of this rapidly expanding field.

7.2 The Technical Basis of Spin Electronics – The Two-spin Channel Model

The basis of spin-polarized transport was established as far back as the 1930s with the observation that features of electric transport in ferromagnets distinguished them from other metals. Mott [1] explained this phenomenon by postulating that the transport in ferromagnetic systems was effected by two independent families of carriers whose members are distinguished by their spin orientation with respect to the local magnetic axis – spin-up (parallel) or spin-down (antiparallel). The key point in Mott's argument is that because the spin-flip processes are rare on the time-scale of the other scattering processes which control the transport, the current in each spin-channel is conserved, and the two spin channels can essentially be regarded as being pseudo-independent.

7.2.1 2.1 Spin Asymmetry

The physical origin of this spin asymmetry in ferromagnets is now known to arise because the ferromagnetic exchange interaction splits the spin-up and spin-down conduction bands, leaving different band structures (and hence densities of states, Fig. 1) evident at the Fermi surface. As a result, the number of available carriers of a particular spin type, or (in a tunneling process) the number of available final states for such carriers, is different for the up-spin and down-spin electrons. In addition, owing to the different densities of final states for each spin type, the two types of carrier are differently affected by momentum-changing scattering processes and hence their mobilities are in general not the same. Most spin electronic phenomena are based on either or both of these asymmetries prevailing in the relevant physical system.

In fact, the two asymmetries often compete with one another in spin electronics. The Fermi surface in most ferromagnetic materials contains components which have both s and d character. The s-like effective masses are small compared with the d-like masses and so any current that flows is primarily mediated by s-electrons. The d-electrons are, however, significantly split by the exchange interaction, and this results in very different densities of states into which the s electrons can be scattered. Thus, from Fig. 1, the down s-channel (the spin type of which has a large d density of

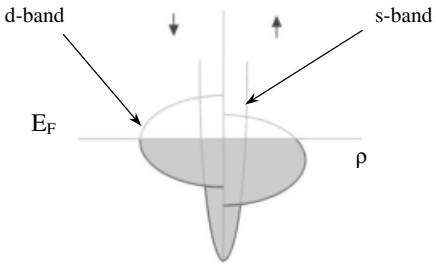

Fig. 1. Spin splitting of the density of states (ρ) in a ferromagnet as a result of the ferromagnetic exchange field.

states at the Fermi energy) suffers the most scattering and hence has lower mobility than the other s-channel; as a consequently the latter carries most of the current. Thus in a system with s and d like character at the Fermi surface, the tendency is for the current to be carried by the minority carriers (where "minority" is taken to mean those with the lower density of states at the Fermi energy) whereas in a half-metallic ferromagnet the current can be carried by majority carriers only.

7.2.2 Spin Injection Across an Interface

Now that we have considered the basic principles behind the origin of spin asymmetry, we can briefly consider an important phenomenon which lies at the heart of early spin electronic devices. If one carrier spin type is dominant in the electrical transport of a ferromagnet, when a current is passed from this ferromagnet to a paramagnetic metal such as silver or aluminum, it brings with it a net injection of spin angular momentum and hence also of magnetization [2]. The magnetization which builds up in the new material is known as a *spin accumulation*. (Fig. 2). Its size is determined by the equilibrium between the net spin injection rate at the interface and the spin flipping rate in the body of the paramagnet. It follows that the spin accumulation decays exponentially away from the interface on a length scale called the "spin diffusion length".

Because of its importance in the field of spin electronic devices, it is instructive to do a rough "back of the envelope" calculation to see how large is this spin diffusion length, l_{sd}, and on what factors it depends. We can consider a newly injected up-spin arriving across the interface into the non-magnetic material. It undergoes a number N of momentum-changing collisions before being flipped (on average after time $\tau_{\uparrow\downarrow}$). The average distance between momentum-scattering collisions is λ, the mean free path. We can now derive two relationships. By analogy with the progress of a drunken sailor leaving a bar and executing a random walk up and down the street, we can say (remembering to include a factor of three because, unlike the

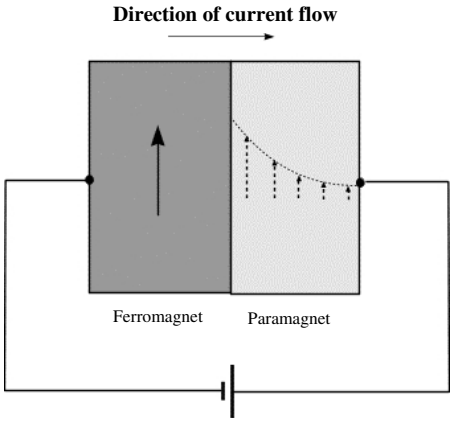

Fig. 2. Illustration of the spin accumulation at the ferromagnet/paramagnet interface.

sailor, our spin can move in three dimensions) that the average distance which the spin penetrates into the non-magnetic material (perpendicular to the interface) is $\lambda\sqrt{N/3}$. This distance is l_{sd}, the spin diffusion length which we wish to estimate. The total distance walked by the spin is, moreover, $N\lambda$ which in turn equals its velocity (the Fermi velocity, v_{F}) multiplied by the spin-flip time $\tau_{\uparrow\downarrow}$. Eliminating the number of collisions, N, gives

$$l_{\mathrm{sd}} = \sqrt{\frac{v_{\mathrm{F}}\tau_{\uparrow\downarrow}\lambda}{3}} \tag{1}$$

For a rigorous analysis of the spin-accumulation length in terms of the respective electrochemical potential of the spin channels, the reader is referred to Valet and Fert [3] from which it can be seen, numerical factors apart, that the crude "drunken sailor" model gives a remarkably accurate insight into the physics of this problem.

Using the above relationship, the resulting magnitude of spin accumulation can be given in terms of the spin density, n, at distance, x, from the interface. It is:

$$n = n_0 e^{-\left(\frac{x}{l_{\mathrm{sd}}}\right)} \tag{2}$$

where n_0, the density at the interface is given by:

$$n_0 = \frac{3\alpha j l_{\mathrm{sd}}}{e v_{\mathrm{F}}\lambda} \tag{3}$$

Here, the coefficient α is the polarization of the ferromagnet and j is current density at the interface. Substituting typical numbers – $j = 1000$ Amps cm^{-2}, $\alpha = 1$, $v_{\mathrm{F}} = 10^6$ m s^{-1}, $\lambda = 5$ nm, $l_{\mathrm{sd}} = 100$ nm gives a value of spin density of 10^{22} m^{-3} as opposed to a total electron density of approximately 10^{28} m^{-3}. That such minute asymmetries in total spin density can give rise to such large electrical transport effects as giant magnetoresistance is yet one more example of the dominance of the electrons at the metal Fermi surface, which is where these spins are concentrated. This small spin density asymmetry also explains why measurement of the spin density, or its associated magnetization, is difficult, owing to problems in distinguishing convincingly the magnetic fields generated by the effect itself (approximately 10 nT for the example above) and those caused by the current which is generating the accumulation.

7.2.3 The Role of Impurities in Spin Electronics

From Eq. (1) it becomes evident that introducing impurities into the paramagnetic material leads to rapid reduction of the spin diffusion length (l_{sd}), because they shorten not only the mean free paths of the charge carriers, but also the spin flip time via the mechanism of spin-orbit scattering. The latter can be thought of as a relativistic effect–under Lorentz transform, electric fields assume a magnetic component. To electrons at the Fermi surface, which have weakly relativistic velocities, the electric fields generated by impurity atoms seem weakly magnetic. If the symmetry of the

impurity site is sufficiently low, this field can Zeeman-couple to the S^+, S^- operators which induce spin-flip transitions. Hence materials with point defects and low symmetry structural disorder are likely to have reduced spin diffusion lengths [4].

7.3 Two Terminal Spin Electronics – Giant Magnetoresistance (GMR)

Having outlined the origins of the spin accumulation length at the interface between a ferromagnet and a normal metal, we can now consider the operation of arguably the simplest spin electronic device – a thin layer of paramagnetic material sandwiched between two ferromagnetic electrodes, such as that shown in Fig. 3.

The device acts as a two-terminal passive spin electronic component which, in some realizations, is known as a "spin valve" and it passes muster in the world of commerce as a giant magnetoresistive hard-disk read-head.

Empirically, the function of the device is simple (Fig. 4). If we measure the electrical resistance between the two terminals in an externally applied magnetic field (supplied for example by the magnetic information bit on the hard disk the orientation of which must be read) we can use the field to switch the relative magnetic orientations of the ferromagnetic layers from parallel to antiparallel. It is observed that the parallel magnetic moment configuration corresponds to a low electrical resistance and the antiparallel state to a high resistance. Changes in electrical resistance of approximately 100 % are possible in quality devices, hence the term giant magnetoresistance, because, by comparison with, for example, anisotropic magnetoresistance in ferromagnets, the observed effects are about two orders of magnitude larger.

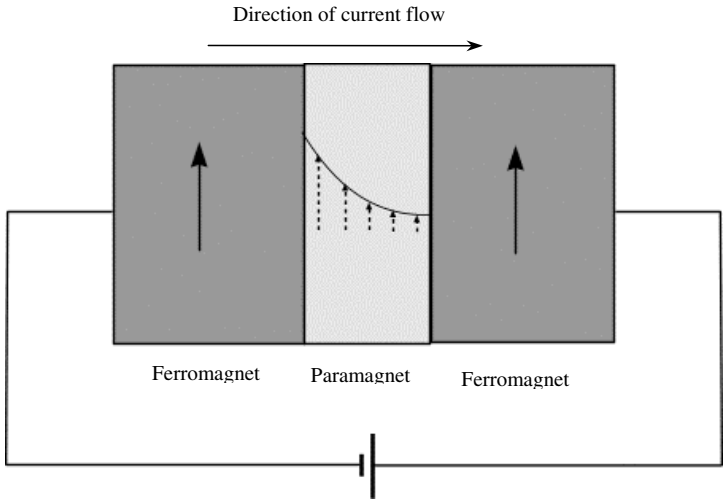

Fig. 3. Schematic diagram of a simple GMR device.

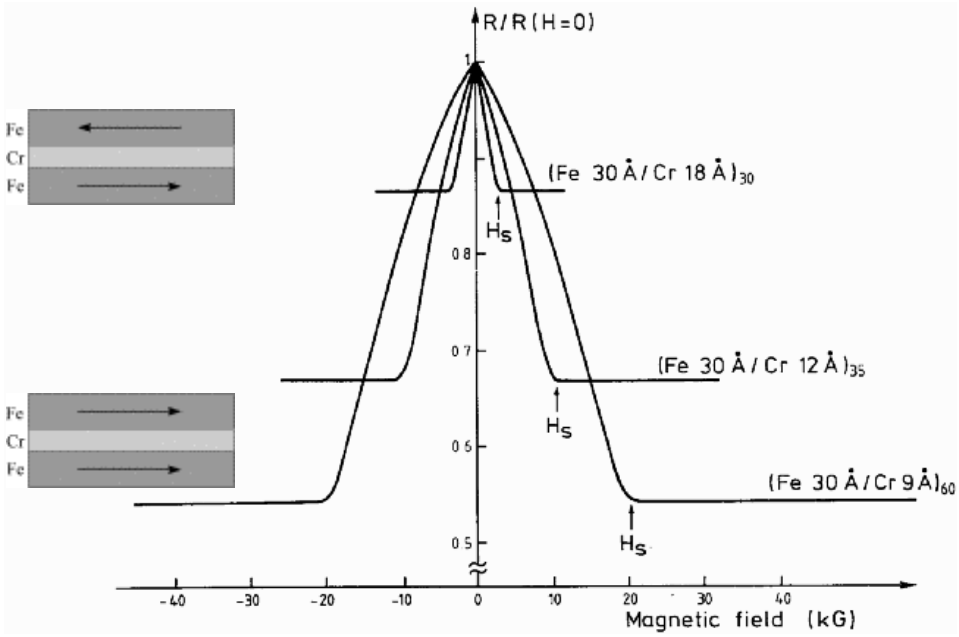

Fig. 4. Experimental illustration of GMR (after Baibich et al. [5]).

7.3.1 The Analogy with Polarized Light

There are several different ways – of varying rigor – of explaining the operation of this spin valve structure. To keep things simple, let us analyze it by analogy with the phenomenon of polarized light. In the limit in which the ferromagnets are half-metallic the left hand magnetic element supplies a current consisting of spin-up electrons only; this causes a spin accumulation in the central layer. If the physical thickness of the silver layer is comparable with or smaller than the spin diffusion length, this spin accumulation reaches across to the right hand magnetic layer which, because it is half-metallic, acts as a spin filter, just as a piece of Polaroid spectacle lens acts as a filter of polarized light. The spin accumulation presents different densities of up and down electrons to this spin filter, which thus lets through different currents depending on whether its magnetic orientation is parallel or antiparallel to the orientation of the polarizer (i. e. the first magnetic layer). The only difference from the example of crossed optical polarizers is that in optics the extinction angle is 90°. In spin electronics it is 180°, which arises because the photon is a spin 1 particle and the electron has spin 1/2.

Alternatively, a simple parallel resistor model, shown in Fig. 5, can be used to describe GMR. The two parallel paths, each consisting of five series resistors, represent the respective spin channels and the resistors in each path represent the resistances which they experience in each of the magnetic layers. If we arbitrarily assign resis-

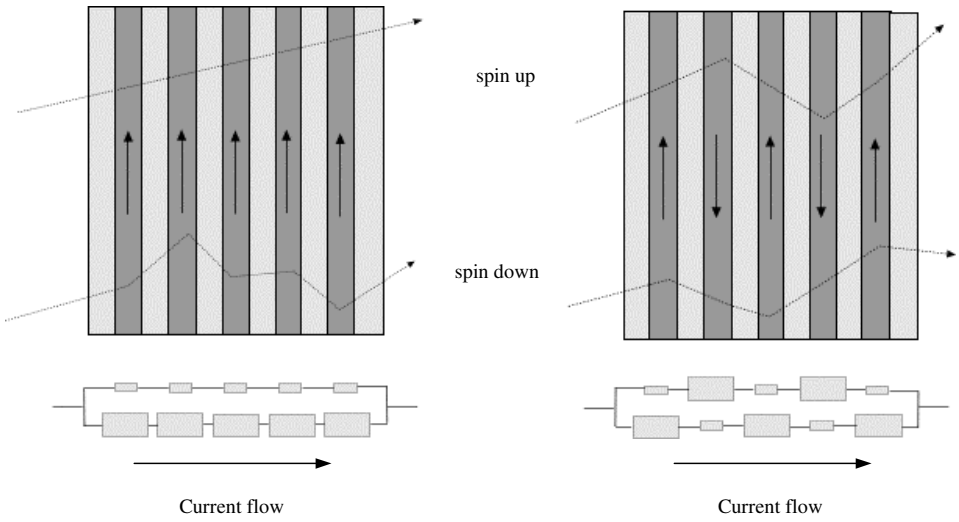

Fig. 5. The two-resistor model of GMR.

tance values of 1 and 10 Ohms to the majority and minority resistances, it is seen that the magnetization parallel and antiparallel configurations have overall resistance of 4.5 and 22.3 Ohms, respectively.

7.3.2 CIP and CPP GMR

It is important to note that there are two configurations in which our simple two-terminal device can work – they are described as current in plane (CIP) and current perpendicular to plane (CPP) configurations. Above, we have discussed only the latter in which the critical length scale for the magnetic phenomena is the spin diffusion length. The physics involved in CIP operation is rather different and the critical length scale here is the mean free path. CIP GMR was, in fact, the first GMR to be experimentally demonstrated, its geometry being easier to realize than CPP geometry, the implementation of which requires sophisticated nanolithography techniques [6].

CIP GMR is characterized by the same drop in electrical resistance of the thin film sample when a magnetic field is applied. The explanation is, however, fundamentally different – symmetry considerations show clearly that no spin accumulation is set up in this instance, because current flow is parallel to the layers. Instead the explanation invokes the different mobilities of the spin-up and spin-down electrons and relies on the non-magnetic interlayer being sufficiently thin that a high proportion of the current-carrying electrons experience successive momentum-scattering events in different magnetic layers. This in turn means that if the layers are antiparallel, neither spin type has high mobility, because each experiences heavy scattering in one or other layer. If, however, the layers are parallel, one spin-type is heavily scattered in both layers and the other spin type is relatively unscattered and hence its high

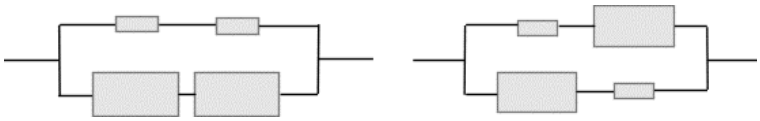

Fig. 6. The two resistor model of GMR in CIP configuration for ferromagnetic (left) and antiferromagnetic (right) layer alignment.

mobility electrically short-circuits the device. The resistor model of Fig. 6 models the CIP geometry – the two parallel paths are representative of the two spin channels in each non-magnetic layer, and each path comprises two resistances which represent the scattering they experience in the adjacent magnetic layers, assuming that their trajectories sample both these magnetic layers.

7.3.3 Comparative Length Scales of CIP and CPP GMR

It is evident from this discussion that two quite different length scales are relevant to CIP and CPP GMR. For CPP GMR, the interlayer must be less than the spin diffusion length whereas for CIP GMR to appear the interlayer must be less than a mean free path, which is a rather shorter distance. As a result the typical CIP GMR multilayers use non-magnetic spacers of approximately 10 Å or less.

7.3.4 Inverse GMR

In the above discussion of GMR it is assumed that the metals in the two ferromagnetic layers are similar, or at least that the signs of their polarizations are the same. In other words, the majority spin for each ferromagnet is parallel to the magnetization (positive polarization) or antiparallel to the magnetization (negative polarization). If a combination of two ferromagnets with opposite polarizations is used to make a GMR trilayer, the GMR is inverted, i. e. the resistance of the device increases on application of an external magnetic field. This is because when the ferromagnets have parallel magnetizations they disagree about which spin direction is the majority type [7, 8].

7.3.5 Methods of Achieving Differential Switching of Magnetization – RKKY Coupling Compared with Exchange Pinning

Two techniques are used to engineer GMR systems such that the two ferromagnetic layers in the trilayer switch differentially in an externally applied field. The first involves making the metallic interlayer of such a thickness (approx. 1 nm) that the RKKY coupling across it between the magnetic layers is antiferromagnetic and so the layers anti-align in zero applied field but align parallel to one another in applied field [9]. This technique imposes constraints on device design which might militate

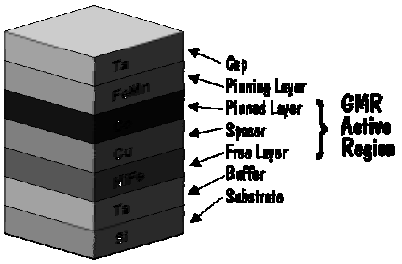

Fig. 7. Schematic diagram of a spin valve [11].

against obtaining the best GMR signal. The other technique is to fabricate one layer magnetically harder by exchange pinning it to an antiferromagnet on the side opposite to that which abuts the GMR device. In this arrangement only the unpinned soft layer moves in small magnetic fields. The resulting device is termed a spin valve (Fig. 7) [10].

There is a third technique, using materials known as artificial antiferromagnets (AAF), which is a clever combination of the other two ideas. Here, no RKKY coupling is used in the GMR spacer layer but one of the ferromagnetic electrodes is rendered magnetically hard by fabricating it from two distinct ferromagnetic layers A and B, of almost identical thickness, which are magnetically coupled such that in zero applied field they are antiparallel and hence their net moment is small. The switching field of this artificial antiferromagnet block (A + B) is thus enhanced by a so-called Q factor, which is the ratio of the total magnetic moment when A and B are aligned in a high field to the net moment when A and B are anti-aligned [12].

7.3.6 GMR in Nanowires

An interesting realization of CPP GMR has been achieved by using electroplating technology to construct metallic nanowires in nanopores of a membrane [13]. With a suitable electrolyte containing a selection of ions, different materials can be deposited with an interspacing of few nanometers along the wire simply by switching the value of the electroplating potential, thereby creating a magnetic multilayer structure. This technique has the added convenience that the geometry of the wires is conducive to easy measurement, unlike thin evaporated films which must be lithographed to obtain specimens whose resistance is high enough for practical purposes.

7.4 Three-terminal Spin Electronics

Electronically, the natural progression is from a two terminal GMR device to a three terminal device, and this step was first achieved by Mark Johnson [14–16] simply by attaching a third contact to the intermediate paramagnetic base layer to create the Johnson transistor (shown in Fig. 8)

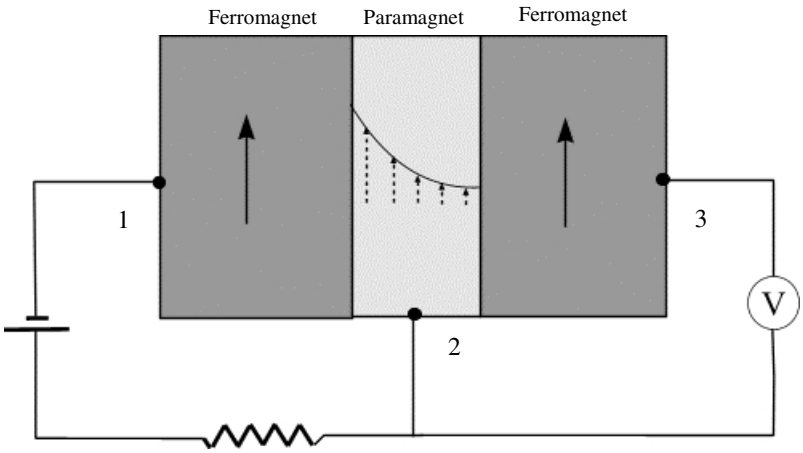

Fig. 8. The Johnson transistor.

In the language of bipolar transistors, we can speak of a base, an emitter, and a collector, the last two being the ferromagnetic layers. Just like its bipolar counterpart, the Johnson transistor can be used in a variety of configurations; the one we discuss here is chosen because it gives insight into yet another way of analyzing spin filtering and spin accumulation. We leave the collector floating and monitor the potential at which it floats by use of a high-impedance voltmeter. Meanwhile a current is pumped round the emitter-base circuit and this leads to spin accumulation in the base layer as before. The floating potential of the collector now depends on whether its magnetic moment is parallel or antiparallel to the magnetization of the polarizing emitter electrode which causes the spin accumulation. Evidently this potential can be altered by using an external magnetic field to switch the relative orientation of the emitter and collector magnetic moments.

To analyze this behavior, consider again the limiting case of a half-metallic ferromagnet as the collector electrode. It floats in equilibrium with the base electrode – in other words, in the steady state no net current flows. But because it is half-metallic it can only trade electrons with the base whose spin is (say) parallel to its magnetization and the "no current" condition then means that its electrochemical potential is equal to the electrochemical potential in the base layer for the same electron spin type. In other words, the collector is sampling the electrochemical potential of the appropriate spin type (spin–up) in the base. Reversing the collector magnetization means it now samples the spin-down electrochemical potential in the base. Because there is spin accumulation in the base, these spin-up and spin-down electrochemical potentials are different [3] and the collector potential thus depends on the orientation of its magnetic moment. Thus we have a three-terminal spin electronic mechanism for which the conditions at terminal 3 can be set by suitable adjustment of the conditions at terminals 1 and 2, as for a traditional electronic three-terminal device. These conditions can also be reversed by applying an external magnetic field. The above encapsulates the essence of spin electronic device behavior.

7.5 Mesomagnetism

Evidently, in the above discussion it is essential that the spin accumulation penetrates right across the thickness of the base layer so that the collector may sample it. Likewise, in the two-terminal device, it was important that the base layer thickness was small on the length scale of the spin diffusion length. This provides us with an interesting new way to view spin electronic devices. We can regard their behavior as a write-read process in which an encoder writes spin information on to the itinerant electrons in one part of the device and this information is then conveyed to a physically different part of the device where it is read off by a decoder. The encoder and decoder elements are nanoscale ferromagnets and the spin information decays in transit on the length scale of the spin diffusion length. The message, then, is that for successful spin electronic device operation, the device **must be physically engineered on this length scale** or smaller.

This is just one particular manifestation of the general phenomenon of mesomagnetism, which concerns itself with the appearance of novel physical phenomena when magnetic systems are reduced to the nanoscale. The underlying tenet of mesomagnetism is that magnetic processes are characterized by a variety of length scales and that when the physical dimensions of a magnetic system are engineered to dimensions comparable with or smaller than these characteristic lengths, new and unusual magnetic phenomena appear, for example giant magnetoresistance, superparamagnetism, and perpendicular recording media. These characteristic length scales have a variety of origins. Many – domain size, domain wall width, exchange length, thin film perpendicular anisotropy threshold – are governed by a balance of energy terms. Others are the result of diffusion processes for energy, momentum, and magnetization.

7.5.1 Giant Thermal Magnetoresistance

As an interesting example of a mesomagnetic phenomenon we consider giant thermal resistance. The Wiedemann- Franz law (WFL) tells us there is a close relationship between electrical transport and heat transport in most materials. Thermal and electrical conductivity are limited in most regimes by the same scattering processes and the WFL tells us that in these circumstances their quotient is a constant times absolute temperature. Moreover, this close relationship extends to magnetotransport in mesomagnetic systems. Figure 9 shows measurement of the giant thermal magnetoresistance in a giant magnetoresistive mechanical alloy.

The analysis is identical to that for the electrical case. Spin information is encoded on to a thermal current in one part of the device and read off again in a different part of the device. The result is a thermal resistance which varies with applied magnetic field by many percent [17].

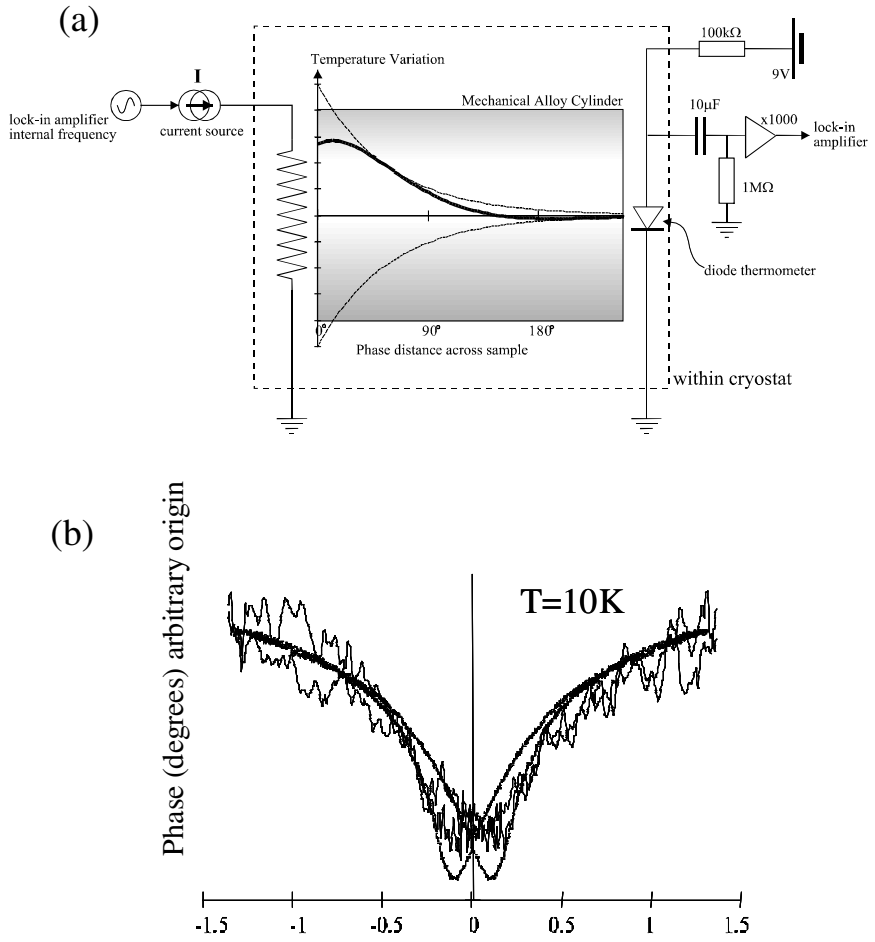

Fig. 9. (a) Schematic diagram of an experiment designed to measure thermal magnetoresistance, and (b) the thermal GMR effect seen in a mechanical alloy. For comparison, the electrical GMR is also shown inverted (dots) and superimposed on the thermal trace.

7.5.2 The Domain Wall in Spin Electronics

Another example of the intrigue of mesomagnetism can be seen by considering the geometrical similarity between a spin-valve structure and a ferromagnetic domain wall, as illustrated in Fig. 10. In both, regions of differential magnetization are separated by an intermediate layer. In the former this layer is in the form of a thin film of non-magnetic metal whereas in the latter it is a region of twisted magnetization.

The spin valve functions if spin conservation occurs across the intermediate zone. By analogy, it is possible to develop a model of domain wall resistance [18–20] in which the value of the resistance is determined by the amount of spin depolarization

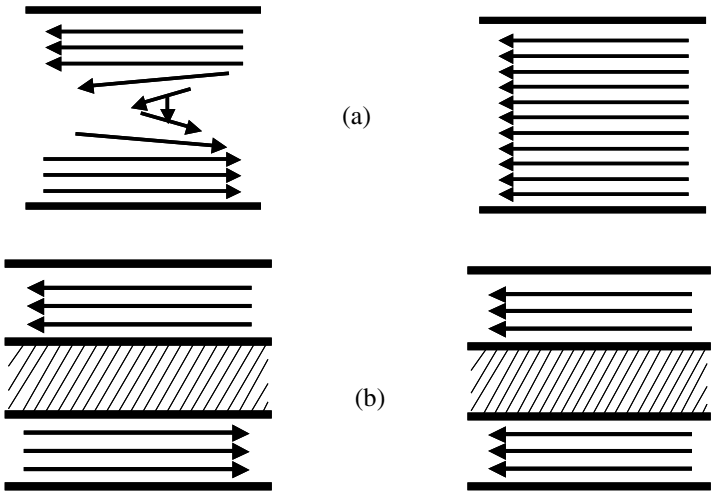

Fig. 10. Geometric similarities between (a) an FM domain wall and (b) a GMR trilayer (courtesy of W. D. Allen).

of the charge carriers in the twisted magnetic structure formed at the heart of the domain wall. The model invokes magnetic resonance in the ferromagnetic exchange field to determine the amount of electron spin mis-tracking on passing through the domain wall. This mis-tracking of, say, an up-spin leads to its making an average angle θ with the local magnetization direction in the domain wall, which is equivalent to its wavefunction being contaminated by a fraction $\sin(\theta/2)$ of the down-spin wavefunction (Fig. 11).

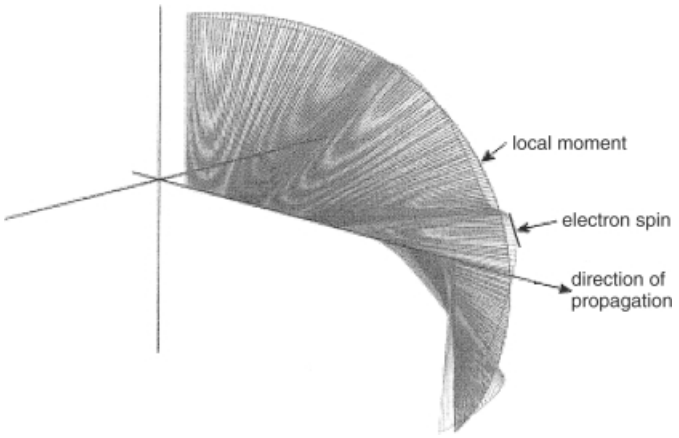

Fig. 11. Spin orientation versus trajectory for the electrical carriers in transit through a domain wall in cobalt. The blue vector represents the cobalt magnetization and the red vector represents the spin orientation (courtesy of W D Allen).

The up-spin is then susceptible to additional scattering by an amount equivalent to $\langle \sin^2(\theta/2) \rangle$ multiplied by the down-spin scattering rate. This model leads to a formula for the spin-dependent contribution to the domain wall resistivity:

$$\frac{\delta\rho_w}{\rho} = \left(\frac{\lambda^*}{\lambda} + \frac{\lambda}{\lambda^*} - 2\right)\left\langle \sin^2\left(\frac{\theta}{2}\right)\right\rangle \tag{4}$$

where λ and λ^* are the majority and minority spin mean free paths, and ρ_0 and $\delta\rho_W$ are, respectively, the bulk ferromagnetic resistivity and the resistivity increase for domain wall material. The varying angle θ has an amplitude which is approximately equal to $h v_F / E_{ex} d$, where d is wall thickness, v_F is Fermi velocity and E_{ex} is ferromagnetic exchange energy [21].

This spin-dependent contribution differs from various other proposed mechanisms for domain wall resistance in that it predicts not a fixed value of resistance for the wall but rather a ratio increase based on the bulk value for the material. In principle, therefore, the validity of the model can be assessed by measuring domain walls in increasingly impure samples of the same ferromagnet and observing if the ratio $\delta\rho_W/\rho_0$ stays fixed. This model has been re-analyzed [22] by replacing this simple rotating frame approach with a more sophisticated quantum mechanical analysis. To within a simple numerical factor, identical results are obtained.

7.6 Spin Tunneling

Tunneling between ferromagnetic electrodes, and the effect of the relative magnetic orientation of the electrodes upon it, was an effect first investigated by Julliere [23] and Maekawa [24]. These early observations (Fig. 12) showed that the tunneling conductance (for these dissimilar electrodes) increases when the relative orientation of the electrodes changes from parallel to antiparallel; the effect was termed tunneling magnetoresistance (TMR).

Julliere was the first to describe the cause of this effect in classical terms. His argument was that the spin splitting of the Fermi level in the magnetic metals led to unequal distribution of up- and down-spin electron states. This, combined with the classical model of tunneling [26], in which the overall tunneling conductance is proportional to the product of the densities of states of the two electrodes, with the assumption that spin is conserved in the process of tunneling, resulted in a simple formula which stated that:

$$\frac{\Delta R}{R} = \frac{\left(R^P - R^{AP}\right)}{\left(R^P + R^{AP}\right)} = \frac{2P_1P_2}{(P_1 + P_2)} \tag{5}$$

where P_i is the polarization of the electrode defined as:

$$P_i = \frac{\rho_i^{\uparrow} - \rho_i^{\downarrow}}{\rho_i^{\uparrow} + \rho_i^{\downarrow}} \tag{6}$$

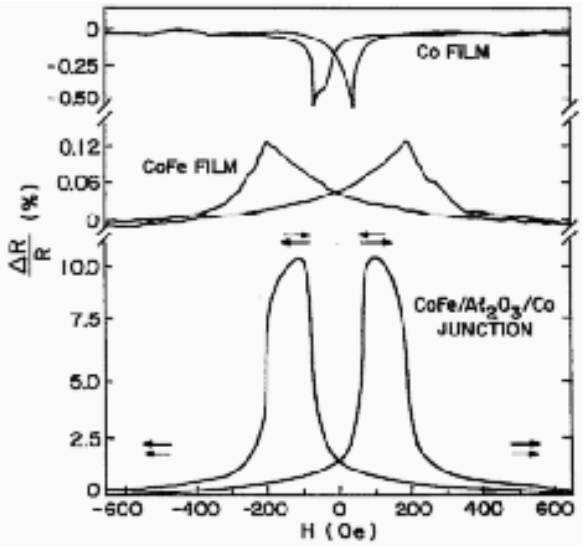

Fig. 12. Experimental signature of spin tunneling [25]; resistance of $CoFe/Al_2O_3/Co$ tunneling junction plotted as a function of H in the film plane, at 295 K. Also shown is the variation of CoFe and Co resistances. The arrows indicate the direction of M in the two films.

and ρ is the density of states. This well known Julliere model was successful in giving physical insight into the possible origin of the effect. Extensive research performed over the last twenty years has, however, posed new questions, some of which remain unexplained even today. For instance, in a classic experiment by Moodera and Kinder [25] it was found that the observed TMR is highly dependent not only on the type of insulator used as a tunnel junction, but also on the barrier height and width. Many workers found that the TMR varies substantially with temperature and applied bias, irrespective of junction quality. In addition, barrier impurities and the introduction of a spacer metal into barriers of controlled thicknesses all affected the measured values. None of these effects is explained by the simple classical model. The search for a comprehensive theoretical model for TMR that can explain all available experimental data is as yet an unresolved challenge.

7.6.1 Theoretical Description of Spin Tunneling

The basic defect in the classical theory of spin tunneling is that it treats the two ferromagnetic electrodes as independent systems [23]. In Julliere's model, the electron wavefunctions within the barrier are treated as evanescent and are assumed not to perturb the electron wavefunction in the other electrode. It also considers only the simple case of a square barrier–i. e. one which is unbiased, or at least where the effect of the bias voltage on the barrier shape can be ignored. As a result, this early model does not predict any barrier width or height dependence of the tunneling magnetoresistance, in clear contradiction of the measured results.

The need to modify Julliere's model was first realized by Slonczewski [27], who argued that because most practical barriers are relatively permeable, wavefunction overlap within the barrier means that wavefunction matching must be considered

across the entire device. Using two parabolic bands (spin up and down) shifted relative to one another by the exchange splitting, Slonczewski solved the Schrödinger equation for the wavefunctions of the polarized electrons tunneling across a rectangular barrier and determined the resulting conductance from the current operator. The principal result of his calculation was that the effective polarization of the tunneling electron (which, when substituted into Eq. (5), gives the TMR) now depends on the height of the barrier, V_b, through an imaginary wavevector in the barrier, κ, defined by:

$$\hbar\kappa = \sqrt{[2m(V_b - E_F)]} \tag{7}$$

by an amount:

$$P_i = \left[\frac{k_i^{\uparrow} - k_i^{\downarrow}}{k_i^{\uparrow} + k_i^{\downarrow}}\right] \times \left[\frac{\kappa^2 - k_i^{\uparrow} k_i^{\downarrow}}{\kappa^2 + k_i^{\uparrow} k_i^{\downarrow}}\right] \tag{8}$$

This equation has a simple physical interpretation–because the magnitude of the Fermi wavevector for a particular spin channel is proportional to the density of states at the Fermi energy, we can see that the first factor $\left(k^{\uparrow} - k^{\downarrow}\right) / \left(k^{\uparrow} + k^{\downarrow}\right)$ is identical to the polarization obtained in Julliere's classical theory of tunneling, but is now multiplied by a new factor $[\kappa^2 - k^{\uparrow}k^{\downarrow}]/[\kappa^2 + k^{\uparrow}k^{\downarrow}]$. Because κ ranges from 0 (low barrier) to infinity (high barrier) we can see that in the limit of high barrier height the effective polarization reduces to Julliere's result; for low barrier height, however, it departs significantly and can even change sign. Hence the matching of the wavefunctions across the tunnel barrier offers a plausible explanation of the observed dependence of TMR on the thickness and height of the tunneling barrier, and hence on the choice of insulator itself.

7.6.1.1 Fowler-Nordheim Tunneling Regime

An additional sophistication, which may be added at will to the Julliere and Slonczewski models alike is the replacement of the simple square barrier with a triangular topped barrier, the shape of which more accurately reflects the applied bias across the tunnel junction. This has the effect that the tunneling electron wavefunction in the barrier is now an Airy function rather than a simple evanescent wave. The circumstances in which this modification is necessary (i. e. when the bias potential term is **not** small compared with the barrier height) is termed the Fowler–Nordheim tunneling regime. The Fowler-Nordheim regime manifests itself experimentally as non-linearity in the current-voltage curve for the tunnel junction.

7.6.1.2 Linear Response Theory

Although Slonczewski's model enables much more realistic treatment of the F/I/F interface than the classical theory of tunneling, its drawback is that it cannot be

readily extended to more complex systems with more than one electron band. Any rigorous model of TMR must, however, include, or at least justify the exclusion of, the multi-orbital structure of ferromagnetic electrodes. It is for this reason that a great majority of the work undertaken in explaining TMR over the last decade was based on the *linear-response* theory of electron tunneling.

The main assumption of this theory (often referred to as the Kubo/Landauer formalism) is that the overall conductance in either spin channel for *any* (insulating or conducting) sample sandwiched between two electrodes can be written in terms of its total transmission coefficient [28]. The basis of the linear response theory states that the expression for the conductance in either spin channel can be written in terms of one-electron Green's functions in the left and right planes of the tunneling junction, in a direction parallel to the current flow [29]:

$$G^{\sigma} = \frac{4e^2}{h} \sum_{k_{\parallel}} Tr \left([T_{\sigma} \mathrm{Im}\mathbf{g}_R^{\sigma}(E_F, \mathbf{k}_{\parallel})] \times \left[\mathbf{T}_{\sigma}^{+} \mathrm{Im}\mathbf{g}_L^{\sigma}(E_F, \mathbf{k}_{\parallel}) \right] \right) \tag{9}$$

The theory includes more essential components necessary to explain the observed effects than any earlier model. The Green functions for each of the-states $\mathrm{Im}\mathbf{g}_{\mathrm{R,L}}^{\sigma}(E_F, k_{\parallel})$, (which are closely related to the densities of states) are multiplied by a matrix $\mathbf{T}_{\sigma}$ whose elements indicate the strength of the tight binding hopping between atomic orbitals in the left and right planes. The matrix also contains an element which is responsible for evaluation of the dependence of TMR on the height and width of the tunneling barrier, as will be shown below. Summation over the two-dimensional Brillouin zone and taking into account the different characteristics of the s, p, and d orbitals yields an overall conductance.

As an illustration, we can simplify the formalism and evaluate the above equation for the simple case of coherent ($k_{\parallel}$ and spin conserved) tunneling through a high barrier, assuming that the electrons originate from only one band. In these circumstances it is found is that the current in each channel is then proportional to the product of the surface densities of states of the two electrodes (as in the classical theory of tunneling), but that the product is scaled by the denominator which describes the mutual interaction of the two electrodes as a result of the overlap of the wavefunctions. Such a model has been used to perform numerical calculations [29] on a structure chosen to resemble a junction with Co electrodes and the result (increasing TMR with increasing barrier height, V_{ins}, saturating when V_{ins} is of the order of the bandwidth of the electrodes) is in excellent agreement with recent experimental results of Sousa et al. [30, 31]. The observed weak variation of TMR with barrier thickness [32] can be explained by the model if we assume that most TMR experiments are performed in the high-barrier regime.

By adding a fully realistic band structure for the ferromagnetic electrodes to the above model (i. e. by distinguishing between s, p, and d orbitals), it is possible to test whether the Kubo/Landauer formula predicts the correct sign for the polarization of the tunneling electrons. Two such calculations have been performed–one dealing with tunneling between Co electrodes through a vacuum gap [29] one through a simple step barrier [33]. The results from the first study are particularly encouraging – the calculated polarization of the tunneling electrons as a function of the tunneling

vacuum gap shows that, when the tunneling gap is small, of the order of the lattice constant, the conductance is dominated by d electrons, and the polarization has the "wrong" sign, i. e. $P < 0$ as in the classical Julliere theory of tunneling. There is a rapid crossover, however, as the width of the gap increases, and the polarization changes to positive values. The calculated saturation value of 35-40 % is, moreover, in excellent agreement with the observed values [34]. The crossover occurs because the overlap of the d-orbitals decreases with increasing gap much faster than that of the s-orbitals, and it is, therefore, s-electrons which determine the conductance in most tunneling experiments. One can therefore deduce that the observed sign of the polarization in junctions between ferromagnets and Al_2O_3 suggests that the sd-hybridization between the two must be weak.

Going a step further in the Kubo/Landauer formalism, it is possible to consider the effect on the observed TMR of disorder in the barrier. In most tunneling experiments the fabricated barriers are amorphous and, therefore, the assumption of conservation of momentum parallel to the tunneling junction ($k_{\|}$) is not satisfied. Advanced studies of the effect of disorder on spin tunneling using a single-orbital tight-binding model and the Kubo formalism, show that, in addition to the mixing of the k// channels, disorder also induces resonant tunneling via localized electronic states [35–37]. These states are formed in the barrier in the presence of impurities or defects. Resonant tunneling results in quasi-one-dimensional high-conductance channels which dominate the overall conductance when the degree of disorder is high and the barrier is thick [38]. It follows that the overall tunneling current, and hence the TMR, is not only determined by the intrinsic properties of the densities of states of the ferromagnet, but also to a large extent by the properties of the insulator.

As a further test of this theory, it is useful to compare its predictions with the experiments performed by several workers [39, 40] in which a thin layer of non-magnetic metal is inserted between one of the ferromagnetic electrodes and the insulating barrier. According to classical theory, because there is no spin asymmetry in one of the metal insulator interfaces, no TMR should be observed; this contradicts the experimental findings. Calculations by Mathon and Umerski [41], using the Kubo formalism, predict that the TMR should oscillate with increasing thickness of the Cu interlayer in a Co junction with a vacuum gap. For a very thin interlayer this leads to a negative TMR. This effect can be explained by considering the Fermi surfaces of Cu and Co. For the majority spin electrons in Co the matching of the surfaces with Cu is good, whereas for the minority spins they are not. It follows that the majority spin electrons can easily cross the Co/Cu interface whereas the poor match for the minority spin electrons results in the formation of down spin quantum well states in the Cu overlayer [42–44]; the loss of transport of these gives rise to a spin asymmetry of the tunneling current, and hence to a non-zero TMR.

We can see, therefore, that the linear response theory is relatively successful in offering explanations of the many subtleties of observed TMR effects. Many questions, however, remain unanswered. One of the more challenging problems is the true origin of the fall in TMR with increasing temperature and applied DC bias. For the former, there are currently two possible explanations. One involves the mechanism of spin-flip scattering arising from magnetic impurities in the barrier [45], which, being an inelastic process, increases with temperature. The other suggests

that the increase in temperature leads to a reduction of overall magnetization in the ferromagnet, because of excitations of magnons [46, 47]. At this stage the extent to which each of these holds true is unclear. In a similar way, bias dependence can be accounted for by Slonczewski's model [25, 48], although the predicted initial decrease of TMR is much slower than is observed [49]. An alternative explanation invokes electron–magnon scattering which (because magnons are spin-1 quasi-particles) flips the electron spin in the process [50]. Because the phase space for electron-magnon scattering increases with increasing bias, the total TMR decreases. Again, the extent to which these mechanisms are responsible for the observed behavior is currently unclear.

7.6.2 Applications of Spin Tunneling

By analogy with the spin valve, the spin tunneling junction acts as an electronic switch the operation of which again mirrors that of a pair of crossed optical polarizers which can be switched on and off by application of external magnetic fields. If the electrodes are not ideal HMFs, the on/off conductance ratio is finite and reflects the majority and minority density of states for the ferromagnet concerned. Spin tunnel junctions as described have the added advantage that their operation depends only on the net properties at the interfaces and does not invoke carrier mobility, hence unlike GMR, there is no competition between these two effects. Unlike all-metal systems, moreover, they have lower conductances per unit area of device and hence larger signal voltages (of the order of millivolts or more) are realizable for practical values of operating current. The device characteristics such as the size of the "on" resistance, current densities, operating voltages, and total current can be tuned by adjusting the device cross-section, the barrier height, and the barrier width. As we shall see below, this is just one reason they are very promising candidates for the spin-injector stages of future spin electronic devices. They are also the basis of the next generation of tunnel MRAM, as illustrated in Figs 13 and 14.

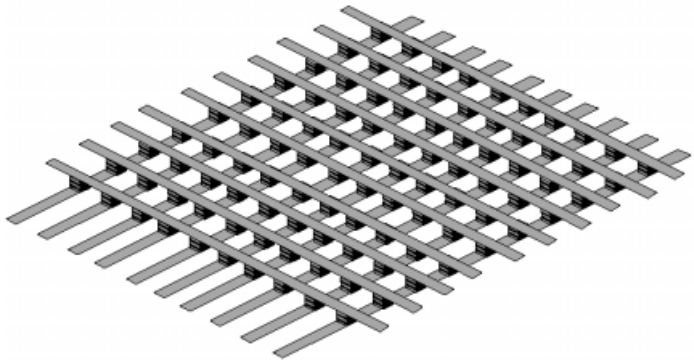

Fig. 13. A 10 × 10 MRAM matrix with tunnel memory elements (courtesy of M. Hehn, Université H. Poincare, France).

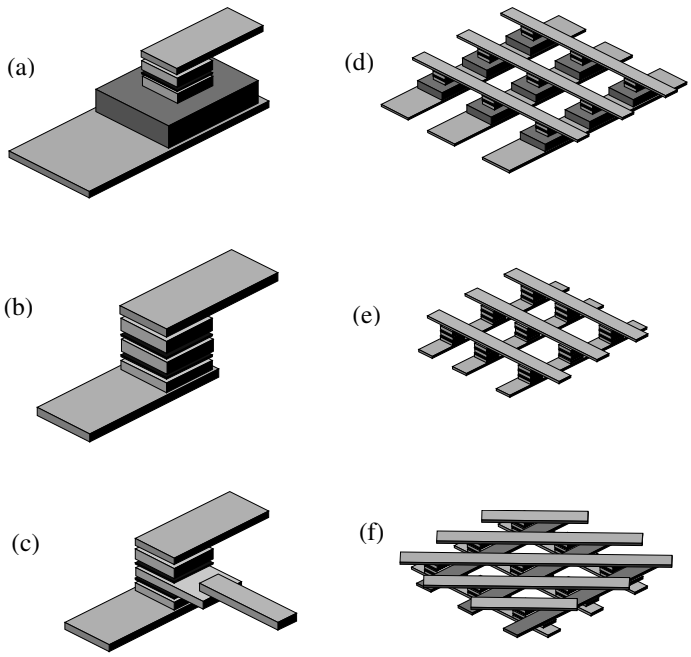

Fig. 14. (a) Current state of the art MRAMs use semiconductor diodes to prevent parasitic current paths during readout. These diodes impede further miniaturization. Alternative options include: (b) MIM diodes and (c) three- terminal spin tunnel transistor TRAM with selective polarization. A selection of array address geometries is shown: (d) TRAM–diode units (e) TRAM–MIM units, and (f) three-terminal spin tunnel transistor TRAM. (Courtesy of M. Hehn)

7.7 Hybrid Spin Electronics

Although the early Johnson transistor is a useful and versatile demonstrator device, it has practical limitations. The voltage changes measured are small and it has no power gain without the addition of two extra electrodes and a transformer structure. The underlying design problem with the device is that it is entirely Ohmic in operation simply because all its constituent parts are metals.

Clearly another technology progression is needed and this is the introduction of hybrid spin electronics-the combination of conventional semiconductors with spin-asymmetric conducting materials. At a stroke this makes the complete armory of semiconductor physics (for example exploitation of diffusion currents, depletion zones, and the tunnel effect in semiconductors) available to the spin electronic designer for the creation of new high-performance spin-devices.

7.7.1 The Monsma Transistor

The first hybrid spin electronic device was the Monsma transistor (Fig. 15) produced by the University of Twente [51–53]. It was fabricated by sandwiching an all-metal spin valve device between two layers of silicon. Three electrical contacts are attached to the spin-valve base layer and to the silicon layers. The spin valve is more sophisticated than that illustrated in Fig. 12 and comprises multiple magnetic/non-magnetic bilayers, but the operating principle is the same. Schottky barriers form at the interfaces between the silicon and the metal structure and these absorb the bias voltages applied between pairs of terminals. The collector Schottky barrier is back-biased and the emitter Schottky is forward biased. This has the effect of injecting (unpolarized) hot electrons from the semiconductor emitter into the metallic base high above its Fermi energy. The question now is whether the hot electrons can travel across the thickness of the base and retain enough energy to surmount the collector Schottky barrier. If not they remain in the base and get swept from the base connection.

By varying the magnetic configuration of the base magnetic multilayer the operator can determine how much energy the hot electrons lose in their passage across the base. If the magnetic layers are antiferromagnetically aligned in the multilayer both spin types experience heavy scattering in one or other magnetic layer orientation, so the density of both spin types with energy greater than the collector barrier E_C as a function of distance into the base follows the heavy exponential decay curve of Fig. 15. If, on the other hand, the magnetic multilayer is in an applied field and its layers are all aligned, one spin class gets scattered heavily in every magnetic layer, whereas the other class has a passport to travel through the structure relatively un-

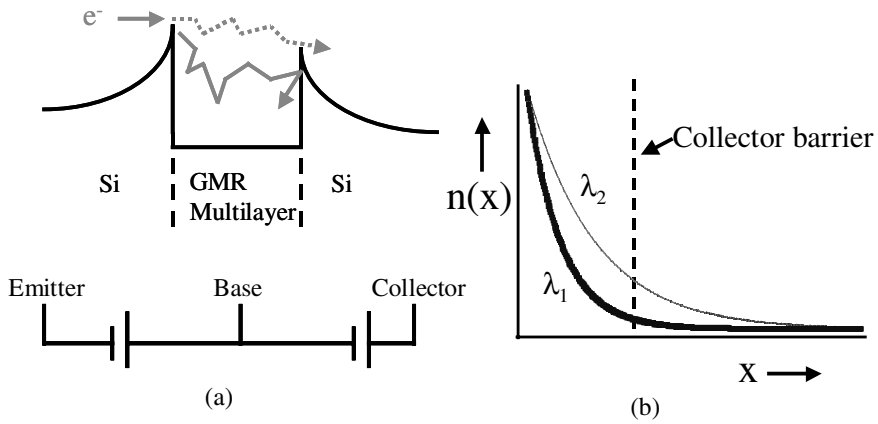

Fig. 15. The Monsma transistor – the first attempt to integrate ferromagnetic metals with silicon (a); (b) shows the density as a function of distance into the base for majority hot spins with energy greater than the collector barrier. The thick line corresponds to an antiferromagnetically aligned multilayer and the thin line to ferromagnetic alignment. There is a clear tradeoff between the size of the collected current and the sensitivity of the collector current to the applied magnetic field.

scathed and the plot of density (with $E > E_C$) against distance for this privileged class follows the thin curve. It can thus be seen that for parallel magnetic alignment more spins with energy $> E_C$ impinge on the collector barrier and the collected current is correspondingly higher. Once again, like the Johnson device, we have a transistor with electrical characteristics that are magnetically tuneable. This time, however, the current gain and the magnetic sensitivity are sufficiently large that, with help from some conventional electronics, this is a candidate for a practical working device.

It can be seen by comparison of the two traces of Fig. 15 that a trade-off must be made in determining the optimum base thickness. A thin base enables a large collector current harvest but affords little magnetic discrimination. A thick base, on the other hand, means a large difference between the collector currents corresponding to the two magnetic states of the multilayer but an abysmally small current gain. The low current gain has always been the Achilles' heel of metal base transistors, and is probably the main reason for their fall from favor as practical devices despite their good high frequency performance which derives from the absence of charge storage in the base.

An interesting feature of the Monsma transistor is that transmission selection at the collector barrier is achieved on the basis of energy. Thus the scattering processes in the base which determine collected current are the inelastic processes. Elastic collisions which change momentum but not energy are of less significance (although spin transmission at the interface is confined to a cone of k-vectors the incident angles of which lie within certain limits). This contrasts with the functioning of a spin valve type system in which all momentum-changing collision processes have the same status in determining device performance [54].

7.7.2 Spin Transport in Semiconductors

The Monsma transistor is a very important step in the evolution of spin electronics. It is the first combination of spin-selective materials with semiconductor. So far, however, the semiconductor has been used solely to generate barriers and to shield the spin-dependent part of the device from electric fields. To release the full potential of hybrid spin electronics we need to make devices which exploit spin-dependent transport in the semiconductor itself.

7.7.3 The SPICE Transistor [55, 56]

The current gain of a conventional bipolar transistor is partly a result of the screening action of the junctions either side of the base which absorb the bias voltages and leave the base region relatively free from electric fields. The current which diffuses across the base is primarily driven by carrier concentration gradient and to a rather lesser extent by electric field. The randomness associated with concentration-driven current flow helps to improve the current gain. The carriers injected by the emitter are forced to wander towards the base along the top of an extended cliff in voltage, at the bottom of which lies the collector. Approximately 99 %, say, of the carriers

stumble over the cliff and are swept out the collector and the remaining 1 % make it to the base connection; this gives a very satisfactory current gain $\beta = I_c/I_b$ of 99.

Implementing spin-polarized current transport in a semiconductor enables a new concept in spin transistor design – the spin polarized injection current emitter (SPICE) device in which the emitter launches a spin-polarized current into the electric field screened region and a spin-selective guard-rail along the top of the cliff determines whether or not these polarized carriers are allowed to fall into the collector. Thus we have a device with a respectable current gain from which power-gain can easily be derived, but whose characteristics may again be switched by manipulating the magnetic guard rail via an externally applied magnetic field. A wide variety of designs is possible which answer to this general principle. For example the emitter and collector interfaces can be realized by p–n junctions, Schottky barriers, or spin tunnel junctions and the geometry of the device can be adjusted to allow a greater or lesser amount of electric field driving component to the diffusion current in the base, depending on the application.

7.7.4 Measuring Spin Decoherence in Semiconductors

The crucial question which must be answered to realize this kind of spin transistor is whether spin transport is possible at all in semiconductors, and, if so, whether it is possible over the sort of physical dimensions on which a typical transistor is built. In other words, we need an estimate of the spin diffusion length in a typical semiconductor. A subsidiary question concerns the role of dopants in the semiconductor and whether they introduce spin-orbit scattering which militates against the spin transport by reducing the spin flip times.

An immediate way of addressing this question is to direct spin-inject into a semiconductor and observe the polarization of the current which emerges on the other side. Figure 16 shows an experiment in which this was performed.

Doped channels of silicon with various types of dopant at different concentrations, and of different lengths (from 1 to 64 microns), were contacted at each end with differentially magnetizable cobalt pads of well defined magnetizing behavior. The transport results shown in Fig. 16 are insensitive to magnetic field direction, have even symmetry (thereby eliminating AMR and the Hall effect as possible causes), and they are compatible with the observed domain magnetization processes for the cobalt pads. They seem to correspond to spin transport through the semiconductor, and as such they correlate well with earlier experiments [57] using nickel injectors. Interestingly, however, the spin transport effects are of order a few percent at best, yet the effect decays only very slightly with silicon channel length and was still well observable for 64-μm channels.

The message would seem to be that the spin diffusion length in silicon is many tens of microns at least, but that the spin injection process at the metal/silicon interface is highly inefficient. This direct injection inefficiency is being widely observed and its cause is still hotly debated. It might arise from spin depolarization by surface states [58], or it might be explainable by the Valet/Fert model in which spin injection is less efficient for materials of very different conductivity [59]. It might also be

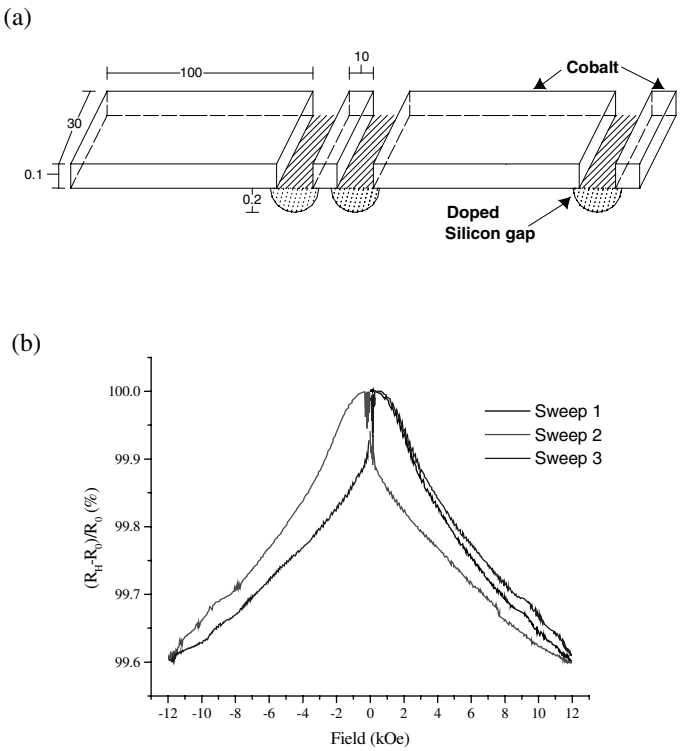

Fig. 16. Geometry of an experiment (dimensions in microns) to investigate the possibility of spin injection across a ferromagnetic/semiconductor interface (a). The transport curves (b) suggest that the spin diffusion length is of the order of tens of microns, but that the spin injection process at the interface is highly inefficient. (Courtesy of C. Sirisathitkul)

because the spin injection is not being implemented at the optimum point in the semiconductor band structure. From the latter standpoint spin tunnel injection into semiconductors is a more versatile technique, because, for a given injected tunnel-current density, the necessary bias (and hence the point in the band-structure where injection occurs) can be tuned by varying the thickness and/or the tunnel barrier height.

A very beautiful direct measurement of semiconductor spin diffusion length has been performed by avoiding the spin injection problem [60, 61] and generating the spin-polarized carriers in the semiconductor itself (Fig. 17). Gallium arsenide, which was used as the host, has the property that, when pumped with circularly polarized light, the selection rules are such as to populate the conduction band with predominantly one spin type.

These spins can be made to precess by application of a small magnetic field. The resulting precessing magnetization is then detected using optical Faraday rotation, by use of a probe beam from the same optics as provides the pump. The magnetization drifts under the application of a driving electric field and the spatial decay

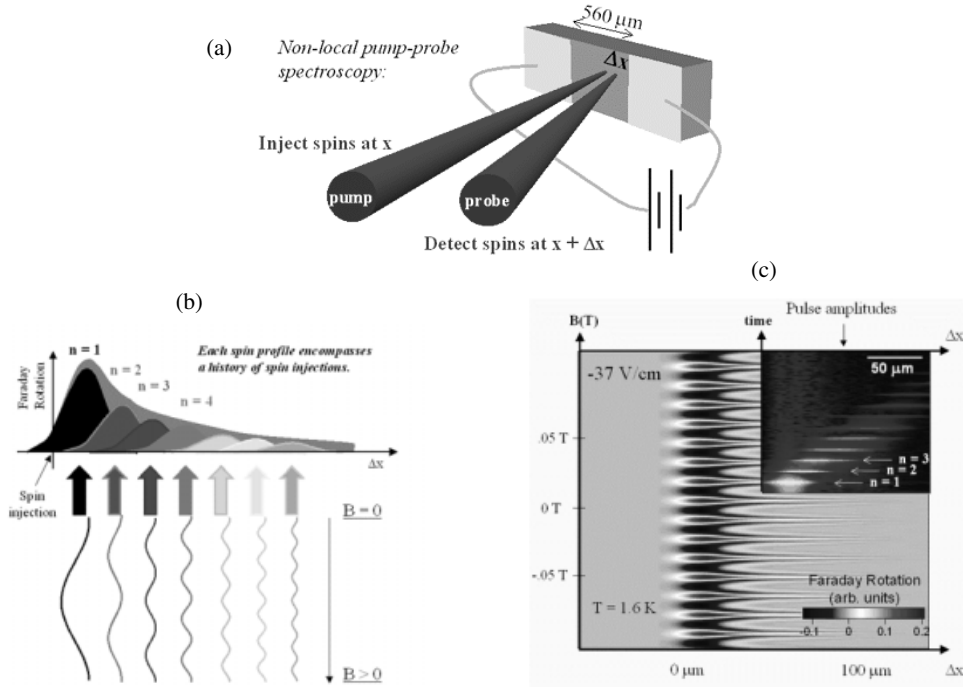

Fig. 17. Lateral drag of spin coherence in gallium arsenide, measured by Faraday rotation [55] (a). Additional population is created every time a pulse hits the sample (b). The electrons in each new population drift along the magnetic field, and the spatial extent of each spin population can be assessed as shown in (c). Spin transport can be observed on length scales exceeding 100 μm.

of the precession signal is a measure of the spin diffusion length. The results are of order many tens of microns, in accordance with the silicon direct injection experiment discussed above.

Thus it would seem beyond doubt that the spin diffusion length in semiconductors is adequate for the design and realization of SPICE type transistor structures – assuming means of efficient delivery of the initial spin polarized current are provided.

7.7.5 Methods of Increasing Direct Spin-injection Efficiency

With this problem in mind it is interesting to examine the results of an experiment which injects spin-polarized carriers from a **magnetic** semiconductor into a normal semiconductor light-emitting diode structure [62–65]. The polarization of the injected carriers depends on the magnetization direction of the magnetic semiconductor which supplies them. This is reflected in the polarization of the light emitted by the LED – its polarization is related to the spin of the electrons which cause it via the same selection rules, as discussed in the Awschalom experiment [60, 61], and as illustrated in Fig. 18.

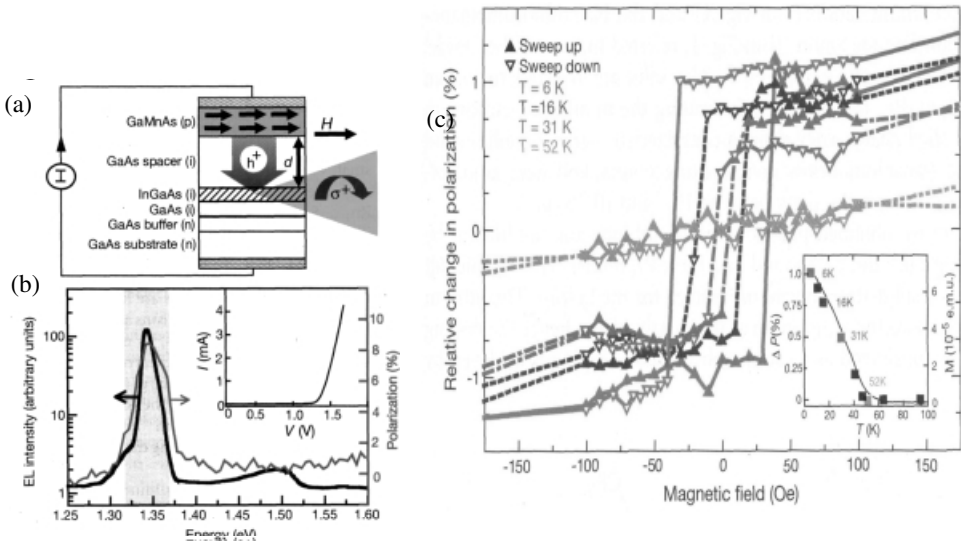

Fig. 18. (a) Electrical spin injection into an epitaxially grown ferromagnetic semiconductor. (b) The photoluminescence of the device as a function of energy. (c) Polarization of the emitted optical radiation decays in accordance with the variation of the semiconductor magnetization with temperature.

The polarization of the light emitted correlates well with the hysteresis loop for the magnetic semiconductor and decays with temperature exactly as the magnetic moment of the magnetic semiconductor, leaving little doubt that successful spin injection has been achieved. The percentage injection achieved here is more favorable than has been possible by direct injection from metals and it might be that magnetic semiconductors have an important role to play in future spin electronics development, notwithstanding the non-negligible materials problems which they pose. Very recent developments [66, 67] would seem to promise workable high-temperature magnetic semiconductor materials.

Otherwise, experiments suggest that spin-tunnel injection into semiconductors is a promising technique with higher injection efficiency than direct spin-injection. Further results in this area are imminent.

7.8 Novel Spin Transistor Geometries – Materials and Construction Challenges

The different spin transistors designed along the SPICE principle all require ferromagnetic polarizer and analyzer stages each side of the semiconductor assemblies. For contamination reasons the magnetic fabrication must be performed only after

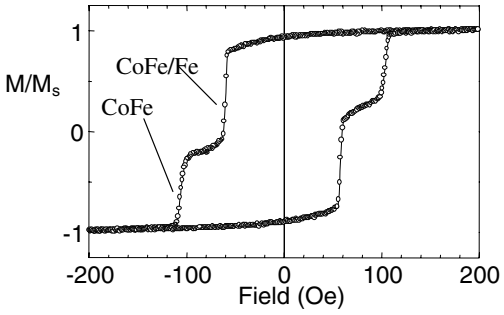

(b)

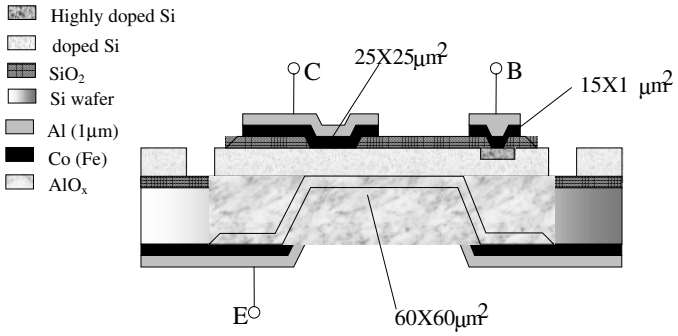

Fig. 19. Schematic illustration of a spin tunneling semiconductor transistor: (a) shows the differential magnetic hysteresis of the transistor before the base and collector were lithographically patterned to produce the structure shown in (b).

semiconductor processing is complete. The materials must be compatible, the process must enable the implementation of high-quality tunnel junctions, the nanomagnetic elements must be differentially magnetizable, the physical dimensions must satisfy spin diffusion length requirements, and the fabrication must comprise a lithographic stage which defines the three distinct electrodes, all with a minimum of processing steps.

Faced with these challenges, the authors and their colleagues in York, Strasbourg, and Southampton have found the configuration illustrated in Fig. 19 most satisfactory for making this type of device. The basis of the structure is a silicon-on-insulator (SOI) wafer into the base of which is etched a micron-sized pit with relieved sides. The spin polarized injection emitter is built into the pit and the base and collector structures are deposited and etched on the device-quality silicon side.

7.9 The Rashba effect and the Spin FET

7.9.1 The Rashba Effect

The Lorentz transform applied to electromagnetism shows that to a relativistic traveller a stationary electric field looks partially magnetic. Because charge-carrier velocities in devices are of the order of 10^6 m s^{-1} or larger, relativistic considerations apply, and electrons in, for example, the channel of a field-effect transistor see the local electric fields in the device as having magnetic components whose orientation depends on the geometry of the observer's travel relative to the field axis. This is known as the Rashba effect. If the electric field in question originates from crystal-field effects or from the depletion layer in a semiconductor structure, the magnetic component which appears to relativistic electrical carriers is capable of spin-splitting the conduction band if it is diagonal and of causing spin precession if it is off-diagonal.

7.9.2 The Datta–Das Transistor or Spin FET [68]

The Rashba effect gives rise to a novel spin electronic device concept proposed by Datta and Das but so far unrealized experimentally. The device has a construction similar to that of a conventional field-effect transistor with source and drain electrodes made in ferromagnetic metals and a semiconductor channel which is subject to a transverse electric field whose magnitude can be tuned by applying a gate voltage. Spin-polarized carriers leave the source with their spins parallel to the source magnetization and precess in transit through the channel owing to the Rashba effect. If the drain magnetization is parallel to that of the source and the carriers perform an integral number of precessions in transit, the conductance of the device is high. Slight modification of the gate voltage changes the precession rate, however, and if the spins now execute $N + 1/2$ precessions in transit the device conductance is minimized. The resulting device thus behaves like a normal FET with the additional feature that the differential magnetization of its electrodes (and hence its electrical characteristics) are sensitive to an externally applied magnetic field.

Although the device has not yet been realized, much groundwork on the materials properties, and principles exist in the literature and spin-valve effects have apparently been observed in experiments involving two-dimensional electron gases in which spin-polarized carriers are injected from permalloy contacts into an AlSb/InAs quantum well and are analyzed by a second permalloy contact with a different switching field [69, 70].

Some scepticism has, however, been voiced by other workers on the spin FET problem [71, 72], and theoretical signposts have been placed to spin precession type data which will confirm unambiguously that Datta/Das type device function has been observed [73]. This is clearly an exciting topic which will continue to attract attention and research activity for the foreseeable future.

7.10 Methods for Measuring Spin Asymmetry

With the caveat, particularly for spin tunneling, that the concept of the amount of spin polarization is more appropriate to combinations of materials [74], it is interesting to establish the expected polarization which a particular material might offer in a device. Several methods exist, including spin-polarized photoemission spectroscopy [75] and Andreev reflection [76], in which the transport properties of an interface between a superconductor and point-contact of the spin-asymmetric material are examined. Another technique involves characterization of tunneling currents from an electrode of the material under investigation to a known electrode/insulator combination [74].

A third technique [77] is to analyze the magnetic variation in the Schottky characteristics of a barrier formed between the ferromagnetic conductor under analysis and a semiconductor. The Schottky current varies as:

$$I = I_0 \exp\left\{\frac{\mu_B B}{k_B T}\left[\frac{\rho_\uparrow - \rho_\downarrow}{\rho_\uparrow + \rho_\downarrow}\right]\right\}\left[e^{\frac{eV}{k_B T}} - 1\right] \tag{10}$$

where V is the bias voltage, B is applied magnetic field and $(\rho_\uparrow - \rho_\downarrow)/\rho_\uparrow + \rho_\downarrow)$ is the required spin asymmetry, which can, therefore, be extracted by observing the modifications to the Schottky characteristic in a magnetic field.

7.10.1 Ferromagnetic Single-electron Transistors (FSETs)

The electrostatic energy of a charged capacitor is $1/2Q^2/C$. If C is sufficiently small, this energy can compete with thermal quanta of size $k_B T$, even for $Q = e$, the electronic charge. Small metallic spheres or pads with physical dimensions in the nanometer range have capacitances in the right range for this condition to be satisfied [78]. If such a metallic island is sandwiched between two physically close metallic electrodes (the source and the drain), we have a single-electron transistor (SET) [79–81] through which current can be made to pass one electron at a time. A third electrode (the gate) which is capacitatively coupled to the metallic island is biased to control the passage of current, as illustrated in Fig. 20.

The physics involved is competition between three energy terms; the electrostatic energy, E_i, of the island, because of the presence on it of just one electron, the thermal quantum, $k_B T$, and the energy, eV_b, gained by an electron in falling through the bias voltage, V_b. The first electron which arrives on the island from the source electrode charges it to a potential e/C which, is sufficient to prevent any further electrons hopping to the island until the first electron has left via the drain electrode. The charges are encouraged to jump from the island to the drain (and hence make room for more charges to arrive from the source) by appropriate bias on the gate electrode. If the thermal quantum size is arranged to be small compared with the electrostatic energies in play, the risk of random thermal interference with the current control is negligible.

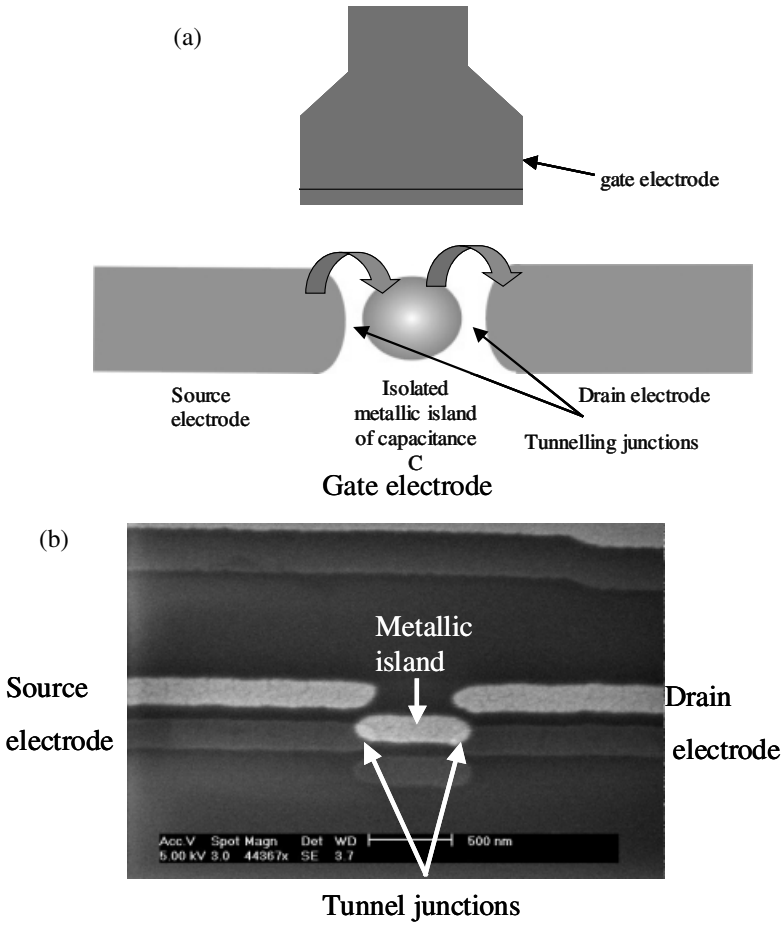

Fig. 20. (a) Schematic diagram of a FSET, and (b) the scanning electron microscope picture of the actual device. (I. Petej)

There is a fourth energy term which we can now introduce to the problem, the electrochemical potential difference for spin-up and spin-down electrons associated with spin accumulation. In practice this is achieved by making the electrodes and/or the island from ferromagnetic material [82–84]. A ferromagnetic source electrode will, in principle, induce spin accumulation on a non-magnetic island and, under certain bias conditions, the associated electrochemical potential divergence holds the balance of power between the main energy terms, and hence has a large amount of control over the current flow to the ferromagnetic drain. Other configurations are possible in which the island also is magnetic. Fert and Barnas [85] have performed extensive calculations for a variety of temperature regimes of the different possible modes of behavior of such devices, which are called ferromagnetic single-electron transistors (FSETs) or spin SETs. They are of particular interest in the experimental

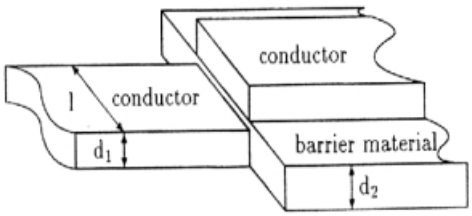

Fig. 21. A conductor of thickness d_1 evaporated on to a previously evaporated step of barrier material of thickness d_2. If $d_1 < d_2$ the two electrodes have no contact at the edge of the step and current is carried by means of tunneling. The capacitance of a SECO capacitor is small compared with those of conventional tunneling elements, because there is no overlap of the electrodes.

development of quantum computing, because they are a means of manipulating spatially localized qubits, as discussed below.

Very recently a completely novel design of an FSET has been considered by the authors; in this the tunnel junction structure is formed by use of the step-edge cut off (SECO) [86] method (Fig. 21).

The main reason for choosing the SECO geometry is that the capacitance of such a junction is dramatically smaller than that of a tunnel sandwich, even with larger line-widths, because of zero overlap of the electrodes, and the fabrication of such a step with a defined interruption of 10 nm is also much easier than that of a tunnel sandwich with 50 nm line widths made by electron beam lithography. This makes it possible to investigate the interplay between spin and charge-tunneling phenomena at higher temperatures; it is also a possible route to a room-temperature single-electron transistor. As an illustration, Fig. 22 shows the results of our numerical simulations of the capacitances of this structure (on the basis of algorithms developed by M. Knoll and H.F. Uhlmann [87, 88]). The predicted capacitance values are 15 aF, which will enable us to observe Coulomb blockade effects at temperatures <100 K (i. e. $e^2/2k_BC$ for 15 aF equals 120 K). The capacitance can be further reduced by reducing the line width of the electrodes.

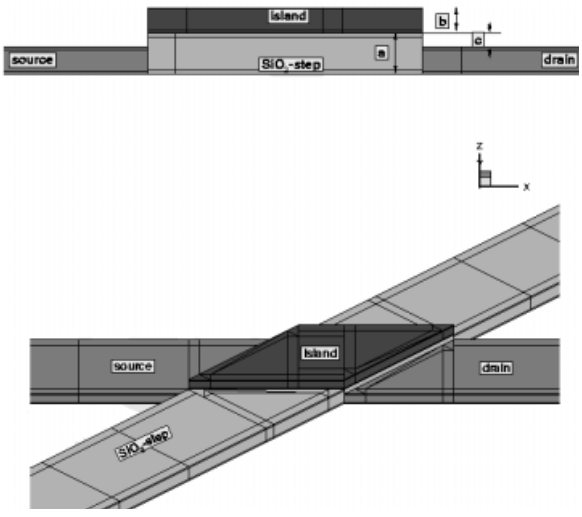

Fig. 22. 3D geometry of the proposed SECO based design of the FSET, indicating the relevant dimensions.

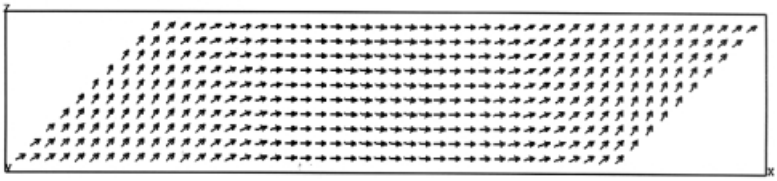

Fig. 23. Result of micromagnetic simulation of a 50-nm wide element showing the direction of local magnetization with the field applied parallel to the long axis

In addition, the SECO geometry is naturally suited to making all three thin-film ferromagnetic electrodes in the required shapes as acicular magnetic thin-film elements in which it is possible to induce quasi-single-domain behavior by modifying the shape of their ends [89]. Figure 23 illustrates a micromagnetic simulation close to the switching point on the type of element to be used.

The field is applied parallel to the long dimension and it is seen that even near switching there are no embryonic domains in the reverse direction and that the magnetization along the tunneling edges is well behaved. For the dimensions modeled, our simulation predicts a difference of 1350 Oe between the switching fields of the island and the electrodes ($H_{S(island)} - H_{S(electrode)}$). (Although this is probably an overestimate, it indicates we have a safety margin of nearly two orders of magnitude.)

Overall this new design hopes to deliver the concept of spin selectivity combined with the operational principles of the now-established single electron transistor (SET) to develop a device which will not only be a veritable playground for investigating the nanomagnetic behavior of single-electron transport, but also promises to be the basic building block of an important future technology.

7.10.2 Spin Blockade

Another interesting possibility which arises also if the magnetic island is itself a ferromagnet is that of a spin-blockaded system in which electrical transport across the device is switched by magnetizing the island [90]. An example of a Schottky barrier at low temperature which has been spin blockaded in this fashion is shown in Fig. 24 [91]. The MR effect is as large as 25 % at 20 K, which is unprecedented in a silicon device (shown in Fig. 25). The band structure consists of the Schottky barrier on the edge of which have been placed a series of magnetic islands which are antiferromagnetically coupled (and hence blockaded) in zero applied magnetic field. Applying a field orients these superparamagnetic particles and the resistance of the structure decreases owing to a tunnel-hopping current between adjacent islands. Exposure to light increases the resistance of the structure owing to photon-promotion of electrons from the islands to the large density of adjacent surface states. The geometry of this system is not unlike that of a high electron mobility transistor (HEMT) in which the performance of the main current channel is controlled by localized states in an adjacent but physically distinct region of the device.

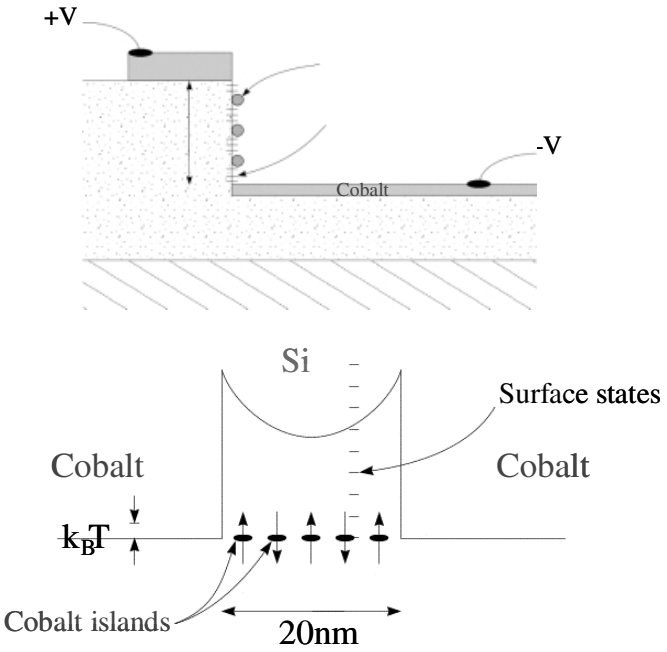

Fig. 24. Proposed band-structure for the spin blockaded Schottky barrier device [91].

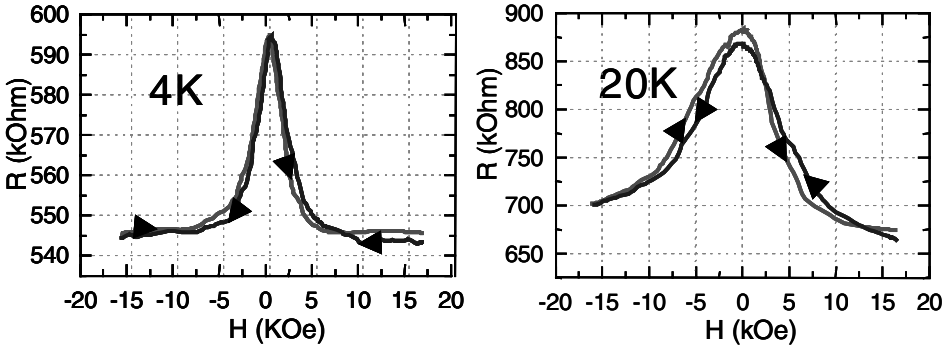

Fig. 25. Spin blockaded Schottky Barrier magnetoresistance measured at (a) 4 K, and (b) 20 K. The MR effect of 25 % in the latter is unprecedented in a silicon device.

7.11 Unusual Ventures in Spin Electronics

Just as conventional electronics insinuates itself into all walks of life, so spin electronics has the same invasive tendency. Even the carbon nanotube has not escaped [92]. Figure 26 shows the spin-valve effect observed from a cobalt-contacted nanotube; from this it is deduced that the spin diffusion length in such nanotubes is a surpris-

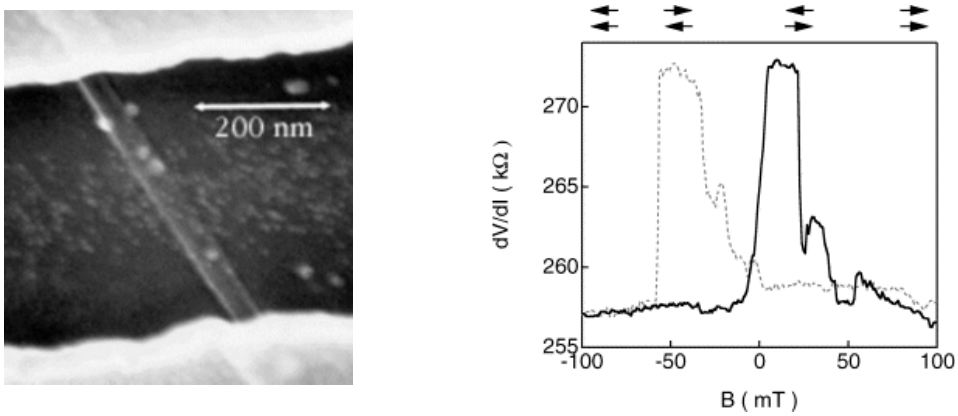

(a) (b)

Fig. 26. (a) Electron microscope picture of a 40-nm carbon nanotube contacted by Co. (b) The measured magnetoresistance [92].

ingly large 130 nm. This would seem to promise well for future device applications of such materials.

7.12 The Future of Spin Electronics

Outside the realms of politics and economics it is most foolhardy to predict the future of anything. Who would have thought that, after a mere decade of existence (starting for real in 1988), spin electronics would underpin a major industry such as hard-disk read technology? It seems clear that its next conquest is likely to be to carve itself a large niche in the MRAM industry using existing tunnel-junction technology and perhaps eventually refinements of the spin-tunnel transistors discussed above. Ultimately it might spawn a new philosophy in computer memory in which the distinction between storage memory and active memory becomes less defined.

7.12.1 Fast Magnetic Switching

A feature of spin electronic device performance which we have not discussed in detail is device bandwidth. There are two aspects to this, device response to electrical and to magnetic signals. The former is determined by the same considerations that govern the speed of conventional electronics – diffusion rate, charge storage, parasitic capacitance, and its spin analog. The magnetic switching time of the spin polarizing nanoelements is, however, another matter which is new to spin electronics, though some analogies may be drawn with the high-frequency response of particu-

late recording media. Analysis of high-speed magnetic switching of nanoelements is widely researched and has been found to be highly dependent on sample shape and coupling of the switching mode to the spin-wave spectrum. MRAM nanoelement access/write times of the order of nanoseconds are routinely achievable; this is highly competitive with other memory technology. In the future, however, higher magnetic switching speeds are desirable.

7.12.2 Optically Pumped Magnetic Switching

In the authors' opinions, one potential option for making a fast write-time magnetic memory is to use a spin electronic device in which one of the magnetic nano-elements is a ferromagnetic spin-split insulator. The memory function is contained in the orientation of this magnetic insulator relative to a metallic ferromagnetic electrode. Because the insulator is optically transparent, however, its moment might be reversed very rapidly by connecting the Zeeman energy reservoir to a suitable optical transition energy reservoir by off-resonance optical irradiation. This would function as a high-frequency analog of dynamic nuclear polarization [93]. An alternative scheme might involve optical-microwave double resonance whereby the device is continuously bathed in microwave radiation and the switching is achieved by exposure to a short pulse of optical radiation. The principle in both is to induce energy transfer between two different energy baths – magnetic and electronic with whose Hamiltonians the operators representing the irradiation do not commute.

7.12.3 Spin Diode

An idea for a two-terminal spin device, which was originally mooted by Roland Mattheis [94], consists of a five-layer magnetic system in which three ferromagnetic metal layers are mutually spaced by thin paramagnetic metal layers (Fig. 27). From left to right the ferromagnetic layer magnetizations point respectively along the y, z, and x directions. y-Polarized spins leaving the first layer precess 90° about the z-

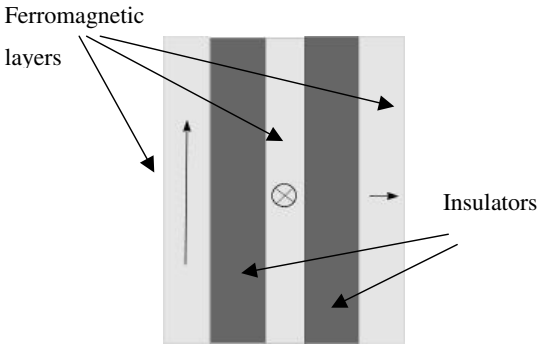

Fig. 27. Schematic illustration of a spin diode device.

oriented magnetization in the second layer (the thickness of which is thus determined by the precession frequency of the spin) and transfer to the x-oriented third layer to whose magnetization they are now parallel. If, however, spins transfer in the opposite direction from the right hand x-oriented layer, these also precess 90° in the center layer and end up antiparallel to the y-orientation of the left-hand layer to which they are unable to transfer owing to the absence of density of states of the right polarization. Thus the entire system functions as a spin diode which is capable of fulfilling the memory and blocking function of a two terminal MRAM element in a single device. Tunnel versions of this device should also be realizable which, because their function is wholly determined by density of states asymmetry, should offer higher on/off ratios.

7.12.4 Spin Split Insulator as a Polarizing Injector – Application to Semiconductor Injection

The transport properties of spin-split Europium-based insulators at low temperatures have been studied [95, 96] and the empirical data obtained would seem to suggest that these–or room-temperature analogs thereof – might act as convincing spin polarizers. To date, however, little practical use has been made of these materials. The physics relies on the fact that, because the insulator band gap is spin-split, a tunneling quasiparticle with its energy in the bandgap sees a different tunnel barrier height depending on its spin (Fig. 28). Accordingly its evanescent wavefunction has a spin-dependent decay constant. For unpolarized electrons incident on a sufficiently thick barrier, this implies a high spin asymmetry for the tunnel current and hence suggests itself as an ideal way to spin inject into materials such as semiconductors. Because no metal is involved, no problems of Schottky barrier interface states and differential material resistivities are called into play and the insulator/semiconductor combination affords a high degree of flexibility in choosing the point on the semiconductor band-structure where spin injection occurs.

7.12.5 Novel Fast-switching MRAM Storage Element

The above ideas could be combined to produce a new type of tunnel MRAM storage element consisting of a ferromagnetic film, a spin-split magnetic insulator and a normal metal. The memory function would then comprise the magnetic configurations of the magnetic metal and the magnetic insulator. The former would be magnetically pinned and the latter would be rapidly switchable by optical double-resonance techniques.

7.12.6 Quantum-coherent Spin Electronics

Perhaps the most far-reaching development in spin electronics will be the establishment of quantum coherent spin devices. By this is meant devices whose construction

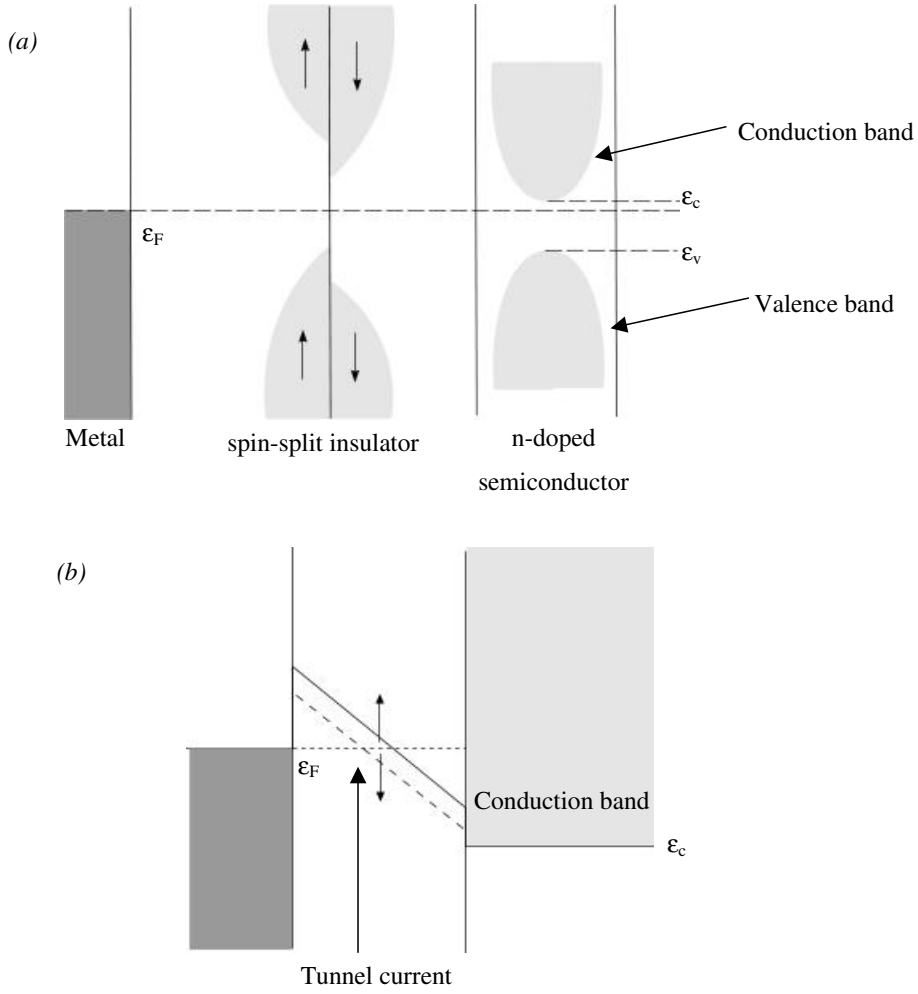

Fig. 28. Spin split insulator injector (a) unbiased, and (b) biased.

is on a sufficiently short length scale that the quantum coherence of the electronic wavefunction is preserved across the device, thereby coupling input and output electrical signals.

Earlier in this chapter we considered the importance of the various mesomagnetic length scales in generating the novel characteristics and properties of spin electronic devices. In fact the spin diffusion length, which is the determining size threshold for spin electronics, is the least exacting length scale to reach, being typically thousands of Angstroms for pure metals. At the other end of the scale of difficulty is the quantum coherence length, which is of order the mean free path, i. e. comparable with the length scale on which momentum scattering events occur, i. e. typically tens

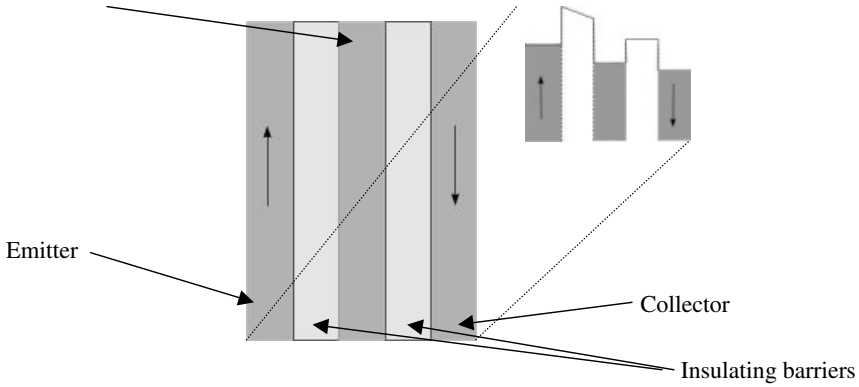

Fig. 29. Tunnel grid spin triode.

of Angstroms upwards. On a slightly longer length scale are inelastic scattering events which change not only the momentum but also the energy of the carriers.

Nanofabrication technology is such that devices can now be constructed with relative ease on the 10-Å scale. A typical example is the double-barrier resonant-tunnel diode – three metal layers sandwiching two insulating layers – which relies for its performance on quantum mechanical interference between opposite faces of the central potential well. Because insulating barriers can now be prepared with Angstrom precision it is but a short step to a three-terminal spin transistor in which the emitter, base and collector are phase-coherent. A foreshadow of this concept is to be found in the patent of Ounadjela and Tiusan [97]. A typical schematic diagram is shown in Fig. 29.

7.12.7 The Tunnel-grid Spin-triode

The authors envisage a device which is essentially the double-barrier resonant-tunnel diode with ferromagnetic collector and emitter and an added electrical contact to the non-magnetic base layer. In operation the base and collector are biased progressively positive relative to the emitter. In line with the above discussion the base layer is thin compared with the mean free path – and here we mean **hot electron** mean free path – so little carrier scattering occurs in the base and the phase coherence of the electrons launched by the emitter is preserved into the collector. Although the base layer does not appreciably scatter the transiting carriers, and so does not demand significant base current, it nonetheless is sufficiently substantial to define the electrostatic potential across the successive barriers and hence to modulate the current tunneling from emitter to collector. In this respect the base is not unlike the grid electrode in a vacuum triode. Thus we have a device in which the emitter-collector conductance can be controlled by applying potential to a high impedance base, thereby affording power gain. Owing to the ferromagnetic nature of the electrodes, moreover, the device characteristics are also switchable by applying an external magnetic field.

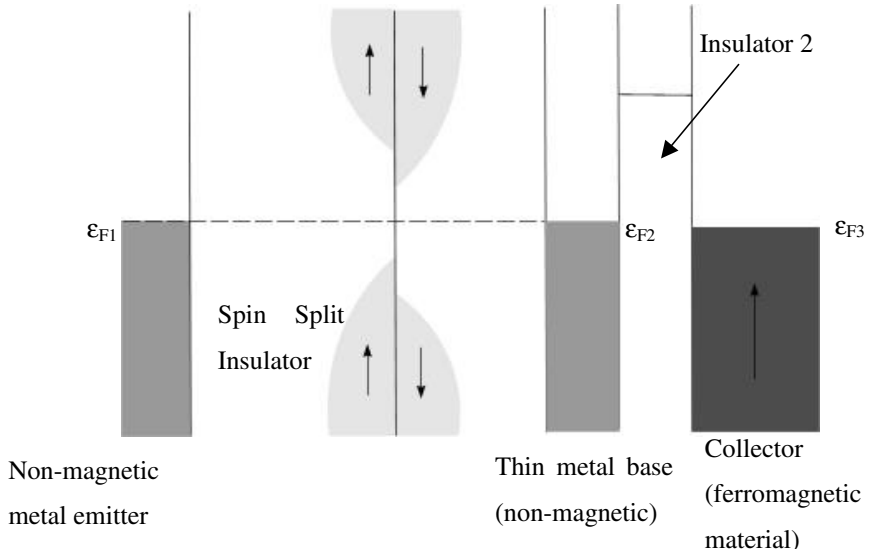

Fig. 30. Tunnel grid spin triode with spin-split insulator injector (no bias).

Other permutations of this basic configuration are imaginable, for example making all three layers – or indeed any pair of them – ferromagnetic. Another coherent spin transistor variant, shown in Fig. 30, uses a spin-split insulator as the spin-polarizing injector stage.

7.12.8 Multilayer Quantum Interference Spin-stacks

More elaborate quantum coherent structures can be made by analogy with optical thin-film interference filters in which stacks of $\lambda/4$ dielectric layers are cascaded to provide special optical transfer functions. In like manner, combinations of $\lambda/4$ metal films and tunnel barriers can achieve analogous electrical transport effects. In particular, use might be made of resonant thin-film structures in which the magnetic "refractive index" changes with change in magnetization or spin direction thereby modifying the resonant conditions and changing the transfer function of the multilayer stack.

7.12.9 Multilayer Tunnel MRAM

This is another possible means of realizing two terminal tunnel MRAM elements in which the memory function and the blocking of parasitic paths is achieved at the same time by realizing a structure which is both a tunnel junction and a MIM diode. The asymmetric characteristic of the MIM relies on the difference between the work-functions of the two magnetic metals either side of the insulating barrier.

Insufficient latitude in work-functions is available to make this viable, assuming that a back-to-front diode asymmetry of at least ten is required. Bruno has proposed a double resonant variant [98] to improve the transport asymmetry. Multilayer constructions analogous to the optical thin film domain might be capable of even better performance.

7.12.10 Quantum Information Technology

On an equally speculative note, it would seem that spin electronics has a bright potential future in the world of quantum information technology [99]. The simple spin electronic devices which have been demonstrated to date–for example GMR devices and the various spin transistors – function by coding spin information on to the electrical carriers in one part of the device and reading it back in another remote region of the device. In short, contemporary spin electronics functions by transfer of streams of single qubits from one part of the spin electronic circuit to another. Viewed thus, this is just the simplest possible type of quantum information transfer in which no entanglement is involved. The next stage in spin electronics is to implement devices which function by displacing spin information by means of entangled qubit pairs. So, for example, multi-terminal spin devices of the future might be envisaged in which streams of entangled qubits enable communication between different device terminals, each of which receives one qubit component of the entangled ensemble. The practical realization of such a device might be attempted by employing combinations of spin SETs.

The FSET (or spin SET) is a particularly important stepping-stone on the path to quantum information processing. Its distinguishing feature is that it is a rare example of a quantum processor in which the qubits (i. e. the spins) can be physically displaced, enabling the gates and their implementation hardware to be spatially localized, as in conventional computing. Competing quantum processor hardware, for example nuclear magnetic resonance processors, have fixed qubits and peripatetic gates. Coupled with this configurational advantage, the Spin SET is also endowed with an automatic electrical facility for measuring and collapsing the qubit. These two attributes alone position it in the forefront of potential candidates for future quantum information-processing hardware.

Although realization of a full-blown quantum computer will be a long way into the future, owing to the monumental problems of overcoming uncontrolled quantum decoherence and parasitic interactions of qubits, the more modest aim of implementing demonstrators of basic quantum information processing hardware is, nonetheless, feasible in the medium term. Particularly intriguing would be to explore their use in quantum dense coding, in which fractions of entangled qubits are used to carry increased information capacity compared with classical bit-streams. This might be achieved by using pairs of spin SETs, each of which is fed entangled qubit spins by a central generator, and each of which is equipped with gate hardware capable of executing the basic single qubit operators X, Y, Z, H, and $P(\theta)$, which are used to decode the entangled dual spin states. In the simplest example the gates might consist

simply of ferromagnetic layer sandwich structures with differing anisotropy axes in combination with ultra-fast switching microwave pulsing.

A rather simpler task, which could be investigated to gain insight into the functioning of this hardware, is the matter of transmitting quantum-encrypted data. This has been achieved experimentally by using polarized light (see, for example, Ref. [100]) but not yet with localized qubits. The problem is one of transmitting single qubits with one of two orthogonal quantization axes and projecting them on arrival on to similar axes. Interception of the data might then be detected by monitoring the bit-stream error rate which must remain lower than 25 % for guaranteed secure transmission. This is a configuration which lends itself to implementation by assemblies of three connected spin SETs.

The main obstacles in quantum information processing are unsolicited interaction, quantum decoherence, and data corruption by noise. A key element in any successful program will be to reduce these effects to a working minimum necessary to demonstrate functioning of such primitive quantum hardware, as has been outlined above. In particular, ways must be developed to introduce quantum error correction and spin regeneration by methods which do not seek to violate the "no-qubit" cloning rule.

References

[1] N. F. Mott, *Proc. Roy. Soc.* **1936**, *153*, 69.
[2] M. Johnson and R. H. Silsbee, *Phys. Rev. Lett.* **1985**, *55*, 1790.
[3] T. Valet and A. Fert, *Phys. Rev. B* **1993** *48*, 7099.
[4] A. Fert, J-L. Duvail, and T. Valet, *Phys. Rev. B* **1991**, *43*, 13124.
[5] M N. Baibich, J. M. Broto, A. Fert, F. Nguyen Van Dau, F. Petroff, P. Etienne, G. Creuzet, A. Friederich, and J. Chazelas, *Phys. Rev. Lett.* **1988**, *61*, 2472.
[6] A. Fert; A. Barthelemy, P. Galtier, P. Holody; R. Loloee, R. Morel, F. Petroff; P. Schroeder; L. B. Steren, and T. Valet, *Mater. Sci. Eng.* **1995**, *B 31*, 1.
[7] J. P. Renard, P. Bruno, R. Megy, B. Bartenlian, P. Beauvillain, C. Chappert, C. Dupas, E. Kolb, M. Mulloy, J. Prieur, P. Veillet, and E. Velu, *J. Appl. Phys.* **1996**, *79*(8), pt. 2A; p. 5270–5.
[8] C. Vouille, A. Fert, A. Barthelemy, S. Y. Hsu, R. Loloee, and P. A. Schroadar, *J. Appl. Phys.* **1997**, *81*(8), 4573–5.
[9] S. S. P. Parkin, N. More, K. P. Roche, *Phys. Rev. Lett.* **1990**, *64*, 2304.
[10] B. Dieny, V. S. Speriosu, S. S. P. Parkin, B. A. Gurney, D. R. Wilhoit, and D. Mauri *Phys. Rev. B* **1991**, *43*,1297–1300.
[11] B. Cywinski, *UK Magnetics Society Meeting on GMR devices*, Leeds, UK, **1998**.
[12] C. Tiusan, M. Hehn, K. Ounadjela, Y. Henry, J. Hommet, C. Meny, H. van den Berg, L. Baer, and R. Kinder, *J. Appl. Phys.* **1999**, *85*(8), 5276–8.
[13] L. Piraux, J. M. George, J. F. Despres, C. Leroy, E. Ferain, R. Legras, K. Ounadjela, and A. Fert, *Appl. Phys. Lett.* **1994**, *65* (19), 1–3.
[14] M. Johnson, *Science*, **1993**, *260*, 320.
[15] M. Johnson, *Mater. Sci. Eng. B*, **1995**, *31*, 199.
[16] M Johnson, *Appl. Phys. Lett.* **1993**, *63*, 1435.

[17] D. S. Daniel, J. F. Gregg, S. M. Thompson, J. M. D. Coey, A. Fagan, K. Ounadjela, C. Fermon, and G. Saux, *J. Mag. Magn. Mater.* **1995**, *140*, 493.
[18] J. F. Gregg, W. Allen, K. Ounadjela, M. Viret, M. Hehn, S. M. Thomson, and J. M. D. Coey, *Phys. Rev. Lett.* **1996**, *77*, 1580.
[19] M. Viret, D. Vignoles, D. Cole, J. M. D. Coey, W. Allen, D. S. Daniel, and J. F. Gregg, *Phys. Rev. B*, **1996**, *53*, 8464.
[20] J. E. Wegrove, A. Comment, Y. Jaccard, J. Ph. Ansernmet, N. M. Dempsey, and J. P. Nozieres, *Phys. Rev. B* **2000**, *61*, 12216.
[21] W. Allen, J. F. Gregg, K. Ounadjela, M. Viret, M. Hehn, S. M. Thompson, and J. M. D. Coey, *J. Magn. Magn. Mater.* **1997**, *165*, 121–124.
[22] S. F. Zhang and P. M. Levy, *Phys. Rev. Lett.* **1997**, *79*, 5110.
[23] M. Julliere, *Phys. Lett.* **1975**, *54 A 3*, 225.
[24] S. Maekawa and U. Gafvert, *IEEE Trans. Mag.* **1982**, *18*, 707.
[25] J. S. Moodera, L. R. Kinder, T. M. Wong, and R. Meservey, *Phys. Rev. Lett.* **1995**, *74*, 3273.
[26] J. G. Simmons, *J. Appl. Phys.* **1963**, *34*(6), 1793–1803.
[27] J. C. Slonczewski, *Phys. Rev. B* **1989**, *39*, 6995.
[28] R. Landauer, IBM *J. Res. Dev.* **1988**, *32*, 306.
[29] J. Mathon, *Phys. Rev. B* **1997**, *56*, 11810.
[30] R. C. Sousa, J. J. Sun, V. Soares, P. P. Freitas, A. Kling, M. F. da Silva, and J. C. Soares, *J. Appl. Phys.* **1999**, *85* 5258.
[31] C. Sousa, J. J. Sun, V. Soares, P. P. Freitas, A. Kling, M. F. da Silva, and J. C. Soares, *Appl. Phys. Lett.* **1995**, *73* 3288.
[32] J. S. Moodera, E. F. Gallagher, K. Robinson, and J. Nowak, *Appl. Phys. Lett.* **1997**, *70*, 3050.
[33] J. M. MacLaren, X.-G. Zhang, and W. H. Butler, *Phys. Rev.* **1997**,*B* 56, 11827.
[34] R. Meservey and P. M. Tedrow, *Phys. Rep.* **1994**, *238*(4), 173.
[35] S. Zhang, P. M. Levy, A. C. Marley, and S. S. P. Parkin, *Phys. Rev. Lett.* **1997**, *79*, 3744.
[36] A. M. Bratkovsky, *Phys. Rev. B* **1997**, *56* 2344.
[37] J. Halbritter, *Surf. Sci.* **1982**, *122*, 80.
[38] E. Yu. Tsymbal and D. G. Pettifor, *Phys. Rev. B* **1998**, *58,* 432.
[39] J. Sun, and P. P. Freitas, *J. Appl. Phys.* **1999**, *85*, 5264.
[40] J. S. Moodera et al., 1999, to be published.
[41] J. Mathon, A. Umerski, to be published.
[42] J. Mathon, M. Villeret, R. B. Muniz, J. d'Albuquerque e Castro, and D. M. Edwards, *Phys. Rev. Lett.* **1995**, *74*, 3696.
[43] J. E. Ortega, F. J. Himpsel, G. J. Mankey, and R. F. Willis, *Phys. Rev. B* **1993**, *47,* 1540.
[44] P. Segovia, E. G. Michel, and J. E. Ortega, *Phys. Rev. Lett.* **1996**, *77,* 3455.
[45] J. Inoue, S. Maekawa, preprint.
[46] J. S. Moodera, J. Nowak, and R. J. M. van de Veerdonk, *Phys. Rev. Lett.* **1998**, *80*, 2941.
[47] A. H. MacDonald, T. Jungwirth, and M. Kasner, *Phys. Rev. Lett.* **1998**, *81* 705.
[48] T. Mitsuzuka, K. Matsuda, A. Kamijo, and H. Tsuge, *J. Appl. Phys.* **1999**, in press.
[49] Xiangdong Zhang, Bo-Zang Li, Gang Sun, and Fu-Cho Pu, *Phys. Rev. B* **1997**, *56* 5484.
[50] S. Zhang, P. M. Levy, A. C. Marley, and S. S. P. Parkin, *Phys. Rev. Lett.* **1997**, *79*, 3744.
[51] D. J. Monsma, J. C. Lodder, J. A. Popma, and B. Dieny, *Phys. Rev. Lett.* **1995**, *74*, 5260.
[52] D. J. Monsma, R. Vlutters, and J. C. Lodder, *Science* **1998**, *281*, 407.
[53] J. C. Lodder, D. J. Monsma, R. Vlutters, and T. Shimatsu, *J. Magn. Magn. Mater.* **1999**, *198*, 119.
[54] R. Jansen, P. S. Anil Kumar, O. M. J. van't Erve, R. Vlutters, P. de Haan, and J. C. Lodder, *Phys. Rev. Lett.* **2000**, *85*, 3277.

[55] J. F. Gregg, W. D. Allen, N. Viart, R. Kirschman, C. Sirisathitkul, J-P. Schille, M. Gester, S. M. Thompson, P. Sparks, V. da Costa, K. Ounadjela, and M. Skvarla, *J. Magn. Magn. Mater.* **1997**, *175*, 1.
[56] J. F. Gregg and P. D. Sparks, Patent Application No 9608716. 8.
[57] Y. Q. Jia, R. C. Shi, and S. Y. Chou, *IEEE Transactions on Magnetics*, **1996**, *32*(5).
[58] F. G. Monzon and M. L. Roukes, *J. Magn. Magn. Mater.* **1999**, *198–199*, 632–5.
[59] G. Schmidt, L. W. Molenkamp, A. T. Filip, and B. J. van Wees, *Phys. Rev. B*, **2000**, *62*, 4790.
[60] J. M. Kikkawa, I. P. Smorchkova, N. Samarth, and D. D. Awschalom, *Science* **1997**, *277*, 1284.
[61] D. D. Awschalom and N. Samarth, *J. Supercon.* **2000**, *13*, 201.
[62] M. Oestreich, J. Hubner, D. Hagele, P. J. Klar, W. Heimbrodt, W. W. Ruhle, D. E. Ashenford, and B. Lunn, *Appl. Phys. Lett.* **1999**, *74*(9), 1251–3.
[63] R. Fiederling, M. Keim, G. Reuscher, W. Ossau, G. Schmidt, A. Waag, and L. W. Molenkamp, *Nature*, **1999**, *402*, 787–790.
[64] Y. Ohno, D. K. Young, B. Beschoten, F. Matsukura, H. Ohno, and D. D. Awschalom, *Nature* **1999**, *402*, 790–2.
[65] B. T. Jonker, Y. D. Park, B. R. Bennett, H. D. Cheong, G. Kioseoglou, and A. Petrou, *Phys. Rev. B*, **2000**, *62*(12), 8180–3.
[66] H. Ohno, *Science* **1998**, *281* p. 951–6.
[67] Y. Matsumoto, M. Murakami, T. Shono, T. Haesegawa, T. Fukumura, M. Kawasaki, P. Ahmet, T. Chikyow, Shin-ya Koshishara, and H. Koinuma, *Science*, **2001**, *291*, p. 854.
[68] S. Datta and B. Das, *Appl. Phys. Lett.* **1990**, *56*, 665.
[69] P. R. Hammar, B. R. Bennett, M. J. Yang, and M. Johnson, *Phys. Rev. Lett.* **1999**, *83*(1), 203–6.
[70] S. Gardelis, C. G. Smith, C. H. W. Barnes, E. H. Linfield, and D. A. Ritchie, *Phys. Rev. B*, **1999**, *60* (11), 7764–7.
[71] F. G. Monzon, H. X. Tang, and M. L. Roukes, *Phys. Rev. Lett.* **2000**, *84* (21), 5022.
[72] B. J. van Wees, *Phys. Rev. Lett.* **2000**, *84* (21), 5022.
[73] H. X. Tang, F. G. Monzon, R. Lifshitz, M. C. Cross, and M. L. Roukes, *Phys. Rev. B*, **2000**, *61 (7)*, 4437–40.
[74] J. M. de Teresa, A. Barthelemy, A. Fert, J. P. Contour, F. Montaigne, and P. Seneor, *Science* **1999**, *286*, 507.
[75] J.-H. Park, E. Vescovo, H.-J. Kim, C. Kwon, R. Ramesh, and T. Venkatesan, *Nature*, **1998**, *392*, 794–6.
[76] R. J. Soulen, J. M. Byers, M. S. Osofsky, B. Nadgorny, T. Ambrose, S. F. Cheng, P. R. Broussard, C. T. Tanaka, J. Nowak, J. S. Moodera, A. Barry, and J. M. D. Coey, *Science* **1998**, *282*, 85–88.
[77] C. Sirisathitkul, W. D. Allen, J. F. Gregg, P. D. Sparks, J. M. D. Coey, R. Kirschman, and S. M. Thompson, *Measuring Spin Asymmetry via the Chemical Potential Zeeman Shift*, in preparation.
[78] J. B. Barner and S. T. Ruggiero, *Phys. Rev. Lett.* **1987**, *59*(7), 807–10.
[79] M. Amman, K. Mullen, and E. Ben-Jacob, *J. Appl. Phys.* **1989**, *65*, 339.
[80] M. H. Devoret and H. Grabert: *Single Charge Tunneling,* (Plenum Press, New York, 1992).
[81] S. Altimeyer, B. Spangenberg, and H. Kurz, *Appl. Phys. Lett.* **1995**, *67*, 569.
[82] J. Barnas and A. Fert, *Phys. Rev. Lett.* **1998**, *80*, 1058.
[83] K. Majumdar and S. Hershfield, *Phys. Rev. B* **1998**, *57*, 11521.
[84] K. Ono, H. Shimada, and Y. Ootuka, *J. Phys. Soc. Jpn* **1998**, *67*, 2852.
[85] J. Barnas and A. Fert, *Europhys. Lett.* **1998**, *44* (1), 85.

[86] Deutsches Patentamt, Aktenzeichen P 44 41 502. 8, 1994.
[87] M. Knoll, H. F. Uhlmann, M. Gotz, and W. Krech, *IEEE Trans. Appl. Superconductivity* **1997**, *7*, 3524.
[88] G. Mader and F. H. Uhlmann, *Adv. Comp. Electromagnetics*, IOS Press, Amsterdam, **1995**, pp. 13–23.
[89] K. J. Kirk, J. N. Chapman, and C. D. W. Wilkinson, *Appl. Phys. Lett.* **1997**, *71* (4), 539.
[90] L. F. Schelp, A. Fert, F. Fettar, P. Holody, S. F. Lee, J. L. Maurice, F. Petroff, and A. Vaures, *Phys. Rev. B* **1997**, *56*, 5747.
[91] C. Sirisathitkul, W. D. Allen, J. F. Gregg, P. D. Sparks, J. M. D. Coey, R. Kirschman, and S. M. Thompson, *Spin Blockaded Silicon Schottky Barrier*, in preparation.
[92] B. W. Alphenaar, K. Tsukagoshi, and H. Ago, *Physica E* **2000**, *6*, 848.
[93] A. Abragam and M. Goldman, *Nuclear Magnetism: Order and Disorder*, OUP, **1982**.
[94] R. Mattheis, EMSA 2000, Dresden.
[95] L. Esaki, P. J. Stiles, and S. von Molnar, *Phys. Rev. Lett.* **1967**, *19*, 852.
[96] J. S. Moodera, X. Hao, G. A. Gibson, and R. Meservey *Phys. Rev. Lett.* **1988**, *61*, 637.
[97] K. Ounadjela and C. Tiusan, French patent office.
[98] P. Bruno and J. Wunderlich, *J. Appl. Phys.* **1998**, *84*(2), 978.
[99] A. Steane, *Rep. Progr. Phys.* **1998**, *61*, 117.
[100] S. J. D. Phoenix and P. D. Townsend, Quantum cryptography: protecting our future networks with quantum mechanics, in: *Cryptography and Coding*, 5th IMA Conference. Springer, Berlin, Germany, **1995**, pp. 112–31; H. Zbinden, J. D. Gautier, N. Gisin, B. Huttner, A. Muller, and W. Tittel, *Elect. Lett.* **1997**, *33*, 586.

Magnetism: Molecules to Materials III. Edited by J.S. Miller and M. Drillon

ISBNs: 3-527-30302-2 (Hardback); 3-527-60014-0 (Electronic)

8 NMR of Nanosized Magnetic Systems, Ultrathin Films, and Granular Systems

Pierre Panissod

8.1 Introduction

Nuclear magnetic resonance investigations cover an extremely broad range of applications reaching from pure nuclear physics to NMR imaging in medicine, including atomic physics, condensed-matter physics, chemical analysis, and structural investigations in biology. Because of the sensitivity of the nuclei to their local electronic environment, NMR (and other hyperfine techniques) is widely used in condensed matter to probe local crystallographic or molecular structures and, particularly in metallic systems, local electronic structure and magnetism.

This chapter is devoted to studies by NMR of the magnetic properties of ferromagnetic systems that are inhomogeneous on a nanometer scale, for example multilayers or granular alloys with a magnetic and a non-magnetic component. Materials of this class are studied intensively for fundamental purposes (surface or interface magnetic anisotropy, exchange coupling through a non-magnetic spacer, spin-dependent scattering or tunneling), and for technological applications (recording media, field sensors and other 'spintronic' devices based on spin-selective electric currents). The composite nature of these systems offers the possibility of tailoring their properties by choosing the appropriate components, structure, and composition, and the way they are arranged in the final material (or device). Considering the intricacy of the two (or more) components in the material, it is obvious that interactions at the interfaces and between the magnetic components through the non-magnetic component largely determine the magnetic and magneto-transport properties of the composite. Indeed the influence of the interface topology and of the detailed microstructure of the components on the aforementioned properties has been demonstrated or, at least, predicted. For example, the roughness of, or compositional intermixing at, the interfaces affects the giant magneto-resistance of the multilayers. Bulk defects also influence the magneto-resistance, as a result of spin-independent scattering and, in some systems, spin-dependent scattering. Changing the structure can, moreover, modify the coupling between the magnetic layers (or grains), their anisotropy, and their coercive field, which will also largely determine the sensitivity of the composite to the external field and its applicability as a magneto-resistive field sensor. This example stresses the need for detailed studies of the composite structure and its consequences on the magnetization process of the magnetic components.

In this respect NMR does provide original insight into the structural and magnetic properties of composite nanostructured materials. In short, the yield of NMR exper-

iments is twofold. On the one hand the NMR spectrum reflects the distribution of the different chemical configurations, the different phases in the sample, their structure, and their defects. On the other hand the dependence of spectral shape on the strength and orientation of external magnetic fields (DC and radio-frequency) enables probing of the magnetization, the magnetic anisotropy, or the magnetic stiffness of the electronic environment of the observed nuclei. Combining both aspects thus makes NMR a unique tool for correlating, on a local scale, the inhomogeneous magnetic properties of a composite sample with its different structural components. For example, one can estimate the magnetization profile at a diffuse interface between a magnetic and non-magnetic phase, measure separately the magnetic anisotropy in different parts of a sample, or monitor the different magnetic hardness of the magnetic clusters in respect of the alloyed matrix in nanogranular alloys.

Although the application of NMR to structural investigations and phase analysis is summarized in Section 8.2, most of the chapter is devoted to the use of NMR to investigate local magnetic properties.

8.2 Local Structure

8.2.1 Introduction

In an NMR experiment, the $2I + 1$ levels of the ground state of a nucleus (spin I) are split by Zeeman interaction with a static field H_0. The energy difference between adjacent levels is $\gamma_n \hbar H_0$ where γ_n is the gyromagnetic ratio of the nucleus. A radio frequency (r. f.) field, H_1, applied perpendicular to H_0, induces dipolar transitions ($\Delta m = \pm 1$) between adjacent levels. The probability of transition and, consequently, the amplitude of the NMR signal are significant only when the frequency is close to $\omega_L = \gamma_n H_0$, the Larmor (precession) frequency of the nuclei [1, 2]. In condensed matter the static field H_0 experienced by nuclei differs from the externally applied field H_{ext} because the electronic magnetization produces additional fields at the nucleus – the classical dipolar field and the hyperfine field HF. HF is brought about by the spatial distribution of electron spin polarization close to the observed nucleus; it is, therefore, indicative of the topological and chemical environment of this nucleus (position, symmetry, number, and nature of neighbors) [3]. In an inhomogeneous material, the distribution of local environments around the nuclei gives rise to a distribution of resonance frequencies, the NMR spectrum. Therefore *specific structural regions* in a sample correspond to *specific frequency ranges* in the spectrum.

It is, therefore, possible to obtain structural information from NMR spectra, if a quantitative relationship is established between the strength of HF and the local chemical and topological structure. This relationship can be deduced from theoretical calculations but, despite recent advances [4–9], ab-initio calculations are still too difficult to perform in systems that are inhomogeneous on the atomic scale. Hence the assignment of a given resonance frequency to a specific local atomic configuration is more generally inferred, phenomenologically, from reference studies of standard

alloys and compounds, the structures of which are known from conventional characterization techniques [10–19]. Subsequently the information is used to analyze the spectrum observed in the unknown system under investigation – the intensity of the lines measures the number of nuclei resonating in each spectral range, which yields the atomic fraction of the various atomic configurations and structural components in the sample.

In magnetic/non-magnetic composites one will first distinguish coarsely the bulk of the magnetic phase from its interface with the other phase; refined analysis of the spectral shape of these two parts will then identify and quantify the defects in the bulk of the magnetic component and characterize the roughness or the interdiffusion at the interfaces. Pioneering works along this line were initiated in Japan [20, 21] using combined NMR and Mössbauer techniques to provide the local information around V and Fe, respectively, in Fe/V multilayers. Since then the method has been used mainly for structural investigations of cobalt-based multilayers and, particularly, their buried interfaces [22–48]. Investigations of nanogranular systems have also been undertaken more recently [49–51].

8.2.2 Local Atomic Configuration and Resonance Frequency

8.2.2.1 The Bulk of the Magnetic Component – Crystallographic Structure and Strains

As far as the influence of the crystallographic structure on the nuclear resonance frequency is concerned, cobalt is exemplary because it can be found in a hexagonal compact phase and a face-centered cubic phase that are almost degenerate in energy. Although the hcp phase is the stable phase below 400 °C, the fcc phase is easily stabilized, particularly in small grains, and many Co-based systems contain both phases. In fcc Co the NMR frequency extrapolated to 0 K is 217 MHz [52]. The hcp Co phase is slightly more compact and anisotropic; as a consequence the hyperfine field has considerable anisotropy that results in an NMR frequency of 220 MHz, when the moment is along the c-axis, and of 228 MHz, when it lies in the c-plane [53–55]. It is thus usually easy to discriminate between the two phases. In samples with some fcc/hcp phase admixture, which is very common, two more lines are observed. These correspond to stacking faults [56–59], i. e. planes that are locally hcp stacked within an fcc grain, and vice versa (Fig. 1). In addition to the two stable crystallographic structures, under some conditions Co can be forced to assume a metastable bcc phase [45–48, 60, 61]. The Co NMR frequency in the less dense bcc Co is lower (198 MHz at 1.4 K) than in the compact hcp or fcc Co phases.

It is apparent that in the different phases of cobalt the resonance frequency increases with the compactness of the structure. Experiments under pressure [62] have also shown that, within the same crystallographic structure, the resonance frequency increases with decreasing atomic volume. For Co, the dependence of the hyperfine field on the change in volume, V, is approximately $\Delta HF/HF \approx -\Delta V/V$. Hence the presence of strains in layers or clusters is immediately apparent, and has actually been studied by NMR [27–30].

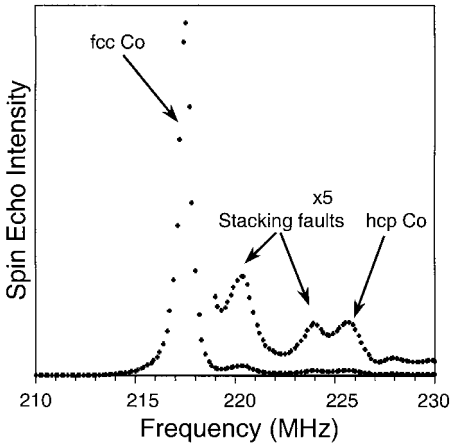

Fig. 1. Example of bulk cobalt spectra (here mostly fcc) showing the lines of the main phases and of stacking faults (see also Fig. 8).

8.2.2.2 The Interface Between Components – Chemical Coordination

In a pure metal sample the NMR spectrum has a single line arising from nuclei that are all equivalent. When foreign atoms are substituted for matrix atoms in the vicinity of the nucleus, HF modifications are reflected on the spectrum by the presence of new lines shifted away from the main line. These new lines are called satellites (Fig. 2). Usually, only satellites arising from substitution in the nearest neighbor (NN) shell are resolved. The influence of further neighbors decreases rapidly with increasing distance and they contribute only to the broadening of the NN satellite lines. Study of reference alloys and compounds shows that the effect of foreign atoms is nearly additive–every atom substituted for a matrix atom in the NN shell shifts the resonance frequency by a given, element specific, amount. In binary alloy the satellite lines corresponding to $1, 2, 3, \ldots$ foreign atoms in the NN shell are thus nearly equally spaced [13–19].

The well studied case of bulk systems can be transposed to the interfaces between two elements. At a perfect interface, all sites are equivalent but different from those in the bulk of the magnetic phase. Hence the spectrum has only one satellite line beside the bulk line. Perfect interfaces are rare and, usually, interface spectra extend over a broad spectral range corresponding to a spread of nearest-neighbor configurations around the probed nuclei. The NN distribution in the sample is measured by the satellite intensities in the spectrum. This, in turn, can be compared with the distribution of local configurations that would result from a model structure of the interface. Indeed modeling the spectral shape does provide more quantitative information about intermixing at the interfaces (short-range admixture). By considering a model (topological and chemical) of the interface structure, configuration probabilities (line intensities) can be calculated, and these are used to reconstruct the spectrum. The spectral refinement procedure is applied to the topological and chemical parameters of the model. The fitting procedure assesses the applicability of the model and, if it can be accepted, its refined parameters give direct insight into the short-range order at the interfaces. Figure 3 illustrates some models that have

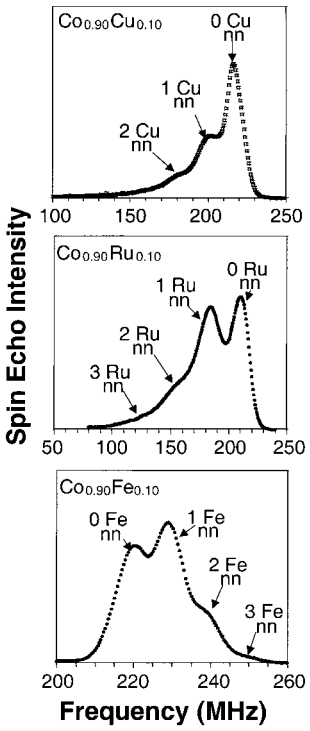

Fig. 2. Co NMR spectra from some fcc CoX diluted alloys showing the presence of satellites on the low frequency side of the main line for Cu and Ru (non-magnetic impurities) and on the high frequency side for Fe (magnetic impurity).

been successfully used to describe the interface spectra of Co/X multilayers [27, 33, 63]. The first interface is sharp with only monoatomic step defects; it is found in epitaxially grown multilayers of non-miscible elements such as Co and Cu. The second is a diffuse interface with a concentration profile over several atomic planes in which atoms are mixed at random; this is commonly found in multilayers of highly miscible elements such as Co and Ru. The last interface model combines the two first – each atomic plane consists of pure and alloyed patches; it is particularly useful for describing rough interfaces and discontinuous layers [44]. It is clearly apparent that the expected spectral shapes are quite different for the different models, which shows that the different types of interface structure can be easily distinguished. Such models can be adapted to spherical granules.

8.2.3 A Typical Example

The Co NMR spectrum observed in a Cu/Co/Cu/NiFe/FeMn spin valve is shown in Fig. 4. The sample comprises small columnar grains with a ⟨111⟩ growth orientation. It is exemplary for two reasons – firstly it is typical of the kinds of device used as reading heads for magneto-recording applications and, secondly, the bulk of the Co layer and the Co/Cu interfaces contain all the structural features and defects which can be found in metallic multilayers.

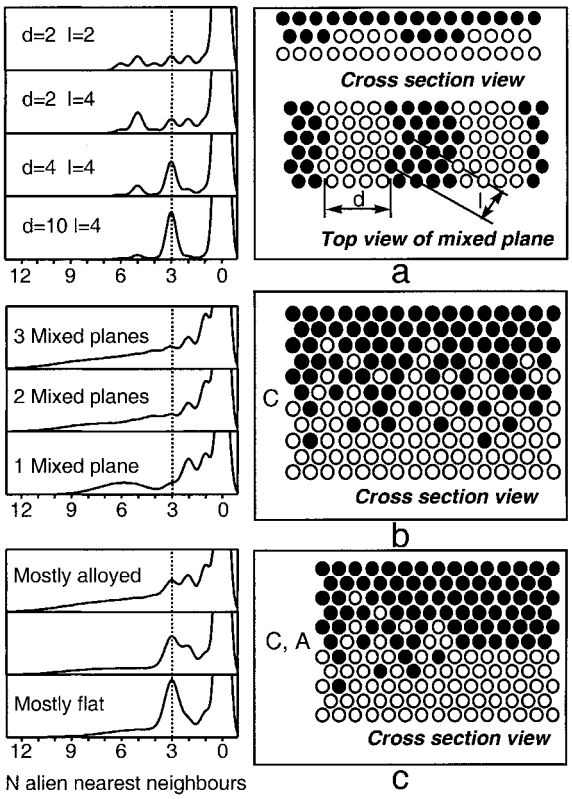

Fig. 3. Basic interface models for the simulation of buried interface spectra. All simulated spectra correspond to nine atomic planes in the magnetic layer. (a) Monoatomic step defect model (d, the average distance between steps, and l, the average distance between kinks, are the variables of the model, in atomic distance units). (b) Diffuse interface model with a linear concentration profile (atomic plane concentrations, C, are the free variables). (c) Alloy and pure Co patches – hybrid model consisting of clusters with sharp interfaces separated by diffuse areas. (C, concentration of the alloy in the atomic plane, and A, surface fraction of the alloy in the plane, are the variables of the model).

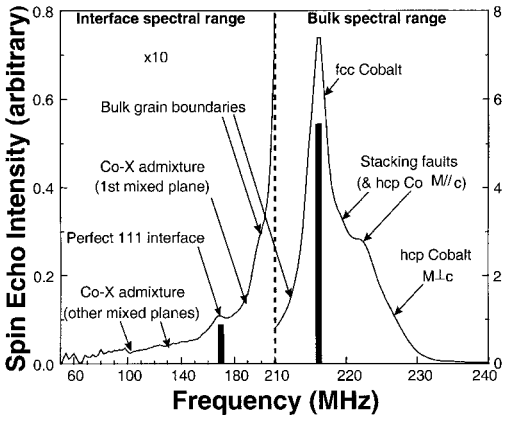

Fig. 4. Co NMR spectrum recorded in a typical Cu/Co multilayer showing indications of many defects present in Co layers. The left part shows the interfacial component magnified ten times relative to the bulk components on the right. The thick vertical bars represent the spectrum that should be observed for a perfect Co/Cu multilayer.

It is clearly apparent that the layered structure is far from perfect. The spectrum can be coarsely separated into three parts:

- a main line at 215 MHz corresponding to bulk Co with the fcc structure. The frequency is slightly lower than that for pure fcc Co (217 MHz), because of the expan-

sive strains resulting from the difference between Co and Cu lattice constants [28, 29];
- a set of shoulders at higher frequencies corresponding to Co in hcp-like environments (bulk hcp Co at 225–228 MHz, stacking faults at 220–225 MHz); and
- a set of lines below 200 MHz corresponding to Co atoms with at least one Cu atom among their 12 nearest neighbors (Co atoms at the Co/Cu interfaces). The relative intensity of this spectral component shows that there is a fraction of Co equivalent to 2.5 monolayers involved per interface instead of 1 monolayer for a perfect interface.

Indeed the shape of this extended tail is typical of diffuse interfaces although a small fraction of sharp interface areas is apparent from the peak at 165 MHz, which corresponds to Co with three Cu nearest neighbors at perfect ⟨111⟩ interfaces.

Figure 4 also contains a significant feature between 200 and 210 MHz. This frequency range corresponds to Co atoms located at the boundaries of the numerous thin columnar grains [33, 36]. The consequences of the detailed structure of such spin valves on their magnetic and magneto-resistive properties will be discussed in Section 8.4.

8.2.4 Summary

Because it probes atomic configurations in real space and at a short distance NMR efficiently complements standard diffraction techniques (and even diffuse scattering investigations) in the absence of translation symmetry. In terms of probed distances and element selectivity NMR can be compared with the EXAFS technique; although, in contrast to EXAFS, it measures distances indirectly only, it furnishes much more detailed information about local chemical configurations than a mere average number of neighbors.

The short presentation above has shown how NMR can be used to investigate the structure of nanocomposites and, in particular, that of buried interfaces. Quantitatively, concentration profiles with atomic resolution, densities of step defects, and sizes of grains, clusters or islands can be evaluated, thus characterizing the interface roughness on the atomic distance scale.

Combined with information about local magnetism, it provides unique insights into the correlation between the structure and magnetic properties, for example the magnetic profile at interfaces or the magnetic anisotropy or exchange stiffness in different parts of the artificial structures. This is the topic of subsequent sections.

8.3 Magnetization and Magnetic Anisotropy

8.3.1 Principles – Hyperfine Field in Ferromagnets

The total static field H_0 experienced by nuclei in condensed matter is expressed as the vectorial sum:

$$H_0 = \mathbf{H}_{\text{ext}} + \mathbf{H}_{\text{M}} = \mathbf{H}_{\text{ext}} + \mathbf{H}_{\text{dip}} + \mathbf{HF} \tag{1}$$

where **HF** is the field resulting from the electron spin and orbital moments within the ion radius and $\mathbf{H}_{\text{dip}}$ is the dipolar field resulting from other moments in the sample.

The classical dipolar field is, for convenience, split into three components:

$$H_{\text{dip}} = H_{\text{dem}} + H_{\text{Lor}} + H_{\text{Loc}} \tag{2}$$

where H_{dem} is the demagnetizing field related to the macroscopic shape of the sample, H_{Lor} is the Lorentz spherical cavity field, $4\pi M/3$ (emu) or $M/3$ (S.I.), and H_{Loc} is the field arising from moments within the Lorentz sphere except the central one. $H_{\text{dem}} + H_{\text{Lor}} = 0$ for a spherical sample and $H_{\text{Loc}} = 0$ for cubic site symmetry.

The hyperfine field HF is the sum of three contributions within the ion radius [64, 65]:

$$HF = HF_{\text{con}} + HF_{\text{dip}} + HF_{\text{orb}} \tag{3}$$

where HF_{dip} is the dipolar field from electron spins outside the nucleus volume, HF_{orb} is the orbital field associated with a not fully quenched orbital moment, and HFcon is the Fermi contact field, which originates from the spin polarization of all electrons (essentially s shells) within the volume of the nucleus.

It is usual to group H_{Loc}, HF_{dip}, and the anisotropic part of HF_{orb} into what is called the anisotropic hyperfine field HF_{ani} (strictly speaking, a traceless second rank tensor). The existence of a finite HF_{ani} is evidence of the low symmetry (lower than cubic) of the site.

The contact field HF_{con}, a spin contribution, is isotropic. For 3d ferromagnetic materials, it is the largest contribution to the hyperfine field (for Co, $HF_{\text{con}} \approx 200$ kOe). Three contributions to the spin polarization at the nucleus can be distinguished:

$$HF_{\text{con}} = HF_{\text{core}} + HF_{\text{cond}} + HF_{\text{tran}} \tag{4}$$

HF_{core} arises from the core polarization because of the exchange interaction between *s* electrons of the inner shells and the outer *non-s* electrons that carry the on-site magnetic moment; it is generally negative, i. e. antiparallel to the local moment. The two other terms originate from the spin polarization of the s conduction electrons in metals–HF_{cond} arises from the *s* spin polarization because of the on-site magnetic moment of the atom itself, and HF_{tran} arises from the s spin polarization because of the neighbor moments (transferred hyperfine field).

In ferromagnetic materials, owing to the spontaneous magnetization, the field experienced by the nuclei is usually largely dominated by HF (100–400 kOe for the magnetic 3*d* elements). The resonance can be, and often is, observed without applying an external magnetic field. Actually the role of an external DC field in ferromagnetic NMR is merely the same as in standard magnetometry – it is used to saturate the magnetization or to follow the magnetization process. All the measurements are, however, performed at selected frequencies and, therefore, yield information about the local magnetization and magnetization process in different parts of the sample.

8.3.2 Local Magnetization

8.3.2.1 Hyperfine Field and Local Magnetic Moments

In Eq. (4) for the contact hyperfine field the magnitude of the first two terms is proportional to the on-site magnetic moment, μ_l, whereas the magnitude of the third term is, crudely, proportional to the number of nearest neighbor magnetic atoms, n_i, and their magnetic moments, μ_j:

$$HF_{\text{con}} = a_{\text{core}}\mu_l + a_{\text{cond}}\mu_l + a_{\text{tran}}\sum n_i\mu_j \tag{5}$$

where the a values are hyperfine coupling coefficients [11–14]. This expression shows immediately that information about the local moment is contained in the measurement of HF. Such an equation should not, however, be interpreted too strictly– lengthy calculations are needed to compute the hyperfine field [4–9] and Eq. (5) should be regarded as an empirical experimental approach. Indeed a_{core} is almost independent of the system in which the element is involved whereas a_{cond} and a_{trans} depend on the detailed electronic structure and hence, for instance, on composition [7]. If HF_{core} dominates HF, which is usual for Co or Fe, it is possible to obtain reasonable estimates of the magnetic moment or, at least, to compare the magnitude of these moments at different sites and/or elements. This should always be done with caution, particularly for metallic systems.

Despite this uncertainty it must be stressed that hyperfine spectroscopy provides the most local information, site and element specific, about electronic magnetic properties. As such it complements macroscopic magnetic measurements, which give spatial (and often orientational) averages, magnetic dichroism experiments, which are element-specific but which yield only a spatial average of the magnetic moment, and neutron diffraction measurements, which are local in the reciprocal space.

8.3.2.2 Hyperfine Field and Magnetization Profile at Interfaces

When interfaces are thick and diffuse (as indicated by the intensity of the interface spectrum), the spectrum shape is analyzed in terms of a concentration profile through several monolayers. The same analysis also yields the average HF in each atomic plane, which gives insight into the magnetization profile at the interfaces.

For example, NMR studies have furnished evidence of large, alloy like, admixtures at the interfaces between Co/Ru multilayers. Table 1 lists the Ru concentration (C_{Ru}) and the hyperfine field profiles deduced from analysis of the spectrum given in Fig. 5. By integration over this HF profile, a loss of magnetization is deduced which compares well with the number of dead (non-magnetic) layers obtained by magnetic measurements. NMR yields more detailed insight into the magnetization at the interface, however, than merely the number of dead layers. Table 1 compares the HF profile with the moment profile computed ab-initio [66] in a multilayer with a comparable concentration profile. Experiment and theory agree rather well although the experimental HF decreases slightly faster than the theoretical moment with increasing Ru concentration. Indeed, HF is not exactly proportional to the local

Table 1. Ru concentration (%) and Co hyperfine field profile at the interface of Co/Ru multilayers as deduced from NMR. Theory: ab-initio calculation of the Co moment at a Co–Ru interface with linear concentration profile [66].

		NMR	Theory	
	C_{Ru}	HF_{Co}/HF_{bulk}	μ_{Co}/μ_{bulk}	C_{Ru}%
Bulk Co	0	1.00	1.00	0
Plane 0	0	0.99	1.03	0
Plane 1	2.5	0.94	0.97	0
Plane 2	17	0.75	0.89	25
Plane 3	50	0.40	0.63	50
Plane 4	82	0.04	0.13	75
Bulk Ru	100	–	–	100

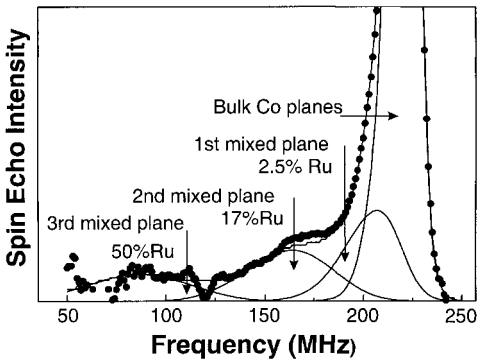

Fig. 5. Reconstruction of a $Co_{32Å}/Ru_{32Å}$ multilayer spectrum showing the contribution of each plane involved in the interface.

moment because of a minor contribution of neighboring moments (the number of which decreases as the Ru content increases); to a first approximation, however, the HF profile is a reasonable estimate of the moment profile.

The existence of a magnetization gradient at thick interfaces has several consequences on the magnetic properties that should be taken into account in the interpretation of the experimental data. The demagnetizing field involves magnetic poles in the interface volume and not only surface poles. This affects estimates of the surface anisotropy, particularly when the thickness of the magnetic layers is comparable with the interface thickness.

The planes that carry a weak moment at liquid He temperatures eventually become non-magnetic at room temperature; this can change the effective thickness of the non-magnetic spacer or introduce a loose-spin type biquadratic coupling [67]. As a consequence the temperature-dependence of the magneto-resistive effect can differ significantly from theoretical expectations that involve only the thermal variation of the spin-dependent scattering. Indeed, whereas the magneto-resistance is expected to decrease with increasing temperature, cases of increasing MR with increasing T have been observed in Co/Ru superlattices, and in some samples with thin Ru layers ferromagnetic coupling is observed at 4.2 K but antiferromagnetic or biquadratic (perpendicular) coupling at 300 K [68].

8.3.3 Local Anisotropy

The three examples described below show how evolution of the spectrum as a function of the DC field strength and orientation enables discrimination between different parts of composite materials, to furnish evidence of their different magnetization processes or to enable measurement of their different magnetic anisotropy.

8.3.3.1 Magnetic Phase Separation – Single-domain and Multidomain Particles

When a small DC external field is applied to a multidomain ferromagnet the resonance frequency does not shift immediately, as expected; this means that the internal field does not increase as immediately as the external field. Indeed, because the domain walls move while the sample magnetizes, the demagnetizing field increases, which compensates more or less for the increase of the external field. In contrast, in a single domain and isotropic particle the resonance line starts shifting as $-\gamma_n H_{\text{ext}}$ from the smallest field values (the minus sign is included, because, in transition metals, HF is antiparallel to the magnetization and to H_{ext}).

The bimodal distribution of the sizes of Co clusters embedded in silica has been demonstrated in this way. The samples were prepared by sol–gel synthesis then reduced in a hydrogen atmosphere at temperatures in the range 600–1000 °C. As is apparent from in Fig. 6 the NMR spectra of the samples comprise two main lines –

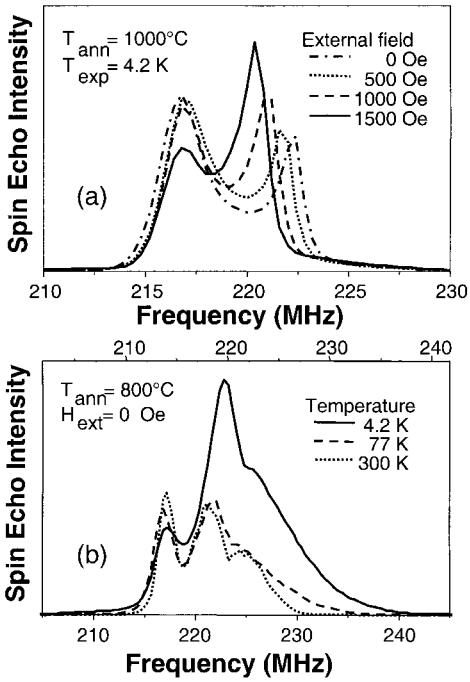

Fig. 6. ^{59}Co spectra of cobalt granules in silica showing two sizes of population – at 217 MHz, large fcc Co clusters, multidomain, at 223 MHz, small fcc Co clusters, single domain and superparamagnetic at high temperature. The high-frequency tail at the lower annealing temperature (800 °C) is a result of bad crystallization (stacking faults). The shift between the two lines in zero field is because of the demagnetizing field (6 kOe) in the single-domain spheres. (a) The dependence of the single domain line (sample annealed at 1000 °C) on the external field. (b) The different temperature dependence of the two populations of granules (sample annealed at 800 °C). The top frequency axis is for the spectrum observed at 300 K (the shift is because of thermal variation of the magnetization).

at 217 MHz a standard line arising from large, multidomain, fcc Co clusters that does not shift with increasing field, and, 6 MHz higher, another line that shifts exactly as $-\gamma_{Co} H_{ext}$ ($\gamma_{Co} \approx 1$ MHz kOe^{-1}).The latter line arises from single-domain fcc Co particles. Without the results of the in-field measurement, the 223 MHz line in zero field could have been misinterpreted as arising from hcp Co. Actually the 6 MHz up shift of this line relative to the 217 MHz line of fcc Co is because of the 6 kOe demagnetizing field that adds to HF [69]. The existence of the two kinds of cluster is explained by the direct reduction of Co ions to metallic Co in the small clusters, and the formation of Co silicide at an early stage of the thermal/reduction treatment; indeed for reduction temperatures below 800 °C small clusters only are observed in the spectrum. The large clusters are subsequently formed after reduction of the silicide at higher reduction temperatures.

The temperature dependence of the line intensities (Fig. 6b) shows that most of the small clusters become superparamagnetic and, hence, disappear from the spectrum between 4 K and 77 K . Assuming that the anisotropy constant of the clusters is equal to that of bulk fcc Co, this range of blocking temperatures implies that the radius of the small grains lies in the 10 to 30-Å range whereas that of the multidomain clusters must be larger than 300 Å, in agreement with electron microscopy observations. In the future such thermal dependence, associated with relaxation measurements, might provide much unique information on the dynamics of small magnetic particles.

8.3.3.2 Local Magnetic Anisotropy – Dependence of NMR on DC Field Strength

When H_{ext} is large enough to yield a single domain state, it can be shown (Section 8.4.1) that the NMR signal intensity varies as $1/(H_{ext} + H_{an})$, where H_{an} is the local anisotropy field. The local magnetic anisotropy can, therefore, be measured by studying the dependence of signal intensity on DC field strength. This has been used by Thomson et al. [70] to measure selectively the magnetic anisotropy of Co/Cu multilayers at the interfaces and in the bulk of the Co layers. Figure 7 shows an example fit of the signal intensity to the theoretical dependence in a Co/Cu multilayer. Results from measurements on two multilayers grown on different substrates are given in Table 2. The data indicate that the two samples have quite different bulk anisotropy (as measured at the bulk frequency) and that the anisotropy at the interfaces (measured on the main interface line – 3 Cu NN) are much lower than in the bulk, and are similar for both samples.

Interestingly, the similar values of the anisotropy fields at the interfaces compares well with the similar values of the coercive fields measured on these multilayers. As

Table 2. Local anisotropy fields measured by NMR in the bulk and at the interfaces of two different Co/Cu multilayers as compared with the macroscopic coercive field (all values in Oe) [70].

Sample	Local H_{an}, bulk	Local H_{an}, interface	Coercive field
Cu/[Co/Cu]$_n$	550	340	260
Au/[Co/Cu]$_n$	1230	360	260

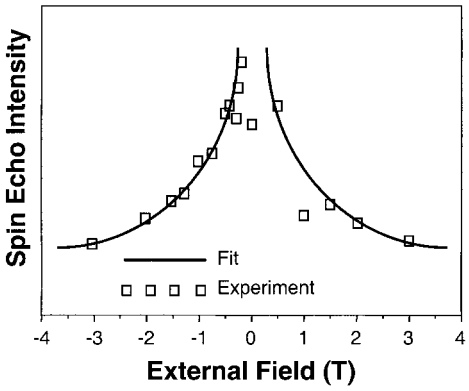

Fig. 7. Variation of the spin echo intensity as a function of the external DC field strength recorded on the bulk peak of a Co/Cu multilayer. The line is a fit to the theoretical dependence $I/(H_{\text{ext}}+H_{\text{an}})$ from which the local anisotropy field H_{an} is deduced [70].

first noticed by the authors, this is a strong indication that the magnetization reversal in the magnetic layer is initiated at the interfaces.

A similar approach has been used to study the orthorhombic distortion and the resulting in-plane anisotropy of Co/Pt superlattices, although, in this case, the external field was applied perpendicular to the easy axis [71].

8.3.3.3 Local Magnetic Anisotropy – Dependence of NMR on DC Field Orientation

When the external field is made still larger, to (nearly) saturate the sample, the local magnetic anisotropy of the various parts of a sample can be investigated by monitoring the dependence of the resonance frequency on the orientation of the field. This kind of experiment closely parallels torque magnetometry measurements. It must be performed on a single crystal, or at least, an oriented sample. Because the resonance frequency is proportional to the vector sum of the external field and the internal fields H_{dip} and HF (Eq. 1), it is possible to measure the angles between HF, the moment, and the external field, which yields quantitatively the magnetic anisotropy.

The method has been used by van Alphen and co-workers [58, 59] to determine local magnetic anisotropy in thin Co films. A typical NMR spectrum of a Co [111] film is shown in Fig. 8. This figure shows two spectra of the same film recorded with the magnetic field applied parallel (circles) and perpendicular (squares), respectively, to the film plane. The overall shift of the spectrum for H_{ext} perpendicular to the film plane is because of the demagnetizing field of 18 kOe, as expected for a Co film. As seen in many imperfect cobalt samples, four distinct resonance lines can be distinguished. The most intense arises from fcc Co. The signals at the high field side of this fcc line arise from stacking faults and the hcp phase. Whereas fcc Co and stacking faults have an isotropic or nearly isotropic (respectively) hyperfine field, the hyperfine field of hcp Co is anisotropic by 8 kOe [54, 55]. This implies that the hcp resonance line shifts 8 MHz less than the isotropic lines when the field is applied perpendicular to the film plane. This is exactly what can be observed in Fig. 8 for

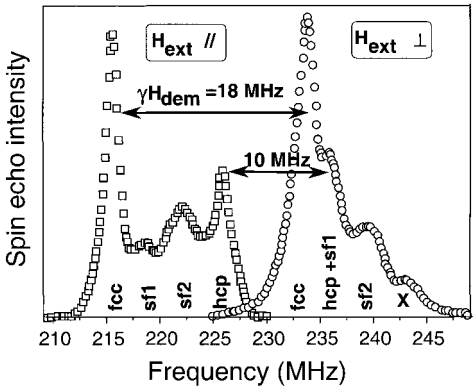

Fig. 8. Spectra of a Co thin film grown along the ⟨111⟩ fcc or ⟨001⟩ hcp orientation with an external field in-plane and perpendicular to the plane (the shift resulting from the external field has been subtracted for comparison with zero field measurements). The overall shift of the spectrum by 18 MHz is because of the demagnetizing field, but the true hcp line shifts only by 10 MHz, because of its hyperfine field anisotropy. The lines labeled fcc and hcp correspond to perfect fcc and hcp structures, sp1 and sp2 are the lines arising from stacking faults. X is an unidentified line that lies at the hcp frequency for M⊥c (H_{ext} in plane) but is isotropic, unlike the true hcp line [58, 59].

the line at 226 MHz (field parallel). From this experiment, performed on series of Co thin films prepared under different conditions, the isotropic and the anisotropic fractions in the spectra have been measured and the overall film anisotropy has been calculated by weighted averaging according to:

$$K_{rmav} = (1 - x)K_{\text{dem}} + xK_{\text{hcp}} \tag{6}$$

where x is the volume fraction of the anisotropic phase, K_{dem} is the shape (dipolar) anisotropy acting on the fcc phase and the defects, and K_{hcp} is the effective anisotropy (magnetocrystalline + dipolar) acting on the hcp fraction. K_{dem} and K_{hcp} have been assumed to take the same values as in perfect fcc and hcp films, respectively. The 'average' anisotropy energy estimated from NMR and the results from direct magnetization measurements are compared in Fig. 9. The agreement between the two determinations is reasonable but not perfect. Perfect agreement is expected only in two limit cases–when the two phases are totally decoupled magnetically (macroscopic average of the anisotropy energy), and when the phases are fully coupled magnetically (self averaging of the anisotropy, because of exchange coupling).

The difference between the two determinations of the film anisotropy shows that none of these cases is valid, because grains of the two phases are magnetically coupled but the exchange coupling length is not large enough compared with the grain size. The effective anisotropy energies within each of the coupled phases has subsequently been measured by analyzing the angular dependence of the resonance frequency of their respective line in the spectrum. Table 3 lists the values found by NMR in two of the previous Co films. It can be seen that the local magnetic anisotropy measured

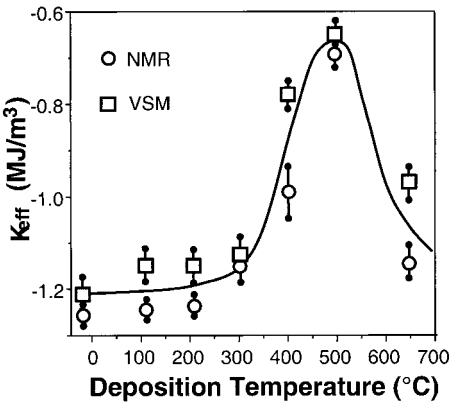

Fig. 9. Magnetic anisotropy of a series of Co thin films, grown on mica, as a function of deposition temperature. Squares, VSM measurements; circles, as deduced from the NMR phase analysis. The line is a guide for the eyes [58, 59].

Table 3. Local magnetic anisotropies (MJ m^{-3}) measured by NMR in thin Co films containing a mixture of hcp and fcc phases [58, 59].

Sample/Phase	fcc K_{loc} NMR	hcp K_{loc} NMR
Co on mica (400 °C)	-1.12 ± 0.04	-0.84 ± 0.15
Co on mica (500 °C)	-0.90 ± 0.06	-0.45 ± 0.09
K_{eff} thin film, pure phase	-1.27	-0.42

on the fcc and hcp lines does, indeed, differ from that of the respective single phase values; there is less difference between the two phases and the values depend on the relative amounts of hcp and fcc phases. This is exactly what is expected from a partial averaging, because of finite exchange coupling between the fcc and hcp grains.

8.4 Magnetic Stiffness – Anisotropy, Coercivity, and Coupling

8.4.1 Principles – NMR in Ferromagnets, Restoring Field, and Enhancement Factor

In magnetic materials [72], the nuclei are not directly excited by the external radio-frequency field H_1 but by the oscillation of HF after the electronic moment response to H_1. The position at rest of the electronic moment is determined by its minimum energy (magnetic anisotropy, dipolar and exchange energy, etc.). Their small oscillation amplitude under the external r. f. field H_1 can be expressed as $\Delta\theta = H_1/Hr$, where Hr is the restoring field traducing the restoring torque exerted on the moments upon small orientation changes. This is the same torque that is probed in ferromagnetic resonance (FMR) but here it is assumed that the electronic moments follow the r. f. field adiabatically, i. e. one is far from any electronic resonance. For example, the restoring field takes the value of the anisotropy field for a uniaxial,

single-domain particle, in other words $1/Hr$ is proportional to the local transverse electronic susceptibility and will obviously be different in different materials. The r. f. oscillation of the electronic moments is. In turn, transferred to the hyperfine field HF, inducing its oscillating transverse component $H_\perp$ that is directly responsible for the nuclear transitions. Hence, the value of $H_\perp$ reads:

$$H_\perp = HF\Delta\theta = H_1(HF/Hr) \tag{7}$$

The ratio $HH_\perp/H_1$ $(= HF/Hr)$ is called the NMR enhancement factor η. As far as the received signal is concerned, the precessing transverse nuclear magnetization exerts a torque on the electronic magnetization which is thus driven into rotation (or oscillation) in accordance with the torque balance equation

$$m_n \times = m_\mathrm{e} \times Hr \tag{8}$$

where m_m and m_e are the transverse (perpendicular to HF and M) components of the nuclear and electronic magnetization respectively. Thus the electronic magnetization acquires an oscillating component η times larger than the rotating nuclear component. The actual signal in the probe coil is mostly induced by m_e and it is thus enhanced by the same factor η as the r. f. excitation. Thus, in ferromagnets, the zero field NMR signal should read:

$$\begin{aligned} S(\omega, H_1) &= \eta\omega\xi_n(\omega)HF.\sin[\theta(\eta H_1)] \\ &= \eta\sin[\theta(\eta H_1)]\omega^2 N(\omega)\gamma\hbar^2 I(I+1)/3k_B T \end{aligned} \tag{9}$$

where $\xi_n(\omega)$ and $N(\omega)$ are, respectively, the nuclear susceptibility and the nucleus density –. the 'true' NMR intensity – and θ is the turn angle of the nuclear magnetization after the pulse sequence. Actually there is a spread of enhancement factor values within a sample, which results from the distribution of magnetization orientation, of demagnetizing field, etc. [73]. The actual distribution of enhancement factors is the convolution product of these distributions and tends to a log–normal distribution. From this it is found [74] that the spin echo intensity in a single phased magnetic material can be expressed as a function of the external r. f. field amplitude, H_1, according to:

$$S(\omega, H_1) = K\langle\eta\rangle\exp[-\log^2(H_1/H_{1\mathrm{opt}})/2\sigma^2]\omega^2 N(\omega)\gamma I(I+1)/T \tag{10}$$

where $H_{1\mathrm{opt}}$ is the r. f. field value for which the signal is maximum, σ is the width of the Gaussian distribution in $\log(H_1)$. The maximum NMR signal is reached when the nuclear spins experience an effective r. f. field strength such that, after the pulse sequence, the nuclear magnetization is perpendicular to HF. This happens when the average $H_\perp$ reaches the value H_opt such that, for a single pulse of duration τ, $H_\mathrm{opt} = \pi(2\gamma\tau)$. The value of Hr can, therefore, be written as:

$$Hr = (2\tau/\pi)\gamma HF.H_{1\mathrm{opt}} = (2\tau/\pi)\omega H_{1\mathrm{opt}} = \beta H_{1\mathrm{opt}} \tag{11}$$

where β is a sample-independent instrumental factor (calibrated against a sample for which Hr is well defined). Measurement of $H_{1\mathrm{opt}}$ enables evaluation of Hr and $\langle\eta\rangle$ for any sample; this is necessary to obtain the true intensity, $N(\omega)$, from raw spectra. NMR results can, moreover, now be discussed in terms of restoring field, a material property that is easily understood, rather than in terms of – instrument dependent – optimum excitation field, or in terms of enhancement factor – a notion for the specialists. Several experiments have shown (Section 8.4.2.1) that the measured Hr is indeed quantitatively comparable with more conventional macroscopic data (for example the anisotropy field, the coercive field, or the exchange bias field) [70, 75]. In the following text, H_1 is always expressed in units of Hr (i. e. βH_1 is used instead of H_1.

From Eq. (10) it follows that, in a single-phase material, the signal intensity has a Gaussian dependence upon $\log(H_1)$. To measure Hr and $\langle\eta\rangle$ one must record a set of spectra for several values of the r. f. power. This set of observed spectra can be plotted as a 3D picture (signal intensity S as a function of frequency and H_1 strength) or contour curves, similar to those shown later in Figs 16, 11, and 12, respectively. If the r. f. field strength is scaled as βH_1, then Hr is directly read as the position of the maximum signal intensity and the variation of Hr with frequency is given by the locus of this maximum. Considering that each frequency range is associated with a specific region of a composite sample, the $S(\omega, \beta H_1)$ curves shed some light on structural properties governing, at the atomic scale, the magnetic stiffness of the composite and the coupling strength between its components. Simply speaking, the 3D curves image directly the structural inhomogeneity, along the frequency axis, and the magnetic inhomogeneity, along the r. f. field axis.

8.4.2 Local Magnetic Stiffness

8.4.2.1 Magnetic Stiffness – Dependence of NMR on r. f. Field Strength

It has been shown above that the local restoring field can be measured in zero external field by monitoring the dependence of the NMR signal on the r. f. field strength. The next examples illustrate three instances in which the dominant contributions to the restoring energy have different origins (from, mostly, coercivity/anisotropy within the layers to, mostly, exchange coupling between layers). Figure 10 shows the dependence of Hr (averaged over the NMR spectrum) on the Co film thickness (t_{Co}) in various spin valves and multilayers.

The first example (Fig. 10, left) is an example of a hard/soft Cu/Co/Cu/NiFe multilayer with nearly uncoupled layers (Cu thickness = 50 Å). The process of magnetization of the Co layer is dominated by coercivity. Hr is roughly independent of Co thickness and corresponds well to the coercive field of the Co layers (200 to 300 Oe) measured in the samples [35].

A contrasting example (Fig. 10, right) is that of Co/Cu multilayers designed to have large antiferromagnetic coupling but a very low coercivity at room temperature [76]. The magnetization process is dominated by the antiferromagnetic coupling between the layers and Hr varies roughly as the reciprocal Co thickness, as expected for a

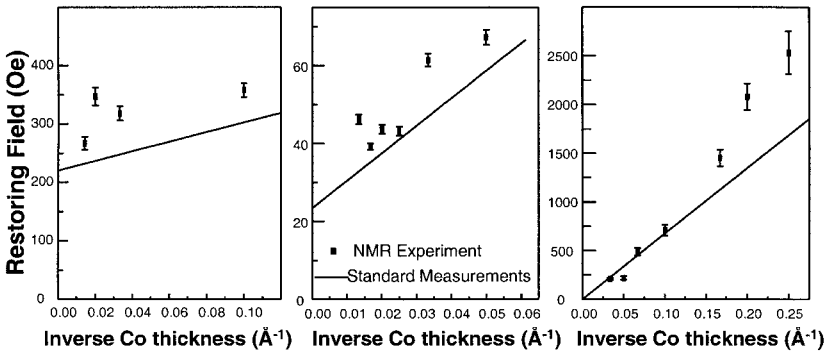

Fig. 10. Restoring field (average value on the Co spectrum) as function of inverse Co thickness in different magneto-resistive multilayers. Full lines are results from macroscopic measurements (coercive and exchange bias field). Left, $Co_x/Cu_{50Å}/NiFe_{50Å}/Cu_{50Å}$ Hard/soft multilayers; center, $Co_x/Cu_{22Å}$/NiFe/FeMn Spin valves; right, $Co_x/Cu_{20Å}$ AF coupled multilayers.

surface mechanism. For Co thicknesses below 10Å, however, Hr increases more than expected from $1/t_{Co}$ behavior and analysis of the spectra [44] shows that Co layers are no longer continuous when the thicknesses is below 10 Å. The observed deviation of 300 to 800 Oe is then attributed to the larger anisotropy of the small Co grains compared with that of the continuous Co layers. The NMR measurements were performed at 4.2 K and, indeed, the coercive field that was measured at 4.2 K on the magneto-resistance loop reaches 700 Oe for the thinnest Co layer, in agreement with the observed departure from linearity in the NMR result. At higher temperatures the coercivity decreases rapidly; it vanishes above 100 K .

The third example (Fig. 10, center) is the intermediate behavior of Co/Cu/NiFe/FeMn spin valves, for which there is residual coupling between Co and NiFe layers (the slope of Hr against $1/t_{Co}$) and the coercivity (the intercept at infinite Co thickness) is weak. The bulk contribution ($H_b = 29 \pm 6$ Oe) and the surface contribution ($A_s = 750 \pm 250$ Oe Å) to Hr agree very well with the coercive field H_c (21 ± 3 Oe) and the residual coupling field H_i ($H_i t_{Co} = 630 \pm 60$ Oe Å), respectively, which are measured directly on the magnetization loop [37].

These examples are given to show how the average Hr can be quantitatively related to more conventional macroscopic data. The average Hr is always found to be slightly larger than the corresponding macroscopic data. Better agreement is always found between the local restoring field measured on the softest part of the layered structure and the macroscopic coercive field. Indeed, the main interest in NMR measurement stems from the possibility of select parts of the sample, i. e. of looking at specific frequencies, and to measure their local magnetic stiffness. This is illustrated in the subsections below.

8.4.2.2 Structure and Magnetic Stiffness

The behavior of the spin valve $Cu_{10Å}/Co_{75Å}/Cu_{22Å}/NiFe_{50Å}/FeMn_{80Å}$ is again presented as a typical example. Figure 11a shows the frequency-dependence of the restoring field acting on Co moments in the sample and Fig. 11b shows the contour curves $S(\omega, \beta H_1)$. Two observations can be made. Firstly, the interface moments (below 190 MHz) are softer than the bulk moments (210–230 MHz). This is a general observation for all the layers, from many sources, which have been investigated and is in full agreement with results obtained in-field (Section 8.3.2.2). Secondly, the moments at grain boundaries in very small grains (190–210 MHz) are even softer than the interface moments and at least twice as soft as regular bulk moments. Because they can involve up to 20 % of the Co atoms in some samples, they are likely to influence substantially the magnetization process of the samples [36].

All studies of Co based multilayers show that the different regions of the Co layers can be classified in order of increasing magnetic stiffness (in the ⟨111⟩ plane) as: (i) regions with a large density of grain boundaries (small grains), (ii) interfaces, (iii) regions with a large density of stacking faults, (iv) hcp phase ($M \perp c$), (v) fcc phase, (vi) hcp phase ($M \| c$). Depending on whether one wants the Co layer soft or stiff, one should use appropriate preparation conditions favoring the former or the latter regions. For example, a large Cu thickness favors the fcc Co phase and increases the Co layer stiffness; in contrast, high deposition rates favor small grains and magnetic softness [34].

Thermal annealing of the same sample results in reduced magneto-resistance, which disappears completely when high annealing temperatures (360 °C) are

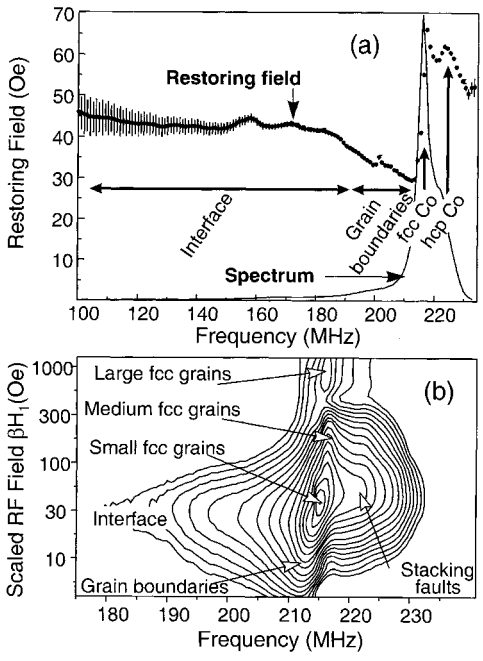

Fig. 11. Structural and magnetic inhomogeneity in the $Cu/Co_{75Å}/Cu_{22Å}/NiFe_{50Å}/FeMn$ spin valve (as deposited). (a) Frequency-dependence of the restoring field strength, showing the magnetic softness of grain boundaries (190–210 MHz) and interfaces (below 190 MHz) and the hardness of the bulk of the layers (above 210 MHz). (b) Detailed contour view (dependence of NMR intensity on frequency and rf field) of the upper frequency range showing the distribution of restoring field corresponding to that of Co grains sizes and other crystallographic defects.

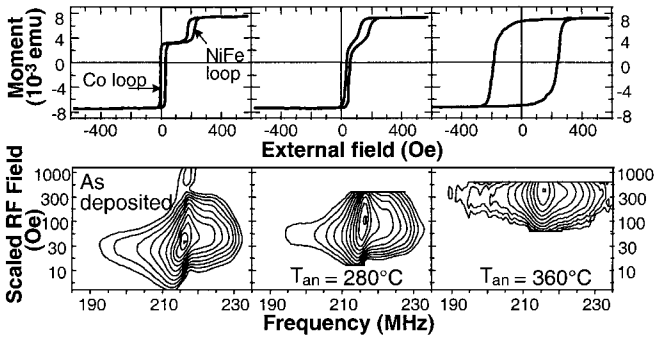

Fig. 12. Top: BH loops observed in $Cu/Co_{75Å}/Cu_{22Å}/NiFe/FeMn$ spin valves (as deposited and after annealing at 280 °C and 360 °C). Bottom: Contour plots of Co NMR intensity against frequency and r. f. field. Annealing at 280 °C results in no significant structural change – the shift of the curves towards larger restoring fields is because of larger coupling with the pinned NiFe layer. After annealing at 360 °C the narrowing of the distribution of restoring field is indicative of better magnetic homogeneity because of the growth of fcc crystal grains and the disappearance of the soft grain boundaries. The coercivity of the Co layer increases considerably.

used [37]. The evolution of the structure and of the magnetization process of the Co layer during the annealing treatment is illustrated by the contour plots $S(\omega, \beta H_1)$ presented in Fig. 12, bottom. After the first annealing step (280 °C) the shape of the contour curve does not change, it is merely shifted towards larger r. f. fields, i. e. the grain structure of the Co layer is not affected nor are its intrinsic magnetic properties. The larger restoring field results mainly from greater coupling between the free Co layer and the pinned NiFe layer – the sub-loops of the two magnetic layers (Co and NiFe) in the magnetization curve (Fig. 12, top) start to merge. In contrast, after annealing at 360 °C the structure of Co changes significantly, the soft grain boundary characteristics disappear (i. e. the average Co grain size has increased considerably) and the $S(\omega, H_1)$ plots are indicative of much better magnetic homogeneity (much narrower distribution of restoring fields) but at the expense of the soft character of the Co layer – indeed the average restoring field reaches values ten times larger (approximately 300 Oe) than in the as-deposited spin valve. The growth of the grains has been confirmed by electron microscopy.

For this spin valve and for other giant magneto-resistance devices a magneto-resistive effect can be observed assuming:

- there is a significant spin-dependent scattering in the bulk or at the interface of the magnetic layers; and
- the magnetization in successive magnetic layers is antiparallel or, at least, largely non-collinear.

The second requirement is fulfilled by different means – by taking advantage of antiferromagnetic coupling between the magnetic layers or, in spin valves, by pinning the magnetization orientation of one of the layers (here NiFe) while leaving the other layer (here Co) free to rotate under the external field.

While modifying the structure of the system, the annealing treatment can affect the spin-dependent scattering as well as the coupling and the magnetization process of the two layers. Observations show that the reduced magneto-resistance is mostly because of changes of the magnetization process of the free layer. At moderate annealing temperature the problem arises mainly from greater coupling between the free and the pinned magnetic layers of the spin valve. Although the structural origin for this increased coupling has not been clearly identified, it is suspected that it results from magnetic bridges, because of diffusion of the magnetic elements in the grain boundaries of the Cu spacer layer. For the highest annealing temperature the reason for the complete loss of magneto-resistance has been clearly identified– the structure of the free Co layer changes and its coercivity increases strongly; this suppresses the possibility of antiparallel alignment of the magnetization of the two magnetic layers.

8.4.2.3 Magnetic Stiffness Profile at Interfaces

The (nearly) universal soft character of the interface planes is shown in Fig. 13 for sputtered $Co_{30\text{Å}}$/Cu multilayers from different sources. Similar behavior has been also observed in Co/Ru and Co/Cr multilayers. All samples in which the interfaces are found to be softer than the bulk of the magnetic layer have different amounts of interfacial admixture (two or more mixed planes).

The general character of the observation shows that the magnetic moments do not rotate coherently in the magnetic layer – in contrast with the behaviour usually assumed; the moments rotate more easily in the interface atomic planes than in bulk planes, which implies that they are partly decoupled. It also implies that the average anisotropy must be weaker in the interface planes than in the bulk planes. These two assessments might be surprising, because of the large exchange coupling in Co and because of the surface anisotropy, respectively. Actually the experimental observation is not unexpected.

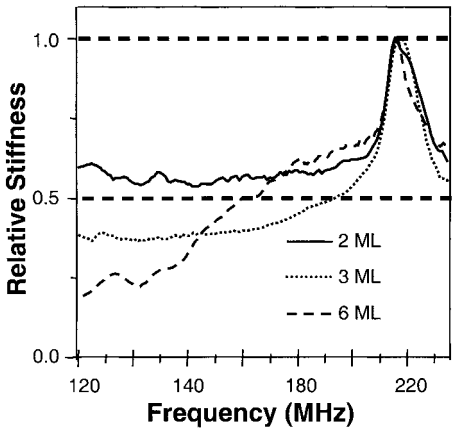

Fig. 13. Frequency dependence of the restoring field (normalized to the value in the bulk of the layer) in different ...Cu/$Co_{30\text{Å}}$/Cu... multilayers. This shows the softer character of the interfaces (below 200 MHz) compared with the bulk of the Co layers (210-230 MHz) as observed in most multilayers. Inserts indicate the number of mixed Co-Cu atomic planes at the interfaces.

As far as the anisotropy is concerned, it must be noted that in the samples studied the magnetization lies in plane and the magnetization process involves in-plane rotations – the anisotropy between in-plane and perpendicular to plane orientations is not relevant. The element admixture also breaks the in-plane symmetry, however, which can result in a large site anisotropy, depending on the arrangement of impurity atoms around each Co atom. This anisotropy is, however, random in strength and orientation and such a random anisotropy is readily averaged out by the exchange coupling as long as the exchange energy is larger than the anisotropy energy. This explains the lower anisotropy at the interface.

As far as the exchange energy is concerned, experimental observation shows that it is considerably reduced relative to the coupling energy in bulk Co. This is certainly a consequence of the smaller number of magnetic neighbors and the reduction of the moment in the mixed interfaces. To estimate the reduction of the exchange energy a simple model of the magnetic layer has been developed. This is built on the basis of a large moment $n\mu$ (for the n bulk planes) coupled on both sides to a moment μ (for the two interface planes). The central moment is pinned by a uniaxial anisotropy and the two interface moments are free from any anisotropy (in accordance with the remark above). Energy minimization, in a Stoner-Wohlfarth approach, shows that the interface moments rotate twice as much as the bulk moments (as is observed experimentally) when the coupling energy is approximately twenty times larger than the anisotropy energy of the central moment. In comparison, the exchange energy in bulk hcp Co is approximately one thousand times larger than the magneto-crystalline anisotropy. Current experimental observations indicate, therefore, that the exchange coupling between external interface planes and inner planes is only a few percent of the bulk Co value as soon as there are two or more mixed planes at the interfaces.

Two exceptions have been found to the softer character of the interface moments; they are, however, consistent with this explanation. The first exception is an example of a well mixed interface but, in contrast with all other samples, the two elements are magnetic (bcc Co/Fe superlattices) [48]. In these circumstances there is absolutely no stiffness difference between bulk and interface planes (Fig. 14a). Indeed the exchange coupling is certainly not reduced at the interface when both atomic species are magnetic, so the interface moments are tightly bound to those in the bulk of the layers. The second exception is the nearly perfect interface in a sample prepared by slow thermal evaporation of a single Co layer on a (111)-oriented single crystal of copper. Despite the presence of some fcc grains in a mostly hcp phase, the experimental spectrum is very close to perfect – in other words there is nearly no Co-Cu admixture at the interface. In these circumstances (Fig. 14b) the restoring field is as large (on average) at the interface as in the bulk (although there is a visible inhomogeneity associated with the hcp/fcc admixture).

It is commonly assumed that thin ferromagnetic layers behave as a single moment along the growth direction, owing to their small thickness compared with the exchange coupling length in bulk samples. NMR observations show that often this is not so. The two exceptions (the only ones yet observed) emphasize the condition that the full layer rotates uniformly under an external field – interdiffusion with non-magnetic atoms must be very weak, otherwise the magnetic moments at the interfaces are partly decoupled from the bulk magnetic moments.

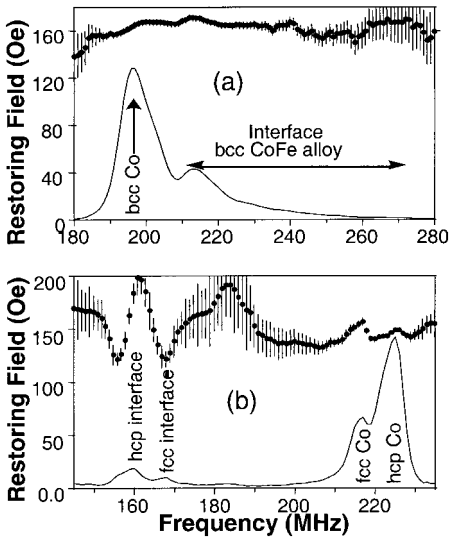

Fig. 14. Spectrum and restoring field in bcc Co/Fe multilayers (a) and in a single Co layer on a ⟨111⟩ single crystal of Cu with nearly perfect interface but a mixture of large hcp and fcc grains (b).

8.4.2.4 Exchange-coupling Oscillations

It is generally found in metallic multilayers that the coupling between the magnetic layers oscillates between ferromagnetic and antiferromagnetic as a function of the non-magnetic spacer thickness: this results from an RKKY- like mechanism [77]. Similar oscillations are found for the magneto-resistance which appears only when the coupling is antiferromagnetic. The exchange coupling strength oscillations are also readily observed on the restoring field measured by NMR.

In Co/Ru multilayers, for example, the coupling between Co layers oscillates with varying Ru thickness between ferromagnetic and antiferromagnetic with a period of approximately 11 Å [78]. Figure 15 shows the variation of the restoring field

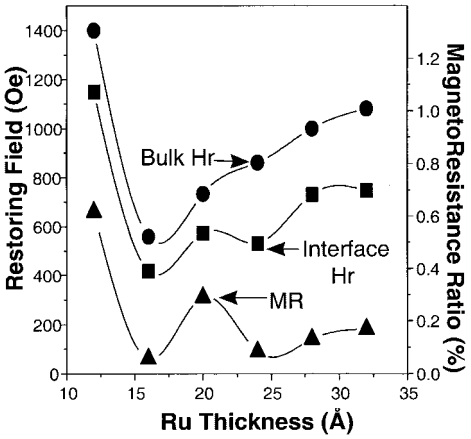

Fig. 15. Magneto-resistance and magnetic stiffness oscillations in $Co_{32Å}/Ru_t$ multilayers as a function of Ru thickness.

strength measured by NMR as a function of Ru thickness in $Co_{32Å}Ru_x$ multilayers. It is apparent that the variation of Hr parallels the oscillating evolution of the magneto-resistance ratio, as expected. Quantitatively, however, the magnetic response of interface and bulk planes are different, i. e. the diffuse interface planes are partly decoupled from the bulk planes. Not only are the interface planes softer, on average, than the bulk planes, it is also apparent that the amplitude of the oscillations of Hr is larger at the interfaces than in the bulk. The reason for this is that the antiferromagnetic coupling acts through the Ru spacer; its contribution to the restoring energy is, therefore, expected to be larger at the interface planes than in the bulk of the Co layers.

Analysis of the magnetization and of magneto-resistance loops in Co/Ru multilayers has already suggested significant spin misorientation inside the Co layers [79]. It was assumed that rotation of the interface moments under the external field was retarded by the AF coupling more than that of the bulk moments. This was interpreted as a result of the competition, at interfaces, between a weakened ferromagnetic coupling with the inner Co planes and strong antiferromagnetic coupling through the Ru spacer.NMR observation confirms this speculation. For samples with thinner (10 Å) Co layers, and according to the analysis of the macroscopic measurements, the interface moments would even be stiffer than the bulk moments when the antiferromagnetic coupling is maximum. Unfortunately, no NMR signal could be observed in these samples because the restoring fields were too large (> 5 kOe), owing to AF coupling, with respect to the available H_1 strength (r. f. power).

8.4.2.5 Inhomogeneity of the Magnetization Process

The examples so far presented have pointed out the magnetic differences between the different parts of magnetic layers (bulk phases, grain boundaries, interfaces) that can be detected as a result of their different NMR frequencies. The variation of the NMR signal with r. f. field strength can also furnish evidence of more global magnetic inhomogeneity, for example distribution of coercive field among layers or distribution of magnetic coupling strength between layers. Such inhomogeneity is revealed by the observation of very broad $S(H_1)$ curves with several peaks, i. e. a large distribution of restoring field at any frequency. The usefulness of the observation is illustrated by the example (Fig. 16) of two Co/Cu multilayers, with a Cu thickness of approximately 10 Å, that is responsible for a strong antiferromagnetic coupling between the Co layers [78]. The magnetization loops of the two samples (Fig. 16, bottom) are quite similar – both increase rapidly at low field and this is followed by a slow saturation up to 5 kOe. Such curves can be interpreted as resulting from coupling inhomogeneities, parts of layers being antiferromagnetically coupled, others being ferromagnetically coupled (because of magnetic bridges, pin-holes in the Cu layer, or fluctuations of Cu thickness). Alternatively, after the experimental evidence for biquadratic coupling, i. e. 90° orientation between the magnetization of adjacent layers [80], and theoretical developments relating to this [67], it is also tempting to interpret magnetization curves like these in terms of homogeneous perpendicular (or non-collinear) coupling.

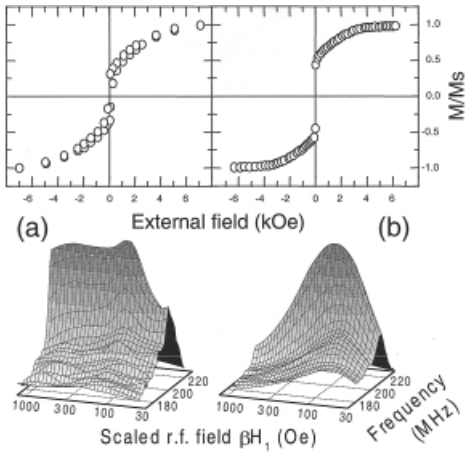

Fig. 16. Co/Cu multilayers with large antiferromagnetic coupling ($t_{Cu} \approx 1$ nm) showing similar magnetization loops (top) but very different amounts of coherence in their magnetization process (bottom). (a) Broad distribution of restoring field (inhomogeneous coupling). (b) Homogeneous magnetization process (homogeneous non collinear coupling).

NMR observation if the first multilayer (Fig. 16a) reveals very broad distribution of the restoring field in the 3D curves $S(\omega, H_1)$, which proves the inhomogeneous nature of the magnetization process. This is because of fluctuations of anisotropy or coupling strength. The magnetization loop can, therefore, hardly be attributed to biquadratic coupling – it results from distribution of anisotropy or coupling strength from place to place in the sample where the magnetization rotates incoherently. In contrast, the distribution of Hr is narrower in the second multilayer (Fig. 16b); this is consistent with a homogeneous, coherent magnetization process. The curves peak at a low value (< 100 Oe), which is expected for biquadratic coupling. This low value of Hr corresponds to the initial rotation of the net moment of the whole multilayer, as for ferromagnetic coupling. The occurrence of biquadratic coupling can, therefore, be considered in this second example. Any other magnetic structure with a net remanent magnetization and tightly coupled magnetic layers is, however, also compatible with the NMR results.

Presently, the kind of analysis illustrated here is often limited to qualitative conclusions about the magnetic homogeneity of the samples and only large inhomogeneities are visible. Indeed, even in homogeneous samples the $S(H_1)$ curve is intrinsically broad and a deconvolution procedure must be applied to extract the true restoring field distribution. As illustrated below, however, it is rather easy to separate two different magnetic phases in a sample if their restoring field differs by more than a factor of three.

8.4.2.6 Magnetic Phase Separation – Soft and Hard Phases

If a material consists of several phases with largely different magnetic stiffness, more than one Gaussian shape is needed to describe the signal intensity as a function of the excitation field. A possible ambiguity of the method arises because in a single-phase, multidomain material two main restoring mechanisms act on the moments; one which acts on the domain wall displacement (the propagation field) and the other on domain rotation (the anisotropy field). Thus if domain rotations and domain wall movements

were both excited in the experiment two Gaussians would also be needed. In such circumstances, however, the two contributions must have the same spectral shape. If the spectra recorded under the different r. f. conditions differ in shape, several magnetic phases are present in the sample. In favorable circumstances, i. e. when the different phases in a sample have largely different structure and magnetic stiffness, it is thus possible to separate the spectra arising from each of the phases and to determine their average restoring field.

The occurrence of granular CoCu alloys, obtained by melt spinning, with giant magneto-resistance [51] illustrates this possibility. The shapes of the spectra of such alloys change substantially as a function of the r. f. field strength (Fig. 17). The H_1 dependence of the spin echo intensity at two exemplary frequencies (200 and 215 MHz) is shown in Fig. 18a. At both frequencies two Gaussian shapes must be used, one corresponding to $Hr \approx 0.9\,\mathrm{kOe}$ and the other to $Hr \approx 6.4\,\mathrm{kOe}$. At 200 MHz the amplitudes of the two components are comparable, whereas at 215 MHz the harder component is clearly dominant. The individual spectra of the two components are obtained by the fitting $S(H_1)$ with two distributions at each frequency. Figure 18b shows the NMR spectrum recorded for $\beta H_1 = 2\,\mathrm{kOe}$, and those of its hard and soft components. The spectrum corresponding to the softer component is typical of a CoCu alloy; it has a characteristic satellite structure separated by approximately 16 MHz on the low-frequency side of the Co peak, corresponding to Co first coordination shells with one, two, etc., Cu neighbors [18]. The other ferromagnetic component in the sample is a hard phase, the dominating feature of which is a strong Co peak, showing the presence of pure fcc Co granules. The low-frequency tail of this line is strikingly similar to the spectrum observed in Co/Cu multilayers with rough interfaces but limited interdiffusion.

The measured restoring field of the hard component is close to that expected for an assembly of non-interacting single-domain particles of fcc Co. Indeed the restoring field in a single domain fcc Co grain is equal to the anisotropy field, i. e. 3 kOe, a value that would be obtained if H_1 was optimally oriented perpendicular to the

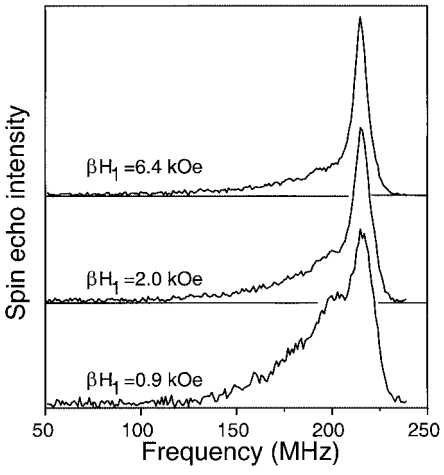

Fig. 17. ^{59}Co NMR spectra from a $Co_{10}Cu_{90}$ melt-spun ribbons recorded at 4.2 K at different r. f. power (H_1 in unit of restoring field). They show the large change in shape arising from a mixture of hard an soft phases.

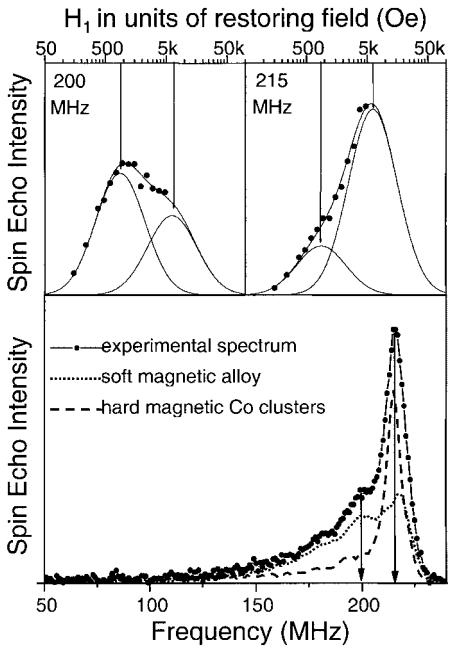

Fig. 18. $Co_{10}Cu_{90}$ melt-spun granular alloy. Top: dependence of spin echo intensity on H_1 strength at two exemplary frequencies, showing the existence of two magnetic phases (two restoring fields). Bottom: ^{59}Co spectrum and its decomposition into the spectra of the soft and hard phases.

magnetization. For an assembly of particles with random magnetization orientation, however, the expected average restoring field is twice as large, i. e. 6 kOe, which is close to the value observed experimentally. The smaller value of the restoring field observed for the alloyed component (approximately 0.9 kOe) is understood to result from self averaging of the random anisotropy due to the CoCu admixture as a result of the exchange interaction.

In contrast with multilayers, in which the geometry of the composite is rather well controlled, the distribution of sizes and the composition of the magnetic clusters in nanogranular alloys prepared by metallurgical means varies considerably; this results in large differences between magnetic properties. The most obvious consequence is distribution of blocking temperatures, i. e. some of the particles are ferromagnetic, blocked, but others are superparamagnetic. It is often speculated that the anisotropy constant of the particles is independent of their size and composition and the distribution of blocking temperatures is analyzed in terms of size distribution only. This example shows that the assumption can be clearly invalid.

8.5 Conclusion

NMR investigations on many Co-X multilayers and granular alloys [81] have shown how the structure of Co layers or clusters can be correlated with their magnetic properties, for example their magnetization profile at the interfaces or the anisotropy

and magnetic stiffness of different parts of the composite structure. In summary, because they contribute to the NMR spectrum at different frequencies, different regions of the magnetic layers can be selected and their magnetic properties can be separately probed.

In the bulk of Co layers, it has been shown that the fcc fraction is usually magnetically stiffer than the hcp fraction. This is observed for most multilayers in which the magnetization lies and rotates in-plane, perpendicular to the hcp c-axis. In samples with numerous small columnar grains the softness of these grains has been proved directly; they lead to very soft layers.

A very general observation is that, unless the interfaces are very sharp, the magnetic layer cannot be considered as rotating as a whole under the external field. In most systems the moments at the interfaces rotate more easily than those in the bulk, despite the small layer thickness compared with the domain wall width in bulk Co. This is interpreted as resulting from reduction of the magnetic moments and weakening of the exchange stiffness, because of element admixture at the interfaces. A consequence of the softer character of the interface moments is that the magnetization reversal of the layer is quite probably initiated at interfaces. Another consequence of the partial decoupling of the interface moments is that the antiferromagnetic coupling through the spacer, which acts primarily on the interfaces, can be transferred only partly to the bulk of the magnetic layers.

In addition to the magnetic inhomogeneity expected from the intrinsic composite design of the nanomaterials, such as the magnetization and magnetic stiffness profiles at multilayer interfaces, NMR can also image directly any large, and usually unwanted, inhomogeneity of coupling and/or anisotropy between the magnetic components. One can then discriminate between various interpretations of the process of magnetization of the composite structure. Ultimately, such studies facilitate identification both structurally (geometry and chemical nature) and magnetically (anisotropy and stiffness) of the different magnetic phases that might be present in a composite sample.

References

[1] For a general introduction to NMR see: A. Abragam, *The Principles of Nuclear Magnetism*, Oxford Clarendon Press, Oxford, **1962**; C. P. Slichter, *Principles of magnetic resonance*, Springer, Heidelberg, **1990**.

[2] For NMR in metals: J. Winter, *Magnetic Resonance in Metals*, Oxford University Press, Oxford, **1971**; P. Panissod in *Microscopic Methods in Metals*, (Ed. U. Gonser) Springer Verlag, Heidelberg, **1986**, pp. 365–408.

[3] The electric field gradient that act on the observed nucleus affects also its resonance frequency. As such it is also a signature of the local atomic configuration. However, in the magnetic materials one is dealing with here, the electric quadrupole interaction is often much weaker than the magnetic hyperfine interaction so that the spectrum shape arises mostly from the distribution of the magnetic hyperfine field.

[4] S. Blügel, H. Akai, R. Zeller, and P. H. Dederichs, *Phys. Rev. B* **1987**, 35, 3271–3283.

[5] B. Drittler, H. Ebert, R. Zeller, and P. H. Dederichs, *Phys. Rev. B* **1989**, 39, 6334–6341.
[6] B. Drittler, N. Stefanou, S. Blügel, R. Zeller, and P. H. Dederichs, *Phys. Rev. B* **1989**, 40, 8203–8212.
[7] H. Ebert, H. Winnert, D. D. Johnson, and F. J. Pinski, *J. Phys. Cond. Matter* **1990**, 2, 443–453.
[8] H. Akai, M. Akai, S. Blügel, B. Drittler, H. Ebert, K. Terakura, R. Zeller, and P. H. Dederichs, *Progr. Theor. Phys.* **1990**, Suppl. 101, 11–77.
[9] P. H. Dederichs, R. Zeller, H. Akai, and H. Ebert, *J. Magn. Magn. Mater.* **1991**, 100, 241–260.
[10] R. C. Laforce, R. F. Ravitz, and G. F. Day, *Phys. Rev. Lett.* **1961**, 6, 226–228.
[11] S. Kobayashi, K. Asayama, and J. Itoh, *J. Phys. Soc. Jpn* **1966**, 21, 65–74.
[12] H. Yasuoka, S. Hoshinouchi, Y. Nakamura, M. Matsui, and K. Adachi, *Phys. Stat. Sol. B* **1971**, 46, K81–84.
[13] V. Niculescu, J. I. Budnick, W. A. Hines, K. Raj, S. Pickart, and S. Skalski, *Phys. Rev. B*, **1979**, 19, 452–464.
[14] P. Panissod, J. Durand, and J. I. Budnick, *Nuclear Inst. Meth.* **1982**, 199, 99–114.
[15] P. C. Riedi and R. G. Scurlock, *J. Appl. Phys.* **1968**, 39, 1241–1242.
[16] M. Kawakami, *J. Phys. Soc. Jpn* **1976**, 40, 56–62.
[17] T. M. Shavishvili, and I. G. Kiliptari, *Phys. Stat. Sol. B* **1979**, 92, 39–47.
[18] C. Mény, E. Jedryka, and P. Panissod, *J. Phys. Cond. Matter* **1993**, 5, 1547–1556.
[19] J. Ph., Jay, M. Wójcik, and P. Panissod, *Z. Phys. B* **1996**, 101, 471–486.
[20] K. Takanashi, H. Yasuoka, K. Kawaguchi, N. Hosoito, and T. Shinjo, *J. Phys. Soc. Jpn* **1982** 51, 3743–3744; *J. Phys. Soc. Jpn* **1984**, 53, 4315–4321.
[21] N. Hamada, K. Terakura, K. Takanashi, and H. Yasuoka, *J. Phys. F* **1985**, 15, 835–850.
[22] K. Le Dang, P. Veillet, C. Chappert, P. Beauvillain, and D. Renard, *J. Phys. F* **1986**, 16, L109–112.
[23] K. Le Dang, P. Veillet, P. Beauvillain, N. Nakayama, and T. Shinjo, *J. Phys. Cond. Matter* **1989**, 1, 6153–6158.
[24] K. Le Dang, P. Veillet, H. Hui He, F. J. Lamelas, C. H. Lee, and R. Clarke, *Phys. Rev. B* **1990**, 41, 12902–12904.
[25] K., Le Dang, P. Veillet, P. Beauvillain, C. Chappert, H. Hui He, F. J. Lamelas, C. H. Lee, and R. Clarke, *Phys. Rev. B* **1991**, 3, 13228–13231.
[26] K. Yoshida, T. Takayama, and H. Yasuoka, *J. Appl. Phys.* **1991**, 69, 5184–5188.
[27] H. A. M. de Gronckel, K. Kopinga, W. J. M de Jonge, P. Panissod, J. P. Schillé, and F. J. A. den Broeder, *Phys. Rev. B* **1991**, 44, 9100–9103.
[28] H. A. M. de Gronckel, B. M. Mertens, P. J. H. Bloemen, K. Kopinga, and W. J. M. de Jonge, *J. Magn. Magn. Mater.* **1992**, 104–107, 1809–1810.
[29] E. A. M. van Alphen, S. G. E. de Velthuis, H. A. M. de Gronckel, K. Kopinga, and W. J. M de Jonge, *Phys. Rev. B* **1994**, 49, 17336–17341.
[30] Y. Saito, K. Inomata, A. Goto, and H. Yasuoka, *J. Phys. Soc. Jpn* **1993**, 62, 1450–1454.
[31] Y. Suzuki, T. Katayama, and H. Yasuoka, *J. Magn. Magn. Mater.* **1992**, 104–107, 1843–1844.
[32] J. P. Renard, P. Beauvillain, K. Le Dang, P. Veillet, E. Velu, C. Marlière, and D. Renard, *J. Magn. Magn. Mater.* **1992**, 115, L147–151.
[33] C. Mény, P. Panissod, and R. Loloee, *Phys. Rev. B* **1992**, 45, 12269–12277.
[34] P. Panissod, and C. Mény, *J. Magn. Magn. Mater.* **1993**, 126, 16–18.
[35] T. Valet, P. Galtier, J. C. Jacquet, C. Mény, and P. Panissod, *J. Magn. Magn. Mater.* **1993**, 121, 402–405.
[36] C. Mény, P. Panissod, P. Humbert, J. P. Noziéres, V. S. Speriosu, B. A. Gurney, and R. Zehringer, *J. Magn. Magn. Mater.* **1993**, 121, 406–409.

[37] C. Mény, J. Ph. Jay, P. Panissod, P. Humbert, V. S. Speriosu, H. Lefakis, J. P. Noziéres, and B. A. Gurney, *Mat. Res. Soc. Symp. Proc.* **1993**, 313, 289–294.
[38] K. Le Dang, P. Veillet, E. Velu, S. S. P. Parkin, and C. Chappert, *Appl. Phys. Lett.* **1993**, 63, 108–110.
[39] J. S. Lord, H. Kubo, P. C. Riedi, and M. J. Walker, *J. Appl. Phys.* **1993**, 73, 6381–6383.
[40] Y. Henry, C. Mény, A. Dinia, and P. Panissod, *Phys. Rev. B* **1993**, 47, 15037–15045.
[41] E. A. M. van Alphen, P. A. A van der Heijden, and W. J. M. de Jonge, J. App. Phys. **1994**, 76, 6607–6609; *J. Magn. Magn. Mater.* **1995**, 140–144, 609–610.
[42] E. A. M. van Alphen and W. J. M. de Jonge, *Phys. Rev. B* **1995**, 51, 8182–8192.
[43] T. Thomson, P. C. Riedi, C. Morawe, and H. Zabel, *J. Magn. Magn. Mater.* **1996**, 156, 89–90.
[44] E. Jedryka, M. Wójcik, S. Nadolski, D. Kubinski, H. Holloway, *J. Magn. Magn. Mater.* **1997**, 165, 292–296.
[45] Ph. Houdy, P. Boher, F. Giron, F. Pierre, C. Chappert, P. Beauvillain, K. Le Dang, P. Veillet, and E. Velu, *J. Appl. Phys.* **1991**, 69, 5667–5669.
[46] P. Boher, F. Giron, Ph. Houdy, F. Baudelet, A. Fontaine, J. M. Ladouceur, E. Dartyge, P. Beauvillain, C. Chappert, P. Veillet, and K. Le Dang, *J. Appl. Phys.* **1992**, 71, 1798–1801.
[47] J. Dekoster, E. Jedryka, C. Mény, and G. Langouche, *Europhys. Lett.* **1993**, 22, 433–438.
[48] J. Ph. Jay, E. Jedryka, M. Wójcik, J. Dekoster, G. Langouche, and P. Panissod, *Z. Phys. B* **1996**, 101, 329–337.
[49] T. Kohara, M. Yamaguchi, and K. Asayama, *J. Phys. Soc. Jpn*, **1985**, 54, 1537–1542.
[50] T. Thomson, P. C. Riedi, S. Sankar, A. E. Berkowitz, *J. Appl. Phys.* **1997**, 81, 5549.
[51] M. Malinowska, M. Wojcik, S. Nadolski, E. Jedryka, C. Mény, P. Panissod, M. Knobel, A. D. C Viegas, J. E Schmidt, *J. Magn. Magn. Mater.* **1999**, 198–199, 599–601.
[52] A. M. Portis and A. C. Gossard, *J. Appl. Phys.* **1961**, 31, 205S–231S.
[53] R. Street, D. S. Rodbell, and W. L. Roth, *Phys. Rev.* **1961**, 121, 84–86.
[54] M. Kawakami, T. Hihara, Y. Koi, and T. Wakiyama, *J. Phys. Soc. Jpn* **1972**, 33, 1591–1598.
[55] D. Fekete, H. Boasson, A. Grayevskey, V. Zevin, and N. Kaplan, *Phys. Rev. B* **1978**, 17, 347–354.
[56] L. E. Toth and S. F. Ravitz, *J. Phys. Chem. Solids* **1963**, 24, 1203–1206.
[57] H. Brömer and H. L. Huber, *J. Magn. Magn. Mater.* **1978**, 8, 61–64.
[58] E. A. M. van Alphen, H. A. M. de Gronckel, P. J. H. Bloemen, A. S. van Steenbergen, and W. J. M. de Jonge, *J. Magn. Magn. Mater.* **1993**, 121, 77–79.
[59] H. A. M. de Gronckel, P. J. H. Bloemen, E. A. M. van Alphen, and W. J. M. de Jonge, *Phys. Rev. B* **1994**, 49, 11327–11335.
[60] P. C. Riedi, T. Dumelow, M. Rubinstein, G. A. Prinz, and S. B. Qadri, *Phys. Rev. B* **1987**, 36, 4595–4599.
[61] M. Wójcik, J. Ph. Jay, P. Panissod, E. Jedryka, J. Dekoster, G. Langouche, *Z. Phys. B* **1997**, 103, 5–12.
[62] J. F. Jauak, *Phys. Rev. B* **1979**, 20, 2206–2208.
[63] P. Panissod, J. Ph. Jay, C. Mény, M. Wójcik, E. Jedryka, *Mater. Res. Soc. Proc.* **1995**, 384, 61–73,; Hyperfine Int. **1996**, 97–98, 75–98.
[64] A. J. Freeman and R. E. Watson in *Magnetism* (eds. G. T. Rado and H. Suhl), Academic Press, New York, **1965**, Vol. 2A, pp. 167–305.
[65] A. Narath in *Hyperfine interactions* (eds. A. J. Freeman and R. B. Frankel), Academic Press, New York, **1967**, pp. 287–363; R. L. Mössbauer, and M. J. Clauser ibid., **1967**, pp. 497–551.
[66] D. Stoeffler, *J. Magn. Magn. Mater.* **1997**, 165, 62–69.
[67] J. C. Slonczewski, *Phys. Rev. Lett.* **1991**, 67, 3172–3175; *J. Appl. Phys.* **1993**, 73, 5957–5962; *J. Magn. Magn. Mater.* **1995**, 150, 13–24.

[68] A. Dinia and K. Ounadjela, *J. Magn. Magn. Mater.* **1995**, 146, 66–76.
[69] A. C. Gossard, A. M. Portis, M. Rubinstein, R. H. Lindquist, *Phys. Rev.* **1965**, 138, 1415–1421.
[70] T. Thomson, H. Kubo, J. S. Lord, and P. C. Riedi, M. J. Walker, *J. Appl. Phys.* **1994**, 76,6504–6506.
[71] K. Le Dang, P. Veillet, C. Chappert, R. F. C. Farrow, R. F. Marks, and D. Weller, *Phys. Rev. B* **1993**, 48, 14023–14026.
[72] For NMR in ferromagnetic materials see: E. A. Turov and M. P. Petrov, *Nuclear Magnetic Resonance in Ferro and Antiferromagnets*, John Wiley and Sons, New York **1972**; A. V. Zalesskij, I. S. Zeludhev, *At. Energy Rev.* **1976**, 14, 133–172; M. A. H. McCausland, I. S. Mackenzie, *Adv. Phys.* **1979**, 28, 305–456.
[73] M. B Stearns, *Phys. Rev.* **1967**, 162, 496.
[74] C. Mény, thesis **1994** and J. Ph. Jay, thesis **1995**, Université Louis Pasteur, Strasbourg, France.
[75] P Panissod, C. Mény, M. Wójcik, E. Jedryka, *Mat. Res. Soc. Symp. Proc.* **1997**, 475, 157–168.
[76] D. Kubinski and H. J. Holloway, *J. Appl. Phys.* **1996**, 79, 1661–1663.
[77] P. Bruno, *Phys. Rev. B* **1995**, 52, 411.
[78] S. S. P. Parkin, N. More, and K. P. Roche, *Phys. Rev. Lett.* **1990**, 64, 2304–2307.
[79] A. Arbaoui, A. Dinia, and P. Panissod, *Solid State Commun.* **1993**, 85, 475–477.
[80] M. Rührig, R. Schäfer, A. Hubert, R. Mosler, J. A. Wolf, S. Demokritov, and P. Grünberg, *Phys. Stat. Sol. A* **1991**, 125, 635.
[81] Reviews on NMR in thin films and multilayers: W. J. M. de Jonge, H. A. M. de Gronckel, and K. Koppinga in *Ultrathin magnetic structures*, (eds. B. Heinrich and J. A. C. Bland), Springer Verlag, Heidelberg **1994**, vol. 2, pp. 279–290; P. P. Panissod in *Frontiers in magnetism of reduced dimension systems* (eds. V. G. Bar'yakhtar, P. E. Wigen, and N. A. Lesnik), Kluwer Academic, Dordrecht **1998**, Nato ASI series 3/49, pp 225–270; P. C. Riedi, T. Thomson, G. J. Tomka in *Handbook of magnetic materials* (ed. K. H. J. Buschow) Elsevier, Amsterdam **1999**, Vol. 12.

Magnetism: Molecules to Materials III. Edited by J.S. Miller and M. Drillon

ISBNs: 3-527-30302-2 (Hardback); 3-527-60014-0 (Electronic)

9 Interlayer Exchange Interactions in Magnetic Multilayers

P. Bruno

9.1 Introduction

Magnetic multilayers typically consist of alternate stacks of ferromagnetic and non-ferromagnetic spacer layers. The typical thickness of an individual layer ranges between a few atomic layers (AL) to a few tens of AL. The magnetic layers usually consist of elemental metallic ferromagnets (Fe, Co, Ni) or alloys thereof (e. g. permalloy). The spacer layers can consist of any transition or noble metal; they are either paramagnetic (Cu, Ag, Au, Ru, Pd, V, etc.) or antiferromagnetic (Cr, Mn).

Because of the spacer layers, the magnetic layers are, to first approximation, magnetically decoupled from each other, i. e. their basic magnetic properties such as magnetization, Curie temperature, magnetocrystalline anisotropy, magneto-optical response, etc., are essentially those of an individual layer. This approximation, however, is not sufficient for accurate descrition of the magnetism of multilayers, and one must consider the magnetic interactions which couple successive magnetic layers through spacer layers.

The various interactions giving rise to an interlayer magnetic interaction are: (i) the dipolar interaction and (ii) the indirect exchange interaction of the Ruderman–Kittel–Kasuya–Yosida (RKKY) type.

For a homogeneously magnetized layer consisting of a continuous medium, there is no dipolar stray field, so that dipolar interlayer coupling can arise only as a result of departures from this idealized situation. This is the case when one considers the real crystalline structure of the layer. It is, however, easy to show that the dipolar stray field decays exponentially as a function of the distance from the magnetic layer, with a decay length of the order of the lattice parameter, so that this effect is completely negligible compared with the interaction as a result of exchange, to be discussed below. Significant dipolar interlayer interactions can, nevertheless, arise from correlated roughness imperfections of the layers ("orange peel" effect) as first pointed out by Néel [1]. This effect, however, becomes negligible for the high quality multilayers that can be fabricated nowadays. Finally, dipolar interactions are important when the magnetic layers are not saturated and split into magnetic domains; this interaction leads in particular to a correlation between the magnetic domains of the successive magnetic layers. This phenomenon is, therefore, extrinsinc and we shall disregard it below by restricting ourselves to homogeneously magnetized layers.

The indirect exchange interaction has a completely different physical origin. It is mediated by conduction electrons which are scattered successively by the mag-

netic layers. Historically, this type of interaction was first proposed by Ruderman and Kittel to describe the indirect interactions between nuclear spins in a metal [2], and then extended to electronic magnetic moments by Kasuya [3] and Yosida [4]. This interaction has received a much attention, in particular in the context of dilute magnetic alloys. Neither theoretical predictions, nor the experiment results, were, however, sufficiently precise to enable fully understanding of this mechanism and quantitative testing of the theoretical predictions. Indirect exchange interactions have received intensly renewed attention since 1990 in the context of magnetic multilayers – indeed, in contrast with the situation of a dilute alloy, in which the distance between magnetic impurities is randomly distributed, multilayers enable controlled variation of the distance between successive magnetic layers and their crystallographic orientation; this enables a very detailled study of indirect exchange interactions.

In this chapter we present an overview of the state-of-the-art of our understanding of interlayer coupling as a result of indirect exchange interactions in transition metal multilayers. In Section 2 we give a short overview of the experimental observations. This is followed by an overview of the theoretical approaches that have been used to describe the interlayer exchange coupling (Section 3). Theoretical description based upon the idea of spin-dependent quantum confinement is presented in Section 4. The behavior obtained in the limit of large spacer thickness is discussed in Section 5, and the dependence of interlayer exchange coupling on magnetic layer thickness and on overlayer thickness are treated in Sections 6 and 7, respectively. The amplitude and phase of interlayer coupling oscillations are discussed in Section 8.

9.2 Survey of Experimental Observations

Interlayer magnetic interactions were first reported in rare-earth superlattices [5, 6]. Rare-earth multilayers will not, however, be considered here, and the reader is refered to recent review papers on this subject [7, 8].

For transition metals systems, antiferromagnetic interlayer exchange coupling in Fe/Cr/Fe layers was first reported by Grünberg et al. [9]. They observed an antiferromagnetic interlayer interaction, decaying regularly with increasing Cr spacer thickness. Phenomenologically, the interlayer interaction energy per unit area can be expressed as

$$E(\theta) = J \cos\theta, \tag{1}$$

where θ is the angle between the magnetizations of the two magnetic layers, and J is called the interlayer coupling coupling constant. With the sign convention adopted here, a positive (negative) value of J relates to an antiferromagnetic (ferromagnetic) type of coupling. One should pay attention to the fact that other conventions for the sign and normalization of the coupling constant are frequently found in the literature.

In practice, an antiferromagnetic interlayer interaction is easily revealed and measured by performing a magnetization measurement (or measurement of any property proportional to the magnetization, for example magneto-optical Kerr or Faraday effect) as a function of an applied magnetic field. In zero field, because of the antiferromagnetic interaction, the magnetization of successive magnetic layers is antiparallel to each other, resulting in zero remanent magnetization (if the magnetic moments of the layers are equivalent). When an external field is applied the Zeeman energy tends to align the magnetization of both layers in the field direction, so that the magnetization progressively increases until a saturation field is reached; the value of the latter gives a quantitative measure of the antiferromagnetic interaction strength. One should be aware, however, that it is not always easy to distinguish this behavior from the effect of magnetocrystalline anisotropy, or magnetic domains. Hence, for a convincing measurement it is necessary to perform a quantitative micromagnetic analysis of the influence of the latter effects [10, 11].

A ferromagnetic interaction is much more difficult to detect and measure quantitatively, because the application of an external magnetic field has no direct action on the mutual orientation of the magnetizations of the successive magnetic layers and thus cannot probe their mutual interaction. It is, nevertheless, possible to measure ferromagnetic interlayer interactions by means of magnetometry by using specially devised structures. This can be achieved by pinning the magnetization of one magnetic layer, leaving the other one free to align itself along an external magnetic field. The pinning of the magnetization of a ferromagnetic layer can be achieved by coupling it to an antiferromagnetic layer [12], or by coupling it to another ferromagnetic layer via a strong antiferromagnetic coupling [13], or by using a magnetic layer with a strong magnetic anisotropy and coercivity [14].

The discovery, by Parkin et al. [15], of spectacular oscillatory variation of the interlayer coupling depending on spacer layer thickness in Fe/Cr and Co/Ru multilayers has stimulated intense research activity in this field. Systematic studies by Parkin revealed, furthermore, that the oscillatory behavior is observed for spacer layers consisting of almost any transition or noble metal and is therefore essentially a universal feature of this phenomenon [16].

The generic behavior of oscillatory interlayer exchange coupling is an interaction which oscillates periodically in sign and magnitude, with an amplitude which decays as $1/D^2$, where D is the spacer thickness. The oscillation periods depend on the nature and crystalline orientation of the spacer metal, but not on the nature or thickness of the magnetic layers. Typical values of oscillation periods are between 2 and 10 AL. The strength of the interaction, on the other hand, depends both on the characteristics of the spacer and of the magnetic layers.

To enable very precise investigation of the dependence on thickness of the interlayer coupling and to avoid problems resulting from unsufficient reproducibility in sample growth conditions and layer thicknesse, Fuss et al. [17] introduced a new technique, which consists in using samples in which the spacer is prepared as a wedge of continuously varying (average) thickness, obtained by moving a shutter close to the sample during deposition. By using Kerr effect, magnetometry can be performed locally by scanning a focused laser on the sample. This ingenious method turned out

to be essential for successfully revealing full richness of thickness variation of the interlayer exchange coupling.

In particular, in confirmation of theoretical predictions (see below) it has been found experimentally that multiperiodic oscillatory coupling exists in Fe/Au(001)/Fe [17–19], Co/Cu(001)/Co [20–22], and Fe/Ag(001)/Fe [23] multilayers.

The dependence on spacer thickness of the coupling constant J can therefore generally be expressed as:

$$J = \sum_{\alpha} \frac{A_\alpha}{D^2} \sin\left(q_\alpha D + \phi_\alpha\right) \tag{2}$$

where the index α labels the various oscillatory components. The strength of interlayer exchange coupling, as expressed by A_α (which the dimension of an energy), is typically of the order of 1 to 10 meV, which (for a spacer thickness of 1 nm) corresponds to a value of the order of 0.1 to 1 mJ m^{-2} for the coupling constant J.

Although the greatest dependence on thickness is the dependence on spacer layer thickness, (weak) oscillatory dependence on magnetic layer thickness has been observed for the Co/Cu(001)/Co system by Bloemen et al. [24] and for the Fe/Cu(001)/Co system by Back et al. [25], and dependende on the thickness of a non-magnetic coverage layer has been observed for the Co/Cu(001)/Co system by de Vries et al. [26], for the Fe/Au(001)/Fe system by Okuno and Inomata [27], and for the Co/Au(111)/Co system by Bounouh et al. [28], in accordance with theoretical predictions (see below for a detailed discussion).

Although the most frequent behavior for the interlayer exchange coupling is of the form given by Eq. (1), Rührig et al. [29] have observed in the Fe/Cr(001)/Fe system a special kind of coupling in which the magnetization of successive magnetic layers tends to be perpendicular to each other, rather than either parallel or antiparallel, as follows from Eq. (1). This behavior can be understood if one assumes that the coupling is of the form

$$E(\theta) = J_1 \cos\theta + J_2 \cos^2\theta \tag{3}$$

In combination with the effect of cubic magnetocrystalline anisotropy, the above coupling can, indeed, lead to a 90 degree configuration for suitable values of the coupling constants J_1 and J_2. This effect has been observed in other systems also. This additional coupling contribution is often dubbed "biquadratic" coupling. Although such coupling can, in principle, arise from intrinsic mechanism, this effect is usually too small to explain the experimental observations, and it is believed that other (extrinsic) mechanisms related to structural defects are responsible. This effect will not be considered further in this paper; the interested reader can find up-to-date discussions on this topic in recent review papers [30, 31].

Note that interlayer exchange coupling has been observed not only for metallic spacer layers, but also for semiconducting spacer layers [32–35]. This effect is, however, believed to have a mechanism different from that operating for metallic spacer layers, and will not be discussed further here.

9.3 Survey of Theoretical Approaches

9.3.1 RKKY Theory

The striking similarity between the oscillatory behavior observed experimentally and that obtained from the RKKY interaction between magnetic impurities suggests, of course, that the two phenomena have a common mechanism. This prompted researchers to attempt to describe interlayer exchange coupling by adapting the RKKY theory [36–40].

This approach rapidly achieved significant success. In particular, Yafet [36] first explained the oscillatory behavior and the $1/D^2$ decay law (compared with a $1/D^3$ decay obtained for the RKKY interaction between impurities). Extending the theory to take proper account of the real electronic structure of the spacer material (as opposed to the free electron approximation used so far), Bruno and Chappert [38, 39] derived the selection rule giving the oscillation period(s) of the oscillatory coupling in terms of the (bulk) Fermi surface of the spacer. By applying this selection rule, they calculated the oscillation periods for noble metal spacers; their results (including the prediction of multiperiodic oscillations) were soon confirmed quantitatively by experiment (see discussion below), giving strong support to the RKKY theory. Because of the approximations used, however, the RKKY theory did not enable quantitative description the amplitude and phase of the oscillatory coupling.

9.3.2 Quantum Well Model

Independently, an (apparently) different mechanism was soon proposed by Edwards et al. [41] and by other authors [42–45]. In this approach the coupling is ascribed to the change of density of states resulting from the spin-dependent confinement of the electrons (or holes) in the quantum well provided by the spacer layer. Remarkably, this approach yielded exactly the same oscillatory behavior and decay as the RKKY interaction. On the other hand, the description of the amplitude and phase was more satisfactory, although early attempts to calculate these were based on assumptions that were too crude (free electron model, single tight-binding model) to yield realistic quantitative results. More realistic calculations have subsequently been performed on the basis of the quantum-well model [46–48].

9.3.3 *sd*-Mixing Model

Yet another approach was based upon the *sd*-mixing model [49–51], proposed earlier by Anderson [52] and Caroli [53] to described the interaction between magnetic impurities in metals. This approach yielded the same result as the RKKY theory for the oscillation periods and decay law of the coupling. Description of the amplitude and phase of the coupling was more physical than that provided by the RKKY theory. Bruno [51], in particular, showed that the amplitude and phase in terms of a (suitably

adapted) Friedel sum rule [54] for the magnetization and charge of an the magnetic "impurities."

9.3.4 Unified Picture in Terms of Quantum Interferences

The coexistence of a variety of apparently different mechanisms predicting essentially similar behavior for the coupling led to a somewhat puzzling and controversial situation regarding the true nature of the mechanism of interlayer exchange coupling. This puzzle was solved when Bruno [55, 56] and subsequently Stiles [57] showed that the different approaches indeed corresponded to different approximations of a same mechanism. They reformulated it in a physically appealing picture in which the amplitude and phase of the oscillatory coupling are expressed in terms of the amplitude and phase of reflection coefficients for the electrons at the interfaces between the spacer and the magnetic layers.

This approach has been used by several authors to perform quantitative calculations for realistic systems [58–60].

Furthermore, thanks to its physical transparency, this approach has enabled qualitative prediction of new behavior, for example oscillations depending on magnetic layer thickness [61] and on overlayer thickness [62].

9.3.5 First-principles Calculations

Finally, numerous authors have performed first-principles calculations of interlayer exchange coupling for realistic systems [63–72]. Besides modeling the approaches mentioned above, first-principles calculation plays a very important rôle in elucidating the mechanism of interlayer exchange coupling: on one hand, it provides a test of the qualitative predictions of the simplified models, while on the other hand it yields quantitative predictions for realistic systems than can be compared critically with experimental observations. The most widely investigated system is the Co/Cu/Co(001) system, which has served as a benchmark for the theory of interlayer exchange coupling. While early attemps yielded doubtful results, essentially because of the great difficulty of such numerical calculation, the most recent results have given results than can be considered satisfactory in many respects (see discussion below).

9.4 Quantum Confinement Theory of Interlayer Exchange Coupling

The purpose of this section is to present as simply as possible the mechanism of interlayer exchange coupling in terms of quantum interferences as a result of electron confinement in the spacer layer. The emphasis here will be on physical concepts rather than on mathematical rigor. This discussion is based on that given in Ref. [74].

9.4.1 Elementary Discussion of Quantum Confinement

For the sake of clarity, we shall first consider an extremely simplified model, namely the one-dimensional quantum well, which nevertheless contains the essential physics involved in the problem. We shall then progressively refine the model to make it more realistic.

The model consists in a one-dimensional quantum well representing the spacer layer (of potential $V = 0$ and width D), sandwiched between two "barriers" A and B of respective widths L_A and L_B, and respective potentials V_A and V_B. Note that we use the term "barrier" in a general sense, i. e., V_A and V_B are not necessarily positive. The barrier widths, L_A and L_B, can, furthermore, be finite or infinite, without any restriction.

9.4.1.1 Change of the Density of States as a Result of Quantum Interferences

Let us consider an electron of wavevector k^+ (with $k^+ > 0$) propagating towards the right in the spacer layer; as this electrons arrives at barrier B, it is partially reflected to the left, with a (complex) amplitude $r_B \equiv |r_B|e^{i\phi_B}$. The reflected wave of wavevector k^- is in turn reflected from barrier A with an amplitude $r_A \equiv |r_A|e^{i\phi_A}$, an so on. (For the one-dimensional model, of course, $k^- = -k^+$; this property will, however, generally not be true for three-dimensional systems to be studied below.) The module $|r_{A(B)}|$ of the reflection coefficient expresses the magnitude of the reflected wave, whereas the argument $\phi_{A(B)}$ represents the phase shift resulting from the reflection (note that the latter is not absolutely determined and depends on the choice of the coordinate origin).

The interferences between the waves as a result of the multiple reflections on the barriers induce a modification of the density of states in the spacer layer, for the electronic state under consideration. The phase shift resulting from a complete round trip in the spacer is

$$\Delta\phi = q\,D + \phi_A + \phi_B \tag{4}$$

with

$$q \equiv k^+ - k^- \tag{5}$$

If the interferences are constructive, i. e., if:

$$\Delta\phi = 2n\pi \tag{6}$$

where n is an integer, one has an increase in the density of states; conversely, if the interferences are destructive, i. e., if

$$\Delta\phi = (2n+1)\pi \tag{7}$$

one has a reduction in the density of states. Thus, to a first approximation, we expect the modification of the density of states in the spacer, $\Delta n(\varepsilon)$, to vary with D in the manner:

$$\Delta n(\varepsilon) \approx \cos\left(qD + \phi_{\mathrm{A}} + \phi_{\mathrm{B}}\right). \tag{8}$$

We expect, furthermore, that this effect will proportional to the amplitude of the reflections at barriers A and B, i. e., to $|r_{\mathrm{A}} r_{\mathrm{B}}|$; finally, $\Delta n(\varepsilon)$ must be proportional to the width, D, of the spacer and to the density of states per unit energy and unit width:

$$\frac{2}{\pi}\frac{\mathrm{d}q}{\mathrm{d}\varepsilon} \tag{9}$$

which includes a factor of 2 for spin degeneracy. We can also include the effect of higher-order interferences, because of n round trips in the spacer; the phase shift $\Delta\phi$ is then multiplied by n and $|r_{\mathrm{A}} r_{\mathrm{B}}|$ is replaced by $|r_{\mathrm{A}} r_{\mathrm{B}}|^n$. Gathering all the terms, we obtain:

$$\begin{aligned}
\Delta n(\varepsilon) &\approx \frac{2D}{\pi}\frac{\mathrm{d}q}{\mathrm{d}\varepsilon}\sum_{n=1}^{\infty} |r_{\mathrm{A}} r_{\mathrm{B}}|^n \cos n\left(qD + \phi_{\mathrm{A}} + \phi_{\mathrm{B}}\right) \\
&= \frac{2}{\pi}\,\mathrm{Im}\left(\mathrm{i}D\frac{\mathrm{d}q}{\mathrm{d}\varepsilon}\sum_{n=1}^{\infty}(r_{\mathrm{A}} r_{\mathrm{B}})^n\ \mathrm{e}^{niqD}\right) \\
&= \frac{2}{\pi}\,\mathrm{Im}\left(\mathrm{i}\frac{\mathrm{d}q}{\mathrm{d}\varepsilon}\frac{r_{\mathrm{A}} r_{\mathrm{B}}\,\mathrm{e}^{\mathrm{i}qD}}{1 - r_{\mathrm{A}} r_{\mathrm{B}}\,\mathrm{e}^{\mathrm{i}qD}}\right)
\end{aligned} \tag{10}$$

As will appear clearly below, it is more convenient to consider the integrated density of states:

$$N(\varepsilon) \equiv \int_{-\infty}^{\varepsilon} n(\varepsilon')\,\mathrm{d}\varepsilon'. \tag{11}$$

The modification $\Delta N(\varepsilon)$ of the integrated density of states because of electron confinement is:

$$\begin{aligned}
\Delta N(\varepsilon) &= \frac{2}{\pi}\,\mathrm{Im}\sum_{n=1}^{\infty}\frac{(r_{\mathrm{A}} r_{\mathrm{B}})^n}{n}\,\mathrm{e}^{niqD} \\
&= -\frac{2}{\pi}\,\mathrm{Im}\ \ln\left(1 - r_{\mathrm{A}} r_{\mathrm{B}}\,\mathrm{e}^{\mathrm{i}qD}\right)
\end{aligned} \tag{12}$$

A simple graphical interpretation of the above expression can be obtained by noting that $\mathrm{Im}\ \ln(z) = \mathrm{Arg}\,(z)$, for z complex; thus, $\Delta N(\varepsilon)$ is given by the argument, in the complex plane, of a point located at an angle $\Delta\phi = qD + \phi_{\mathrm{A}} + \phi_{\mathrm{B}}$ on a circle of radius $|r_{\mathrm{A}} r_{\mathrm{B}}|$ centred in Fig. 1. This graphical construction is shown in Fig. 1.

The variation of $\Delta N(\varepsilon)$ as a function of D is shown in Fig. 2, for different values of the confinement strength $|r_{\mathrm{A}} r_{\mathrm{B}}|$. For weak confinement (a), $\Delta N(\varepsilon)$ varies with D in sinusoidal manner. As one the confinement strength is increased (b), the oscillations are distorded, because of higher-order interferences. Finally, for full confinement (c), $\Delta N(\varepsilon)$ contains jumps that correspond to the appearance of bound states. We note, however, that the period, Λ, of the oscillations of $\Delta N(\varepsilon)$ does not depend on the confinement strength, but only on the wavevector $q \equiv k^+ - k^-$, i. e. $\Lambda = 2\pi/q$.

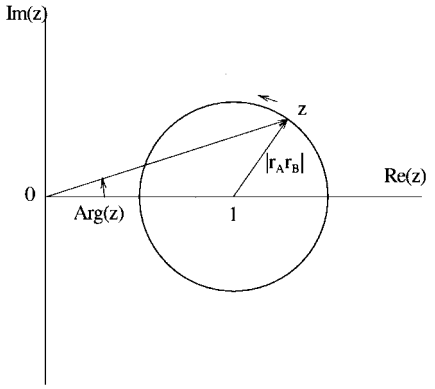

Fig. 1. Graphical interpretation of Eq. (12).

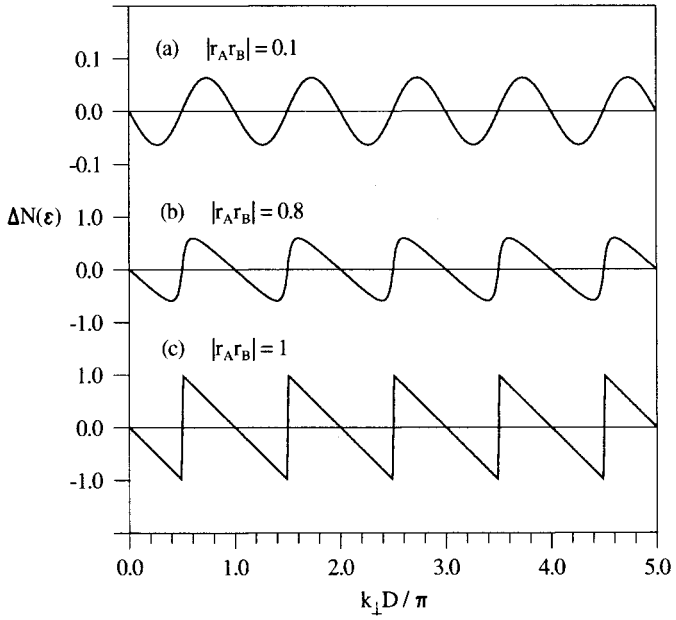

Fig. 2. Variation of $\Delta N(\varepsilon)$ as a function of D, for different values of the confinement strength: (a) $|r_A r_B| = 0.1$, (b) $|r_A r_B| = 0.8$, (c) $|r_A r_B| = 1$ (full confinement). Note the different scales along the ordinate axis.

So far, we have implicitely restricted ourselves to positive energy states. Negative energy states (i. e., of imaginary wavevector) are forbidden in the absence of barriers A and B, because their amplitude diverges either on the right or on the left, so that they cannot be normalized. This matter of fact is no longer-true in the presence of the barriers if V_A (or V_B, or both V_A and V_B) is negative – the negative energy states, i. e. varying exponentially in the spacer, can be connected to allowed states of A or B. To treat these states consistently we simply have to extend the concept of reflection

coefficient to states of an imaginary wavevector, which is straightforward. One can check that, with this generalization, Eq. (12) acounts properly for the contribution of the evanescent states. Physically, this can be interpretated as coupling of A and B by a tunnel effect [73, 74].

9.4.1.2 Energy Associated with the Quantum Interferences in the Spacer

Let us now study the modification of the energy of the system which results from the quantum interferences. To conserve the total number of electrons it is convenient to work within the grand-canonical ensemble, and to consider the thermodynamic grand-potential, which is given by:

$$\begin{aligned}\Phi &\equiv -k_{\mathrm{B}}T\int_{-\infty}^{+\infty}\ln\left[1+\exp\left(\frac{\varepsilon_F-\varepsilon}{k_{\mathrm{B}}T}\right)\right]n(\varepsilon)\,\mathrm{d}\varepsilon\\ &= -\int_{-\infty}^{+\infty}N(\varepsilon)\,f(\varepsilon)\,\mathrm{d}\varepsilon.\end{aligned}\tag{13}$$

At $T=0$, this reduces to:

$$\begin{aligned}\Phi &\equiv \int_{-\infty}^{\varepsilon_F}(\varepsilon-\varepsilon_F)\;n(\varepsilon)\,\mathrm{d}\varepsilon\\ &= -\int_{-\infty}^{\varepsilon_F}N(\varepsilon)\,\mathrm{d}\varepsilon\end{aligned}\tag{14}$$

The energy ΔE associated with the interferences is the contribution to Φ corresponding to $\Delta N(\varepsilon)$:

$$\Delta E=\frac{2}{\pi}\,\mathrm{Im}\int_{-\infty}^{+\infty}\ln\left(1-r_{\mathrm{A}}r_{\mathrm{B}}\,\mathrm{e}^{\mathrm{i}qD}\right)\,\mathrm{d}\varepsilon.\tag{15}$$

9.4.1.3 Three-dimensional Layered System

Generalization of the above discussion to the more realistic case of a three-dimensional layered system is immediate. Because the system is invariant by translation parallel to the plane, the in-plane wavevector $\mathbf{k}_\parallel$ is a good quantum number. Thus, for a given $\mathbf{k}_\parallel$, one has an effective one-dimensional problem analogous to that discussed above. The resulting effect of quantum intereferences is obtained by summing on $\mathbf{k}_\parallel$ over the two-dimensional Brillouin zone. The modification of the integrated density of states per unit area is:

$$\Delta N(\varepsilon)=-\frac{1}{2\pi^3}\,\mathrm{Im}\int\mathrm{d}^2\mathbf{k}_\parallel\,\ln\left(1-r_{\mathrm{A}}r_{\mathrm{B}}\,\mathrm{e}^{\mathrm{i}q_\perp D}\right)\tag{16}$$

and the interference energy per unit area is:

$$\Delta E=\frac{1}{2\pi^3}\,\mathrm{Im}\int\mathrm{d}^2\mathbf{k}_\parallel\int_{-\infty}^{+\infty}f(\varepsilon)\,\ln\left(1-r_{\mathrm{A}}r_{\mathrm{B}}\,\mathrm{e}^{\mathrm{i}q_\perp D}\right)\,\mathrm{d}\varepsilon\tag{17}$$

9.4.1.4 Quantum Size Effect in an Overlayer

A thin overlayer deposited on a substrate is a system of considerable interest. One of the barriers (say, A) is the vacuum, and barrier B is the substrate itself. The potential of the vacuum barrier is $V_{\text{vac}} = \varepsilon_F + W$, where W is the the work function; thus it is perfectly reflecting for occupied states, i. e. $|r_{\text{vac}}| = 1$. The reflection on the substrate (or coefficent r_{sub}) can, on the other hand, be total or partial, depending on the band matching for the state under consideration.

The spectral density of the occupied states in the overlayer can be investigated experimentally by photoemission spectroscopy; in addition, by using inverse photoemission one can study the unoccupied states. If, furthermore, these techniques are used in the "angle-resolved" mode, they give information about the spectral density *locally in the* $\mathbf{k}_\parallel$ *plane*.

For an overlayer of given thickness, the photoemission spectra (either direct or inverse) contain maxima and minima corresponding, respectively, to the energies for which the interferences are constructive and destructive. When the confinement is total, narrow peaks can be observed; these correspond to the quantized confined states in the overlayer, as was pointed out by Loly and Pendry [75].

Quantum size effects arising because of electron confinement in the photoemission spectra of overlayers have been observed in a variety of non-magnetic systems [76–84]. The systems Au(111)/Ag/vacuum and Cu(111)/Ag/vacuum, in particular, are excellent examples of this phenomenon [81, 83].

9.4.1.5 Paramagnetic Overlayer on a ferromagnetic Substrate – Spin-polarized Quantum Size Effect

So far our discussion has been concerned with non-magnetic systems exclusively. Qualitatively new behavior can be expected when some of the layers are ferromagnetic. An example of particular interest is that of a paramagnetic overlayer on a ferromagnetic substrate.

In the interior of the overlayer the potential is independent of the spin; the propagation of electrons is, therefore, described by a wavevector $k_\perp$, which is spin-independent. The reflection coefficient on the vacuum barrier, r_{vac}, is also spin-independent. The ferromagnetic substrate, however, constitutes a spin-dependent potential barrier; thus the substrate reflection coefficients for electrons with a spin parallel to the majority and minority spin directions of the substrate are, respectively, $r_{\text{sub}}^{\uparrow}$ and $r_{\text{sub}}^{\downarrow}$. It is convenient to define the spin average:

$$\overline{r}_{\text{sub}} \equiv \frac{r_{\text{sub}}^{\uparrow} + r_{\text{sub}}^{\downarrow}}{2} \tag{18}$$

and the spin asymmetry:

$$\Delta r_{\text{sub}} \equiv \frac{r_{\text{sub}}^{\uparrow} - r_{\text{sub}}^{\downarrow}}{2}. \tag{19}$$

In this case the electron confinement in the overlayer gives rise to a spin-dependent modulation of the spectral density as the overlayer thickness is changed; the period of the modulation is the same for both spins, whereas the amplitude and phase are expected to be spin-dependent.

The quantum size effects in paramagnetic overlayers on a ferromagnetic substrate have been investigated by several groups [85–98]. The systems studied most are Cu overlayers on a Co(001) substrate and Ag overlayers on a Fe(001) substrate. Ortega and Himpsel [86, 87] observed a quantum size effect in the normal-emission photoelectron spectra of a copper overlayer on a fcc cobalt (001) substrate. They observed peaks arising as a result of quantum size effects, and an oscillation of the photoemission intensity in both, the photoemission and in the inverse photoemission spectra. These quantum size effects manifest themselves also in the form of oscillatory behavior in the photoemission intensity at the Fermi level; because the observed oscillation period (5.9 atomic layers) is close to the long period of interlayer exchange coupling oscillations in Co/Cu(001)/Co, it was suggested that the two phenomena should be related to each other: Ortega and Himpsel also claimed that the observed oscillations in photoemission are spin-dependent and mostly arise from minority electrons. This conjecture has been confirmed directly, by Garrison et al. [89] and by Carbone et al. [90], independently, by means of spin-polarized photoemission. They found that both the intensity and the spin-polarization have oscillatory behavior with the same period (5–6 atomic layers) but opposite phases; this indicates that the quantum-size effect does indeed take place predominantly in the minority-spin band, as proposed by Ortega and Himpsel [86, 87]. Kläsges et al. [96] and Kawakami et al. [98] have recently observed spin-polarized quantum-size effects in a copper overlayer on cobalt (001) for a non-zero, in-plane wavevector corresponding to the short period oscillation of interlayer exchange coupling in Co/Cu(001)/Co; they observed short-period oscillations of the photoemission intensity, in good agrement with the short-period oscillations of interlayer coupling. This observation provides a further confirmation of the relationship between quantum-size effects in photoemission and oscillation of interlayer exchange coupling.

Photoemission studies of quantum size effects have also been performed on other types of system, e. g. a ferromagnetic overlayer on a non-magnetic substrate, or systems comprising more layers [99–103].

Photoemission spectroscopy undoubtedly constitutes a method of choice for investigating quantum-size effects in metallic overlayers; this is because its unique features enable selectivity in energy, in-plane wavevector, and spin.

Besides photemission, spin-polarized quantum-size effects in paramagnetic overlayers on a ferromagnetic substrate also cause oscillatory behavior (which depends on overlayer thickness) of spin-polarized secondary electron emission [104, 105], linear [106–111], and non-linear [112, 113] magneto-optical Kerr effect, and magnetic anisotropy [114, 115]. These effects usually, however, involve a summation over all electronic states, and so quantitative analysis of these quantum-size effects may be fairly complicated.

9.4.2 Interlayer Exchange Coupling Because of Quantum Interferences

Let us now consider a paramagnetic layer sandwiched between two ferromagnetic barriers A and B. The reflection coefficients on both sides of the paramagnetic spacer layer are now spin dependent. A priori the angle, θ, between the magnetizations of the two ferromagnetic barriers can take any value; for the sake of simplicity, however, we shall restrict ourselves here to the ferromagnetic (F) (i.e. $\theta = 0$) and the antiferromagnetic (AF) (i. e. $\theta = \pi$) configurations.

For the ferromagnetic configuration, the energy change per unit area because of quantum interference is easily obtained from Eq. (17), i. e.:

$$\Delta E_F = \frac{1}{4\pi^3}\,\mathrm{Im}\int \mathrm{d}^2\mathbf{k}_\parallel \int_{-\infty}^{+\infty} f(\varepsilon) \times \left[\ln\left(1 - r_\mathrm{A}^{\uparrow} r_\mathrm{B}^{\uparrow} \mathrm{e}^{\mathrm{i}q_\perp D}\right) + \ln\left(1 - r_\mathrm{A}^{\downarrow} r_\mathrm{B}^{\downarrow} \mathrm{e}^{\mathrm{i}q_\perp D}\right)\right] \mathrm{d}\varepsilon \tag{20}$$

In this equation the first and the second terms correspond, respectively, to majority- and minority-spin electrons. The antiferromagnetic conguration is obtained by reversing the magnetization of B, i. e. by interchanging $r_\mathrm{B}^{\uparrow}$ and $r_\mathrm{B}^{\downarrow}$; thus the corresponding energy per unit area is:

$$\Delta E_{AF} = \frac{1}{4\pi^3}\,\mathrm{Im}\int \mathrm{d}^2\mathbf{k}_\parallel \int_{-\infty}^{+\infty} f(\varepsilon) \times \left[\ln\left(1 - r_\mathrm{A}^{\uparrow} r_\mathrm{B}^{\downarrow} \mathrm{e}^{\mathrm{i}q_\perp D}\right) + \ln\left(1 - r_\mathrm{A}^{\downarrow} r_\mathrm{B}^{\uparrow} \mathrm{e}^{\mathrm{i}q_\perp D}\right)\right] \mathrm{d}\varepsilon \tag{21}$$

Thus, the interlayer exchange coupling energy is

$$E_F - E_{AF} = \frac{1}{4\pi^3}\,\mathrm{Im}\int \mathrm{d}^2\mathbf{k}_\parallel \int_{-\infty}^{+\infty} f(\varepsilon) \times \ln\left[\frac{\left(1 - r_\mathrm{A}^{\uparrow} r_\mathrm{B}^{\uparrow} \mathrm{e}^{\mathrm{i}q_\perp D}\right)\left(1 - r_\mathrm{A}^{\downarrow} r_\mathrm{B}^{\downarrow} \mathrm{e}^{\mathrm{i}q_\perp D}\right)}{\left(1 - r_\mathrm{A}^{\uparrow} r_\mathrm{B}^{\downarrow} \mathrm{e}^{\mathrm{i}q_\perp D}\right)\left(1 - r_\mathrm{A}^{\downarrow} r_\mathrm{B}^{\uparrow} \mathrm{e}^{\mathrm{i}q_\perp D}\right)}\right] \mathrm{d}\varepsilon \tag{22}$$

which can be simplified to:

$$E_F - E_{AF} \approx -\frac{1}{\pi^3}\,\mathrm{Im}\int \mathrm{d}^2\mathbf{k}_\parallel \int_{-\infty}^{\infty} f(\varepsilon)\,\Delta r_\mathrm{A}\Delta r_\mathrm{B}\,\mathrm{e}^{\mathrm{i}q_\perp D}\,\mathrm{d}\varepsilon \tag{23}$$

in the limit of weak confinement. The above expression for the IEC has a rather transparent physical interpretation. First, as the integrations on $\mathbf{k}_\parallel$ over the first two-dimensional Brillouin zone and on the energy up to the Fermi level show, the IEC is a sum of contributions from all occupied electronic states. The contribution of a given electronic state, of energy ε and in-plane wavevector $\mathbf{k}_\parallel$, consists of the product of three factors – the two factors Δr_A and Δr_B express the spin-asymmetry of the confinement, because of the magnetic layers A and B, respectively, whereas the exponential factor $\mathrm{e}^{iq_\perp D}$ describes the propagation through the spacer and is responsible for the interference (or quantum-size) effect. Thus, this approach establishes

an explicit and direct link between oscillatory IEC and quantum size effects such as are observed in photoemission.

9.5 Asymptotic Behavior for Large Spacer Thicknesses

In the limit of large spacer thickness, D, the exponential factor oscillates rapidly with ε and $\mathbf{k}_\parallel$, which leads to substantial cancellation of the contributions to the IEC because of the different electronic states. Because the integration over energy is abruptly stopped at ε_F, however, states located at the Fermi level give predominant contributions. Thus the integral on ε can be calculated by fixing all other factors to their value at ε_F, and by expanding $q_\perp \equiv k_\perp^+ - k_\perp^-$ around ε_F, i. e.:

$$q_\perp \approx q_{\perp F} + 2\frac{\varepsilon - \varepsilon_\mathrm{F}}{\hbar v_{\perp F}^{+-}}, \tag{24}$$

with:

$$\frac{2}{v_{\perp F}^{+-}} \equiv \frac{1}{v_{\perp F}^{+}} - \frac{1}{v_{\perp F}^{-}}. \tag{25}$$

The integration (see Ref. [74] for details) yields:

$$\begin{aligned} E_\mathrm{F} - E_{AF} = \frac{1}{2\pi^3}\,\mathrm{Im}\int \mathrm{d}^2\mathbf{k}_\parallel\, \frac{i\hbar v_{\perp F}^{+-}}{D}\,\Delta r_\mathrm{A}\Delta r_\mathrm{B} e^{iq_{\perp F}D} \\ \times F(2\pi\, k_\mathrm{B} T\, D/\hbar v_{\perp F}^{+-}), \end{aligned} \tag{26}$$

where:

$$F(x) \equiv \frac{x}{\sinh x}. \tag{27}$$

In the above equations, $q_{\perp F}$ is a vector spanning the *complex Fermi surface*; the velocity $v_{\perp F}^{+-}$ is a combination of the group velocities at the points $(\mathbf{k}_\parallel, k_{\perp F}^{+})$ and $(\mathbf{k}_\parallel, k_{\perp F}^{-})$ of the Fermi surface.

Next, the integration on $\mathbf{k}_\parallel$ is performed by noting that for large spacer thickness D the only significant contributions arise from the neighboring critical vectors $\mathbf{k}_\parallel^\alpha$ for which $q_{\perp F}$ is stationary. Around such vectors, $q_{\perp F}$ may be expanded as

$$q_{\perp F} = q_{\perp F}^\alpha - \frac{\left(k_x - k_x^\alpha\right)^2}{\kappa_x^\alpha} - \frac{\left(k_y - k_y^\alpha\right)^2}{\kappa_y^\alpha} \tag{28}$$

where the crossed terms have been canceled by proper choice of the x and y axes; κ_x^α and κ_y^α are combinations of the curvature radii of the Fermi surface at $(\mathbf{k}_\parallel^\alpha, k_\perp^{+\alpha})$ and $(\mathbf{k}_\parallel^\alpha, k_\perp^{-\alpha})$.

The integral is calculated by using the stationary phase approximation [74], and one obtains:

$$E_{\mathrm{F}} - E_{AF} = \mathrm{Im} \sum_{\alpha} \frac{\hbar v_{\perp}^{\alpha} \kappa_{\alpha}}{2\pi^2 D^2} \Delta r_{\mathrm{A}}^{\alpha} \Delta r_{\mathrm{B}}^{\alpha} e^{i q_{\perp}^{\alpha} D} \times F(2\pi k_{\mathrm{B}} T D/\hbar v_{\perp}^{\alpha}) \tag{29}$$

where $q_{\perp}^{\alpha}$, $v_{\perp}^{\alpha}$, $\Delta r_{\mathrm{A}}^{\alpha}$, $\Delta r_{\mathrm{B}}^{\alpha}$ correspond to the critical vector $\mathbf{k}_{\parallel}^{\alpha}$, and:

$$\kappa_{\alpha} \equiv \left(\kappa_x^{\alpha}\right)^{1/2} \left(\kappa_y^{\alpha}\right)^{1/2} \tag{30}$$

in Eq. (30), one takes the square root with an argument between 0 and π.

This analysis shows that *in fine*, the only remaining contributions in the limit of large spacer thickness D arise from the neighborhood of states having in-plane wavevectors $\mathbf{k}_{\parallel}^{\alpha}$ such that the spanning vector of the Fermi surface $q_{\perp F} = k_{\perp F}^{+} - k_{\perp F}^{-}$ is stationary with respect to $\mathbf{k}_{\parallel}$ for $\mathbf{k}_{\parallel} = \mathbf{k}_{\parallel}^{\alpha}$, and the corresponding contribution oscillates with a wavevector equal to $q_{\perp F}^{\alpha}$. This selection rule was first derived in the context of the RKKY model [117]; it is illustrated in Fig. 3. There may be several such stationary spanning vectors and, hence, several oscillatory components; they are labelled by the index α.

The above selection rule enables prediction of the dependence of the oscillation period(s) of the interlayer exchange coupling on spacer thickness, merely by inspecting the bulk Fermi surface of the spacer material. In view of an experimental test of these predictions, noble metal spacer layers seem to be the best suited candidates; there are several reasons for this choice:

- Fermi surfaces of noble metals are known very accurately from de Haas-van Alphen and cyclotron resonance experiments [116];
- because only the *sp* band intersects the Fermi level, the Fermi surface is rather simple, and does not depart very much from a free-electron Fermi sphere; and
- samples of very good quality with noble metals as a spacer layer could be prepared.

Fig. 4 shows a cross-section of the Fermi surface of Cu, indicating the stationary spanning vectors for the (001), (111), and (110) crystalline orientations [117]; the Fermi surfaces of Ag and Au are qualitatively similar. For the (111) orientation, a single (long) period is predicted; for the (001) orientation, both a long period and a

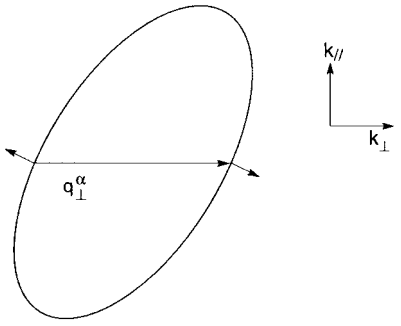

Fig. 3. Sketch showing the wavevector $q_{\perp}^{\alpha}$ giving the oscillation period of the oscillatory interlayer exchange coupling for a non-spherical Fermi surface.

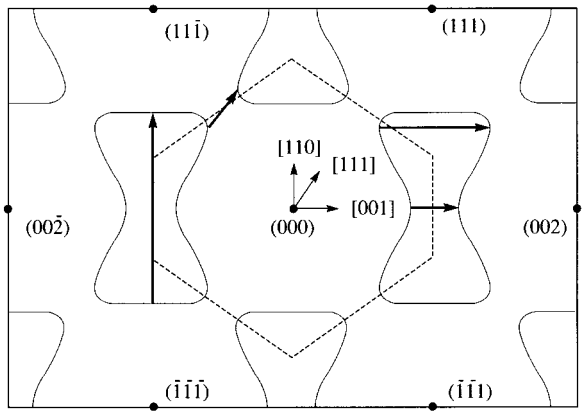

Fig. 4. Cross-section of the Fermi surface of Cu along the (1$\bar{1}$0) plane passing through the origin. The solid dots indicate the reciprocal lattice vectors. The dashed lines indicate the boundary of the first Brillouin zone. The horizontal, oblique, and vertical, solid arrows indicate the vectors $q_{\perp}^{\alpha}$ giving the oscillation period(s) for the (001), (111), and (110) orientations, respectively.

short period are predicted; for the (110) orientation, four different periods are predicted (only one stationary spanning vector is seen in Fig. 4, the three others being located in other cross-sections of the Fermi surface). These theoretical predictions have been confirmed successfully by numerous experimental observations. In particular, the coexistence of a long and a short period for the (001) orientation has been confirmed for Cu [20–22, 98, 122], Ag [23], and Au [17–19]; and the experimental periods have been found to be in excellent agreement with the theoretical predictions. Theoretically predicted and experimentally observed oscillation periods in Table 1.

Table 1. Comparison of the theoretical predictions of Ref. [117] with experimental observations of the dependence of oscillation periods of interlayer exchange coupling on spacer thickness.

Spacer	Theoretical periods	System	Experimental periods	Ref.
Cu(111)	$\Lambda = 4.5$ AL	Co/Cu/Co(111)	$\Lambda \approx 5.$ AL	[118]
		Co/Cu/Co(111)	$\Lambda \approx 6.$ AL	[119]
		Fe/Cu/Fe(111)	$\Lambda \approx 6.$ AL	[120]
Cu(001)	$\Lambda_1 = 2.6$ AL	Co/Cu/Co(001)	$\Lambda \approx 6.$ AL	[121]
	$\Lambda_2 = 5.9$ AL	Co/Cu/Co(001)	$\Lambda_1 \approx 2.6$ AL	[20]
			$\Lambda_2 \approx 8.$ AL	
		Co/Cu/Co(001)	$\Lambda_1 \approx 2.7$ AL	[22]
			$\Lambda_2 \approx 6.1$ AL	
		Fe/Cu/Fe(001)	$\Lambda \approx 7.5$ AL	[106]
Ag(001)	$\Lambda_1 = 2.4$ AL	Fe/Ag/Fe(001)	$\Lambda_1 \approx 2.4$ AL	[23]
	$\Lambda_2 = 5.6$ AL		$\Lambda_2 \approx 5.6$ AL	
Au(001)	$\Lambda_1 = 2.5$ AL	Fe/Au/Fe(001)	$\Lambda_1 \approx 2.$ AL	[17]
	$\Lambda_2 = 8.6$ AL		$\Lambda_2 \approx 7$–8 AL	
		Fe/Au/Fe(001)	$\Lambda_1 \approx 2.5$ AL	[18, 19]
			$\Lambda_2 \approx 8.6$ AL	
Au(111)	$\Lambda = 4.8$ AL	Co/Au/Co(111)	$\Lambda \approx$ 4.5 AL	[14]

In a further attempt to test theoretical predictions of the periods of oscillatory coupling, several groups [123–125] have undertaken to modify, in a controlled manner, the size of the Fermi surface (and hence, the period of the coupling) by alloying the spacer noble metal (Cu) with a metal of lower valence (Ni); in both experiments, the change in oscillation period as a result of alloying has been found to be in good agreement with the expected change in the Fermi surface.

9.6 Effect of Magnetic Layer Thickness

As already mentioned, the influence of the IEC on the ferromagnetic layer thickness is contained in the reflection coefficients Δr_A and Δr_B. If the ferromagnetic layers are of finite thickness, reflections usually occur at the two interfaces bounding the ferromagnetic layers, giving rise to interferences [61] and, hence, to oscillations of the IEC which depend on ferromagnetic layer-thickness. A more detailed discussion of this effect is given in Refs. [74, 61]. This behavior was first predicted from calculations based on a free-electron model [126]. The dependence of the amplitude of the oscillations of the IEC on ferromagnetic layer-thickness is generally much smaller than the dependence on spacer thickness, and does not give rise to changes of the sign of the IEC. Experimentally this effect was confirmed by Bloemen et al. [24] for Co/Cu/Co(001) and by Back et al. [25] for Fe/Cu/Co(001). It has also been confirmed theoretically by Nordström et al. [127], Lang et al. [128], Drchal et al. [129], and Lee and Chang [59].

9.7 Effect of Overlayer Thickness

More surprising behavior (at first sight) is the dependence of the IEC on the thickness of an external overlayer. One might naïely believe that layers external to the basic ferromagnet/spacer/ferromagnet sandwich should not influence the interaction between the two ferromagnetic layers. This view is incorrect, in particular when the system is covered by an ultrathin protective overlayer. In these circumstances, the electrons can to reach the vacuum barrier, which is perfectly reflecting, so that strong confinement and interference effects occur in the overlayer; this leads to weak but significant oscillatory variation of the IEC as a function of the overlayer thickness [62].

This effect, which follows directly from the quantum interference (or quantum size-effect) mechanism, has been proposed and experimentally confirmed independently by de Vries et al. [26] for the Co/Cu/Co(001) system with a Cu(001) overlayer, by Okuno and Inomata [27] for the Fe/Au/Fe(001) system with an Au(001) overlayer, and by Bounouh et al. [28] for Co/Au/Co(0001) with an Au(111) overlayer. In all this work, the dependence of the observed period(s) of the oscillations on overlayer

Table 2. Comparison of theoretical predictions of Ref. [62] and experimental observations of the dependence of the oscillation periods of interlayer exchange coupling overlayer thickness.

Overlayer	Theoretical periods	System	Experimental periods	Ref.
Cu(001)	$\Lambda_1 = 2.6\,\mathrm{AL}$ $\Lambda_2 = 5.9\,\mathrm{AL}$	Cu/Co/Cu/Co/Cu(001)	$\Lambda \approx 5.\,\mathrm{AL}$	[26]
Au(001)	$\Lambda_1 = 2.5\,\mathrm{AL}$ $\Lambda_2 = 8.6\,\mathrm{AL}$	Au/Fe/Au/Fe/Au(001)	$\Lambda_1 \approx 2.6\,\mathrm{AL}$ $\Lambda_2 \approx 8.0\,\mathrm{AL}$	[27]
Au(111)	$\Lambda = 4.8\,\mathrm{AL}$	Au/Co/Au/Co/Au(111)	$\Lambda \approx 5.\,\mathrm{AL}$	[28]

thickness were found to be in good agreement with theoretically predicted values. This effect has also been confirmed by means of first-principles calculations for the Co/Cu/Co(001) system with different types of overlayer [130–132]. The dependence of the oscillation periods on overlayer thickness predicted theoretically are compared with those observed experimentally in Table 2. A more detailed discussion of this effect can be found in Refs. [62, 130, 132].

9.8 Strength and Phase of Interlayer Exchange Coupling

In contrast with the excellent agreement between theory and experiment obtained for oscillation periods, the situation for the amplitude and phase of oscillations is less satisfactory. According to the theory expounded above, the coupling takes the following form in the limit of large spacer thickness (asymptotic limit):

$$J = \sum_{\alpha} \frac{A_\alpha}{D^2} \sin\left(q_\alpha D + \phi_\alpha\right). \tag{31}$$

Because the coupling constant J has the dimension of energy per unit area, the parameters A_α characterizing the coupling strength of the different components of the oscillation have the dimensions of energy. By taking typical values of the Fermi wavevector and velocity, it is easy to see from Eq. (29) that they are typically of the order of 1 to 10 meV.

Theoretical and experimental values of the oscillation amplitude strengths, A_α, for different systems are compared in Table 3. (Note that different theoretical results with each other we include in this discussion only calculations pertaining to semi-infinite magnetic layers.) We observe a variety of rather strong discrepancy between theory and experiment, and also among various theoretical studies. Although the agreement seems to be rather good for the Co/Cu(111)/Co system, more experimental and theoretical data are required to disclose whether the apparent agreement is conclusive or accidental.

Table 3. Comparison of theoretical predictions and experimental observations for the dependence of oscillation amplitudes, A_α, of interlayer exchange coupling on spacer thickness. For Cu(001) and Au(001) spacers A_1 and A_2 correspond, respectively, to the short-period and long-period oscillations.

System	Theory	Ref.	Experiment	Ref.
Co/Cu(111)/Co	$A \approx 3.7$ meV	[133]	$A \approx 7.6$ meV	[20]
	$A \approx 4.2$ meV	[60]	$A \approx 3.4$ meV	[137]
			$A \approx 2.5$ meV	[138]
Co/Cu(001)/Co	$A_1 \approx 42.$ meV	[133]	$A_1 \approx 1.6$ meV	[20, 21, 122]
	$A_2 \approx 0.13$ meV		$A_2 \approx 1.4$ meV	
	$A_1 \approx 72.$ meV	[60]		
	$A_2 \approx 0.75$ meV			
	$A_1 \approx 35.$ meV	[129]		
	$A_2 \approx 3.5$ meV			
	$A_1 \approx 35.$ meV	[47]		
	$A_2 \approx 0.035$ meV			
Fe/Au(001)/Fe	$A_1 \approx 12.5$ meV	[60]	$A_1 \approx 8.1$ meV	[19]
	$A_2 \approx 6.9$ meV		$A_2 \approx 1.1$ meV	

9.8.1 Co/Cu(001)/Co

The Co/Cu(001)/Co system has been most investigated theoretically and is considered to be a model system to test the predictions of theory. The theoretical results reported in Table 3 correspond to semi-infinite magnetic layers, whereas the experimental data have been obtained for magnetic layers of finite thickness. As discussed in Section 6 the strength of the coupling varies with magnetic layer thickness, which can be a source of discrepancy between theoretical and experimental results. Another possible source of discrepancy arises from unavoidable imperfections (roughness, intermixing) of the experimental samples.

Let us first address the short-period oscillatory component (labeled with the subscript 1). As discussed in Section 5 above, this component arises from four equivalent in-plane wavevectors $\mathbf{k}_{\parallel 1}$ located on the $\overline{\Gamma} - \overline{X}$ high-symmetry line of the two-dimensional Brillouin zone [74]. Because the majority-spin band structure of fcc Co well matches that of Cu, $|r_1^{\uparrow}| \approx 0$. For minority-spin fcc Co, on the other hand, there is a local gap in the band structure of symmetry compatible with the Cu states, which leads to total reflection, i. e., $|r_1^{\downarrow}| = 1$. Thus, $|\Delta r_1| \approx 0.5$ [133, 134] and $|\Delta r_1|$ is (almost) independent of Co thickness [129]. The various theoretical values for the amplitude A_1 listed in Table 3 agree rather well with each other, except for that from Ref. [60] which is almost a factor of 2 larger than the values obtained by other authors [129, 133, 47]. This discrepancy might be because of an error in the estimation of the radius of curvature κ_1, of the Fermi surface, and of the Fermi velocity, $v_{\perp 1}$, which are quite tricky to obtain accurately for $\mathbf{k}_{\parallel 1}$.

Turning now to the comparison between theory and experiment, we notice that the calculated values of A_1 are considerably larger than those measured. There might be

at least two reasons for this discrepancy. The first is the effect of interface roughness, which generally tends to reduce the amplitude of the coupling oscillations [117]; this effect is particularly pronounced for short-period oscillatory components, as is indeed confirmed experimentally [22]. The second reason is of intrinsic character – the theoretical values of A_1 given in Table 3 correspond to the asymptotic limit, whereas the experimental data have been obtained for spacer thicknesses below 15 AL. As is clearly apparent from Fig. 6a of Ref. [129] and from Fig. 13 (bottom) of Ref. [47], the asymptotic regime is attained only for thicknesses above 20 to 40 AL; below this value the envelope of the oscillations deviates significantly from D^{-2} behavior, and the apparent amplitude in the range relevant to experiments is typically a factor of 2 smaller than the asymptotic amplitude. This pre-asymptotic correction is attributed to the strong energy-dependence of $r_1^{\downarrow}$ [47].

Let us now discuss the long-period oscillatory component. As appears from Table 3, the situation is quite confusing – not only do the various theoretical results disagree with each other, but some [133, 60, 47] *underestimate* the coupling strength compared with the experimental result [20, 21, 122], a difference which cannot be explained by the effect of roughness or interdiffusion.

The long-period oscillatory component arises from the center $\overline{\Gamma}$ of the two-dimensional Brillouin zone. Here again, for the same reason as above, $|r_2^{\uparrow}| \approx 0$. The minority-spin reflection coefficient, is on the other hand, considerably smaller than for the short-period oscillation, and $|r_2^{\downarrow}| \approx 0.15$ [74], so that $|\Delta r_2| \approx 0.05$ [74, 133]. This very small spin-dependent confinement explains the very small values of A_2 obtained by authors who rely on the asymptotic expression, Eq. (29), obtained from the stationary phase approximation [133, 60, 47]. As seen from Fig. 2 of Ref. [135] and from Fig. 2 of Ref. [60], however, $r_2^{\downarrow}$ increases very strongly with $\mathbf{k}_{\|}$ and full reflection is reached at a distance $0.1 \times \pi/a$ from $\overline{\Gamma}$; indeed, the low reflectivity arises only in a narrow window around $\overline{\Gamma}$. As discussed in Ref. [136], this gives rise to a strong preasymptotic correction, and explains why the stationary-phase approximation yields an *underestimated* value of A_2. If, on the other hand, the $\mathbf{k}_{\|}$ integration is performed without using the stationary-phase approximation, as in Ref. [129], a much higher value of A_2 is obtained; the latter is larger than the experimental value [20, 21, 122] by a factor of 2.5, which seems plausible in view of the effect of roughness and interdiffusion.

Our knowledge of the phase of the oscillations is much more restricted as this aspect of the problem has so far attracted little attention, with the notable exception of the work of Weber et al. [22]. On general grounds, for total reflection (as for $r_{1\downarrow}$), one expects the phase to vary with magnetic layer thickness and/or with the chemical nature of the magnetic layer; conversely, for weak confinement (as for $r_2^{\downarrow}$), one expects the phase to be almost invariant [74]. These general trends were, indeed, confirmed experimentally by Weber et al. [22].

9.8.2 Fe/Au(001/Fe

Because of the excellent lattice matching between Au and bcc Fe (with rotation of the cubic axes of the latter by 45°), and the availability of extremely smooth Fe substrates (whiskers) [18, 19], Fe/Au(001)/Fe is an excellent system for a quantitative testing of theory.

In contrast with Co/Cu(001) discussed above, for Fe/Au(001) one has total reflection of minority-spin electrons both at $\mathbf{k}_{\parallel 1}$ (short-period oscillation) and $\mathbf{k}_{\parallel 2}$ (long-period oscillation), and $|r^{\downarrow}|$ is almost independent of $\mathbf{k}_{\parallel}$ around these points, as is clearly apparent from Fig. 1 of Ref. [134]. The associated preasymptotic correction should, therefore, not be very strong.

Indeed, as is apparent from Table 3, the predicted amplitudes are quite large, both for the short-period and long-period oscillatory components [60]. These predictions are fairly well confirmed by state-of-the-art experimental studies [19], although the predicted amplitude of the long-period component is too large by a factor of 6.

Clearly, even for this almost ideal system, further work is required to achieve satisfactory quantitative agreement between theory and experiment.

9.9 Concluding Remarks

As has been discussed in detail in this review, there is much experimental evidence that the mechanism of quantum confinement presented above is actually appropriate for explaining the phenomenon of oscillatory interlayer exchange coupling. This mechanism is entirely based upon a picture of independent electrons. This might seem paradoxical at first sight, because exchange interactions are ultimately a result of Coulomb interaction between electrons. This independent-electron picture can in fact be, justified theoretically and is based upon the "magnetic force theorem." A thorough discussion of this fundamental (but somewhat technical) aspect of the problem is given elsewhere [139, 140].

Despite the successes of the quantum confinement mechanism, several questions remain to be clarified for full understanding of the phenomenon. In particular, the validity of the asymptotic expression (29) must be assessed more quantitatively than has been achieved so far; a first attempt at addressing this issue is given in Ref. [136].

Acknowledgements

I am grateful to Claude Chappert, Josef Kudrnovský, Vaclav Drchal, and Ilja Turek for their collaboration in the work presented in this chapter.

References

[1] L. Néel, *C. R. Acad. Sci. (Paris)* **255**, 1545 (1962); *C. R. Acad. Sci. (Paris)* **255**, 1676 (1962).
[2] M.A. Ruderman and C. Kittel, *Phys. Rev.* **96**, 99 (1954).
[3] T. Kasuya, *Prog. Theor. Phys.* **16**, 45 (1956).
[4] K. Yosida, Phys. Rev. **106**, 893 (1957).
[5] C.F. Majkrzak, C.W. Cable, J. Kwo, M. Hong, B.D. McWhan, Y. Yafet, J.V. Waszak, and C. Vettier, *Phys. Rev. Lett.* **56**, 2700 (1986).
[6] M.B. Salamon, S. Sinha, J.J. Rhyne, J.E. Cunningham, R.W. Erwin, J. Borchers, and C.P. Flynn, *Phys. Rev. Lett.* **56**, 259 (1986).
[7] C.F. Majkrzak, J. Kwo, M. Hong, Y. Yafet, D. Gibbs, C.L. Chein, and J. Bohr, *Adv. Phys.* **40**, 99 (1991).
[8] J.J. Rhyne and R.W. Erwin, in *Magnetic Materials*, Vol. 8, Ed. K.H.J. Buschow, North Holland, Amsterdam, 1995, p. 1.
[9] P. Grünberg, R. Schreiber, Y. Pang, M.B. Brodsky, and H. Sower, *Phys. Rev. Lett.* **57**, 2442 (1986).
[10] B. Dieny, J.-P. Gavigan, and J.-P. Rebouillat, *J. Phys.: Condens. Matter* **2**, 159 (1990); B. Dieny and J.-P. Gavigan, *J. Phys.: Condens. Matter* **2**, 178 (1990).
[11] W. Folkerts, *J. Magn. Magn. Mater.* **94**, 302 (1990).
[12] B. Dieny, V.S. Speriosu, S.S.P. Parkin, and B.A. Gurney, *Phys. Rev. B* **43**, 1297 (1991).
[13] S.S.P. Parkin and D. Mauri, *Phys. Rev. B* **44**, 7131 (1991).
[14] V. Grolier, D. Renard, B. Bartenlian, P. Beauvillain, C. Chappert, C. Dupas, J. Ferré, M. Galtier, E. Kolb, M. Mulloy, J.P. Renard, and P. Veillet, *Phys. Rev. Lett.* **71**, 3023 (1993).
[15] S.S.P. Parkin, N. More, and K.P. Roche, *Phys. Rev. Lett.* **64**, 2304 (1990).
[16] S.S.P. Parkin, *Phys. Rev. Lett.* **67**, 3598 (1991).
[17] A. Fuss, S. Demokritov, P. Grünberg, and W. Zinn, *J. Magn. Magn. Mater.* **103**, L221 (1992).
[18] J. Unguris, R.J. Celotta, and D.T. Pierce, *J. Appl. Phys.* **75**, 6437 (1994).
[19] J. Unguris, R.J. Celotta, and D.T. Pierce, *Phys. Rev. Lett.* **79**, 2734 (1997)
[20] M.T. Johnson, S.T. Purcell, N.W.E. McGee, R. Coehoorn, J. aan de Stegge, and W. Hoving, *Phys. Rev. Lett.* **68**, 2688 (1992).
[21] M.T. Johnson, P.J.H. Bloemen, R. Coehoorn, J.J. de Vries, N.W.E. McGee, R. Jungblut, A. Reinders, and J. aan de Stegge, *Mat. Res. Soc. Proc.*, Vol. 313, Materials Research Society, San Francisco, 1993, p. 93.
[22] W. Weber, R. Allenspach, and A. Bischof, *Europhys. Lett.* **31**, 491 (1995).
[23] J. Unguris, R.J. Celotta, and D.T. Pierce, *J. Magn. Magn. Mater.* **127**, 205 (1993).
[24] P.J.H. Bloemen, M.T. Johnson, M.T.H. van de Vorst, R. Coehoorn, J.J. de Vries, R. Jungblut, J. aan de Stegge, A. Reinders, and W.J.M. de Jonge, *Phys. Rev. Lett.* **72**, 764 (1994).
[25] C.H. Back, W. Weber, A. Bischof, D. Pescia, and R. Allenspach, *Phys. Rev. B* **52** R13114 (1995).
[26] J.J. de Vries, A.A.P. Schudelaro, R. Jungblut, P.J.H. Bloemen, A. Reinders, J. Kohlhepp, R. Coehoorn, and de W.J.M. Jonge, *Phys. Rev. Lett.* **75**, 1306 (1995).
[27] S.N. Okuno and K. Inomata, *J. Phys. Soc. Japan* **64**, 3631 (1995).
[28] A. Bounouh, P. Beauvillain, P. Bruno, C. Chappert, R. Mégy, and P. Veillet, *Europhys. Lett.* **33**, 315 (1996).
[29] M. Rührig, R. Schäfer, A. Hubert, R. Mosler, J.A. Wolf, S. Demokritov, and P. Grünberg, *Phys. Status Solidi A* **125**, 635 (1991).

[30] J.C. Slonczewski, *J. Magn. Magn. Mater.* **150**, 13 (1995).
[31] S.O. Demokritov, *J. Phys. D: Appl. Phys.* **31**, 925 (1998).
[32] S. Toscano, B. Briner, H. Hopster, and M. Landolt, *J. Magn. Magn. Matter.* **114**, L6 (1992).
[33] S. Toscano, B. Briner, and M. Landolt, in *Magnetism and Structure in Systems of Reduced Dimensions*, Ed. R.F.C. Farrow, B. Dieny, M. Donath, A. Fert, and B.D. Hermsmeier, Vol. 309 of *NATO Advanced Study Institute, Series B: Physics*, Plenum Press, New York, 1993, p. 257.
[34] J.E. Mattson, S. Kumar, E.E. Fullerton, S.R. Lee, C.H. Sowers, M. Grimditch, S.D. Bader, and F.T. Parker, *Phys. Rev. Lett.* **71**, 185 (1993).
[35] B. Briner and M. Landolt, *Phys. Rev. Lett.* **73**, 340 (1994).
[36] Y. Yafet, *Phys. Rev. B* **36**, 3948 (1987).
[37] C. Chappert and J.P. Renard, *Europhys. Lett.* **15**, 553 (1991).
[38] P. Bruno and C. Chappert, *Phys. Rev. Lett.* **67**, 1602 (1991); **67**, 2592(E) (1991).
[39] P. Bruno and C. Chappert, *Phys. Rev. B* **46**, 261 (1992).
[40] R. Coehoorn, *Phys. Rev. B* **44**, 9331 (1991).
[41] D.M. Edwards, J. Mathon, R.B. Muniz, and M.S. Phan, *Phys. Rev. Lett.* **67**, 493 (1991).
[42] J. Mathon, M. Villeret, and D.M. Edwards, *J. Phys.: Condens. Mat.* **4**, 9873 (1992).
[43] J. Barnaś, *J. Magn. Magn. Mater.* **111**, L215 (1992).
[44] R.P. Erickson, K.B. Hathaway, and J.R. Cullen, *Phys. Rev. B* **47**, 2626 (1993).
[45] J.C. Slonczewski, *J. Magn. Magn. Mater.* **126**, 374 (1993).
[46] J. d'Albuquerque e Castro, J. Mathon, M. Villeret, and A. Umerski, *Phys. Rev. B* **53**, R13306 (1996).
[47] J. Mathon, M. Villeret, A. Umerski, R.B. Muniz, J. d'Albuquerque e Castro, and D.M. Edwards, *Phys. Rev. B* **56**, 11797 (1997).
[48] A.T. Costa, Jr., J. d'Albuquerque e Castro, and R.B. Muniz, *Phys. Rev. B* **56**, 13697 (1997).
[49] Y. Wang, P.M. Levy, and J.L. Fry, *Phys. Rev. Lett.* **65**, 2732 (1990).
[50] Z.P. Shi, P.M. Levy, and J.L. Fry, *Phys. Rev. Lett.* **69**, 3678 (1992).
[51] P. Bruno, *J. Magn. Magn. Mater.* **116**, L13 (1992).
[52] P.W. Anderson, *Phys. Rev.* **124**, 41 (1961).
[53] B. Caroli, *J. Phys. Chem. Solids* **28**, 1427 (1967).
[54] J. Friedel, *Nuovo Cimento Suppl.* **7**, 287 (1958).
[55] P. Bruno, *J. Magn. Magn. Mater.* **121**, 248 (1993).
[56] P. Bruno, *Phys. Rev. B* **52**, 411 (1995).
[57] M.D. Stiles, *Phys. Rev. B* **48** 7238 (1193).
[58] B. Lee and Y.-C. Chang, *Phys. Rev. B* **52**, 3499 (1995).
[59] B. Lee and Y.C. Chang, *Phys. Rev. B* **54**, 13034 (1996).
[60] M.D. Stiles, *J. Appl. Phys.* **79**, 5805 (1996).
[61] P. Bruno, *Europhys. Lett.* **23**, 615 (1993).
[62] P. Bruno, *J. Magn. Magn. Mater.* **164**, 27 (1996).
[63] F. Herman, J. Sticht, and M. van Schilfgaarde, *J. Appl. Phys.* **69**, 4783 (1991); in *Magnetic Thin Films, Multilayers and Surfaces*, Ed. S.S.P. Parkin, H. Hopster, J.P. Renard, T. Shinjo, and W. Zinn, Symposia Proceedings No. 231, Materials Research Society, Pittsburg, 1992.
[64] S. Krompiewski, U. Krey, and J. Pirnay, *J. Magn. Magn. Mater.* **121**, 238 (1993).
[65] S. Krompiewski, F. Süss, and U. Krey, *Europhys. Lett.* **26**, 303 (1994).
[66] M. van Schilfgaarde and F. Herman, *Phys. Rev. Lett.* **71**, 1923 (1993).
[67] P. Lang, L. Nordström, R. Zeller, and P.H. Dederichs, *Phys. Rev. Lett.* **71**, 1927 (1993).
[68] L. Norström, P. Lang, R. Zeller, and P.H. Dederichs, *Phys. Rev. B* **50**, 13058 (1994).
[69] J. Kudrnovský, V. Drchal, I. Turek, and P. Weinberger, *Phys. Rev. B* **50**, 16105 (1994).
[70] J. Kudrnovský, V. Drchal, I. Turek, M. Šob, and P. Weinberger, *Phys. Rev. B* **53**, 5125 (1996).

[71] P. Lang, L. Nordström, K. Wildberger, R. Zeller, P.H. Dederichs, and T. Hoshino, *Phys. Rev. B* **53**, 9092 (1996).
[72] V. Drchal, J. Kudrnovský, I. Turek, and P. Weinberger, *Phys. Rev. B* **53**, 15036 (1996).
[73] P. Bruno, *Phys. Rev. B* **49**, 13231 (1994).
[74] P. Bruno, *Phys. Rev. B* **52**, 411 (1995).
[75] P.D. Loly and J.B. Pendry, *J. Phys. C: Solid State Phys.* **16**, 423 (1983).
[76] A.L. Wachs, A.P. Shapiro, T.C. Hsieh, and T.-C. Chiang, *Phys. Rev. B* **33**, 1460 (1986).
[77] S.Å Lindgren and L. Walldén, *Phys. Rev. Lett.* **59**, 3003 (1987).
[78] S.Å Lindgren and L. Walldén, *Phys. Rev. Lett.* **61**, 2894 (1988).
[79] S.Å Lindgren and L. Walldén, *Phys. Rev. B* **38**, 3060 (1988).
[80] S.Å Lindgren and L. Walldén, *J. Phys.: Condens. Matter* **1**, 2151 (1989).
[81] T. Miller, A. Samsavar, G.E. Franklin, and T.-C. Chiang, *Phys. Rev. Lett.* **61**, 1404 (1988).
[82] M.A. Mueller, A. Samsavar, T. Miller, and T.-C. Chiang, *Phys. Rev. B* **40**, 5845 (1989).
[83] M.A. Mueller, T. Miller, and T.-C. Chiang, *Phys. Rev. B* **41**, 5214 (1990).
[84] M. Jalochowski, E. Bauer, H. Knoppe, and G. Lilienkamp, *Phys. Rev. B* **45**, 13607 (1992).
[85] N.B. Brookes, Y. Chang, and P.D. Johnson, *Phys. Rev. Lett.* **67**, 354 (1991).
[86] J.E. Ortega and F.J. Himpsel, *Phys. Rev. Lett.* **69**, 844 (1992).
[87] J.E. Ortega, F.J. Himpsel, G.J. Mankey, and R.F. Willis, *Phys. Rev. B* **47**, 1540 (1993).
[88] J.E. Ortega, F.J. Himpsel, G.J. Mankey, and R.F. Willis, *J. Appl. Phys.* **73**, 5771 (1993).
[89] K. Garrison, Y. Chang, and P.D. Johnson, *Phys. Rev. Lett.* **71**, 2801 (1993).
[90] C. Carbone, E. Vescovo, O. Rader, W. Gudat, and W. Eberhardt, *Phys. Rev. Lett.* **71**, 2805 (1993).
[91] N.V. Smith, N.B. Brookes, Y. Chang, and P.D. Johnson, *Phys. Rev. B* **49**, 332 (1994).
[92] P.D. Johnson, K. Garrison, Q. Dong, N.V. Smith, D. Li, J. Mattson, J. Pearson, and S.D. Bader, *Phys. Rev. B* **50**, 8954 (1994).
[93] F.J. Himpsel and O. Rader, *Appl. Phys. Lett.* **67**, 1151 (1995).
[94] S. Crampin, S. De Rossi, and F. Ciccaci, *Phys. Rev. B* **53**, 13817 (1996).
[95] P. Segovia, E.G. Michel, and J.E. Ortega, *Phys. Rev. Lett.* **77**, 3455 (1996).
[96] R. Kläsge, D. Schmitz, C. Carbone, W. Eberhardt, P. Lang, R. Zeller, and P.H. Dederichs, *Phys. Rev. B* **57**, R696 (1998).
[97] R.K. Kawakami, E. Rotenberg, E.J. Escocia-Aparicio, H.J. Choi, T.R. Cummins, J.G. Tobin, N.V. Smith, Z.Q. and Qiu, *Phys. Rev. Lett.* **80**, 1754 (1998).
[98] R.K. Kawakami, E. Rotenberg, E.J. Escocia-Aparicio, H.J. Choi, J.H. Wolfe, N.V. Smith, and Z.Q. Qiu, *Phys. Rev. Lett.* **82**, 4098 (1999).
[99] F.J. Himpsel, *Phys. Rev. B* **44**, 5966 (1991).
[100] J.E. Ortega and F.J. Himpsel, *Phys. Rev. B* **47**, 16441 (1993).
[101] D. Li, J. Pearson, J.E. Mattson, S.D. Bader, and P.D. Johnson, *Phys. Rev. B* **51**, 7195 (1995).
[102] F.J. Himpsel, *J. Electr. Microsc. and Rel. Phenom.* **75**, 187 (1995).
[103] D. Li, J. Pearson, S.D. Bader, E. Vescovo, D.-J. Huang, P.D. Johnson, and B. Heinreich, *Phys. Rev. Lett.* **78**, 1154 (1997).
[104] K. Koike, T. Furukawa, G.P. Cameron, and Y. Murayama, *Phys. Rev. B* **50**, 4816 (1994).
[105] T. Furukawa and K. Koike, *Phys. Rev. B* **54**, 17896 (1996).
[106] W.R. Bennett, W. Schwarzacher, and W.F. Egelhoff, Jr., *Phys. Rev. Lett.* **65**, 3169 (1990).
[107] T. Katayama, Y. Suzuki, M. Hayashi, and A. Thiaville, *J. Magn. Magn. Mater.* **126**, 527 (1993).
[108] A. Carl and D. Weller, *Phys. Rev. Lett.* **74**, 190 (1995).
[109] R. Mégy, A. Bounouh, Y. Suzuki, P. Beauvillain, P. Bruno, C. Chappert, B. Lécuyer, and P. Veillet, *Phys. Rev. B* **51**, 5586 (1995).
[110] P. Bruno, Y. Suzuki and C. Chappert, *Phys. Rev. B* **53**, 9214 (1996).

[111] Y. Suzuki, T. Katayama, P. Bruno, S. Yuasa, and E. Tamura, *Phys. Rev. Lett.* **80**, 5200 (1998).
[112] T.A. Luce, W. Hübner, and K.H. Bennemann, *Phys. Rev. Lett.* **77**, 2810 (1996).
[113] A. Kirilyuk, Th. Rasing, R. Mégy, and P. Beauvillain, *Phys. Rev. Lett.* **77**, 4608 (1996).
[114] W. Weber, A. Bischof, R. Allenspach, C. Würsch, C.H. Back, and D. Pescia, *Phys. Rev. Lett.* **76**, 3424 (1996).
[115] C.H. Back, W. Weber, C. Würsch, A. Bischof, D. Pescia, and R. Allespach, *J. Appl. Phys.* **81**, 5054 (1997).
[116] M.R. Halse, *Philos. Trans. R. Soc. London A* **265**, 507 (1969).
[117] P. Bruno and C. Chappert, *Phys. Rev. Lett.* **67**, 1602 (1991); **67**, 2592(E) (1991).
[118] S.S.P. Parkin, R. Bhadra, and K.P. Roche, *Phys. Rev. Lett.* **66**, 2152 (1991).
[119] D.H. Mosca, F. Pétroff, A. Fert, P.A. Schroeder, W.P. Pratt, Jr., R. Laloee, and S. Lequien, *J. Magn. Magn. Mater.* **94**, L1 (1991).
[120] F. Pétroff, A. Barthéémy, D.H. Mosca, D.K. Lottis, A. Fert, P.A. Schroeder, W.P. Pratt, Jr., R. Laloee, and S. Lequien, *Phys. Rev. B* **44**, 5355 (1991).
[121] J.J. de Miguel, A. Cebollada, J.M. Gallego, R. Miranda, C.M. Schneider, P. Schuster, and J. Kirschner, *J. Magn. Magn. Mater.* **93**, 1 (1991).
[122] J.J. de Vries, PhD Thesis, Eindhoven University of Technology (1996).
[123] S.N. Okuno and K. Inomata, *Phys. Rev. Lett.* **70**, 1771 (1993).
[124] S.S.P. Parkin, C. Chappert, and F. Herman, *Europhys. Lett.* **24**, 71 (1993).
[125] J.-F. Bobo, L. Hennet, and M. Piécuch, *Europhys. Lett.* **24**, 139 (1993).
[126] J. Barnaś, *J. Magn. Magn. Mater.* **111**, L215 (1992).
[127] L. Norström, P. Lang, R. Zeller, and P.H. Dederichs, *Phys. Rev. B* **50**, 13058 (1994).
[128] P. Lang, L. Nordström, K. Wildberger, R. Zeller, P.H. Dederichs, and T. Hoshino, *Phys. Rev. B* **53**, 9092 (1996).
[129] V. Drchal, J. Kudrnovský, I. Turek, and P. Weinberger, *Phys. Rev. B* **53**, 15036 (1996).
[130] J. Kudrnovský, V. Drchal, P. Bruno, I. Turek, and P. Weinberger, *Phys. Rev. B.* **56**, 8919 (1997).
[131] J. Kudrnovský, V. Drchal, P. Bruno, R. Coehoorn, J.J. de Vries, and P. Weinberger, *Mater Res. Soc. Symp. Proc. Vol.* **475**, 575 (1997).
[132] J. Kudrnovský, V. Drchal, P. Bruno, I. Turek, and P. Weinberger, *Comp. Matter Sci.* **10** 188 (1998).
[133] B. Lee and Y.-C. Chang, *Phys. Rev. B* **52**, 3499 (1995).
[134] M.D. Stiles, *J. Magn. Magn. Mater.* **200**, 322 (1999).
[135] P. Bruno, *J. Magn. Magn. Mater.* **148**, 202 (1995).
[136] P. Bruno, *Eur. Phys. J. B* **11**, 83 (1999).
[137] A. Schreyer, K. Bröhl, J.F. Ankner, C.F. Majkrzak, T. Zeidler, P. Bödeker, N. Metoki, and H. Zabel, *Phys. Rev. B* **47**, 15334 (1993).
[138] A.J.R. Ives, R.J. Hicken, J.A.C. Bland, C. Daboo, M. Gester, and S.J. Gray, *J. Appl. Phys.* **75**, 6458 (1994).
[139] P. Bruno, in *Magnetische Schichtsysteme*, Ed. P.H. Dederichs and P. Gruenberg, Forschungszentrum Jülich, 1999, Chap. B8; cond-mat/9905022.
[140] P. Bruno, *Eur. Phys. J. B* **11**, 83 (1999).

Magnetism: Molecules to Materials III. Edited by J.S. Miller and M. Drillon

ISBNs: 3-527-30302-2 (Hardback); 3-527-60014-0 (Electronic)

10 Magnetization Dynamics on the Femtosecond Time-scale in Metallic Ferromagnets

Jean-Yves Bigot, Eric Beaurepaire, Luca Guidoni, and Jean-Claude Merle

10.1 Introduction

The prospect of improving the switching speed of magnetic devices used for the storage of digital information has instigated several investigations during recent years. To change the magnetic state of such devices one can either use a time-dependent magnetic field or a light pulse simultaneously with a biased static magnetic field. In both instances several factors intrinsic to the magnetic material and to the interaction process between the applied fields and the material, influence the switching behavior of the device. In this context it is important to investigate the fundamental mechanisms involved in the magnetization dynamics of ferromagnetic metals. The techniques which are based on modification of the magnetization induced by a short optical pulse are particularly interesting, because progress in laser technology over the past 20 years now enable unprecedented temporal resolution on the femtosecond time-scale. The application of these techniques to the study of magnetic materials therefore provides deeper insights into the physical mechanisms responsible for the energy relaxation associated with the magnetization dynamics. Let us consider first the different time-scales which can be associated with a change of the magnetic state of a ferromagnetic metallic thin film. Figure 1 shows different mechanisms and their corresponding temporal ranges. Starting with the slowest mechanisms, the first time-scale is that of the motion of magnetic domains in an applied field. This corresponds to the propagation of domain walls and results in an increase in the size of those domains which have a net magnetization parallel to the applied field. More rigorously, one must distinguish between the nucleation of the domains and the propagation of the domain walls [1]. The fundamental processes involved are dipolar magnetic interaction and magnetocrystalline anisotropy. The time-scale for the motion of magnetic domains ($>10^{-8}$ s) varies depending on the structure and inhomogeneity of the particular film which is being considered [2]. For example, the presence of structural defects or chemical inhomogeneity (for alloys) tends to pin the domain walls, resulting in slower and more complex switching patterns.

The second mechanism concerns the magnetization reversal of a single domain. For magnetic inhomogeneous films this corresponds to the rotation of domains with magnetization misaligned with the applied field; it occurs when the energy brought by the field overcomes the anisotropy energy barrier. The time-scale associated with this mechanism (10^{-10}–10^{-8} s) also depends on extrinsic factors. In particular, it is shorter when the demagnetizing field associated with surrounding domains and/or

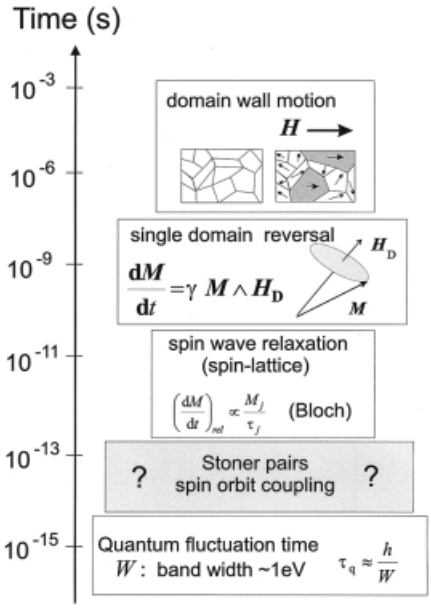

Fig. 1. Characteristic time-scales of dynamic magnetic phenomena.

the particular geometry of the domain itself is important [3]. A lower limit for the time associated with the magnetization reversal can be obtained by considering the dynamics of a single domain. Assuming that the switching occurs within a period T of the magnetization precession around the demagnetizing field H_D, then $T = 2\pi/\gamma H_\mathrm{D}$ with $\gamma = gm_\mathrm{B}/\hbar$, and one obtains for a field $H_\mathrm{D} \approx 350\,\mathrm{Oe}$ ($\sim 2.8 \times 10^4\,\mathrm{A\,m^{-1}}$) a typical time-scale of $T \approx 10^{-9}\,\mathrm{s}$. A third important mechanism shown in Fig. 1 is the damping of the magnetization dynamics. At the microscopic level, this corresponds to dissipation of the energy stored in the magnetic system into the lattice vibrations. The corresponding fundamental process is the interaction between the spin-waves and the phonons. The quantum description of this interaction process gives an expected time-scale of (10^{-11}–$10^{-10}\,\mathrm{s}$). Several phenomenological models can be used to describe the magnetization damping. They all consist in adding a relaxation term to the derivative of the magnetization vector $\mathrm{d}\mathbf{M}/\mathrm{d}t$. In the Bloch model [4] this is taken into account by means of a term $-\mathbf{M}/\tau_1$ or $-\mathbf{M}/\tau_2$ where τ_1 and τ_2 are the relaxation of magnetization parallel and perpendicular, respectively, to the quantification axis. In the Landau-Lifshitz [5] and Gilbert [6] models, the damping of the magnetization dynamics is taken into account via the phenomenological relaxation terms $(\lambda/M_\mathrm{s}^2)\mathbf{M} \wedge (\mathbf{M} \wedge \mathbf{H})$ or $(\alpha/M_\mathrm{s}^2)\mathbf{M} \wedge \mathrm{d}\mathbf{M}/\mathrm{d}t$. In the semiclassical description of magnetization dynamics both the precession and the damping have to be taken into account.

The shortest delays shown in Fig. 1, are the quantum fluctuations of the magnetization. They correspond to local changes of the magnetization which result from the broad energy spectrum, W, associated with the spin distribution. Because the spin density operator does not commute with the Hamiltonian, local spin fluctuations on a time-scale $\tau_\mathrm{q} \approx 2\pi\hbar/W$ are expected. For itinerant ferromagnetic materials, the

bandwidth of the spin density of states is typically of the order of 1 eV (1.6×10^{-19} J), corresponding, therefore, to fluctuations of $\sim 10^{-15}$ s. This quantum process is too fast to be observed with the conventional techniques used in magneto-optics and the magnetization dynamics is averaged over this time-scale.

More interesting is the temporal region represented by the grey area in Fig. 1. So far little information has been obtained in this temporal range lying between 10^{-14} and 10^{-11} s. It is an interesting range to explore using the techniques available in ultrafast optical spectroscopy. Although the transitions induced in the ferromagnetic metal with an optical pulse of a few tens of femtoseconds conserve the spin, rapid changes of the magnetization can occur. Such changes occur via the electron–electron interaction in the non-equilibrium electron system. Several mechanisms can participate in this ultrafast magnetization dynamics. For instance, the excitation of Stoner pairs via the Coulomb and exchange interaction, the scattering of d electrons by conduction quasi-particles, and the spin-orbit interaction have to be considered on a time-scale of a few hundreds of femtoseconds. Finally, energy relaxation from the electrons to the lattice also influences the dynamics of the magnetization. The typical relaxation time for this process is a few picoseconds.

The aim of this paper is to consider modifications of the magnetic properties of ferromagnetic thin films associated with the ultrafast processes mentioned above, i. e. in the temporal range 10^{-14}–10^{-11} s. In particular, we focus on experimental results obtained during the last five years in this field, which we term femtomagnetism [7–11]. The paper is organized as follows. In Section 2 we introduce some theoretical aspects of magnetization dynamics. We first describe the process of heating a metal with an ultrashort laser pulse (Section 2.1). A phenomenological model consisting of three interacting reservoirs enables us to define the relevant processes leading to optically induced demagnetization (Section 2.2). In Section 2.3 we describe a model of spin dephasing which takes into account the electron correlation [12]. In this model, the loss of coherence of the initially excited states leads to an ultrafast charge and spin dynamics with a characteristic time of $\sim$10 fs. In Section 3 we describe different techniques which enable measurement of spin dynamics (Section 3.1) and we describe in detail the techniques used for the time-resolved magneto- optical Kerr effect (MOKE) (Section 3.2). The electron and spin relaxation observed is reported in Section 4. Electron dynamics in thin nickel films after excitation with femtosecond laser pulses without applied magnetic field, is first considered (Section 4.1). Two distinct regimes are considered, corresponding to electron thermalization and energy transfer to the lattice. In addition, coherent effects in which a polarization rotation is associated with pure non-linear optical effects is discussed. The magnetization dynamics of several ferromagnetic materials is then reported (Section 4.2). In Section 5 we conclude by focusing on some of the questions raised and indicating future directions.

10.2 Models

10.2.1 Heating Metals with Ultrashort Laser Pulses

In this section we discuss relaxation processes after the absorption of an ultrashort laser pulse by a metal. Four steps are usually considered in the laser heating of metals; in some circumstances these might overlap in time [13–22]:

1. the photon energy is deposited within the skin-depth of the metal ($\sim$20 nm), exciting electron–hole pairs (quasi-particles);
2. electron–electron interaction leads to the thermalization of the quasi-particles;
3. the energy is exchanged between the quasi-particles and the phonons;
4. the energy propagates in the medium.

The absorption of energy occurs via intra- and inter-band optical transitions. The energy distribution of the excited states then changes in time, because of electron–electron scattering, until it reaches a Fermi–Dirac distribution. This process is characterized by a thermalization time τ_{th} after which the electrons have a well-defined high temperature. The energy then relaxes from the electrons to the lattice, because of the electron–phonon interaction with a characteristic relaxation time τ_{el}. The next step is heat propagation, when the energy is dissipated into the environment. In the context of this paper, this propagation effect, which can be described by the Fourier equation and which occurs in the nanosecond time-scale, will be ignored.

Historically, athermal electron distribution was originally neglected. The problem was formulated in the so-called two- temperature model [23] and was solved to compare the rates of thermionic and thermoelectric emission from laser-exposed surfaces [24]. In this model, the rate equations for the electron and lattice temperatures (T_{e} and T_{l}) are given by:

$$C_{\mathrm{e}}(T_{\mathrm{e}})\mathrm{d}T_{\mathrm{e}}/\mathrm{d}t = -G_{\mathrm{el}}(T_{\mathrm{e}} - T_{\mathrm{l}}) + P(t) \tag{1a}$$

$$C_{\mathrm{l}}(T_{\mathrm{l}})\mathrm{d}T_{\mathrm{l}}/\mathrm{d}t = G_{\mathrm{el}}(T_{\mathrm{e}} - T_{\mathrm{l}}) \tag{1b}$$

where C_{e} and C_{l} are the electronic and lattice specific heats, G_{el} is the electron–phonon coupling constant and P the laser power density absorbed by the material. The laser power density is included in Eq. (1a) only, because the energy is initially deposited in the electron system. G_{el} is related to the microscopic behavior of the electron–phonon interaction [25]; typical values for metals are 10^{16}–10^{17} W m^{-3} K^{-1}. Measurements of G_{el} from ultrafast spectroscopy provide valuable information about the electron–phonon coupling strength [17]. In the perturbative limit, i. e. for a weak temperature elevation $T_{\mathrm{e}}(t) - T_{\mathrm{l}}(t) \ll T_{\mathrm{l}}(0)$, the specific heat coefficients are constant and Eqs (1a) and (1b) become linear. T_{e} decays exponentially with a characteristic time $\tau_{\mathrm{el}} = C_{\mathrm{el}}/G_{\mathrm{el}} \approx 1$ ps.

A more detailed approach consists in taking into account the athermal electron population. The relevant dynamic quantity is now the number of excited particles $n(\epsilon, t)$ per energy unit. The time dependence of n is divided into contributions arising from electron–electron and electron–phonon scattering:

$$\mathrm{d}n/\mathrm{d}t = (\mathrm{d}n/\mathrm{d}t)_{\mathrm{e\text{-}e}} + (\mathrm{d}n/\mathrm{d}t)_{\mathrm{e\text{-}ph}} \tag{2}$$

The computation of n from this rate equations model requires knowledge of the electron and phonon spectra and a many-body description of the quasiparticle interactions. Only for free electron metals has it been considered in some detail [26, 27]. Within the random phase approximation the electron–electron term in Eq. (2) is given by:

$$\left(\frac{\mathrm{d}n}{\mathrm{d}t}\right)_{\text{e-e}} = \frac{n}{\tau_0(\varepsilon_F^2/\varepsilon^2)} + \frac{6}{\tau_0\varepsilon_F^2}\int_{\varepsilon}^{\infty}(\varepsilon\prime - \varepsilon)n(\varepsilon\prime, t)d\varepsilon\prime \tag{3}$$

The first term in Eq. (3) represents the scattering of electrons with excess energy ε by the ground-state electrons. The quantity $\tau_0(\varepsilon_F^2/\varepsilon^2)$ has the physical meaning of an energy-dependent lifetime and it can be described within the Fermi liquid theory [28]. For gold, τ_0 is typically 0.6 fs but the average value $\langle\tau_{\text{ee}}\rangle = \tau(\varepsilon_F^2/\langle\varepsilon^2\rangle)$ amounts rather to ~100 fs. The second term arises from electrons excited into levels at energy ε in the scattering process. The electron–phonon scattering rate is given by:

$$\left(\frac{\mathrm{d}n}{\mathrm{d}t}\right)_{\text{e-ph}} \approx -\dot{q}\frac{\partial n}{\partial\varepsilon} \approx -\frac{\dot{q}n(\varepsilon, t)}{\langle\varepsilon\rangle}$$

where q is the rate of energy transfer from the particle to the lattice and is proportional to the usual McMillian's coefficient. The corresponding relaxation time is, therefore, given by $\langle\tau_{\text{ep}}\rangle = \langle\varepsilon\rangle/\dot{q}$.

Computations of $\langle\tau_{\text{ee}}\rangle$ and $\langle\tau_{\text{ep}}\rangle$ with values realistic for gold show that the electron–electron interaction dominates at short times (less than a few hundreds of femtoseconds) only [26]. When an energy-resolved description of the athermal electron population is not necessary, a phenomenological description can be used. The electronic distribution is separated into a thermalized part, characterized by its temperature T_{e}, and an athermal contribution characterized by a parameter, N, which represents the volumic density of the non-thermal electrons. In this case, three coupled differential equations are necessary [21]:

$$\mathrm{d}N/\mathrm{d}t = -\alpha N - \beta N \tag{4a}$$

$$C_{\text{e}}(T_{\text{e}})\mathrm{d}T_{\text{e}}/\mathrm{d}t = -G_{\text{el}}(T_{\text{e}} - T_{\text{l}}) + \alpha N \tag{4b}$$

$$C_{\text{l}}(T_{\text{l}})\mathrm{d}T_{\text{l}}/\mathrm{d}t = G_{\text{el}}(T_{\text{e}} - T_{\text{l}}) + \beta N \tag{4c}$$

where α (or β) describes coupling between the non-thermalized and thermalized electrons (or phonons).

To describe accurately the dynamics of the optical response of a metallic film, one must consider Eqs (4a)-(4c) together with a model for the medium dielectric function. Two contributions, associated with intra-band and inter-band optical transitions, must be considered. The intra-band term is usually taken into account by use of a Drude-like dielectric function. The inter-band term concerns mostly transitions from the d bands to the conduction states. The occupation of these states depends on the temperature $T_{\text{e}}(t)$.

10.2.2 Three-temperature Model of Ferromagnets

Because the specific heat of ferromagnetic metals is usually split into electronic, magnetic and lattice contributions [29] a first approach to modeling the ultrafast spin dynamics is to extend the two-temperature model by adding an equation related to the spin subsystem.

$$C_e(T_e)\mathrm{d}T_e/\mathrm{d}t = -G_{el}(T_e - T_l) - G_{es}(T_e - T_s) + P(t) \quad (5a)$$

$$C_l(T_l)\mathrm{d}T_l/\mathrm{d}t = G_{el}(T_e - T_l) - G_{sl}(T_l - T_s) \quad (5b)$$

$$C_s(T_s)\mathrm{d}T_s/\mathrm{d}t = G_{es}(T_e - T_s) + G_{sl}(T_l - T_s) \quad (5c)$$

It is straightforward to incorporate in Eqs (5a)–(5c) an additional equation, in the same way as in Eqs (4a)–(4c), to take into account the nascent non-equilibrium electron population [30]. Figure 2a shows a numerical solution to Eqs (5a)–(5c) applied to a nickel film, using a predictor corrector Adam method. The laser source term is a Gaussian pulse of 100-fs duration. The values of the electronic and lattice specific heats used are: $C_e = \gamma T_e$, with $\gamma = 6 \times 10^3\ \mathrm{J\,m^{-3}\,K^{-2}}$; $C_l = C(300\mathrm{K}) - C_e(300\mathrm{K}) = 2 \times 10^6\ \mathrm{J\,m^{-3}\,K^{-1}}$, where the total specific heat C at 300 K is $\sim 4 \times 10^6\ \mathrm{J\,m^{-3}\,K^{-1}}$. The spin specific heat, C_s, which has a pronounced peak at the Curie temperature, $T_c = 631$ K, is deduced from the temperature-dependent total specific heat by subtracting the linear contributions from C_e and C_l. The coupling constants G_{ij} $(i, j = e, l, s)$ are, respectively: $G_{el} = 8 \times 10^{17}\ \mathrm{W\,m^{-3}\,K^{-1}}$;

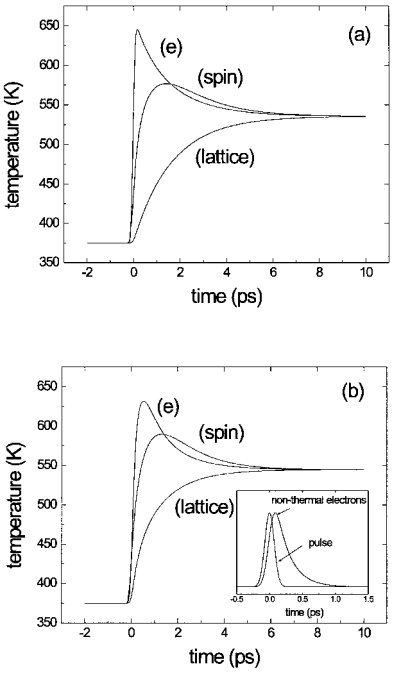

Fig. 2. Simulated time evolution of the electron, spin and lattice temperatures. The numerical solutions are obtained by use of a set of values corresponding to Ni films. (a) Numerical solutions of Eqs (5a)–(5c) (three baths model). (b) Numerical solutions obtained taking into account the nascent non-equilibrium electronic population (inset). The solutions are calculated using a predictor corrector Adam method; in (b) $1/\alpha = 70$ fs.

$G_{es} = 6 \times 10^{17}\,\mathrm{W\,m^{-3}\,K^{-1}}$; $G_{sl} = 0.3 \times 10^{17}\,\mathrm{W\,m^{-3}\,K^{-1}}$. The value of G_{el} is compatible with those generally obtained for the cooling of the electron gas in metals [17, 18]. G_{es} and G_{sl} are two free variables which have been adjusted to reproduce the observed dynamics which we will describe in Section 4.

The temporal behavior in Fig. 2a shows that initially the energy is deposited in the electron subsystem, leading to a maximum of T_e (650 K) which is reached just after excitation. The increase of spin temperature, T_s, is delayed in respect of T_e. It reaches its maximum value (580 K) in ~1 ps. Simultaneously, the energy is transferred from the electrons and spins to the lattice, and T_e, T_s, and T_l slowly, i. e. in a few picoseconds, reach the equilibrium temperature 540 K. When the initial non-thermal electron distribution is taken into account via a rate equation similar to Eq. (4a), the dynamics are different only within the first few hundred femtoseconds. Figure 2b shows the corresponding simulation with $1/\alpha = 70$ fs. The inset represents the time evolution of the non-equilibrium population $N(t)$ which is delayed compared with the pulsed excitation $P(t)$. To estimate the effect of the electronic specific heat on the dynamic behavior of the three baths we have considered a temperature variation $C_e(T_e)$ beyond the low-temperature linear regime. This is achieved by use of the definition $C_e = \mathrm{d}U/\mathrm{d}T_e$, with the energy, U, given by $U = \int ED(E)f(E, T_e, \mu)\mathrm{d}E$. D is the density of energy and f is the Fermi–Dirac distribution at temperature T_e, and depends on the chemical potential, $\mu(T_e)$, which is computed self-consistently. Using the density of states of nickel [31] we obtain the electronic specific heat shown in Fig. 3a. The corresponding linear model $C_e = \gamma T_e$ is displayed for comparison. As seen in Fig. 3b, taking into account this more accurate description of the electronic specific heat C_e, does not alter the qualitative temporal behavior of the three baths.

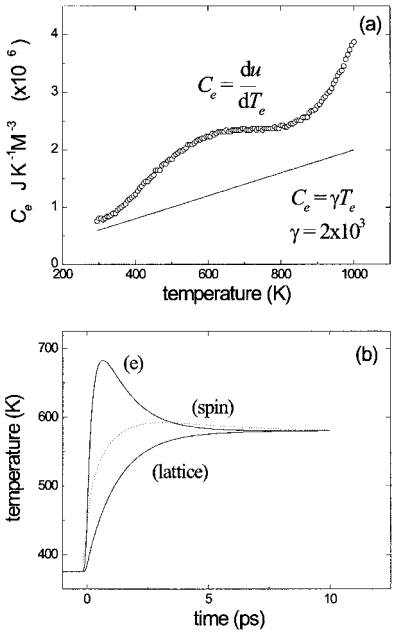

Fig. 3. (a) Electronic specific heat of nickel calculated from the density of states reported in Ref. [31]. The corresponding linear approximation $C_e = \gamma T_e$ is shown for comparison. (b) Numerical solutions of the three-baths model obtained by taking into account the more accurate description of the electronic specific heat, C_e. Comparison with Fig. 2a shows that the qualitative temporal behavior of the three baths model is unchanged.

The above model raises two important questions. First, is it legitimate to describe the dynamics with three different temperatures? Second, what is the physical meaning of the electron–spin and spin–lattice coupling constants G_{es} and G_{sl}? These two questions are at the center of recent observations of ferromagnetic films which we will describe in detail in Section 4. There is currently no satisfying microscopic theory which accounts for the observed spin dynamics induced by femtosecond optical pulses. Our current understanding of the situation, based on experimental results, is: (i) energy is initially deposited in the electron subsystem only, because the spins are conserved in the optical transitions; (ii) the magnetization is strongly modified on a time-scale during which the lattice temperature has not yet changed significantly. These two facts argue in favor of a mechanism involving efficient transfer of the energy from the electrons to the spins, without any major contribution from the lattice. The corresponding coupling, G_{es}, might then correspond to the spin–orbit interaction. One should not, however, exclude spin-flip processes occurring in the interacting electron gas. Such processes can be assisted by the scattering between the d electrons with the conduction electrons, leading to a change of the majority ($N_{d\uparrow}$) and minority ($N_{d\downarrow}$) spin populations and therefore in the magnetization $M_d \approx (N_{d\uparrow} - N_{d\downarrow})$. In these circumstances there is a priori no reason for the electron and spin temperatures to follow the same dynamics. In addition, the relative electron and spin dynamics may be different depending on the populations which are involved or probed with the laser pulses.

Concerning the coupling, G_{sl}, between the spins and the lattice, the mechanism generally considered is the interaction between phonons and spin waves. It is important to stress that in the ultrafast dynamic regime the concept of spin waves might not apply. Indeed, for short temporal delays, the low-frequency magnons are not involved. The rate of energy transfer between the spin subsystem and the lattice might, therefore, be different, depending on the conditions of excitation. When using nanosecond or subnanosecond optical pulses [32], the slow increase of the lattice temperature induces a corresponding change in the magnetization with a time constant τ_m. The microscopic mechanism is the coupling of the spins with the anisotropic fluctuations of the crystal field produced by the phonons. This coupling is mediated by spin-orbit interaction [33, 34]. Microscopic calculation shows that τ_m scales with the magnetocrystalline anisotropy energy. Typical values are $\tau_m = 48$ ps for Gd and 310 ps for Ni, in agreement with experimental results [32, 35]. These values are also compatible with the 45-ps spin–lattice relaxation time in gold [36]. Except for materials with very large magnetocrystalline anisotropy, this mechanism is not expected to play an important role in the ultrafast regime described in this review. Note that the anisotropic fluctuations of the magnetization correspond to the damping mechanism which appears in the phenomenological models of Landau–Lifschitz or Gilbert, which were mentioned in the introduction. Another effect which might influence the spin–lattice relaxation is the dependence of the phonon frequency on the magnetization [37]. This is because of a modification of the screened ion-ion interaction by the magnetization associated with the itinerant electrons in the ferromagnet. This correction should not, however, significantly alter the spin dynamics on the sub-picosecond time-scale.

10.2.3 Model of Spin Dephasing

As detailed in Section 4, an out-of-equilibrium regime is experimentally observed for the ultrafast heating of the electrons, spins, and phonons. This requires a mechanism for coupling electrons and spins. In the preceding section we suggested that it could be modeled with two baths (electrons and spins) with different temperatures. This phenomenological model, however, does not give any insight into the underlying microscopic processes. Ideally, one should consider the full time-dependent many-body problem of interacting charges and spins. For 3d ferromagnets the main difficulty is that several aspects should be considered simultaneously:

- The band structure of ferromagnetic transition metals comprises exchange splitting d and s bands; crystal field, exchange, and hybridization play an equally important role.
- The description of electron correlation should take into account d-s interactions and inter- and intra-site Coulomb interaction.
- Magneto-optical properties can be computed only if spin–orbit interaction is taken into account.

A first approach to this problem was proposed by Hubner and Zang [12]. They considered the electronic Hamiltonian:

$$\sum_{i,j,k,l,\sigma\prime,\sigma'',\sigma'''} U_{i\sigma,j\sigma\prime,l\sigma''',k\sigma''} c^{+}_{i\sigma} c_{j\sigma\prime} c_{k\sigma''} c_{l'''} + \sum_{\nu,\sigma,k} E_{\nu}(k) n_{\nu,\sigma}(k) + H_{\mathrm{so}}$$

where i, j, k, l are orbital indices and σ the spin index ($\sigma = \uparrow$ or $\downarrow$). $U_{i\sigma,j\sigma\prime,l\sigma''',k\sigma''}$ is the intra-site electron interaction described by three parameters (Coulomb repulsion, U, exchange energy, J, and exchange anisotropy, ΔJ) obtained from spectroscopic data for the atom (for Ni, $U_0 = 12\,\mathrm{eV}$, $J_0 = 0.99\,\mathrm{eV}$, $\Delta J_0 = 0.12\,\mathrm{eV}$). $E_{\nu}(k)$ is the single-particle energy dispersion of band ν, $n_{\nu\sigma}$ the particle number operator, and H_{so} the spin-orbit Hamiltonian. A further approximation has been made to enable solution of this Hamiltonian. It consists in neglecting the off-diagonal terms in the momentum space for the electron interaction. The properties of the ground state are discussed in ref. [34]. The time-dependent calculations have been performed assuming an excitation centered 2 eV above the ground state. The excited state is prepared by assuming a Gaussian distribution of width W ($W = 0.1$–$20\,\mathrm{eV}$) which mimics the wavelength dispersion of a short pulse.

The spin and charge dynamics can be characterized by the intrinsic quantities $S_z(t) = \langle\Phi(0)|\hat{S}_z|\Phi(t)\rangle$ and $N(t) = \langle\Phi(0)|\hat{N}|\Phi(t)\rangle$. $|\Phi(0)\rangle$ is the initial state many-body wave function; $|\Phi(t)\rangle = \mathrm{e}^{-iHt/h}|\Phi(0)\rangle$; $\hat{S}_z$ is the spin operator in the direction of the quantification axis, and $\hat{N}$ the electron number operator. The time evolution of S_z and N, during the first 100 fs, computed for a Gaussian width of 0.1 eV, is depicted in Fig. 4 [38]. Both dynamics are characterized by rapid decay and weak oscillations. The decay time of the spins (50 fs) is, however, larger than the decay time of the charges (20 fs). The relaxation of $N(t)$ and $S_z(t)$ has been attributed to a dephasing process between the different excited eigenstates: the more eigenstates contribute to the excited state (namely for the shortest pulses), the faster is the dephasing. The longer dephasing time for the spin can be explained qualitatively,

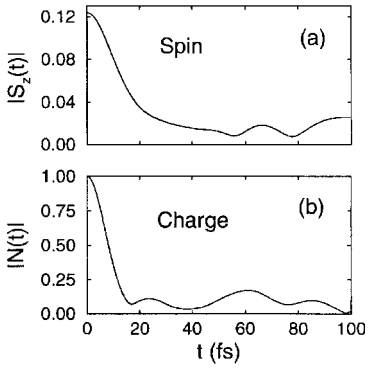

Fig. 4. Intrinsic physical quantities as defined in text: (a) $|S_z(t)|$ and (b) $|N(t)|$, as a function of time, t. The initial state is prepared 2 eV above the ground state with a Gaussian broadening of 0.1 eV [38].

because fewer excited eigenstates (singlets are excluded) are involved for $S_z(t)$ than for the computation of $N(t)$.

10.3 Magneto-optical Response and Measurement Techniques

10.3.1 Magneto-optical Response

10.3.1.1 Linear Magneto-optics

Magneto-optical (MO) techniques are popular tools for probing the magnetic properties of thin films. They are very sensitive and enable the measurement of minute quantities of materials (down to a fraction of a monolayer). The linear magneto-optical effects (the Faraday effect in transmission geometry or the Kerr effect in reflection geometry) produce a modification of the state of polarization of a probe beam after its interaction with a magnetized sample. Experimentally the Faraday and polar Kerr effects result from the application of a magnetic field perpendicular to the plane of the film. They usually produce larger effects than the longitudinal Kerr effect, which is obtained with a magnetic field which lies both in the plane of incidence and in the plane of the film [39]. The simplest description of the MO effect is the classical Voigt model [40], in which the electrons of the metal, with density N, are submitted to a friction force $-m\gamma \mathrm{d}r/\mathrm{d}t$ and the Lorentz force $-e(v \wedge \mathbf{B}_0 + \mathbf{E})$. The solution of the equation of the electron motion enables computation of the dielectric tensor from the expression for the polarization $\mathbf{P}(\omega) = \hat{\chi}(\mathbf{B}_0)\mathbf{E}$. In the presence of a uniform magnetic field of module $B_0 = |\mathbf{B}_0|$ along the z direction, the dielectric tensor of an isotropic medium with permittivity ε_{xx} acquires non-diagonal elements:

$$\hat{\varepsilon} = 1 + 4\pi\hat{\xi} = \begin{bmatrix} \varepsilon_{xx} & \varepsilon_{xy} & 0 \\ \varepsilon_{yx} & \varepsilon_{xx} & 0 \\ 0 & 0 & \varepsilon_{xx} \end{bmatrix}$$

With, to first order in B_0:

$$\varepsilon_{xy}(\omega) = \frac{\omega_p^2 \Omega \omega}{\left(\omega^2 + \mathrm{i}\omega\gamma\right)^2 - \Omega^2\omega^2}$$

where $\omega_p^2 = Ne^2/m\varepsilon_0$, is the plasma frequency and $\Omega = eB_0/m$, is the cyclotron resonance frequency. Knowledge of $\hat{\varepsilon}$ enables determination of the transmitted and reflected waves for a thin film, even for complex geometry, from the use of the Fresnel relations (although closed formulas cannot necessarily be obtained) [41, 42]. For example, for a planar Kerr effect at normal incidence, it is found that the eigenmodes of the electric field are circular waves (σ^+, σ^-). The Kerr rotation and ellipticity are given by:

$$\Phi_K = \theta_K + i\varepsilon_k = \frac{-\sigma_{xy}}{\sigma_{xx}\sqrt{1 + i\frac{4\pi}{\omega}\sigma_{xx}}} \tag{6}$$

where $\hat{\sigma}$ is the conductivity tensor: ($\hat{\varepsilon} = 1 + 4\pi i\hat{\sigma}/\omega$) and n the complex refractive index. Measurement of these quantities enables determination of the non-diagonal part of the dielectric tensor $\hat{\varepsilon}$. Experimental Kerr rotations in metals do not exceed 1° for wavelengths ranging from the near-ultraviolet (UV) to the near-infrared (IR). The ratio of the diagonal to non-diagonal elements of the dielectric tensor is typically of the order of 10^{-2}. The corresponding B_0 is typically 10^3 T and its origin is the Weiss molecular field rather than an external applied magnetic field. We also note that the microscopic mechanism responsible for the friction force in the Voigt model is related to the electron–electron collisions. In metals the electromagnetic absorption originates from this mechanism via intra-band transitions. These transitions dominate optical spectra in the IR. In the visible and UV parts of the spectrum, inter-band transitions are also important.

The calculation of the Kerr or Faraday rotation requires that inter-band optical transitions using a microscopic model of the susceptibility tensor should be taken into account. In metals, it is a difficult task because the strong correlation between the electrons and the coupling of the optical and magnetic fields with the charges and spins must be taken into account. This many-body problem is generally treated with a simplified Hamiltonian model. For example, Bennet and co-workers [43] considered a sum of one-body Hamiltonians, H_{0n}, where the Coulomb interaction e^2/r_{nm} between the electrons is replaced by an effective one-body operator:

$$H_{0n} = \frac{p_{\mathrm{n}}^2}{2m_n} + V(\mathbf{r}_n) + \frac{\hbar \mathbf{P}_n}{4m_n^2c^2}\mathbf{s}_n \times \nabla V(\mathbf{r}_n) + V_{eff}(\mathbf{r}_n)$$

where $\mathbf{P}_{\mathrm{n}} = \mathbf{p}_{\mathrm{n}} + \frac{\mathrm{e}}{\mathrm{c}}\mathbf{A}_{\mathrm{mag}}(\mathbf{r}_{\mathrm{n}})$. The light- matter interaction is treated by a semi-classical Hamiltonian H_{Rn} for each electron n ($n = 1, N$):

$$\mathrm{H_{Rn}} = \frac{\mathrm{e}}{\mathrm{m_n c^2}}\Pi_{\mathrm{n}} \cdot \mathbf{A}_{\mathrm{light}}(\mathbf{r}_{\mathrm{n}})$$

where $\Pi_{\mathrm{n}} = \mathbf{P_n} + \mathbf{s_n} \times \nabla \mathrm{V}(\mathbf{r_n})$. P_n, s_n, and $V(\mathbf{r_n})$ are, respectively, the momentum, the Pauli spin operator, and the periodic potential of the electron, n, of mass m_n. The

vectors $A_{\mathrm{mag}}(\mathbf{r_n})$ and $A_{\mathrm{light}}(\mathbf{r_n})$ are the potential vectors of the applied magnetic and radiation fields. The term $\mathbf{s_n} \times \nabla V(\mathbf{r_n})$ represents the spin-orbit interaction.

Neglecting local field effects, the conductivity tensor components σ_{ij} are related to the density of power P absorbed at the photon energy $\hbar\omega$ in the metal by:

$$\mathrm{P} = \frac{\mathrm{N}}{2}\Re\mathrm{e}\sum_{ij}\sigma_{ij}^{*}\mathrm{E}_j^{*}\mathrm{E}_i = \mathrm{N}\hbar\omega\sum_{\alpha\neq\beta}\mathrm{W}_{\beta\alpha}$$

Application of time-dependent perturbation theory to the Hamiltonian H_{Rn} gives the transition probabilities $W_{\beta\alpha}$ per unit time at energy $\hbar\omega$ between the states $|\alpha\rangle$ and $|\beta\rangle$ separated by the energy $\hbar\omega_{\beta\alpha}$:

$$W_{\beta\alpha} = \frac{2\pi}{\hbar}\frac{EE*e^2}{4m^2\omega^2}\,|\langle\beta|\pi_\nu|\alpha\rangle|^2\left[\delta(\hbar\omega_{\beta\alpha}-\hbar\omega)+\delta(\hbar\omega_{\beta\alpha}+\hbar\omega)\right]$$

where π_ν ($\nu = x$, y, or $\nu = +$, $-$) are the components of the generalized momentum Π with the definition $\pi_\pm = (\pi_x \pm \pi_y)/\sqrt{2}$. The real and imaginary parts of the non-diagonal component of the conductivity are then given by:

$$\Re\mathrm{e}\sigma_{xy} = \frac{\mathrm{N}\pi e^2}{\hbar m^2}\sum_{\beta\neq\alpha}\left\{\frac{|\langle\beta|\pi_-|\alpha\rangle|^2}{(\omega_{\beta\alpha}^2-\omega^2)}-\frac{|\langle\beta|\pi_+|\alpha\rangle|^2}{(\omega_{\beta\alpha}^2-\omega^2)}\right\} \tag{7a}$$

$$\Im\mathrm{m}\sigma_{xy} = \frac{\mathrm{N}\pi e^2}{2\hbar m^2}\sum_{\beta\neq\alpha}\delta(\omega_{\beta\alpha}-\omega)\left[|\langle\beta|\pi_-|\alpha\rangle|^2-|\langle\beta|\pi_+|\alpha\rangle|^2\right] \tag{7b}$$

These two expressions enable deduction of the Kerr and Faraday rotations as described above. The important quantities to determine are the inter-band probability transitions $|\langle\beta|\pi_\pm|\alpha\rangle|$ which contain two different contributions, associated, respectively, with a splitting of the states and with the spin–orbit coupling of the electron. Argyres [44] has shown that it is the spin–orbit coupling which dominates for ferromagnetic materials.

Ab initio calculation of the dielectric tensor has been performed for ferromagnetic 3d metals and wavelengths in the IR to the UV region. Agreement with experimental results is good. The important result is that inter-band transitions dominate the magneto-optical response in the visible part of the optical spectrum.

The theory above applies to the magneto-optical response of a ferromagnetic material excited with a plane wave. In the dynamic case one would, ideally, have to consider time-dependent interactions between the excited electrons. This difficult task can, to a first approximation, be reduced to a simpler one by considering a time-dependent electron temperature by using, for instance, the two-temperature model of Section 2.1. The time-dependent magnetization then depends on the dynamics of the electronic population distributed apart from the Fermi level. This approach is, however, valid only when the electrons are thermalized and it does not, therefore, enable description of the early spin dynamics. It also does not take into account the

dynamic aspect of the coupling between the electron and spin systems which was introduced qualitatively in Section 2.2 with a three-temperature model.

10.3.1.2 Non-linear Magneto-optics

Magnetic second-harmonic generation (M-SHG) is a recent tool which enables study of the magnetic properties of surfaces [45] and buried interfaces [46]. The specificity of this method comes from the non-centrosymmetry of the interfaces, which is at the origin of SHG. Because non-linear optical effects require a large peak power and short pulses, they are a priori compatible with pump and probe measurements of ultrafast dynamics.

The second-order non-linear polarization is given by:

$$P_i(2\omega) = \chi^{(2)}_{ijk}(M) E_j(\omega) E_k(\omega)$$

The term $\chi^{(2)}$ can be split into the contributions, even ($\chi^{(2)}_{\text{even}}$) and odd ($\chi^{(2)}_{\text{odd}}$) with respect to the magnetization. To the lowest order in the magnetization, $\chi^{(2)}_{\text{even}}$ is regarded as independent of the magnetization and $\chi^{(2)}_{\text{odd}}$ as proportional to the magnetization. Denoting by ϕ the phase difference between the complex quantities $\chi^{(2)}_{\text{even}}$ and $\chi^{(2)}_{\text{odd}}$, and disregarding Fresnel factors that take into account the actual experimental geometry, the second-harmonic intensity $I(2\omega)$ is given by:

$$I(2\omega, \pm M) \propto I^2(\omega) \left[\left| \chi^{(2)}_{\text{even}} \right|^2 + \left| \chi^{(2)}_{\text{odd}}(M) \right|^2 \pm 2 \left| \chi^{(2)}_{\text{even}} \right| \left| \chi^{(2)}_{\text{odd}}(M) \right| \cos\phi \right] \quad (8)$$

This expression shows that $I(2\omega)$ provides direct magnetic information. Despite very low efficiency (typically, $I(2\omega)/I(\omega) \approx 10^{-14}$ even for a peak power of $\sim 10^{12}\,\mathrm{W\,m^{-2}}$), M-SHG furnishes detailed surface/interface-sensitive magnetic information. It has also been shown experimentally [46] and theoretically [47] that non-linear MO effects give rise to non-linear Kerr rotations which can be two orders of magnitude larger than linear Kerr rotation. Recent significant experiments related, for example, to surface magnetism, quantum-well states or imaging of surface domains can be found in refs. [48–50].

10.3.2 Time-resolved magneto-optical techniques

In this section, we describe different techniques which enable determination of the time-dependent magnetization. In particular, we describe in detail the apparatus used by the authors to perform the time-resolved magneto-optical measurements reported in Section 4.

10.3.2.1 Time-resolved Magneto-optical Measurements

Time-resolved magneto-optical measurements have been performed using a femtosecond laser system and a static magnetic field. The femtosecond pulses are produced by use of a tunable titanium sapphire laser. The pulses issued from an oscillator operating at 80 MHz are amplified in a regenerative amplifier pumped by a Nd:YLF (yttrium lithium fluoride) laser with a repetition rate of 5 kHz. The maximum energy per pulse is ~200 μJ tunable in the range 760–860 nm and the pulse duration is ~100 fs. Part of the amplified beam can be frequency-doubled (380–430 nm) in a 1-mm thick BBO crystal to enable frequency non-degenerate pump–probe measurements. The intensity ratio of the pump and probe beams is 20:1 and their spot diameters focused on the samples are, respectively, ~100 μm and ~50 μm. The overlap of the two beams is monitored with a CCD camera. Figure 5 shows the laser arrangement and the experimental configuration.

Early experiments performed in nickel films used a different laser system. The femtosecond pulses were produced by a colliding pulsed mode locked cavity operating at 620 nm and amplified at 5 kHz with a copper vapor laser. The duration of the amplified pulses was 80 fs and the maximum pulse energy was 10 μJ, with a central wavelength at 620 nm. Both laser set-ups enabled the performance of different types of measurement.

(i) When measuring electron dynamics no magnetic field is applied. The differential transmission of a thin film $\Delta T/T(t) = (T_{on} - T_{off})/T_{off}$ is measured as a function

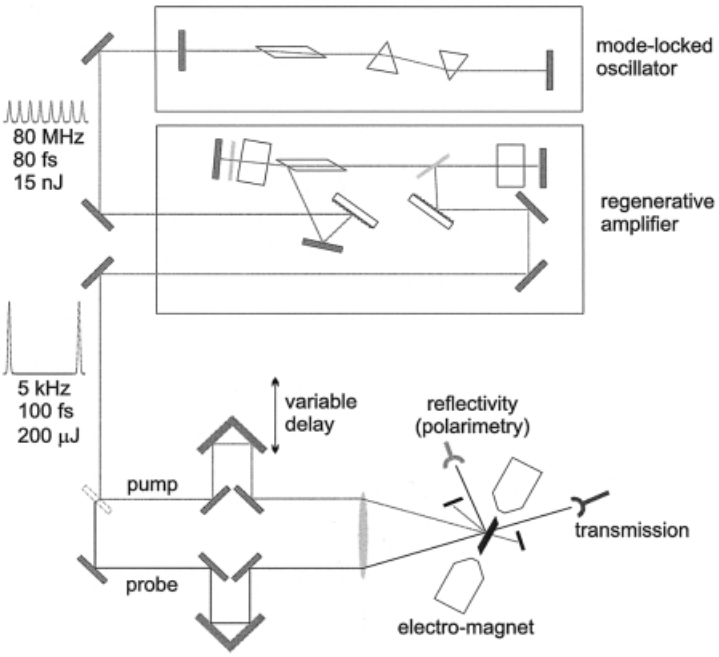

Fig. 5. Laser arrangement and experimental configuration used in order to measure the spin dynamics and transient reflectivity/transmittivity in ferromagnetic thin films.

of the temporal delay, t, between the pump and probe, T_{on} or T_{off}, respectively, being the probe transmission with or without the pump. Similarly the differential reflection $\Delta R/R(t)$ is measured simultaneously. The detection scheme is a synchronous detection using a chopper and a lock-in amplifier. The simultaneous measurement of the differential transmission and reflection as a function of pump-probe delay enables retrieval of the time-dependent complex dielectric function $\varepsilon(t)$ of the metal. We note $\Delta\varepsilon_1$ and $\Delta\varepsilon_2$, the corresponding changes of the real and imaginary part of $\varepsilon(t)$ induced by the pump pulse. They are the physical quantities of interest in understanding the electron dynamics. The dielectric function is retrieved by following the same procedure that was used by Rosei and Lynch [51] to analyze static thermomodulation measurements. In this procedure the Fabry-Pérot transmission, T, and reflection, R, of a thin metallic film of thickness, l, are functions of the refractive index, n, the wavelength, λ, and the film thickness, l. They can be differentiated with respect to a small variation of the refractive index $\Delta n = \Delta n_1 + i\Delta n_2$ to give:

$$(BC - AD)\Delta\varepsilon_1 = B(\Delta T/T) - D(\Delta R/R) \tag{9a}$$

$$(BC - AD)\Delta\varepsilon_2 = C(\Delta R/R) - A(\Delta T/T) \tag{9b}$$

where A, B, C, and D depend on n, λ, and l, and the dielectric function is obtained from $\varepsilon = \varepsilon_1 - i\varepsilon_2 = n^2$. This procedure requires that the properties of the material are known. In particular the thickness of the film and its linear complex refractive index must be determined accurately. In our experiments they were determined by a combination of X-ray diffraction at grazing incidence and by ellipsometric measurements. In the static thermomodulation experiments, in which the temperature of the lattice, Θ_l, is increased by application of a current to the sample, Eqs (9a) and (9b) correspond to the spectral variation of the dielectric functions $\Delta\varepsilon_1(\omega)$and $\Delta\varepsilon_2(\omega)$. Here they correspond to the temporal variation $\Delta\varepsilon_1(t)$ and $\Delta\varepsilon_2(t)$. In this case the change of the dielectric function comes from modification of the electronic distribution induced by the laser pulse or, equivalently, induced by a change of the electronic temperature $\Delta\Theta_e = \Theta_e(t) - \Theta_e(\alpha)$ when the electrons are in a well-defined thermal distribution.

(ii) When measuring the spin dynamics an electromagnet enables variation of the static magnetic field H in the range ± 3 kOe ($\pm 240\,\mathrm{A\,m^{-1}}$), which is set parallel to the plane of the sample. The polarizations of the pump and probe beams are either s, p or σ^+ and they can be varied independently. As sketched in Fig. 6, the magneto-optical signal is obtained by analyzing the probe beam at an angle of $90^\circ + \theta_\varepsilon$ relative to its incident polarization direction, θ_ε, being set to a few degrees.

The signal can be written:

$$I(H,t) = I_0 \sin^2(\theta_\varepsilon + \Theta_K(H,t)) \approx I_0\theta_\varepsilon + 2I_0\Theta_K(H,t)$$

where I_0 is the transmitted probe intensity and Θ_k is the Kerr rotation ($\Theta_K \ll \theta_\varepsilon$). The Kerr signal is superposed on a background and the sensitivity of this method is, therefore, limited by the fluctuations of the laser. Improvement of the technique by use of a polarization-sensitive balanced optical bridge, consisting of a Wollaston prism and a low-noise differential detector, has been proposed [10]. For a high repetition rate laser system the technique can be further improved by modulation of the

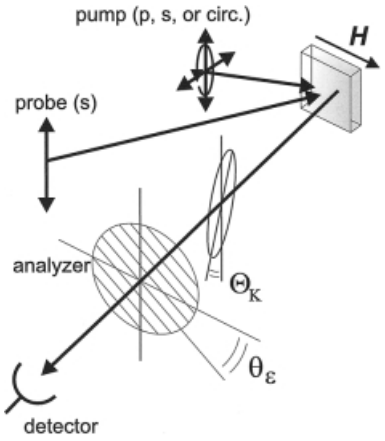

Fig. 6. Polarimetric configuration used in the time-resolved magneto-optical Kerr measurements.

polarization [52], which has the additional advantage of enabling simultaneous measurement of both the Kerr ellipticity and rotation. The Kerr configuration enables two types of measurement. The "magnetization" curve $M(H, t_0) \approx I(H, t_0) - I_0\theta_\varepsilon$ can be measured for a fixed pump–probe delay, t_0, as a function of the magnetic field, which is varied slowly. Alternatively, the magnetization dynamics, $M(H_0, t)$, can be measured for a fixed magnetic field, H_0, as a function of the pump-probe delay, t. In both each data point corresponds to an average over ~1000 pulses.

Fig. 7 shows the typical Kerr hysteresis obtained at room temperature for the 22-nm thick Ni film (Fig. 7a) and the 48-nm thick $CoPt_3$ film (Fig. 7b). The nickel

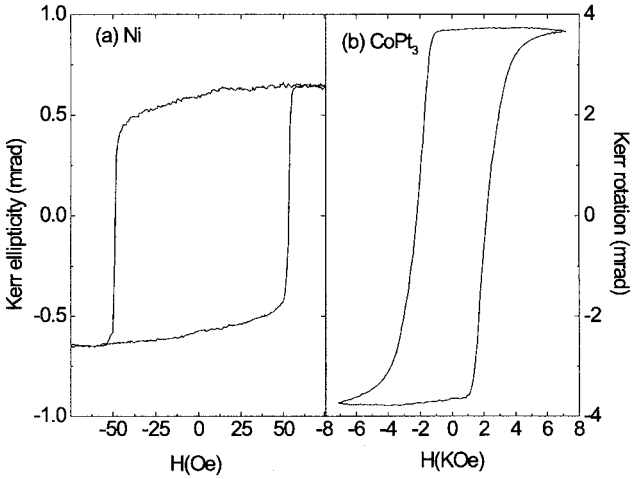

Fig. 7. Typical hysteresis loops obtained by the magneto-optical Kerr effect (MOKE), using a continuous wave (CW) laser ($\lambda = 670$ nm). (a) Longitudinal Kerr ellipticity for a 22-nm thick Ni film covered by a 100-nm thick MgF_2 protective layer. (b) Polar Kerr rotation for a 48-nm thick $CoPt_3$ film.

polycrystalline thin films were evaporated on to a glass substrate under high vacuum. The $CoPt_3$ films, consisting of the alloy $Co_{0.25}Pt_{0.75}$, were grown at 690 K on a 16-nm Ru (0001) buffer layer deposited on a mica substrate. The growth conditions were chosen to optimize the perpendicular anisotropy [53]. Characterization of the magnetization as a function of temperature shows that the remanence magnetization vanishes at 635 K. The ferroparamagnetic transition occurs over a broad temperature range, which can be explained by the chemical disorder present in the alloy.

10.3.2.2 Time-resolved Second-harmonic Generation

Magnetic second-harmonic generation is another technique which has been used to perform measurements of magnetization dynamics on a femtosecond time-scale on Ni and Co surfaces [8, 54]. In these experiments, the temporal resolution is also obtained by a pump-probe technique but, instead of measuring the modifications induced by the pump on the probe, the intensity variations of the second harmonic field generated by the probe are detected. Both the pump and the probe beams must be of high intensity (so that the second-harmonic generation (SHG) yield is measurable). They are produced by a Ti:sapphire regenerative amplifier. Temporal resolution down to 40 fs has been reported [55]; the typical energy density on the sample is $\sim$6 mJ cm^{-2}. In this type of experiment, the raw signal is the SHG intensity obtained with different orientations of a static magnetic field, H, parallel to the plane of the sample. Careful filtering of the fundamental component $I(\omega)$ is achieved with color filters and spatial dispersion with a prism. $I(2\omega)$ is measured with a photomultiplier and the probe beam is chopped to enable phase-sensitive detection. Experimental results using these techniques are reported in Section 4.

10.3.2.3 Spin-resolved Photoemission

Spin-resolved photoemission is a well-known technique for study of the electronic and magnetic properties of ferromagnets [56, 57]. More recently, it has been used to study dynamic effects [9, 32, 58]. In such experiments, an intense pump pulse excites the sample and electrons are photoexcited in the vacuum by use of a time-delayed probe pulse of shorter wavelength. The spin polarization of the photoelectrons is then measured by a spin detector (e. g. a Mott detector). Because most metals have work functions in the range 4–6 eV, UV laser pulses must be used. This can be achieved, for instance, with the fourth harmonic of a Ti:sapphire laser. The photoelectrons emitted by the sample have a short mean free path in metals (typically a few interatomic distances), so the technique is very sensitive to the surface. This technique is powerful, because it enables direct measurement of the spin polarization in the energy–momentum space. It suffers, however, from the very low efficiency of the spin detection, and also from experimental difficulties inherent in the detection of electrons in the presence of an applied magnetic field. Experimental results using these techniques are reported in the next section.

10.4 Experimental Studies – Electron and Spin Dynamics in Ferromagnets

10.4.1 Electron Dynamics

In this section, we consider pump-probe dynamics in d-band metallic thin films in the absence of an applied magnetic field. As discussed in Section 2.1, two main temporal regimes must be distinguished during the first few picoseconds: the initial thermalization of the electron gas to a hot Fermi-Dirac distribution, and the energy transfer to the lattice. The first regime is characterized by electron–electron scattering whereas the temperature equilibrium between the electron and lattice subsystems is achieved via the electron–phonon interaction. We now analyze these two regimes in more detail.

10.4.1.1 Electron Thermalization and Relaxation to the Lattice

In Fig. 8a we have depicted the dynamics of the differential transmission $\Delta T/T(t)$ and reflection $\Delta R/R(t)$, obtained with a nickel film with a thickness, l, of 22 nm, covered with a 100-nm thick MgF_2 protecting layer.

The density of the pump energy absorbed by the film is 0.8 mJ cm^{-2}. The pump and probe are linearly polarized and parallel to each other. The corresponding temporal variation of the real and imaginary parts of the dielectric function, $\Delta\varepsilon_1(t)$ and $\Delta\varepsilon_2(t)$,

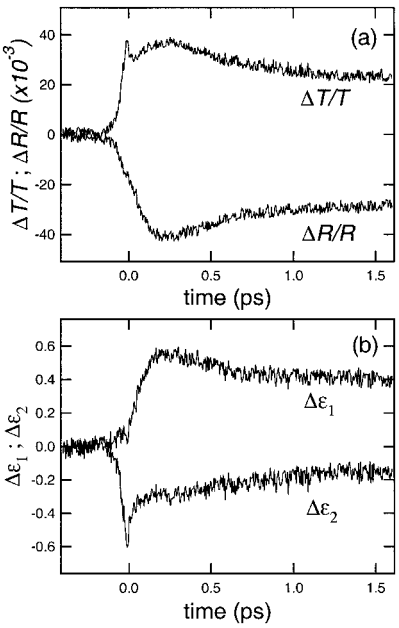

Fig. 8. Optical transients for a 22-nm thick Ni film measured with pulses of duration 60 fs at $\lambda = 620$ nm. (a) Differential transmission $\Delta T/T(t)$ and reflection $\Delta R/R(t)$, measured for a nickel film with a thickness, l, of 22 nm. (b) Temporal variation of the real and imaginary parts of the dielectric function, $\Delta\varepsilon_1(t)$ and $\Delta\varepsilon_2(t)$, calculated using Eqs (7a) and (7b).

obtained by use of Eq. (9), are represented in Fig. 8b. Several features can be observed in Figs 8a and 8b. First, a coherent peak is present in the transmission signal at $t = 0$. It is present only when the pump and probe pulses overlap in time. Second, the maxima of both the transmission and reflection signals occur with a time delay of ~250 fs. Finally both $\Delta T/T$ and $\Delta R/R$ relax with a longer time constant. The first effect corresponds to the non-linear coherent interaction between the pump and probe pulses. Formally, it can be accounted for in the time-dependent perturbation of the material polarization via third-order terms with the following time ordering of the pump and probe field amplitudes: $E_{\text{pump}}(t_1)E_{\text{probe}}(t_2)E^*_{\text{pump}}(t_3)$ with $t_1 < t_2 < t_3$ [59, 60]. It shows up as a coherent peak in the temporal variation of the imaginary part of the dielectric function which has an important contribution near $t = 0$. It is, on the other hand, hardly visible in $\Delta\varepsilon_1$, which has a weak contribution during the pump and probe overlap.

The effect of temporal delay between the maxima of $\Delta\varepsilon_1$ and $\Delta\varepsilon_2$ is related to the thermalization of the electron gas. As mentioned in Section 1.2, the primary step in the electron dynamics is redistribution of the electrons which have been excited with a large excess of energy relative to the Fermi level. This process is mediated via the electron–electron interaction. It lasts a few hundred femtoseconds, because it depends on phase space filling, owing to Pauli exclusion. To understand how this thermalization process influences the dynamics of the real and imaginary parts of the dielectric function, one must decompose the dynamics of the optical processes into two components corresponding to intra-band and inter-band transitions [61, 62]. As seen in Fig. 8b for $\Delta\varepsilon_2$, a fast decrease of the signal occurs during the first 250 fs. This contribution can be attributed to the dynamics of the non-thermalized electrons probed via inter-band transitions from the d levels to the conduction band. After ~250 fs, the value of $\Delta\varepsilon_2$ is essentially related to the thermalized electrons as probed via the intra-band processes. The succeeding dynamics then correspond to the cooling of the electrons via the electron–phonon interaction.

For $\Delta\varepsilon_1$, the situation is different because the signal reaches its maximum value within the first 250 fs. According to the preceding remarks it is indicated that it is mostly the intra-band component which is probed. It should, however, be stressed that the dynamics of $\Delta\varepsilon_1$ can be very different, depending on the probe wavelength. A first intuitive thought is that $\Delta\varepsilon_1$ should also be sensitive to the thermalization process via all the inter-band transitions, because $\Delta\varepsilon_1$ can be obtained by a Kramers–Kronig transform of $\Delta\varepsilon_2$. This is, however, precisely at the root of the complex spectral behavior of the inter-band part of $\Delta\varepsilon_1$, as is known, for instance, for the noble metals [61, 62]. With nickel, the complicated density of states of the 3d bands might be the origin of the negligible contribution of the inter-band component of $\Delta\varepsilon_1$ when the probe energy is close to 2 eV.

Let us now focus on another ultrafast mechanism, which is not related to the magnetization of the material and which is observed when analyzing the state of polarization of the pump-probe transmission and reflectivity signals.

10.4.1.2 Optical Orientation

As detailed in Section 3.2, the magneto-optical techniques used to measure the magnetization of a ferromagnetic material are based on the modification of the state of polarization of an incident beam when it is reflected or transmitted by the sample. In such experiments it is important to study the polarization changes of the laser beam for different applied magnetic fields to obtain reliable information about the magnetization. This point becomes particularly relevant when several laser fields interact in the metal. In these circumstances pure optical effects, which do not require any magnetization of the sample, also lead to a change in the polarization of the incident beams. Such effects, which in non-linear optics have the generic name of optical orientation, might hinder the true modification of the magnetization in a ferromagnetic material. To illustrate this aspect we consider in this section the effect of an intense laser beam (the pump) on the state of polarization of a second weak laser beam (the probe).

Let us assume that the two incident fields are degenerate monochromatic fields of frequency ω and respective complex amplitudes $E_{\mathrm{P}}(\omega)$ and $E_{\mathrm{S}}(\omega)$. In the direction of the probe beam, E_{S}, the component $P_{\mathrm{i}}^{(3)}(\omega)$ $(i = x, y, z)$ of the third order polarization is given by:

$$P_{\mathrm{i}}^{(3)} = \sum_{\mathrm{jkl}} \mathcal{P}\chi_{\mathrm{ijkl}}^{(3)}(\omega, \omega, -\omega, \omega) E_{\mathrm{Pj}}(\omega) E_{\mathrm{Pk}}^{*}(\omega) E_{\mathrm{Sl}}(\omega)$$

where $\mathcal{P}$ indicates the permutations of the fields and $\chi^{(3)}(\omega)$ is the third-order non-linear susceptibility tensor. Using the intrinsic permutation symmetry and assuming an isotropic medium, only two components of $\chi^{(3)}$ are linearly independent; we designate these by χ_{1122} and χ_{1221}. When the pump and probe fields propagate along z, and using the basis of linear polarizations, it is easy to show that [63, 64]:

$$\begin{pmatrix} P_x^{(3)} \\ P_y^{(3)} \end{pmatrix} = 6 \begin{bmatrix} (2\chi_{1122} + \chi_{1221}) E_{Px} E_{Px}^{*} + \chi_{1122} E_{Py} E_{Py}^{*} & \chi_{1122} E_{Px} E_{Py}^{*} + \chi_{1221} E_{Px}^{*} E_{Py} \\ \chi_{1122} E_{Py} E_{Px}^{*} + \chi_{1221} E_{Px} E_{Py}^{*} & (2\chi_{1122} + \chi_{1221}) E_{Py} E_{Py}^{*} + \chi_{1122} E_{Px} E_{Px}^{*} \end{bmatrix} \begin{pmatrix} E_{Sx} \\ E_{Sy} \end{pmatrix}$$

Let us now determine the amplitudes of the probe beam E_{Si} $(i = x, y)$ after propagation. When the pump is polarized along the x axis the Maxwell equations for a probe field E_{Si} $(i = x, y)$ lead to an equation of propagation which can be decomposed along the normal axis Ox and Oy:

$$\frac{\partial^2 \mathrm{E_{Si}}}{\partial \mathrm{z}^2} - \frac{\varepsilon_{\mathrm{L}}}{c^2} \frac{\partial^2 \mathrm{E_{Si}}}{\partial t^2} = \frac{4\pi}{\mathrm{c}^2} \frac{\partial^2 \mathrm{P_i^{(3)}}}{\partial t^2}$$

where ε_{L} is the linear dielectric function. For a probe polarized parallel either to the Ox or to the Oy axis the solution is a plane wave propagating with a velocity $c/\sqrt{\varepsilon_{\mathrm{i}}}$ $(i = x, y)$, with:

$$\varepsilon_x = \varepsilon_{\mathrm{L}} + 24\pi |E_P|^2 (2\chi_{1122} + \chi_{1221});\ \varepsilon_y = \varepsilon_{\mathrm{L}} + 24\pi |E_P|^2 \chi_{1122}$$

Because the non-linear dielectric functions ε_x and ε_y are complex quantities, the pump beam induces both birefringence and dichroism in the non-linear material.

A probe beam which is initially polarized in a direction different from Ox and Oy therefore acquires an elliptic polarization. An induced elliptic probe polarization also occurs when the pump beam has circular polarization. It is then easier to decompose the probe polarization into its right and left circular components E_{S+} and E_{S-} which propagate with different velocities $c/\sqrt{\varepsilon_{\pm}}$.

The extension of the above considerations to pulsed pump and probe excitation is straightforward. The pump pulse induces a time-dependent polarization anisotropy in the non-linear medium which induces rotation of the polarization axis of a linearly polarized probe beam. It must be pointed out that this coherent effect is different from the coherent peak mentioned in the preceding section. The optical orientation is a process which is present during the relaxation time of the polarization anisotropy, that is during the dephasing time T_2 of the electronic states involved in the non-linear process. The coherent peak is, in contrast, present during pump and probe temporal overlap only. Because the dephasing time of the non-linear polarization is extremely fast in metals ($T_2 < 20$ fs), both effects are generally mixed in pump-probe experiments where the pulse duration is longer. Therefore the temporal profile of the probe beam-induced ellipticity follows the envelope of the pump pulse.

The important point we have stressed in this paragraph is that the optical orientation is a coherent effect which might have no connection with the sample magnetization. One should not, therefore, draw any conclusion about the spin dynamics from such effects. It is only when resonant optical processes occur, for example the excitonic transitions in semiconductors, that a circularly polarized optical pulse can induce spin effects related to the conservation of the orbital and spin momentum [71]. In ferromagnetic materials it is via the spin–orbit coupling and exchange interaction that one expects to obtain optically induced spin dynamics.

10.4.2 Demagnetization Dynamics

In this section, we discuss experimental results concerning the ultrafast magnetization dynamics of Ni and $CoPt_3$ thin films.

10.4.2.1 Nickel Films

Spin dynamics in thin and ultrathin Ni films has been studied by several groups [7–9, 52, 55]. This material has the lowest Curie temperature among ferromagnetic transition metals (631 K).

The first report on the spin dynamics of a metallic ferromagnet on the femtosecond time-scale can be found in ref. [7]. Measurements were performed on a 22-nm Ni film deposited on optical glass and protected by a dielectric layer. The experimental conditions used are detailed in Section 3.2. In Fig. 9, the remanence Kerr signal M_M is presented as a function of pump-probe delay. M_M, which is obtained from the hysteresis loops measured at each delay t, drops by approximately 40 % during the first picosecond. Its recovery time is much longer (several tens of picoseconds). To gain more insight into the magnetization dynamics, in Fig. 10 we compare the saturation

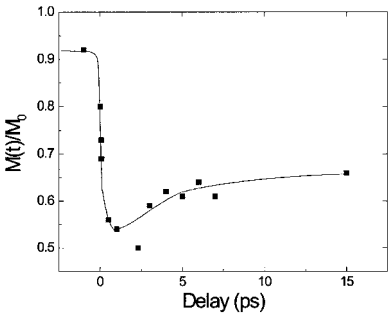

Fig. 9. Remanence Kerr signal as a function of delay for a 22-nm thick Ni film after excitation by a 60-fs pump pulse at 620 nm with an intensity of 7 mJ cm^{-2}. Each data point, corresponding to a time delay, is obtained from the measurement of a complete hysteresis loop (see text) [7]. The line is a visual guide.

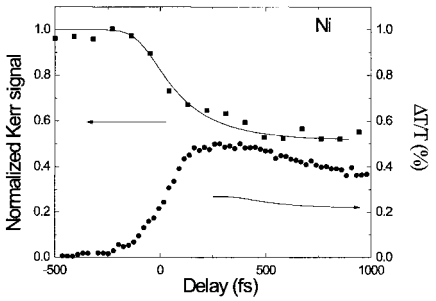

Fig. 10. Comparison of the transient reflectivity ($\Delta R/R(t)$) (circles) and the MOKE signal (squares) of a 22-nm Ni film after excitation by 120-fs duration pump pulses at 800 nm. Pump and probe beams are p polarized. The line is a fit assuming exponential relaxation of the magnetization.

magneto-optical Kerr effect (MOKE) signal $M_S(t)$ with the differential transmission signal during the first picosecond. In this experiment $M_S(t)$ is measured in a static saturating magnetic field. $\Delta T/T$ reaches a maximum at $t \approx 250$ fs with a rising time only limited by the temporal resolution of 120 fs, and then decreases. $M_S(t)$, on the other hand, decreases continuously over the entire temporal range displayed. The characteristic time of this magnetization dynamics, measured at 800 nm, is $t_m \approx 200$ fs. It is obtained by a convolution of the pulse envelope with an exponential decay (solid line in Fig. 10).

The magnetization dynamics of two Ni films of thickness 0.6 and 1.2 nm, deposited on a Ag(100) single crystal was also studied by femtosecond time- and spin-resolved two-photon photoemission [9]. Two distinct types of magnetization dynamics were observed in this experiment:

(i) the spin polarization of photoemitted electrons drops rapidly (<300 fs), in agreement with the previous MOKE experiment [7]; and

(ii) a plateau then occurs until ~300 ps, which is followed by a smoother magnetization decrease. The magnetization of a 0.6-nm film, which has a low Curie temperature ($T_c = 360$ K) vanishes after a delay of ~800 ps.

J. Hohlfeld and co-workers conducted pump and probe second-harmonic generation experiments. They considered both a polycrystalline bulk Ni–air interface [8] and epitaxial Ni ultrathin films (studied in ultrahigh vacuum) [54]. The measured quantity is the time- and magnetization-dependent SHG intensity $I(2\omega, M, t)$. The

following normalized quantities can be defined: $\Delta I^{\pm}(t) = [I^{\pm} - I_0^{\pm}]/I_0^{\pm}$, where:

$$I^{\pm} = I(2\omega, M, t) \pm I(2\omega, -M, t)$$

and $I(2\omega, \pm M)$ are defined in Eq. (8). The 0 subscript corresponds to the signal measured in the absence of the pump beam. To the lowest order in M and with the definitions of Section 3.1, $\chi^{(2)}_{\text{odd}}(t, M) = \chi^{(2)}_{\text{odd},0}(t)M(t)$ and $\chi^{(2)}_{\text{even}}(t, M) = \chi^{(2)}_{\text{even},0}(t)$. This approximation leads to:

$$I^{+} = \frac{|\chi^{(2)}_{\text{odd},0}(t)|^2 M(t)^2 - |\chi^{(2)}_{\text{odd},0}(0)|^2 M(0)^2 + |\chi^{(2)}_{\text{even},0}(t)|^2 - |\chi^{(2)}_{\text{even},0}(0)|^2}{\chi^{(2)}_{\text{odd},0}(0)|^2 M(0)^2 + |\chi^{(2)}_{\text{even},0}(0)|^2} \tag{10a}$$

$$I^{-} = \frac{|\chi^{(2)}_{\text{even},0}(t)||\chi^{(2)}_{\text{odd},0}(t)|M(t)\cos[\phi(t)] - |\chi^{(2)}_{\text{even},0}(0)||\chi^{(2)}_{\text{odd},0}(0)|M(0)\cos[\phi(0)]}{\chi^{(2)}_{\text{even},0}(0)||\chi^{(2)}_{\text{odd},0}(0)|M(0)\cos[\phi(0)]} \tag{10b}$$

With the further assumption that $\chi^{(2)}_{\text{odd},0}(t)$ and $\chi^{(2)}_{\text{even},0}(t)$ are time- independent and that the magnetization has a square-root dependence on the electron temperature:

$$M(t) = M(T_0)[1 - \text{const}(T_e(t) - T_0)]^{1/2} \tag{11}$$

Hohlfeld and co-workers [8] found that:

$$\Delta I^{+} = \text{const}[T_0 - T_e(t)] \tag{12a}$$

$$\Delta I^{-} = M(T_e(t))/M(T_0)\cos\phi - 1 \tag{12b}$$

With the above assumptions, the authors discovered, for temporal delays $t > 300$ fs, quadratic dependence of $1\Delta I^{+}$ on ΔI^{-}, which they interpreted as variation of the magnetization with the electron temperature similar to the static curve $M(T)$. For short time delays the deviation from this quadratic behavior was interpreted as a magnetic response faster than the electron thermalization. As discussed below, this interpretation is misleading.

Later results obtained by the same group, using the same technique with a time resolution of 40 fs showed no detectable delays between the magnetization and the electron temperature [55]. In that paper, the magnetic and electronic responses are associated with other quantities. Instead of using Eqs (12a) and (12b) they used:

$$S^{\pm} = [I(2\omega, M, t)]^{1/2} \pm [I(2\omega, -M, t)]^{1/2}$$

Assuming $|\chi^{(2)}_{\text{even},0}(t)| \gg |\chi^{(2)}_{\text{odd},0}(t)|M(t)$ they found $S^{+}(t)$ and $S^{-}(t)$ related respectively to the electronic and magnetic dynamics.

B. Koopmans et al. measured the spin dynamics from time-resolved MOKE experiments for buried Ni layers (thickness in the nanometer range) epitaxially grown on Cu(111) [52]. The system is interesting because an unusual spin reorientation, because of the strains induced by the lattice mismatch, occurs as a function of thickness. The easy magnetic axis is out of plane for a film thickness in the range 0.9–4 nm. The authors used a double modulation set-up – the pump beam intensity is modulated

by means of a mechanical chopper and the probe beam polarization is modulated by means of a photoelastic device. This configuration enables measurement of the dynamics of both rotation and Kerr ellipticity. During the first 500 fs the results show that these two quantities have different dynamics. The authors therefore concluded that there is no simple relationship between the magneto-optical signals and the magnetization on the sub-picosecond time-scale.

10.4.2.2 $CoPt_3$ Alloy Films

Co_xPt_{1-x} compounds have enhanced magnetic properties because of the combination of the high exchange energy of Co and the high spin-orbit energy of Pt. It was shown in the early 1990s that $CoPt_3$ alloy films have large perpendicular magnetocrystalline anisotropy, large Kerr rotations at short wavelengths, and a Curie temperature close to room temperature [65]. These properties make them good candidates for high-density magneto-optical recording. The ultrafast spin dynamics of these systems have been studied by two groups [10, 66].

G. Ju et al. studied 20-nm thick (poly-)crystalline $CoPt_3$ films deposited on glass substrates, using optical pulses at 434 nm with the high repetition rate of 76 MHz. They measured the differential reflectivities of the sample $\left(\frac{\Delta R}{R}(t)\right)_{\sigma_{\text{pump}},\sigma_{\text{probe}}}$ in four different combinations of pump and probe polarizations: $\sigma_{\text{pump}} = \sigma^{\pm}$, $\sigma_{\text{probe}} = \sigma^{\pm}$. The sample was placed in a static magnetic field. The transient Kerr ellipticity was given by:

$$\Delta\varepsilon_{K,\sigma^{\pm}}(t) = \left(\frac{\Delta R}{R}(t)\right)_{\sigma^{\pm},\sigma^{+}} - \left(\frac{\Delta R}{R}(t)\right)_{\sigma^{\pm},\sigma^{-}}$$

With a pump intensity of $\sim 1\,\mu\text{J cm}^{-2}$, the authors observed that the measured transient Kerr ellipticity depends on the pump polarization only for the shortest time delay ($\leq$ 1 ps). From this, it was inferred that the response can be split into a thermalized spin population $\Delta\varepsilon_{Kth}(t) = \frac{1}{2}\left[\Delta\varepsilon_{K\sigma^{+}}(t) + \Delta\varepsilon_{K\sigma^{-}}(t)\right]$, and a non-thermal spin population $\Delta\varepsilon_{Knonth}(t) = \frac{1}{2}\left[\Delta\varepsilon_{K\sigma^{+}}(t) - \Delta\varepsilon_{K\sigma^{-}}(t)\right]$. The non-thermal contribution appears as a nearly symmetric peak, with FWHM $\approx$ 1 ps. On the other hand, the thermalized spin contribution has a rise time of 1.6 ps and a longer decay time ($\sim$10 ps).

The authors of this present review studied epitaxial $CoPt_3$ films of thickness 48 nm under much higher pump intensity ($\sim 10\,\text{mJ cm}^{-2}$ at $\lambda = 800$ nm) using the experimental technique described in Section 3.2 [66]. Under these conditions, the magnetic hysteresis of the film disappears for a pump-probe time delay of approximately 500 fs. It was observed that the film can be driven to the paramagnetic phase with a characteristic time of 100 ± 60 fs, comparable with the duration of the pulses used in the experiment (120 fs). The observed dynamics are also only weakly dependent on the polarization state (circular or linear) of the pump beam. This suggests that the dominant mechanism of the spin dynamics does not imply direct transfer of angular momentum from the photon to the spins.

10.4.2.3 Discussion

As reported in the preceding paragraphs, the experimental results obtained by the different groups led to a variety of interpretations of the spin dynamics. In this context, two main questions should be addressed. How accurate is the interpretation of a magneto-optic signal, obtained with a given technique, in terms of spin dynamics? How much is the spin dynamics influenced by the particular sample which is studied? We will now discuss the different results with these two questions in mind.

To attribute the observed magneto-optical signals to a magnetization effect it is important to study the dynamics for different conditions of the applied magnetic field, H. Even though ferromagnetic materials have a spontaneous magnetization, this magnetization is sensitive to extrinsic parameters which lead to different magnetic domains and which might be altered after each pump pulse excitation. It is, therefore, important to restore the initial magnetic state of the sample between each laser pulse. Another advantage is that the symmetry of the pump-probe response can be checked under a reversed applied field, $\pm H$. It is with this in mind that the time-resolved magneto-optic Kerr experiments were performed on Ni and $CoPt_3$ by the authors of this review [7, 66]. In each experiment full magnetic hysteresis $M(H)$ was measured as a function of the pump probe delay, t. For $CoPt_3$, the disappearance of the hysteresis for $t > 500$ fs can be unambiguously related to complete demagnetization of the sample, irrespective of domain structure. Let us emphasize that in these experiments it is the probe beam which is frequency modulated and not the pump as in conventional transmission or reflectivity pump-probe experiments.

The magneto-optic SHG experiments, performed with a reversed applied field, also furnish information about the magnetization dynamics. Different results have, however, been obtained with the same technique but using a different temporal resolution. In a first experiment [8] the magnetization dynamics were found to precede those of the electrons. In a later experiment [55], performed with 40-fs temporal resolution, no delay between $M(t)$ and the electron dynamics was observed. In both experiments the magnetization response to the pump pulse is shorter than that observed in ref. [7]. This discrepancy might be explained by two major differences between the techniques. First, with magneto-optic SHG it is the surface of the sample which is mainly probed, rather than the bulk as in the linear Kerr or Faraday pump-probe geometry. The faster magnetization dynamics reported by Holfeld and co-workers might, then, be related to a different behavior of magnetic states at the surface as compared to the bulk. Second, the interpretation of the SHG experiments in terms of separated electronic and magnetic contributions must to be viewed cautiously. The expressions for $\Delta I^{\pm}(t)$ in Eqs (10a) and (10b) contain mixed electronic and magnetic terms. A first analysis of the SHG experiments [8] assumes two strong approximations: $\chi^{(2)}_{\mathrm{even},0}$ and $\chi^{(2)}_{\mathrm{odd},0}$ are independent of time, and the electronic temperature, $T_{\mathrm{e}}(t)$, has parabolic dependence on the magnetization. The first assumption is certainly not valid for early time delays. The second approximation is not consistent, because substitution of Eq. (11) into Eq. (10b) instead of Eq. (10a) would lead to the opposite interpretation, that the electronic response precedes the magnetic response. Another analysis of the SHG experiments [55] assumes the weaker approximation: $|\chi^{(2)}_{\mathrm{even},0}(t)| \gg |\chi^{(2)}_{\mathrm{odd},0}(t)|$ to separate the electronic and magnetic contributions.

The work of Koopmans and co-workers [52] shows that even though the Kerr rotation and ellipticity have different dynamics in nickel it is difficult to extract independent information about the magnetization and electronic contributions at early time delays. This is mainly because of the contribution of a non-magnetic Kerr rotation. Such a contribution is discussed in Section 4.1 where we have stressed the effects of the coherent pump-probe coupling and the optical orientation, which are not related to the magnetization. These remarks show that to determine the magnetization dynamics, determination of the ferromagnetic hysteresis loops $M(H, t)$ is a key measurement [7].

The photoemission experiments performed by Scholl and co-workers [9] have focused both on the short- and long-term delay behavior of the magnetization. The initial sub-picosecond demagnetization observed is consistent with the Kerr pump-probe results [7]. The authors attribute it to the excitation of Stoner pairs. This explanation is compatible with ultrafast demagnetization of the metal related to the initial hot electron distribution induced by the pump pulse [67]. To evaluate this effect we have considered a d-band model with spin-up N^+ and spin-down N^- distributions similar to nickel. The magnetization dynamics $M(t)$ are then simply assumed to be given by $M(t) \approx [N^+(T_e) - N^-(T_e)]$ where the time-dependent electronic temperature $T_e(t)$ is given by the two-temperature model (Section 2.1). The corresponding dynamics are presented in Fig. 11, which shows that the right order of magnitude for the demagnetization is obtained with this simple Stoner-like model. We also find that when the electronic temperature is increased the maximum demagnetization which is attained is ~60 %. This value is close to that observed in nickel films up to the breaking threshold of the samples [7]. The model does not, however, enable reproduction of the observed delay between the electronic and magnetic responses which, as stressed earlier might depend on the particular electron population which is probed.

Photoemission experiments performed on ultrathin films of nickel [9] also reveal reduction of the spin polarization on the time-scale of 500 ps; this is attributed to phonon-magnon scattering. This mechanism is consistent with the fact that the interaction of the long-wavelength spin waves with the lattice is effective for long temporal delays. Similar observations have been reported recently for antiferromagnetic spin waves in Cr_2O_3 [68]. One should stress that the long time-scale which is necessary to obtain a complete demagnetization of ultrathin Ni films is not observed with the

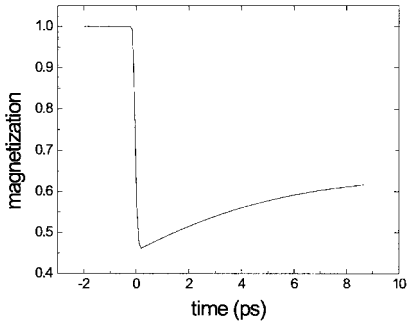

Fig. 11. Magnetization dynamics in a metallic film calculated by taking into account the hot electron distribution induced by the pump pulse. The data are computed considering a d-band metal with spin-up N^+ and spin-down N^- distributions similar to the distributions of nickel. The basic assumption is that $M(t) \approx [N^+(T_e) - N^-(T_e)]$ depends on t only via the time-dependent electronic temperature $T_e(t)$ (obtained using a two-temperature model).

thicker films studied by Beaurepaire et al. and by Hohlfeld and co-workers [7, 55]. This might be because of the low Curie temperature of the ultrathin films or possible heat propagation effects in the metallic Cu substrate supporting the 1.2-nm Ni films.

Finally, let us return to the question of out-of-equilibrium dynamics of the charges and spins. As mentioned earlier, it is now well-accepted that femtosecond pulses excite nascent electron distributions which are not thermalized and that the corresponding thermalization time, because of electron–electron scattering, lasts a few hundred femtoseconds. One might wonder if in this athermal regime non-equilibrium spin populations are also manifested. An attempt to observe this regime has been made with $CoPt_3$ films [10] (Section 4.2). The authors observed a peak in the $\Delta\varepsilon_{\mathrm{Knonth}}(t)$ signal which is interpreted as manifestation of a coherent spin population relaxing with a time constant of ~600 fs. Such a "long" coherence time is, however, in disagreement with recent similar studies of nickel films performed without an applied magnetic field [69]. In these experiments, the coherent contribution lasts during the pulse excitation, i. e. 40 fs. Both results raise the question of the distinction between electronic and spin coherence effects in connection with the discussion of optical orientation described in Section 4.1.

10.5 Conclusion

In conclusion, we have reviewed different experiments showing that ultrafast demagnetization of ferromagnetic metallic thin films can be induced with femtosecond optical pulses. In particular, we have focused on the demagnetization dynamics observed in Ni and $CoPt_3$ thin films [7, 66]. This effect is determined by comparing the time-dependent polarization anisotropy, measured in the magneto-optical Kerr configuration, obtained with the two polarities $\pm H$ of an applied static magnetic field. This configuration enables us to distinguish between true magnetic effects and spurious polarization rotation effects associated with optical orientation of a probe beam induced by the pump. The demagnetization process is complete in $CoPt_3$ thin films and occurs within ~150 fs. More importantly, the demagnetization occurs before heating of the lattice occurs via the electron–phonon interaction. In addition, the electron dynamics, measured without a magnetic field, is faster than the magnetization dynamics.

These experimental results show unambiguously that the two components of the electron gas corresponding to the charges and the spins do not follow the same dynamics. Other experiments, based on the time-resolved non-linear magneto-optical Kerr effect [8, 55] and on spin-resolved photoemission [9], lead to different spin dynamics for nickel. For magnetic second-harmonic generation the authors conclude that there is no significant delay between the electron and spin responses. We believe that this different behavior is because of the surface sensitivity of the technique and/or the difficulty in separating the electronic and magnetic components of the non-linear response. The spin-resolved photoemission results confirm the initial ultrafast demagnetization. Scholl et al. [9] have also studied the long delay magne-

tization dynamics which is interpreted by magnon–phonon interactions. This long delayed spin behavior has not, however, been reproduced by the second-harmonic studies. These discrepancies emphasize the need for further experimental work to clarify the initial magnetization dynamics in ferromagnets.

The understanding of ultrafast demagnetization of ferromagnetic materials sets new challenges, both fundamental and from the standpoint of applications. A first approach to describing the dynamic behavior of the magnetization has been to consider three distinct reservoirs, which exchange energy via coupling terms which at the microscopic level correspond to electron–spin, electron–phonon, and spin-phonon interaction. This phenomenological approach, however, raises the question of the electron–spin interaction. A first possibility is that spin-orbit coupling might be important. This requires systematic study of magnetization in metals with different spin-orbit coupling. A second possibility is that the initial hot electron distribution which is excited by the pump pulse leads to the excitation of Stoner pairs (via additional scattering processes). Both mechanisms require spin-flip processes and, therefore, the total angular momentum is expected to change. One might wonder if such a change is correlated with excitation by light. The demagnetization observed with the pump-probe Kerr configuration on $CoPt_3$, using different pump polarizations (linear or circular), does not reveal such an effect. The question of the conservation of the total momentum in the time-scale when the lattice is still cold thus remains an open question.

Acknowledgments

Many results presented in this review rely on original data obtained at the Institut de Physique et Chimie des Matériaux, and the authors thank all the colleagues who participated to this work In particular we are grateful to A. Daunois for his help in the preparation of the manuscript. Stimulating discussions with G. P. Zhang and W. Hubner are acknowledged.

References

[1] A. H. Morrish, *The Physical Principles of Magnetism,* R. E. Krieger, Huntington, New York, **1980**.
[2] J. Ferré, V. Grolier, P. Meyer, S. Lemerle, A. Maziewski, E. Stefanowicz, S. V. Tarasenko, V. V. Tarasenko, M. Kisielewski, D. Renard, *Phys. Rev. B* **1997**, *55*, 15092–15102.
[3] J. F. Dillon Jr in *Magnetism,* (Eds.: G. T. Rado, H. Suhl), Academic Press, New York **1963**, pp 415–461.
[4] F. Bloch, *Phys. Rev.* **1946, 70**, 460.
[5] L. Landau, L. Lifshitz, *Phys. Z. Sowjetunion* **1935, 8**, 153.
[6] T. L. Gilbert, *Phys. Rev.* **1955, 100**, 1243.
[7] E. Beaurepaire, J.-C. Merle, A. Daunois, J.-Y. Bigot, *Phys. Rev. Lett.* **1996**, *76*, 4250–4253.

[8] J. Hohlfeld, E. Matthias, R. Knorren, K. H. Bennemann, *Phys. Rev. Lett.* **1997**, *78*, 4861–4864.
[9] A. Scholl, L. Baumgarten, R. Jacquemin, W. Eberhardt, *Phys. Rev. Lett.* **1997**, *79*, 5146–5149.
[10] G. Ju, A. Vertikov, A. V. Nurmikko, C. Canady, G. Xiao, R. F. C. Farrow, A. Cebollada, *Phys. Rev. B* **1998**, *57*, R700–R703.
[11] D. Guarisco, R. Burgermeister, C. Stamm, F. Meier, *Appl. Phys. Lett.* **1996**, *68*, 1729–1731.
[12] W. Hübner, G. P. Zhang, *Phys. Rev. B* **1998**, *58*, R5920–R5923.
[13] G. L. Eesley, *Phys. Rev. Lett.* **1983**, *51*, 2140–2143.
[14] E. J. Heilweil, R. M. Hochstrasser, *J. Chem. Phys.* **1985**, *82*, 4762–4770.
[15] H. E. Elsayed-Ali, T. B. Norris, M. A. Pessot, G. A. Mourou, *Phys. Rev. Lett.* **1987**, *58*, 1212–1215.
[16] R. W. Schoenlein, W. Z. Lin, J. G. Fujimoto, G. L. Eesley, *Phys. Rev. Lett.* **1987**, *58*, 1680–1683.
[17] S. D. Brorson, A. Kazeroonian, J. S. Moodera, D. W. Face, T. K. Cheng, E. P. Ippen, M. S. Dresselhaus, G. Dresselhaus, *Phys. Rev. Lett.* **1990**, *64*, 2172–2175.
[18] R. H. M. Groeneveld, R. Sprik, A. Lagendijk, *Phys. Rev. B* **1992**, *45*, 5079–5082.
[19] W. S. Fann, R. Storz, H. W. K. Tom, J. Bokor, *Phys. Rev. Lett.* **1992**, *68*, 2834–2837.
[20] T. Q. Qiu, C. L. Tien, *Int. J. Heat Mass Transfer* **1992**, *35*, 719–725.
[21] C.-K. Sun, F. Vallée, L. H. Acioli, E. P. Ippen, J. G. Fujimoto, *Phys. Rev. B* **1994**, *50*, 15337–15348.
[22] For a recent review on the electron dynamics in metals, see *Chem. Phys.* **2000**, *251*.
[23] M. I. Kaganov, I. M. Lifshits, L. V. Tanatarov, *Sov. Phys. JETP* **1957**, *4*, 173.
[24] S. I. Anisimov, B. L. Kapeliovich, T. L. Perel'man, *Sov. Phys. JETP* **1974**, *39*, 375–377.
[25] P. B. Allen, *Phys. Rev. Lett.* **1987**, *59*, 1460–1463.
[26] C. Suarez, W. E. Bron, T. Juhasz, *Phys. Rev. Lett.* **1995**, *75*, 4536–4539.
[27] V. E. Gusev, O. B. Wright, *Phys. Rev. B* **1998**, *57*, 2878–2888.
[28] D. Pines, P. Nozières, *The Theory of Quantum Liquids*, Benjamin, New York, **1966**.
[29] N. W. Ashcroft, N. D. Mermin, *Solid State Physics*, Saunders College, Philadelphia, **1976**.
[30] J.-Y. Bigot, E. Beaurepaire, A. Daunois, J.-C. Merle, in *Ultrafast Phenomena X*, Springer Series in Chemical Physics, Vol. 62 (Eds.: P. F. Barbara, J. G. Fujimoto, W. H. Knox, W. Zinth), Springer, Berlin, **1996**, pp. 414–415.
[31] V. L. Moruzzi, J. F. Janak, A. R. Williams, *Calculated Electronic Properties of Metals*, Pergamon Press, New York, **1978**.
[32] A. Vaterlaus, T. Beutler, D. Guarisco, M. Lutz, F. Meier, *Phys. Rev. B* **1992**, *46*, 5280–5286.
[33] W. Hübner, K. H. Bennemann, *Phys. Rev. B* **1996**, *53*, 3422–3427.
[34] G. P. Zhang, W. Hübner, E. Beaurepaire, J.-Y. Bigot, Femto- and Picosecond Phenomena, in *Spin Dynamics in Confined Magnetic Structures* (Eds.: B. Hillebrands, K. Ounadjela), Springer, Berlin, to be published.
[35] M. B. Agranat, S. I. Ashitkov, A. B. Granovskii, G. I. Rukman, *Sov. Phys. JETP* **1984**, *59*, 804–806.
[36] A. Y. Elezzabi, M. R. Freeman, M. Johnson, *Phys. Rev. Lett.* **1996**, *77*, 3220–3223.
[37] D. J. Kim, *J. Magn. Magn. Mater.* **1993**, *125*, L257–L262.
[38] W. Hübner, G. P. Zhang, *J. Magn. Magn. Mater.* **1998**, *189*, 101–105.
[39] Some reviews can be found in: Z. Qiu, S. D. Bader, *MRS Bull.* Oct. **1995**, pp 34–37.
[40] W. Voigt, *Magneto- und Electro-Optik*, Teubner, Leipzig, **1908**.
[41] G. Metzger, P. Pluvinage, R. Torguet, *Ann. Phys.* (*Paris*) **1965**, *10*, 5–12.
[42] J. Zak, E. R. Moog, C. Liu, S. D. Bader, *Phys. Rev. B* **1991**, *43*, 6423–6429.
[43] H. S. Bennett, E. A. Stern, *Phys. Rev.* **1965**, *137*, A448–A461.

[44] P. N. Argyres, *Phys. Rev.* **1955**, *97*, 334–345.
[45] J. Reif, C. Rau, E. Matthias, *Phys. Rev. Lett.* **1993**, *71*, 1931–1934.
[46] B. Koopmans, A. M. Janner, H. A. Wierenga, T. Rasing, G. A. Sawatzky, F. van der Woude, *Appl. Phys. A* **1995**, *60*, 103–111.
[47] W. Hübner, K. H. Bennemann, *Phys. Rev. B* **1995**, *52*, 13411–13418.
[48] T. Rasing, *Appl. Phys. B* **1999**, *68*, 477–484.
[49] Q. Y. Jin, H. Regensburger, R. Vollmer, J. Kirschner, *Phys. Rev. Lett.* **1998**, *80*, 4056–4059.
[50] V. V. Pavlov, G. Tessier, C. Malouin, P. Georges, A. Brun, D. Renard, P. Meyer, J. Ferré, P. Beauvillain, *Appl. Phys. Lett.* **1999**, *75*, 190–192.
[51] R. Rosei, D. W. Lynch, *Phys. Rev. B* **1972**, *5*, 3883–3894.
[52] B. Koopmans, M. van Kampen, J. T. Kohlhepp, W. J. M. de Jonge, 44th Conference on Magnetism and Magnetic Materials, San Jose, USA, November 15–18, 1999, *J. Appl. Phys.* **2000**, *87*, 5070–5072.
[53] M. Maret, M.-C. Cadeville, R. Poinsot, A. Herr, E. Beaurepaire, C. Monier, *J. Magn. Magn. Mater*. **1997**, *166*, 45–52
[54] U. Conrad, J. Güdde, V. Jähnke, E. Matthias, *Appl. Phys. B* **1999**, *68*, 511–517.
[55] a) J. Hohlfeld, J. Güdde, U. Conrad, O. Dühr, G. Korn, E. Matthias, *Appl. Phys. B* **1999**, *68*, 505–510; b) J. Güdde, U. Conrad, V. Jähnke, J. Hohlfeld, E. Matthias, *Phys. Rev. B* **1999**, *59*, R6608–R6611.
[56] J. Kessler, *Polarized Electrons*, 2nd edn., Springer, Berlin, **1985**.
[57] M. Campagna, D. T. Pierce, F. Meier, K. Sattler, H. C. Siegmann, in *Advances in Electronics and Electron Physics*, *Vol. 41*, Academic Press, London, **1976**, pp. 113–165.
[58] M. Aeschlimann, M. Bauer, S. Pawlik, W. Weber, R. Burgermeister, D. Oberli, H. C. Siegmann, *Phys. Rev. Lett.* **1997**, *79*, 5158–5161.
[59] C. V. Shank, D. H. Auston, *Phys. Rev. Lett.* **1975, 34**, 479–481.
[60] C. H. Brito-Cruz, J.-P. Gordon, P. C. Becker, R. L. Fork, C. V. Shank, *IEEE J. Quantum Electron.* **1988, 24**, 261–266.
[61] J.-Y. Bigot, V. Halté, J.-C. Merle, A. Daunois, *Chem. Phys.* **2000**, *251*, 181–203.
[62] N. Del Fatti, R. Bouffanais, F. Vallée, C. Flytzanis, *Phys. Rev. Lett.* **1998**, *81*, 922–925.
[63] Y. R. Shen, *The Principles of Nonlinear Optics*, John Wiley & Sons, New York, **1984**.
[64] Yu. P. Svirko, N. I. Zheludev, *Polarization of Light in Nonlinear Optics*, John Wiley & Sons, Chichester, **1998**.
[65] C. J. Lin, G. L. Gorman, *Appl. Phys. Lett.* **1992**, *61*, 1600–1602.
[66] E. Beaurepaire, M. Maret, V. Halté, J.-C. Merle, A. Daunois, J.-Y. Bigot, *Phys. Rev. B* **1998**, *58*, 12134–12137.
[67] K. H. Bennemann, *Rev. Mex. Fis.* **1998**, *44*, 533–539.
[68] J. S. Dodge, A. B. Schumacher, J.-Y. Bigot, D. S. Chemla, N. Ingle, M. R. Beasley, *Phys. Rev. Lett.* **1999**, *83*, 4650–4653.
[69] P. J. Bennett, V. Albanis, Yu. P. Svirko, N. I. Zheludev, *Opt. Lett.* **1999**, *24*, 1373–1375.
[70] M. R. Freeman, *J. Appl. Phys.* **1994**, *75*, 6194–6198.
[71] J. J. Baumberg, D. D. Awschalom, N. Samarth, *J. Appl. Phys.* **1994**, *75*, 6199–6204.

Magnetism: Molecules to Materials III. Edited by J.S. Miller and M. Drillon

ISBNs: 3-527-30302-2 (Hardback); 3-527-60014-0 (Electronic)

Subject Index